

Gran Sasso Science Institute  
**ASTROPARTICLE PHYSICS**  
**DOCTORAL PROGRAMME**  
Cycle XXIX - AY 2013/2016

# Precision Measurement of Solar $v$ Fluxes with Borexino and Prospects for $0\nu\beta\beta$ Search with $^{136}\text{Xe}$ -loaded Liquid Scintillators

PHD CANDIDATE  
**Simone Marcocci**

PhD Thesis submitted  
October 30, 2016

## ADVISORS

**Aldo Ianni**  
Laboratori Nazionali del Gran Sasso  
**Marco Pallavicini**  
Università e Sezione INFN di Genova

## TUTOR

**Gemma Testera**  
Sezione INFN di Genova



*Science is the belief in the ignorance of experts.*

*Richard P. Feynman*



## Abstract

After its successful Phase-I (2007-2011), Borexino has further improved its unprecedentedly low background and has entered the solar neutrino precision measurement era. Thanks to the developments in the data analysis and to a better understanding of the detector response, a global analysis of Borexino Phase-II data (2011-2016) was carried out, yielding to the simultaneous determination of  ${}^7\text{Be}$ , pep and pp neutrino fluxes. This PhD thesis describes the achievements (mainly regarding an improved simulation of the experiment) which made these accurate measurements possible. Furthermore, a more long term future for a Borexino-like experiment hunting for neutrinoless double beta decay ( $0\nu\beta\beta$ ) is discussed. The current status of uncertainties and experimental/theoretical expectations on  $0\nu\beta\beta$  is summarized, and the possible sensitivity of a large, next generation  ${}^{136}\text{Xe}$ -loaded liquid scintillator detector is assessed and compared to present and near future experiments. The results of the experimental investigations of optical properties of liquid scintillators loaded with xenon at high pressure are also presented, in view of possible future applications.



# Contents

<b>Introduction</b>	<b>vii</b>
<b>1 Solar neutrinos and oscillations</b>	<b>1</b>
1.1 Introduction . . . . .	1
1.2 Neutrino sources . . . . .	2
1.3 Neutrino mixing and oscillations . . . . .	4
1.3.1 Neutrino oscillations in vacuum . . . . .	6
1.4 Oscillation in matter: the MSW effect . . . . .	9
1.4.1 Two-neutrino matter effects . . . . .	10
1.4.2 MSW resonance . . . . .	11
1.5 The Standard Solar Model . . . . .	12
1.5.1 Solar abundances and helioseismology . . . . .	13
1.6 Production of solar neutrinos . . . . .	15
1.6.1 The pp-chain . . . . .	16
1.6.2 The CNO cycle . . . . .	18
1.6.3 Solar fluxes predictions from the Standard Solar Models . . . . .	20
1.7 The solar metallicity problem . . . . .	20
1.8 The propagation of solar neutrinos . . . . .	22
1.9 Experimental observations of solar neutrinos . . . . .	24
1.10 Outlook on solar neutrino measurements . . . . .	28
<b>2 Neutrinoless double beta decay experimental status and Borexino</b>	<b>29</b>
2.1 Introduction . . . . .	29
2.2 Majorana neutrinos . . . . .	31
2.2.1 Leptogenesis and right-handed neutrinos . . . . .	32
2.2.2 Neutrino nature and cosmic neutrino background . . . . .	32
2.3 Particle physics mechanisms for $0\nu\beta\beta$ . . . . .	33
2.4 Present knowledge on neutrino masses . . . . .	34
2.4.1 The parameter $m_{\beta\beta}$ . . . . .	34
2.4.2 Oscillations . . . . .	35
2.4.3 Cosmology and neutrino masses . . . . .	37
2.4.4 Other non-oscillation data . . . . .	38
2.5 The role of nuclear physics . . . . .	39

---

2.5.1	Recent developments on the phase space factor calculations . . . . .	40
2.5.2	Models for the NMEs . . . . .	40
2.5.3	Theoretical uncertainties . . . . .	42
2.6	Experimental search for $0\nu\beta\beta$ . . . . .	43
2.6.1	Sensitivity estimation . . . . .	45
2.6.2	Experimental techniques and requirements . . . . .	47
2.6.3	Experiments: a brief review . . . . .	47
2.6.4	Present sensitivity on $m_{\beta\beta}$ . . . . .	48
2.6.5	Future (planned) experiments . . . . .	49
2.7	Interplay with cosmology . . . . .	50
2.8	Search for Majorana neutrinos with Borexino . . . . .	54
2.8.1	The new concept: increasing the pressure . . . . .	55
2.8.2	Pros and cons of the technique . . . . .	56
2.8.3	Xenon’s dissolution in the liquid scintillator . . . . .	58
2.8.4	Borexino’s expected sensitivity and comparison with other experiments . . . . .	60
2.9	Conclusions and outlook . . . . .	63
<b>3</b>	<b>Measurements of optical properties of scintillators doped with xenon</b>	<b>65</b>
3.1	Description of the setup . . . . .	65
3.1.1	The large chamber . . . . .	66
3.1.2	The small chamber . . . . .	69
3.1.3	Hydraulics system . . . . .	70
3.1.4	Sensors . . . . .	71
3.2	Electronics . . . . .	73
3.3	Gas dissolution and mass control . . . . .	73
3.4	Measurements with the large chamber . . . . .	75
3.4.1	Measurements as a function of xenon concentration . . . . .	77
3.5	Small chamber measurement campaign . . . . .	79
3.5.1	Light yield variation vs xenon concentration in Borexino’s scintillator	81
3.6	Light yield measurements as a function of the PPO concentration . . . . .	86
3.7	Borexino’s scintillator time response . . . . .	89
3.7.1	The time response of the detector . . . . .	89
3.7.2	Time response of nitrogen saturated liquid scintillator as a function of PPO concentration . . . . .	91
3.7.3	Time response as a function of the xenon concentration . . . . .	92
3.7.4	Timing and spectral response . . . . .	94
3.8	Characterization of the LAB+PPO scintillator doped with xenon at high pressure . . . . .	97
3.8.1	Xenon solubility in LAB . . . . .	97
3.8.2	LAB light yield variation as a function of the xenon concentration . . . . .	98
3.8.3	LAB time response as a function of the xenon concentration . . . . .	99
3.9	Conclusions and outlook . . . . .	100

---

<b>4 The Borexino experiment</b>	<b>101</b>
4.1 Detection methods in Borexino . . . . .	101
4.2 Description of the setup . . . . .	103
4.3 Purity levels in Borexino and major contaminants . . . . .	106
4.4 The data acquisition system . . . . .	110
4.5 Event structure and energy estimators . . . . .	112
4.6 Position reconstruction . . . . .	114
4.7 $\alpha/\beta$ discrimination . . . . .	115
4.7.1 The Gatti parameter . . . . .	117
4.7.2 MLP discrimination variable . . . . .	119
4.8 $\beta^+/\beta^-$ discrimination . . . . .	120
4.9 Thermal stability, $^{210}\text{Po}$ evolution and $^{210}\text{Bi}$ constraint . . . . .	122
4.9.1 $^{210}\text{Po}$ time and space evolution . . . . .	124
4.9.2 Borexino thermal insulation . . . . .	124
4.9.3 $^{210}\text{Po}$ distribution in Borexino . . . . .	127
4.10 Borexino Phase-I results . . . . .	128
4.10.1 $^7\text{Be} \nu$ . . . . .	128
4.10.2 pep $\nu$ and CNO $\nu$ . . . . .	129
4.10.3 pp $\nu$ . . . . .	129
4.10.4 $^8\text{B} \nu$ . . . . .	130
4.10.5 Geo-neutrinos . . . . .	130
4.10.6 Other Borexino measurements . . . . .	130
4.11 Outlook and Phase-II goals . . . . .	130
4.12 Borexino (near) future: the SOX project . . . . .	131
<b>5 The Borexino full Monte Carlo simulation</b>	<b>135</b>
5.1 Simulation principles and structure . . . . .	136
5.2 Detailed geometry simulation . . . . .	137
5.2.1 Outer Detector geometry . . . . .	138
5.2.2 Inner Detector Geometry . . . . .	138
5.3 Energy loss and light generation . . . . .	140
5.3.1 Generation of scintillation light . . . . .	141
5.3.2 Generation of Čerenkov light . . . . .	145
5.3.3 Algorithm optimization . . . . .	146
5.4 Light tracking and propagation . . . . .	147
5.4.1 Effective Quantum Efficiencies . . . . .	149
5.5 Refractive index dependence upon the temperature . . . . .	150
5.5.1 Simple model for the effect of $n(z)$ on the reconstruction . . . . .	151
5.5.2 Density effect and $dn/d\lambda$ . . . . .	152
5.5.3 The experimental setup and the measurements . . . . .	153
5.5.4 Outlook . . . . .	155
5.6 Event generators . . . . .	155
5.6.1 Solar neutrino generation . . . . .	156

---

5.6.2	“Special” radioactive decays . . . . .	156
5.6.3	Positron generator . . . . .	157
5.6.4	Anti-neutrino generator . . . . .	157
5.6.5	Radioactive source generator . . . . .	158
5.7	Electronics simulation . . . . .	158
5.7.1	<code>bxelec</code> operation and features . . . . .	158
5.8	Tuning of the MC simulation . . . . .	160
5.8.1	The calibration campaigns . . . . .	162
5.8.2	Non uniformity of the energy response within the inner vessel . . . . .	163
5.8.3	Time distribution of the collected light . . . . .	165
5.8.4	The energy scale . . . . .	167
5.8.5	Outlook . . . . .	170
5.9	$^{210}\text{Po}$ simulation . . . . .	170
5.10	External background simulation . . . . .	172
5.10.1	Biasing strategy: importance sampling . . . . .	173
5.10.2	Steps of the simulation . . . . .	175
5.10.3	Further optimization strategies . . . . .	177
5.10.4	Validation of the procedure through comparisons with calibrations	179
5.10.5	Source-induced background simulation for the SOX experiment . .	181
5.11	Monte Carlo pileup production . . . . .	182
5.11.1	Data-driven methods for pileup spectra production . . . . .	183
5.11.2	Introduction on MC pileup production . . . . .	184
5.11.3	Pileup spectral composition . . . . .	185
5.11.4	Validation of the MC pileup with the synthetic pileup . . . . .	189
5.11.5	Pileup constraint in the fit . . . . .	191
5.12	Outlook . . . . .	191
<b>6</b>	<b>Precision measurement of solar neutrino fluxes with Borexino</b>	<b>193</b>
6.1	Data selection . . . . .	193
6.2	Event selection . . . . .	194
6.2.1	Effects of the cuts . . . . .	195
6.2.2	Fiducial Volume cut . . . . .	196
6.3	Three-Fold Coincidence veto . . . . .	199
6.4	Choice of the spectrum binning . . . . .	201
6.5	Effect of the normalization: “PDF masking” . . . . .	202
6.6	Radial distribution of events and $\beta^+/\beta^-$ pulse shape discrimination . . . . .	205
6.6.1	Radial versus energy distribution of events . . . . .	205
6.6.2	$\beta^+/\beta^-$ pulse shape discrimination: the likelihood of the position reconstruction . . . . .	205
6.7	Fitting procedure . . . . .	209
6.7.1	MC PDF production . . . . .	211
6.8	Validation of the fit procedure . . . . .	212
6.9	Goodness of fit evaluation . . . . .	217

---

6.10	TFC parameter optimization	217
6.11	The spectral fit	218
6.12	Systematic uncertainties	225
6.12.1	Uncertainty on the exposure	226
6.12.2	Fit configuration	226
6.12.3	Energy scale	228
6.12.4	Multivariate fit options	229
6.12.5	$^{85}\text{Kr}$ and $^{210}\text{Bi}$ spectral shapes	229
6.12.6	$^{85}\text{Kr}$ external constraint	229
6.12.7	Oscillation parameters and $^8\text{B}$ $\nu$ rate	230
6.12.8	Systematics budget for $^7\text{Be}$ $\nu$	230
6.12.9	Systematics budget for pp $\nu$	231
6.12.10	Systematics budget for pep $\nu$	231
6.13	Likelihood profile for pep $\nu$ and CNO $\nu$ limit	232
6.14	Results	235
6.15	Outlook	236
7	Conclusions	239
A	Coherence and decoherence in neutrino oscillations	241
B	Parameters in the Monte Carlo simulation after the tuning	243
C	Fit results with $npmts$ , $npmts\_dt1$ and $npmts\_dt2$ variables	245
	Bibliography	251
	Acknowledgments	267



# Introduction

Neutrinos are unique in the particle world. They are neutral particles with very little mass and their interaction cross section with standard matter is tiny, since they are coupled in practice only to the weak interaction force. Despite being so elusive, neutrinos pervade the Universe and are quite abundant, since they can be produced in many processes, such as radioactive decays or nuclear reactions powering the stars.

The Sun is the most intense neutrino source close to the Earth. Neutrinos are produced in the Sun as a consequence of the nuclear reactions which take place in its core. Therefore, solar neutrinos carry information about the Sun interior: they reach us (almost) without interacting from the production to the detection point. The only delay is of  $\sim 8$  minutes and is simply due to the time of flight. This is much different with respect to what happens to photons, for which it takes  $\sim 100000$  years to reach the Earth after they are produced in the Sun's core. As a consequence, studying the Sun through neutrinos allows to acquire information which is not accessible in the photon channel.

Solar neutrinos offer unique chances also for studying neutrino particle physics through the observation of solar neutrino oscillations. Actually, before oscillations were discovered, several experiments observing solar neutrinos detected a deficit of electron solar neutrinos with respect to the theoretical predictions. This was historically referred to as “The Solar Neutrino Problem”. Subsequent investigations found out that this phenomenon was explained by the existence of neutrino oscillations. Thus, solar neutrinos became pivotal for the study of oscillations and for the measurement of the matter effect in solar neutrino oscillations. Experimental observations are consistent with the Mikheyev-Smirnov-Wolfenstein Large-Mixing-Angle (MSW-LMA) model, which describes the role of matter in neutrino oscillations. The situation of solar neutrinos is particularly fortunate, since the various reactions taking place in the Sun produce neutrinos in a window from a few hundreds of keV to  $\sim 20$  MeV. This lies in the same energy range where the transition from the vacuum to matter dominated oscillations is predicted by the MSW-LMA model. Therefore studying solar neutrinos also allows to assess the role of matter in neutrino oscillations.

The Sun's energy is produced through the fusion of protons into helium nuclei. This happens through a series of reactions called “pp chain” in  $\sim 99\%$  of the cases. The remaining part of the energy is produced through a subdominant ( $\sim 1\%$ ) set of reactions, the “CNO cycle”. The ratio between pp chain and CNO cycle contributions depend on the star's mass. As anticipated above, neutrinos are the only direct mean of investigation of

the reactions taking place in the Sun core. Neutrinos produced by pp chain reactions were observed already, while neutrinos produced in the CNO cycle have not been detected yet. Besides its importance in principle, since it is supposed to be the main energy production mechanism in massive stars, the CNO cycle allows to test the Sun internal composition, since the predicted values of CNO neutrino fluxes strongly depend on the solar modeling. Different observations of the Sun not based on neutrinos led to contradictory results and the “low” and “high” metallicity models for the solar composition cannot be disentangled without the measurement of CNO neutrinos. For these reasons, the direct detection of CNO neutrinos would represent a major milestone in stellar astrophysics.

The Borexino experiment at Laboratorio Nazionali del Gran Sasso was designed to study low energy solar neutrinos. The key feature of Borexino is the unprecedently low background level, which allows to measure count rates as low as a few counts per day per 100 ton of liquid scintillator. Borexino started taking data in 2007 and after its successful Phase-I (which lasted until 2011), it has further improved its ultra low background and has entered the solar neutrino precision measurement era. This PhD thesis presents the developments in the data analysis which led to a better understanding of the detector response, particularly referring to the improvements achieved in the full Monte Carlo simulation of the experiment. This allowed to perform, for the first time, a global analysis of Borexino Phase-II data (2011-2016), yielding to the simultaneous determination of  ${}^7\text{Be}$ , pep and pp neutrino fluxes. This is quite an important result, since it demonstrates that the Borexino spectrum and response are understood in the energy range  $\sim 200\text{ keV} \div 2.6\text{ MeV}$ . Furthermore, it strengthens the previous results, which were obtained with different analyses. The Borexino Collaboration has worked very hard for the goal of the CNO neutrino determination since the very first early stages of Phase-II. However, this goal is tremendously challenging and by the time this PhD thesis had to be completed, no final result was available on this topic. This effort is still ongoing, and improvements with respect to the past findings will be published in the next months.

As early as the 1990’s, R. Raghavan suggested that after its solar neutrino phase Borexino could be turned into a very powerful neutrinoless double beta decay ( $0\nu\beta\beta$ ) experiment.  $0\nu\beta\beta$  is a hypothetical decay forbidden in the Standard Model of particle physics, which would consist in a nuclear decay with the emission of only two electrons. Its existence would prove lepton number violation and would be extremely precious for studying the origin of neutrino masses. In fact,  $0\nu\beta\beta$  can occur only if neutrinos are endowed with Majorana mass, rather than Dirac. Therefore, studying  $0\nu\beta\beta$  is very interesting, also considering that to date this is the only known practical way which allows to investigate the origin of neutrino masses. The sensitivity level reached by  $0\nu\beta\beta$  experiments is very high, but still it is not sufficient to hope to catch a  $0\nu\beta\beta$  signal in the near future.<sup>1</sup> As forecasted more than 20 years ago, Borexino would have the potential to look for  $0\nu\beta\beta$  very proficiently. In particular, it would be possible to load Borexino’s liquid scintillator with  ${}^{136}\text{Xe}$  at high pressure and reach a sensitivity better than that of current experiments by at least an order of magnitude. The potential for

---

<sup>1</sup>This is true in the standard hypothesis that the exchange of light Majorana neutrinos dominates the transition.

Borexino as a future  $0\nu\beta\beta$  hunter is assessed in this PhD thesis. In parallel, an R&D setup for the characterization of liquid scintillators loaded with xenon at high pressure was developed, put in operation and used for characterizing Borexino's liquid scintillator and the LAB+PPO mixture.<sup>2</sup> Results on this experimental effort are presented in the context of assessing the expected sensitivity for Borexino for the search of  $0\nu\beta\beta$ .

## Experimental activity

The PhD work presented in this thesis was carried out mainly at the Laboratori Nazionali del Gran Sasso (for the Borexino data analysis) and at the University of Genova (for the R&D activities) in the context of the Borexino Collaboration. I also spent a quite significant amount of time at the Gran Sasso Science Institute, studying the phenomenology of neutrinoless double beta decay.

I played a leading role in the improvement of the Borexino Monte Carlo simulation, in order to match adequate precision levels for the Phase-II analysis. The simulation is coded in C++ and it is based on the Geant4 framework. The innovative advancements for which I contributed the most include the development of a novel algorithm for the external background simulation and the Monte Carlo reproduction of the pileup spectrum. The external background in Borexino is mostly due to gammas originating in the photomultipliers or in the stainless steel sphere which supports the detector. These gammas can reach the innermost fiducial volume, after traveling some meters in the liquid scintillator. Because of the thick shielding, a brute force approach in the simulation is impossible. On the contrary, by exploiting variance reduction techniques, the new algorithm is able to simulate these events very efficiently. Regarding the low energy part of the Borexino spectrum, an important feature to be understood for the pp neutrino measurement is the event pileup. In the past, it was addressed by using real data artificially and randomly overlapped. A more careful data analysis and simulation allowed to reproduce the pileup spectral shape a priori with the Monte Carlo. A paper describing these achievements is in preparation.

In the framework of the Borexino analysis working group, I was involved in the data selection (cuts and efficiencies) and spectral fit activities. The Borexino energy spectrum is fitted with many background and neutrino components and it is performed with a multivariate approach, i.e. together with the spectral information, the radial distribution of events and the shape of a pulse shape discrimination parameter are fitted simultaneously. The radial distribution is important for disentangling the contribution of the external background, while the pulse shape discrimination is developed in order to separate electrons from positrons, and thus remove the residual cosmogenic beta plus decays.

I also worked on the development, realization and commissioning of an experimental apparatus for the measurement of optical properties of liquid scintillators doped with xenon at high pressure. The goal was to test the possibility of dissolving xenon at

---

<sup>2</sup>This scintillator cocktail will be used in the near future in upcoming large scintillator detectors such as SNO+ and JUNO.

high pressure in Borexino’s liquid scintillator in order to look for  $0\nu\beta\beta$  with very high sensitivity. I followed all the steps of the realization of the setup, starting from the project, construction and assembling. The system allowed to carry out many measurements (light yield, attenuation length, time response, test of different scintillator cocktails) which are discussed in this PhD thesis.

The results on the study of phenomenology, experimental status and theoretical uncertainties on  $0\nu\beta\beta$  are summarized in Refs. [1, 2, 3]. The main motivation for these works was the need of assessing the experimental expectations for the next decade and the theoretical uncertainties in the phenomenon description (the nuclear physics explaining the decay, and the long standing issue of the “quenching” of the axial vector coupling constant in the nuclear medium). Furthermore, the recent developments in cosmological survey sensitivity could provide tight constraints on the sum of the three active neutrino masses. This in turn reflects on tight bounds on  $0\nu\beta\beta$ , and in small indications for the normal mass ordering, as it is also weakly suggested from oscillation experiments. The net output of these investigations is the requirement of ton or multi-ton scale experiments in order to hope to catch a  $0\nu\beta\beta$  signal in the next decades. On the other hand, a discovery of double beta decay with a much smaller exposure than this could indicate very exciting scenarios, such as mechanisms mediating the decay other than the light neutrino exchange, an absent quenching of the axial vector coupling constant or the wrongness of current standard models in cosmology.

## Thesis layout

The thesis is structured as follows. Chapter 1 introduces neutrinos, their main sources and neutrino oscillations. The MSW effect is discussed, together with an introduction to Standard Solar Models and to solar neutrinos production, propagation and detection. Chapter 2 discusses the current phenomenology and experimental status of  $0\nu\beta\beta$ , together with the expected sensitivity for a new generation experiment based on the dissolution of gaseous  $^{136}\text{Xe}$  in Borexino. Chapter 3 describes the R&D developed at the University of Genova for the characterization of liquid scintillators doped with xenon at high pressure and reports the results of the measurements carried out. Chapter 4 illustrates the main features and performances of the Borexino detector. Previous achievements of the experiment are also mentioned. Chapter 5 details the Borexino Monte Carlo simulation structure and reports about the recent improvements. Particular emphasis is put on the tuning procedure of the algorithm, its validation on calibration data, the novel approach for the external background simulation and on the Monte Carlo pileup modeling. Chapter 6 describes the data analysis procedure that yields to the Borexino spectral fit which allows to determine solar neutrino fluxes. Chapter 7 summarizes the conclusions.

# Chapter 1

## Solar neutrinos and oscillations

In this chapter, the basic phenomenology of solar neutrinos and neutrino oscillations is introduced. In particular, some attention is devoted to highlighting the theoretical and experimental achievements in the understanding of neutrino production in the Sun and of neutrino oscillations. The open scientific questions which should be addressed in the near future are also discussed.

The chapter is structured as follows. Section 1.1 introduces neutrinos, Sec. 1.2 discusses the main neutrino production mechanisms, Sec. 1.3 introduces the theory of neutrino oscillations, Sec. 1.4 presents matter effects, Sec. 1.5 describes the framework of Standard Solar Models, Sec. 1.6 discusses the production of solar neutrinos, Sec. 1.7 mentions the solar metallicity problem, Sec. 1.8 is about the propagation of solar neutrinos towards the Earth, Sec. 1.9 shows some historical results on solar neutrino measurements and in Sec. 1.10 possible future developments are considered.

### 1.1 Introduction

In 1914, Chadwick established experimentally that the electrons emitted in radioactive  $\beta$  decays have a continuous spectrum, unlike what happens in  $\alpha$  and  $\gamma$  decays. In December 1930, Pauli proposed a “desperate way out” to save energy conservation, postulating the existence of a new neutral particle, named “neutron”, with a mass “of the same order of magnitude as the electron mass” and maybe a “penetrating power equal or ten times bigger than a  $\gamma$  ray” [4].

In 1934, Fermi formulated the first effective theory able of predicting neutrino couplings in terms of  $\beta$ -decay lifetimes. The new particle was renamed “neutrino”, after Chadwick’s discovery in 1932 of what now we call “neutron”. Anti-neutrinos were finally directly observed by Cowan and Reines in 1956 [5, 6].

The neutrinos which take part in the standard weak interactions are of three different types or flavors [7]:  $\nu_e$  and  $\bar{\nu}_e$  (electron),  $\nu_\mu$  and  $\bar{\nu}_\mu$  (muon),  $\nu_\tau$  and  $\bar{\nu}_\tau$  (tau). These are the neutrino flavor eigenstates produced in weak interactions, since the  $\nu_e$  ( $\nu_\mu$ ,  $\nu_\tau$ ) neutrino is produced together with  $e^+$  ( $\mu^+$ ,  $\tau^+$ ) or can produce an  $e^-$  ( $\mu^-$ ,  $\tau^-$ ). The same holds for anti-neutrinos and the respective charged leptons. Already in 1958, neutrinos were

found to be mostly left-handed [8], this meaning that only the neutrino left-handed component is coupled to the weak force. In general, for a massless particle, the concepts of chirality (property of the field with respect to the operators  $P_{R/L} = (1 \pm \gamma_5)/2$ ) and helicity (projection of the spin along the direction of motion) coincide. In the case of a massless spin-1/2 particle, such as neutrinos were believed to be before the discovery of oscillations, the left-handed neutrino produced in a weak interaction process would have a fixed (-1/2) helicity. If the particle has a non-zero mass, the left-handed state is a superposition of both the helicity eigenstates, with the (+1/2) helicity component entering the superposition with a coefficient  $\propto m/E$ , where  $m$  is the particle mass and  $E$  its energy. In the practical case of neutrinos,  $m/E \ll 1$ , thus the (+1/2) helicity component is strongly suppressed.

At present, there is no evidence for the existence of right-handed (left-handed) relativistic neutrinos (anti-neutrinos) [7]. If they exist, their interaction with matter has to be much weaker than the interaction of the left-handed components. In the Standard Model (SM) of particle physics, the right-handed component is described as a singlet of the  $SU(2)_L$  symmetry group, and thus it has no coupling with the weak bosons. If right-handed neutrinos exist, they might be important for explaining e.g. the generation of neutrino masses and mixing and the generation of the matter/anti-matter asymmetry in the Universe [7].

## 1.2 Neutrino sources

Neutrinos are unique particles for many reasons. They are several orders of magnitude lighter than all the other fermions, and in fact no direct measurement has found evidence for a non-zero neutrino mass yet. Neutrinos are also neutral, do not feel strong interactions, and interact only weakly. The typical orders of magnitude of the cross sections of  $\sim 1$  MeV neutrinos with electrons are  $10^{-44} \div 10^{-45} \text{ cm}^2$ . This corresponds to a probability  $\sim 10^{-18}$  to interact in a solid detector within the thickness of one meter, or to a probability  $\sim 10^{-11}$  to interact inside the Earth traveling along one of its diameters.

Neutrinos are therefore “elusive” particles, but they are very abundant in the universe and are produced in several different physical processes. A sketch of the energy spectrum of neutrinos at the Earth’s surface is shown in Fig. 1.1.

When the universe was sufficiently hot, neutrinos were kept in equilibrium with electrons and positrons through reactions such as  $e^+ + e^- \rightarrow \nu_\alpha + \bar{\nu}_\alpha$  [10]. Neutrinos got out of the thermal equilibrium when the temperature dropped below  $T \sim 10^{10}$  K and they essentially decoupled from the rest of the universe, starting to cool down with the universe expansion reaching the current value of  $T_\nu \sim 1.95$  K. The neutrino temperature is cooler than the photon one ( $T_\gamma \sim 2.7$  K), because the photon component was heated by the annihilation of the electron and positron components of the “cosmic soup” that happened at a temperature  $T_\gamma \sim m_e$ .

In the Sun innermost core, various nuclear reactions produce a huge amount of electron neutrinos, with energies  $0.1 \div 20$  MeV. The order of magnitude of the flux of these neutrinos at the Earth’s surface is around  $60 \times 10^9 \text{ cm}^{-2}\text{s}^{-1}$ . Since the measurement

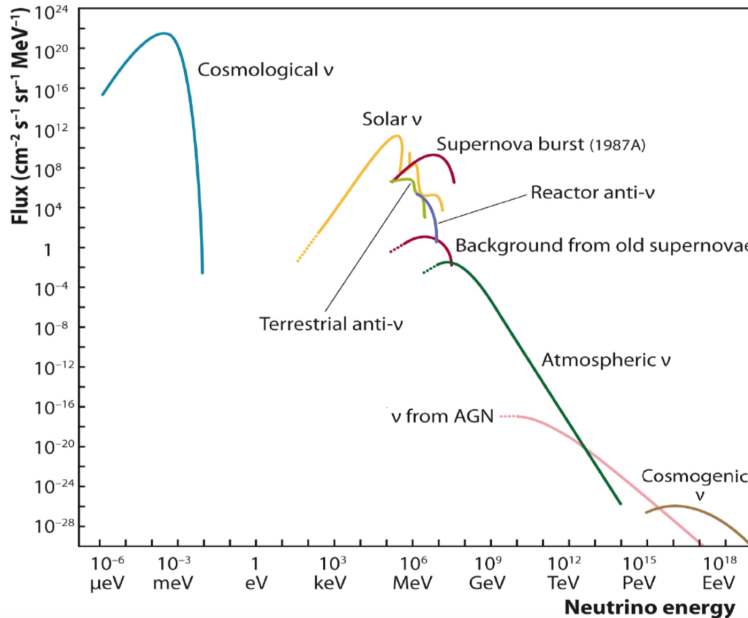


**Fig. 1.1:** Measured or expected fluxes of natural and reactor neutrinos, spanning a large amount of orders of magnitude in energy. The energy range from hundreds of keV to several GeV is the domain of underground detectors. The region from tens of GeV to about 100 PeV is addressed by Čerenkov light detectors underwater and in ice [9].

of solar neutrino fluxes is one of the main aims of this PhD thesis, more details can be found in Sec. 1.6.

An impressive number of neutrinos ( $\sim 10^{58}$ ) is emitted following the gravitational collapse of a massive star that triggers a supernova explosion. The energy release in the explosion is around  $\sim 10^{51} \div 10^{53}$  ergs with a sudden burst of neutrinos of all flavors of  $\sim 10$  s duration. The Sun and the closest supernova in the last three centuries (SN1987A in the Large Magellanic Cloud) have been the first two astrophysical objects to be “seen” in neutrinos. The neutrino burst from SN1987A was observed in the Kamiokande II detector, and the signal consisted of 11 electron neutrino events with energies from 7.5 to 36 MeV [11]. The relic flux of neutrinos emitted by the explosion of supernovae in all the universe history should correspond to several tens per squared centimeter per second. However, it has not been observed yet [12].

Geo-neutrinos originate from the radioactive  $\beta$  decays of  ${}^{40}K$  and of several nuclides in the decay chains of the long-lived radioactive isotopes  ${}^{238}U$  and  ${}^{232}Th$  naturally present on Earth. These electron anti-neutrinos have energies of the order of a few MeV and carry information which is not accessible to geological investigations.  $\bar{\nu}_e$ ’s from uranium and thorium can be detected through inverse beta decay, while anti-neutrinos from potassium cannot, because of their low energy, although they are presumed to be the most abundant geo-neutrinos. More details on geo-neutrinos and on Borexino’s contribution on their measurement are discussed in Sec. 4.10.5.

The Earth receives an approximately isotropic and constant flux of cosmic rays (with an intensity of  $\sim 0.5$  particles  $\text{cm}^{-2}\text{s}^{-1}\text{sr}^{-1}$ ). Interactions of the primary cosmic ray protons with nitrogen nuclei in the atmosphere generate a number of secondary particles, including charged pions and kaons, that in turn produce neutrinos in decays such as:

$$\begin{aligned}\pi^+ &\rightarrow \mu^+ + \nu_\mu \\ \mu^+ &\rightarrow e^+ + \nu_\mu + \nu_e.\end{aligned}$$

These “atmospheric” neutrinos are electron and muon neutrinos and anti-neutrinos with energies  $0.05 \div 1000$  GeV.

Recently, the IceCube detector at the South Pole, got the first evidence for a high energy neutrino flux of extraterrestrial origin [13]. In particular, results are consistent with an astrophysical flux in the  $100 \text{ TeV} \div \text{PeV}$  range at the level of  $10^{-8} \text{ cm}^{-2}\text{s}^{-1}\text{sr}^{-1}$  per flavor and a purely atmospheric explanation is rejected at  $5.7\sigma$ . The origin of these ultra high energy neutrinos is a lively source of scientific debate, since there is no established explanation yet. The data are consistent with equal fluxes of all three neutrino flavors and with isotropic arrival directions, suggesting either numerous or spatially extended sources.

Neutrinos can also be man-made. In nuclear reactors, uranium and plutonium undergo fission reactions after absorbing neutrons. Fission products are generally unstable and thus they  $\beta$  decay, emitting one  $\bar{\nu}_e$  per decay. On average, each fission releases  $\sim 200$  MeV and  $\sim 6 \bar{\nu}_e$ . Considering a nominal thermal power per reactor of 1 GW, the correspondent neutrino flux is around  $\sim 2 \times 10^{20} \text{ s}^{-1}$ .

Neutrinos can be produced at accelerators. In practice, they are produced from the in-flight decay of charged pions and kaons, thus sort of emulating the natural production of neutrinos in the atmosphere. The past, present and future experiment based on neutrinos produced at accelerators were, are and will be of extreme importance in studying neutrino oscillations and mixing parameters [14].

A quantitative compilation with a direct comparison of the most important sources of neutrinos is shown in Tab. 1.1.

### 1.3 Neutrino mixing and oscillations

The Hamiltonian causing the weak charged current transitions in the original Fermi theory is [15]

$$H_{cc} = \frac{G_F}{\sqrt{2}} \sum_{\mu=0,1,2,3} \int d^3x (J_{cc}^\mu)^\dagger J_{cc,\mu}. \quad (1.1)$$

As a consequence, the amplitude of any weak transition at low energy is proportional to the Fermi coupling,  $G_F \sim 1.16 \cdot 10^{-5} \text{ GeV}^{-2}$  [7]. The weak charged current  $J_{cc}$  decreases the electric charge of the fermionic state by one unit. It contains two parts, one leptonic

Neutrino Source	Flux ( $\text{cm}^{-2}\text{s}^{-1}$ )	Average energy	Typical target and type	Distance	Cross section ( $\text{cm}^2$ )
Sun (pp reaction)	$3 \times 10^{10}$	0.2 MeV	$3 \times 10^{31}$ , e <sup>-</sup>	$1.5 \times 10^8$ , km	$10^{-45}$ (ES)
Earth	$3 \times 10^5$	2 MeV	$10^{31}$ , p	?	$3 \times 10^{-44}$ (IBD)
Reactor	$3 \times 10^4$	4 MeV	$10^{31}$ , p	$1 - 1000$ , km	$7 \times 10^{-43}$ (IBD)
Relic SN	2.5	10 MeV	$10^{33}$ , p	300, kpc	$7 \times 10^{-42}$ (IBD)
Galactic SN	$10^{10}$	20 MeV	$10^{33}$ , p	10, kpc	$3 \times 10^{-41}$ (IBD)
Atmosphere	1	1 GeV	$10^{34}$ , N	500, km	$10^{-38}$ (QEL+DIS)
Accelerators $\nu_\mu$	0.1	10 GeV	$6 \times 10^{32}$ , N	500, km	$10^{-37}$ (DIS)
Accelerators $\nu_\tau$	0.01	120 GeV	$10^{34}$ , N	700, km	$10^{-38}$ (DIS)
Galactic sources	$10^{-12}$	3 TeV	$2 \times 10^{39}$ , N	1, kpc	$10^{-35}$ (DIS)
High energy neutrinos	$2 \times 10^{-12}$	100 TeV	$6 \times 10^{38}$ , N	?	$10^{-34}$ (DIS)

**Tab. 1.1:** A list of neutrino sources and their properties from [15]. In the target column, e<sup>-</sup> stands for electrons, p for protons and N for nucleons. The cross sections are quoted for the particular processes used to detect the particular kind of neutrinos they refer to: ES indicates elastic scattering, IBD inverse beta decay, QEL quasi elastic nucleon interaction and DIS deep inelastic scattering. The distances and the target masses given in the table are indicative and refer to particular experimental conditions. As a reference, for atmospheric and  $\nu_\mu$  accelerator neutrinos the number for Super-Kamiokande is quoted, the distance for the  $\nu_\tau$  from accelerator refers to the OPERA experiment, the masses for solar-Earth-reactor neutrinos are that of Borexino, while for the investigation of galactic sources or ultra high energy neutrinos, the IceCube experiment is taken as a reference.

and one hadronic. The leptonic one, which is interesting for the purpose of this work, is

$$J_{cc}^\mu = 2 \left( \bar{e} \gamma^\mu \frac{1 - \gamma^5}{2} \nu_e + \bar{\mu} \gamma^\mu \frac{1 - \gamma^5}{2} \nu_\mu + \bar{\tau} \gamma^\mu \frac{1 - \gamma^5}{2} \nu_\tau \right) \quad (1.2)$$

where  $e$ ,  $\mu$ ,  $\tau$ ,  $\nu_e$ ,  $\nu_\mu$  and  $\nu_\tau$  are relativistic quantum fields. Within the framework of the SM, the interaction described in Eq. (1.1) derives from the (tree-level) exchange of a  $W^\pm$  boson in the low energy limit. The corresponding Lagrangian in the SM is [7]

$$- \frac{g}{2\sqrt{2}} \left( W_\mu^- \bar{e} \gamma^\mu (1 - \gamma^5) \nu_e + W_\mu^- \bar{\mu} \gamma^\mu (1 - \gamma^5) \nu_\mu + W_\mu^- \bar{\tau} \gamma^\mu (1 - \gamma^5) \nu_\tau + c.c. \right), \quad (1.3)$$

where  $g \sim 0.65$  is one of the gauge coupling constants of the SM,  $W_\mu$  is the relativistic field of the  $W$  boson and “c.c.” indicates the charge conjugated of all the terms expressed before. If one considers small momenta compared to the mass of the  $W$  boson ( $M_W \sim 80 \text{ GeV}/c^2$ ), this Lagrangian term gives rise to the effective four-fermion interaction described in Eq. (1.1) with

$$\frac{G_F}{\sqrt{2}} = \frac{g^2}{8M_W^2}. \quad (1.4)$$

The weak charged current interactions and the current in Eq. (1.2) provide a definition of neutrino flavor: the electron neutrino field is the one associated to the electron field, and similarly for the other ones. Thus, by definition, the neutrino emitted in the pion

decay  $\pi^+ \rightarrow \mu^+ + \nu_\mu$  is a muon neutrino, whereas the one emitted in the beta decay of the neutron  $n \rightarrow p + e^- + \bar{\nu}_e$  is an electron anti-neutrino. Neutrinos are also coupled to the neutral massive boson of the SM, the  $Z^0$ : this interaction is usually referred to as weak neutral current interaction.

The neutrino-electron cross section as computed in the framework of the SM is discussed in Sec. 4.1, when introducing the neutrino detection methods of the Borexino experiment.

### 1.3.1 Neutrino oscillations in vacuum

A complete and theoretically clean description of neutrino oscillations could be quite heavy and difficult. Fortunately, except for a few cases (e. g. supernovae explosions or Big Bang nucleosynthesis), neutrino fluxes are usually *weak*, in the sense that multi-particle Fermi-Dirac effects can be neglected. This means that without any loss of generality, one-particle quantum mechanics is a right framework to describe neutrino oscillations. In addition, if one focuses on a stationary neutrino flux or on experiments which only measure time-averaged observables, it is possible to describe oscillations in terms of plane waves. For a more detailed explanation, see e. g. Ref. [16].

#### Two-neutrino mixing

In this section, the case of only two active neutrinos is analyzed. This situation is much simpler from the computational point of view with respect to the three-neutrino scenario, but the physical phenomena are quite similar. Supposing to be dealing only with  $\nu_e$  and  $\nu_\mu$ , it is possible to project such states on the free Hamiltonian eigenstates  $\nu_1$  and  $\nu_2$ :

$$\begin{pmatrix} \nu_e \\ \nu_\mu \end{pmatrix} = \begin{pmatrix} \cos \theta & \sin \theta \\ -\sin \theta & \cos \theta \end{pmatrix} \begin{pmatrix} \nu_1 \\ \nu_2 \end{pmatrix}, \quad (1.5)$$

where the  $2 \times 2$  mixing matrix is described by just one mixing angle,  $\theta$ .

If, for the initial state, the following equation holds:

$$|\nu(x=0)\rangle = |\nu_e\rangle = \cos \theta |\nu_1\rangle + \sin \theta |\nu_2\rangle, \quad (1.6)$$

at a generic position  $x$  it is possible to write <sup>1</sup>

$$|\nu(x)\rangle = e^{ip_1 x} \cos \theta |\nu_1\rangle + e^{ip_2 x} \sin \theta |\nu_2\rangle, \quad (1.7)$$

where  $p_1$  and  $p_2$  are the mass eigenstate momenta.

In the ultra-relativistic approximation, the probability of transition from  $\nu_e$  to  $\nu_\mu$  after  $x \simeq L$  is the square of the amplitude  $A_{e\mu} = \langle \nu_\mu | \nu(L) \rangle$ :

$$P_{\nu_e \rightarrow \nu_\mu} \simeq \sin^2(2\theta) \sin^2 \left( \frac{\Delta m_{12}^2 L}{4E} \right), \quad (1.8)$$

---

<sup>1</sup>The time dependence is not written explicitly since it is just an overall phase.

where  $\Delta m_{12}^2 \equiv m_2^2 - m_1^2$ .

As it can be seen from Eq. (1.8), neutrinos must have different masses in order for oscillations to occur. In addition to that, the formula is symmetric for  $\theta \leftrightarrow (\pi/2 - \theta)$  and so two-neutrino oscillations cannot discriminate whether  $\theta > \pi/4$  or  $\theta < \pi/4$ . Of course, oscillation effects are maximal for  $\theta = \pi/4$ .

From Eq. (1.8), one can get the oscillation wavelength as

$$\lambda = \frac{4\pi E}{\Delta m_{12}^2} = 2.48 \text{ km} \frac{E}{\text{GeV}} \frac{\text{eV}^2}{\Delta m_{12}^2}. \quad (1.9)$$

This expression is convenient for evaluating the order of magnitude of the oscillation length as a function of energy, provided the value of the mixing angle  $\theta$ .

In the (very well in agreement with data) hypothesis that neutrinos cannot decay, the survival and appearance probability have to sum to unity:

$$P_{\nu_e \rightarrow \nu_e} + P_{\nu_e \rightarrow \nu_\mu} = 1. \quad (1.10)$$

### Three neutrino families

In the case of three types of neutrinos, Eq. (1.5) becomes

$$|\nu_l\rangle = \sum_{j=1}^3 U_{lj}^* |\nu_j\rangle, \quad (1.11)$$

where  $l = e, \mu, \tau$  and  $U$  is the neutrino mixing matrix (Pontecorvo-Maki-Nakagawa-Sakata matrix or PMNS matrix). If the number of leptonic eigenstates is equal to the number of mass eigenstates,  $U$  is a unitary matrix, i. e.  $UU^\dagger = U^\dagger U = 1$ , because of probability conservation. This kind of formalism for the description of neutrino oscillations can be easily adapted to the most general case of  $n$  families, simply by adding dimensions to the PMNS matrix. Since  $U$  is unitary, it can be shown that the number of free parameters needed for its description consists in  $n(n-1)/2$  angles and  $(n-1)(n-2)/2$  physical phases in the case of Dirac neutrino fields, or in  $n(n-1)/2$  phases in the case of Majorana neutrino fields.

For the case of 3 neutrino families, the usual parametrization of  $U$  is the following:

$$\begin{aligned} U &\equiv \begin{pmatrix} U_{e1} & U_{e2} & U_{e3} \\ U_{\mu 1} & U_{\mu 2} & U_{\mu 3} \\ U_{\tau 1} & U_{\tau 2} & U_{\tau 3} \end{pmatrix} \\ &= R_{23}(\theta_{23}) \cdot R_{13}(\theta_{13}) \cdot \text{diag}(1, e^{i\phi}, 1) \cdot R_{12}(\theta_{12}) \cdot \text{diag}(e^{i\alpha_1/2}, e^{i\alpha_2/2}, 1) \\ &= \begin{pmatrix} c_{12}c_{13} & c_{13}s_{12} & s_{13}e^{-i\phi} \\ -c_{23}s_{12}e^{i\phi} - c_{12}s_{13}s_{23} & c_{12}c_{23}e^{i\phi} - s_{12}s_{13}s_{23} & c_{13}s_{23} \\ s_{23}s_{12}e^{i\phi} - c_{12}c_{23}s_{13} & -c_{12}s_{23}e^{i\phi} - c_{23}s_{12}s_{13} & c_{13}c_{23} \end{pmatrix} \cdot \begin{pmatrix} e^{i\alpha_1/2} & 0 & 0 \\ 0 & e^{i\alpha_2/2} & 0 \\ 0 & 0 & 1 \end{pmatrix} \end{aligned} \quad (1.12)$$

where  $s_{ij}$  and  $c_{ij}$  stand for  $\sin \theta_{ij}$  and  $\cos \theta_{ij}$ , while  $\phi$  and  $\alpha_{1,2}$  are the Dirac and Majorana phases respectively. This parametrization holds for  $\theta_{ij} = [0, \pi/2]$  and  $\phi = [0, 2\pi]$ .

The most updated experimental values for the oscillation parameters are presented in Sec. 2.4.2.

A couple of general remarks coming from first principles are in order. First of all, probability conservation implies:

$$\sum_{l'} P(\nu_l \rightarrow \nu_{l'}) = \sum_{l'} P(\bar{\nu}_l \rightarrow \bar{\nu}_{l'}) = 1. \quad (1.13)$$

In the assumption of CPT invariance, one can also write:

$$P(\nu_l \rightarrow \nu_{l'}) = P(\bar{\nu}_{l'} \rightarrow \bar{\nu}_l). \quad (1.14)$$

For simplicity, it is possible to assume that at  $t = 0$ , a neutrino is produced in a flavor eigenstate, e.g.  $|\nu_l\rangle$ , with a well defined momentum  $\vec{p}$ , and consider the probability to find the neutrino in a different flavor state  $|\nu_{l'}\rangle$  at a later time  $t$ .<sup>2</sup> According to Eq. (1.11), the flavor eigenstate  $|\nu_l\rangle$  has not a defined energy. Its time evolution is

$$|\nu_l(t)\rangle = \sum_{j=1}^3 U_{lj}^* e^{-iE_j t} |\nu_j\rangle, \quad (1.15)$$

where  $E_j = \sqrt{m_j^2 + p^2}$  are the energies of the single mass eigenstates. Eq. (1.15) shows that the different components get different phases, thus giving rise to oscillations. The amplitude of finding the neutrino at the time  $t$  in a flavor state  $|\nu_{l'}\rangle$  is

$$\begin{aligned} A(\nu_l \rightarrow \nu_{l'}, t) &= \langle \nu_{l'} | \nu_l(t) \rangle \\ &= \sum_{j=1}^3 \sum_{k=1}^3 \langle U_{l'k} \nu_k | e^{-iE_j t} U_{lj}^* \nu_j \rangle \\ &= \sum_{j=1}^3 \sum_{k=1}^3 U_{l'k} U_{lj}^* e^{-iE_j t} \langle \nu_k | \nu_j \rangle \\ &= \sum_{j=1}^3 U_{l'j} U_{lj}^* e^{-iE_j t}. \end{aligned} \quad (1.16)$$

---

<sup>2</sup>The condition that the neutrino is produced with a well defined momentum can be dropped. See e.g. the discussions in Refs. [10, 16].

Explicitly, the oscillation probability turns out to be [10]

$$\begin{aligned}
P(\nu_l \rightarrow \nu_{l'}) &= \left| \sum_{j=1}^3 U_{l'j} U_{lj}^* e^{-iL \frac{m_j^2}{2E\nu}} \right|^2 \\
&= \sum_{j=1}^3 |U_{l'j}|^2 |U_{lj}|^2 \\
&\quad + \sum_{j < k} 2 \operatorname{Re} [U_{l'j} U_{l'k}^* U_{lj}^* U_{lk}] \cos \left( \frac{\Delta m_{jk}^2 L}{2E} \right) \\
&\quad + \sum_{j < k} 2 \operatorname{Im} [U_{l'j} U_{l'k}^* U_{lj}^* U_{lk}] \sin \left( \frac{\Delta m_{jk}^2 L}{2E} \right), \tag{1.17}
\end{aligned}$$

where  $\Delta m_{jk}^2 \equiv m_k^2 - m_j^2$ , the relativistic approximation is used and  $t \sim L$  since  $c = 1$ .

## 1.4 Oscillation in matter: the MSW effect

The impact of matter in neutrino propagation is here discussed in the simplest formalism possible, in order to highlight the physics concepts which are useful for the scopes of this thesis. Further details can be found in Ref. [16].

Neutrinos from the Sun or the atmosphere cross the Earth or the Sun without being significantly absorbed. But since matter is composed by electrons (rather than by muons and taus), electron neutrinos interact differently than muon or tau neutrinos, giving rise to a flavor-dependent propagation. The scattering of  $\nu_l$  on electrons and quarks mediated by the  $Z$  boson is the same for all flavors  $l = e, \mu, \tau$ , and therefore it does not affect flavor transitions between active neutrinos. In the case of charged current interactions mediated by the  $W$  boson, the situation is different. The forward scattering of  $\nu_e$  on electrons is described at low energy ( $E \ll M_W$ ) by the effective contact Hamiltonian

$$H_M = \frac{G_F}{\sqrt{2}} \int d^3x \bar{\nu}_e \gamma^\mu (1 - \gamma^5) \nu_e \langle \bar{e} \gamma_\mu (1 - \gamma^5) e \rangle, \tag{1.18}$$

where  $\langle \bar{e} \gamma_\mu (1 - \gamma^5) e \rangle$  indicates the average on the electron state. The only non-zero term for ordinary matter, i. e. non-polarized and at rest, is  $\langle \bar{e} \gamma_0 e \rangle = \langle e^\dagger e \rangle = n_e$ , where  $n_e$  is the volume density of electrons. In conclusion, the effective Hamiltonian in the matter is<sup>3</sup>

$$\langle H_M \rangle = \sqrt{2} n_e G_F \int d^3x \sum_{j=e,\mu,\tau} \bar{\nu}_j \delta_{j,e} \gamma^\mu \left( \frac{1 - \gamma^5}{2} \right) \nu_j. \tag{1.19}$$

The difference of potentials between the interaction of electron and muon/tau neutrinos with electrons leads to the appearance of an additional non-zero phase in the neutrino

---

<sup>3</sup>The contribution of neutral currents is neglected, since it cannot induce modifications in the oscillations.

system,  $\Delta\varphi = (H_M - H)t$ , where  $H$  is the Hamiltonian given in Eq. (1.1). In the ultra-relativistic approximation, one gets  $\Delta\varphi = \sqrt{2}n_e G_F L$ , where  $L$  is the distance between the neutrino production and observation points. This term leads to matter effect on neutrino oscillations, usually referred to as matter effect or MSW effect after Wolfenstein [17], Mikheev and Smirnov [18]. In the vacuum, the phase difference between two neutrino mass eigenstates with a fixed momentum<sup>4</sup> is

$$(E_1 - E_2)t = \frac{E_1^2 - E_2^2}{E_1 + E_2}t = \frac{m_1^2 - m_2^2}{E_1 + E_2}t \approx \frac{\Delta m^2}{2E}L. \quad (1.20)$$

The size of the matter phase  $\Delta\varphi$  can be compared with the vacuum phase of Eq. (1.20) as follows [15]

$$\varepsilon \equiv \frac{\sqrt{2}G_F n_e}{\Delta m^2/2E} \sim \begin{cases} \left(\frac{7.5 \times 10^{-5} \text{eV}^2}{\Delta m^2}\right) \left(\frac{E}{5 \text{MeV}}\right) \left(\frac{\rho_e}{100 \text{mol} \cdot \text{cm}^{-3}}\right) \\ \left(\frac{2.4 \times 10^{-3} \text{eV}^2}{\Delta m^2}\right) \left(\frac{E}{5 \text{GeV}}\right) \left(\frac{\rho_e}{3 \text{mol} \cdot \text{cm}^{-3}}\right), \end{cases} \quad (1.21)$$

where  $\rho_e$  is the molar density of electrons, namely the Avogadro number times  $n_e$ . The numerical parametrization shown in Eq. (1.21) is very useful, since it shows the numbers to be used as a reference for understanding the importance of matter effects for solar neutrinos (top) and atmospheric neutrinos (bottom). Regarding e.g. solar neutrinos, for which  $\Delta m^2 = 7.5 \times 10^{-5} \text{eV}^2$  and at the production point  $\rho_e \sim 100 \text{mol/cm}^3$ , if one considers energies around  $\sim 0.2 \text{MeV}$  (e.g. pp neutrinos, see Sec. 1.6), the matter effect can be neglected. Instead, for  ${}^8\text{B}$  neutrinos with energies above 5 MeV it is important. The effect exists also for high energy neutrinos that cross the Earth (where  $\rho_e \sim 3 \text{mol/cm}^3$  and  $\Delta m^2 = 2.4 \times 10^{-3} \text{eV}^2$ ) but this has still to be observed. It depends on the neutrino mass ordering, which is more extensively discussed in Sec. 2.4.2.

#### 1.4.1 Two-neutrino matter effects

The description of the matter effect is discussed here in detail only in the case of two-neutrino mixing, since this is sufficient to explain the physics phenomena induced on flavor oscillations by the interaction between neutrinos and matter. The notation follows that of Sec. 1.3.1.

The full Hamiltonian is

$$H = H_0 + H_M = V(\theta) \begin{pmatrix} E_1 & 0 \\ 0 & E_2 \end{pmatrix} V^\dagger(\theta) + \begin{pmatrix} \sqrt{2}G_F n_e & 0 \\ 0 & 0 \end{pmatrix}, \quad (1.22)$$

where  $V$  is the  $2 \times 2$  mixing matrix. By recasting Eq. (1.22) and dropping all the terms which are proportional to the unity matrix, and thus do not contribute to flavor oscillations, one gets [10, 16]

$$H \sim \frac{\Delta m_{12}^2}{4E} \begin{pmatrix} -\cos 2\theta & \sin 2\theta \\ \sin 2\theta & \cos 2\theta \end{pmatrix} + \frac{\sqrt{2}G_F n_e}{2} \begin{pmatrix} 1 & 0 \\ 0 & -1 \end{pmatrix} = \frac{\Delta m_{12}^2}{4E} \begin{pmatrix} -\cos 2\theta + \varepsilon & \sin 2\theta \\ \sin 2\theta & \cos 2\theta - \varepsilon \end{pmatrix}, \quad (1.23)$$

---

<sup>4</sup>This condition simplifies the calculations but it is not absolutely needed to draw these very same conclusions, as it is discussed in the footnote 2 of Sec. 1.3.1.

where  $\varepsilon$  is defined in Eq. (1.21). It is now fairly easy to diagonalize  $H$ , since it is very similar to the free one. By dividing and multiplying by  $\sqrt{\sin^2 2\theta + (\cos 2\theta - \varepsilon)^2}$ , Eq. (1.23) becomes:

$$H = \frac{(\Delta m_{12}^2)_{\text{eff}}}{4E} \begin{pmatrix} -\cos 2\theta_m & \sin 2\theta_m \\ \sin 2\theta_m & \cos 2\theta_m \end{pmatrix}, \text{ where } \begin{cases} (\Delta m_{12}^2)_{\text{eff}} &= \Delta m_{12}^2 \sqrt{\sin^2 2\theta + (\cos 2\theta - \varepsilon)^2} \\ \sin^2 2\theta_m &= \frac{\sin^2 2\theta}{\sin^2 2\theta + (\cos 2\theta - \varepsilon)^2} \end{cases} \quad (1.24)$$

and the situation is identical to the free neutrino case. Note that in matter the neutrino and anti-neutrino mixings are different because they have opposite effective potentials. In particular, the eigenvalues and the eigenvectors for anti-neutrinos can be obtained with the replacements  $H_M \rightarrow -H_M$  and  $\varepsilon \rightarrow -\varepsilon$ . Another important aspect is that unlike vacuum oscillations, matter oscillations distinguish  $\theta$  from  $\pi/2 - \theta$ .

Without any loss of generality it is possible to assume that  $\Delta m_{12}^2$  is positive, if the mixing angle  $\theta \in [0, \pi]$ .  $\theta = 0$  corresponds to the situation where the lightest neutrino is a pure  $\nu_e$  and  $\theta = \pi/2$  to the situation where the lightest state is a  $\nu_\mu$ . Within this convention,  $\varepsilon$  is always positive for neutrinos and negative for anti-neutrinos.

### 1.4.2 MSW resonance

Equation (1.24) shows that even in the case of a very small mixing angle, namely  $\theta \ll 1$ , there exists a condition in the matter for which the effective mixing is maximal. This condition is achieved when  $\varepsilon = \cos 2\theta$  and thus  $\sin^2 2\theta_m = 1$ . This situation is usually referred to as “matter resonant oscillations” and it happens when

$$E \sim \frac{\Delta m_{12}^2}{2\sqrt{2}G_F n_e} = 3 \text{ GeV} \frac{\Delta m_{12}^2}{10^{-3} \text{ eV}^2} \frac{1.5 \text{ g/cm}^3}{\rho f_e}, \quad (1.25)$$

where  $\rho$  is the density of the material and  $f_e$  is the fraction of electrons with respect to nucleons. If the neutrino energy is fixed, the resonant density for which the effective mixing is maximal is defined directly from Eq. (1.25), i. e.  $n_e^{\text{res}} = \Delta m_{12}^2 / 2\sqrt{2}G_F E$ . It is interesting to note that when the vacuum mixing approaches the maximal value,  $\theta \sim \pi/4$ , the resonance shifts to zero density,  $n_e^{\text{res}} \rightarrow 0$ .

Some limits of Eq. (1.24) are here discussed. The low density (or low energy) limit can be obtained for  $\varepsilon \rightarrow 0$ , in which the vacuum case is recovered. The limit  $\varepsilon \rightarrow \infty$  corresponds to very high density (or very high energy). The effective mixing parameters become:

$$\begin{aligned} \sin^2 2\theta_m &\rightarrow 0 \\ \Delta m_{12}^2 &\rightarrow \pm \Delta m_{12}^2 \cdot \varepsilon = \pm 2\sqrt{2}G_F n_e E, \end{aligned} \quad (1.26)$$

where “+”(“−”) holds for neutrinos (anti-neutrinos). In this situation, neutrinos oscillate in matter with an energy-independent wavelength  $\lambda = \pi / \sqrt{2}G_F n_e$ , and  $\nu_e$  ( $\bar{\nu}_e$ ) becomes an eigenvector of propagation.

## 1.5 The Standard Solar Model

A lot of papers have been published throughout the years concerning the theoretical modeling of the Sun and the birth of a standard framework for describing our star's interiors. J. Bahcall pioneered these developments [19] and after many years of both theoretical and experimental efforts, still there are some issues to be solved. Some of the past achievements can be found e. g. in Refs. [20, 21, 22, 23, 24, 25, 26, 27, 28, 29, 30, 31, 32, 33, 34, 35, 36, 37].

In this section, the contributions of Refs. [20, 21] are discussed, with the aim of highlighting the milestones and the open problems in the understanding of the mechanisms that make the Sun shine.

Solar models trace the evolution of the Sun throughout its whole history, since the collapse of the pre-solar gas cloud and the turn-on of thermonuclear reactions. This allows to predict some observable solar properties such as the composition, temperature, pressure, sound-speed profiles and neutrino fluxes. The concept behind Standard Solar Models (SSMs) is that of a well-defined framework within which a physical description of the Sun can be constructed and predictions be made as a function of a few varying parameters. SSMs are essentially based on four assumptions [38]:

1. The Sun generates energy in hydrostatic equilibrium, thus maintaining a local balance between the gravitational force and the pressure gradient. A mathematical description of the equilibrium is provided through an equation of state. Even if hydrogen and helium in the Sun's core are nearly completely ionized because of the high temperature ( $\sim 10^7$  K), an ideal gas equation of states with some corrections (incomplete ionization of metals, radiation pressure and screening) is found to be a good approximation.
2. Energy is carried out through radiation and convection and the innermost part of the Sun (i. e. around 98% by mass or 71% by radius) is radiative. The radiative transport can be described only if the opacity is known as a function of temperature, density, and composition. In addition to elementary processes such as Thomson scattering off electrons and inverse Bremmstrahlung off fully ionized hydrogen and helium, more complex processes such as bound-free scattering off metals are important contributors to the opacity in the Sun's central regions. Modifications of the opacity could influence important helioseismic properties such as the sound speed and the location of the convective zone boundary. In the outermost part of the Sun, convection dominates the energy transport.
3. The Sun produces its energy by fusing protons into  ${}^4\text{He}$

$$2\text{e}^- + 4\text{p} \rightarrow {}^4\text{He} + 2\nu_e + 26.73 \text{ MeV}, \quad (1.27)$$

via the pp-chain ( $\sim 99\%$ ) and CNO cycle ( $\sim 1\%$ ). See Sec. 1.6 for details about these processes. The nuclear cross sections come from experimental data (see e. g. the results and prospects of the LUNA experiment at the Laboratori Nazionali

del Gran Sasso [39, 40, 41, 42]) or, when the measurement is particularly difficult, they are computed theoretically. It must be noted that this kind of laboratory astrophysics is challenging because reaction rates are needed for energies well below the Coulomb barrier. This makes the achievements of the LUNA experiment (which is able to measure at “astrophysical energies”, i. e. “low energies”), very precious and important, otherwise the measurements would have to be made at higher energies, with theory guiding the extrapolations to the solar Gamow window.

4. Boundary conditions include the modern Sun’s mass, age, radius  $R_\odot$ , and luminosity  $L_\odot$ . The pre-solar composition is divided into hydrogen  $X_{ini}$ , helium  $Y_{ini}$ , and metals  $Z_{ini}$ , with  $X_{ini} + Y_{ini} + Z_{ini} = 1$ . The relative metal abundances can be determined from a combination of the photospheric (coming from analyses of the absorption lines) and chondritic abundances, and are generally assumed to have been constant since the Sun formation. The photospheric abundances and the assumption of a homogeneous Sun at its formation then constrain the Sun’s initial core composition. In fact, one can equate the Sun’s pre-solar core metallicity  $Z_{ini}$  to its present photospheric metallicity  $Z_S$ , both correcting for the effects of diffusion over the Sun’s lifetime, and imposing the constraints on the observed solar radius and luminosity.

The resulting model is dynamic and follows the Sun evolution. For example,  $L_\odot$  increases by  $\sim 40\%$  over the solar lifetime, the helium synthesis alters the mean molecular weight and opacity in the core and the ratios between the various thermo-nuclear reactions taking place inside the core change.

The SSM plays a fundamental role for stellar models in general. This is most evident when considering that convection theories used to model stars still rely on a free parameter that is calibrated by forcing solar models to reproduce the present-day solar radius and temperature. Also, the calibrated initial solar composition is often used as an anchor point, together with results from Big Bang Nucleosynthesis. The SSM is also used as a benchmark against which it is possible to test additional physical processes in stars.

### 1.5.1 Solar abundances and helioseismology

The determination of the chemical element abundances in the Sun is achieved primarily through spectroscopy of the solar photosphere. The analysis of this data relies on the modeling of the solar atmosphere, for the determination of temperature and density stratifications, and on detailed radiation transfer calculations. This is needed to link elemental abundances with the observed spectral line intensities and shapes. Recently, there have been some improvements in these data analyses, especially thanks to the introduction of three-dimensional radiation hydrodynamic (3D-RHD) models of the solar atmosphere and of new non-local thermodynamic equilibrium calculations, see e. g. Refs. [43, 44]. Tab. 1.2 from Ref. [20] lists the abundances for the most relevant metals in solar modeling determined by different authors with spectroscopical analyses of the solar

Element	GN93	GS98	AGSS09	C11
C	8.55	8.52	8.43	8.50
N	7.97	7.92	7.83	7.86
O	8.87	8.83	8.69	8.76
Mg	7.58	7.58	7.60	7.54
Si	7.55	7.55	7.60	7.52
S	7.33	7.33	7.13	7.16
Fe	7.50	7.50	7.50	7.52
$(Z/X)_{\odot}$	0.0245	0.0230	0.0180	0.0209

**Tab. 1.2:** Solar photospheric composition in different models for most relevant metals in the Sun. Abundances are given in the standard astronomical scale,  $\log \epsilon_i = \log (n_i/n_{\text{H}}) + 12$ , where  $n_i$  is the number density of a given atomic species. Note that from spectroscopy it is only possible to obtain abundances relative to that of hydrogen, since the spectroscopic line intensities is measured relative to the continuum of lines determined by the hydrogen abundance in the solar atmosphere. Table from Ref. [20].

photosphere. The considered models are: GN93 [45], GS98 [46], AGSS09 [43], C11 [44].<sup>5</sup> The introduction of the 3D-RHD models around the year 2001 is a crucial point for the values determined for abundances of volatile elements, particularly C, N, and O. Results from AGSS09, in particular, give large reductions, grater than 30% with respect to the older generation analyses (GN93, GS98). C11, based on 3D-RHD independent models, finds CNO abundances at intermediate values between older results and those of AGSS09. In Ref. [47], three different 3D-RHD solar model atmospheres are compared, showing that minimal variations in the 3D-RHR modeling explain the differences on CNO between AGSS09 and C11.

The last row of Tab. 1.2 gives the total photospheric metal-to-hydrogen ratio  $(Z/X)_{\odot}$  at present and it is the quantity used as observational constraint to construct solar models. It is difficult to quantify uncertainties in the element abundances of Tab. 1.2. A detailed study of systematics is not available, and therefore the quoted uncertainties in works on solar abundances are only indicative [20]. Typical values quoted by AGSS09 for volatile elements are around 0.05 (standard astronomical scale, see the caption of Tab. 1.2 for details).

Refractory elements<sup>6</sup> play a very important role in solar models. They amount to about 20% of the total metal mass fraction and are determinant contributors to the radiative opacity in the solar interior, particularly Si and Fe and, to a lesser extent, Mg and S [20]. Abundances for refractories can be determined very precisely from chondritic meteorites, which can provide robust results. It is therefore desirable to combine the spectroscopic measurements of volatiles with the more robust meteoritic results for

<sup>5</sup>The number in the names of the models is simply referring to the year in which the model was proposed.

<sup>6</sup>The refractory group includes elements and compounds like metals and silicates (commonly termed rocks) which make up the bulk of the mass of terrestrial planets and asteroids in the inner belt of the Solar System.

refractories. The solar abundance composition thus constructed is the one typically used in SSMs. In the case of GS98, results from meteorites and from spectroscopy are very similar. Instead, in the case of AGSS09, some differences are present, as shown in Tab. 1.2. Therefore, it is common to identify the combination of AGSS09 photospheric abundances for volatiles and the meteoritic ones for refractories as “AGSS09met” [20]. In relation to AGSS09 values given in Tab. 1.2, AGSS09met has lower Mg and Fe and  $(Z/X)_\odot = 0.0178$ .

In the last few decades, helioseismology has provided the most stringent constraints on the interior structure of the Sun [35, 48]. Helioseismology can measure the frequencies of thousands of global acoustic “p-modes”<sup>7</sup>, with angular momentum from  $\ell = 0$  up to several hundreds and with precisions of the order of  $10^{-5}$  [20]. These measurements allow to probe the innermost part of the Sun with excellent precision, since modes with different angular momentum and frequency behave differently depending on the density and the position inside the star. In particular, low angular momentum modes can reach the solar core, where solar neutrinos are produced.

Some interesting observables for testing the quality of solar models include the solar sound speed profile inside the Sun, the depth of the convective region  $R_{CZ}$  with respect to the radiative region and the abundance of helium in the outermost parts of the Sun (usually referred to as  $Y_S$ ). The solar density profile can also be used as a probe for solar models, but there are large correlations in the derived profiles in different parts of the Sun. More details on these techniques and on helioseismology in general can be found e. g. in Refs. [49, 50].

The discussion on interaction and compatibility of the photospheric and helioseismic results regarding the Sun composition are postponed to Sec. 1.7.

## 1.6 Production of solar neutrinos

The Sun produces  $\sim 3.8 \times 10^{26}$  W by means of the thermo-nuclear reactions which take place in its center. Like approximately the 80% of the observed stars, the Sun produces most of its energy (99%) through the pp-chain, i. e. a chain of reactions which has the net effect of fusing 4 protons into a helium nucleus and releasing energy, as shown in Eq. (1.27). The subdominant CNO cycle accounts for the remaining 1% of energy production. In the case of the CNO cycle, the heavier elements present inside the star, such as C, N and O act only as catalysts of nuclear reactions which result also in this case in burning 4 protons per cycle into helium. The CNO cycle is more important in the energetic balance of stars more massive than the Sun ( $M \gtrsim 1.5 M_\odot$ ). In Fig. 1.2, sketches of both the pp-chain and the CNO cycle are shown. In the next subsections, the various reactions which make the Sun shine are described, with a special emphasis on those producing neutrinos.

---

<sup>7</sup>“p-mode” indicates a pressure wave. Unlike seismic waves on Earth, solar waves have practically no shear component (s-mode).

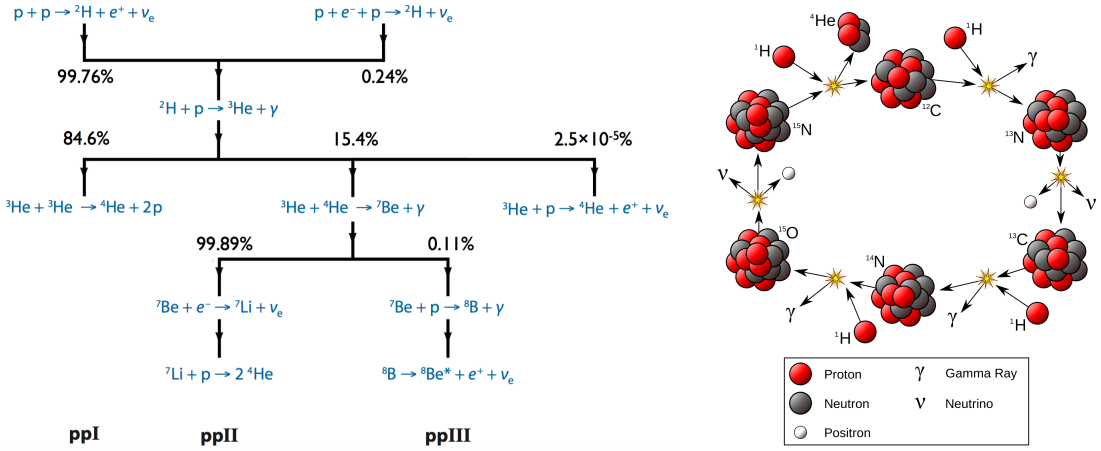


**Fig. 1.2:** Sketch of the pp-chain (left) and the CNO cycle (right). The left picture comes from Ref. [21] while the rightmost one is from Wikipedia.

### 1.6.1 The pp-chain

The first step of the chain is the fusion of two protons, forming deuterium:

$$p + p \rightarrow ^2H + e^+ + \nu_e \quad (Q = 0.42 \text{ MeV}), \quad (1.28)$$

where  $Q$  is the Q-value of the reaction. The reaction in Eq. (1.28), called pp reaction, is the basis of the whole pp chain, since in  $\sim 99.76\%$  of the cases, a termination of the pp-chain passes through it. The cross section for this key-stone reaction is too low in order to perform a direct measurement in the laboratory at the same energies of the Sun's core. The neutrino emitted in this process, called pp  $\nu$ , has a continuous spectrum with a maximum energy correspondent to the Q-value,  $Q = 0.42 \text{ MeV}$ . This reaction is the most probable inside the Sun (thanks to the very high density of hydrogen) and, therefore, the associated neutrino flux, despite the quite low energy, is the highest. Interestingly, the reaction in Eq. (1.28) is induced by a weak process, and this allows to power the Sun in a quiescent equilibrium for many years, thanks to the very low rate of reaction.

The pp-chain can be entered also through another much rarer reaction, ( $\sim 0.24\%$  of the cases):

$$p + e^- + p \rightarrow ^2H + \nu_e \quad (Q = 1.44 \text{ MeV}). \quad (1.29)$$

In this case the neutrino is emitted monochromatically with an energy of  $1.44 \text{ MeV}$ . Neutrinos produced in this reaction (pep reaction) are called pep  $\nu$  and are of particular importance because of their energy. In fact, at around  $1 \text{ MeV}$ , the electron neutrino survival probability has the transition from vacuum towards matter dominated oscillations (see Sec. 1.8). For this reason, pep  $\nu$  are important for studying neutrino particle physics other than solar astrophysics. As a final remark, given the difference in the branching ratios between the pp and pep reactions, the flux of pep  $\nu$  is much weaker than that of pp  $\nu$ .

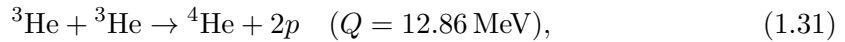
Once  $^2\text{H}$  is produced, the only way to proceed further consists in the absorption of a proton by the deuteron,



This reaction was directly measured at energies relevant for solar astrophysics by the LUNA Collaboration [51]. At this point, the pp-chain splits into three different terminations, called pp-I, pp-II and pp-III, with different subsequent reactions. These are determined by the different ways in which  $^3\text{He}$  interacts.

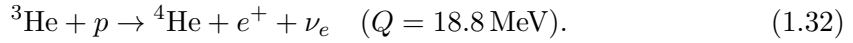
### The pp-I branch

The most probable termination of the chain ( $\sim 84.6\%$ ) consists in the reaction



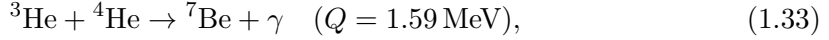
whose cross section was measured experimentally [52]. In this case, there is no more neutrino emission.

However, this is not the only reaction which could take place. With a very low probability ( $\approx 10^{-7}$ ),  $^3\text{He}$  could react with a proton and do



This reaction is usually called hep reaction, and it produces hep neutrinos (hep  $\nu$ ). They have a continuous spectrum which extends up to more than 18 MeV, but because of their very low production rate, they have not been observed yet [53, 54, 55].

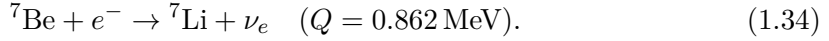
In the remaining  $\sim 15.4\%$  of the cases,  $^3\text{He}$  can undergo the following reaction:



which was measured in Ref. [56]. This reaction is the cornerstone which brings to the last two branches of the pp-chain and to the production of other solar neutrinos.

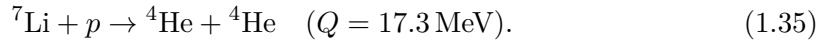
### The pp-II branch

$^7\text{Be}$  decays via electron capture to  $^7\text{Li}$ ,



This reaction emits a mono-energetic neutrino, called  $^7\text{Be}$  neutrino ( $^7\text{Be} \nu$ ). The neutrinos emitted in this reaction are monochromatic, with an energy of 862 keV in  $\sim 90\%$  of the cases. In the remaining  $\sim 10\%$  of decays, the lithium is produced in an excited state and thus the neutrino emitted has an energy of 384 keV.

The final reaction leading to the production of  $^4\text{He}$  is the following:

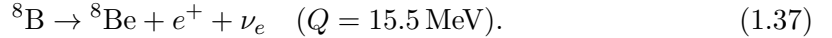


### The pp-III branch

There is a little probability ( $\sim 0.11\%$ ) that a  ${}^7\text{Be}$  nucleus, before decaying, captures a proton, thus producing  ${}^8\text{B}$ ,



${}^8\text{B}$  is unstable and it  $\beta$  decays pretty quickly:



This reaction is called  ${}^8\text{B}$  reaction. It produces a continuous spectrum of electron neutrinos with energies up to almost 16 MeV. Naturally, these neutrinos are called  ${}^8\text{B}$  neutrinos ( ${}^8\text{B} \nu$ ). They have an extremely historical importance since they are the first detected solar neutrinos and their later detection in different channels in the SNO experiment led to the first evidence of neutrino oscillations. More details are in Sec. 1.9. The branch ends either with the  ${}^8\text{Be}$  decay, i. e.  ${}^8\text{Be} \rightarrow {}^4\text{He} + {}^4\text{He}$ , or with the capture of a  ${}^4\text{He}$  nucleus by  ${}^8\text{Be}$  yielding to the production of  ${}^{12}\text{C}$ .

### 1.6.2 The CNO cycle

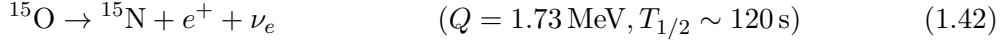
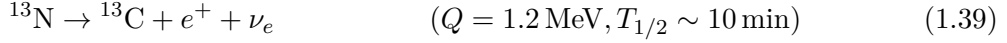
The CNO cycle is a set of reactions which result, exactly as the pp-chain, in the fusion of four protons into helium. In Sun-like stars, the CNO cycle is subdominant, while in bigger stars with higher temperatures in their cores, it actually represents the largest way of energy production.

What is commonly referred to as the CNO cycle, is actually an ensemble of different cycles, which involve slightly different reactions but end up in the fusion of four protons, using carbon, nitrogen and oxygen isotopes as catalysts. Since one of these cycles (CNO-I) is the dominant one and the total CNO contribution in the Sun is small, one usually refers to the CNO-I cycle with the global name of CNO cycle. Under typical conditions found in most of stars, the amount of hydrogen burnt by the CNO cycle is limited by the rate of proton captures by the catalyst nuclei. In fact, the timescale of  $\beta$  decays of the radioactive nuclei produced is faster than the timescale for proton capture. The detection of the solar neutrinos emitted in the CNO cycle would be very important for stellar astrophysics. The discussion on this is postponed to Sec. 1.7.

#### CNO-I cycle

The first proposed catalytic cycle for the conversion of hydrogen into helium was initially called the carbon-nitrogen cycle (CN cycle or CNO-I cycle), since oxygen is produced and decays, but does not capture any proton within this cycle. This is the set of reactions which contribute the most to the total energy production through the CN

cycle:

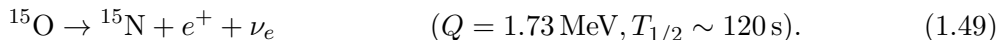
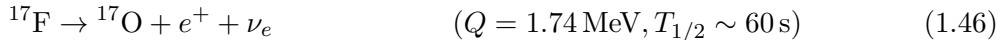


A certain amount of  $^{12}\text{C}$  is supposed to be present inside the Sun (depending on the metallicity, see Sec. 1.7). A  $^{12}\text{C}$  nucleus is used in the first reaction of the CNO-I cycle and it is created back at the end, closing the loop. Summing up the whole released energies (taking into account also the positron annihilation), one obtains once again a total energy release of 26.73 MeV per cycle, exactly as in the pp-chain case. The reaction in Eq. (1.41) was studied experimentally in Ref. [57], while the one in Eq. (1.43) in Ref. [58].

Within the CNO-I cycle, two solar neutrinos are produced. They have continuous spectra with endpoints 1.2 MeV ( $^{13}\text{N}$  neutrinos) and 1.73 MeV ( $^{15}\text{O}$  neutrinos). The theoretical predictions on their fluxes depend pretty much on the inputs given to the solar model, especially regarding the metal composition of the Sun (see Sec. 1.7 for a deeper discussion).

### CNO-II (and III+IV) cycle

The CNO-II cycle (also called NO cycle, since the two nuclei involved in the capture of protons are nitrogen and oxygen) is subdominant with respect to the CNO-I cycle. Its contribution accounts for the  $\sim 2\%$  of the total CNO energy production (which is around 1% of the total energy production in the Sun). The reactions involved are the following:



At the end of this cycle, other than an  $^{15}\text{O}$  neutrino, an additional neutrino with a maximum energy of 1.74 MeV from the  $\beta$  decay of  $^{17}\text{F}$  is produced. In stars bigger and hotter than the Sun, other cycles (CNO-III and CNO-IV) can produce energy. They involve heavier elements (mostly fluorine and oxygen) with respect to those involved in the CNO-I and CNO-II cycles and thus they are suppressed in the Sun, since the temperature in the core is relatively low and the Coulomb barrier of heavier elements is higher.

Neutrino component	$E_\nu^{max}$ (MeV)	GS98 model	AGSS09 model	Units ( $\text{cm}^{-2} \text{s}^{-1}$ )
pp $\nu$	0.42	$5.98(1 \pm 0.006)$	$6.03(1 \pm 0.006)$	$10^{10}$
pep $\nu$	1.44	$1.44(1 \pm 0.012)$	$1.47(1 \pm 0.012)$	$10^8$
$^7\text{Be} \nu$	0.862 ( $\sim 90\%$ )	$5.00(1 \pm 0.07)$	$4.56(1 \pm 0.07)$	$10^9$
	0.384 ( $\sim 10\%$ )			
$^8\text{B} \nu$	15.5	$5.58(1 \pm 0.14)$	$4.59(1 \pm 0.14)$	$10^6$
hep $\nu$	18.77	$8.04(1 \pm 0.30)$	$8.31(1 \pm 0.30)$	$10^3$
$^{13}\text{N} \nu$	1.20	$2.96(1 \pm 0.14)$	$2.17(1 \pm 0.14)$	$10^8$
$^{15}\text{O} \nu$	1.73	$2.23(1 \pm 0.15)$	$1.56(1 \pm 0.15)$	$10^8$
$^{17}\text{F} \nu$	1.74	$5.52(1 \pm 0.17)$	$3.40(1 \pm 0.16)$	$10^6$

**Tab. 1.3:** Theoretical neutrino fluxes from the GS98 and AGSS09 SSMs, with associated uncertainties (averaging over asymmetric uncertainties). In the second column, the endpoint of the  $\beta$  decay is shown apart from the cases of pep  $\nu$  and  $^7\text{Be} \nu$ , in which their monochromatic energies are reported. This table is from Ref. [21].

### 1.6.3 Solar fluxes predictions from the Standard Solar Models

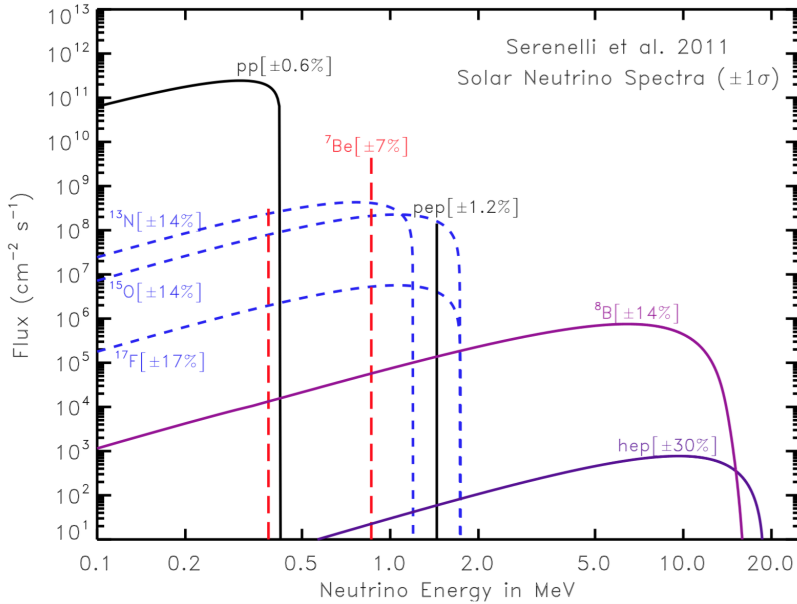
Table 1.3 summarizes the predictions on solar neutrino fluxes from two of the versions of the SSMs introduced in Sec. 1.5.1. The two models, GS98 and AGSS09, mainly differ for the amount of metals<sup>8</sup>. All the main components of the total neutrino flux are not very affected by this difference, apart from the neutrinos from the CNO-I and CNO-II cycles. In this case, the differences in the predictions reach  $\sim 40\%$ . It might seem that Tab. 1.3 is outdated, but actually these models are still the reference concerning theoretical predictions on solar neutrino fluxes, as they are used as benchmarks in a quite recent review work [59].

Figure 1.3 shows the spectral composition of the total solar neutrino flux.

## 1.7 The solar metallicity problem

As discussed already in Sec. 1.5.1, after the pretty recent developments in the 3D analysis of the photospheric data, the theoretical modeling of the Sun is left with basically two scenarios: the “*high metallicity*” (*high-Z*) and the “*low metallicity*” (*low-Z*) ones. In particular, the *high-Z* model refers to the GS98 prediction, where the volatile abundances (especially for C, N and O) are  $\sim 30 \div 40\%$  higher than those predicted in AGSS09 (*low-Z*) models. Figure 1.4 shows the relative difference in sound speed profiles for *low-Z* and *high-Z* models. The newest models (AGSS09met and CO5BOLD, representative of the *low-Z* models) do not match as well as the older model (GS98) the observed sound speed profile in the Sun. The large differences in SSMs between *high-Z* and *low-Z* models is known under the name of “solar abundance problem” or “solar metallicity problem”.

<sup>8</sup>In Sun’s astrophysics, a metal is any element heavier than helium.



**Fig. 1.3:** Solar neutrino spectrum for the components in Tab. 1.3, along with the SSM uncertainties [60]. Units for continuous spectra are  $\text{cm}^{-2} \text{s}^{-1} \text{MeV}^{-1}$ . Picture from Ref. [21].

Most seismic probes do not directly depend on the metal composition of the Sun but rather on its opacity profile [20], which is the result of atomic calculations of radiative opacities, given the composition of the solar interior. Helioseismology can constrain the metal composition and opacity combination, but cannot disentangle the two contributions. Ref. [61] shows how, by modifications in the opacity profile, a *low-Z* SSM could reproduce the *high-Z* model behavior while keeping a *low-Z* composition. Changes of the order of 15  $\div$  20% (decreasing inwards to a few percents in the solar core) in the radiative opacity are required to bring back the agreement between helioseismology and SSMs if the *low-Z* solar composition is adopted [20]. As it is also discussed in Ref. [62], even taking into account all the sources of uncertainties in SSMs, there is no freedom to compensate for the reduction in  $(Z/X)_\odot$  other than a change in opacity. Typically, two sets of atomic opacity calculations are used, OPAL and OP. The differences between the two are never larger than 3% [20]. This does not seem to leave room for an error in opacity big enough to restore the accordance between SSMs and helioseismology. However, the experimental determination of opacities in the solar conditions is extremely challenging. Some very recent data regarding the wavelength dependence of the iron opacity [63] seems to show that radiative opacities could be underestimated in atomic calculations by a fraction much larger than differences between the different theoretical calculations.

The solar metallicity problem has a direct impact on solar neutrino fluxes. Differences in the predicted fluxes of neutrinos belonging to the pp-chain are exclusively related to changes in the core temperature in the models (of the order of 1%). These differences are due to modified values of the radiative opacities, which are lower for *low-Z* models than

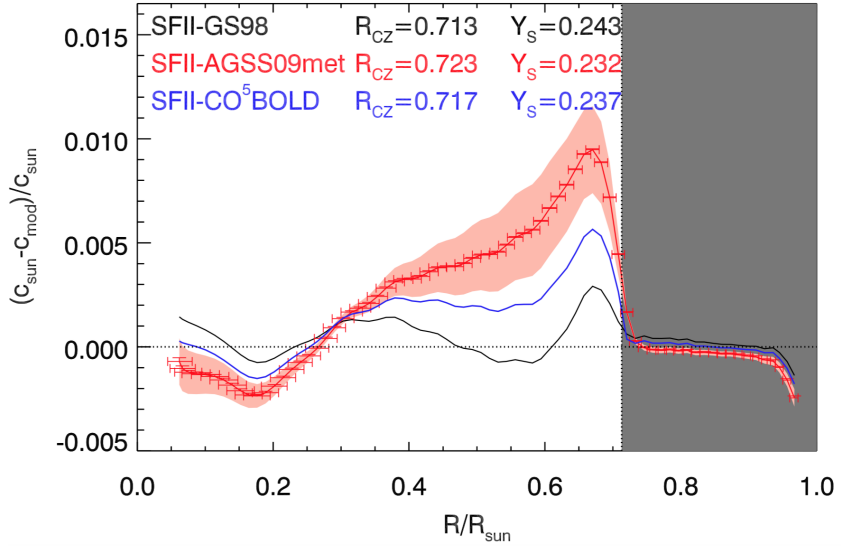


**Fig. 1.4:** Sound speed profiles in the Sun relative to the measured one for different SSMs. Picture from Ref. [20].

they are in *high-Z* models [20]. This means that pp-chain neutrinos cannot probe directly the solar composition, since it is degenerate with the opacity. The advantage of CNO neutrinos, instead, is that the physical conditions in the solar core are established by the pp-chain. Therefore, the CNO cycle keeps a linear dependence on the volatile abundances in the solar core that cannot be washed out by temperature variations. For this reason, CNO neutrino fluxes could be of essential importance if discriminating between *low-Z* and *high-Z* models, especially since the theoretical predictions on the CNO fluxes differ of  $\sim 30 \div 40\%$ , as it is shown in Tab. 1.3. However, an experimental detection of CNO  $\nu$  is particularly tough, as it is detailed in Sec. 4.9.

## 1.8 The propagation of solar neutrinos

Solar neutrinos are direct probes of the mechanisms that make the Sun shine. They are also very effective means for testing particle physics of neutrinos themselves. Observations of solar neutrinos led to the discovery of neutrino oscillations and to the establishment of the current paradigm which describes this phenomenon also in matter, i. e. the MSW model with Large Mixing Angles (MSW-LMA). In this section, the physical processes happening between neutrino production in the core of the Sun and their detection on Earth are briefly discussed. They are of great importance in assessing the particle physics of neutrinos.

The physical picture of solar neutrino propagation and flavor evolution is the following [16]:<sup>9</sup>

<sup>9</sup>The discussion will be restricted to the two-neutrino case as it is done in the reference. Results are

- Neutrinos are produced in the core of the Sun ( $R \sim 0$ ), with probabilities of being  $\nu_{1m}$  or  $\nu_{2m}$  (eigenstates of the Hamiltonian in Eq. (1.24)) of  $\cos^2 \theta_m$  and  $\sin^2 \theta_m$  respectively.  $\theta_m$  is the effective mixing angle at the production point.
- The oscillation wavelength is much smaller than the solar radius. Therefore, neutrinos propagate for many oscillation wavelengths and the eigenstates do not interfere with each other.<sup>10</sup> In the adiabatic approximation, i. e. if the density is a “slow-varying” function of the radius, each neutrino mass eigenstate stays the same. Otherwise, neutrinos can flip to the other mass eigenstate with some level-crossing probability, say  $P_C$ .
- Neutrinos propagate from the Sun to the Earth, and possibly inside the Earth before reaching the detector.
- $\nu_1$  ( $\nu_2$ ) is detected as  $\nu_e$  with probability  $\cos^2 \theta$  ( $\sin^2 \theta$ ).

The result for the survival probability of  $\nu_e$  is [16]

$$P(\nu_e \rightarrow \nu_e) = \frac{1}{2} + \left( \frac{1}{2} - P_C \right) \cos 2\theta \cos 2\theta_m. \quad (1.50)$$

It is interesting to study some of the limit cases for Eq. (1.50) in order to have a picture of the phenomenology of solar neutrino oscillations:

1.  $\theta_m \sim \theta$  and  $P_C = 0$ . In this case matter effects are negligible and this is representative for solar neutrinos at lower energies.  $P(\nu_e \rightarrow \nu_e) = 1 - \frac{1}{2} \sin^2 2\theta$ .
2.  $\cos 2\theta_m = -1$  and neutrinos propagate adiabatically ( $P_C = 0$ ):  $P(\nu_e \rightarrow \nu_e) = \sin^2 \theta$ . This is realized for solar neutrinos at higher energies ( $\gtrsim 1$  MeV).
3.  $P(\nu_e \rightarrow \nu_e) = 1 - \frac{1}{2} \sin^2 2\theta$ , when  $\cos 2\theta_m = -1$  and neutrinos are in the extreme non-adiabatic limit. In this case, one can assume a very high density suddenly terminating in vacuum. The produced neutrino, which is produced in the  $\sim \nu_{2m}$  eigenstate since the matter effect is dominant, does not change flavor at the transition region, because it is negligibly short. For this reason,  $P_C$  can be evaluated as  $|\langle \nu_e | \nu_1 \rangle|^2 = \cos^2 \theta$ .

Figure 1.5 shows the energy dependence of  $P(\nu_e \rightarrow \nu_e)$  as a function of energy for solar neutrinos.

The crossing probability  $P_C$  can be evaluated in any situation [16]. However, since for solar neutrinos the adiabatic approximation is a very good approximation, a discussion on  $P_C$  is not carried out here. Some remarks on the adiabatic approximation are anyway necessary. In particular, in the Sun, the condition of smallness of the density gradient is satisfied, i. e. [64]

$$n_e \left( \frac{dn_e}{dr} \right)^{-1} \gg \frac{2\pi}{\Delta_m}, \quad (1.51)$$

---

easily generalized for the realistic three-neutrino mixing.

<sup>10</sup>The coherence between the eigenstates is lost and oscillations are suppressed, see App. A for details.

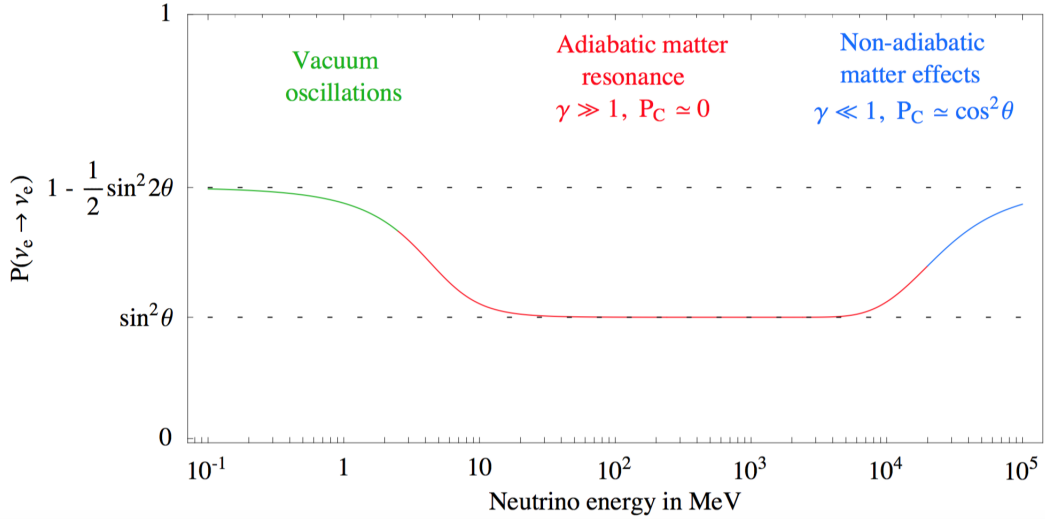


**Fig. 1.5:** Behavior of the survival probability for solar neutrinos ( $P(\nu_e \rightarrow \nu_e)$ ) as a function of energy. Picture from Ref. [16].

where  $2\pi/\Delta_m$  represents the oscillation length in the matter, with  $\Delta_m \equiv H_{im} - H_{jm}$ , i.e. the difference of the matter Hamiltonian (see Eq. (1.24)) for two consecutive shells  $i, j$  inside the Sun. Note that the strongest flavor change occurs when neutrinos cross the MSW resonance layer centered at the resonance density given by the resonance condition of Eq. (1.25). The adiabatic condition for solar neutrinos would cease at around 10 GeV, thus well above the solar neutrinos maximum energy [16].

In order to generalize the results here reported, the density matrix formalism should be adopted. The final result from Ref. [16] is reported here. The full derivation is beyond the scopes of this PhD thesis. The survival probability for low energy solar neutrinos ( $E \lesssim 10$  MeV) where matter effects are negligible is

$$P(\nu_e \rightarrow \nu_e) = \sin^4 \theta_{13} + \cos^4 \theta_{13} \left[ \frac{1}{2} + \left( \frac{1}{2} - P_C \right) \cos 2\theta_{12} \cos 2\theta_{12}^m \right]. \quad (1.52)$$

The formula for “high energy” solar neutrinos reaching the detector at night would be a little different, in order to take into account the “regeneration effect” induced by neutrino oscillations in the Earth mantle [16].

## 1.9 Experimental observations of solar neutrinos

The direct study of solar neutrinos began with the pioneering work of the radiochemical chlorine experiment at Homestake [65]. The Homestake Solar Neutrino Detector measured the total flux of solar neutrinos above 0.814 MeV in the period 1970 ÷ 1994. A radiochemical technique was used, based on the following inverse  $\beta$  reaction:



This method was first suggested by Pontecorvo already in 1946. The detector was located in the Homestake Gold Mine, at a depth of 1478 m. The apparatus consisted in a single horizontal steel tank 6.1 m in diameter and 14.6 m long, containing 615 tons of tetrachloroethylene,  $C_2Cl_4$ . The tetrachloroethylene filled about 95% of the detector volume, while the remaining 5% was filled with helium gas at 1.5 atm pressure (absolute). The design and construction of the detector were driven by two paramount concerns. First, because the Earth's atmosphere contains 0.934% of argon, it was essential that all the system was absolutely leakproof. This is a rigid requirement because the sensitivity of the detector depends upon extracting a small volume of argon carrier gas and on placing the final sample into a proportional counter with an internal volume of only  $0.5\text{ cm}^3$ . The system was helium vacuum-leak tested, with an upper limit on the in-leakage of helium less than  $10^{-6}\text{ cm}^3\text{ s}^{-1}$ . The second major concern in constructing the tank was to minimize the radioactivity of the materials, in order to ensure that the non-solar production of  $^{37}\text{Ar}$  from these sources was less than that from solar neutrinos. As anticipated, the measurement of the total solar neutrino flux was done through the careful measurement of the number of  $^{37}\text{Ar}$  atoms produced inside the detector. Since the  $^{37}\text{Ar}$  atoms decay back to  $^{37}\text{Cl}$  via electron capture with a half-life of  $\sim 35$  days as they are created, the total number of  $^{37}\text{Ar}$  atoms in the tank grows only to a saturation level where the production rate is equal to the decay rate. Of course, since the signal in the chlorine detector is due to a number of source reactions in the Sun, this measurement alone does not uniquely determine the flux from any of the sources, but can be considered as an upper limit on the flux of electron neutrinos from each source. The solar neutrino-induced  $^{37}\text{Ar}$  production rate was found to be  $0.478 \pm 0.030(\text{stat.}) \pm 0.029(\text{sys.})\text{ day}^{-1}$ . This is equivalent to a neutrino capture rate of  $2.56 \pm 0.16(\text{stat.}) \pm 0.16(\text{sys.})\text{ SNU}^{11}$ . This measurement has to be compared with the solar model predictions for the chlorine detector of  $9.3 \pm 1.3\text{ SNU}$  [65]. This was the “Solar Neutrino Problem” which was already indicating the presence of neutrino oscillations. More details on the innovative techniques adopted in the Homestake experiment, which led to the first observation of solar neutrinos, can be found in Ref. [65].

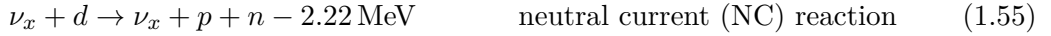
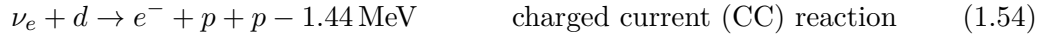
The subsequent generation of radiochemical experiment consisted in the gallium based experiments Gallex/GNO [66] and SAGE [67]. These experiments are based on the inverse beta decay reaction on  $^{71}\text{Ga}$ , i. e.  $\nu_e + ^{71}\text{Ga} \rightarrow ^{71}\text{Ge} + e^-$ . The threshold of this reaction is 233 keV and thus,  $^{71}\text{Ga}$ -based experiments can detect also the low-energy pp  $\nu$ , while the chlorine experiment could detect mostly  $^8\text{B} \nu$  and  $^7\text{Be} \nu$ . These detectors were the first ones able to detect the most abundant component of the solar neutrino flux, the pp  $\nu$ . Gallex and his successor GNO measured solar neutrinos at Laboratori Nazionali del Gran Sasso from 1992 to 2003. The combined Gallex/GNO result on solar neutrino interaction rate (123 solar runs, 3307 days of exposure time) is  $69.3 \pm 4.1(\text{stat.}) \pm 3.6(\text{sys.})\text{ SNU}$ . This is only slightly more than half of the expected rate assuming no neutrino oscillation. The significance of this deficit was assured directly by the results from two  $^{51}\text{Cr}$ -neutrino source run with the same detector (at the 10% level). The SAGE experiment measured solar neutrinos during almost a full 22-year cycle of solar activity, between 1990 and 2010.

<sup>11</sup>1 SNU corresponds to a rate of  $10^{-36}$  neutrino-induced captures per target atom per second.

The result on the flux,  $65.4 \pm 2.7(\text{stat.}) \pm 2.7(\text{syst.})$  SNU [68], is well in agreement with the Gallex/GNO result.

The study of solar neutrinos grew with the observation of high energy ( $E > 5$  MeV) events by means of water Čerenkov detectors at the Kamioka mine in Japan (KamiokaNDE 1983-1995 [69, 70] and Super-KamiokaNDE 1996-present [71, 72]). These water Čerenkov detectors consist of a welded stainless-steel tank filled with pure water. Neutrino interactions are detected via the Čerenkov light emitted by the charged particles produced. The light emitted via Čerenkov effect is revealed by photomultipliers (PMTs) and it arranges in cones, whose orientation depends on the direction of the incoming particle. Thus, other than providing a spectroscopical information of neutrino interactions, it is possible to measure the direction of the incoming neutrino. The main drawback of this technique is the relatively high energy threshold (some MeV), which does not allow to measure the main components of the solar neutrino spectrum. This kind of detectors, and especially the KamiokaNDE detector, is very sensitive to the more energetic atmospheric neutrinos. In fact, KamiokaNDE's results on atmospheric neutrinos led to the unambiguous discovery of neutrino oscillations [73] together with the solar neutrino observations of the SNO experiment [74]. These results were celebrated with the Nobel Prize in physics in 2015, obtained by Takaaki Kajita for the KamiokaNDE experiment and by Arthur B. McDonald for the SNO experiment.

The SNO detector was a water Čerenkov neutrino detector with a design similar to those of KamiokaNDE and Super-KamiokaNDE. However, the strength and innovation of SNO consisted in the use of heavy water as a target (namely,  $\text{D}_2\text{O}$  at  $> 99.92\%$ , i. e. with deuterium instead of simple hydrogen). In heavy water, neutrinos can interact via the following processes:



where  $x = e, \mu$  or  $\tau$ . The CC process in Eq. (1.54) is sensitive only to electron neutrinos and produces a high energy electron, observable through Čerenkov light. The NC process in Eq. (1.55) is equally sensitive to all neutrino flavors and produces a free neutron, that was observed in different ways in the three phases of the SNO detector operation. By comparing appropriately calibrated rates for these two reactions it was possible to determine whether solar electron neutrinos had changed into other flavors before reaching the detector. The ES process of Eq. (1.56) is much weaker than the other two and is mostly sensitive to electron neutrinos. It produces an energetic electron, which is pointing the forward direction relative to the incident neutrino and therefore can be distinguished from the other two reactions by reference to the direction from the Sun [74].

The smoking gun of the observation of solar neutrino oscillations is Fig. 1.6. In this picture, a comparison of the measured solar neutrino fluxes from different experiments is shown, relative to the predicted flux from the SSM calculations from J. Bahcall of 2004. The analysis of the SNO data in the CC channel, the gallium and chlorine based radiochemical experiments, the KamiokaNDE and Super-KamiokaNDE water Čerenkov

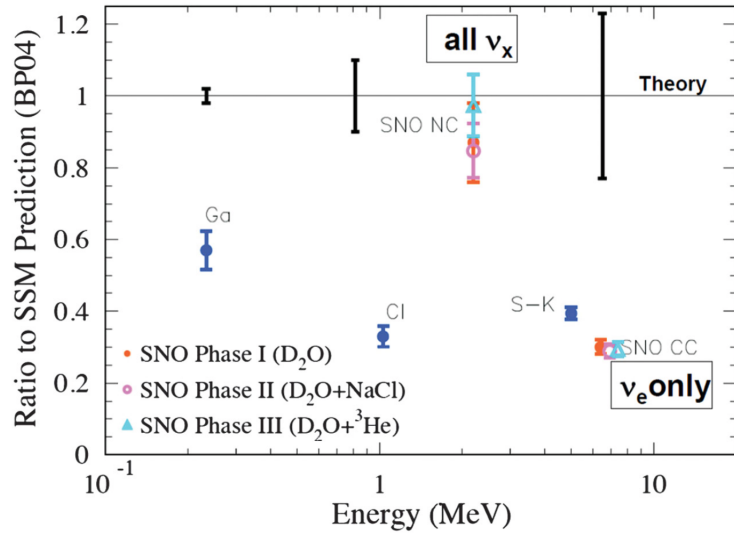


**Fig. 1.6:** Ratios of measurements of solar neutrino fluxes to calculations of electron neutrino fluxes in the core of the Sun using a SSM of 2004 from J. Bahcall. All the experiments sensitive to electron neutrinos only (gallium and chlorine radiochemical experiment, KamiokaNDE and Super-KamiokaNDE) show results in agreement with the CC measurement from SNO, but much below the predicted fluxes from the SSM. The SNO result on all neutrino species, instead, matches quite well the theoretical expectation. Picture from Ref. [74].

detectors, are sensitive only to electron neutrinos. The measured flux in this channel is a factor  $2 \div 3$  below the expectations. Instead, the inclusive analysis of all neutrino flavors done in SNO is in very good agreement with the SSM calculation, thus proving the existence of neutrino oscillations, since  $\nu_\mu$  and  $\nu_\tau$  cannot be produced in the nuclear reactions which power the Sun. As a final remark, SNO's analysis allowed to prove the existence of neutrino oscillations independently of any SSM assumption. The oscillation picture was then confirmed by the KamLAND reactor experiment [75].

After this golden era for neutrino physics, the development of new, more sensitive detectors started, with the aim of entering the precision age of solar neutrino measurements. Currently, the running solar neutrino experiments are Borexino, SAGE, Super-KamiokaNDE and KamLAND. Borexino and KamLAND are liquid scintillator detectors. The former one is one of the subjects of this PhD thesis and it is discussed in the following sections in greater details. The latter is a 1 kton liquid scintillator detector placed in the Kamioka mine in Japan, which was built for the detection of electron anti-neutrinos from nuclear reactors. Nonetheless, it could provide a measurement of the  $^8\text{B}$   $\nu$  flux above 5.5 MeV [76] and also an evidence of geo-neutrinos [77]. KamLAND has also measured  $^7\text{Be}$   $\nu$  with an error of  $\sim 15\%$ . At present, KamLAND is focused on the search for neutrinoless double beta decay, changing its name to KamLAND-Zen as it is discussed in Sec. 2.8.

## 1.10 Outlook on solar neutrino measurements

As discussed extensively in the previous Sec. 1.7, SSMs have progressed a lot in the last decades but still, there are some incompatibilities among the different sources of experimental data on the Sun composition and their interpretation. These problems might be solved with a high precision solar neutrino spectroscopy. Borexino gave and is expected to give a big contribution to this scientific developments. In particular, Borexino Phase-I achievements are discussed in Sec. 4.10, while the results on the longer and cleanest ever<sup>12</sup> Borexino Phase-II are the subject of this PhD thesis.

Another project which is just about to start is SNO+ [78]. SNO+ is a large liquid scintillator-based experiment located 2 km underground at SNOLAB, Sudbury, Canada. It reuses the SNO detector facility, consisting of a 12 m in diameter acrylic vessel which is filled with about 780 tonnes of ultra-pure liquid scintillator. Even if the ultimate goal is the search for the neutrinoless double-beta decay of  $^{130}\text{Te}$  (see Sec. 2.6.3), in the first filling phase of the detector, the possible impact of SNO+ for solar neutrino physics will be evaluated. In particular, if the background levels are low enough (i. e. at the level of Borexino or better), it will be possible for SNO+ to perform very accurate measurements of solar neutrino fluxes, given the huge sensitive mass.

On a longer time-scale, new technologies for the measurement of solar neutrinos are considered, see e. g. Ref. [79]. High precision solar neutrino spectroscopy requires exposures of the order of  $1\text{ kton} \cdot \text{yr}$ , with good energy resolution and extremely low background. Two-phase liquid argon time projection chambers are under development for direct Dark Matter WIMP searches [80]. They have large sensitive masses, high scintillation light yield, good energy resolution, and good spatial resolution in all three cartesian directions. Such detectors could reach a level of sensitivity extending to the “neutrino floor”<sup>13</sup> and could also enable precision measurements of solar neutrino fluxes in the neutrino-electron elastic scattering channel. In the example of Ref. [79], the authors suggest that a 100 ton liquid argon time projection chamber operating at Laboratori Nazionali del Gran Sasso at a depth of 3800 m of water equivalent could measure the CNO neutrino rate with  $\sim 15\%$  precision, and significantly improve the precision of the  $^7\text{Be} \nu$  and pep  $\nu$  rates compared to the currently available results from the Borexino organic liquid scintillator detector.

Solar neutrinos were pivotal to the discovery of neutrino oscillations and for establishing the MSW-LMA solution of the neutrino oscillation problem in the matter. After a few decades, the scientific community is still very active in improving the precision of both the experimental results and theoretical predictions on solar neutrinos, since this channel of observation can provide other very important inputs regarding the neutrino particle physics and the physics of the Sun’s interior.

---

<sup>12</sup>This refers to the fact that between Phase-I and Phase-II there were scintillator purifications which reduced some of the background contaminants.

<sup>13</sup>This terminology is often used in direct-search dark matter experiments to indicate the unavoidable background for dark matter created by the rate of nuclear recoil events from solar neutrino coherent scattering.

## Chapter 2

# Neutrinoless double beta decay experimental status and Borexino

In this chapter, the basic phenomenology and the current theoretical and experimental status on neutrinoless double beta decay ( $0\nu\beta\beta$ ) are discussed. The results reported here are fully based on the work presented in Refs. [1, 2, 3], which I contributed to develop. The main motivation for this apparent deviation from the main purpose of this PhD thesis, which is the precision measurement of solar neutrino fluxes with Borexino, comes from Borexino’s proposal of 1991 [81] and more directly from Ref. [82]. Already at the beginning of the 90’s, R. Raghavan suggested that the upcoming Borexino experiment could have been turned into a  $0\nu\beta\beta$  experiment, looking for the  $0\nu\beta\beta$  decay of  $^{136}\text{Xe}$  dissolved in the liquid scintillator. At the end of this chapter, some projected sensitivities for a “Borex-Xenon” like detector looking for  $0\nu\beta\beta$  of  $^{136}\text{Xe}$  are presented. In chapter 3, some experimental results on optical properties of liquid scintillators loaded with xenon are also discussed.

The chapter is structured as follows. Section 2.1 introduces the  $0\nu\beta\beta$ , Sec. 2.2 discusses the Majorana hypothesis for the neutrino mass term, Sec. 2.3 introduces possible mechanisms generating the  $0\nu\beta\beta$ , Sec. 2.4 highlights the present experimental knowledge on neutrino masses, Sec. 2.5 underlines the role of nuclear physics for  $0\nu\beta\beta$  investigations, Sec. 2.6 discusses the experimental search for  $0\nu\beta\beta$ , Sec. 2.7 shows the importance of cosmological surveys in assessing neutrino masses and  $0\nu\beta\beta$ , Sec. 2.8 introduces the strategy to look for  $0\nu\beta\beta$  with Borexino and Sec. 2.9 discusses the possible outlook for  $0\nu\beta\beta$  searches.

### 2.1 Introduction

In 1937, almost ten years after Paul Dirac’s “The quantum theory of electron” [83, 84], Ettore Majorana proposed a new way to describe fermions in a relativistic quantum field theory [85], and remarked that this could be especially useful for neutral particles. A single Majorana quantum field models the situation in which particles and antiparticles coincide. Giulio Racah stressed that such a field could fully describe massive neutrinos,

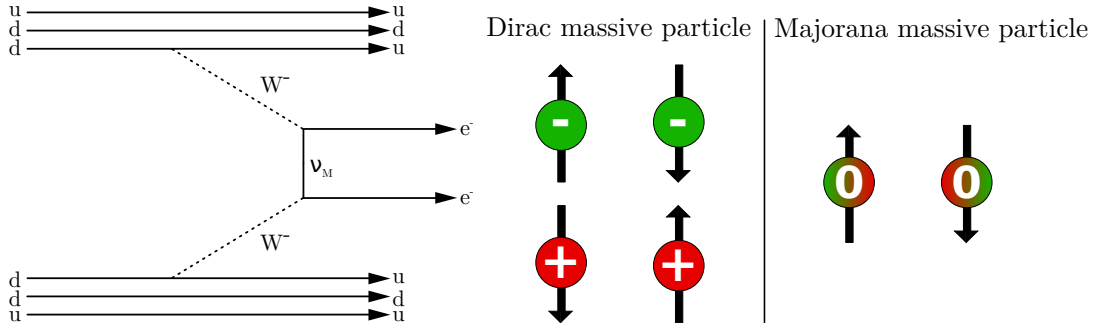


**Fig. 2.1:** *Left panel:* Diagram of the  $0\nu\beta\beta$  process due to the exchange of massive Majorana neutrinos, here denoted generically by  $\nu_M$ . *Right panel:* Massive fields in their rest frames. Arrows show the possible directions of the spin. (Left) The 4 states of a Dirac massive field. The signs indicate the charge that distinguishes particles and antiparticles, e.g. the electric charge of an electron. (Right) The 2 states of Majorana massive field. The symbol “zero” indicates the absence of any  $U(1)$  charge: particles and antiparticles coincide. Pictures taken from [3].

noting that Majorana’s theory leads to physical predictions essentially different from those coming from Dirac theory [86]. Two years later, Wendell Furry [87] studied within this scenario a new process similar to the “double beta disintegration”, introduced by Maria Goeppert-Mayer in 1935 [88]. It is the double beta decay without neutrino emission, or *neutrinoless double beta decay* ( $0\nu\beta\beta$ ). This process assumes a simple form:

$$(A, Z) \rightarrow (A, Z + 2) + 2e^- . \quad (2.1)$$

The Feynman diagram of the  $0\nu\beta\beta$  process, written in terms of massive Majorana neutrinos, is given in the left panel of Fig. 2.1.

The main feature of the  $0\nu\beta\beta$  transition is the explicit violation of lepton number through the creation of only a pair of electrons. A discovery of  $0\nu\beta\beta$  would therefore demonstrate that lepton number is not a symmetry of nature. This would support the exciting theoretical picture according to which leptons played a role in the creation of the matter-antimatter asymmetry in the universe [3].

On the theoretical side, the operator which gives rise to Majorana neutrino masses is the only one which is suppressed only by one power of the new mass scale [89]. On the experimental side, the discovery of neutrino oscillations and thus of non-zero neutrino masses strengthened the case for light massive neutrinos playing a major role for the  $0\nu\beta\beta$  transition. For these reasons  $0\nu\beta\beta$  is a key tool for studying neutrinos, probing whether their nature is the one of Majorana particles and providing precious information on the neutrino mass scale and ordering.

In the next sections, the available information on neutrino masses is considered and discussed, with particular emphasis on that coming from cosmological surveys. The nuclear matrix elements for  $0\nu\beta\beta$  have to be calculated (rather than measured) and are thus subject to uncertainties which are difficult to assess reliably. Moreover, the adopted methods of calculation do not precisely reproduce other measurable quantities (e.g. single beta decay or two-neutrino double beta decay). Therefore, a cautious/conservative

assessment of the theoretical ranges of these matrix elements is adopted and investigated here.

## 2.2 Majorana neutrinos

No elementary process leading to a variation either of the number of leptons or that of hadrons has been observed yet. The SM in its minimal formulation has various global symmetries, including  $B$  (baryon number) and  $L$  (lepton number), which are called “accidental”.<sup>1</sup> This is sufficient to forbid the  $0\nu\beta\beta$  transition completely in the SM. In other words, a hypothetical evidence for such a transition would directly point out to physics beyond the SM.

Majorana’s theory of massive and “real” fermions [85] contains less fields than the one used by Dirac for the description of the electron [83, 84] and, in this sense, it is simpler. Following the formalism introduced in 1933 by Fermi when describing the  $\beta$  decay [90], the condition of reality for a quantized fermionic field can be written as:

$$\chi = C\bar{\chi}^t, \quad (2.2)$$

where  $C$  is the charge conjugation matrix, while  $\bar{\chi} \equiv \chi^\dagger \gamma_0$  is the Dirac conjugate of the field. In particular, Majorana advocated a specific choice of the Dirac  $\gamma$ -matrices, such that  $C\gamma_0^t = 1$ , which simplifies various equations. The free particle Lagrangian density formally coincides with the usual one:

$$\mathcal{L}_{\text{Majorana}} = \frac{1}{2}\bar{\chi}(i\partial - m)\chi. \quad (2.3)$$

The right panel of Fig. 2.1 illustrates the comparison between the particle content both of a Dirac and a Majorana field in the case of the rest frame. Evidently, a Majorana neutrino is incompatible with any  $U(1)$  transformation, e. g.  $L$  or the weak hypercharge. In general,  $L$  is violated by the presence of a Majorana mass.

In the SM, only the left-handed components of neutrino fields ( $\psi_L$ ) are coupled to weak interactions. It is possible to implement the hypothesis of Majorana in the most direct way by defining the real field

$$\chi \equiv \psi_L + C\bar{\psi}_L^t. \quad (2.4)$$

The SM field can be easily obtained with a projection:

$$\psi_L \equiv \frac{1 - \gamma^5}{2}\chi. \quad (2.5)$$

---

<sup>1</sup> Actually  $B$  and  $L$  individually are not conserved in the SM, see Sec. 2.2.1.

### 2.2.1 Leptogenesis and right-handed neutrinos

Although particles and anti-particles have the same importance in the current understanding of particle physics, the Universe contains mostly baryons rather than anti-baryons.<sup>2</sup> In 1967, Sakharov proposed a set of necessary conditions to generate the cosmic baryon asymmetry [91]:

- Existence of at least one  $B$  violating process.
- Existence of  $C$  and  $CP$  violations.
- Existence of interactions outside of thermal equilibrium during baryogenesis.

In the SM, although  $L$  and  $B$  are not conserved separately at the non-perturbative level [92, 93, 94], the observed value of the Higgs mass is not big enough to account for the observed baryon asymmetry [95, 96]. An attractive theoretical possibility is that right-handed neutrinos not only enhance the SM endowing neutrinos with Majorana mass, but also produce a certain amount of leptonic asymmetry in the Universe. This is subsequently converted into a baryonic asymmetry thanks to  $B + L$  violating effects, which are built-in in the SM. It is the so called “leptogenesis mechanism”. The initial proposal of leptogenesis dates back to 1980s [97], and there is a large consensus that this type of idea is viable and attractive. Subsequent investigators showed that the number of alternative theoretical possibilities is very large and, in particular, that there are other possible sources of  $L$  violations besides right-handed neutrinos. Conversely, the number of testable possibilities is quite limited [98].

### 2.2.2 Neutrino nature and cosmic neutrino background

The Big Bang theory predicts that the present Universe is left with a residual population of  $\sim 56$  non-relativistic neutrinos and antineutrinos per  $\text{cm}^3$  and per species. It constitutes a Cosmic Neutrino Background (CνB). The detection of the CνB could allow to understand which hypothesis (Majorana or Dirac) applies for the neutrino description. Electron neutrinos of the CνB could be detected through the reaction [99, 100]



In the standard assumption of a homogeneous Fermi-Dirac distribution of the CνB, one expects  $\sim 8$  events per year per 100g of  ${}^3\text{H}$ , if neutrinos are Majorana particles, and about half if the Dirac hypothesis applies [101]. In the former case, the states with positive helicity (by definition, antineutrinos) act just as neutrinos, since they are almost at rest. Instead, in the latter case, *they are antineutrinos* and thus they do not interact.

It can be noticed that the signal rate is not prohibitively small, but the major difficulty consists in attaining a sufficient energy resolution to keep at a manageable level the background from beta decay (for further details see Refs. [100, 101]).

---

<sup>2</sup>The lepton number in the Universe is probed much less precisely. Cosmic neutrinos and anti-neutrinos are abundant, but it is not easy to measure their asymmetry which, according to standard cosmology, should be very small.

## 2.3 Particle physics mechanisms for $0\nu\beta\beta$

The exchange of light Majorana neutrinos is up to now the most appealing mechanism to possibly explain the  $0\nu\beta\beta$ . Other theoretical explanations are possible, but they are less probable according to the present evidence. In this section, the basic aspects of the light neutrino exchange mechanism for  $0\nu\beta\beta$  are reviewed and alternatives to this model are briefly mentioned.

Due to the reality condition, Eq. (2.3) can lead to new types of propagators that do not exist within the Dirac theory [3]. In the low energy limit (relevant for  $\beta$  decay processes) neutrino interactions are well described by the current-current 4-fermion interactions, corresponding to the Hamiltonian of Eq. (1.1). In order to implement the Majorana hypothesis, one can use Eq. (2.4) and introduce the field  $\chi = \psi_L + C\bar{\psi}_L^t$ .

A contribution to the  $0\nu\beta\beta$  transition arises at the second order of the Fermi interaction. The core of the operator describing the  $0\nu\beta\beta$  process through the exchange of neutrinos is essentially the ordinary propagator sandwiched between two chiral projectors<sup>3</sup> [3]:

$$P_L \Delta(x) P_L = P_L \int \frac{d^4 q}{(2\pi)^4} \frac{i m}{q^2 - m^2 + i0} e^{-iqx}. \quad (2.7)$$

The momentum  $q$  represents the virtuality of the neutrino, whose value is connected to the momenta of the final state electrons and to those of the intermediate virtual nucleons. In particular, since the latter are confined in the nucleus, the typical 3-momenta are of the order of the inverse of the nucleonic size, namely

$$|\vec{q}| \sim \hbar c/\text{fm} \sim \text{a few } 10^2 \text{ MeV}, \quad (2.8)$$

whereas the energy ( $q_0$ ) is smaller (a few MeV). The comparison of this scale with the one of neutrino mass identifies and separates “light” from “heavy” neutrinos for what concerns  $0\nu\beta\beta$ .

The most interesting mechanism for  $0\nu\beta\beta$  is the one that sees light neutrinos as mediators, and it is described in greater detail in the next sections. It is the one originally considered in Ref. [87] and the main reason for which the hypothesis that the  $0\nu\beta\beta$  receives its main contribution from light Majorana neutrinos is the fact that experiments point out the existence of three light massive neutrinos. In the case of a heavy neutrino mixing with active neutrinos, the propagator of Eq. (2.7) simply becomes proportional to  $1/M_H$ , where  $M_H$  is the heavy neutrino mass. More in general, such a definition can be used in an effective formula<sup>4</sup>, but a gauge model requires to express  $M_H$  in terms of the single right-handed neutrino mass  $M_I$  and of the mixing between the left-handed neutrino  $\nu_{eL}$  and the heavy neutrino:

$$\frac{1}{M_H} = \frac{U_{eI}^2}{M_I}. \quad (2.9)$$

---

<sup>3</sup> $P_L = \frac{1-\gamma^5}{2}$ .

<sup>4</sup>This means that  $M_H$  is the “effective” heavy neutrino mass for the  $0\nu\beta\beta$ . This is exactly the same as the effective Majorana mass introduced in Sec. 2.4.1.

In particular, in typically considered Seesaw type I models, the mixings are small if  $M_I$  is large, since  $U_{ei} \propto 1/M_I$  [3]. This suggests a suppression of the above effective operator with the cube of  $M_I$ , whereas the light neutrino exchange mechanism leads to a milder suppression, linear in  $M_I$ .

Alternative mechanisms for allowing the  $0\nu\beta\beta$  without the exchange of neutrinos have been proposed throughout the years. A review about the most significative ones can be found in Ref. [3].

A final remark concerns the result of the well-known work of Ref. [102] by Schechter and Valle, where it is shown that from the  $0\nu\beta\beta$  observation it is possible to conclude the existence of a Majorana mass. The size of the neutrino masses is not indicated in the original work, but a rough estimation shows that they are so small that they have no physical interest, being of the order of  $10^{-24}$  eV [103, 3].

## 2.4 Present knowledge on neutrino masses

The crucial parameter describing the  $0\nu\beta\beta$  if the process is mediated by light Majorana neutrinos is discussed. Also, the present information coming from the oscillation parameters, cosmology and other data is reported.

### 2.4.1 The parameter $m_{\beta\beta}$

The Majorana mass term in the Lagrangian density is described by a symmetric matrix:

$$\mathcal{L}_{\text{mass}} = \frac{1}{2} \sum_{\ell, \ell' = e, \mu, \tau} \nu_{\ell}^t C^{-1} M_{\ell \ell'} \nu_{\ell'} + h. c.. \quad (2.10)$$

The only term that violates the electronic number by two units is  $M_{ee}$ , and this simple consideration motivates the fact that the amplitude of the  $0\nu\beta\beta$  decay has to be proportional to this parameters, while the width to its squared modulus. One can diagonalize the neutrino mass matrix by means of a unitary matrix:

$$M = U^t \text{diag}(m_1, m_2, m_3) U^{\dagger}. \quad (2.11)$$

It is therefore useful to define:

$$m_{\beta\beta} \equiv \left| \sum_{i=1,2,3} U_{ei}^2 m_i \right|, \quad (2.12)$$

where the index  $i$  runs on the 3 light neutrinos with given masses. This parameter is often called “effective Majorana mass”.

The previous intuitive argument in favor of this definition is corroborated by calculating the Feynman diagram of Fig. 2.1. The neutrino propagator of Fig. 2.1 brings a factor  $m_i$ , while in the two leptonic vertices the mixing  $U_{ei}$  must be considered. Taking the product of these factors, one gets the expression given in Eq. (2.12).

In the case of  $0\nu\beta\beta$ , the two Majorana phases introduced in Eq. (1.12) cannot be rotated away and have a physical role. This is not true in the case of oscillation experiments, as anticipated in Sec. 1.3.1.

### 2.4.2 Oscillations

In Ref. [104], a complete analysis of the current knowledge of oscillation parameters and of neutrino masses is performed. Although the absolute neutrino mass scale is still unknown, oscillation experiments measured the squared mass splittings between the three active neutrinos. In Tab. 2.1, the results are reported. The mass splittings are labeled by  $\delta m^2$  and  $\Delta m^2$ . The former is measured through the observation of solar neutrino oscillations, while the latter comes from atmospheric neutrino data.

Parameter	Best fit	$1\sigma$ range	$\sigma_{\text{symmetric}}$
$\mathcal{NH}$			
$\sin^2(\theta_{12})$	$2.97 \cdot 10^{-1}$	$(2.81 - 3.14) \cdot 10^{-1}$	$0.17 \cdot 10^{-1}$
$\sin^2(\theta_{13})$	$2.14 \cdot 10^{-2}$	$(2.05 - 2.25) \cdot 10^{-2}$	$0.10 \cdot 10^{-2}$
$\sin^2(\theta_{23})$	$4.37 \cdot 10^{-1}$	$(4.17 - 4.70) \cdot 10^{-1}$	$0.33 \cdot 10^{-1}$
$\delta m^2$ [eV $^2$ ]	$7.37 \cdot 10^{-5}$	$(7.21 - 7.54) \cdot 10^{-5}$	$0.17 \cdot 10^{-5}$
$\Delta m^2$ [eV $^2$ ]	$2.50 \cdot 10^{-3}$	$(2.46 - 2.54) \cdot 10^{-3}$	$0.04 \cdot 10^{-3}$
$\mathcal{IH}$			
$\sin^2(\theta_{12})$	$2.97 \cdot 10^{-1}$	$(2.81 - 3.14) \cdot 10^{-1}$	$0.17 \cdot 10^{-1}$
$\sin^2(\theta_{13})$	$2.18 \cdot 10^{-2}$	$(2.06 - 2.27) \cdot 10^{-2}$	$0.11 \cdot 10^{-2}$
$\sin^2(\theta_{23})$	$5.69 \cdot 10^{-1}$	$(5.18 - 5.97) \cdot 10^{-1}$	$0.32 \cdot 10^{-1}$
$\delta m^2$ [eV $^2$ ]	$7.37 \cdot 10^{-5}$	$(7.21 - 7.54) \cdot 10^{-5}$	$0.17 \cdot 10^{-5}$
$\Delta m^2$ [eV $^2$ ]	$2.46 \cdot 10^{-3}$	$(2.42 - 2.51) \cdot 10^{-3}$	$0.05 \cdot 10^{-3}$

**Tab. 2.1:** Results of the global  $3\nu$  oscillation analysis, in terms of best-fit values and allowed  $1\sigma$  range for the  $3\nu$  mass-mixing parameters as reported in Ref. [104]. The last column is our estimate of the  $\sigma$  while assuming symmetric uncertainties. Note that  $\theta_{23}$  flips from the first to the second octant when assuming  $\mathcal{NH}$  or  $\mathcal{IH}$  respectively. However, there is no statistical significance in this fact.

The definitions of these two parameters are the following:

$$\delta m^2 \equiv m_2^2 - m_1^2 \quad \text{and} \quad \Delta m^2 \equiv m_3^2 - \frac{m_1^2 + m_2^2}{2}. \quad (2.13)$$

In practice,  $\delta m^2$  is the splitting between  $\nu_1$  and  $\nu_2$ , while  $\Delta m^2$  refers to the distance between the  $\nu_3$  mass and the mid-point of  $\nu_1$  and  $\nu_2$  masses.

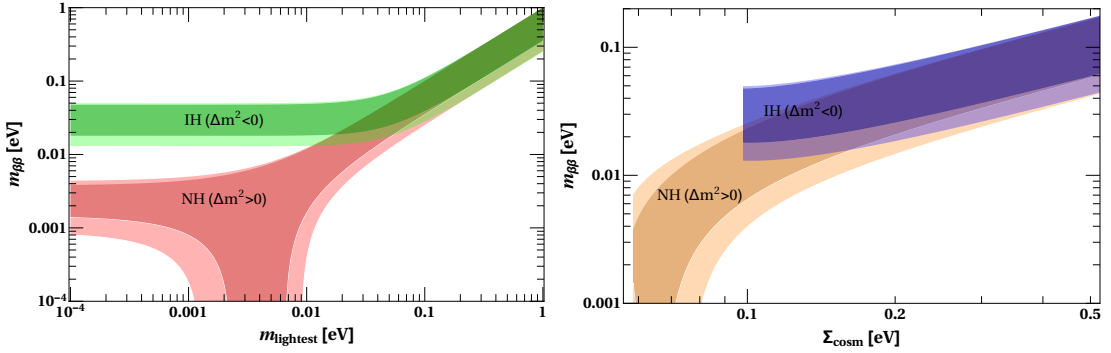


**Fig. 2.2:** *Left Panel:* Updated predictions on  $m_{\beta\beta}$  from oscillations as a function of the lightest neutrino mass in the two cases of  $\mathcal{NH}$  and  $\mathcal{IH}$ . The shaded areas correspond to the  $3\sigma$  regions due to error propagation of the uncertainties on the oscillation parameters. *Right Panel:* Updated predictions on  $m_{\beta\beta}$  from oscillations as a function of the cosmological mass  $\Sigma$  in the two cases of  $\mathcal{NH}$  and  $\mathcal{IH}$ . The shaded areas correspond to the  $3\sigma$  regions due to error propagation of the uncertainties on the oscillation parameters.

The sign of  $\delta m^2$  can be determined by observing matter enhanced oscillations as explained within the MSW theory introduced in Sec. 1.4. It turns out that  $\delta m^2 > 0$  [105]. The sign of  $\Delta m^2$  is still unknown and it is not simple to measure it. However, it was argued (see e. g. Ref. [106]) that by carefully measuring the oscillation pattern, it could be possible to distinguish between the two possibilities,  $\Delta m^2 > 0$  and  $\Delta m^2 < 0$ . This is a very promising perspective in order to solve this ambiguity, which is sometimes referred to as the “mass hierarchy problem”, since the two mentioned possibilities for the neutrino mass spectra are usually referred to as “Normal Hierarchy” ( $\mathcal{NH}$ ) for  $\Delta m^2 > 0$  and “Inverted Hierarchy” ( $\mathcal{IH}$ ) for  $\Delta m^2 < 0$ .

The experimental values of  $\delta m^2$  and  $\Delta m^2$  (see Tab. 2.1) clarify why it is possible to refer just to the two neutrino mixing scenario for most of the oscillation experiments. The oscillation probability of  $\nu_i$  into  $\nu_j$  depends on the parameter  $\frac{\Delta m_{ij}^2 L}{4E}$ , where  $\Delta m_{ij}^2 = m_i^2 - m_j^2$ ,  $E$  is the neutrino energy and  $L$  is the travelled distance. Therefore, with a proper choice of the beam energy and of the distance between production and detection points, one can enhance a particular oscillation channel, making the others negligible. For instance, for experiments sensitive to  $\Delta m^2$ , i. e. those for which  $\frac{\Delta m^2 L}{4E} \sim 1$ ,  $\frac{\delta m^2 L}{4E} \ll 1$ , meaning that the contribution from the mixing angle  $\theta_{12}$  is negligible in this regime. On the contrary, when  $\frac{\delta m^2 L}{4E} \sim 1$ , oscillations induced by  $\theta_{23}$  are averaged out.

Thanks to the knowledge of the oscillation parameters, it is possible to put a first series of constraints on  $m_{\beta\beta}$ . However, since Majorana phases cannot be probed by oscillations, the allowed region for  $m_{\beta\beta}$  is obtained letting them vary freely. The expressions for the resulting extremes (i. e. the  $m_{\beta\beta}$  maximum and minimum values due to the phase variation) can be found in Ref. [3]. In the left panel of Fig. 2.2,  $m_{\beta\beta}$  is plotted as a function of the mass of the lightest neutrino, both for the cases of  $\mathcal{NH}$  and of  $\mathcal{IH}$ . The uncertainties on the various parameters are propagated using the procedures described

in Ref. [3]. This results in a wider allowed region, which corresponds to the shaded parts in the picture.

### 2.4.3 Cosmology and neutrino masses

#### The parameter $\Sigma$

The three light neutrino scenario is consistent with all experimental evidences, including the new measurements by Planck [107]. Thus, the physical quantity probed by cosmological surveys,  $\Sigma$ , is the sum of the masses of the three light neutrinos:

$$\Sigma \equiv m_1 + m_2 + m_3. \quad (2.14)$$

Depending on the mass hierarchy, it is possible to express  $\Sigma$  as a function of the lightest neutrino mass  $m$  and of the oscillation mass splittings. In particular, in the case of  $\mathcal{NH}$  one gets:

$$\begin{cases} m_1 = m \\ m_2 = \sqrt{m^2 + \delta m^2} \\ m_3 = \sqrt{m^2 + \Delta m^2 + \delta m^2/2}, \end{cases} \quad (2.15)$$

while, in the case of  $\mathcal{IH}$ :

$$\begin{cases} m_1 = \sqrt{m^2 + \Delta m^2 - \delta m^2/2} \\ m_2 = \sqrt{m^2 + \Delta m^2 + \delta m^2/2} \\ m_3 = m. \end{cases} \quad (2.16)$$

It can be useful to compute the mass of the lightest neutrino, given a value of  $\Sigma$ . This can be convenient in order to compute  $m_{\beta\beta}$  as a function of  $\Sigma$  instead of  $m$ .<sup>5</sup> In this way,  $m_{\beta\beta}$  is expressed as a function of a directly observable parameter.

The close connection between the neutrino mass measurements obtained in laboratory and those probed by cosmological observations was outlined long ago [108]. Furthermore, the measurements of  $\Sigma$  have recently reached important sensitivities, as discussed in Sec. 2.7. In the right panel of Fig. 2.2, an updated version of the plot ( $m_{\beta\beta}$  vs.  $\Sigma$ ) originally introduced in Ref. [109] is shown.

#### Constraints from cosmological surveys

Indications for neutrino masses from cosmology have kept changing for 20 years. A comprehensive review on the topic can be found in Ref. [114]. In Fig. 2.3 the values for  $\Sigma$  given in Refs. [110, 111, 112, 113] are shown. The scientific literature contains several authoritative claims for a non-zero value for  $\Sigma$  but, being different among each others,

---

<sup>5</sup>In Ref. [3], an approximate (but accurate) alternative method for the numerical calculation needed to make this conversion is given.

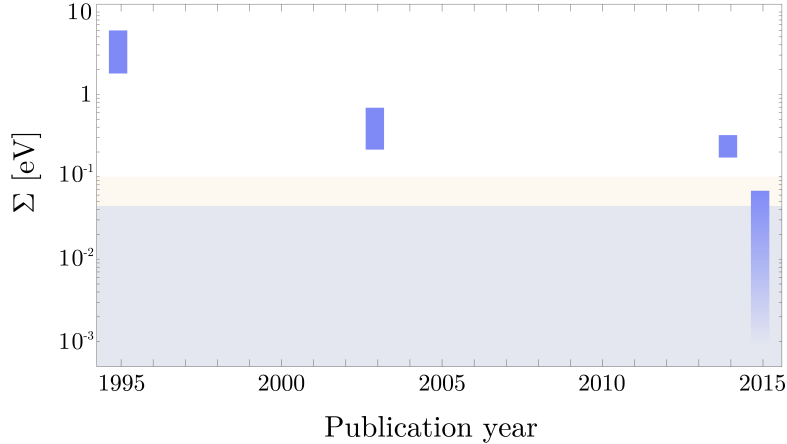


**Fig. 2.3:** Evolution of some significant values for  $\Sigma$  as indicated by cosmology, based on Refs. [110, 111, 112, 113]. Whenever not reported in the reference, an error of 50% is assumed for the purpose of illustration. The yellow region includes values of  $\Sigma$  compatible with the  $\mathcal{NH}$  spectrum, but not with the  $\mathcal{IH}$  one. The light blue band includes values of  $\Sigma$  incompatible with the standard cosmology and with oscillation experiments.

these values cannot be all correct (at least) and this calls for a cautious attitude in their interpretation.

The most recent limit on  $\Sigma$  is so stringent, that it better agrees with the  $\mathcal{NH}$  spectrum, rather than with the  $\mathcal{IH}$  one (see the discussion in Sec. 2.7).<sup>6</sup>

Quite recently, a very stringent limit  $\Sigma < 146$  meV ( $2\sigma$  C. L.) was set by Palanque-Delabrouille and collaborators [113].

Some of the most significant results on  $\Sigma$  from various analyses are reported in Tab. 2.2. The bounds on  $\Sigma$  indicated by these post-Planck 2015 studies are quite small, but they are still larger than the final sensitivities expected, especially thanks to the inclusion of other cosmological data sets probing smaller scales (see e. g. Refs. [116, 117] for review works). Therefore, these small values cannot be considered surprising and, conversely, further progress should be expected.

#### 2.4.4 Other non-oscillation data

For the sake of completeness, there are other two potential sources of information on neutrino masses:

- the study of kinematic effects (in particular of supernova neutrinos).
- the investigation of the effect of mass in single beta decay processes.

<sup>6</sup>It was shown in Ref. [115] that the presence in the nuclear medium of  $L$ -violating four-fermion interactions could account for an apparent incompatibility between the  $0\nu\beta\beta$  searches in the laboratory and the cosmological data. The net effect of these interactions would be the generation of an effective “in-medium” Majorana neutrino mass matrix with a corresponding enhancement of the  $0\nu\beta\beta$  rate.

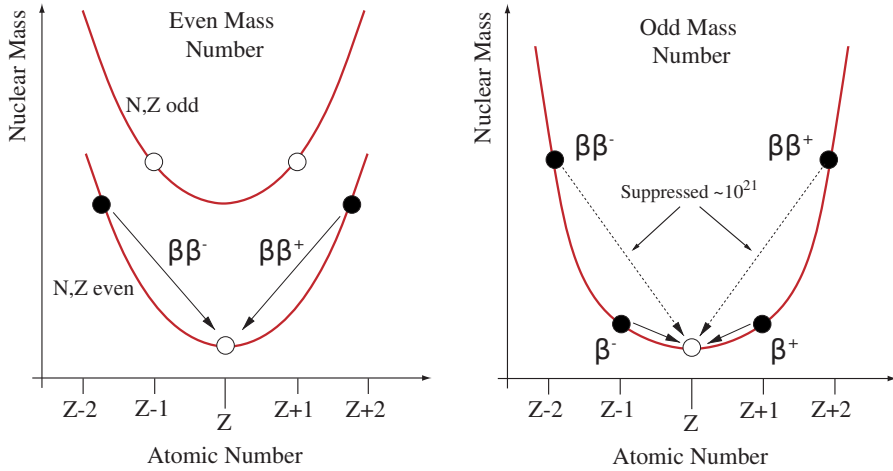


**Fig. 2.4:** Nuclear mass as a function of the atomic number  $Z$  in the case of an isobar candidate with  $A$  even (left) and  $A$  odd (right).

The first type of investigations, applied to SN1987A, produced a limit of about 6 eV on the electron antineutrino mass [122, 123]. Future prospects are connected to new detectors, or to the existence of antineutrino pulses in the first instants of a supernova emission. The second approach, instead, is presently limited to about 2 eV [124, 125], even having the advantage of being obtained in laboratory conditions. Its future is currently in the hands of new experiments based on a  ${}^3\text{H}$  source [126] and on the electron capture of  ${}^{163}\text{Ho}$  [127, 128, 129], which have the potential to reach a sub-eV sensitivity.

## 2.5 The role of nuclear physics

$0\nu\beta\beta$  is first of all a nuclear process. The transition has to be described taking into account the relevant aspects that concern nuclear structure and dynamics. In particular, it is a second order nuclear weak process and it corresponds to the transition from a nucleus  $(A, Z)$  to its isobar  $(A, Z + 2)$  with the emission of two electrons. In principle,

upper bound on $\Sigma$ ( $2\sigma$ C. L.)	included dataset
153 meV [107] <sup>a</sup>	SNe, BAO, $H_0$ prior
120 meV [118]	Lyman- $\alpha$
126 meV [119]	BAO, $H_0, \tau$ priors, Planck SZ clusters
177 meV [120]	BAO
110 meV [121]	BAO, galaxy clustering, lensing

<sup>a</sup>Results as reported in [wiki.cosmos.esa.int/planckpla2015](http://wiki.cosmos.esa.int/planckpla2015), page 311.

**Tab. 2.2:** Tight constraints on  $\Sigma$  obtained in 2015, by analyzing the data on the CMB by the Planck Collaboration [107], polarization included, along with other relevant cosmological data sets probing smaller scales.

a nucleus ( $A, Z$ ) can decay via double beta decay as long as the nucleus ( $A, Z + 2$ ) is lighter. However, if the nucleus could also decay by single beta decay, the  $0\nu\beta\beta$  would be too difficult to be observed due to the overwhelming background rate from the single beta decay. Therefore, candidate isotopes for detecting the  $0\nu\beta\beta$  are even-even nuclei<sup>7</sup> that, due to the nuclear pairing force, are lighter than the odd-odd ( $A, Z + 1$ ) nucleus, making single beta decay kinematically forbidden (see Fig. 2.4). However, it is worth to mention that single beta decays of  $^{48}\text{Ca}$  and  $^{96}\text{Zr}$  are kinematically allowed, but strongly suppressed because of a “big” change in spin. As a result, the  $2\nu\beta\beta$  decay was already observed for these nuclei, while the single beta decay was not (see Ref. [130]).

The theoretical expression of the half-life of the process in a certain nuclear species can be factorized as [1]:

$$[t_{1/2}]^{-1} = G_{0\nu} |\mathcal{M}|^2 |f(m_i, U_{ei})|^2, \quad (2.17)$$

where  $G_{0\nu}$  is the phase space factor (PSF),  $\mathcal{M}$  is the nuclear matrix element (NME) and  $f(m_i, U_{ei})$  is an adimensional function containing the particle physics beyond the SM that could explain the decay through the neutrino masses  $m_i$  and the mixing matrix elements  $U_{ei}$ . In this section, the discussion is restricted to the case of light neutrino exchange as candidate process for mediating the  $0\nu\beta\beta$  transition, as already discussed in Sec. 2.3. Therefore, the factor  $f$  is proportional to  $m_{\beta\beta}$ :

$$f(m_i, U_{ei}) \equiv \frac{m_{\beta\beta}}{m_e} = \frac{1}{m_e} \left| \sum_{k=1,2,3} U_{ek}^2 m_k \right|, \quad (2.18)$$

where the electron mass  $m_e$  is taken as a reference value.

### 2.5.1 Recent developments on the phase space factor calculations

The first calculations of PSFs date back to the late 1950s [131] and used a simplified description of the wave functions. Recent developments in the numerical evaluation of Dirac wave functions and in the solution of the Thomas-Fermi equation allowed to calculate accurately the PSFs both for single and double beta decay. The new calculations take into account relativistic corrections, the finite nuclear size and the effect of the atomic screening on the emitted electrons. The main difference between these calculations and the older ones is of the order of a few percent for light nuclei ( $Z = 20$ ), about 30% for Nd ( $Z = 60$ ), and a rather large 90% for U ( $Z = 92$ ).

In Refs. [132, 133, 134], the most up to date calculations of the PSFs for  $0\nu\beta\beta$  can be found. For obtaining all the results presented in this PhD thesis, the values from the first reference are used.

### 2.5.2 Models for the NMEs

The calculation of the NMEs for the  $0\nu\beta\beta$  is a difficult task because the ground and many excited states of open-shell nuclei with complicated nuclear structures have to

---

<sup>7</sup>Note that this automatically implies that their spin is zero.

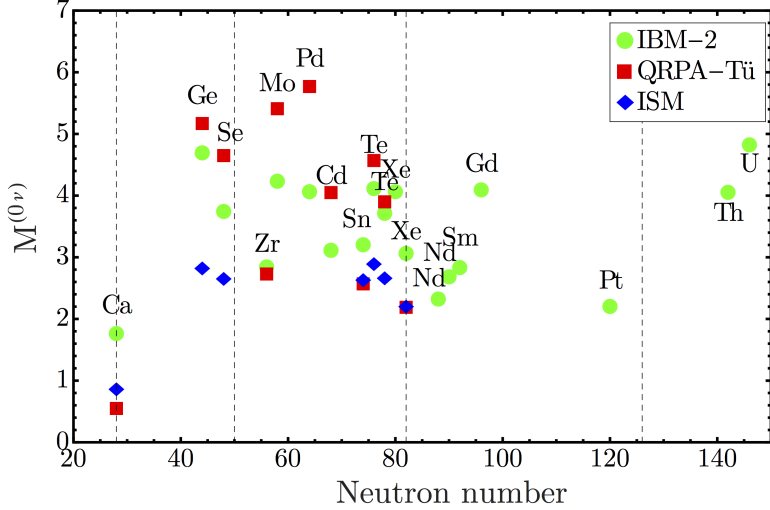


**Fig. 2.5:** Most updated NMEs calculations for the  $0\nu\beta\beta$  with the IBM-2 [135], QRPA-Tü [136] and ISM [137] models. The results somehow differ among the models, but are not too far away. Figure from Ref. [135].

be considered. The problem is faced by using different approaches and, especially in the last few years, the reliability of the calculations improved a lot. The most relevant theoretical models are the Interacting Shell Model (ISM, [138, 137]), the Quasiparticle Random Phase Approximation (QRPA, [136, 139, 140]) and the Interacting Boson Model (IBM-2, [135]). A short description of the main features of these models (and others) can be found in Ref. [3].

A convenient parametrization for the NMEs is the following [141]:

$$\mathcal{M} \equiv g_A^2 \mathcal{M}_{0\nu} = g_A^2 \left( M_{GT}^{(0\nu)} - \left( \frac{g_V}{g_A} \right)^2 M_F^{(0\nu)} + M_T^{(0\nu)} \right), \quad (2.19)$$

where  $g_V$  and  $g_A$  are the axial and vector coupling constants of the nucleon,  $M_{GT}^{(0\nu)}$  is the Gamow-Teller (GT) operator matrix element between initial and final states (spin-spin interaction),  $M_F^{(0\nu)}$  is the Fermi contribution (spin independent interaction) and  $M_T^{(0\nu)}$  is the tensor operator matrix element. The form of Eq. (2.19) emphasizes the role of  $g_A$ . In fact,  $\mathcal{M}_{0\nu}$  mildly depends on  $g_A$  and can be evaluated by modeling theoretically the nucleus. Actually, it is independent on  $g_A$  if the same quenching is assumed both for the vector and axial coupling constants [142].

In Fig. 2.5, a comparison among the most recent NME calculations computed with these three models is shown. The disagreement can be generally quantified in some tens of percents, instead of the factors  $2 \div 4$  of the past. As discussed in Sec. 2.5.3, the main source of uncertainty in the inference does not rely in the NME calculations anymore, and for this reason in the next sections only the results from IBM-2 [135] are used, without any loss of generality.

### 2.5.3 Theoretical uncertainties

From Eq. (2.17), it follows that an experimental limit on the  $0\nu\beta\beta$  half-life implies a limit on the effective Majorana mass:

$$m_{\beta\beta} \leq \frac{m_e}{\mathcal{M} \sqrt{G_{0\nu} t_{1/2}}}. \quad (2.20)$$

In order to constrain  $m_{\beta\beta}$ , the estimation of the uncertainties both on  $G_{0\nu}$  and  $\mathcal{M}$  is crucial.

The PSFs can be assumed quite well known, being the error on their most recent calculations around  $\sim 7\%$  [132].

The main sources of uncertainties on  $m_{\beta\beta}$  are the NMEs. A comparison of the calculations from 1984 to 1998 revealed an uncertainty of more than a factor 4 [143]. An important step forward was made with the first calculations that estimated also the errors, see Refs. [144, 145]. These works, based on the QRPA model, assessed a relatively small intrinsic error of  $\sim 20\%$ . The validity of these conclusions has been recently supported by the (independent) calculation based on the IBM-2 description of the nuclei [132, 135], which assesses an intrinsic error of 15% on  $\mathcal{M}_{0\nu}$ . However, each scheme of calculation can estimate its own uncertainty, but it is still hard to understand the differences in the results among the models (Fig. 2.5) and thus give an overall error.

Recently, there has been a lively interest in a specific and important reason of uncertainty, the value of the axial coupling constant  $g_A$ . If the value of the axial coupling in the nuclear medium is decreased by a factor  $\delta$ , namely  $g_A \rightarrow g_A \cdot (1 - \delta)$ , the expected decay rate and therefore the number of signal events  $S$  also decreases, approximatively as  $S \cdot (1 - \delta)^4$ . The statistical significance of a hypothetical measurement, instead, changes only with the square root of the time or of the mass, in the typical case in which there are also background events  $B$  (see Sec. 2.6.1 for further details). For instance, a decrease by  $\delta = 10$  (20)% of the axial coupling, means that the same sensitivity can be achieved after a time that is larger by a factor of  $1/(1 - \delta)^8 = 2.3$  (6).

It is commonly expected that the value  $g_A \simeq 1.269$  measured in the weak interactions and decays of nucleons is “renormalized” in the nuclear medium towards the value appropriate for quarks [144, 145, 146]. It was argued in Ref. [142] that a further modification (reduction) is rather plausible. This is in agreement with what was stated some years before in Ref. [147], where the possibility of a “strong quenching” of  $g_A$  (i. e.  $g_A < 1$ ) is actually favored. The same was also confirmed by recent study on single beta decay and  $2\nu\beta\beta$  [148]. It has to be noticed that within the QRPA framework, the dependence of  $\mathcal{M}$  upon  $g_A$  is actually milder than quadratic, because the model is calibrated through the experimental  $2\nu\beta\beta$  decay rates using also another parameter, the particle-particle strength  $g_{pp}$  [149].

There could be different causes for the quenching of  $g_A$ . It was found that it can be attributed mainly to the limited model space (i. e. the size of the basis of the eigenstates) in which the calculation is done, to the contribution of non-nucleonic degrees of freedom and to the renormalization of the GT operator due to two-body currents. More details are given in Refs. [142, 150]. It is still not clear if the quenching observed in  $2\nu\beta\beta$  transitions

is the same as the one expected for the  $0\nu\beta\beta$ .  $2\nu\beta\beta$  can occur only through a GT ( $1^+$ ) transition. Instead, the  $0\nu\beta\beta$  could happen through all the possible intermediate states, so one could argue that the transitions through states with spin parity different from  $1^+$  can be unquenched or even enhanced. Incidentally, it turns out that the dominant multipole in the  $0\nu\beta\beta$  transition is the GT one, thus making the hypothesis that the quenching in  $2\nu\beta\beta$  and  $0\nu\beta\beta$  is the same quite solid. This is what is found within the IBM-2 model [135], however some indications that the quenching might be different in the  $0\nu\beta\beta$  and  $2\nu\beta\beta$  transitions are present in other models [151, 137]. It would be extremely precious if these theoretical questions could be answered by some experimental data. Experimental studies of nuclear transitions where the nuclear charge is changed by two units leaving the mass number unvaried in analogy to the  $0\nu\beta\beta$  decay, could give important information. Despite the Double Charge Exchange reactions and  $0\nu\beta\beta$  processes are mediated by different interactions, some similarities between the two cases are present. These could be exploited to assess effectively the NME for the  $0\nu\beta\beta$  (and, more specifically, the entity of the quenching of  $g_A$ ). In the near future, a new project will start at the Laboratori Nazionali del Sud (Italy) [152] with the aim of getting some inputs to deepen our theoretical understanding of this nuclear process.

For the above reasons, the value of  $g_A$  in the nuclear medium cannot be regarded as a quantity that is known reliably. It is rather an *important reason of uncertainty in the predictions*. In a conservative treatment, at least three cases should be considered,

$$g_A = \begin{cases} g_{\text{nucleon}} & = 1.269 \\ g_{\text{quark}} & = 1 \\ g_{\text{phen.}} & = g_{\text{nucleon}} \cdot A^{-0.18}, \end{cases} \quad (2.21)$$

where the last formula includes phenomenologically the effect of the atomic number  $A$ . The  $g_{\text{phen.}}$  parametrization as a function of  $A$  comes directly from the comparison between the theoretical half-lives for  $2\nu\beta\beta$  and their observations in different nuclei, as reported in Ref. [142]. From the comparison between the theoretical half-life for the process and the experimental value it was possible to extract an effective value for  $g_A$ , thus determining its quenching. This is just a phenomenological description of the quenching, since the specific behavior is different in each nucleus and it somewhat differs from this parametrization [142]. The question of which is the “true value” of  $g_A$  is still open and introduces a considerable uncertainty in the inferences concerning massive neutrinos. The implications are discussed in Sec. 2.6.4 and Sec. 2.6.5.

## 2.6 Experimental search for $0\nu\beta\beta$

The searches for a  $0\nu\beta\beta$  signal rely on the detection of the two emitted electrons. In fact, the energy of the recoiling nucleus is negligible, and the sum of the kinetic energies of the two electrons is equal to the Q-value of the transition (computed according to the atomic masses of the involved nuclei). Therefore, considering the two electrons as a single body, a monochromatic peak at the Q-value is the expected signature of the decay (Fig. 2.6).

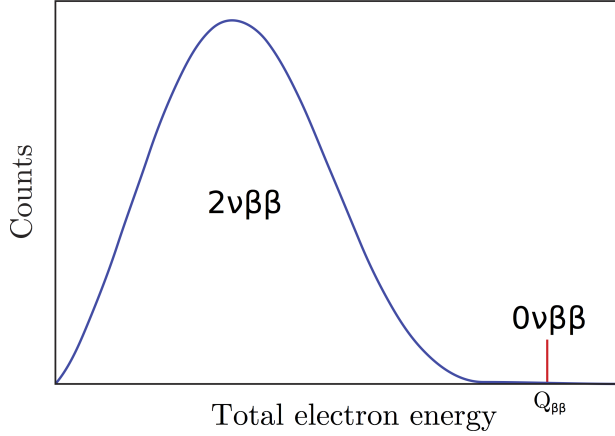


**Fig. 2.6:** Schematic view of the  $2\nu\beta\beta$  and the  $0\nu\beta\beta$  spectra.

In addition to the rarity of the process, the detection of the two electrons is complicated by the presence of background events in the same energy region, which can mask the  $0\nu\beta\beta$  signal. The main contributions to the background come from the environmental radioactivity, the cosmic rays, and the  $2\nu\beta\beta$  itself. In particular, the last contribution has the problematic feature of being unavoidable in presence of finite energy resolution, since it is originated by the same isotope which is expected to undergo  $0\nu\beta\beta$ . It is interesting to notice that in next generation experiments, if the time resolution is bad, pileups from two  $2\nu\beta\beta$  events might create another unavoidable background to  $0\nu\beta\beta$ . This could be the biggest intrinsic background in future experiments using “slow” bolometers (see Ref. [153]).

The choice for the best isotope to look for  $0\nu\beta\beta$  must take into account a set of criteria. First of all, the isotope must provide a high Q-value ( $Q_{\beta\beta}$ ), possibly above the 2615 keV line of  $^{208}\text{Tl}$ , which represents the end-point of the natural gamma radioactivity.

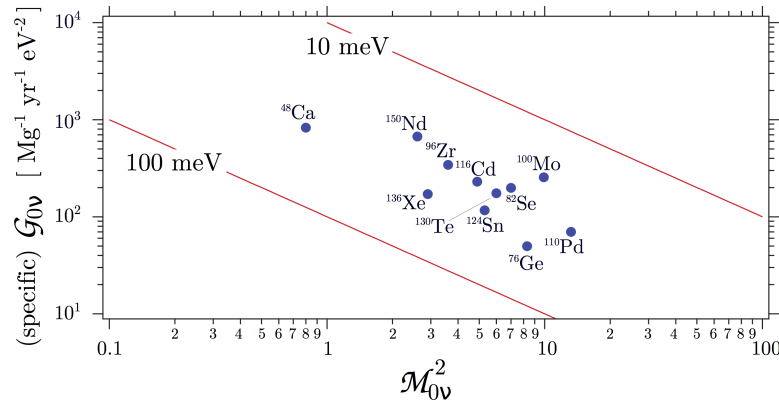


**Fig. 2.7:** Geometric mean of the squared  $\mathcal{M}_{0\nu}$  considered in Ref. [154] vs. the respective  $G_{0\nu}$ . The case  $g_A = g_{\text{quark}}$  is assumed. Adapted from Ref. [154].

Isotope	isotopic abundance (%)	$Q_{\beta\beta}$ (MeV)
$^{48}\text{Ca}$	0.187	4.263
$^{76}\text{Ge}$	7.8	2.039
$^{82}\text{Se}$	9.2	2.998
$^{96}\text{Zr}$	2.8	3.348
$^{100}\text{Mo}$	9.6	3.035
$^{116}\text{Cd}$	7.6	2.813
$^{130}\text{Te}$	34.08	2.527
$^{136}\text{Xe}$	8.9	2.459
$^{150}\text{Nd}$	5.6	3.371

**Tab. 2.3:** Isotopic abundance and Q-value for the known  $2\nu\beta\beta$  emitters [155].

This is important in order to minimize the radioactivity contribution in the region of interest. The isotope must also be isotopically abundant or easy to enrich, in order to build an experiment with a sufficiently high mass. Furthermore, it must be possible to integrate the material in a working detector, preferably with the potential of mass scalability. These requirements result in a group of “commonly” studied isotopes among all the possible  $0\nu\beta\beta$  candidate emitters, which are summarized in Tab. 2.3.

From the theoretical side, referring to Eq. (2.17), one should also try to maximize both the PSF and the NME in order to get stricter bounds on  $m_{\beta\beta}$  with the same sensitivity in terms of half-life time. However, as recently discussed in Ref. [154], a uniform inverse correlation between the PSF and the square of the NME emerges in all nuclei (Fig. 2.7). This happens to be more a coincidence than something physically motivated and, as a consequence, no isotope is either favored or disfavored for the search for the  $0\nu\beta\beta$ . It turns out that all isotopes have qualitatively the same decay rate per unit mass for any given value of  $m_{\beta\beta}$ .

### 2.6.1 Sensitivity estimation

In the fortunate case of a  $0\nu\beta\beta$  peak showing up in the energy spectrum, the law of radioactive decay reads as

$$t_{1/2} = \ln 2 \cdot T \cdot \varepsilon \cdot \frac{N_{\beta\beta}}{N_{\text{peak}}}, \quad (2.22)$$

where  $T$  is the measuring time,  $\varepsilon$  is the detection efficiency,  $N_{\beta\beta}$  is the number of  $\beta\beta$  decaying nuclei under observation, and  $N_{\text{peak}}$  is the number of observed decays in the region of interest. If the detector features are known reasonably well (i. e. the number of decaying nuclei, the efficiency and the time of measurement), the uncertainty on  $t_{1/2}$  is only due to the statistical fluctuations of the counts:

$$\frac{\delta t_{1/2}}{t_{1/2}} = \frac{\delta N_{\text{peak}}}{N_{\text{peak}}}. \quad (2.23)$$

If no peak is detected, the sensitivity of a given  $0\nu\beta\beta$  experiment is usually expressed in terms of the “detector factor of merit”,  $S^{0\nu}$  [156]. This can be defined as the process half-life corresponding to the maximum signal that could be hidden by the background fluctuations  $n_B$  (at a given statistical C. L.). Hereafter, with a little of abuse of notation,  $S^{0\nu}$  is intended either as the expected sensitivity than an experiment is supposed to reach or, in the case of a running experiment, as the limit on  $t_{1/2}$  obtained from real data. It has to be clear, however, that the concepts of “sensitivity” and of “experimental limit” are different, and that their specific values are likely not to be the same, simply because of statistical fluctuations on the data realization from which the limit is extracted.

In order to obtain an estimation for  $S^{0\nu}$  as a function of the experimental parameters, it is sufficient to require that the  $0\nu\beta\beta$  signal exceeds the standard deviation of the total detected counts in the interesting energy window. At the confidence level  $n_\sigma$ , this means:

$$n_{\beta\beta} \geq n_\sigma \sqrt{n_{\beta\beta} + n_B}, \quad (2.24)$$

where  $n_{\beta\beta}$  is the number of  $0\nu\beta\beta$  events. Note that it is possible to use the “ $n_\sigma \cdot \sigma$ ” concept even if the statistics is Poissonian with a low count rate. In fact, the difference is below 1% already with 5 real counts. Assuming that the background counts scale linearly with the mass of the detector,<sup>8</sup> from Eq. (2.22) it is easy to find an expression for  $S^{0\nu}$ :

$$S^{0\nu} = \ln 2 \cdot T \cdot \varepsilon \cdot \frac{N_{\beta\beta}}{n_\sigma \cdot n_B} = \ln 2 \cdot \varepsilon \cdot \frac{1}{n_\sigma} \cdot \frac{x \eta N_A}{\mathcal{M}_A} \cdot \sqrt{\frac{M \cdot T}{B \cdot \Delta}}, \quad (2.25)$$

where  $B$  is the background level per unit mass, energy, and time,  $M$  is the detector mass,  $\Delta$  is the FWHM energy resolution,  $x$  is the stoichiometric multiplicity of the element containing the  $\beta\beta$  candidate,  $\eta$  is the  $\beta\beta$  candidate isotopic abundance,  $N_A$  is the Avogadro number and, finally,  $\mathcal{M}_A$  is the compound molecular mass. Equation (2.25) emphasizes the role of all the essential experimental parameters.

A particularly interesting case is that in which the background level  $B$  is so low that the expected number of background events in the region of interest along the experiment life is of the order of unity:

$$M \cdot T \cdot B \cdot \Delta \lesssim 1. \quad (2.26)$$

This is called “zero background” experimental condition. In this case,  $n_B$  is a constant, Eq. (2.25) is no more valid and the sensitivity is given by:

$$S_{0B}^{0\nu} = \ln 2 \cdot T \cdot \varepsilon \cdot \frac{N_{\beta\beta}}{n_\sigma \cdot n_B} = \ln 2 \cdot \varepsilon \cdot \frac{x \eta N_A}{\mathcal{M}_A} \cdot \frac{M T}{N_s}. \quad (2.27)$$

The constant  $N_s$  is the number of observed events in the region of interest.

---

<sup>8</sup>This is reasonable since, a priori, impurities are uniform inside the detector but, of course, this might not always be true (e. g. for external background).

### 2.6.2 Experimental techniques and requirements

Desirable features for a  $0\nu\beta\beta$  detector are good energy resolution, very low background and large isotope mass. The energy resolution is a fundamental requirement to identify the sharp  $0\nu\beta\beta$  peak over an almost flat background from contaminants and from the (intrinsic) background induced by the tail of the  $2\nu\beta\beta$  spectrum. It can be shown that the ratio of counts due to  $0\nu\beta\beta$  and those due to  $2\nu\beta\beta$  in the peak region ( $R_{0\nu/2\nu}$ ) can be approximated by [157]:

$$R_{0\nu/2\nu} \propto \left( \frac{Q_{\beta\beta}}{\Delta} \right)^6 \frac{t_{1/2}^{2\nu}}{t_{1/2}^{0\nu}}, \quad (2.28)$$

which indicates that a good energy resolution is critical. Present experiments have masses of the order of some tens of kg up to a few hundreds of kg. Tons will be required for experiments aiming at covering the  $\mathcal{IH}$  region (see Sec. 2.6.5).

It is impossible to optimize the listed features simultaneously in a single detector. Therefore, it is up to the experimentalists to choose which ones to privilege in order to get the best sensitivity.

All the modern  $0\nu\beta\beta$  experiments are conceived on a calorimetric technique<sup>9</sup>, in which the source is embedded in the detector itself. Among the most successful examples, there are Ge-diodes, bolometers, Xe liquid and gaseous TPCs and loaded liquid scintillators. Ge-diodes can be of very large volume, high-purity and wonderful energy resolution, so that the relatively low  $Q_{\beta\beta}$  of  $^{76}\text{Ge}$  is not really a problem. Bolometers, mainly based on the isotope  $^{130}\text{Te}$  within  $\text{TeO}_2$  crystals, also have a very good energy resolution. In Xe liquid and gaseous TPCs the energy resolution is worse, but event topology discrimination capabilities are available. Liquid scintillators loaded with the isotope of interest (usually  $^{136}\text{Xe}$  or  $^{130}\text{Te}$ ) are the worst in energy resolution, but a huge amount of material can be dissolved and, thanks to the purification processes, the lowest levels of background are achievable.

### 2.6.3 Experiments: a brief review

The first attempt to observe the  $0\nu\beta\beta$  process dates back to 1948 [182, 183]. Actually, the old geochemical experiments aiming to set a limit on the double beta decay half-lives could not distinguish between  $2\nu\beta\beta$  and  $0\nu\beta\beta$ . The considerable technological improvements allowed to increase the half-life sensitivity of several orders of magnitude. The  $2\nu\beta\beta$  was first observed in the laboratory in  $^{82}\text{Se}$  in 1987 [184], and in many other isotopes in the subsequent years.

Tab. 2.4 summarizes the main characteristics and performances of some selected and recent experiments. Because of their different specific features, the actual comparison among all the values is not always possible. The table tries to overcome this problem by choosing a common set of units of measurement.

---

<sup>9</sup>Technically, this is not entirely accurate since SuperNEMO and NEXT are supposed to provide tracking capability.

Experiment	Isotope	Technique	Total mass [kg]	Exposure [kg yr]	FWHM @ $Q_{\beta\beta}$ [keV]	Background [counts/keV/kg/yr]	$S^{0\nu}$ (90% C. L.) [ $10^{25}$ yr]
<i>Past</i>							
Cuoricino, [158]	$^{130}\text{Te}$	bolometers	40.7 ( $\text{TeO}_2$ )	19.75	$5.8 \pm 2.1$	$0.153 \pm 0.006$	0.24
CUORE-0, [159]	$^{130}\text{Te}$	bolometers	39 ( $\text{TeO}_2$ )	9.8	$5.1 \pm 0.3$	$0.058 \pm 0.006$	0.29
Heidelberg-Moscow, [160]	$^{76}\text{Ge}$	Ge diodes	11 ( $^{enr}\text{Ge}$ )	35.5	$4.23 \pm 0.14$	$0.06 \pm 0.01$	1.9
IGEX, [161, 162]	$^{76}\text{Ge}$	Ge diodes	8.1 ( $^{enr}\text{Ge}$ )	8.9	$\sim 4$	$\lesssim 0.06$	1.57
GERDA-I, [163, 164]	$^{76}\text{Ge}$	Ge diodes	17.7 ( $^{enr}\text{Ge}$ )	21.64	$3.2 \pm 0.2$	$\sim 0.01$	2.1
NEMO-3, [165]	$^{100}\text{Mo}$	tracker + calorimeter	6.9 ( $^{100}\text{Mo}$ )	34.7	350	0.013	0.11
<i>Present</i>							
EXO-200, [166]	$^{136}\text{Xe}$	LXe TPC	175 ( $^{enr}\text{Xe}$ )	100	$89 \pm 3$	$(1.7 \pm 0.2) \cdot 10^{-3}$	1.1
KamLAND-Zen, [167, 168, 169]	$^{136}\text{Xe}$	loaded liquid scintillator	348 ( $^{enr}\text{Xe}$ )	89.5	$244 \pm 11$	$\sim 5 \cdot 10^{-4}$	11
GERDA-II (first release), [170]	$^{76}\text{Ge}$	Ge diodes	37.8 ( $^{enr}\text{Ge}$ )	10.8	3.5	0.001	5.3
<i>Future</i>							
CUORE, [171]	$^{130}\text{Te}$	bolometers	741 ( $\text{TeO}_2$ )	1030	5	0.01	9.5
CUPID-0, [172, 173]	$^{82}\text{Se}$	bolometers	17 ( $\text{Zn}^{82}\text{Se}$ )	18	10	0.001	1.8
MAJORANA D., [174]	$^{76}\text{Ge}$	Ge diodes	44.8 ( $^{enr/\text{nat}}\text{Ge}$ )	100	4	0.003	12
NEXT, [175]	$^{136}\text{Xe}$	Xe TPC	100 ( $^{enr}\text{Xe}$ )	300	$12.3 - 17.2$	$4 \cdot 10^{-4}$	6
AMoRE-II, [176]	$^{100}\text{Mo}$	bolometers	200 ( $\text{Ca}^{enr}\text{MoO}_4$ )	1000	6	$1 \cdot 10^{-4}$	110
nEXO, [177]	$^{136}\text{Xe}$	LXe TPC	4780 ( $^{enr}\text{Xe}$ )	12150	58	$1.7 \cdot 10^{-5}$	66
PandaX-III, [178]	$^{136}\text{Xe}$	Xe TPC	1000 ( $^{enr}\text{Xe}$ )	3000	$12 - 76$	0.001	11
SNO+, [78]	$^{130}\text{Te}$	loaded liquid scintillator	2340 ( $^{nat}\text{Te}$ )	3980	270	$2 \cdot 10^{-4}$	9
KamLAND2-Zen, [179]	$^{136}\text{Xe}$	loaded liquid scintillator	1000 ( $^{enr}\text{Xe}$ )	5000	150	$\sim 5 \cdot 10^{-4}$	100
SuperNEMO, [180, 181]	$^{82}\text{Se}$	tracker + calorimeter	100 ( $^{82}\text{Se}$ )	500	120	0.01	10

**Tab. 2.4:** This table from Ref. [3] shows the main features and performances of some past, present and future  $0\nu\beta\beta$  experiments.

## 2.6.4 Present sensitivity on $m_{\beta\beta}$

Once the experimental sensitivities are known in terms of  $S^{0\nu}$ , it is possible to find lower bounds on  $m_{\beta\beta}$  thanks to Eq. (2.20). Figure 2.8 shows the most stringent limits to date. They come from  $^{76}\text{Ge}$  [170],  $^{130}\text{Te}$  [159] and  $^{136}\text{Xe}$  [169] and they are reported in Tab. 2.5. In the figure, the case  $g_A = g_{\text{nucleon}}$  (unquenched value) is assumed. As the plot shows, the current generation of experiments is probing the quasi degenerate part of the neutrino mass spectrum.

The effect of the quenching of  $g_A$  is compared with the effect of the usage of different models in Fig. 2.9, where the sensitivity coming from  $^{136}\text{Xe}$  experiments in the two cases

Experiment	Isotope	$S^{0\nu}$ (90% C. L.) [ $10^{25}$ yr]	Lower bound for $m_{\beta\beta}$ [eV]		
			$g_{\text{nucleon}}$	$g_{\text{quark}}$	$g_{\text{phen.}}$
GERDA-II first release, [170]	$^{76}\text{Ge}$	5.3	$0.19 \pm 0.02$	$0.30 \pm 0.03$	$0.91 \pm 0.08$
Cuoricino + CUORE-0, [159]	$^{130}\text{Te}$	0.4	$0.36 \pm 0.03$	$0.58 \pm 0.05$	$2.07 \pm 1.05$
KamLAND-ZEN, [169]	$^{136}\text{Xe}$	11	$0.08 \pm 0.01$	$0.13 \pm 0.02$	$0.48 \pm 0.05$

**Tab. 2.5:** Lower bounds on  $m_{\beta\beta}$  for  $^{76}\text{Ge}$ ,  $^{130}\text{Te}$  and  $^{136}\text{Xe}$  from the most competitive experimental results. Ref. [132] and Ref. [135] were used for the evaluation of the PSFs and for the NME, respectively. The different results correspond to different values of  $g_A$  according to Eq. (2.21).

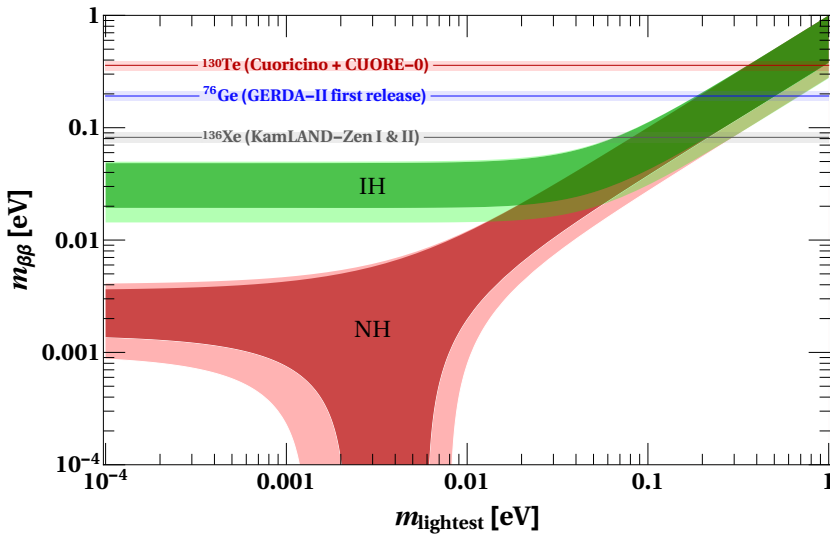


**Fig. 2.8:** The colored regions show the predictions on  $m_{\beta\beta}$  from oscillations as a function of the lightest neutrino mass with the corresponding  $3\sigma$  uncertainty regions. The horizontal bands show the current experimental limits (referred to the values reported in Tab. 2.5) with the spread due to the theoretical uncertainties on the NMEs [135] and PSFs [132].

of  $g_{\text{nucleon}}$  and  $g_{\text{phen}}$  differs of a factor  $\gtrsim 5$ . It is clear from the figure that this is the biggest uncertainty, with respect to all the other theoretical ones.

### 2.6.5 Future (planned) experiments

The expected bounds on  $m_{\beta\beta}$  coming from projection of future experiment sensitivities are shown in Tab. 2.6. The mass region below 100 meV will be probed in many isotopes in case of unqueched value for  $g_A$ <sup>10</sup>, while in case  $g_A$  is maximally quenched, the situation is much worse.

What should be the target for the next generation of experiments? Referring to Ref. [1], besides the hope of discovering the  $0\nu\beta\beta$ , the most exciting investigation that can be imagined at present is the exclusion of the  $\mathcal{IH}$  case. This is the goal that most of the experimentalists are trying to reach with future  $0\nu\beta\beta$  experiments (see e. g. Ref. [186]). For this purpose, one can require a sensitivity  $m_{\beta\beta} = 8$  meV. By choosing this value, even taking into account the residual uncertainties on the NMEs and on the PSFs, the overlap between the allowed band for  $m_{\beta\beta}$  and the  $\mathcal{IH}$  allowed region is excluded at more than  $3\sigma$ . Within these assumptions, one could consider a next generation experiment (say a “mega” experiment) and a next-to-next generation one (an “ultimate” experiment) with enhanced sensitivity. The mega experiment is the one that satisfies this requirement assuming that the quenching of  $g_A$  is absent. Instead, the ultimate experiment assumes

<sup>10</sup>Up to now, the only experiment which could put a bound on  $m_{\beta\beta} < 100$  meV in the assumption of null quenching of  $g_A$  is KamLAND-Zen [169].

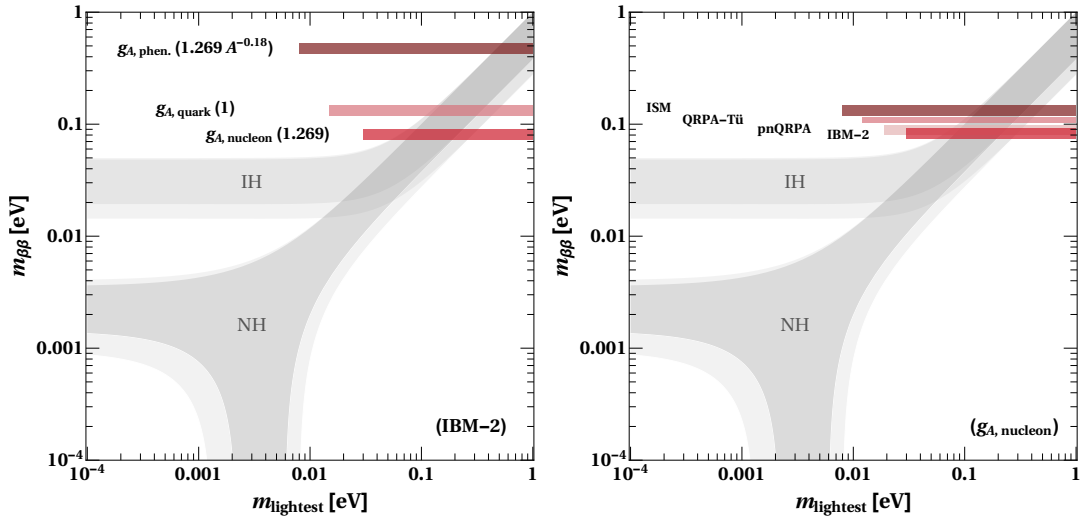


**Fig. 2.9:** *Left Panel:* Limit on  $m_{\beta\beta}$  from Ref. [169] computed within the IBM-2 model for the different values of  $g_A$  reported in Eq. (2.21). *Right Panel:* Limit on  $m_{\beta\beta}$  from Ref. [169] with  $g_A = g_{\text{nucleon}}$ , while assuming the different theoretical calculations of NMEs discussed in Sec. 2.5.2.

that  $g_A$  is maximally quenched. Using Eq. (2.20), the corresponding values of  $t_{1/2}$  and the relative exposures needed in order to reach the 8 meV goal are calculated and reported in Tab. 2.7 for different isotopes. Note that in the table the zero background condition is assumed. The last column of the table gives the maximum allowed value of the product  $B \cdot \Delta$  that satisfies Eq. (2.26).

## 2.7 Interplay with cosmology

The knowledge on the neutrino cosmological mass is important in order to make inferences on some  $0\nu\beta\beta$  experiment results (or expected ones). This is more extensively discussed in Ref. [2]. The tight limit on  $\Sigma$  reported in Ref. [113] was obtained by combining the Planck 2013 results [187] with the one-dimensional flux power spectrum measurement of the Lyman- $\alpha$  forest extracted from the BAO Spectroscopic Survey of the Sloan Digital Sky Survey [188]. In particular, the data from a new sample of quasar spectra were analyzed and a novel theoretical framework which incorporates neutrino non-linearities self consistently was employed. The authors of Ref. [113] computed a probability for  $\Sigma$  that can be summarized to a very good approximation by [2]:

$$\Delta\chi^2(\Sigma) = \frac{(\Sigma - 22 \text{ meV})^2}{(62 \text{ meV})^2}. \quad (2.29)$$

Experiment	Isotope	$S^{0\nu}_{(90\% \text{ C.L.})}$ [ $10^{25}$ yr]	Lower bound for $m_{\beta\beta}$ [eV]		
			$g_{\text{nucleon}}$	$g_{\text{quark}}$	$g_{\text{phen.}}$
GERDA-II (final, expected), [185]	$^{76}\text{Ge}$	15	$0.11 \pm 0.01$	$0.183 \pm 0.017$	$0.54 \pm 0.05$
CUORE, [171]	$^{130}\text{Te}$	9.5	$0.074 \pm 0.007$	$0.12 \pm 0.01$	$0.43 \pm 0.04$
CUPID-0, [172, 173]	$^{82}\text{Se}$	1.8	$0.199 \pm 0.018$	$0.32 \pm 0.03$	$0.97 \pm 0.09$
MAJORANA D., [174]	$^{76}\text{Ge}$	12	$0.13 \pm 0.01$	$0.20 \pm 0.02$	$0.61 \pm 0.06$
NEXT, [175]	$^{136}\text{Xe}$	6	$0.111 \pm 0.012$	$0.18 \pm 0.02$	$0.65 \pm 0.07$
AMoRE-II, [176]	$^{100}\text{Mo}$	110	$0.018 \pm 0.002$	$0.029 \pm 0.003$	$0.094 \pm 0.009$
nEXO, [177]	$^{136}\text{Xe}$	660	$0.011 \pm 0.001$	$0.017 \pm 0.002$	$0.062 \pm 0.007$
PandaX-III, [178]	$^{136}\text{Xe}$	11	$0.082 \pm 0.009$	$0.13 \pm 0.01$	$0.48 \pm 0.05$
SNO+, [78]	$^{130}\text{Te}$	9	$0.076 \pm 0.007$	$0.12 \pm 0.01$	$0.44 \pm 0.04$
SuperNEMO, [180]	$^{82}\text{Se}$	10	$0.084 \pm 0.008$	$0.14 \pm 0.01$	$0.41 \pm 0.04$

**Tab. 2.6:** Lower bounds for  $m_{\beta\beta}$  for the closer (upper group) and further (lower group) future  $0\nu\beta\beta$  experiments. Refs. [132, 135] were used for the PSFs and for the NMEs, respectively. The different results correspond to different values of  $g_A$  according to Eq. (2.21).

Experiment	Isotope	$S^{0\nu}_{0B}$ [yr]	Exposure (estimate)		
			$M \cdot T$ [ton·yr]	$B \cdot \Delta_{(\text{zero bkg})}$ [counts $\text{kg}^{-1} \text{yr}^{-1}$ ]	
mega Ge	$^{76}\text{Ge}$	$3.0 \cdot 10^{28}$	5.5		$1.8 \cdot 10^{-4}$
mega Te	$^{130}\text{Te}$	$8.1 \cdot 10^{27}$	2.5		$4.0 \cdot 10^{-4}$
mega Xe	$^{136}\text{Xe}$	$1.2 \cdot 10^{28}$	3.8		$2.7 \cdot 10^{-4}$
ultimate Ge	$^{76}\text{Ge}$	$6.9 \cdot 10^{29}$	125		$8.0 \cdot 10^{-6}$
ultimate Te	$^{130}\text{Te}$	$2.7 \cdot 10^{29}$	84		$1.2 \cdot 10^{-5}$
ultimate Xe	$^{136}\text{Xe}$	$4.0 \cdot 10^{29}$	130		$7.7 \cdot 10^{-6}$

**Tab. 2.7:** Sensitivity and exposure necessary to reach the goal of  $m_{\beta\beta} = 8$  meV. The two cases refer to the unquenched value of  $g_A = g_{\text{nucleon}}$  (mega) and  $g_A = g_{\text{phen.}}$  (ultimate). The calculations are performed assuming *zero background* experiments with 100% detection efficiency and no fiducial volume cuts. The last column shows the maximum value of the product  $B \cdot \Delta$  in order to actually comply with the zero background condition.

From the likelihood function  $\mathcal{L} \propto \exp{-(\Delta\chi^2/2)}$ , one can obtain the following limits:

$$\begin{aligned}
 \Sigma < & 84 \text{ meV} & (1\sigma \text{ C. L.}) \\
 \Sigma < & 146 \text{ meV} & (2\sigma \text{ C. L.}) \\
 \Sigma < & 208 \text{ meV} & (3\sigma \text{ C. L.})
 \end{aligned} \tag{2.30}$$

which are very close to those predicted by the Gaussian  $\Delta\chi^2$  of Eq. (2.29). In particular, even if this measurement is compatible with zero at less than  $1\sigma$ , the best fit value is different from zero, as expected from the oscillation data and as evidenced by Eq. (2.29). Despite the impact of systematic versus statistical errors on the estimated flux power is considered and discussed [188], it is anyway advisable to take these results from cosmology with the due caution.

Considering again the plot showing  $m_{\beta\beta}$  as a function of  $\Sigma$  in the right panel of Fig. 2.2, it has to be noted that together with the uncertainties on the oscillation parameters,

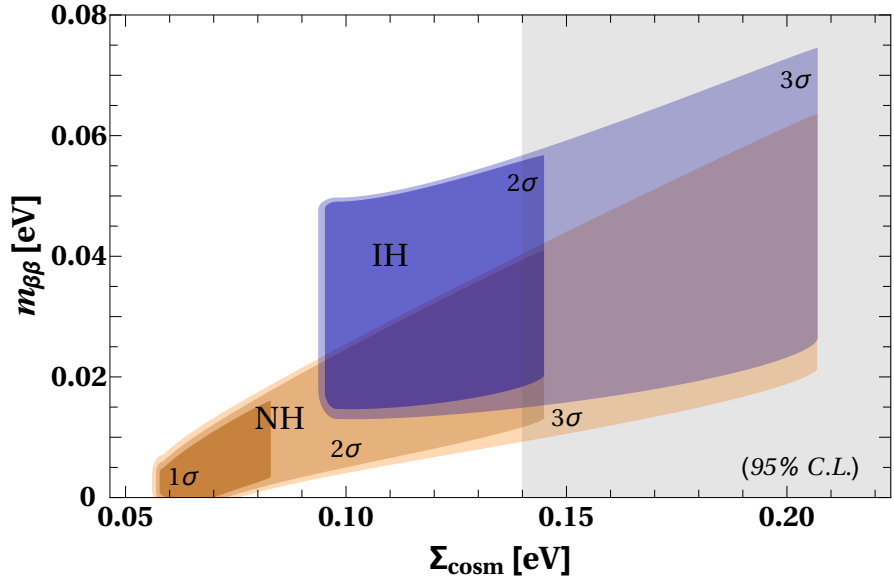


**Fig. 2.10:** Constraints from cosmological surveys on  $m_{\beta\beta}$  are added to those from oscillations. Different C. L. contours are shown for both hierarchies. Notice that the  $1\sigma$  region for the  $\mathcal{IH}$  case is not present, being the scenario disfavored at this confidence level. The dashed band signifies the 95% C. L. excluded region coming from Ref. [113]. Figure from Ref. [2].

the error on  $\Sigma$  contributing to the total uncertainty should be taken into account. Its effect is a broadening of the light shaded area on the left side of the minimum allowed value  $\Sigma(m = 0)$  for each hierarchy. In order to compute this uncertainty, it is sufficient to consider Gaussian errors on the oscillation parameters, namely

$$\delta\Sigma = \sqrt{\left(\frac{\partial\Sigma}{\partial\delta m^2}\sigma(\delta m^2)\right)^2 + \left(\frac{\partial\Sigma}{\partial\Delta m^2}\sigma(\Delta m^2)\right)^2}. \quad (2.31)$$

It is possible to include the new cosmological constraints on  $\Sigma$  from Ref. [113] considering the following inequality:

$$\frac{(y - m_{\beta\beta}(\Sigma))^2}{(n\sigma[m_{\beta\beta}(\Sigma)])^2} + \frac{(\Sigma - \Sigma(0))^2}{(\Sigma_n - \Sigma(0))^2} < 1, \quad (2.32)$$

where  $m_{\beta\beta}(\Sigma)$  is the Majorana Effective Mass as a function of  $\Sigma$  and  $\sigma[m_{\beta\beta}(\Sigma)]$  is the  $1\sigma$  associated error, computed as discussed in Ref. [1].  $\Sigma_n$  is the limit on  $\Sigma$  derived from Eq. (2.29) for the C. L.  $n = 1, 2, 3, \dots$ . By solving Eq. (2.32) for  $y$ , it is thus possible to get the allowed contour for  $m_{\beta\beta}$  considering both the constraints from oscillations and from cosmology. In particular, the Majorana phases are taken into account by computing  $y$  along the two extremes of  $m_{\beta\beta}(\Sigma)$ , namely  $m_{\beta\beta}^{\max}(\Sigma)$  and  $m_{\beta\beta}^{\min}(\Sigma)$ , and then connecting the two contours. The resulting plot is shown in Fig. 2.10. The most evident feature of Fig. 2.10 is the clear difference in terms of expectations for both  $m_{\beta\beta}$  and  $\Sigma$  in the two

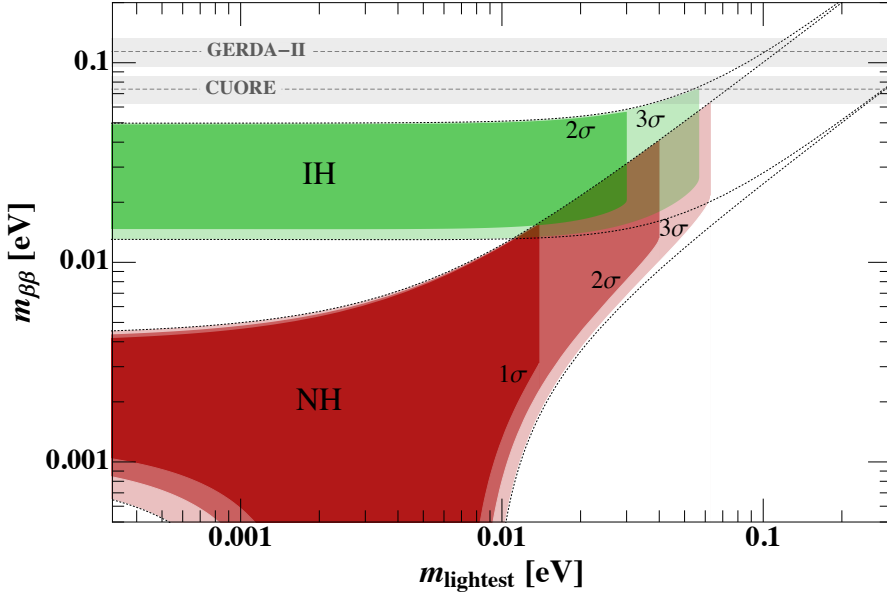


**Fig. 2.11:** Constraints from cosmological surveys are added to those from oscillations in the representation of  $m_{\beta\beta}$  as a function of the lightest neutrino mass. The dotted contours represent the  $3\sigma$  regions allowed considering oscillations only. The shaded areas show the effect of the inclusion of cosmological constraints at different C. L.. The horizontal bands correspond to the expected sensitivity for future experiments. Figure from Ref. [2].

hierarchy cases. The relevant oscillation parameters (mixing angles and mass splittings) are well known and they induce only minor uncertainties on the expected value of  $m_{\beta\beta}$ . These uncertainties widen the allowed contours in the upper, lower and left sides of the picture. The boundaries in the rightmost regions are due to the new information from cosmology and are cut at various confidence levels. It is notable that at  $1\sigma$ , due to the exclusion of the  $\mathcal{IH}$ , the set of plausible values of  $m_{\beta\beta}$  is highly restricted.

The impact of the new constraints on  $\Sigma$  appears even more evident by plotting  $m_{\beta\beta}$  as a function of the mass of the lightest neutrino. In this case, Eq. (2.32) becomes:

$$\frac{(y - m_{\beta\beta}(m))^2}{(n \sigma[m_{\beta\beta}(m)])^2} + \frac{m^2}{m(\Sigma_n)^2} < 1. \quad (2.33)$$

The plot in Fig. 2.11 globally shows that the next generation of experiments will have small possibilities of detecting a signal of  $0\nu\beta\beta$  due to light Majorana neutrino exchange. Therefore, if the new results from cosmology are confirmed or improved, ton or even multi-ton scale detectors will be needed [1].

On the other hand, a  $0\nu\beta\beta$  signal in the near future could either disprove some assumptions of the present cosmological models, or suggest that a different mechanism other than the light neutrino exchange mediates the transition. New experiments are seeking to test the latter possibility by probing scenarios beyond the SM [189, 190, 191].

## 2.8 Search for Majorana neutrinos with Borexino

Already before the construction of the Borexino experiment, the idea of exploiting its experimental facility to search for the  $0\nu\beta\beta$  was considered. This was pointed out already in the Borexino proposal [81] and more extensively in Ref. [82] by Raghavan. The criteria of a large source mass, very low background and good energy resolution, which are needed for a successful  $0\nu\beta\beta$  experiment, are also basic for the design of very low energy (sub-MeV) solar neutrino detectors. This idea can be realized in practice with  $^{136}\text{Xe}$  “since large masses of  $^{136}\text{Xe}$  gas can be loaded into a large-scale liquid scintillation detector such as Borexino. Such an experiment is, in fact, less demanding than the detection of  $< 1$  MeV solar neutrinos because of the higher energy of the  $^{136}\text{Xe}$   $0\nu\beta\beta$  line signal at 2.45 MeV, which also opens other facilities such as Kamiokande (K-II)...” [82].

The idea of dissolving gaseous xenon in a liquid scintillator is thus quite old. It was applied firstly in the KamLAND-Zen experiment [167, 168, 169]. This technique is so powerful that the best limit on the half-life ever measured in the search for  $0\nu\beta\beta$ , has just been obtained by the KamLAND-Zen Collaboration in 2016 [169] (see Tab. 2.5). Potentially, such a technique can provide a way to build a 100-ton scale experiment looking for  $0\nu\beta\beta$ , as discussed in Sec. 2.8.4. As already mentioned within Sec. 2.6.5 and it is clear from Tab. 2.7, the next generation of experiments must have huge masses, of the order of tens or hundreds of tons.

This approach has basically two key advantages. The solubility as high as  $\sim 2\%$  of xenon in organic liquid scintillators [192] makes it possible to have a xenon source mass possibly of many tons (in fact, e. g. in the case of Borexino the amount of liquid scintillator is  $\sim 300$  ton). This has to be compared to the hundred-kg size of the next generation of  $0\nu\beta\beta$  detectors reported in Tab. 2.4. In addition to this, the specific background is lower by many orders of magnitude with respect to what can be achieved in solid state detectors, because of the high radio-purity of liquid scintillators (see e. g. Ref. [193]) and the massively shielded environment in a direct-counting facility for low energy solar neutrinos such as Borexino. These two factors more than offset the much poorer energy resolution and the relatively low concentration of xenon in the liquid scintillator.

There have been other proposals for the next life of Borexino, when all the solar neutrino measurements will be over. In Ref. [194], preliminary studies for what is called the CAMEO project are presented. In particular, the unique features (super-low background and large sensitive volume) of the CTF<sup>11</sup> and Borexino setups could be used for a high sensitivity search of  $0\nu\beta\beta$  in  $^{100}\text{Mo}$  and  $^{116}\text{Cd}$ . The main concept foresees the deployment of crystals containing the isotope of interest in the middle of the liquid scintillator detector, so that the large liquid volume can act as a light guide and contemporarily as a shield against the external backgrounds.

---

<sup>11</sup>CTF stands for Counting Test Facility. It is the old prototype for Borexino and it is now hosting the DarkSide experiment.

### 2.8.1 The new concept: increasing the pressure

The Borexino experiment has set unprecedented limits on the radio-purity of its organic liquid scintillator [193]. This was achieved by a really careful choice of all the materials involved in the realization of the detector and by a huge development of purification techniques. In addition to this, Borexino achieved a good energy resolution ( $\sigma$  of 5% at 1 MeV), among (if not) the best for liquid scintillator based experiments. These features make the case for studying the possibility of using the Borexino facility to develop a new generation  $0\nu\beta\beta$  experiment.

A smart and innovative way to exploit the potential of the Borexino facility for  $0\nu\beta\beta$  consists in dissolving  $^{136}\text{Xe}$  inside the scintillator *at high pressure*. This makes it possible to take advantage of Henry's law, which states that the solubility of a gas in a liquid grows linearly with the pressure. This means that just by increasing the pressure, one could increase almost arbitrary the target mass, without touching the detector, and thus keeping under control the systematics. For instance, it is possible to perform a source-in/source-out approach, which would allow to measure the main backgrounds, the detector response and resolution with and without the  $^{136}\text{Xe}$ , providing a smoking gun for the possible discovery of the  $0\nu\beta\beta$  in the case of a peak showing up in the spectrum. In fact, most of the scientific community is sort of skeptical about the discovery potential of scintillator detectors mainly because of their energy resolution. The source-in/source-out approach with  $^{136}\text{Xe}$  could eliminate this ambiguity. Indeed, it would be possible to load the detector either with natural or  $^{136}\text{Xe}$ -depleted xenon and then compare the observed spectrum with the case of enriched  $^{136}\text{Xe}$ . The relative easiness<sup>12</sup> of the enrichment of the gaseous xenon in  $^{136}\text{Xe}$  is another advantage of the choice of this isotope.

When adding several tons of xenon inside the scintillator, one must assure that the hydrostatic equilibrium is guaranteed. In principle, one could dissolve xenon in all the volume containing liquid scintillator, but the cost of such an amount of inactive xenon would be prohibitive. Due to the fiducialization procedure, most of the outer volume is usually not used in the analysis, since only the innermost, cleaner parts are considered. The KamLAND-Zen Collaboration solved this problem by developing a small vessel, which is suspended in the middle of the detector and which is the only part which contains the doped liquid scintillator [167] (see the right panel of Fig. 2.12).

In the case of pseudocumene (PC), the aromatic liquid used in Borexino as solvent for the scintillator PPO, assuming that the volume of the xenon loaded scintillator does not change with the increase of xenon concentration, the density increases at a pressure of 5 bar as much as 100 g per kg of solution. One possible solution to compensate this could consist in adding a suitable solute in the buffer liquid (see the schematic drawing of Borexino in the left panel of Fig. 2.12) to compensate for the different densities. Also, the tightness of nylon vessels against xenon diffusion should be demonstrated, even if the xenon atom is relatively “big” and thus this should not represent a real concern.

It is of course possible to apply these ideas to future large liquid scintillator detectors

---

<sup>12</sup>Actually, the only real obstacle is the amount of money needed to enrich many tons of xenon, but the technology is available.

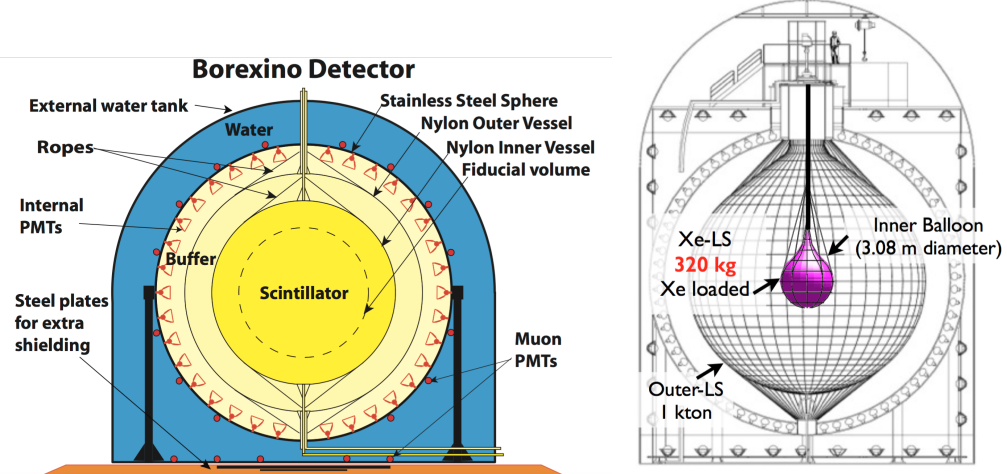


**Fig. 2.12:** Schematic view of the Borexino (left) and of the KamLAND-Zen (right) detectors.

as e.g. JUNO [195]. In particular, JUNO aims at reaching an unprecedentedly low energy resolution for a liquid scintillator detector ( $\sim 3\%$  at 1 MeV, to be compared to Borexino's  $\sim 5\%$  at 1 MeV) and having a huge mass of  $\sim 20$  kton of liquid scintillator. In principle, this could be the golden experiment to perform a  $0\nu\beta\beta$  search with a huge amount of target mass. Preliminary studies about this possibility have been presented very recently [196]. In Sec. 3.8 some results on the optical properties of the JUNO-like liquid scintillator doped with xenon at high pressure are reported.

As a final remark concerning backgrounds, Borexino is the current world leader in terms of radio-purity. In addition, the favorable environment of the Laboratori Nazionali del Gran Sasso with an overburden of  $\sim 3800$  m w.e. makes the cosmogenic background contribution in the  $0\nu\beta\beta$  region of interest negligible in practice. Instead, the radioactive decays of cosmogenic isotopes such as  $^{10}\text{C}$ ,  $^6\text{He}$ ,  $^{12}\text{B}$  and  $^{137}\text{Xe}$  in the KamLAND-Zen experiment [169] give a contribution to the background budget at the level of the radioactivity coming from the small vessel. In fact, flux reduction at the Kamioka Observatory is around  $\sim 10$  times worse than that of Laboratori Nazionali del Gran Sasso. The situation is even worse in the case of JUNO [196], where the rock overburden is almost a factor of two less than Kamioka's one.

### 2.8.2 Pros and cons of the technique

The technique discussed above has many pros and a few challenges to face. In this section, a summary of its main features is presented.

The advantages of this method include:

- a well established know-how in the construction and operation of ultra-pure, large liquid scintillator detectors.
- a superb radio-purity level in the Region Of Interest (ROI) as demonstrated by

Borexino (see Sec. 4.3).

- the fact that xenon is a noble gas, thus easy to purify. In addition, the xenon can be easily enriched to levels as high as 90% or even more. Its Q-value is pretty high, above most of the natural radioactive contaminations (see Tab. 2.3).
- an almost free and arbitrary scalability in mass, just by increasing the gaseous pressure of the isotope of interest.
- the possibility to operate in a source-in/source-out mode to study the detector with and without the presence of the isotope of interest. While the detector is operating, it would be possible to load it with xenon depleted or enriched in  $^{136}\text{Xe}$  without modifying any other experimental condition, thus being able to verify that a potentially non-null signal is in fact produced by the sought process (or decay).
- the possibility of reusing the Borexino facilities and plants<sup>13</sup>, thus making the active isotope one of the most important part of the required budget.
- the loading of the scintillator with xenon at high pressure, making it possible to keep the detector relatively small despite having a huge mass, and therefore reducing possible non-uniformity effects which could spoil the energy resolution.
- the possibility of extended calibrations of the detector in the whole volume by using internal source insertion systems.
- the possibility to improve the results and thus the background performances only by fiducializing a small enough volume inside the detector while keeping the mass high just by increasing the pressure. This is possible because the Borexino scintillator is so pure that the only background contribution in the ROI is external (see Sec. 2.8.4).<sup>14</sup>

The challenges of the project are:

- commonly to all  $^{136}\text{Xe}$  based experiments, xenon is expensive. This is a problem which has to be faced anyhow by all the next generation of experiments, because of the increase in the active mass.
- the energy resolution must be improved as much as possible (100 – 150 keV). This is achievable (geometrical coverage, modifications in the scintillator cocktail) but challenging.
- the development of a smart system for balancing the hydrostatic pressure induced by the presence of xenon in the inner volume (a dedicated nylon balloon or a buffer scintillator with appropriate density).

---

<sup>13</sup>Borexino is mentioned here as an example, this holds for every Borexino-like experiment which could be turned into a  $0\nu\beta\beta$  experiment.

<sup>14</sup>The background due to  $^8\text{B}$   $\nu$  is here neglected, since it is still too small with respect to the foreseen sensitivity.

### 2.8.3 Xenon's dissolution in the liquid scintillator

In a large detector, the gaseous part dissolved in the liquid scintillator is not homogeneous throughout the volume. In fact, since Henry's law states that the solubility grows linearly with the pressure, the hydrostatic pressure induced by gravity on the liquid creates automatically a non uniform mass distribution of the dissolved gas. It is possible to quantify this effect for a detector such as Borexino within easy but reasonable assumptions. The hydrostatic equilibrium is described by

$$\frac{\vec{\nabla}p}{\rho} = -\vec{\nabla}\phi \quad (2.34)$$

where  $p = p(\vec{r})$  is the pressure,  $\rho = \rho(\vec{r})$  is the density and  $\phi$  is the potential in which the liquid is immersed in, i. e. the gravitational one. Therefore, both the pressure and the density fields can actually be assumed symmetric in  $x$  and  $y$ , with a non trivial dependence only left on the vertical coordinate  $z$ . In the assumption that the volume of the liquid is not modified by the dissolution of the xenon, Henry's law can be expressed directly in terms of the density of the mixture liquid-gas. In this case, the density of the liquid is modified proportionally to the pressure, such as

$$\rho(z) = \rho_0 (1 + ap(z)) \quad (2.35)$$

where  $\rho_0$  is the density of the scintillator and  $a = k/p_{ref}$ , with  $k$  being the solubility in mass of the gas in the liquid at the pressure  $p_{ref}$ . The implementation of the hypothesis of Eq. (2.35) in Eq. (2.34) yields

$$\frac{dp}{dz} = -g\rho_0(1 + ap), \quad (2.36)$$

where  $g$  is the gravitational acceleration at Earth's surface. Eq. (2.36) can be easily solved by variable separation. The solution is

$$p(z) = \frac{1}{a} \left( e^{-g\rho_0 a(z - z_{top})} (1 + ap_0) - 1 \right). \quad (2.37)$$

$z_{top}$  is the  $z$  coordinate of the top of the detector where the pressure is  $p_0$ . In the case of Borexino, the volume in which the xenon can be dissolved is the innermost one, i. e. a sphere of 8.5m in diameter, and thus the  $z$  coordinate would span on the vertical diameter of the sphere in the interval  $[-4.25 \text{ m}, 4.25 \text{ m}]$ . In the left panel of Fig. 2.13, the behavior of the pressure predicted by Eq. (2.37) is compared to the one observable in the case of absence of dissolved gas in the liquid. The effect of the gas extra-mass is clearly visible in the deviation from the standard Stevin trend. Since the amount of dissolved gas as a function of the vertical coordinate is directly proportional to the pressure, Eq. (2.37) shows that the xenon is actually stratified and not uniform in space.

In a simple case such as Borexino's, i. e. a spherical symmetry from the geometrical point of view and a pure dependence on  $z$  of the pressure, the total mass of scintillator

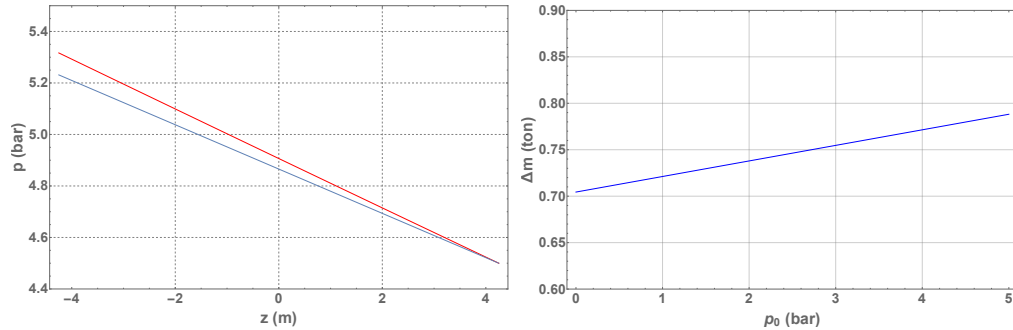


**Fig. 2.13:** *Left Panel:* Pressure of the mixture liquid-gas in Borexino's inner vessel as a function of the vertical coordinate. The red line shows the behavior described in Eq. (2.37), while the blue line shows the prediction in the case of Stevin's law, when no gas is dissolved in the liquid. In this example, it was assumed that the liquid at the top of the detector is in equilibrium with xenon at a pressure of 4.5 bar. *Right Panel:* Mass difference as a function of the pressure  $p_0$  between the realistic calculation of Eq. (2.38) and the one done in the assumption of uniform xenon pressure, neglecting the hydrostatic pressure.

plus dissolved gas can easily be computed as

$$M = \int_{z_{bottom}}^{z_{top}} \pi R^2 \left(1 - \frac{z^2}{R^2}\right) \rho(z) dz, \quad (2.38)$$

where  $R$  is the vessel's radius and  $\rho$  can be obtained by putting together Eq. (2.35) and Eq. (2.37). It is possible to use Eq. (2.38) to estimate the deviations from the trivial computation of the mass that one would get in the assumption of uniform dissolution of the gas. This is shown in the right panel of Fig. 2.13. In particular, the plot shows the difference between the total xenon mass evaluated according to Eq. (2.38) and that obtained assuming uniform pressure and gaseous density in a spherical volume of 2.8 m. The offset of  $\sim 700$  kg<sup>15</sup> is due to the fact that, in the homogenous assumption, at  $p_0 = 0$  there is no gas dissolved at all, while in the realistic case, it is possible to have xenon dissolved throughout the detector in such a way that at the hydrostatic equilibrium the amount of gas at the top of the detector is negligible. This can be understood by looking at the pressure behavior in the left panel of Fig. 2.13, which is proportional to the amount of dissolved gas. In practice, the amount of xenon which can be inserted in the detector without modifying any infrastructure is as high as a few tons.

It has to be noted that in general, the solubility of gases in liquids depends on the temperature. For instance, CO<sub>2</sub> solubility increases of  $\sim 30\%$  if the temperature decreases from 18° C to 8° C. In addition, it is known since the very beginning of Borexino, that a significant thermal gradient along the vertical axis is present (see Sec. 4.9.2 for more details). The thermal gradient in Borexino is pretty much linear in space, meaning in practice that considering a possible temperature effect is totally equivalent to a rescaling

<sup>15</sup>This amount of xenon would be dissolved in a sphere of 2.8 m. In the total vessel volume of Borexino, the amount of xenon would be around 2ton.

of the value of the solubility. Therefore, apart from the quantitative conclusions, the above discussion is not modified in the substance by a possible temperature effect.

An effect which should be taken into account carefully is the energy reconstruction dependence upon the position. The stratification of the gas in layers, in fact, could induce different energy responses in the detector depending on the vertical coordinate. As it is discussed e. g. in Sec. 3.5.1, the addition of xenon to the liquid scintillator actually alters the light yield by an amount which depends on the pressure. For this reason, in order to have the lowest energy resolution, the energy reconstruction should be designed in order to take into account of the different energy response depending on the position of the event.

#### 2.8.4 Borexino’s expected sensitivity and comparison with other experiments

In this section, the expected performances in terms of energy resolution, backgrounds in the ROI and ultimately the sensitivity to  $0\nu\beta\beta$  of a possible Borexino-like experiment whose scintillator is loaded with  $^{136}\text{Xe}$  at high pressure are presented.

Given the most important features of a specific detector (energy resolution, background and so on, see Tab. 2.4) it is possible to use Eq. (2.24) to estimate its sensitivity to  $0\nu\beta\beta$ . In this case, the term  $n_B$  accounts for two different contributions, namely the counts in the ROI coming from contaminations and those coming from the intrinsic  $2\nu\beta\beta$  decay events. In order to estimate this last contribution, the resolution, approximated with a gaussian with a given width, was convolved with the  $2\nu\beta\beta$  summed electron spectrum, i. e. the spectrum of the sum of the energies of the two electrons. Its shape for the  $^{136}\text{Xe}$  is obtained from Ref. [197] which refers to Ref. [132]. The result of this computation is in substantial agreement with the approximated formula of Eq. (2.28). In Tab. 2.8, the main features of the present or next future  $^{136}\text{Xe}$  based experiment are shown.

The same approach was followed for three different scenarios concerning a possible Borex-Xenon experiment looking for  $0\nu\beta\beta$  of  $^{136}\text{Xe}$ . The performances of the resulting detectors are shown in Tab. 2.9, with the same format of Tab. 2.8. The first scenario, the one labelled “Current-Borex”, refers to the hypothesis in which the scintillator is loaded with xenon at a pressure  $p_0 = 0.5$  bar (see Sec. 2.8.3) and all the detector performances are untouched, i. e. energy resolution and backgrounds at the same level as Borexino’s. The quoted number for the background in this configuration is extracted directly from Borexino data. Already without modifying the Borexino facility, the sensitivity on the half-life would already be better by a factor of 4 than the current best limit from KamLAND-Zen (see Tab. 2.8). The main motivation for this good performance is the very good energy resolution<sup>16</sup> and the lowest background. However, KamLAND-Zen has already run for some years and by the time the potential Borex-Xenon takes data, KamLAND-Zen’s statistics (and possibly also the detector) might be improved, thus resulting in a better performance than the present one.

---

<sup>16</sup>This statement evidently is referred at liquid scintillator detectors, since with other techniques the energy resolution could be way better.

Feature	EXO-200 [166]	KamLAND Zen [169]	NEXT-100 [198] (assumed)	nEXO <sup>d</sup> (from EXO-200)	nEXO <sup>e</sup> [177] (assumed)
Total Mass [kg]	200	344	100	12000 <sup>f</sup>	12000 <sup>f</sup>
Fiducial Mass [kg, $^{136}\text{Xe}$ ]	76.5	94 <sup>b</sup>	80	4302	4302
Enrichment [%]	80.6	90.77	90	90	90
FWHM Energy resolution [%]	3.6	11	0.5	3.6	2.35
$2\nu\beta\beta$ in ROI [counts ton( $^{136}\text{Xe}$ ) $^{-1}$ y $^{-1}$ ]	0.1	75	<0.1	0.1	$\sim 10^{-2}$
Other bkg in ROI [counts ton( $^{136}\text{Xe}$ ) $^{-1}$ y $^{-1}$ ]	229	108	6.8	229	4.5-1.2 <sup>g</sup>
Bkg in ROI [c ton( $^{136}\text{Xe}$ ) $^{-1}$ y $^{-1}$ ]	229	183 <sup>c</sup>	6.8	229	4.5-1.2 <sup>g</sup>
Total bkg in ROI 5 y [c]	88	86	2.7	4926	91-16 <sup>g</sup>
$S^{0\nu}_{(90\% \text{ C.L.})}$ [yr]	$1.1 \cdot 10^{25}$	$9.2 \cdot 10^{25}$ <sup>d</sup>			
$S^{0\nu}_{(90\% \text{ C.L.})}$ [yr]	$3.3 \cdot 10^{25}$ <sup>a</sup>	$4.3 \cdot 10^{25}$ <sup>e</sup>	$2.8 \cdot 10^{26}$	$5.6 \cdot 10^{26}$	$3.7-5 \cdot 10^{27}$ <sup>g</sup>
computed according to Eq. (2.24)					

<sup>a</sup>The reported value of the mean sensitivity for the experiment is  $1.9 \cdot 10^{25}$  yr [166].

<sup>b</sup>This value refers to the amount of  $^{136}\text{Xe}$  in the innermost 1 m.

<sup>c</sup>The background is the mean value of the PhaseII of the data taking: assuming the values as low as the ones reported for Period-2 in Ref. [169], this value would become 57.

<sup>d</sup>The limit quoted in Ref. [169] is better than the one reported here, since this one refers to PhaseII only, without any combination with PhaseI.

<sup>e</sup>The mean sensitivity quoted in Ref. [169] is  $5.6 \cdot 10^{25}$  yr.

<sup>f</sup>Assuming the same volume efficiency cut as EXO-200.

<sup>g</sup>The first number is computed assuming a background of  $6.1 \cdot 10^{-4}$  counts yr $^{-1}$  mol $^{-1}$  ( $^{136}\text{Xe}$ ) and a fiducial mass of 4302 kg, while the second one assumes  $1.6 \cdot 10^{-4}$  counts yr $^{-1}$  mol $^{-1}$  ( $^{136}\text{Xe}$ ) and a fiducial mass of 2700 kg.

**Tab. 2.8:** Sensitivities and backgrounds for some present and near future  $^{136}\text{Xe}$ -based  $0\nu\beta\beta$  experiments. ROI is intended here as the region in a FWHM with respect to the  $0\nu\beta\beta$  Q-value. The “other background in ROI” row refers to the contaminants different from the  $2\nu\beta\beta$  itself. The second to last row indicates the experimental limit possibly achieved by the experiment, while the last row is computed according to Eq. (2.24) and assumes the actual live time if an experimental limit exists otherwise 5 years running time are hypothesized. The “assumed” comment in parenthesis recalls that the feasibility of the performances reported has still to be demonstrated experimentally.

If one considers an improved situation, say “Borex-Xe 4ton”, in which the light collection is better (e.g. thanks to the addition of more PMTs) by a factor of two<sup>17</sup> and where the xenon is dissolved with  $p_0 = 2.5$  bar, the results are one order of magnitude better than the present and next-future sensitivity. In fact, apart from nEXO, which still has to prove to be able to push the energy resolution and the backgrounds as down as claimed in the last column on Tab. 2.8, all the other future experiments do not seem to be able to do much better.

The last scenario considered in Tab. 2.9 foresees  $p_0 = 4.5$  bar and assumes to be able to reduce the background of a factor of  $\sim 20$  (in addition to an improved energy resolution). This is actually still a conservative assumption. In fact, as discussed in Ref. [199], the main background in Borexino for the  $0\nu\beta\beta$  is due to external gammas of  $^{208}\text{Tl}$ , which is mostly concentrated on the PMTs light concentrators and the Stainless Steel Sphere (SSS). Intrinsically, the scintillator is almost background free around the  $0\nu\beta\beta$  Q-value (see Sec. 4.3). Concerning cosmogenic backgrounds, extensive studies

<sup>17</sup>This is actually possible, since the present Borexino geometrical coverage is around 30%.

Feature	Current Borex <sup>a</sup>	Borex-Xe 4t <sup>b</sup>	Borex-Xe 7t <sup>c</sup>
Total Mass [kg]	5847 <sup>d</sup>	19375 <sup>d</sup>	32900 <sup>d</sup>
Fiducial Mass [kg, $^{136}\text{Xe}$ ]	1504	4471	7592
Enrichment [%]	90	90	90
FWHM Energy resolution [%]	6.7	4.2	4.2
$2\nu\beta\beta$ in ROI [counts ton( $^{136}\text{Xe}$ ) $^{-1}$ y $^{-1}$ ]	4	0.25	0.25
Other bkg in ROI [counts ton( $^{136}\text{Xe}$ ) $^{-1}$ y $^{-1}$ ]	122	29	1.3
Bkg in ROI [counts ton( $^{136}\text{Xe}$ ) $^{-1}$ y $^{-1}$ ]	126	29	1.5
Total bkg in ROI 5 y [c]	948	648	57
$S^{0\nu}$ (90% C. L.) [yr]			
computed according to Eq. (2.24)	$4.4 \cdot 10^{26}$	$1.6 \cdot 10^{27}$	$8.3 \cdot 10^{27}$
$t_{1/2}(3\sigma \text{ C. L.})$ [yr]			
computed according to Eq. (2.39)	$1.7 \cdot 10^{26}$	$6.1 \cdot 10^{26}$	$3.2 \cdot 10^{27}$

<sup>a</sup> Assumes a spherical fiducial volume with  $R = 2.8$  m and a pressure  $p_0 = 0.5$  bar.

<sup>b</sup> Assumes a spherical fiducial volume with  $R = 2.7$  m and a pressure  $p_0 = 2.5$  bar. Light yield doubled with respect to Borexino.

<sup>c</sup> Assumes a spherical fiducial volume with  $R = 2.7$  m and a pressure  $p_0 = 4.5$  bar. Light yield doubled with respect to Borexino and background at the level of Borexino's  $R < 1$  m.

<sup>d</sup> This number assumes that Borexino geometry is not changed at all. With a modification of the project, this number could be dramatically decreased.

**Tab. 2.9:** Sensitivities and backgrounds for some possible configuration of the Borexino detector adapted to look for the  $0\nu\beta\beta$  of  $^{136}\text{Xe}$ . ROI is intended here as the region in a FWHM with respect to the  $0\nu\beta\beta$  Q-value. The “other background in ROI” row refers to the contaminants different from the  $2\nu\beta\beta$  itself. The second to last row indicates the experimental limit possibly achievable, while the last row shows the  $0\nu\beta\beta$  discovery potential.

were carried out for the  $^8\text{B} \nu$  analysis (see Sec. 4.10 and Refs. [200, 201]). The most critical contribution in the  $0\nu\beta\beta$  region of interest is due to  $^{10}\text{C}$  decays. However, it is quite small<sup>18</sup> compared to that of external backgrounds and can be substantially decreased by applying a Three Fold Coincidence veto (see Sec. 6.3) and by the usage of  $\beta^+/\beta^-$  pulse shape discrimination (see Sec. 4.8). The addition of xenon to the liquid scintillator might also lead to the production of Xe-correlated cosmogenic backgrounds. The most important one for the  $0\nu\beta\beta$  search is  $^{137}\text{Xe}$ , generated via neutron capture. The production rate of  $^{137}\text{Xe}$  is lower than that of  $^{10}\text{C}$  (also considering the relative abundances of  $^{136}\text{Xe}$  and  $^{12}\text{C}$ ) and it can be removed very efficiently (> 90%) by the Three Fold Coincidence. Therefore, it does not represent a real concern for Borex-Xenon.

As studied in Ref. [199] by means of the Borexino Monte Carlo simulation, if one replaced the light concentrators with much purer aluminum and the SSS with one made out of titanium, the level of the external gammas would be reduced at least by a factor of  $\sim 20$ . The “Borex-Xe 7ton” configuration assumes as background level the one measured today in the innermost 1 m sphere of the fiducial volume, and thus around a factor of  $\sim 20$

<sup>18</sup>It is almost at the same level of the unavoidable  $^8\text{B} \nu$  rate.

less than the previous configurations (where the background is predominantly coming from outside). “Borex-Xe 7ton” could have approximately the performance of the “mega” experiment discussed in Sec. 2.6.5.

It is interesting to investigate the discovery potential of Borex-Xenon in the fortunate case of a peak showing up at the Q-value. As anticipated in Sec. 2.8.1, Borex-Xenon might exploit the source-in/source-out approach, which could provide a smoking gun for the discovery. In principle, one should subtract the spectra obtained with and without  $^{136}\text{Xe}$  dissolved in the scintillator, taking into account that some backgrounds might be Xe- or  $^{136}\text{Xe}$ -correlated. The only non-negligible Xe-correlated background is given by the  $2\nu\beta\beta$  decay, since the cosmogenic  $^{137}\text{Xe}$  can be almost completely removed by the Three Fold Coincidence, as discussed above. The  $2\nu\beta\beta$  contribution can be subtracted away with quite good accuracy thanks to the knowledge of its half-life and of the amount of  $^{136}\text{Xe}$  present in the detector. Therefore, the main uncertainty introduced by the subtraction is the statistical one. Within these assumptions and in the hypothesis that both the source-in and the source-out phases have the same exposure, it is possible to estimate the discovery potential by modifying Eq. (2.24) as follows:

$$n_{\beta\beta} \geq n_\sigma \sqrt{n_{\beta\beta} + 2n_B + n_{2\nu}}, \quad (2.39)$$

where  $n_{2\nu}$  is the number of  $2\nu\beta\beta$  events in the region of interest and  $n_B$  (in this case) accounts for intrinsic, external and cosmogenic backgrounds only. Equation (2.39) states that the  $0\nu\beta\beta$  signal must exceed the total statistical uncertainty introduced by the background subtraction in the interesting energy window. The maximum half-lives of the hypothetical  $0\nu\beta\beta$  decay which Borex-Xenon could discover with this approach are reported in the last row of Tab. 2.9. The values are slightly smaller than those which can be probed if no peak is observed.

Figure 2.14 shows  $m_{\beta\beta}$  as a function of the lightest neutrino mass together with the performances in terms of  $m_{\beta\beta}$  of the possible Borex-Xenon’s listed in Tab. 2.9. The bands shown in Fig. 2.14 correspond to the  $S^{0\nu}$  row of Tab. 2.9 and thus refer to the sensitivity on the  $0\nu\beta\beta$  exclusion. Here,  $g_A = 1.269$ , and PSFs and NMEs come from Ref. [132] and Ref. [135] respectively.

## 2.9 Conclusions and outlook

A cautious attitude in dealing with the results from cosmological surveys is highly advisable. However, the newest analyses confirm and strengthen the limits on  $\Sigma$ , pointing down to low values, somehow incompatible with the  $\mathcal{IH}$  scenario. From the point of view of  $0\nu\beta\beta$ , these results show that ton or multi-ton scale detectors are needed in order to probe the range of  $m_{\beta\beta}$  now allowed by cosmology. In addition to this, a better understanding of the quenching of  $g_A$  in the nuclear medium is very urgent. If this turns out to be negligible, it will be possible to start probing the  $\mathcal{IH}$  region with the next generation of experiments, otherwise it will be unlikely to be able to reach the minimum sensitivity required to probe the  $\mathcal{IH}$  region within the next 20 years. Results on  $\Sigma$  from

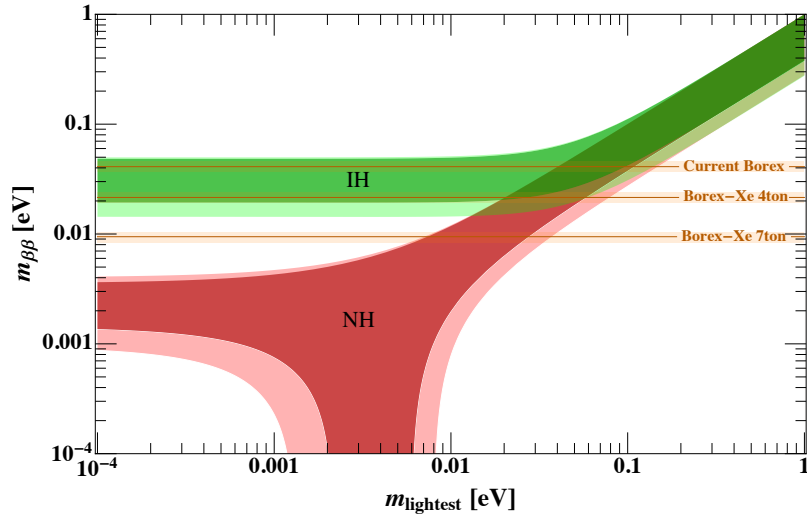


**Fig. 2.14:**  $m_{\beta\beta}$  as a function of the lightest neutrino mass with the bands corresponding to the projected sensitivities of the possible Borex-Xenon's presented in Tab. 2.9.

cosmology could be precious to understand (and possibly quantify) the actual quenching of  $g_A$ . Given the current bound on  $\Sigma$ , if next generation experiments see a signal, it will likely be a  $0\nu\beta\beta$  signal of new physics different from the light Majorana neutrino exchange, or, conversely, this will indicate that the present cosmological modeling is wrong. Within this scenario, it is clear that searching for  $0\nu\beta\beta$  with different isotopes is the key strategy in order to being able to understand the mechanism generating the  $0\nu\beta\beta$  in the fortunate case of a positive signal.

A Borexino-like  $0\nu\beta\beta$  experiment would be very powerful and have great sensitivity, as discussed in Sec. 2.8.4. Particularly, the relatively good energy resolution and the superb radio-purity (already demonstrated experimentally by almost 10 years of Borexino) are the key elements. The main disadvantage of the technique comes from the cost of the isotope, which would be the most demanding item in the budget. Apart from this, the technique is solid, well demonstrated, and the risk of failure is pretty low. In fact, since the main background in Borexino is external, even in the worst case in which one failed in the reduction of the gamma contaminants coming from the aluminum and the steel, it would be possible to reach the highest level of purity just by fiducializing the innermost part of the active volume. Furthermore, just by increasing the pressure without modifying anything in the setup, one would always be able to reach the planned exposure. It has to be noted that the potential development of a new, smaller inner vessel could allow to have the same fiducial volume mass, while using a smaller amount of xenon. Anyhow, this would not be trivial, since the new vessel should be much purer than the present one (especially in  $^{232}\text{Th}$  and  $^{238}\text{U}$ ) being it closer to the fiducial volume. Alternatively, if no other small vessel able to support the xenon weight is developed, the buffer liquid can be slightly modified in order to have a density such that the hydrostatic equilibrium between the buffer and the inner vessel is assured.

# Chapter 3

## Measurements of optical properties of scintillators doped with xenon

In this chapter, the details of an R&D project designed and developed in Genova are described. The aim consisted in the characterization of liquid scintillator's optical properties when doped with gaseous xenon at high pressure. Particularly, the measurements were focused on the light yield, attenuation length and time response variations as a function of the xenon concentration in the liquid scintillator. Preliminary results were already presented in Refs. [202, 203].

The chapter is structured as follows. Section 3.1 describes the experimental setup, Sec. 3.2 discusses the electronics used for the data acquisition, Sec. 3.3 describes how the thermodynamics of the setup is modeled, Sec. 3.4 reports the results obtained with the “large chamber”, Sec. 3.5 shows the measurements carried out with the “small chamber”, Sec. 3.6 discusses the investigations on scintillator samples with different PPO concentrations, Sec. 3.7 describes the measurement of Borexino's scintillator time response, Sec. 3.8 shows the LAB+PPO scintillator characterization and Sec. 3.9 discusses the results and provides a possible outlook for the development of this technique for  $0\nu\beta\beta$  investigations.

### 3.1 Description of the setup

The setup consists in two chambers containing liquid scintillator and able to reach a pressure of 5 bar. They share a common hydraulics system which allows the management of the liquid and the gas inside the apparatus and are equipped with photosensors in order to measure the scintillation light. One chamber is 50 L in volume (“large chamber”), while the other one is just 0.25 L (“small chamber”). They are cylinders, and while the larger one has bases with 5” diameters, the smaller one has a base diameter of 3”.

The need for two different chambers has both scientific and practical motivations. In

order to test the liquid scintillator optical properties, a chamber with the size of the order of meters is needed, since the Borexino scintillator attenuation length at the wavelengths of interest is around  $\sim 7$  m. Therefore, for the sake of possibly appreciating little changes in the attenuation length due to the introduction of the xenon inside the liquid, the chamber must have a size similar to the scale of the attenuation length. As detailed in Sec. 3.1.1, there is the possibility to study events in selected locations along the large chamber length. This would allow to study attenuation effects to some extent, even if it would not be possible to completely decouple propagation and generation of light effects. This fact explains scientifically the need for the smaller chamber. In addition, the small chamber allows to save a consistent amount of money. When performing a “cycle of measurements”, that is measuring some optical property as a function of the amount of xenon dissolved in the scintillator (or the pressure), a quite large amount of xenon is needed in the case of the large chamber (around 3 kg). It is unreasonable to just buy “new” xenon for every cycle of measurement and, also, the construction of a certified, cryogenic xenon recovery system would be too expensive. For these reasons the small chamber was constructed, providing also the scientific advantages described above.

### 3.1.1 The large chamber

The project of the large chamber is shown in Fig. 3.1. It is a cylinder about  $\sim 1$  m long and with a diameter of  $\sim 20$  cm. It can contain around 50 L of liquid scintillator. It

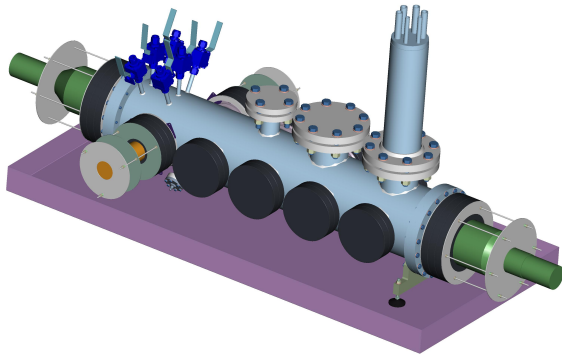


**Fig. 3.1:** Rendering of the large chamber.

is realized with 3 mm-thick steel. 11 quartz windows are left on the sides, in order to collect the scintillation light produced inside. Two 5" PMTs are put in front of the two windows at the bases of the cylinder, while the 9 lateral windows can house 3" PMTs. All the material was chosen to be compatible with Borexino’s liquid scintillator (PC, with the addition of PPO at 1.5 g/L) which is a quite aggressive solvent. The windows are made with quartz, since the glass is not transparent enough to the next-to-UV light produced by the scintillator (see Sec. 5.3.1).

Orthogonally to the main body of the chamber, a smaller steel cylinder allows to create a liquid-gas interface through which the equilibrium between the two phases can be reached. Other appendixes and openings are left in various places on the chamber: these allow the positioning of sensors and are useful when loading and unloading the liquid scintillator.

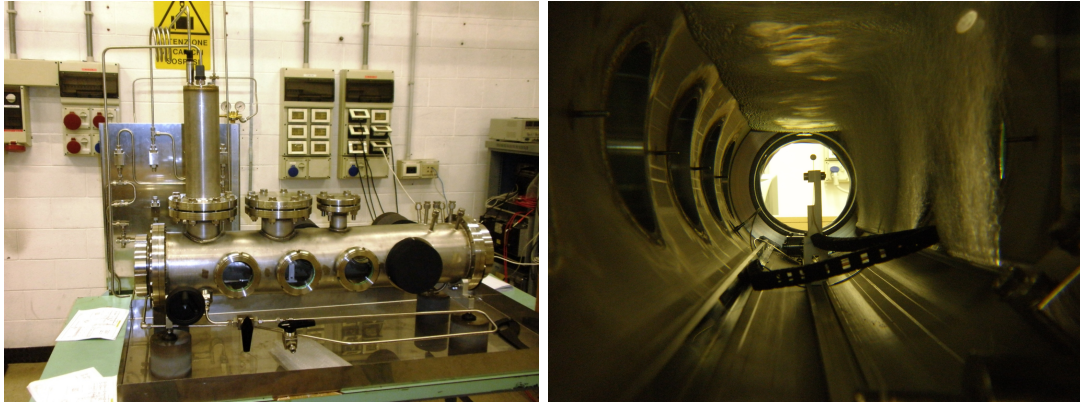


**Fig. 3.2:** *Left panel:* Picture of the large chamber completed and assembled. *Right panel:* View inside the large chamber filled with PC during nitrogen bubbling of the scintillator.

On the left panel of Fig. 3.2 a picture of the actual large chamber is shown. The right panel shows the inside, filled with PC, during nitrogen bubbling. At the bottom of the cylinder, inside the chamber, a little pipe drilled with lots of small holes is placed. The gas enters the chamber through this pipe and through the holes it can bubble inside the scintillator. This is needed in order to make the nitrogen bubbling effective<sup>1</sup>: the sparging of the liquid with nitrogen is essential, since during transportation and loading in the apparatus the liquid scintillator might have got in contact with air and especially with oxygen. The scintillation of PC, but in general of organic liquid scintillators, is pretty much affected by even a little presence of oxygen, which alters the temporal response and the light yield of the scintillator cocktail.

In the right panel of Fig. 3.2 it is possible to note a little movable carriage that holds a tiny teflon sphere on the top. This sphere is linked to a light pulse generator through an optical fiber that gets out of the chamber. By using this source of light, it is possible to calibrate the PMTs and to study the light propagation inside the scintillator.

As a source of energy deposit inside the chamber, it is possible to use gamma radioactive sources or, more conveniently, the natural cosmic muon flux. The dimensions and the geometry of the chamber, in fact, allow an interaction rate of muons inside the scintillator of about 30 Hz. The usage of radioactive sources is in principle possible, but because of the geometrical construction of the chamber and the positioning of the PMTs, the light produced by an energy release of a few hundreds of keV is not enough to generate a sufficiently high number of detected photoelectrons. The main limitation

<sup>1</sup>The efficiency of gas sparging increases if the surface of the bubbles is big and thus it is higher when there are many small bubbles, as opposed to few larger ones.

is the geometrical coverage of the photosensors with respect to a point-like interaction inside the chamber. This is not a problem in the case of muon interactions, since in that case the energy release is of the order of a few MeV per cm.

A set of eight plastic scintillators for the tagging of muons crossing the chamber was developed at Laboratori Nazionali del Gran Sasso. Particularly, plastic rectangular prism scintillators of about  $5 \times 30 \times 0.5$  cm are instrumented with a light guide passing through their longest symmetry axis. At one end of the fiber optics some reflective aluminum is placed, while at the other end the fiber is coupled to a silicon photomultiplier (SiPM) which is able to detect the light. By putting together the eight plastic bars and looking for time coincidences of the signals, it is possible to track muons quite efficiently. In particular, by placing bars above and below the chamber, muon events in the liquid scintillator can be tagged. This gives also the opportunity to study events in different positions along the chamber axis. The plastic scintillators mounted to form crosses and thus tag muons only in the overlapping region are visible in Fig. 3.3. Extensive tests were performed in order to be sure that the working condition of these detectors (SiPM voltage breakdown, amplification, threshold) were optimized for the detection of muons. In particular, the coincidence rate of events in two or more plastic bars in different geometrical configurations (such as piles of two or more bars, crosses of two bars in different location with respect to the bar lengths, bars placed one next to the other, bars put at different heights) was measured and was found to agree pretty well with the theoretical prediction. Of course, each bar has a unique detection efficiency, but this fact is not critical, since a measurement of the rate of the events is not carried out.

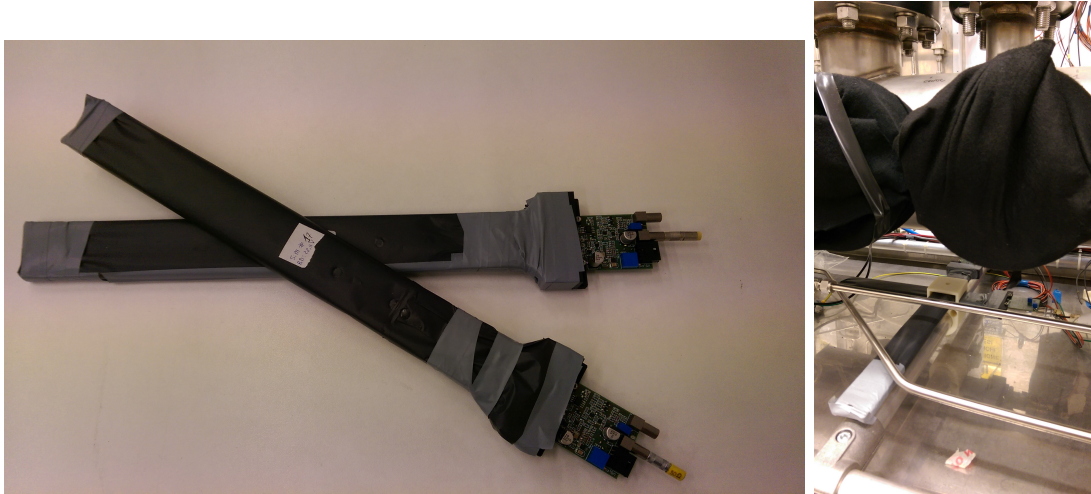


**Fig. 3.3:** The external muon tagging system through plastic scintillators coupled with SiPMs.

In steady working condition, the large chamber is equipped with two 5" PMTs (HAMAMATSU R1584 [204]) looking inside from the two cylinder basis windows. This kind of PMT has a good temporal resolution and a good quantum efficiency also in the near UV region.

### 3.1.2 The small chamber

A schematic view of the project of the small chamber is presented in Fig. 3.4. The design is very similar to that of the larger one, apart from the dimensions. In this case, the cylinder holding the scintillator has a diameter of about  $\sim 10$  cm and a height of approximately 5cm. A little expansion volume is placed on top of the cylinder, in order to establish an interface between the liquid and gaseous part, exactly as it is done for the larger chamber. A “gas sparger” was designed and placed at the bottom of the chamber (see Fig. 3.5): it is very useful in order to limitate the gaseous flux in the small liquid volume hosted inside the cylinder and, more importantly, it allows the creation of many small bubbles, thus increasing the surface of the gas fluxing through the liquid and incrementing the stripping efficiency.

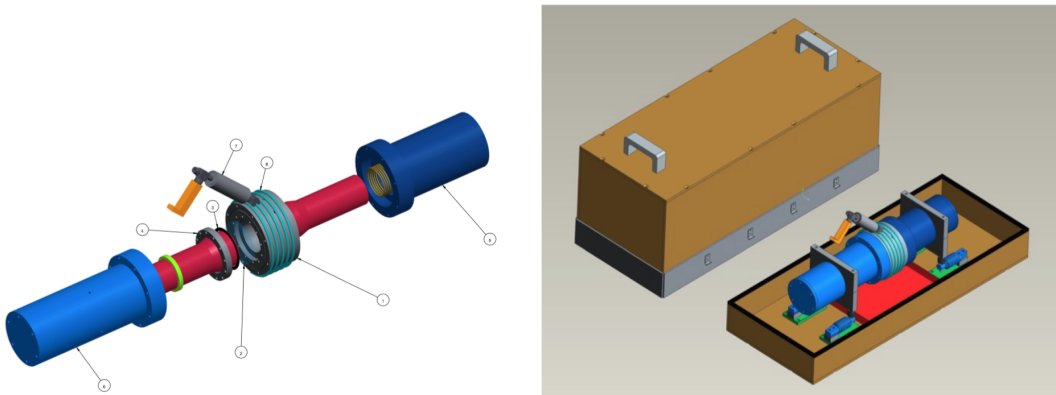


**Fig. 3.4:** Schematic view of the project for the realization of the small chamber. As visible from the figure on the right, the chamber is encapsulated in a dark box, in order to gaurantee easily the light tightness.

The scintillation light can be detected by two 3" PMTs (HAMAMATSU R6091 [205]) placed at the basis of the chamber, where instead of stainless steel, the scintillator is in contact with quartz windows. Thanks to its small dimensions, the whole system is placed in a dark box (see the right panel of Fig. 3.4), thus making it easier to avoid light leaks inside the apparatus from the external environment. This was not possible for the larger chamber, and thus much more care was needed in that case in order to optically seal all the junctions. Figure 3.6 shows the actual small chamber completed and assembled.

A critical difference with respect to the large chamber is in the rate of cosmic muons. Because of the small dimensions, the rate of this kind of events is too low ( $\sim 0.5$  Hz) to be used in practice to study the scintillation process. Conversely, the geometrical coverage of the photosensors is pretty high, and thus it is possible to use collimated gamma sources in order to scatter off electrons and produce scintillation light in the liquid scintillator.

This chamber was projected in order to make measurements in different modes. In fact, besides the measurement of the scintillation light yield as a function of the xenon concentration in the liquid scintillator, it is possible to perform the measurement of the scintillator time response (see Sec. 3.7). This goal is achieved by using one of the two

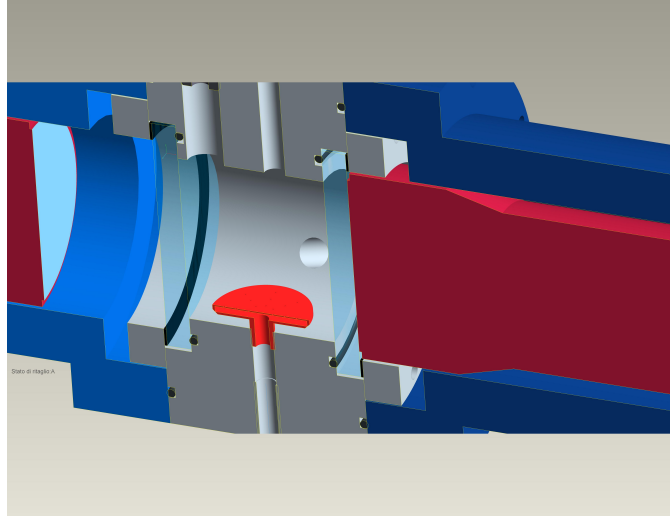


**Fig. 3.5:** Rendering of the gas sparger on the bottom of the small chamber.

PMTs as a trigger (keeping it very well optically coupled) and the other one as light detector in the single photoelectron regime (degrading the optical coupling between it and the chamber). This is technically impossible to be done in the larger chamber, since the system is not contained in an external dark box and thus the light tight is provided by a close contact of the PMTs and the chamber<sup>2</sup>.

### 3.1.3 Hydraulics system

The hydraulics system is meant to control all the fluid movements inside the chambers. The two chambers are connected in parallel to the hydraulics apparatus, thus making it possible to use them independently. The system allows to load, unload and recirculate nitrogen and xenon in the liquid scintillator. A complete hydraulic scheme of the system is shown in Fig. 3.7.

In the top left corner of Fig. 3.7 there are two bottles that contain nitrogen and xenon. Nitrogen is used for test purposes and for gas stripping of the liquid scintillator. As detailed in Ref. [206], the stripping of the liquid scintillator with nitrogen is very important in order to eliminate impurities (e.g. oxygen) which could create light quenching. In addition to this scientific requirement, using nitrogen is convenient in a commissioning stage because of its cheapness. The two bottles are linked to the main pipe circuit which is basically a closed loop. A pump allows the recirculation of the gas introduced inside the system and inside the chambers. Thanks to the spargers placed at the bottom of the chambers, the gas can bubble inside the liquid and so dissolve into it. The expansion volumes at the top of the two chambers allow the gas to circulate inside the pipes, while the liquid is confined inside the main chambers' volume.

---

<sup>2</sup>Theoretically, it would be possible to worsen the optical coupling within the mentioned experimental constraint of light tightness by the usage of optical filters, but they were not available.

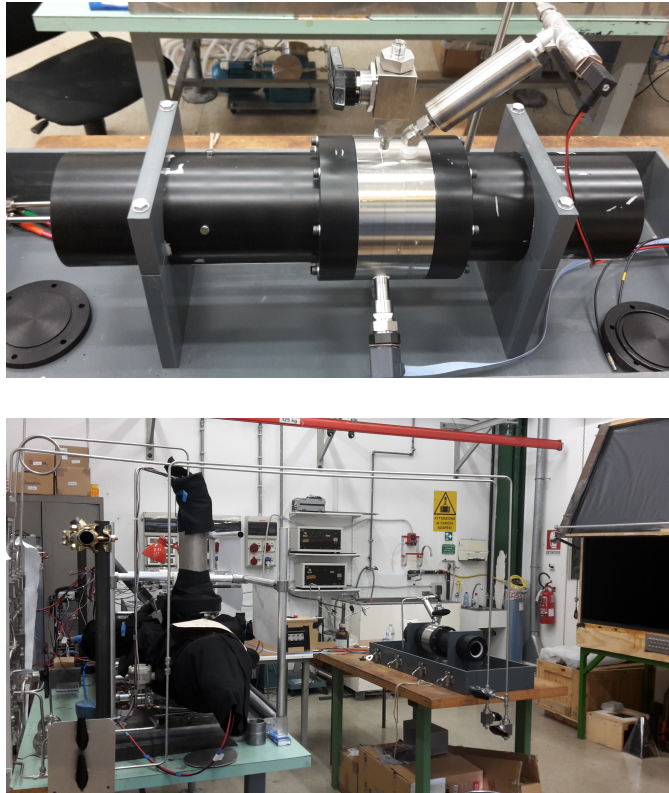


**Fig. 3.6:** *Top panel:* View of the small chamber, equipped with temperature and pressure sensors. *Bottom panel:* The large chamber is shown on the left, while the small one is on the right. The pipes connecting both the chambers to the hydraulics panel (which is on the left) are visible.

The system allows to control the xenon and the nitrogen partial pressures inside the chamber by means of a set of valves all along the hydraulics circuit. The hydraulic part was commissioned using water as emulator of the liquid scintillator and it is able to handle pressures up to about 5 bar.

### 3.1.4 Sensors

The system is equipped with a variety of sensors, both for monitoring the setup during operations and for measuring the apparatus conditions while acquiring measurements. All the sensors are interfaced with a computer and either acquired with a serial RS-232 connection or through a standard 4 – 20 mA loop. A custom software developed within the “LabVIEW” environment controls the readout of these devices. More details are given in Ref. [202]. The system is provided with the following sensors (the letter followed by a number in the parenthesis provides the label with which the sensor is tagged in the hydraulics scheme of Fig. 3.7):

- 3 pressure sensors ( $S1$  [large chamber],  $S5$  [hydraulics panel] and  $S7$  [small chamber], precision 0.25%).

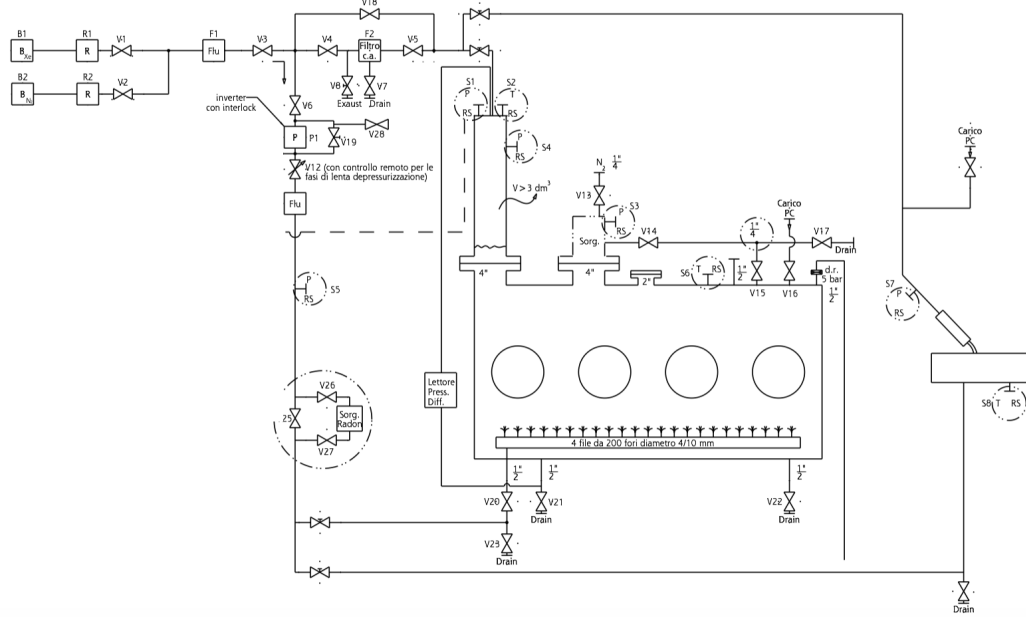


**Fig. 3.7:** Hydraulics scheme of the system. The plant is essentially a closed loop. The gas (either nitrogen or xenon) enters from the top left part of the scheme. It then flows through a pump which injects it either in the large or in the small chamber. The pipes are instrumented with various automatic sensors as outlined in Sec. 3.1.4.

- 2 temperature sensors ( $S_2$  [large chamber] and  $S_8$  [small chamber], precision 0.1%).
- 1 differential pressure sensor (“*Lettore Press. Diff.*” in the scheme [large chamber], precision  $\sim 1$  mm for  $\sim 20$  cm).
- 1 flux-meter (“*Flu*” in the scheme [hydraulics loop], operated by Coriolis effect, precision 0.1%).
- 4 strain gauges to measure the mass of the large chamber (not in the scheme, precision of 1 g for  $\sim 200$  kg).
- 1 high precision scale to measure the mass of the small chamber (not in the scheme, precision of 0.1 g for  $\sim 20$  kg).

The differential pressure sensor constantly monitors the liquid height inside the big chamber, when the PMTs are on and thus the innermost part of the chamber is not visible. The height of the liquid in the small chamber is not measured. The flux-meter allows the measurement of the amount of xenon introduced in the system and, most importantly, allows the monitoring of the gas circulation inside the circuit. In order to have a precise measurement of the amount of gas actually present inside the chambers (both in a gaseous phase and dissolved in the liquid), the system is also constantly weighed (the large chamber with 4 strain gauges and the small chamber with a precise scale).

More details are given in Sec. 3.3. In conclusion, the sensors allow the measurement of the following parameters of scientific interest:

- Amount of scintillator inside the chambers.
- Gaseous xenon/nitrogen partial pressures.
- Amount of xenon/nitrogen dissolved in the scintillator.

Note that nitrogen is almost unavoidably present inside the scintillator because its inevitable (but harmless) dissolution in the liquid during nitrogen stripping.

## 3.2 Electronics

An electronic chain able to handle the readout of 4 PMTs and 8 muon taggers was developed. The acquisition system cannot operate the two chambers simultaneously. The front end electronics is handled by “NIM” modules, which provide amplification and logical operations on the signals. This allows the generation of the trigger, too. The main trigger logic is based on the coincidence of the discriminated signals on the two PMTs. The trigger logic is slightly modified during time response measurements as described in Sec. 3.7. The PMT waveforms are fed into a digitizer (ADC, CAEN, V1731) and the logic signals generated by a constant fraction discriminator are recorded by a Time to Digital Converter (TDC, CAEN V1290n) module, which stores the times in which the PMTs were hit.

The plastic scintillator detectors for the muon tagging are individually equipped with dedicated chips which provide power to the SiPMs and amplify and discriminate their signals. The discriminated signals (with adjustable threshold) carry the information of the time of the muon crossings in each bar, which is then recorded by the TDC.

All the signals are acquired by a custom LabVIEW software, which was developed in order to get the data from the ADC and TDC boards in addition to other ancillary information on the trigger and on the PMTs status (thanks to the usage of a scaler). The data acquisition system described above produces raw data in ASCII format on a run basis. A very simple reconstruction algorithm was developed, in order to analyze systematically the data and store the information in a ROOT TTree (see Ref. [207]) container. Further details on the electronic boards and chain can be found in Ref. [202].

## 3.3 Gas dissolution and mass control

The thermodynamics of the system can be summarized by the following equations:

$$m_{tot}^{gas} = m_{sc} (k_{Xe}^{sc} p_{Xe} + k_{N_2}^{sc} p_{N_2}) + A_{Xe} n_{Xe}^{gas} + A_{N_2} n_{N_2}^{gas} \quad (3.1)$$

$$p_{tot} = p_{Xe} + p_{N_2} \quad (3.2)$$

$$p_{Xe/N_2} V_{gas} = n_{Xe/N_2}^{gas} RT, \quad (3.3)$$

Measurements with $N_2$ dissolved in PC			
Pressure (bar)	Measured Mass (kg)	Predicted Mass (kg)	$\frac{M_{predicted}}{M_{measured}}$
$1.02 \pm 0.02$	$167.253 \pm 0.001$	-	-
$2.04 \pm 0.02$	$167.271 \pm 0.001$	$167.272 \pm 0.002$	$1.000006 \pm 0.000018$
$3.96 \pm 0.02$	$167.288 \pm 0.001$	$167.288 \pm 0.002$	$1.000000 \pm 0.000018$
$4.06 \pm 0.02$	$167.305 \pm 0.001$	$167.308 \pm 0.003$	$1.000018 \pm 0.000019$
$4.92 \pm 0.02$	$167.321 \pm 0.001$	$167.324 \pm 0.004$	$1.00002 \pm 0.00003$

Tab. 3.1: Measurements with nitrogen in PC ( $k_{N_2}^{PC} \sim 1 \cdot 10^{-4}$ ). Table from Ref. [202].

where  $m_{tot}^{gas}$  is the total mass (both dissolved and gaseous) of nitrogen and xenon inside the system,  $m_{sc}$  is the mass of scintillator inside the chamber,  $p_{Xe}$  and  $p_{N_2}$  are the xenon and nitrogen partial pressures,  $A_{Xe}$  and  $A_{N_2}$  are the molecular masses of xenon and nitrogen,  $n_{Xe}^{gas}$  and  $n_{N_2}^{gas}$  are the number of gaseous moles of xenon and nitrogen and  $k_{Xe}^{sc}$  and  $k_N^{sc}$  are the mass solubility of xenon and nitrogen in the liquid scintillator (Henry's constants).

Equation (3.1) states that the total mass inside the chamber as a function of the pressure is simply the sum of the masses of nitrogen and xenon both in gaseous and dissolved forms. The fraction of gas dissolved inside the liquid phase can be computed from Henry's law. It is proportional to the liquid mass and to the partial pressure of the gas itself. The Henry's constant which describes this process depends both on the liquid and on the gas. Equation (3.2) is Dalton's law of partial pressures and Eq. (3.3) is the ideal gas state equation. In the working condition of the experimental apparatus, the ideal gas equation of state is true with a high accuracy. Ideally, it would not be difficult to implement a Van der Waals state equation, but it is not needed at this stage.

The scintillator mass is evaluated at the time of the filling and the amount of mass inside the chambers is monitored by the scale and the strain gauges. Furthermore, the large chamber is equipped with the differential pressure sensor, which allows to measure the liquid height and thus to monitor more precisely the stability of the liquid mass.<sup>3</sup> The small chamber is almost entirely filled with liquid scintillator. Therefore in this case the contribution to the total mass of the gaseous part is negligible as it would be less than 1 g.

Thanks to the sensors (see Sec. 3.1.4) the apparatus is equipped with, and since Henry's constants can be known from literature, it is possible to reconstruct  $p_{Xe}$  and  $p_{N_2}$  straightforwardly.

In order to perform the commissioning of the system and test the precision of the method, some nitrogen was dissolved in PC in the large chamber. The mass of the system was monitored as a function of the gas pressure. The increase in the system mass due to an increase of pressure is described by the following equation (which follows directly

<sup>3</sup>In case of wrong operations on the hydraulics system, it could be possible to spill some of the scintillator from the chamber to the pipes.

from Eq. (3.1) ):

$$\Delta m = k_{N_2}^{PC} m_{PC} \frac{p_{N_2}}{p_{ref}} + A_{N_2} n_{N_2}, \quad (3.4)$$

where  $p_{ref}$  is the pressure for which the value of the solubility is known. As shown in Tab. 3.1, Eq. (3.4) is able to predict the mass variations as a function of the pressure with a precision of a few grams over about 200 kg. It is important to notice that particular care has to be taken in reaching the thermodynamic equilibrium, in order to be sure that the gaseous partial pressure in the liquid matches the one in the gas phase.

### 3.4 Measurements with the large chamber

Preliminary measurements of the Borexino scintillator light yield as a function of the xenon concentration were already reported in Refs. [202, 203]. The strategy for performing this kind of measurements foresees the usage (and tagging) of muons crossing the chamber and releasing energy in the liquid scintillator. As reported in Ref. [202], the number of photoelectrons produced by the electron recoil induced by an ordinary gamma source outside of the chamber (a few tens) is not high enough to have a good precision on the light yield measurement. On the contrary, the signal generated by muons in the scintillator is *huge*. The goal of the measurements presented in this section is that of assessing the light yield variation of the scintillator cocktail as a function of the xenon concentration.

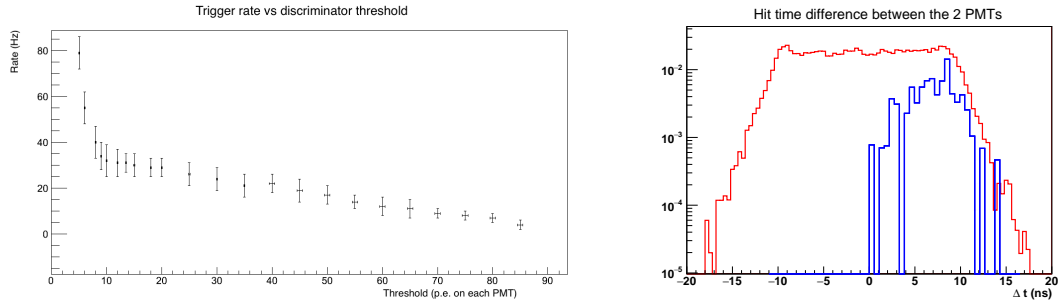


**Fig. 3.8:** *Left panel:* Trigger rate (coincidence rate between the two PMT signals) as a function of the threshold on each tube (in photoelectrons). *Right panel:* Time difference in ns between the recorded hit times on the PMTs. The red curve shows a flat distribution obtained with no position cut, compatible with muons uniformly distributed along the cylinder. The blue line refers to events tagged by the external muon plastic scintillators at one end of the chamber. The scale on the y-axis is on arbitrary unit, and thus the normalizations of the two curves has no physical meaning.

As a preparatory operation, the PMTs were calibrated with the usage of the light diffuser inside the chamber and the LED connected to it. Particularly, the time response and the single photoelectron peak position were studied. These were continuously monitored with dedicated acquisition runs between normal physics run, in order to assure

the stability and the calibration of the system. Furthermore, with the aim of monitoring the electronics stability, a dedicated random trigger was always operating, in order to study possible baseline and noise fluctuations.

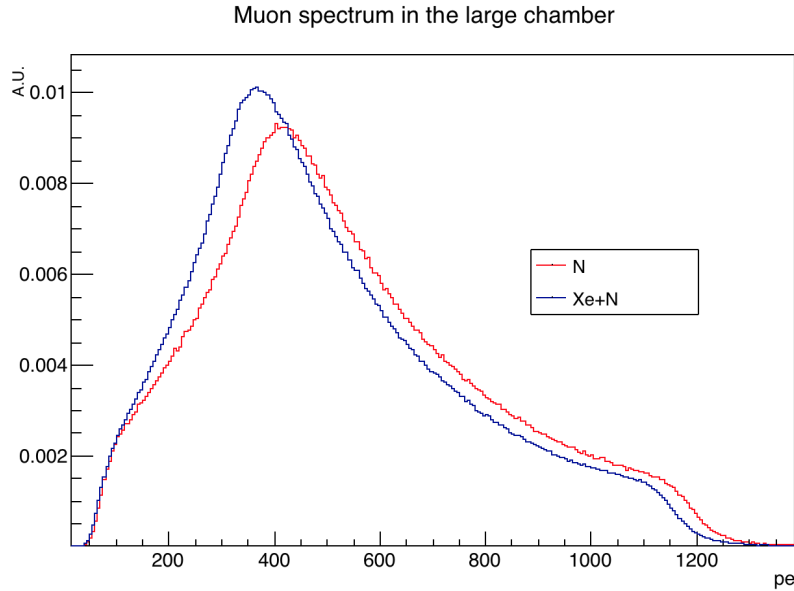


**Fig. 3.9:** Muon spectrum in photoelectrons. The Borexino scintillator condition is plotted in red, while the muon spectrum in the scintillator where  $\sim 0.5$  bar of xenon was dissolved is in blue. The curves are both normalized to 1 in area.

Many checks were performed in order to assure that the light signal seen by the PMTs was due to muons. First of all, the trigger rate as a function of the threshold on each PMT signal was studied. Since the amount of light produced is pretty high (many hundreds of detected photoelectrons), after a fast fall of the rate when increasing the threshold from low values (where noise and natural radioactivity dominate), the trigger rate should stay almost flat while increasing the threshold. The trigger rate as a function of the threshold is shown in the left panel of Fig. 3.8. Another check was performed by looking at the mean time difference between the signals on the two PMTs generated by events tagged by the plastic scintillators in different positions along the cylinder. An example is shown on the right panel of Fig. 3.8. After performing these preliminary controls, the spectrum of the muon energy release in the liquid scintillator was recorded as a function of the nitrogen and xenon pressures.

A comparison between the muon spectrum acquired with the scintillator in standard Borexino conditions (also in the next chapters and sections, this means saturated with nitrogen at 1 bar) and with xenon dissolved at a partial pressure of about  $\sim 0.5$  bar is shown in Fig. 3.9. The spectrum shows the evident features of an endpoint (corresponding to those muon events which release the biggest amount of energy in the scintillator, by crossing the chamber obliquely and thus traveling more in the liquid) and a peak

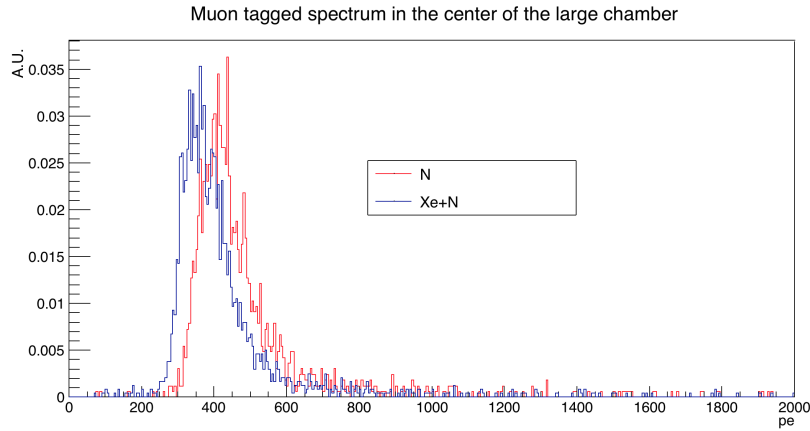


**Fig. 3.10:** Muon spectrum tagged by external  $\mu$  detectors in the center of the chamber in photoelectrons. The Borexino scintillator condition is plotted in red, while the muon spectrum in the scintillator where  $\sim 0.5$  bar of xenon was dissolved is in blue. The curves are both normalized to 1 in area.

structure (corresponding to the vertical crossing of the chamber). Also, Fig. 3.9 shows the quenching effect on the light yield induced by the presence of the xenon which was already presented in Refs. [202, 203]. The spectrum of muon events tagged by the external detectors in the middle of the chamber and with a vertical direction is presented in Fig. 3.10. As expected, the structure of the spectrum for this class of events is peak-like. In fact, the external muon tag system selects events in a well established direction and in a fixed position along the chamber, making the tagged events sort of monochromatic. Some higher energy events, in which some daughters produced by the muon in the scintillator release additional energy, are still visible. Also in this case, the quenching effect induced by the presence of the xenon is present. The magnitude of the effect does not depend on the data selection, as it is explained below and visible in Fig. 3.9 and 3.10.

### 3.4.1 Measurements as a function of xenon concentration

An independent set of measurements was acquired with the large chamber, in order to confirm the preliminary results presented in Ref. [202]. The muon spectrum in the liquid scintillator was measured continuously as a function of the pressure (i.e. dissolved gas concentration). A “cycle of measurements” is intended here to be a set of runs acquired in different pressure conditions, ranging in the interval  $1 \div 5$  bar, going up from the atmospheric pressure to the maximum and then coming back down. It is very important to acquire runs both when the pressure is increased and when it is decreased in order to test their reproducibility. Regarding the filling and emptying of the system with gas, the procedure is well summarized in Fig. 3.11. Some amount of gas, either xenon or nitrogen, is inserted into the system. In the figure, this corresponds to the steps in the mass curve and to the spikes in the pressure. After that, the pump is turned on, and the gas is let recirculate inside the chamber. This allows the dissolution of the gas inside the

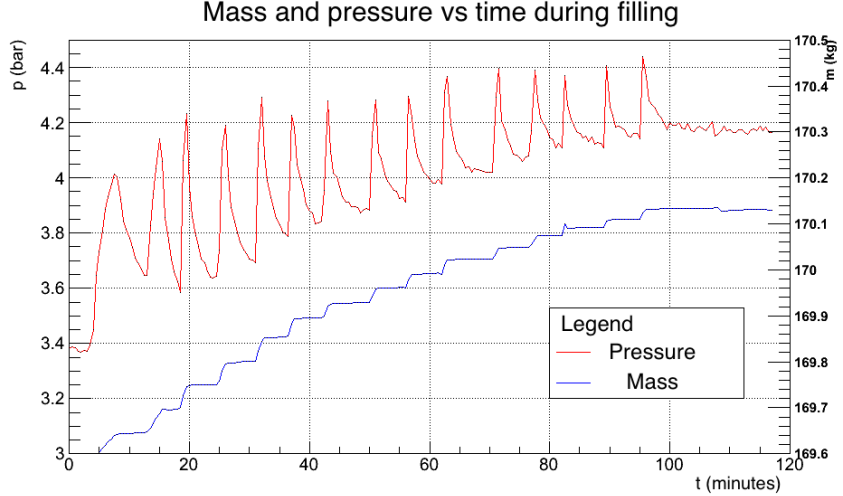


**Fig. 3.11:** The red line indicates the pressure as a function of the time, while the blue line shows the mass as a function of the time. More explanations on the trend are given in the text.

liquid thanks to the spargers at the bottom of the chambers. This phase is visible in the picture as a plateau concerning the mass, and as an exponential decrease after the spike in the pressure. Particular care has to be adopted in this procedure in order to reach the thermodynamic equilibrium. When the equilibrium is reached, the procedure starts again from the beginning. A very similar approach is used during emptying operations.

As estimators for the light yield, the positions of the peaks of Fig. 3.9 and Fig. 3.10 were used. All the light yield measurements are relative to the standard Borexino condition, since the first purpose is to make a differential measurement of the light yield of the scintillator between the condition in which it is saturated with nitrogen and when it is charged with xenon at high pressure. In the case of the spectrum without external muon tag, the peak position was determined with a fit using a Landau function plus an exponential. In the muon tagged spectrum, the fit was performed with a Landau plus constant function. In Ref. [202], the systematics associated to this specific choice of fitting functions are evaluated and the validity of the linearity response of PMTs to muon signals is discussed. The Landau function describes phenomenologically the visible energy released by muons crossing the chamber mostly vertically (corresponding to the events in the peak) and obliquely (generating the tail because of the longer travelled distance in the scintillator).

Figure 3.12 shows the first result of the measurement on the light yield which was already reported in Refs. [202, 203]. The errors on the light yield determination are mainly due to the systematics associated with the fitting procedure (see Ref. [202]). The nitrogen case was studied here in deeper detail acquiring more data points and the lowest pressure xenon point was acquired again, too. The main purpose of this measurement consisted in cross checking the behavior as a function of the nitrogen pressure and in evaluating the possibility that the quenching observed in Fig. 3.12 was due to the injection

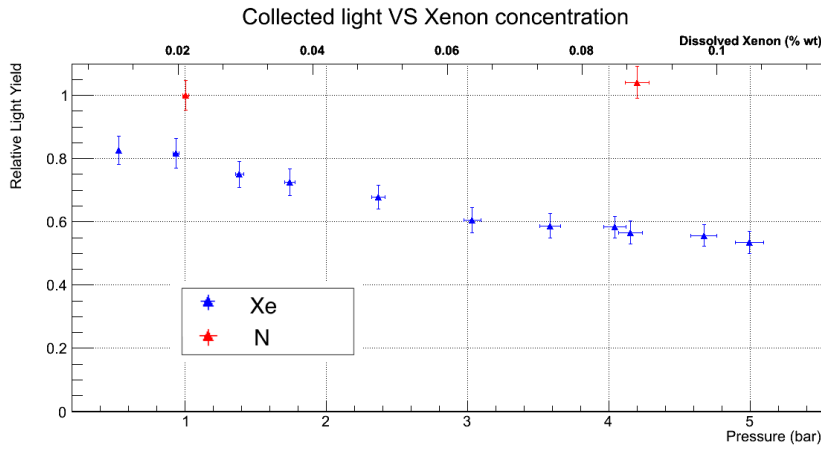


**Fig. 3.12:** The plot shows in red the measurements done with the nitrogen dissolved in the scintillator, while blue dots refer to the xenon measurements. On the x-axis there is the nitrogen/xenon partial pressure while on the y-axis all the measurements are relative to the condition in which the scintillator is full of nitrogen at atmospheric pressure.

(by mistake) of some oxygen inside the system during the xenon filling. The result is shown in Fig. 3.13. Note that in this kind of plots, around half of the measurements were acquired while increasing the pressure, and the remaining ones while the pressure was being decreased<sup>4</sup>. This assures the reproducibility and stability of the system.

The results do not depend on the choice of the set of data, or on the independent selection made with the muon detectors (see especially Fig. 3.13, but it can be seen also in Ref. [202]). The addition of nitrogen does not modify the scintillator optical properties, whereas the addition of xenon quenches the signal. The loss of light yield is of  $\sim 15\%$  at 1 bar and of  $\sim 46\%$  at 5 bar. The two sets of independent measurements agree, and thus any possibility of contamination of the scintillator by oxygen during the filling operations is ruled out<sup>5</sup>. As a final remark, note that a given pressure, the amount of xenon dissolved is almost two order of magnitudes higher than that of nitrogen. This is due to the higher solubility of xenon in the liquid scintillator.

### 3.5 Small chamber measurement campaign

The setup of the small chamber can be used for extensive tests and crosschecks of the results obtained with the large chamber. Diverse measurements on Borexino's liquid scintillator doped with xenon were performed and are here reported. In addition, the solvent usually called LAB (linear alkylbenzene) with the addition of PPO was studied. This scintillator cocktail will be used in next generation large liquid scintillator detectors

<sup>4</sup> The pressure is changed between two different runs, which are acquired in equilibrium conditions.

<sup>5</sup>This does not exclude possible contaminations in the xenon bottle, which are very improbable since latter measurements, as reported in the next sessions, show exactly the same results.

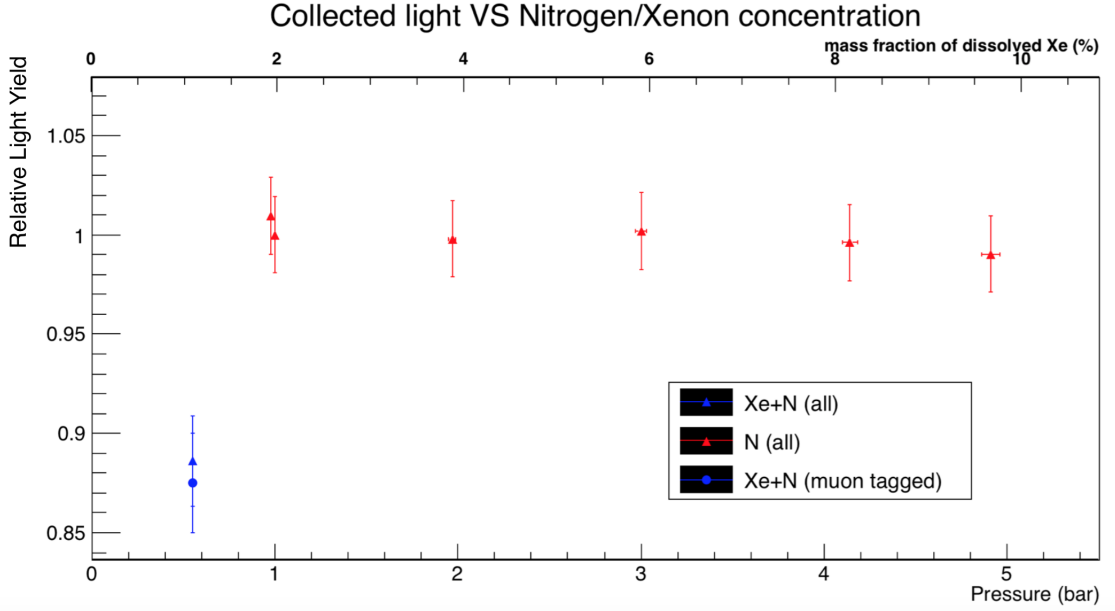


**Fig. 3.13:** The plot shows in red the measurements done with the nitrogen dissolved in the scintillator, while blue dots refer to the xenon measurements. On the x-axis there is the nitrogen/xenon partial pressure while on the y-axis all the measurements are relative to the condition in which the scintillator is full of nitrogen at atmospheric pressure.

such as SNO+ [78] and JUNO [195].

The main goals of the set of measurements presented below include:

- The crosscheck of the measurements reported in Sec. 3.4 and the decoupling between light generation and light propagation effects.
- The measurement of the light yield variation as a function of the xenon concentration for varying densities of PPO dissolved in the PC.
- The measurement of the time response of the scintillator as a function of the nitrogen/xenon/PPO concentrations.
- The measurement of the time response of the scintillator in different ranges of optical photon wavelengths.
- The measurement of the light yield and time response variations as a function of the xenon concentration in LAB+PPO.

Before carrying out any kind of measurement, the liquid scintillator used to fill the chamber was carefully flushed with nitrogen, in order to assure the absence of quenchers, such as oxygen.

### 3.5.1 Light yield variation vs xenon concentration in Borexino's scintillator

In the case of the small chamber, muons cannot be used as source of signal for at least two reasons. The first one is related to the very low rate of muons in the chamber (given the small dimensions,  $\sim 0.5$  Hz) and the second one is due to the fact that Monte Carlo simulations (in agreement with data) show that the muon spectrum does not have a clear signature to be exploited to evaluate the light yield. In the case of the large chamber, instead, the geometry made it possible to observe a clear peak. In the small chamber, simulations show that the spectrum would be continuous with a not very steep endpoint. For these reasons, the measurements were carried out using radioactive gamma sources, and more specifically  $^{137}\text{Cs}$  (662 keV) and  $^{60}\text{Co}$  (1.17 MeV and 1.34 MeV). Due to the geometry of the system, the  $\gamma$  energy and the composition of the scintillator (both in terms of density and elements composing it), the main channel of interaction between the gammas and the scintillator molecules is Compton scattering. Thus, the feature that one should notice in the spectrum is the Compton shoulder, rather than then photoelectric full absorption peak. This is also confirmed by Monte Carlo simulations.

The gamma source is positioned externally with respect to the dark box in which the chamber is held. The source is shielded by a lead container, which has a hole directed towards the chamber. This allows the collimation of photons towards the center of the liquid scintillator volume. A picture of the source container is shown in the left panel of Fig. 3.14.

The scintillation light is detected by 3" PMTs. The system does not allow their calibration when they are mounted on the chamber. For this reason, special calibration runs have to be acquired. The light pulse from an external LED source is brought inside the dark box through a fiber optics on top of which a teflon diffuser is placed. PMTs are positioned so that they face the teflon diffuser and can be calibrated, both in timing and in the single photoelectron response. The stability of the system during different cycles of measurements is guaranteed by the fact that PMTs are not turned off between different cycles and, more importantly, the usage of the radioactive sources allows the measurements to be much faster (tens of minutes) with respect to the ones performed with muons in the large chamber (tens of hours). For this reason, the impossibility to perform PMT calibrations in the middle of measurement runs without turning off the PMTs is not really a concern, since a full cycle of measurements lasts no more than a few hours, compared to the few days necessary in the case of the large chamber. A picture of the teflon diffuser in front of the PMTs inside the dark box is shown in the right panel of Fig. 3.14.

The tests performed to assure that the measured spectrum was due to the source  $\gamma$  interactions were done comparing the background spectrum with the one obtained with the source in place. Also, the shapes of the Compton edges in the cases of the two sources were checked. In particular, the smoking gun is given by the left panel of Fig. 3.15, which shows that the position of the Compton edge changes significantly (as expected) as a function of the source used. Particularly, the maximum energy of an electron recoiling

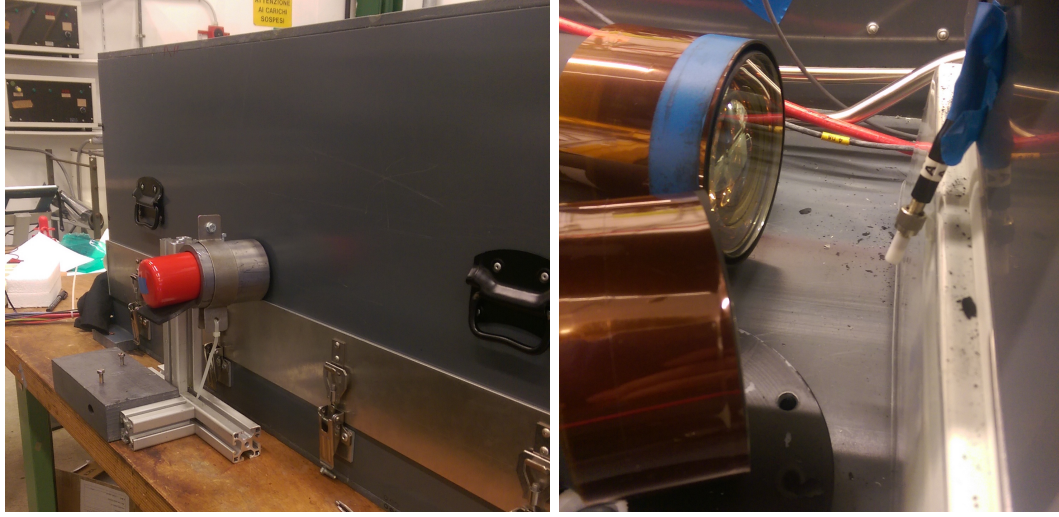


**Fig. 3.14:** *Left panel:* The  $^{137}\text{Cs}$  gamma source is encapsulated in the red lead shield and collimated towards the chamber, which is contained in the dark box. *Right panel:* The calibration system for the 3" PMTs. The light from an LED is fed to a teflon diffuser which is pointed in front of the photocathodes. Everything is contained in the dark box.

by Compton effect is given by

$$E_{max} = E_0 \left( 1 - \frac{1}{1 + \frac{2E_0}{m_e c^2}} \right), \quad (3.5)$$

where  $E_0$  is the energy of the incident gamma. This means that when comparing  $^{60}\text{Co}$  and  $^{137}\text{Cs}$ , one should expect the Compton edge of the latter to end approximately at an energy which is half of the one of the former. This is roughly the case in Fig. 3.15<sup>6</sup>.

Another check which needs to be performed regards the possible biases introduced in the spectrum due to the saturation of the acquisition electronics. In particular, the electronics settings must be chosen so that the Compton edge is always well far away from the saturation region. It is possible to check a possible saturation of the ADC signal directly in the reconstruction algorithm (which was mentioned briefly in Sec. 3.2). The right panel of Fig. 3.15 shows that indeed the saturation cut is not removing many events, and particularly it is not removing events at all in the Compton edge region which is the interesting one as light yield estimator.

Some cycles of measurements with different concentrations of nitrogen and xenon dissolved in the scintillator were carried out, exactly as in the case of the large chamber. The spectra resulting from the different measurements are shown in Fig. 3.16. Whereas there is no appreciable difference in the case of varying concentration of nitrogen, the spectrum is pretty much distorted by the addition of the xenon. In particular, the effect somehow agrees with the one observed in Sec. 3.4 and by increasing the xenon

<sup>6</sup>A more accurate analysis would need to be done in order to estimate the position of the Compton edge in both cases, but this is beyond the purpose of this work.

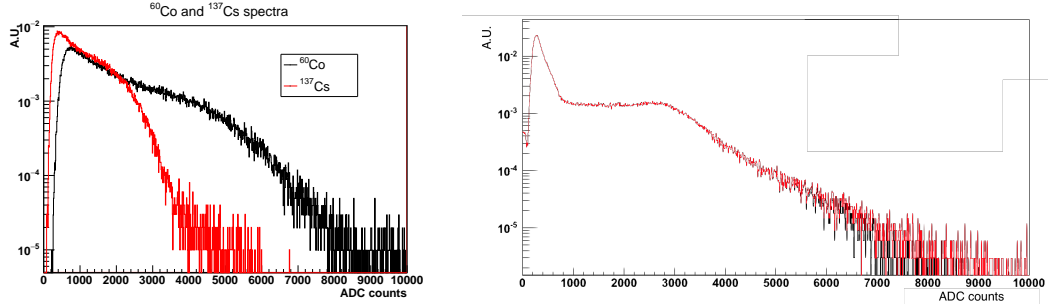


**Fig. 3.15:** *Left panel:* Spectrum for the  $^{60}\text{Co}$  (black) and  $^{137}\text{Cs}$  (red) in the same experimental conditions. The x-axis reports ADC counts (roughly proportional to the visible energy). The curves are normalized to 1 in area. *Right panel:* The addition of the saturation cut (black spectrum) removes very few events and well above the signature of the Compton edge, thus ensuring that the spectrum is not biased by saturation effects.

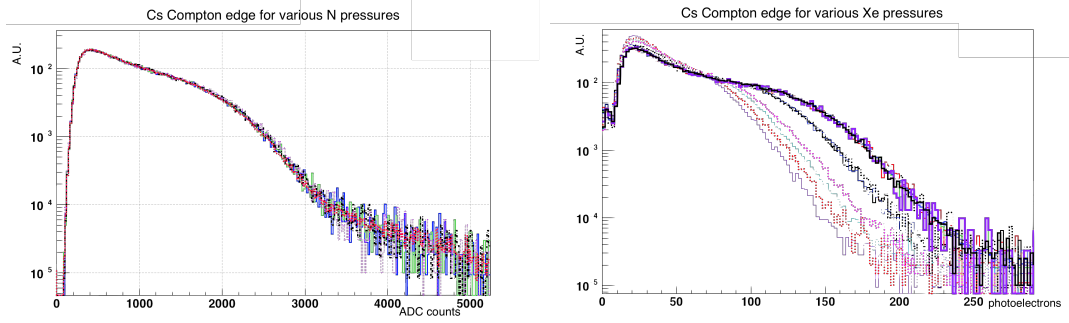


**Fig. 3.16:** *Left panel:* Compton spectra induced by  $^{137}\text{Cs}$  gammas for various nitrogen pressures from 1 to 5 bars. All the spectra are normalized to 1 in area and on the x-axis ADC counts are reported. *Right panel:* Compton spectra induced by  $^{137}\text{Cs}$  gammas for various xenon pressures from 1 to 5 bars. All the spectra are normalized to 1 in area and on the x-axis the number of detected photoelectrons is reported.

concentration the quenching increases, while a reduction in the pressure results in a growth of the light yield, well reproducibly. The tail of events above the Compton edge is due to natural radioactivity in the steel of the chamber and to “low energy” muons, i. e. those muon events which do not cross the entire scintillator volume. Standard muon events were cut out with the saturation cut mentioned above.

Also in this case, a cycle of measurement was performed between a minimum pressure of 1 bar and a maximum pressure of  $\sim 5$  bar. The Compton edge must be fitted with some phenomenological formula in order to quantify the quenching effect.

### Parameterization of the Compton edge

In the literature, many different phenomenological parameterization of the Compton edge are commonly suggested. It is not trivial to predict an accurate theoretical shape,

since it for sure depends on the geometry of the system and on the energy response of the detector. One possibility is to compare the data with the shape predicted by a Monte Carlo simulation. Another possibility is to describe phenomenologically the Compton edge features together with the detector response. Typically, experimentalists use functions such as lines or exponentials multiplied by a Heaviside function then convolved with a Gaussian, in order to describe the energy resolution. Many other combinations are possible. A good compromise which was adopted in this work is the usage of a Fermi distribution multiplied by a line:

$$f(E) = \frac{a - bE}{1 + e^{\frac{E - E_c}{\sigma_E}}}, \quad (3.6)$$

where  $E$  is the visible energy (actually the number of detected photoelectrons),  $E_c$  is the position of the Compton edge and  $\sigma_E$  an additional parameter describing the energy resolution. From the statistical mechanics point of view,  $E_c$  is the equivalent of the Fermi energy and  $\sigma_E \sim k_B T$ . The more the “temperature” is increased (i.e. the worse the resolution) the less evident the step at the Compton edge energy is.

The parameter  $E_c$  is the one which carries the information on the light yield. All the acquired data runs have a statistics high enough so that the statistical error on  $E_c$  returned by the fit is much lower than the systematic error associated with it. In order to estimate the systematic uncertainty, fits in many different configurations were performed. For instance, the range of integration was modified and  $f(E)$  was slightly changed by inserting an exponential function plus a constant instead of the line term. Test fits were also performed with functions different from that of Eq. (3.6), such as convolutions of Heaviside functions with Gaussians. The fit in this condition returns values of  $E_c$  always consistent with those of Eq. (3.6), but the fit stability is worse, since the fit procedure is complicated by the introduction of the convolution. Another crosscheck which was performed is related to  $\sigma_E$ . In fact,  $E_c$  and  $\sigma_E$  are parameters somewhat anti-correlated when using  $f(E)$  as a fitting function. In all the fits shown below,  $\sigma_E$  is a free parameter, but actually  $\sigma_E$  can be related to  $E$ , since the resolution is strictly connected to the number of observed photoelectrons (this fact is clearly visible by comparing the two pictures in Fig. 3.17). Fits with a parameterization like  $\sigma_E = \sqrt{r_0 + r_1 E}$ , where  $r_0$  and  $r_1$  are constant left free in the fit, were performed. They showed results very well in agreement with those performed with  $\sigma_E$  left free, and for this reason any kind of assumption on the behavior of the energy resolution as a function of the energy was dropped in what follows. As a goodness of fit estimator, the  $\chi^2/NDF$  was adopted. The error on the light yield estimated in various experimental conditions can be evaluated directly by the dispersion induced by the usage of different fitting procedures. The average uncertainty can be quantified in  $\pm 3\%$ , which is good enough for the purposes of the present work.

### Light yield results with the small chamber

Two cycles of measurements were carried out, with the usage of the  $^{137}\text{Cs}$  source. One of the cycles from 1 to 5 bar was done with nitrogen, and the other one with xenon.

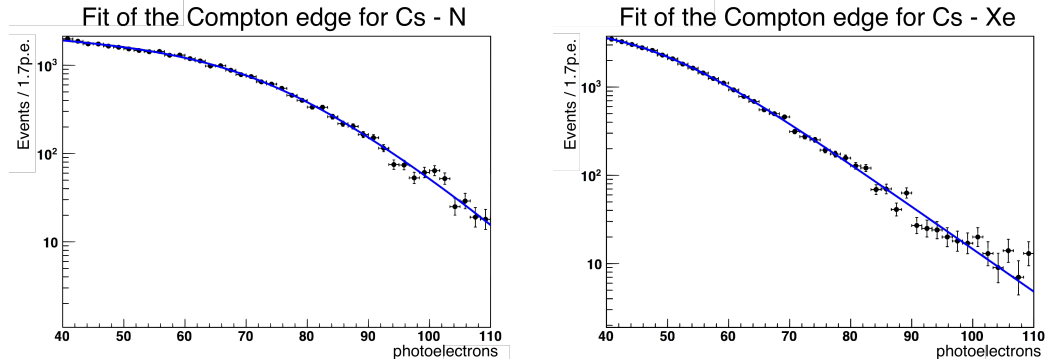


**Fig. 3.17:** *Left panel:* Example of the fit of the Compton edge with the function  $f(E)$  of Eq. (3.6) for the spectrum acquired with the scintillator in Borexino’s standard conditions. *Right panel:* Example of the fit of the Compton edge with the function  $f(E)$  of Eq. (3.6) for the spectrum acquired with the scintillator containing a few percent contamination of xenon. The quenching of the light yield and the worsening of the energy resolution with respect to the picture in the left panel are clearly visible.

The light yield variation as a function of the pressure was estimated according to the procedure described in the previous section. The experimental uncertainty on each point is around 3%. Figure 3.18 shows the comparison between the measurements performed with the small chamber (labelled as “new measurements”) with those obtained with the large chamber (labelled as “old measurements”) and presented in Fig. 3.12. All the points are normalized to the standard Borexino condition.

The two sets of measurements (“old” and “new”) were obtained with independent systems, scintillators and xenon (two different bottles were used). Still, the effect is absolutely indistinguishable, within the experimental errors. Because of the difference in size of the two chambers, this allows already to conclude that the light quenching cannot be caused by meter-scale propagation effects. It must be due to processes happening at the very moment of the scintillation light generation, possibly at the level of the wavelength shifting process (which means a few mm distance from the interaction point for most of the wavelengths, see Sec. 5.4).

The agreement between the results of the small and the large chambers allows to put a limit on the additional attenuation length for the light propagation in the scintillator induced by the presence of the xenon. A precise estimation of this quantity should be obtained with the comparison with Monte Carlo simulations, because of the non trivial geometry. However, it is possible to quantify roughly the effect in very basic assumptions. For instance, one could assume that the mean travelled distance of photons in the small chamber is  $\sim 5$  cm (reasonable, since the gammas are collimated towards the center of the chamber), while for the large chamber is  $\sim 50$  cm (the highest trigger efficiency for muon events is around the center of the cylinder, see Ref. [202]). Even at the maximum concentration of xenon ( $\sim 10\%$  in mass), the results of the large and small chambers are identical within the experimental uncertainty of  $\sim 3\%$ . Therefore, a lower limit on the

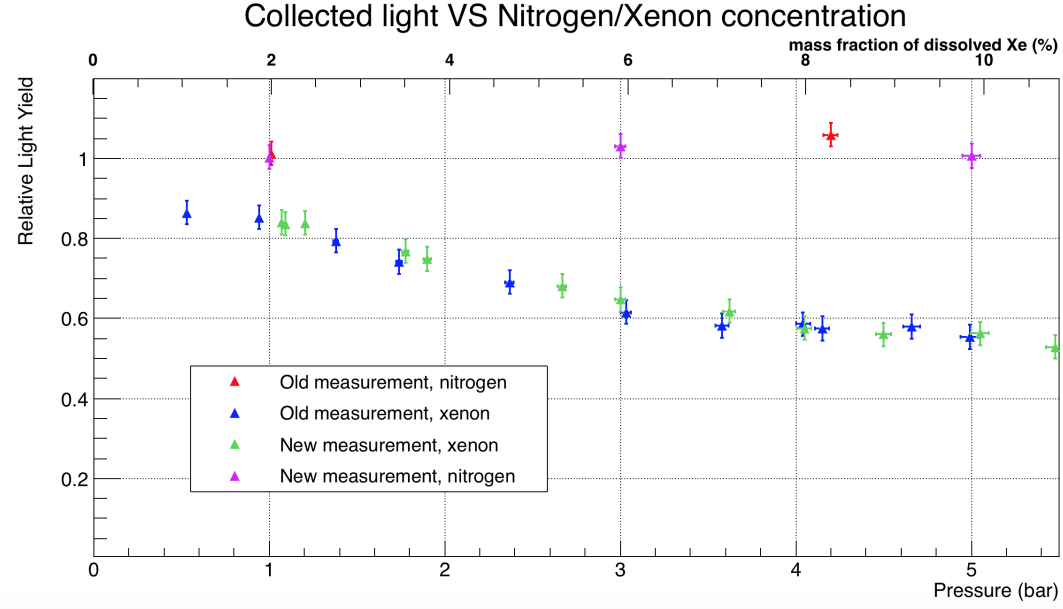


**Fig. 3.18:** Light yield variation as a function of xenon concentration or nitrogen pressure. Note that at a given pressure, the amount of nitrogen dissolved in the scintillator is about two orders of magnitude lower than the amount of xenon which would dissolve at the same pressure. The “new measurements” label refers to those obtained with the small chamber and the method described in Sec. 3.5.1, whereas “old measurements” is referred to those obtained with the large chamber and shown already in Fig. 3.12.

attenuation length induced by the presence of the xenon can be derived:

$$\left| \frac{e^{-\mu d_1} - e^{-\mu d_2}}{\frac{1}{2} (e^{-\mu d_1} + e^{-\mu d_2})} \right| < \delta, \quad (3.7)$$

where  $d_1 = 5 \text{ cm}$ ,  $d_2 = 50 \text{ cm}$ ,  $\delta = 0.03$  and  $\lambda = 1/\mu$  is the lower limit. With the experimental values mentioned above, the solution of Eq. (3.7) yields to a lower limit  $\lambda \gtrsim 15 \text{ m}$ . This value is much higher than the attenuation length of the scintillator itself (around 7 m for the wavelengths of interest, see Sec. 5.4) and for this reason the xenon introduction is definitely not a concern regarding light propagation in the potential usage in a large liquid scintillator detector.

### 3.6 Light yield measurements as a function of the PPO concentration

The Borexino liquid scintillator is made of PC, which acts like a solvent, with the addition of 1.5 g/L of PPO, which is the wavelength shifter and, ultimately, the *real scintillator*. The concentration of 1.5 g/L chosen for Borexino was essentially a compromise between light yield performances and radio-purity, i.e. this was found to

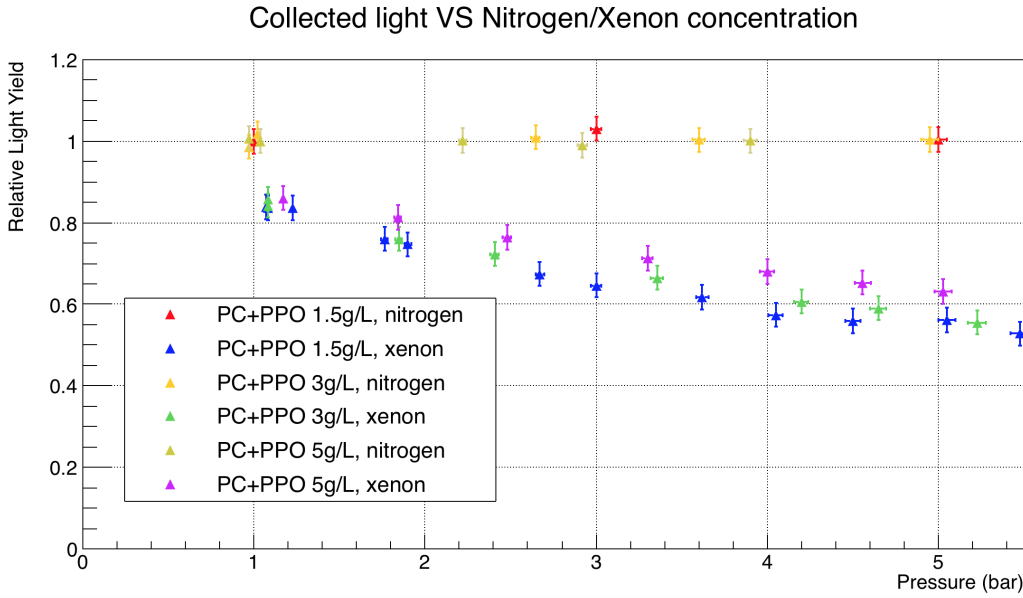


**Fig. 3.19:** Light yield variation as a function of xenon/nitrogen pressure. The different series of points refer to cycles of measurements obtained in the small chamber setup with scintillator cocktails containing different amounts of PPO. For each scintillator cocktail, the points are normalized to the light yield obtained with the scintillator saturated with nitrogen at 1 bar.

be the lowest concentration giving a high enough number of scintillation photons. For a  $0\nu\beta\beta$  experiment, the radio-purity constraints are much less demanding than those of a solar neutrino detectors, and thus it is interesting to study the effect of an increase of the solute concentrator. The main aim of this study is the investigation of the possibility of recovering some of the light lost due to the high concentration of dissolved xenon in the scintillator.

The scintillator cocktails were prepared in Genova's laboratory from a sample of pure PC and some PPO powder. Within those particular experimental conditions, it was not possible to control properly the relative purity of the cocktails, and thus to measure the absolute light yield difference between them. For this reason, in the results shown in Fig. 3.19 every point relative to a particular scintillator cocktail was normalized to the light yield observed with that particular scintillator saturated with nitrogen at 1 bar. Figure 3.19 shows, very similarly to the plots shown above, the results of different cycles of measurements, both with nitrogen and xenon, for three different concentrations of PPO in the scintillator, i. e. 1.5 g/L, 3 g/L and 5 g/L. The plot shows that a higher concentration of PPO reduces the effect of the quenching induced by the xenon, thus suggesting that the xenon does not interact optically with the scintillator, but it is somehow preventing the energy transfer between PC and PPO. In this sense, Fig. 3.19 is pessimistic, since it does not take into account the intrinsic growth of light yield due to an increased amount of PPO. Note that as already reported in Refs. [208, 209], the light yield stops to increase already around a few g/L of PPO concentration, and thus it would not make a lot of

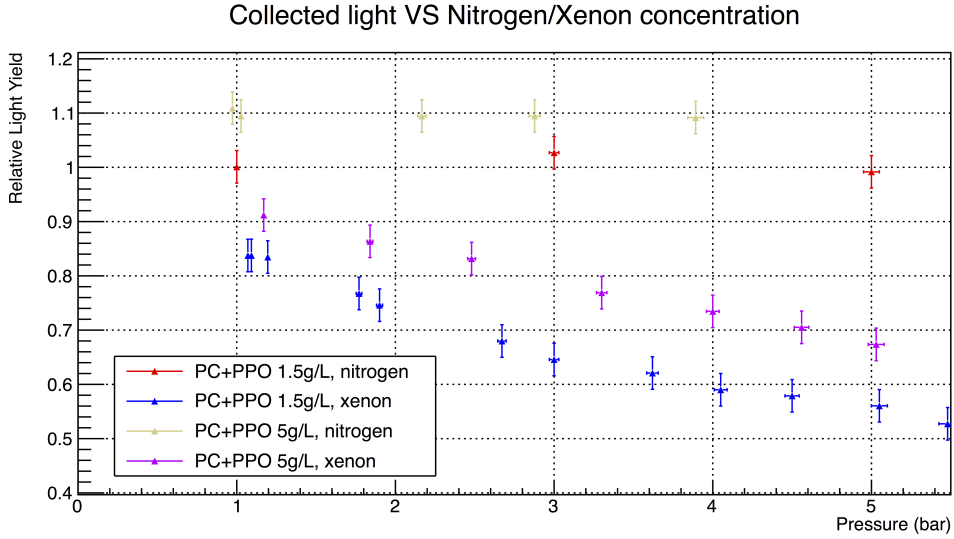


**Fig. 3.20:** Light yield variation as a function of xenon/nitrogen pressure. The different series of points refer to cycles of measurements obtained in the small chamber setup with scintillator cocktails containing different amounts of PPO. The points are normalized to the standard Borexino condition (the red point at 1 bar) and take into account the intrinsic light yield increase induced by a high amount of PPO, as quantified in Ref. [208].

sense to study much higher concentrations. Furthermore, as shown in Sec. 5.4, the more the PPO, the lower the attenuation length, which at some point could be a problem in a very large detector.

As mentioned before, it is not trivial to assure an absolute calibration of the light yield among the various scintillator cocktails. It is anyhow interesting to try to compare the light yield loss as a function of the PPO and xenon concentrations. In practice, the intrinsic increase in the fluorescence due to a denser PPO (from 1.5 g/L to 5 g/L) was estimated to be of around  $\sim 8\%$  from Ref. [208]. This number has anyway to be taken cautiously, for the reasons mentioned above and as also reported in Ref. [208]. The plot which compares the results of the cycles of measurements in xenon and nitrogen with Borexino's scintillator and PC+PPO at 5 g/L can be found in Fig. 3.20. This time all the points are relative to the Borexino standard condition (i.e. the red point at 1 bar in the plot).

In conclusion, a scintillator doped with xenon at high pressure with a larger density of wavelength shifter would have a consistently better light yield, even if the quenching effect would still be important. It has also to be reminded that with xenon dissolved at 1 bar in PC+PPO at 1.5 g/L, there are about 200 xenon atoms per PPO molecule.

In a detector such as Borexino, the scintillator light yield is not the only parameter which can be optimized in order to have a better energy resolution. For instance, the average quantum efficiency could be increased and the geometrical coverage (today of about  $\sim 30\%$ ) could be improved. From the scintillation process point of view, a

higher density of fluor dissolved inside the PC reduces the effect of the xenon quenching, thus suggesting that the xenon atoms interfere in the processes of energy transfer and wavelength shifting between the PC and PPO molecules.

### 3.7 Borexino's scintillator time response

The small chamber setup allows to measure the time response of the scintillator. The two PMTs are not used in the same way as it is done for the light yield measurements described above. One of the two PMTs, say the trigger PMT, is setup to have a high threshold (tens of photoelectrons) and it is used directly as trigger. In this way, noise and very low energy events are removed. The other PMT, say the timing PMT, records hits with a very low threshold (some fractions of a photoelectron, anyway not too low to avoid to be dominated by dark noise) and it is *badly* optically coupled to the chamber. Basically, it is placed some tens of cm away from the small chamber, so that the probability that many photons per event can reach it is very low. Furthermore, a software cut is applied, so that only real single photoelectron events are selected. This is useful also to remove the residual jitter created by the discriminator. In this way, by recording the relative time of the hit on the timing PMT with respect to the trigger PMT, it is possible to build the so called scintillation curve, which describes the time response of the scintillator. Liquid scintillators have generally fast time responses (a few ns typically) and this makes it possible to develop pulse shape discrimination and position reconstruction variables which are quite precise. The determination of possible modifications induced by the xenon presence in the time response is therefore important.

#### 3.7.1 The time response of the detector

The timing response function of the system was measured using the LED, as shown in the right panel of Fig. 3.14. A very narrow light pulse (750 ps) is injected inside the timing PMT, and the time<sup>7</sup> of the recorded hit after the whole electronics chain is saved. This procedure allows to measure directly the time resolution of the system PMT+front end electronics+digital electronics. The result is reported in the left panel of Fig. 3.21.

The transfer function is characterized by the exponential (with  $\sim 4$  ns time constant) response of the RC-circuit embedded in the PMT voltage divider. A second peak structure is clearly visible around  $t \sim 40$  ns, which is approximately equal to the transit time of the PMT. As shown in the right panel of Fig. 3.21, the position of this peak is pretty influenced by the supply voltage of the PMT, and in particular, the peak is moved towards lower times as the high voltage is increased. This makes the case for a connection between the position of this peak and the characteristic PMT transit time (which, in turn, depends on the high voltage value). This effect is thus only related to the PMT itself and not to any physical mechanisms of scintillation. Furthermore, the jitter on the LED output signal is well below the ns.

<sup>7</sup>Relative to the firing time of the LED.

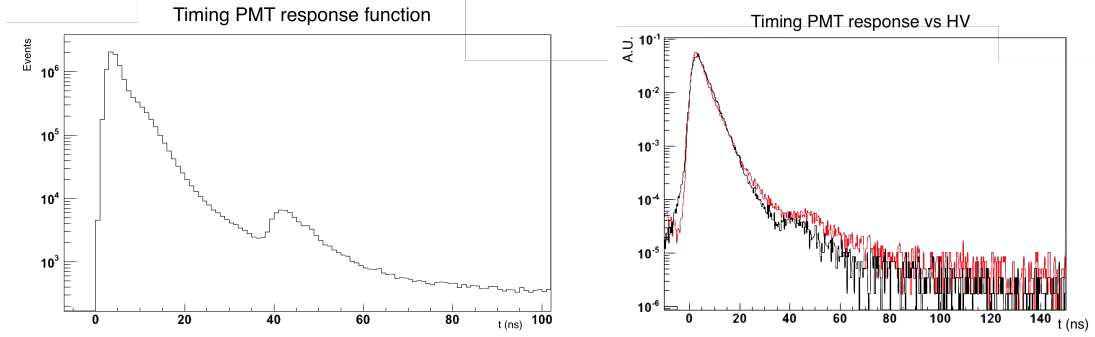


**Fig. 3.21:** *Left panel:* Timing PMT response to the LED narrow pulses. *Right panel:* Time response as a function of the high voltage supplying the PMT. The red curve corresponds to 1900 V while the black one to 2300 V.

Following Ref. [208] and subsequent works, the scintillator time response is modeled here with a sum of three exponentials, namely

$$S(t) = \sum_{i=1,2,3} \frac{q_i}{\tau_i} e^{-t/\tau_i}, \quad (3.8)$$

with  $q_1 + q_2 + q_3 = 1$ . In the model with three exponentials, only the first one, i. e. the fastest, has the physical meaning of time constant needed for the energy transfer from the solvent to the solute. The other two exponentials describe phenomenologically the very complex process of scintillation. Note that the aim of this work is studying if the addition of xenon alters substantially the timing properties of the scintillator cocktail. For this reason, the attention is focused on the first few hundreds of ns in the temporal response of the system. Studying the response for longer time would require a more careful treatment of dark noise and random coincidences. In some more recent works such as Ref. [210], a model with four exponential is adopted, in order to study the scintillation curve on the scale of a few  $\mu$ s.

The response function measured in Fig. 3.21, say  $R(t)$ , is then convolved with  $S(t)$  of Eq. (3.8) in order to obtain the fitting function to be used to extract the weights  $q_i$  and the corresponding time constants  $\tau_i$ , which describe the time response of the system. Therefore, the fitting function is:

$$f(t) = S \star R(t) = \int dy S(y) R(t - y) = \int dy \sum_{i=1,2,3} \frac{q_i}{\tau_i} e^{-y/\tau_i} R(t - y). \quad (3.9)$$

A fit example is shown in Fig. 3.22.

In the subsequent sections, measurements of the time constants  $\tau_i$  and weights  $q_i$  are carried out with the strategy described above. Typically, the statistics is pretty high and thus the statistical error on the parameters coming out of the fit is not a good estimate of the actual uncertainty. Similarly as what already discussed in Sec. 3.5.1, the parameter errors are dominated by systematic uncertainties, such as range of the fit, parameter constraints and convolution range. Another variability comes from the shape of  $R(t)$ ,

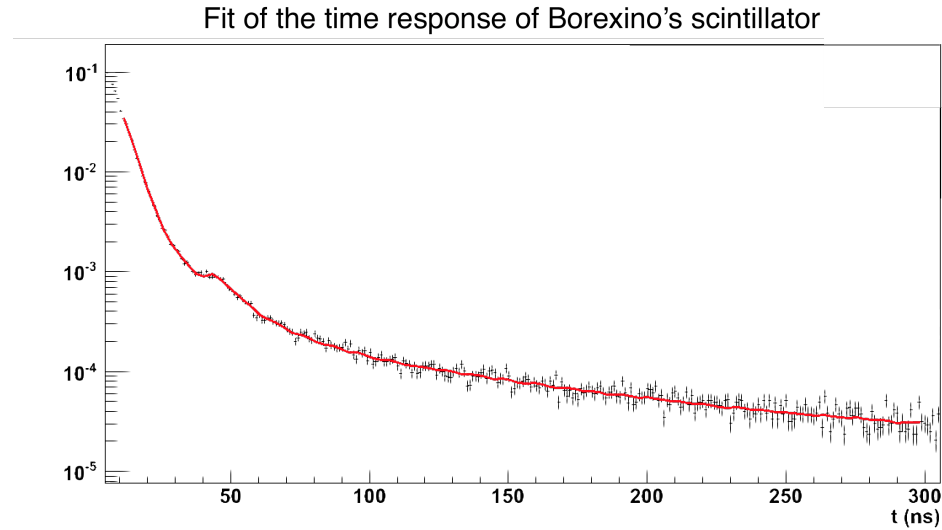


**Fig. 3.22:** Example of fit of the hit time distribution recorded by the timing PMT with the function in Eq. (3.9).

which has been acquired several times after well defined time intervals. The shapes thus obtained are consistent, but sometimes slightly different. This results in a little modified fit results after the convolution. For these reasons, a very conservative estimate of the uncertainty on the parameters can be assessed around 10%. In the following tables reporting results, the errors are not quoted and the reader should refer to this number. As a final remark, one should notice that the specific values of the time constants of a scintillator mixture highly depend on the purity (mainly in terms of oxygen) of the sample under study. This means that usually the values reported are just a reference and it is possible to get quite different results by using a better/worse quality sample.

### 3.7.2 Time response of nitrogen saturated liquid scintillator as a function of PPO concentration

In this section, time constants and weights are measured for PC saturated with nitrogen at 1 bar and with PPO concentrations of 1.5 g/L, 3 g/L and 5 g/L. This allows to understand phenomenologically the impact of the addition of the PPO to the scintillator mixture.

Figure 3.23 shows the comparison of the light curves obtained with the three different scintillators. The curves are normalized to the peak. The addition of PPO makes the fast component even faster. This agrees with what was observed in the past [208] and finds its explanation in the fact the a higher PPO concentration makes the energy transfer from PC easier, and so a faster fluorescence is observed.

Table 3.2 summarizes and quantifies the trends visible in Fig. 3.23. In particular,  $\tau_1$  and  $\tau_2$  diminish as the PPO concentration increases, while  $q_2$  increases, thus making the longer time constant  $\tau_3$  less important. The results of Tab. 3.2 substantially agree

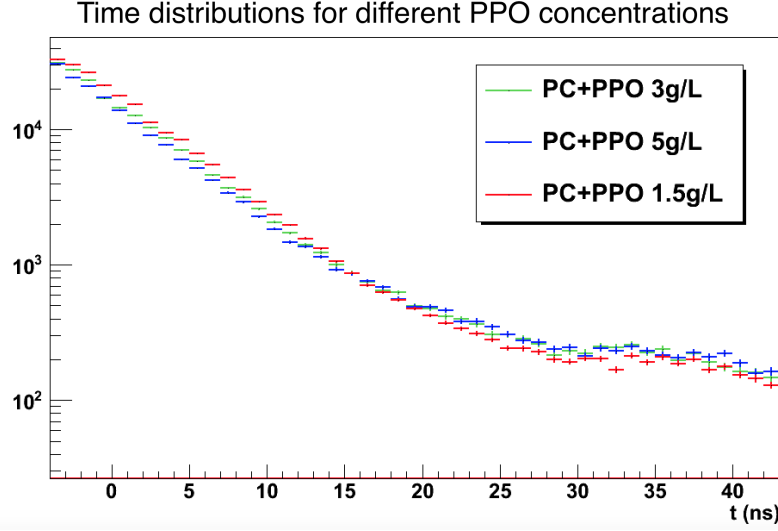


**Fig. 3.23:** Comparison of the scintillation light curves for PC doped with different concentrations of PPO and saturated with nitrogen at 1 bar. The curves are normalized to the peak, which is not at  $t = 0$  simply because of an offset in the time definition.

with those of Ref. [208], but they slightly differ from those of Ref. [210]. Whereas the scintillator used in this last reference was taken directly from Borexino, the sample used here was prepared from pure PC. This might explain the slight difference in the results, which could be due to the different purity of the samples.

PPO [g/L]	$\tau_1$ [ns]	$\tau_2$ [ns]	$\tau_3$ [ns]	$q_1$	$q_2$
1.5	2.7	29.3	34.8	0.91	0.08
3	2.2	8.4	30.6	0.86	0.11
5	1.6	7.1	25.9	0.8	0.16

**Tab. 3.2:** Time constants resulting from the fit for different PPO concentrations. As discussed in the text, uncertainties can be assumed of the order of 10%. Note that  $q_3 = 1 - q_1 - q_2$ .

### 3.7.3 Time response as a function of the xenon concentration

Since the PPO impact on the time response was established independently, it is possible to focus on studying the time response variation as a function of the xenon concentration only in the case of the Borexino liquid scintillator, i. e. PC+PPO at 1.5 g/L. The standard Borexino condition is compared with the cases in which xenon is dissolved in the liquid scintillator at 1 bar, 3 bar and 5 bar.

Figure 3.24 shows a comparison of the data points for different nitrogen/xenon concentrations. The fit results are then summarized in Tab. 3.3. The effect due to the xenon dissolution is very small. This is great news, since it means that while the light yield is quite influenced by the xenon presence, the goodness of the scintillator time

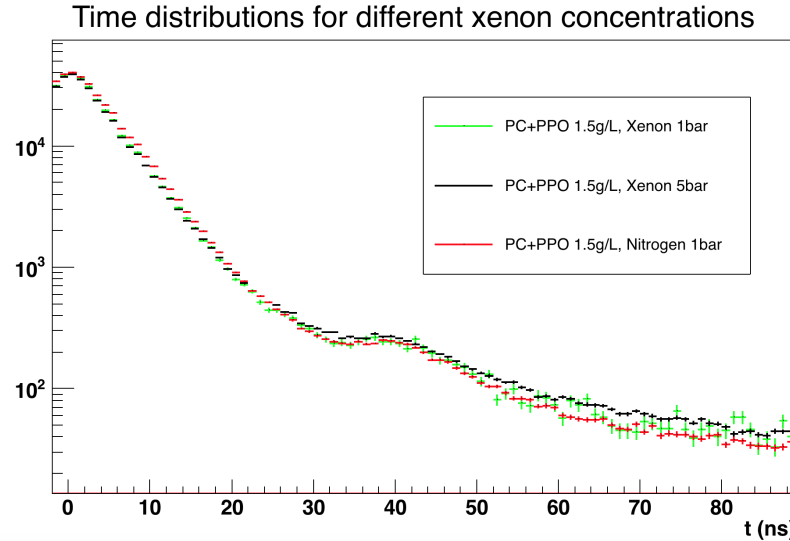


**Fig. 3.24:** Comparison of the scintillation light curves for PC+PPO at 1.5 g/L doped with nitrogen or xenon at high pressure. The curves are normalized to the peak, which is not at  $t = 0$  simply because of an offset in the time definition.

response is not modified. The main phenomenological effect induced by the xenon is a decrease of the weight of the fastest time component, in favor of an increase of the slowest ones. This happens smoothly as the xenon concentration increases, but the decrease is almost sudden, if one compares to the nitrogen case.  $\tau_2$  decreases also significantly with respect to the nitrogen case, but the net effect is that of a little slower mean scintillation times.

The (measured) theoretical curves, computed according to Eq. (3.8) and to the parameters in Tab. 3.3, are shown in Fig. 3.25. From the picture, it is clear that with more xenon, the slower components have more importance. Conversely, this could also be interpreted as a suppression of the faster component. These results might suggest that:

- The xenon presence inhibits the primary energy transfer from PC to PPO, thus suppressing the fast component, which describes exactly this energy transfer.

	p [bar]	$\tau_1$ [ns]	$\tau_2$ [ns]	$\tau_3$ [ns]	$q_1$	$q_2$
N	1	2.7	29.3	34.8	0.91	0.08
Xe	1	2.2	7.5	31.6	0.62	0.28
Xe	3	2.2	10.2	39.6	0.59	0.30
Xe	5	2.0	8.7	43	0.51	0.33

**Tab. 3.3:** Time constants resulting from the fit for different gaseous dopant in PC+PPO at 1.5 g/L. As discussed in the text, uncertainties can be assumed of the order of 10%. Note that  $q_3 = 1 - q_1 - q_2$ .

- The xenon introduction does not interfere optically with the PPO excitation and light emission, since the light curves are modified, but not significantly.
- The very good timing properties of the scintillator are not heavily altered by the presence of xenon.

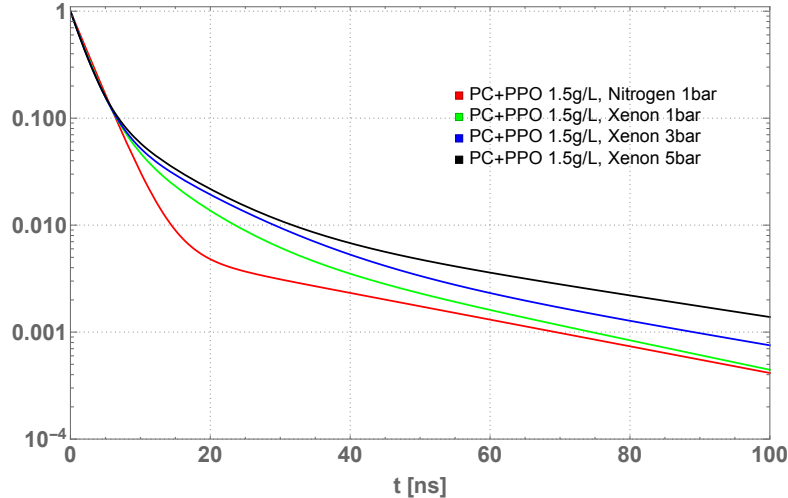


**Fig. 3.25:** “Theoretical” scintillation light curves computed according to Eq. (3.8) and to the parameters in Tab. 3.3. The curves are normalized to 1 at  $t = 0$  by definition.

### 3.7.4 Timing and spectral response

In this section, measurements of the timing properties of the scintillator in given wavelength ranges are reported. In particular, optical filters with a bandpass width of 10 nm and the following central values: 365 nm, 375 nm, 400 nm and 420 nm, were placed in front of the timing PMT, thus allowing to measure the scintillator time constants in the different regions of the emission spectrum.

Measurements were performed for PC+PPO at 1.5 g/L both saturated with nitrogen at 1 bar and xenon at 5 bar. The results concerning the standard Borexino condition are reported in Tab. 3.4, while those related to the xenon are in Tab. 3.5.

As done previously, the results reported in Tab. 3.4 and Tab. 3.5 are used to plot the “theoretical” scintillation curves according to Eq. (3.8). The resulting plots are shown in the right and left panels of Fig. 3.26, respectively. In the case of scintillator saturated with nitrogen, it is clearly possible to notice both from the plot and from the table, the effect of the wavelength shifting due to the PPO. The scintillation times, and particularly  $\tau_1$ , are higher for photons with higher wavelengths. This is coherent with the wavelength shifting mechanism, for which the more infra-red<sup>8</sup> (IR) the photons are, the more likely they were absorbed and reemitted. Of course, absorption and reemission cause a delay

<sup>8</sup>In this case it simply is intended as “higher wavelengths”.

N at 1 bar	$\lambda (\pm 5)$ [nm]	$\tau_1$ [ns]	$\tau_2$ [ns]	$\tau_3$ [ns]	$q_1$	$q_2$
	365	1.3	11.5	40	0.90	0.05
	375	1.5	17.2	61	0.91	0.05
	400	1.6	24	80	0.93	0.06
	420	2.3	28.6	248	0.92	0.07

**Tab. 3.4:** Time constants resulting from the fit in different wavelength ranges for PC+PPO at 1.5 g/L saturated with nitrogen at 1 bar. As discussed in the text, uncertainties can be assumed of the order of 10%. Note that  $q_3 = 1 - q_1 - q_2$ .

Xe at 5 bar	$\lambda (\pm 5)$ [nm]	$\tau_1$ [ns]	$\tau_2$ [ns]	$\tau_3$ [ns]	$q_1$	$q_2$
	365	1.3	33	41	0.86	0.13
	375	1.4	21	40	0.84	0.07
	400	1.4	21	40	0.86	0.07
	420	1.5	20	41	0.81	0.10

**Tab. 3.5:** Time constants resulting from the fit in different wavelength ranges for PC+PPO at 1.5 g/L saturated with xenon at 5 bar. As discussed in the text, uncertainties can be assumed of the order of 10%. Note that  $q_3 = 1 - q_1 - q_2$ .

which is visible as higher mean scintillation times. In the xenon case, instead, this effect seems to be almost absent. The curves obtained with the optical filters, in different wavelength regions, agree pretty much with each other and are substantially different from the one obtained without any optical filters. These observations could suggest that xenon alters the absorption and reemission mechanisms of the light and/or the energy transfer from PC to PPO. The xenon could actually absorb some of the lower wavelength light, reemitting it in the IR region, since gaseous xenon has a spectrum mostly peaked in the IR.

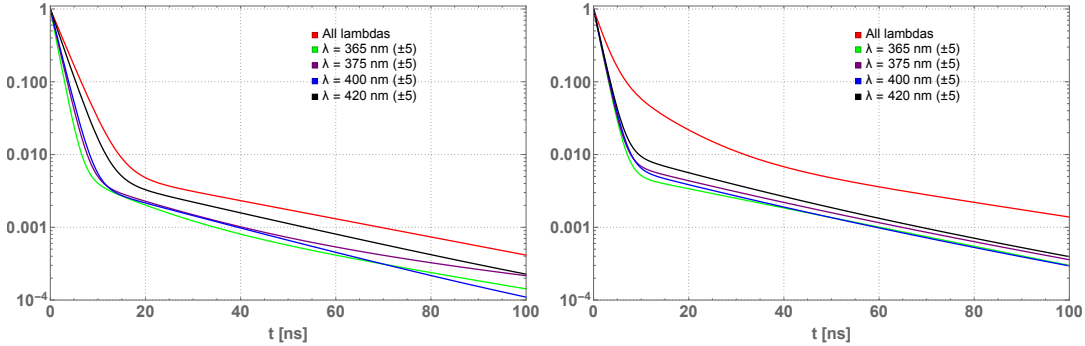


**Fig. 3.26:** *Left panel:* “Theoretical” scintillation light curves computed according to Eq. (3.8) and to the parameters in Tab. 3.4. The curves are normalized to 1 at  $t = 0$  by definition. *Right panel:* “Theoretical” scintillation light curves computed according to Eq. (3.8) and to the parameters in Tab. 3.5. The curves are normalized to 1 at  $t = 0$  by definition.

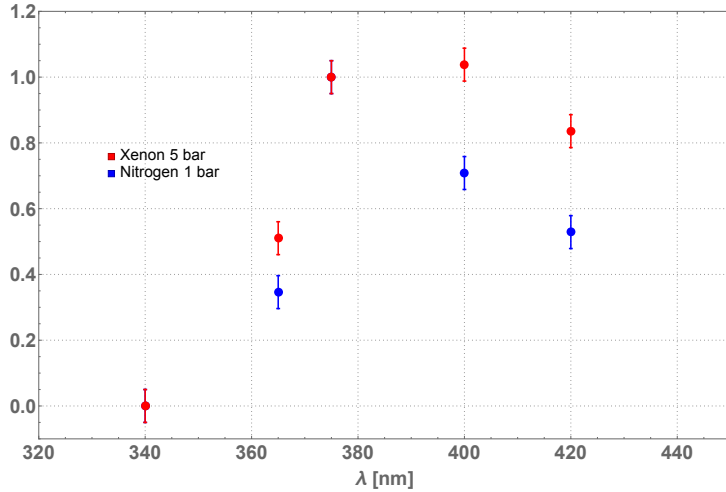


**Fig. 3.27:** “Emission spectrum” of the scintillator doped with nitrogen or xenon. These experimental points have not been corrected by the PMT quantum efficiency curve, since for the purposes of this work only the relative comparison between nitrogen and xenon is relevant. The points are normalized at 1 at 375 nm. Since the two data points are overlapped, the blue one is not visible, but is actually present.

Another test evaluating the amount of light emitted at various wavelengths is shown in Fig. 3.27. This plot was obtained by measuring the trigger rate on the timing PMT with different optical filters placed between itself and the quartz window. More accurate measurements are for sure possible (e. g. a spectral measurement), but considering that the timing PMT is kept in the single photoelectron regime, significant distortions induced by this approach are not expected. Figure 3.27 compares the “scintillation spectrum” (actually, the positions of the experimental points have not been corrected by the PMT quantum efficiency curve) for the cases of PC+PPO at 1.5 g/L and nitrogen at 1 bar or xenon at 5 bar. From the figure, a surplus of higher wavelength photons in the case of xenon with respect to the nitrogen one seems to be present. Conversely, as shown before, it seems that this “IR component” is not due to the normal wavelength shifting process, since the scintillation times do not vary much as a function of  $\lambda$  (as shown in Tab. 3.5). These data are in agreement with the hypothesis that the xenon absorbs some of the low wavelength light emitted either by the PC or the PPO. Part of this light is probably reemitted at lower energies and, therefore, a great part of it is lost.

As a conclusion, it is important to remark that the results reported here show that PC+PPO in various concentrations doped with xenon at high pressure has very good timing capability. From the experimental data shown here, the timing response of the scintillator doped with xenon is practically as good as the Borexino one. Of course, the investigation of the mechanisms which cause the light yield quenching by the xenon is as much interesting as difficult, because of the main mechanisms which enter the game. This is somewhat decoupled from the main aim of this set of measurements, which had the purpose of characterizing the various mixtures from an experimental point of view.

## 3.8 Characterization of the LAB+PPO scintillator doped with xenon at high pressure

In this section, the first measurements of LAB+PPO at 3 g/L doped with xenon are presented. They include the first determination of the xenon solubility in LAB, the light yield variation as a function of the xenon concentration and the time response characterization. These measurements can be of importance for future large liquid scintillators, such as JUNO [195] or SNO+ [78]. With this respect, the concentration of 3 g/L was chosen as a reference, since the concentration of PPO in SNO+ is of 2 g/L while there is no final decision yet regarding JUNO, but higher concentrations are being explored.

### 3.8.1 Xenon solubility in LAB

While a 10% measurement of the xenon solubility in PC+PPO is known in literature [192], no experimental data is available for the solubility in LAB. Therefore, the setup of the small chamber was used to measure it. Note that a better sensitivity could be achieved by using a larger mass of xenon (and thus the large chamber apparatus), but this was not needed at this stage.

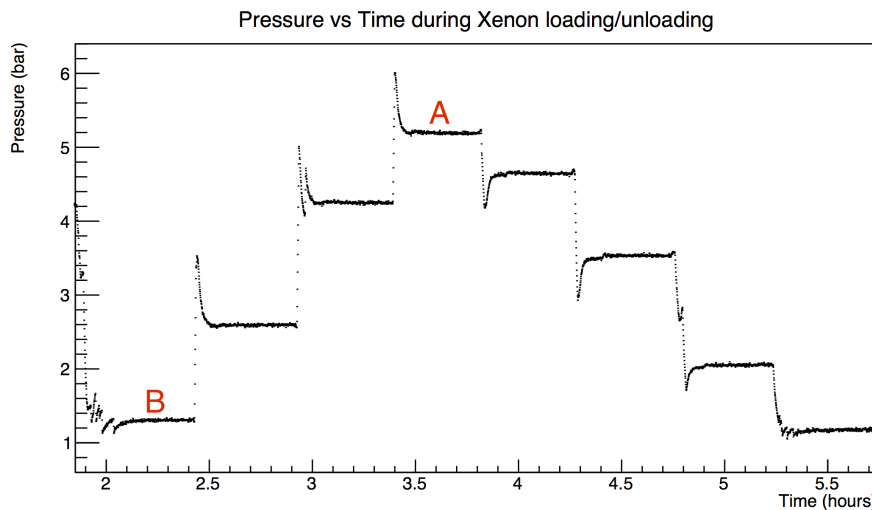


**Fig. 3.28:** Pressure as a function of time inside the small chamber during a full cycle of measurements with xenon in LAB. The labels “A” and “B” indicate the experimental conditions used in order to estimate the xenon solubility in LAB.

The solubility measurement reported here is done in the assumption of (the well verified experimentally) Henry’s law. In practice, the amount of xenon introduced in the system is measured. By knowing the pressure difference between the starting and the ending situation, it is possible to reconstruct the solubility. Figure 3.28 shows the behavior of the pressure in the small chamber as a function of time, during a whole cycle

of measurements. In particular, it is possible to recognize the plateaus associated to the various optical measurements performed at the equilibrium. The transient spikes show the dissolution of the xenon after the injection inside the system. As soon as the gas is inserted in the system, the pressure suddenly increases. After some time, with an exponential trend, the pressure is reduced, since the recirculation of the gas in the system allows its dissolution inside the liquid. After reaching the highest pressure, the amount of xenon is progressively reduced, and the curve's behavior is inverted with respect to the previous part of the chart. In fact, when the valve is open, and the xenon is let out of the system, the pressure drops. But the recirculation of the remaining gas in the system allows the xenon still dissolved in the scintillator to go back to the gaseous part, thus increasing the pressure. The solubility measurement was carried out considering the conditions labelled as “A” and “B” in Fig. 3.28:

$$\begin{aligned}
 p_A &= (5.2 \pm 0.05) \text{ bar} \\
 m_A &= (1.915 \pm 0.001) \text{ kg} \\
 p_B &= (1.3 \pm 0.03) \text{ bar} \\
 m_B &= (1.891 \pm 0.001) \text{ kg} \\
 m_{LAB} &= (260 \pm 10) \text{ g.}
 \end{aligned} \tag{3.10}$$

The mass of the scintillator was measured at the time of filling. The mass determination represents the biggest source of uncertainty. The solubility  $k_{LAB}^{Xe}$  at 1 bar can be easily obtained by Henry's law:

$$m_A - m_B = k_{LAB}^{Xe} \times m_{LAB} \times (p_A - p_B). \tag{3.11}$$

At 1 bar the mass solubility is then  $k_{LAB}^{Xe} = (2.4 \pm 0.25) \%$ . In order to compare it with the one measured for PC in Ref. [192], it is useful to express the xenon solubility in LAB at 900 mbar,  $k_{LAB}^{Xe} (900 \text{ mbar}) = (2.1 \pm 0.2) \%$ . This value is completely compatible with the solubility of xenon in PC, which is  $k_{PC}^{Xe} (900 \text{ mbar}) = (1.97 \pm 0.20) \%$ .

### 3.8.2 LAB light yield variation as a function of the xenon concentration

The measurement of the LAB+PPO light yield as a function nitrogen and xenon concentrations was performed exactly as reported above for PC+PPO. The gains of the PMTs and of the electronics chain were a little increased, in order to exploit better the dynamics of the apparatus, since the LAB cocktail with 3 g/L of PPO resulted to have a lower light yield than that of PC+PPO. Probably the purity of the LAB sample is not as high as that of the PC or it can be an intrinsic feature of the scintillator, since the adopted nitrogen fluxing procedures were exactly the same for both cocktails.

Figure 3.29 compares the light yield as a function of xenon in LAB and in PC with the same PPO concentration. The results are very similar, even if the LAB points seem a little more quenched than those obtained with PC.

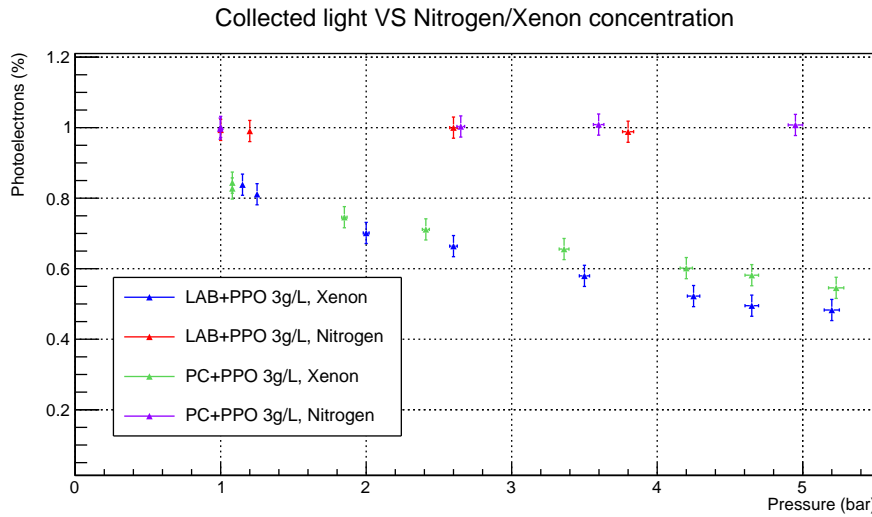


**Fig. 3.29:** Light yield variation in LAB and PC with PPO at 3 g/L as a function of xenon/nitrogen pressure. The two series of points are normalized to the standard case of scintillator saturated with nitrogen at 1 bar.

### 3.8.3 LAB time response as a function of the xenon concentration

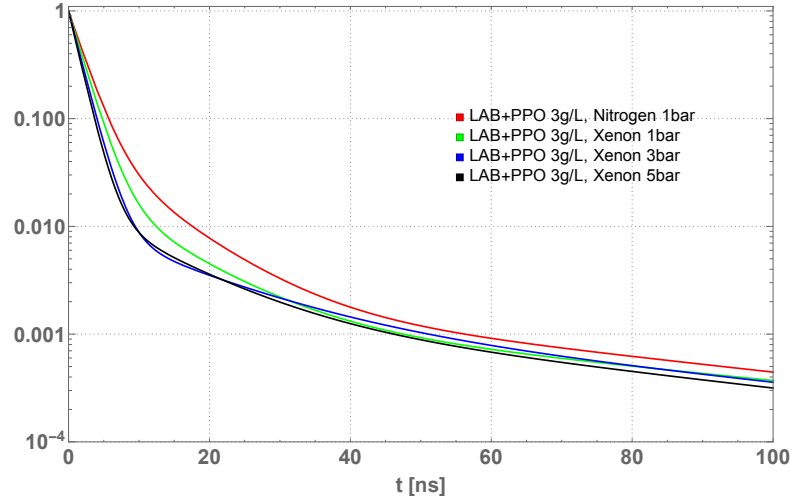
The time response of the LAB+PPO mixture was measured as a function of nitrogen and xenon concentrations exactly with the same technique presented for the PC+PPO scintillator. The measurements reported here regard the integrated (with respect to the optical photon wavelengths) response of the scintillator, since no spectral response studies were carried out yet.

Table 3.6 reports the values of the fitted parameters for the light curves obtained with the LAB+PPO. Figure 3.30 shows the “theoretical” scintillation light curve computed according to Eq. (3.8) and to the parameters in Tab. 3.6. As visible both in the table and in the plot, the qualitative behavior of the parameters as a function of the xenon concentration is identical to that observed in PC (the more the xenon, the faster the fast component). The absolute values of the parameters obtained for the case of scintillator saturated with nitrogen are not far from those reported in Ref. [210] and the qualitative

	p [bar]	$\tau_1$ [ns]	$\tau_2$ [ns]	$\tau_3$ [ns]	$q_1$	$q_2$
N	1	2.1	8.6	60.7	0.75	0.20
Xe	1	1.9	9.8	67.6	0.84	0.11
Xe	3	1.7	14	64	0.87	0.07
Xe	5	1.5	11	59	0.85	0.09

**Tab. 3.6:** Time constants resulting from the fit for different gaseous dopants in LAB+PPO at 3 g/L. As discussed in the text, uncertainties can be assumed of the order of 10%. Note that  $q_3 = 1 - q_1 - q_2$ .

effect of increase of the weights of the slower components is observed as well as in the PC case. The fact that, besides the numbers which are of course different, the qualitative phenomena observed in PC are essentially observed also with the LAB, might suggest that probably the mechanism generating the light yield quenching is the same for both the scintillator mixtures.



**Fig. 3.30:** “Theoretical” scintillation light curves computed according to Eq. (3.8) and to the parameters in Tab. 3.6. The curves are normalized to 1 at  $t = 0$  by definition.

### 3.9 Conclusions and outlook

In this chapter, PC+PPO and LAB+PPO doped with xenon at high pressure were characterized. Particularly, the light yield and time response variations induced by the dissolution of xenon were investigated experimentally. From the liquid scintillator point of view, the main advantages are the high xenon solubility in mass in both the mixtures (around 2% in mass at 1 bar) and the fact that the scintillator time response is not altered substantially by the presence of the dissolved gas. The challenge is the light yield loss. It is not a dramatic loss, i. e. the scintillator still emits a pretty high amount of light, and there is no evidence of a worsening of the liquid transparency on at least a  $\sim 15$  m length scale. The requirement of a superb energy resolution, in fact, would need the highest light collection possible, and thus the number of detected photons per unity of energy should be maximized. As discussed in Sec. 2.8.4, great results could be obtained if the present Borexino energy resolution is improved. This might not be trivial at the pressure of 5 bar, where big improvements in the PMTs quantum efficiency and geometrical coverage could probably bring the light yield up only to the Borexino level. Despite this challenge, which anyhow could probably be solved by studying other kinds of scintillators other than PPO, the technique is solid and is probably the only known at present, which can guarantee the investigation of the  $\mathcal{TH}$  region in the next decade.

## Chapter 4

# The Borexino experiment

In this chapter, the basic details of the Borexino experiment performance, construction, physics goals and achievements are provided. The key features of the detector operation are discussed, with the aim of introducing the physics analysis methods used in the subsequent chapters.

Borexino is a large liquid scintillator detector, whose primary scientific goal was the detection of  ${}^7\text{Be} \nu$  [81]. However, the measured radioactive backgrounds were much lower than expected. This resulted in a wide broadening of the scientific contribution of the experiment, which could perform an almost complete solar neutrino spectroscopy<sup>1</sup>. Besides solar physics, Borexino is very competitive in the detection of anti-neutrinos (geo and supernova) and in addition to providing the first  $5\sigma$  evidence of the existence of geo-neutrinos, it will turn in the near future into the SOX experiment, measuring the (potential) short baseline oscillations in sterile states of anti-neutrinos produced with a radioactive source. The physics goals of the experiment also included the test of very rare phenomena, such as the electron decay.

The chapter is structured as follows. Section 4.1 discusses how neutrinos are detected, Sec. 4.2 describes the Borexino experimental facility, Sec. 4.3 shows the superb radio-purity achieved, Sec. 4.4 mentions some details of the data acquisition system, Sec. 4.5 introduces the main parameters used in the data analysis, Sec. 4.6 briefly describes the position reconstruction algorithm, Sec. 4.7 discusses  $\alpha/\beta$  discrimination, Sec. 4.8 discusses  $\beta^+/\beta^-$  discrimination, Sec. 4.9 introduces Borexino's thermal stability issues, Sec. 4.10 mentions Borexino's physics achievements, Sec. 4.11 discusses the prospects for Borexino Phase-II and Sec. 4.12 describes the future of Borexino, i. e. the SOX experiment.

### 4.1 Detection methods in Borexino

Solar neutrinos are detected by Borexino through elastic scattering off electrons:

$$\nu_x + e \rightarrow \nu_x + e, \quad (4.1)$$

---

<sup>1</sup>The hep  $\nu$  flux is anyway too small to be observed by a detector with the size of Borexino.

where  $x = e, \mu, \tau$ . Only a fraction of the primary neutrino energy  $E_\nu$  is transferred to the electron, which is then stopped by the scintillator, giving rise to the scintillation signal. The electron recoil spectrum is continuous even in the case of mono-energetic neutrinos, very similarly to what happens in the case of Compton effect. Actually, neglecting neutrino masses<sup>2</sup>, the end point of the electron recoil spectrum can be obtained exactly through Eq. (3.5) by replacing  $E_0$  with  $E_\nu$ .

The cross section of the process in Eq. (4.1) can be derived in the framework of the SM. At the lowest order in perturbation theory, the differential cross section is [211, 212]:

$$\frac{d\sigma}{dT_e}(E_\nu, T_e) = \frac{2G_F^2 m_e}{\pi} \left( g_L^2 + g_R^2 \left( 1 - \frac{T_e}{E_\nu} \right)^2 - g_L g_R \frac{m_e T_e}{E_\nu^2} \right), \quad (4.2)$$

where  $T_e$  is the electron kinetic energy,  $g_L = \pm \frac{1}{2} + \sin^2 \theta_W$  (“+” holds for  $\nu_e$  and “-” holds for  $\nu_\mu$  and  $\nu_\tau$ ),  $g_R = \sin^2 \theta_W$  and  $\sin^2 \theta_W \sim 0.23$  is the Weinberg angle. Radiative corrections both for Eq. (4.2) and for the electron recoil shape are computed in Ref. [213]. Their contribution is of the order of a few percents and is relevant only for the higher part of the  $^8\text{B}$   $\nu$  spectrum.

If one considers solar neutrino oscillations, the expected neutrino interaction rate in Borexino  $R_\nu$  is [214]:

$$R_\nu = N_e \int dE_\nu \frac{d\Phi_\nu}{dE_\nu} \int dT_e \left( \frac{d\sigma_e}{dT_e}(E_\nu, T_e) P_{ee}(E_\nu) + \frac{d\sigma_{\nu/\tau}}{dT_e}(E_\nu, T_e) (1 - P_{ee}(E_\nu)) \right), \quad (4.3)$$

where  $N_e$  is the number of target electrons,  $d\Phi_\nu/dE_\nu$  is the SSM differential energy spectrum of solar neutrinos as discussed in Sec. 1.6.3 and  $P_{ee}$  is the electron neutrino survival probability as of Eq. (1.52).

Table 4.1 summarizes the weighted cross sections for each solar neutrino species and the expected count rates in Borexino according to the *high-Z* (GS98) and *low-Z* (AGSS09) SSMs already discussed in Sec. 1.6.3. Borexino can detect all kinds of neutrinos, but the interaction probability increases with energy and it is about 4-5 times larger for  $\nu_e$  than for  $\nu_{\mu/\tau}$  in the energy region of interest. The low count rate of a few or a few tens of counts-per-day per 100 ton (cpd/100 ton) defines the need of a superb radio-purity for the detector. In fact, scintillation light is isotropic and any information about the initial direction of the incoming particle is lost. Thus, neutrino-induced events in liquid scintillators are intrinsically indistinguishable on an event-by-event basis from radioactive backgrounds.

The activity corresponding to the interaction rate of solar neutrinos in Borexino is equivalent to a few  $10^{-9}$  Bq/kg [215]. If this number is compared with the typical radioactivity of materials (ranging from a few Bq/kg to hundreds of Bq/kg), it is immediately clear that in order to accomplish its goals, the Borexino detector must be at least 9  $\div$  10 orders of magnitude less radioactive than anything on Earth. Typical

<sup>2</sup>This is an excellent approximation, being the precision goals of Borexino around the % level while the ratio of neutrino masses and solar neutrino energies is  $< 10^{-6}$ .

Solar $\nu$	$T_e^{\max}$ [keV]	$\sigma_e$ [ $10^{-46}$ cm $^2$ ]	$\sigma_{\mu/\tau}$ [ $10^{-46}$ cm $^2$ ]	$P_{ee}$	GS98 rate [cpd/100 t]	AGSS09 rate [cpd/100 t]	Main background
$pp$	261	11.38	3.22	$0.542 \pm 0.016$	$130.8 \pm 2.4$	$131.9 \pm 2.4$	$^{14}\text{C}$ , pileup
$^7\text{Be}$ (384 keV)	231	19.14	5.08	$0.537 \pm 0.015$	$1.90 \pm 0.14$	$1.73 \pm 0.12$	$^{85}\text{Kr}$ , $^{210}\text{Bi}$
$^7\text{Be}$ (862 keV)	665	57.76	12.80	$0.524 \pm 0.014$	$46.48 \pm 3.35$	$42.39 \pm 3.05$	$^{85}\text{Kr}$ , $^{210}\text{Bi}$
$pep$	1220	108.49	22.08	$0.514 \pm 0.012$	$2.73 \pm 0.05$	$2.79 \pm 0.06$	$^{11}\text{C}$ , $^{210}\text{Bi}$ , ext $\gamma$
CNO <sup>a</sup>	1517	$\sim 70$	$\sim 15$	$\sim 0.517$	$5.24 \pm 0.54$	$3.74 \pm 0.37$	$^{11}\text{C}$ , $^{210}\text{Bi}$
$^8\text{B}$	14500	596.71	106.68	$0.384 \pm 0.009$	$0.44 \pm 0.07$	$0.37 \pm 0.05$	ext $\gamma$

<sup>a</sup>The cross sections and the survival probability are relative to the higher energy components ( $^{15}\text{O}$  and  $^{17}\text{F}$ ) since they are “easier” to be measured.

**Tab. 4.1:** For each solar neutrino component, the table shows the maximum energy of the recoiled electrons  $T_e^{\max}$ , the total cross sections  $\sigma_e$  averaged on the spectral shape and  $\sigma_{\mu/\tau}$ , the electron neutrino survival probability  $P_{ee}$  (weighted for the spectral shape) and the predicted solar neutrino interaction rates in Borexino (in counts-per-day per 100 ton) according to the *high-Z* (GS98) and *low-Z* (AGSS09) SSMs already presented in Sec. 1.6.3. The values reported in this table are computed in Ref. [214].

radioactive contaminants are  $^{238}\text{U}$  and  $^{232}\text{Th}$  daughters, and  $^{40}\text{K}$ . Gaseous contaminants are commonly  $^{222}\text{Rn}$ ,  $^{39}\text{Ar}$  and  $^{85}\text{Kr}$ . The design goal was  $< 10^{-16}$  g/g in  $^{238}\text{U}$  and  $^{232}\text{Th}$  and  $< 10^{-16}$  g/g in natural K [215].

The experimental technique adopted for the unambiguous detection of anti-neutrinos (such as geo-neutrinos) does not exploit the elastic scattering off electrons. Borexino detects  $\bar{\nu}_e$  via the inverse neutron  $\beta$  decay (IBD),

$$\bar{\nu}_e + p \rightarrow n + e^+. \quad (4.4)$$

The threshold for this process is 1.806 MeV. The positron from the IBD promptly loses its energy in the liquid scintillator and annihilates emitting two back-to-back 511 keV gammas, yielding a prompt event, with a visible energy of  $E_{\bar{\nu}_e} - 0.782$  MeV.<sup>3</sup> The neutron is typically captured on protons with a mean time of  $\sim 256\ \mu\text{s}$  in Borexino, ending up in the emission of a 2.22 MeV de-excitation gamma, which provides a coincident delayed event. The characteristic time and spatial correlations of prompt and delayed events offer a clean signature of the  $\bar{\nu}_e$  detection.

## 4.2 Description of the setup

Borexino is widely described in Ref. [215]. A scheme of the detector can be found in the left panel of Fig. 2.12 and a complete 3D rendering is presented in Fig. 4.1.

It is located at the Laboratori Nazionali del Gran Sasso (LNGS) in central Italy, at a depth of 3800 m w.e. . The inner part (inner detector, ID) is an unsegmented Stainless Steel Sphere (SSS) of radius 6.85 m, that contains the liquid scintillator and supports mechanically the PMTs. Inside the SSS, two thin nylon vessels (with a 125  $\mu\text{m}$  thickness) divide the scintillator volume in three shells of radii 4.25 m, 5.50 m and 6.85

<sup>3</sup>The scintillation light related to the proton recoil is quenched and practically negligible.

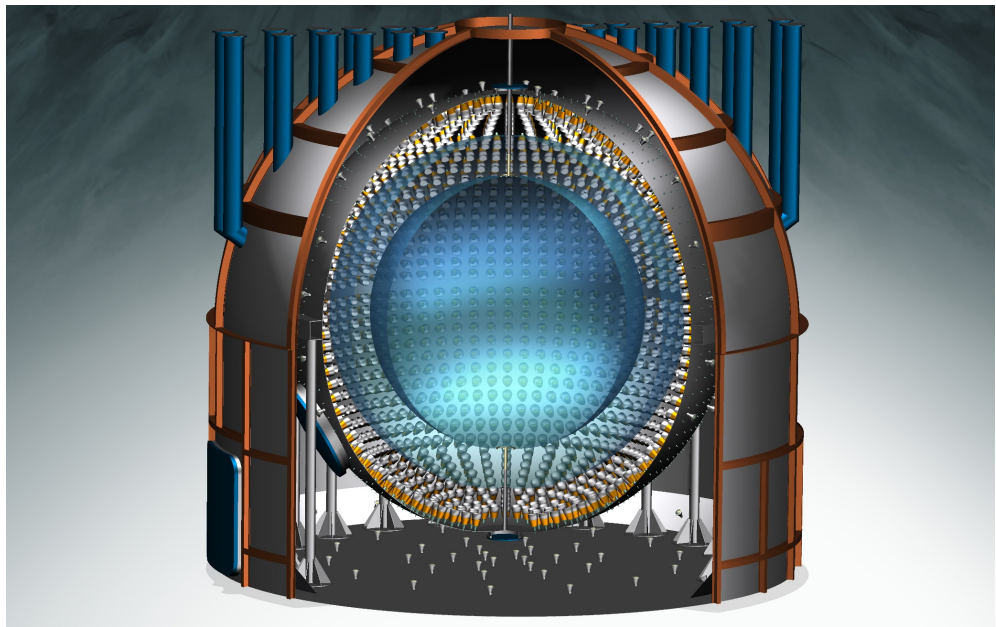


**Fig. 4.1:** 3D rendering of the whole Borexino detector, including the SSS, the two nylon vessels, the PMTs and the outer detector.

m. The inner vessel (IV) contains around 300 tons of the liquid scintillator solution: PC (pseudocumene, 1,2,4-trimethylbenzene  $C_6H_3(CH_3)_3$ ) as a solvent and the fluor PPO (2,5-diphenyloxazole,  $C_{15}H_{11}NO$ ) as a solute at a concentration of 1.5 g/L. The second and the third shells (“inner and outer buffers”) contain PC with a small amount (a few g/L) of DMP (dimethylphthalate,  $C_6H_4(COOCH_3)_2$ ) which is added as a light quencher. The addition of the DMP quenches the scintillation yield of the buffer fluid by a factor of 20. This is crucial in order to suppress the extremely high rate of events due to the radioactivity of the PMTs. Note that the choice of nylon as material for the vessel construction is particularly convenient, since its index of refraction is very similar to that of the scintillator. As already extensively discussed in chapter 3, the PC+PPO cocktail satisfies specific requirements such as high scintillation yield ( $\sim 10^4$  photons/MeV), high light transparency (mean free path of  $\sim 7$  m) and fast decay time ( $\sim 3$  ns), all essential for good energy resolution, precise spatial reconstruction and good  $\alpha/\beta$  discrimination. Since the PC+PPO solution is slightly lighter (about 0.4%) than the PC+DMP solution, the IV is anchored to the bottom, with a set of nylon strings. The outer nylon vessel (OV) is a barrier that prevents the diffusion of  $^{222}\text{Rn}$  emanated from external materials (steel, glass, PMTs) into the fiducial volume.

A leak of scintillator from the IV to the buffer region within the OV started approximately in 2008. The small hole in the IV was reconstructed to have location of  $26^\circ < \theta < 37^\circ$  and  $225^\circ < \phi < 270^\circ$ . The leak was detected based on a large rate of events reconstructed out of the IV. In order to minimize the leak rate, the density difference between the scintillator and the buffer fluids was reduced by partial removal of

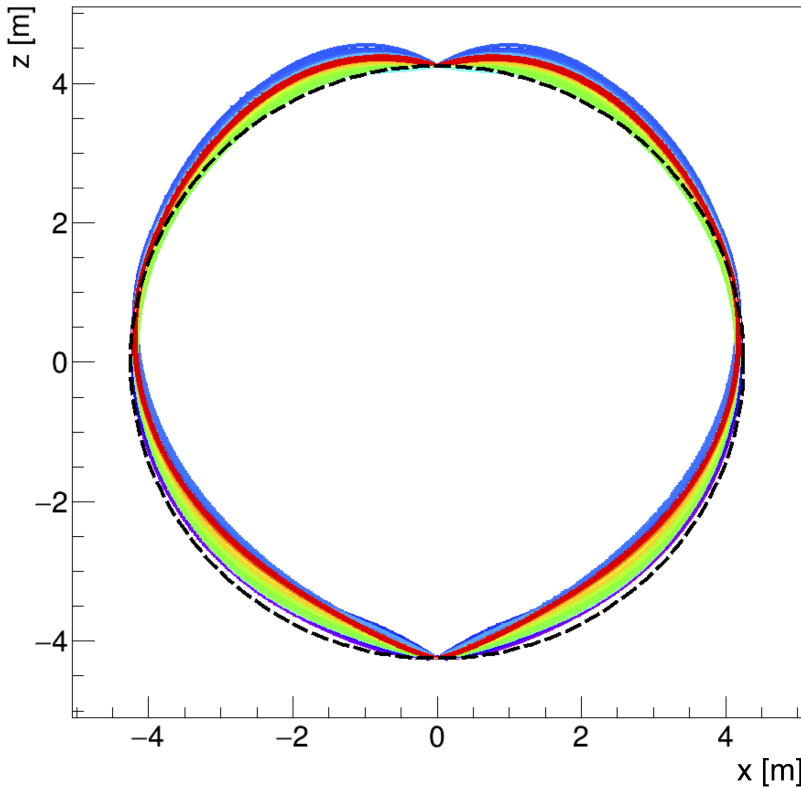


**Fig. 4.2:** Borexino's vessel reconstructed shape as a function of time. The black dashed line corresponds to the ideal situation of spherical vessel, which is very similar to the real vessel shape before the leak (violet band, almost invisible in the picture). The blue band corresponds to the leak period and the green refers to the time between the leak and the end of 2015 (red lines).

DMP from the buffer by distillation, with negligible consequences on the buffer optical behavior. Although the phenomenon has been under control since the DMP concentration decrease in the buffer, due to the presence of the hole and buoyancy effects, the IV profile is not precisely that of a sphere. Its shape is determined dynamically by identifying background events reconstructed on the vessel surface. They are mainly identified as  $^{210}\text{Bi}$  decays. The position of these events is fitted assuming uniformity on  $x - y$  planes so that the  $z$ -dependence of the vessel radius can be determined. The detailed procedure is described in Ref. [214] and was calibrated with ID pictures taken with CCD cameras [216]. A weekly basis monitoring of the vessel shape is performed, in order to check its stability and prevent further damages. Figure 4.2 shows the time evolution of the vessel shape, from 2007 to 2015. The violet bands<sup>4</sup> correspond to periods before the leak, the blue situation is the worst, corresponding to the months in which the leak was present.

The scintillation light is collected by nominally 2212 photomultipliers (PMTs) that are uniformly attached to the inner surface of the SSS. All but 384 PMTs are equipped

<sup>4</sup>They are almost not visible, since they almost completely overlap with the black spherical contour.

with light concentrators that are designed to reject photons not coming from the active scintillator volume and to make the light collection for events in the fiducial volume (FV) as uniform as possible. The 384 PMTs without concentrators are used to study radioactive decays in the buffer liquid or gammas from the PMTs and to identify muons that cross the buffer, but not the IV.

The SSS is supported by 20 steel legs and enclosed within a large tank (WT) which is filled with ultra-pure water. The WT has a cylindrical base with a diameter of 18 m and a hemispherical top with a maximum height of 16.9 m. The WT is a powerful shielding against external backgrounds ( $\gamma$  rays and neutrons from the rock) and is also used as a Čerenkov muon counter and tracker (outer detector, OD). The muon flux, although reduced by a factor of  $10^6$  by the 3800 m w.e. depth of LNGS, is of the order of  $1 \text{ m}^{-2} \text{ h}^{-1}$ , corresponding to about 4000 muons per day crossing the detector. This flux is well above Borexino's requirements and a strong additional reduction factor (about  $10^4$ ) is necessary. Therefore, the WT is equipped with 208 photomultipliers that collect the Čerenkov light emitted by muons in the water.

### 4.3 Purity levels in Borexino and major contaminants

The achievement of extremely low background levels in Borexino was crucial for the success in obtaining solar neutrino results. The different components can be classified as external and surface backgrounds (coming from outside the scintillator, i.e. from the SSS, PMTs and nylon vessels), internal backgrounds (due to radioactive decays of nuclei contaminating the liquid) and cosmogenic backgrounds (associated with the creation of unstable elements by muon interactions).

The main source of external background is the radioactivity contained in the SSS, PMTs and light concentrators. Since the radioactive decays occur outside the scintillator, only gammas can reach the innermost fiducial volume, and particularly those of  $^{208}\text{Tl}$ ,  $^{214}\text{Bi}$  and  $^{40}\text{K}$ . The contribution of the external background is not very important for the  $^7\text{Be} \nu$  measurement, while it is crucial for the determination of pep  $\nu$  and CNO  $\nu$ . It is possible to reduce the contribution of external gammas by choosing smaller fiducial volumes or inserting the radial distribution of the events in the fit procedure with a multivariate approach, as discussed in Sec. 6.6.

The contribution of internal backgrounds producing electrons or gammas can be disentangled from neutrino interactions only through their spectral shapes. In the case of  $\alpha$  particles or positrons, it is possible to develop pulse discrimination techniques to further suppress them (see Sec. 4.7 and Sec. 4.8).

Table 4.2 shows the major sources of contaminants in Borexino, the strategies adopted for reaching the scientific purity requirement of the experiment and the results actually achieved in the two phases of data acquisition. Borexino started the data taking in May 2007 and terminated its Phase-I in May 2010. The results achieved on solar neutrinos with this first data set are well summarized in Ref. [214]. Between May 2010 and the end of 2011, calibrations and purification campaigns took place, leading to a further reduction of the radioactive contaminants. The improvements of Phase-II in the detector

Type	Background	Concentration/Flux		Strategy	Result	
		Source	Typical amount		Requirement	Phase-I
$\mu$	cosmic	~ 200 s <sup>-1</sup> m <sup>-2</sup>	< 10 <sup>-10</sup> s <sup>-1</sup> m <sup>-2</sup>	underground, WT	< 10 <sup>-10</sup> (eff.>0.9992)	< 10 <sup>-10</sup> (eff.>0.9992)
$\gamma$	rock	—	—	WT, FV	negligible	negligible
$\gamma$	PMTs, SSS	—	—	buffer, FV	negligible	negligible
$^{14}\text{C}$	intrinsic PC	~ 10 <sup>-12</sup> g/g	< 10 <sup>-18</sup> g/g	PC selection	~ 2 · 10 <sup>-18</sup> g/g	~ 2 · 10 <sup>-18</sup> g/g
$^{238}\text{U}$	dust, metals	~ 10 <sup>-5</sup> g/g	< 10 <sup>-16</sup> g/g	purifications, tagging	1.6±0.1 10 <sup>-17</sup> g/g	< 9.5 · 10 <sup>-20</sup> g/g
$^{232}\text{Th}$	dust, metals	~ 10 <sup>-6</sup> g/g	< 10 <sup>-16</sup> g/g	purifications, tagging	5±1 10 <sup>-18</sup> g/g	< 7.2 · 10 <sup>-19</sup> g/g
$^7\text{Be}$	cosmogenic	~ 3 · 10 <sup>-2</sup> Bq/ton	< 10 <sup>-6</sup> Bq/ton	distillation	not seen	not seen
$^{40}\text{K}$	dust, PPO	~ 2 · 10 <sup>-6</sup> g/g(dust)	< 10 <sup>-18</sup> g/g	distillation	not seen	not seen
$^{210}\text{Po}$	$^{222}\text{Rn}$	—	<1 cpd/ton	purifications, tagging	~1 cpd/ton	< 1 cpd/ton
$^{222}\text{Rn}$	material emanation	10-1000 Bq/kg (rock)	<10 cpd/100 ton	< 1cpd/100 ton	< 1cpd/100 ton	< 0.1 cpd/100 ton
$^{39}\text{Ar}$	air, cosmogenic	17 mBq/m <sup>3</sup> (air)	<1 cpd/100 ton	$\text{N}_2$ stripping	$\ll^{85}\text{Kr}$	$\ll^{85}\text{Kr}$
$^{85}\text{Kr}$	air, nuclear reactions	~ 1 Bq/m <sup>3</sup> (air)	<1 cpd/100 ton	$\text{N}_2$ stripping	30±5 cpd/100 ton	< 5 cpd/100 ton
$^{210}\text{Bi}$	$^{222}\text{Rn}$	—	—	water extraction	40 cpd/100 ton	~ 20 cpd/100 ton

**Tab. 4.2:** The table shows Borexino’s main sources of contaminations with the relative requirements in terms of interaction rates or concentration. The main strategies for the background reduction, together with the actual achievements both for Phase-I and Phase-II, are also highlighted.

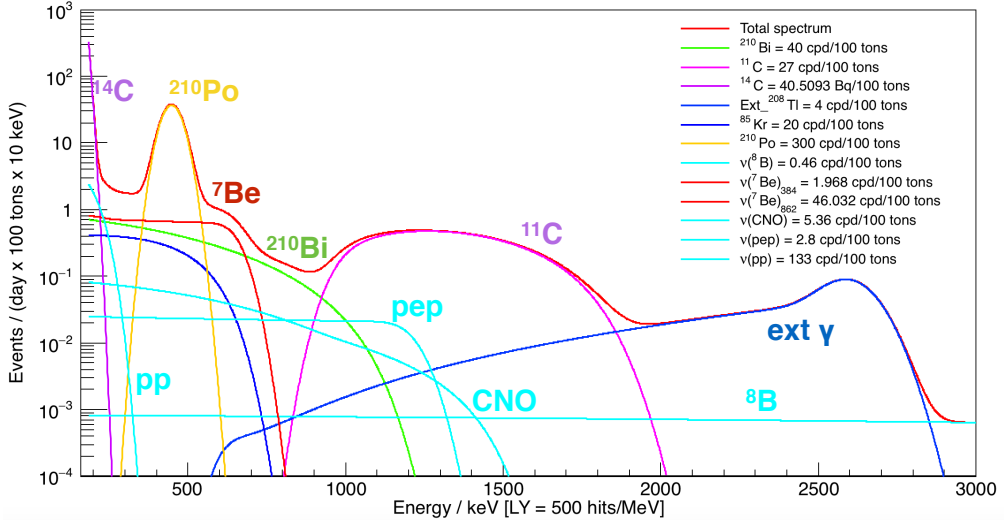
radio-purity are clearly visible in the last column of Tab. 4.2. Phase-II started at the end of 2011 and it is coming to its end, with the preliminary results on the precision global analysis of solar neutrinos being one of the goals of this PhD thesis.

Figure 4.3 shows the expected energy spectrum in Borexino including solar neutrinos and the relevant internal and cosmogenic background sources, taking into account the realistic energy resolution of the detector. The rates of solar neutrinos correspond to the SSM expectations while those of background components are set to values typical for Borexino Phase-I period.

At low energy, the main background is  $^{14}\text{C}$ . It is a  $\beta$ -emitter, with 156 keV end point and a half life of  $\sim 5700$  years.  $^{14}\text{C}$  is chemically identical to  $^{12}\text{C}$  and thus the only way to reduce the levels of contamination consisted in deriving the Borexino scintillator from crude oil from deep underground. The measured level of  $^{14}\text{C}$  in the Borexino scintillator is as low as  $10^{-18}$  [217]. Still, even with this large reduction in contamination,  $^{14}\text{C}$  is by far the largest Borexino background. Being its rate of  $(3.46 \pm 0.09) 10^6$  cpd/100 ton [218], it limits the detector low-energy threshold at around  $\sim 50$  keV.

$^{85}\text{Kr}$  is a  $\beta$ -emitter with 687 keV end point in 99.57% of the cases and  $\sim 10.8$  years half life. This background is crucial for the measurement of  $^7\text{Be} \nu$ , since its  $\beta$  spectrum is very similar to that of recoiled electrons by  $^7\text{Be} \nu$ .  $^{85}\text{Kr}$  can also decay (with a branching ratio of just 0.43%) into  $^{85m}\text{Rb}$ , emitting an electron with maximum kinetic energy of 173 keV.  $^{85m}\text{Rb}$  then de-excites by emitting a 514 keV gamma with a mean life of  $\sim 2 \mu\text{s}$ . This coincidence (both in space and in time) can be used to obtain an independent measurement of the  $^{85}\text{Kr}$  concentration in the scintillator. The very low branching ratio, and the relatively low energy of the prompt and delayed events, make this tagging not very easy, since accidental coincidences of  $^{14}\text{C}$  and  $^{210}\text{Po}$  might mimic this signature.<sup>5</sup> In the case of Borexino Phase-I, the level of contamination in  $^{85}\text{Kr}$  obtained with this method was quantified to be  $(30.4 \pm 5.3(\text{stat.}) \pm 1.5(\text{sys.}))$  cpd/100 ton. After purifications, only

<sup>5</sup>Actually,  $^{210}\text{Po}$  events might be tagged thanks to the pulse shape, see Sec. 4.7.



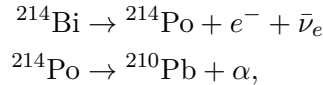
**Fig. 4.3:** Simulated spectrum of solar neutrino components according to SSM and radioactive backgrounds with Borexino Phase-I contamination levels. Note that the event pileups at low energy are not present here. The resolution assumed ( $\sim 500$  p.e./MeV) is very close to the one observed with real data.

a limit for Phase-II is available:  $< 5$  cpd/100 ton at 95% C.L. .

$^{40}\text{K}$  has a dominant pure  $\beta$ -decay (89% branching ratio and 1310 keV end point) and can also decay by electron capture to an excited state of  $^{40}\text{Ar}$ , which in turn can de-excite emitting a mono-energetic 1460 keV gamma. The  $^{40}\text{K}$  contamination was reduced through distillation, filtration, and water extraction of the scintillator. Phase-I results show only a limit for this component of 0.4 cpd/100 ton at 95% C.L. [214]. A little more 1460 keV gamma events are observed in the external background components, since potassium is present in the PMT glass [214].

The isotope  $^{39}\text{Ar}$  is a pure  $\beta$ -emitter with a Q value of 565 keV. A great effort was done in ensuring that the  $^{39}\text{Ar}$  contamination was as low as possible, since its spectral shape and end point are very close to that of  $^7\text{Be}$   $\nu$  [214]. The argon levels in the specially prepared low Ar/Kr nitrogen used for the stripping of the scintillator was found to be  $\sim 0.005$  ppm (in volume). Assuming an activity of  $1.4 \text{ Bq}/\text{m}^3$  in atmospheric argon, this translates to an expected rate of less than 0.02 cpd/100 ton in the scintillator, which is totally negligible [214].

The concentration of contaminants due to the  $^{238}\text{U}$  chain in secular equilibrium can be measured thanks to the coincidence of  $^{214}\text{Bi}$  and  $^{214}\text{Po}$  decays:



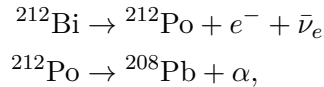
with  $\tau = 238 \mu\text{s}$ .  $^{214}\text{Bi}$  is a  $^{222}\text{Rn}$  daughter and the hypothesis of secular equilibrium is often invalid due to radon diffusion through surfaces or scintillator contaminations from

the air.  $^{210}\text{Pb}$  is a  $\beta$ -emitter with a very low energy end point (63.5 keV), and thus it does not represent a problem for solar neutrinos. The number of  $^{214}\text{Bi}$ - $^{214}\text{Po}$  coincidences is continuously monitored in Borexino. A sharp increase followed by the decay with the 5.5 days mean life of  $^{222}\text{Rn}$  is always observed in correlation with operations performed on the detector (e.g. purifications, water extractions or calibrations). No persistent contamination is observed, suggesting that the increase in the rate of tagged  $^{214}\text{Bi}$ - $^{214}\text{Po}$  events is due to  $^{222}\text{Rn}$  insertion in the detector. The presence of these events is particularly useful for developing pulse shape discrimination for  $\alpha/\beta$  and  $\beta^+/\beta^-$ , as discussed in Sec. 4.7 and Sec. 4.8.

$^{210}\text{Bi}$  is a pure  $\beta$ -emitter created by the disintegration of  $^{210}\text{Pb}$ . Its mean life is 7.23 days and the emitted electrons have an end point of 1160 keV. It represents a crucial background for solar neutrino detection: its spectrum spans through the energy range of interest for  $^7\text{Be} \nu$ , pep  $\nu$  and CNO  $\nu$ . Particularly, its spectral shape is almost degenerate to that of CNO  $\nu$  interactions with electrons in the liquid scintillator.  $^{210}\text{Bi}$  contamination can be measured only through the spectral fit. A possible approach for an independent constraint on the  $^{210}\text{Bi}$  concentration in the liquid scintillator is presented in Sec. 4.9.

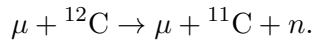
$^{210}\text{Po}$  is produced by  $^{210}\text{Bi}$  decays and, besides  $^{14}\text{C}$ , it is the most abundant component in the Borexino spectrum. It is a mono-energetic 5300 keV  $\alpha$ -emitter with  $\sim 138$  days half life. The pulse-shape discrimination is very effective in reducing this background component. More details on  $^{210}\text{Po}$  in Borexino are given in Sec. 4.9.

The primordial  $^{232}\text{Th}$  isotope content in Borexino can be estimated by the fast decay sequence of  $^{212}\text{Bi}$ - $^{212}\text{Po}$ :

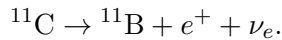


with  $\tau = 433$  ns, very similarly to the  $^{214}\text{Bi}$ - $^{214}\text{Po}$  case. The observed  $^{232}\text{Th}$  rate in the innermost FV is not constant in time and it changes as a consequence of operations on the detector. Also in this case, no time persistent contamination is introduced since the  $^{212}\text{Bi}$ - $^{212}\text{Po}$  rate recovers the initial value very quickly, being the longest lived isotope among thoron daughters  $^{212}\text{Pb}$  with  $\tau = 15.4$  hours.

The dominant muon-induced cosmogenic background in Borexino is  $^{11}\text{C}$ , which represents the biggest challenge for the measurement of pep  $\nu$  and CNO  $\nu$ . In 95% of the cases,  $^{11}\text{C}$  is produced together with at least one neutron:



Then,  $^{11}\text{C}$  decays with  $\tau = 29.4$  minutes via  $\beta^+$ -decay:



The  $\beta^+$  decay has a Q value of 960 keV and it is always associated with the emission of two 511 keV gamma rays from the  $e^+$  annihilation. The interaction of the residual muons which can reach Borexino is expected to produce a few tens of  $^{11}\text{C}$  nuclei per day. The continuous cosmogenic production and the short  $^{11}\text{C}$  half life create an equilibrium

concentration of  $^{11}\text{C}$  that cannot be reduced by any purification procedure. On the other hand,  $^{11}\text{C}$  tagging through spatial and time coincidence with muons and captured neutrons is possible [219] and very well performing, as described in Sec. 6.3. Other cosmogenic backgrounds are present in Borexino [201], such as  $^{10}\text{C}$  or  $^7\text{Be}$ , but their relevance is much lower for low energy solar neutrino spectroscopy [214].

## 4.4 The data acquisition system

The ID and OD electronics are two independent systems with two different designs. A complex trigger system takes care of their integration.

The ID electronics is organized in 14 identical racks, each of them handling 160 PMTs. Each rack supplies the high voltage (HV) to the PMTs, processes the signals through the front ends and possibly records the event information with dedicated digital boards (“Laben boards”). Borexino PMTs are AC coupled, i. e. the signal and the HV travel along the same cable. After the decoupling stage, the negative signal has therefore a bipolar shape with a positive overshoot and a null area. The overshoot is however small and long ( $\sim\text{ms}$ ) and its interference in the signal processing can be easily minimized. The PMT operating voltage is regulated in order to obtain a gain of  $\sim 10^7$  and the gain equalization is performed on a weekly basis. Typically, after the decoupling, Borexino PMT signals have an amplitude of  $-12\text{ mV}$ , a  $4\text{ ns}$  rise time and  $10\text{ ns}$  fall time, with a charge of  $1.6\text{ pC}$ . The number of photoelectrons collected by the Borexino detector is approximately 500 per MeV and the interesting energy range extends from a few tens of keV up to a few MeV. Therefore, Borexino PMTs work mostly in single photoelectron regime. In case of a 1 MeV event at the center of the detector, the probability of multiple photoelectrons originating within the same PMT is below 10%. This number scales with the energy of the event and increases with the radial distance as the solid angle seen by PMTs closer to the event is bigger.

In order to determine the energy and the position of a scintillation event, the amount of collected charge and the time of the detected photoelectrons must be recorded. For this reason, the front end boards provide a timing signal, which is simply an inverted,  $\sim 20$  times amplified copy of the PMT waveform, together with an integrated signal. This latter is built with the principle of the gate-less integrator described in Ref. [220] and depicted in Fig. 4.4. This device has zero dead time and does not need a gate. Once a pulse reaches the front end (leftmost picture in Fig. 4.4), the signal is integrated and the full charge plateau is kept for  $T = 80\text{ ns}$ . After that, the integrator discharges with a time constant  $\tau = 500\text{ ns}$ . The digital electronics of the Laben boards samples this signal twice (points  $B_0$  and  $P_0$  in Fig. 4.4), with the measured charge corresponding to the two samples difference, i. e.  $Q_0 = P_0 - B_0$ . This filters out any offset along with all possible baseline drifts and low frequency noise. The bipolar shape of the PMT signal actually disturbs slightly the charge evaluation (i.e. the flat top is not entirely flat), but as the undershoot time constant is much longer than  $T$ , the effect is negligible. In case of pileup photoelectrons with time distance  $\Delta t < 80\text{ ns}$ , the double sampling methods keeps working fine as it can be noted in the middle picture of Fig. 4.4. Instead, for pileup

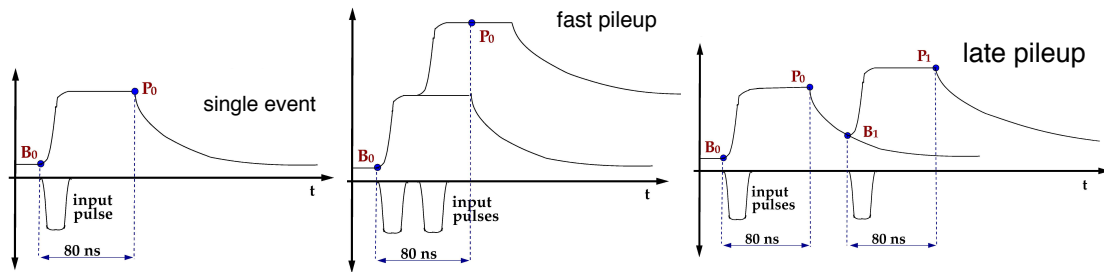


**Fig. 4.4:** Principle of operation of the gate-less charge integrator used in Borexino. The integrated output is shown as a function of time for various photoelectron arrival time combinations.

signals with  $\Delta t > 80$  ns (rightmost picture of Fig. 4.4), a software correction must be applied to the second hit charge in order to cancel out the discharge effect of the previous hit. Therefore,  $Q_1$  becomes:

$$Q_1 = (P_1 - B_1) - Q_0 e^{-\frac{\Delta t}{\tau}} \left[ 1 - e^{-\frac{T}{\tau}} \right]. \quad (4.5)$$

The goal of the digital electronics is to digitize time and charge information for every PMT signal and to provide information to the trigger system on the number of channels firing in coincidence. Each channel functional block of the Laben boards receives the linear amplified pulse and the integrated pulse from a front-end channel. The linear signal is fed to a programmable dual threshold discriminator, whose high and low thresholds are set to 50mV and 20mV respectively. These values correspond roughly to 0.25 and 0.1 of the average (amplified) single photoelectron signal. The high threshold corresponds to the valley between the exponential and the Gaussian components of the single photoelectron charge spectrum. The discriminator fires if the signal crosses the high threshold, but the time of the signal is measured in relation to the low threshold crossing. In this way the dark noise component under the exponential is filtered out and at the same time the amplitude walk is kept small. When the discriminator fires, the timing information is stored with a nominal resolution of 0.2 ns.<sup>6</sup> A second ADC samples the peak ( $P_0$ ) and the base ( $B_0$ ) of the integrated signal, associating to the timing information also its charge. This explains the concept of “hit” in Borexino data analysis, i. e. the time information of the Laben threshold crossing by a PMT output signal, together with the associated charge measurement. In order for the Laben boards to work properly, a hardware dead time of 140 ns must be issued, after each high threshold crossing. This means that the minimum time distance of two hits occurring on the same channel (which can be thought as the union of a PMT and the front end) is 140 ns. Therefore, the effective dead time of the system is limited to the interval between 80 ns and 140 ns from the first high threshold crossing. If more photoelectrons pileup in a time window shorter than 80 ns, only one hit is recorded, the time information being relative to the first photoelectron. Anyhow, the charge associated with the hit is the sum of all the piled-up signals in the 80 ns, as illustrated in the middle picture of Fig. 4.4. The dead time interval between 80 ns and

<sup>6</sup>It has to be noted that the intrinsic PMT time resolution is worse.

140 ns translates only to a few percent overall dead time for a typical physics event in Borexino.

The main acquisition system of Borexino was designed and optimized for the detection of low energy solar neutrinos in the sub-MeV range. It is possible to extend the energy region of interest to higher energies than a few MeV by taking into account the effect of saturated channels. However, this might not be accurate enough for very high energies (e.g.  $\gtrsim 10$  MeV). For this reason, a separate system was designed, based on the idea that at high energies it is possible to retain precision even without recording all the channels individually. The photomultiplier signals are therefore grouped by solid angle sectors, and each of these sums is recorded by a 400 MHz, 8-bit waveform digitizer.

The OD is composed of 208 additional PMTs arranged on the outer side of the SSS and on the floor of the WT. The front-end electronics of the OD is constituted by 14 Charge-to-Time Converters (QTCs), each of which is made of 16 channels. The output of the QTC is connected to a commercial double-edge TDC, which measures the time of the rising and falling edges of the signal. The first rising edge yields the time of the PMT pulse, while the time distance to the second falling edge yields the charge.

The Borexino triggering system has to identify scintillation events that are detected by the quasi simultaneous occurrence of several PMT hits in the ID. The trigger fires when a programmable number of photomultipliers (typically 20  $\div$  30) are hit within a short trigger time window. Being the total transit time of photons throughout the SSS at most about 50 ns, the system allows trigger time windows only in the range 48  $\div$  99 ns. The Borexino Trigger Board (BTB) handles several additional triggers, such as random triggers, electronic pulse triggers and timing laser triggers which are fired for monitoring purposes.

## 4.5 Event structure and energy estimators

The acquisition gate in Borexino is  $16.5\ \mu\text{s}$  long. The averaged hit time distribution (the concept of hit being that defined in Sec. 4.4) for typical Borexino events is shown in the left panel of Fig. 4.5. In the picture, the trigger happens at  $t = 0$ : the baseline due to PMT dark noise is clearly visible, as well as the main peak structure for scintillation events. An additional feature is present a few  $\mu\text{s}$  later than the physical scintillation pulse and it is due to the PMT after-pulses. The typical dark rate of internal PMTs is around a few hundreds Hz which yields, on average,  $\sim 15$  random hits per event within the acquisition gate.

The reconstruction algorithm developed for Borexino (i. e. `echidna`) is able to analyze the hit time distribution on an event basis, in order to identify scintillation pulses against noise. The raw hits acquired by the Laben boards are scanned, and *bad* hits are removed thanks to the decoding algorithm.<sup>7</sup> The ensemble of hits which are recognized to belong to the same scintillation pulse are grouped in the so called “cluster”. The clustering

---

<sup>7</sup>The procedure for the selection of the raw hits is complicated. In practice, unphysical hits are removed, e. g. those with too low or too high charge.

algorithm is quite sophisticated, but in practice, after binning the decoded hit time distribution in 16 ns bins, the following conditions are checked:

- a bin exceeds  $3\sigma$  the average dark noise.
- at least 20 decoded hits ( $\sim 50$  keV) are found in the first 48 ns.
- the sum of the hits exceeds the 80% of the trigger threshold (only for the first cluster in the gate).
- the cluster start time lies within a few  $\mu$ s after the start of the gate (only for the first cluster in the gate).

The last two conditions apply only to the first physical event in the gate and are not applied in case another cluster is found within the same acquisition window, as for example in the case presented in the right panel of Fig. 4.5, where two independent clusters are identified. Dedicated functions determine the cluster start time and its end. The typical cluster duration lies between  $\sim 100$  ns and  $\sim 1 \mu$ s.

Clusters are the primary objects used in Borexino's data analysis, since they contain information about the real scintillation events. It can happen that two distinct events are so close in time (a few hundreds of ns) that the clustering algorithm is not able to decouple them: these are the pileup events, which are more extensively addressed in Sec. 5.11. The time and charge information of all the hits which are grouped in a cluster is used to estimate the event energy, position, topology and so on.

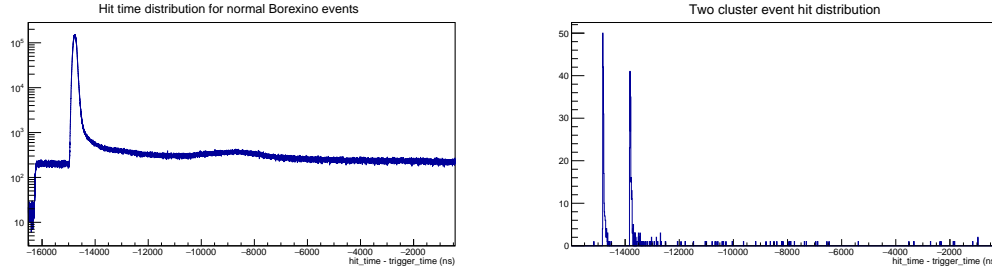


**Fig. 4.5:** *Left panel:* Hit time distribution averaged for many Borexino events. The trigger condition is realized at  $t = 0$ . *Right panel:* Hit time distribution for a two-cluster event.

The Borexino energy estimators are essentially of three kinds, and are commonly referred to as *npmts* ( $N_p$ ), *nhits* ( $N_h$ ) and *charge* ( $N_{pe}$ ). They are evaluated for each identified cluster. *nhits* corresponds to the number of decoded hits (as defined in Sec. 4.4) which are grouped in the same cluster. *npmts* is the number of PMTs which recorded at least one hit. In general, *npmts* and *nhits* are different, since this latter can detect some of the possibly piled-up photoelectrons (see Sec. 4.4), while *npmts* is either 0 or 1 for each channel. On an event basis, the number of actually working channels ( $N_{live_{pmt}}$ ) is recorded and an equalization factor is computed, so that the effects of temporarily disabled channels or the death of PMTs along the years are reduced. The adopted procedure

consists in equalizing  $nhits$  and  $npmts$  to 2000 working channels. This operation is often called “normalization”. In practice, e. g. in the case of  $npmts$ , one simply computes:

$$N_p^{\text{norm}} = f_{eq}(t)N_p, \quad \text{where } f_{eq}(t) = \frac{2000}{N_{\text{live}_{pmt}}}. \quad (4.6)$$

The *charge* variable  $N_{pe}$  corresponds to the sum of the recorded charge of all the decoded hits in the cluster. Also in this case, the normalization procedure is performed, but the equalization coefficient is slightly different from  $f_{eq}(t)$ , not because of a different definition, but because while in the case of  $nhits$  and  $npmts$  only the timing information recorded by the Laben boards is needed, a full working channel for the evaluation of  $N_{pe}$  must collect properly also the charge information. This causes a slight disalignment between  $N_{\text{live}_{pmt}}$  and  $N_{\text{live}_{charge}}$ , which is taken into account. In order to suppress the dark noise contribution to the charge evaluation, an additional variable, say  $N_{pe}^d$ , is calculated by subtracting the expected number of photoelectrons due to dark noise during the cluster duration. From these variable definitions, it is immediately clear that while *charge* is expected to be linear in a wider energy range (being less affected by saturation effects),  $npmts$  and  $nhits$  are actually better at lower energies, where the dark noise contribution spoils *charge*.

Other variables with a “fixed duration” are usually defined. They were useful for the low energy analysis for the first measurement of  $pp \nu$  of Ref. [218], and particularly for studying the event pileup spectral shape and composition.  $npmts\_dt1$  is the sum of the fired PMTs within the first 230 ns from the beginning of the cluster.  $npmts\_dt2$  sums the number of PMTs which collected at least a hit in the first 400 ns from the beginning of the cluster. Of course, the normalization procedure can take place for these variables in the same way as it does for  $npmts$  and  $nhits$ . These variables can be convenient, since the fixed cluster duration allows a simpler study of the event pileup and the dark noise is lowered by the relatively small time window considered. The drawback is a larger loss of linearity at higher energies than that of the whole-cluster based variables.

## 4.6 Position reconstruction

Event position reconstruction in Borexino is based on the time distribution of collected photons. The algorithm maximizes the likelihood ( $\mathcal{L}_{\text{pos}}(\vec{r}_0, t_0 | (\vec{r}_i, t_i))$ ) that given the measured decoded hit time pattern  $(\vec{r}_i, t_i)$  ( $\vec{r}_i$  is the position of the PMT which fired for the hit  $i$ , and  $t_i$  is the hit time), the event occurs at  $t_0$  in the position  $\vec{r}_0$  [216]. The object of the maximization is thus the couple  $t_0, \vec{r}_0$ . In the likelihood computation, for each hit  $i$  in the cluster, the time of flight  $T_i^f$  is subtracted to the hit time  $t_i$ .  $T_i^f$  can be easily computed as

$$T_i^f = |\vec{r}_i - \vec{r}_0| \frac{n_{\text{eff}}}{c}. \quad (4.7)$$

$n_{\text{eff}}$  takes into account the fact that optical photons travel with the group velocity, their energy spectrum is not trivial and the index of refraction is a function of the wavelength

$\lambda$ , i.e.  $n = n(\lambda)$ . At a given  $\lambda$ , the definition of  $n_{eff}$  comes directly from the group velocity definition:

$$v_g(\lambda) = \frac{c}{n - \lambda \frac{dn}{d\lambda}} \rightarrow n_{eff}(\lambda) \equiv n - \lambda \frac{dn}{d\lambda}. \quad (4.8)$$

The  $n_{eff}(\lambda)$  as defined in Eq. (4.8) is still a function of the wavelength, while the parameter needed in Eq. (4.7) is an effective one, which does not distinguish upon  $\lambda$ . In practice,  $n_{eff}(\lambda)$  must be averaged over the spectrum of photons which are detected by the PMTs, so taking into account the scintillator primary spectrum, the absorption and reemission phenomena and the quantum efficiency of the PMTs. In principle, it could be predicted efficiently by means of accurate Monte Carlo simulations, but for sure the most reliable method is the use of calibrations. During the calibration campaigns described in Ref. [216], various radioactive sources were placed in more than 200 positions inside the detector, and the position reconstruction algorithm was tested and  $n_{eff}$  measured.  $n_{eff}$  was found to be significantly larger (1.68) than the index of refraction of PC measured at 600 nm (1.50). More details on  $n(\lambda)$  and  $n_{eff}$  are discussed in Sec. 5.5.

In order to perform the likelihood maximization, probability density functions (PDF) of the hit detection as a function of time elapsed from the emission of scintillation light, are used. The PDF shapes depend on the amount of charge collected within the hit, as shown in the left panel of Fig. 4.6. The starting values of  $t_0$  and  $\vec{r}_0$  for the maximization algorithm are computed with a barycenter of light method. The right panel of Fig. 4.6 shows the method accuracy on an event basis as a function of energy as estimated during the calibration campaign. Naturally, the more available hits, i.e. the higher the energy, the better the accuracy is.

During the calibration campaign, the source positions are evaluated according to an independent CCD camera system [216]. The  $x$  and  $y$  coordinates turned out to be very well reconstructed, while a significant bias of approximately  $-3$  cm in the reconstructed  $z$  coordinate is observed. The origins of this effect have not yet been understood: it may be the result of a small offset in the position of the PMT coordinate system, a problem of the CCD camera system or a physical effect which is not taken into account properly (such as the temperature dependence of the refraction index, see Sec. 5.5). Nevertheless, as pointed out e.g. in Ref. [214], the observed  $z$ -shift negligibly contributes to the systematic uncertainty in Borexino physics results.

As a final remark, it was recently found out that the value of the maximized likelihood  $\mathcal{L}_{pos}$  can be a very good pulse shape discrimination parameter, able to disentangle different event topologies, such as those of  $\beta^+$  and  $\beta^-$ . This is discussed more extensively in Sec. 6.6.2.

## 4.7 $\alpha/\beta$ discrimination

The time distribution of the scintillation photons depends on the details of the energy loss and of the interaction that takes places, which in turn depend on the particle interacting with the liquid scintillator. Particularly, the energy loss for unit path,  $dE/dx$ ,

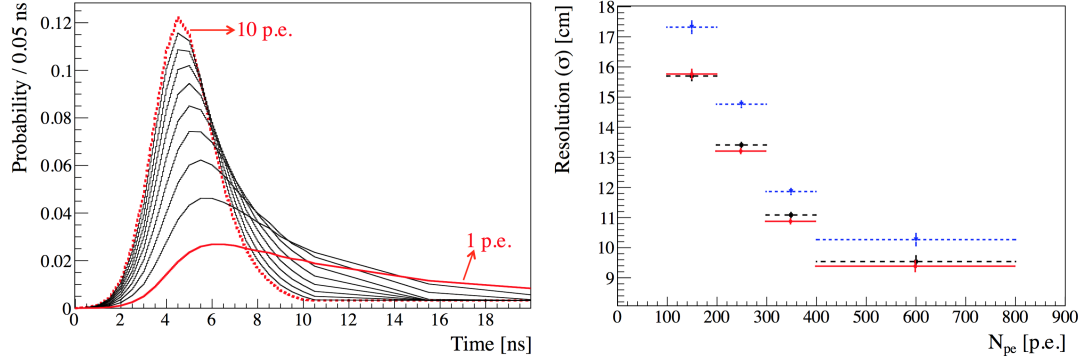


**Fig. 4.6:** *Left panel:* Probability density functions for the hit time detection as a function of the collected charge in the hit. Picture from Ref. [214]. *Right panel:* Position reconstruction algorithm accuracy as a function of the event energy. Picture from Ref. [214].

is very different between  $\alpha$  and  $\beta$ . Theoretically, the mean energies of alpha particles are pretty high ( $\gtrsim 4$  MeV) and thus one would not expect an  $\alpha$  presence in the solar neutrino region of interest. However, as discussed in Sec. 5.3.1, the higher  $dE/dx$  compared to  $\beta$  particles quenches  $\alpha$ 's by a factor of  $\sim 10$ , thus bringing their reconstructed energy exactly in the sub-MeV part of the spectrum. Anyhow, the different interaction mechanism of  $\alpha$ 's creates a hit time distribution pattern within the cluster which is quite distinguishable from that of  $\beta$ 's. By selecting  $^{214}\text{Bi}$ - $^{214}\text{Po}$  fast coincidences as briefly described in Sec. 4.3, it is possible to observe the two different hit time distributions which are shown in Fig. 4.7. Particularly,  $\alpha$  interactions have a much bigger light contribution at later times than those from  $\beta$ 's.

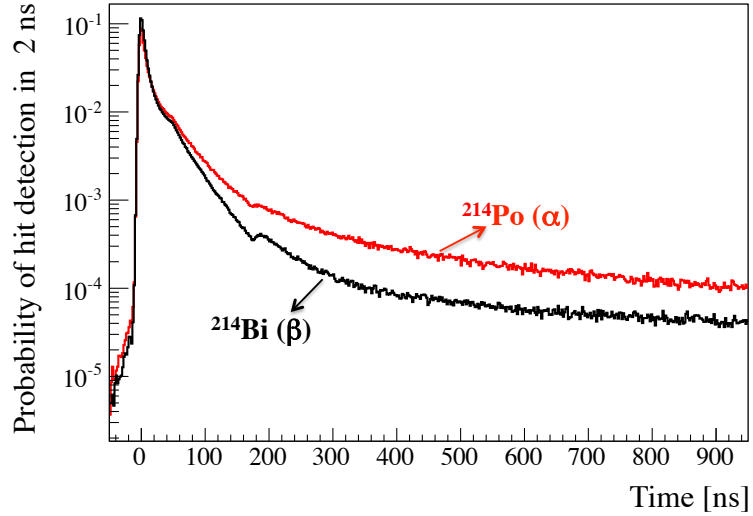


**Fig. 4.7:** Hit time distributions for alphas ( $^{214}\text{Po}$ ) and betas ( $^{214}\text{Bi}$ ) selected through their fast coincidence. Picture from Ref. [214].

The shapes of the time distributions for  $\alpha$ 's and  $\beta$ 's are so different, that some very basic variables could be used quite efficiently as pulse shape discriminator. For instance, as shown in the left panel of Fig. 4.8, the mean time of the hit times in the cluster or a “tail to total” (i.e. the fraction of hits in the tail of the time distribution with respect to the total number of hits in the cluster) are already performing quite well. Nonetheless, an effective  $\alpha/\beta$  discrimination is not so trivial as it might appear. First of all, a crucial point is the selection of the  $\alpha$  and  $\beta$  samples to be used as a reference for the pulse shape. In the case of  $\alpha$ 's and  $\beta$ 's, the  $^{214}\text{Bi}$ - $^{214}\text{Po}$  fast coincidences which are present inside the detector during calibrations and especially purification/water extraction campaigns can be used. As mentioned in Sec. 4.3, spikes in the  $^{214}\text{Bi}$ - $^{214}\text{Po}$  count rate are associated to the introduction of  $^{222}\text{Rn}$  inside the liquid scintillator during operations. Thus, the rate of  $^{214}\text{Bi}$ - $^{214}\text{Po}$  events is strictly correlated with the  $^{222}\text{Rn}$  half life of 3.8 days. Since during purification cycles the scintillator is introduced from the top of the detector and it is taken out from the bottom, the  $^{222}\text{Rn}$  potentially diffusing in the liquid must come from the top. The right panel of Fig. 4.8 shows the  $^{214}\text{Bi}$ - $^{214}\text{Po}$  position distribution in a  $x - z$  plane, thus confirming that the most of the events are in the northern hemisphere of the FV. The liquid movements and the radon diffusion in the scintillator are much slower than the  $^{222}\text{Rn}$  decay time, and thus only a low portion of the events can reach the bottom. This is a first source of systematics one has to deal with, when developing a pulse shape discrimination parameter. In fact, the detector response over the  $z$  coordinate is not uniform, mainly because of more dead PMTs at the bottom. Another source of systematics comes from the energy dependence of the pulse shape discrimination parameters. In fact, by optimizing a parameter with  $^{214}\text{Bi}$ - $^{214}\text{Po}$  coincidences<sup>8</sup>, one should expect some deviations in the discrimination power e.g. at lower energies, such as those of  $^{14}\text{C}$  and  $^{210}\text{Po}$ . More sophisticated methods which have been developed in Borexino for  $\alpha/\beta$  identification are briefly introduced below. In Borexino,  $\alpha/\beta$  discrimination is very important, mostly because of  $^{210}\text{Po}$ , which lies in the middle of the  $^7\text{Be} \nu$  spectral shape.

#### 4.7.1 The Gatti parameter

The Gatti optimal filter [221, 222] is a linear discrimination technique, which allows to separate two classes of events with different time shapes. The two normalized references of the decoded hit time distributions,  $P_\alpha(t)$  and  $P_\beta(t)$ , are obtained by averaging on the totality of the clusters selected in the  $^{214}\text{Bi}$ - $^{214}\text{Po}$  coincidence sample.  $P_\alpha(t)$  and  $P_\beta(t)$  are the probabilities that a photoelectron is detected at the time between  $t$  and  $t + dt$  for  $\alpha$  and  $\beta$  events, respectively. In reality, since it comes from experimental data,  $P_{\alpha/\beta}(t)$  is a binned function, whose time dependence could be described by the discrete variable  $t_n$ , where  $n$  is the bin number. If  $f(t_n)$  is the measured binned time distribution for a

---

<sup>8</sup>This is anyway the best strategy which could be adopted with Borexino data.

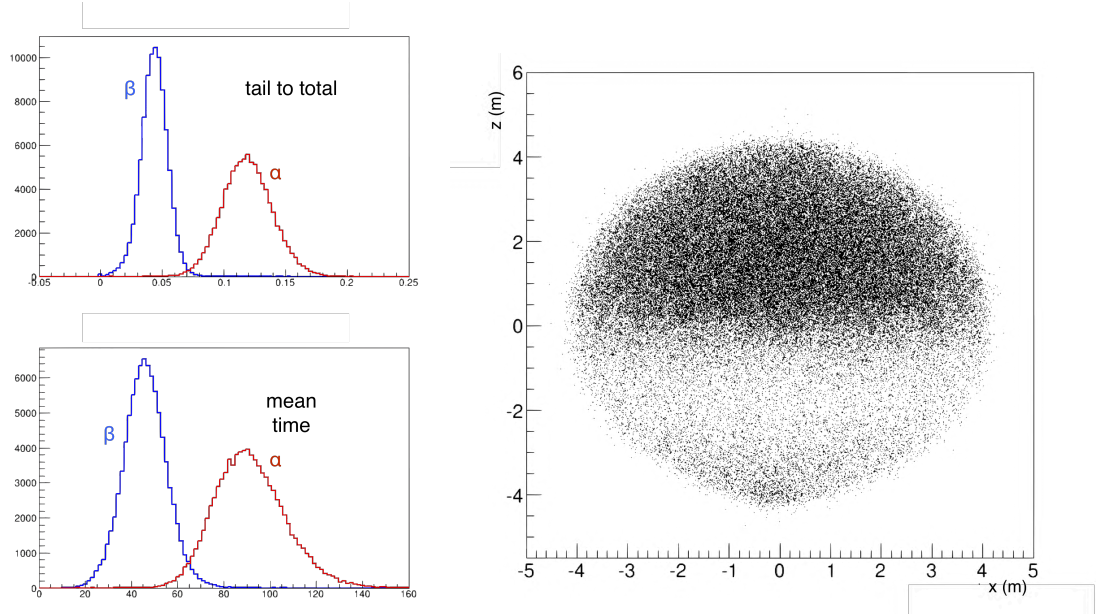


**Fig. 4.8:** *Left panel:* Plots of a tail to total parameter and the hit mean time in the cluster for  $\beta$ 's (blue) and  $\alpha$ 's (red). *Right panel:* Distribution in the  $x - z$  plane of the position of the  $^{214}\text{Bi}$ - $^{214}\text{Po}$  coincidences identified during the scintillator purification campaign and used as references for the development of the pulse shape.

generic event, then the Gatti parameter  $G$  is defined as [214]

$$G = \sum_n f(t_n) w(t_n) \quad \text{where} \quad w(t_n) \equiv \frac{P_\alpha(t_n) - P_\beta(t_n)}{P_\alpha(t_n) + P_\beta(t_n)}. \quad (4.9)$$

The large separation between the  $G_\alpha$  and  $G_\beta$  distributions, which are shown in the left panel of Fig. 4.9, is due to different weight of the delayed scintillation light for  $\alpha$  and  $\beta$  particles, which is clearly visible in Fig. 4.7. The variance of  $G_{\alpha/\beta}$  depends on the energy and it slightly increases as the energy decreases, thus reducing the discrimination power. This fact can be taken into account in order not to bias the analysis, but it is anyway a source of systematics. The Gatti parameter was used for the Borexino Phase-I analysis, as reported in Ref. [214].

Within the same procedure described above, it is possible to develop an optimal Gatti filter to try to discriminate positrons from electrons. More details on this topic are discussed in Sec. 4.8, both as regards the differences in event topology, time distributions and reference samples selection. However, the hit time distributions of positrons produced in the scintillator is quite similar to that of electrons. Moreover, the actual differences take place in a short time at the beginning of the scintillation pulse. For these reasons, in this case the Gatti parameter is not a very efficient discrimination variable, as shown in the right panel of Fig. 4.9.

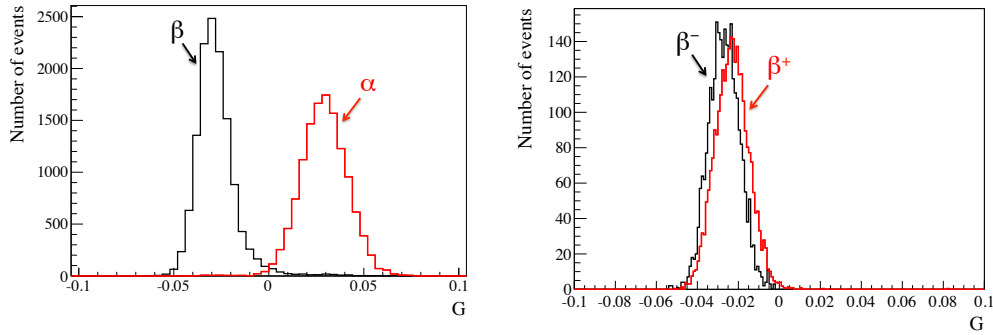


**Fig. 4.9:** *Left panel:* Gatti parameter distributions for  $\alpha$  and  $\beta$  events, built according to Eq. (4.9) with the reference sample selected by the search of  $^{214}\text{Bi}$ - $^{214}\text{Po}$  coincidences. Picture from Ref. [214]. *Right panel:* Gatti parameter distributions developed for  $\beta^+/\beta^-$  discrimination. In this case, the approach is not very powerful. Picture from Ref. [214].

#### 4.7.2 MLP discrimination variable

A novel very efficient approach has been developed recently for improving  $\alpha/\beta$  discrimination. This method is non linear, and it is based on the training of a neural network. The machine learning algorithms are part of the ROOT CERN libraries in the “TMVA” package. The algorithm selected for Borexino is the Multi Layer Perceptron (MLP) which was developed for supervised learning of binary classifiers, i. e. functions that can decide whether an input (represented by a vector of numbers) belongs to one class or another. One of the advantages of this approach is that it is possible to input to the neural network many variables, such as different tail to totals, mean time of the hits in the cluster, kurtosis, variance, skewness and so on. The neural network is then trained on two different reference samples (again those coming from  $^{214}\text{Bi}$ - $^{214}\text{Po}$  coincidences). The two different classes of events are processed on the basis of the potential discrimination variables selected by the user. The output of the MLP is the automatic definition of an algorithm which computes one single value which can be used for the pulse shape discrimination similarly to the Gatti variable. This value is usually called “MLP variable”. The discrimination power provided by the MLP variable is much better than that of the Gatti parameter and it is shown in Fig. 4.10 (compare with the left panel of Fig. 4.9).

Since the method is so powerful, one must be very careful regarding systematics. First of all, the training sample must be completely independent with respect to the events on which the variable is then computed and it must be as large as possible, in order to improve the discrimination parameter. Care must anyway be adopted: the sample cannot contain too high statistics, otherwise the neural network could become overtrained, i. e. the model could start memorizing the training data rather than learning how to generalize their features. Furthermore, the energy dependence of the shape variables used to train the neural network can be important in determining the energy dependence of the MLP parameter. For example, since the  $^{214}\text{Bi}$ - $^{214}\text{Po}$  events used for training are more energetic than the  $^{210}\text{Po}$  events for which the discriminator is developed, a slight

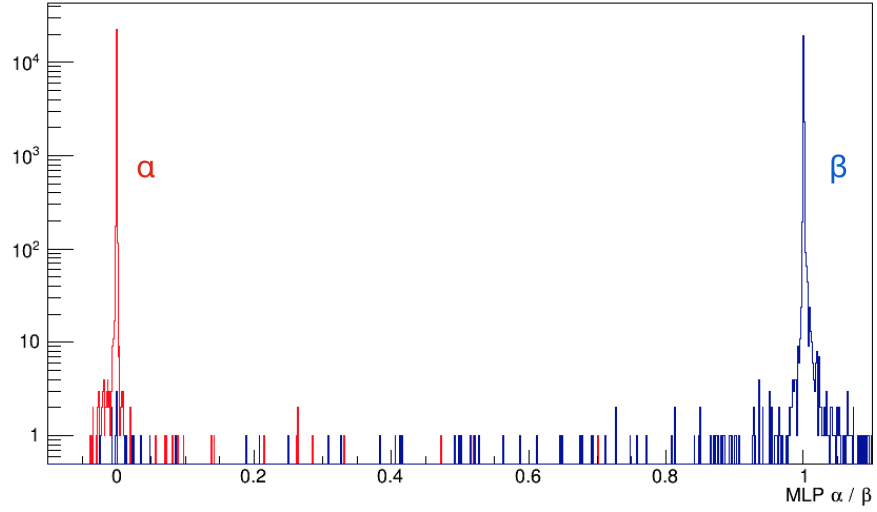


**Fig. 4.10:**  $\alpha/\beta$  separation achieved with the training of the MLP neural network.

energy dependence inefficiency of the MLP should be expected. This can be studied e. g. with comparison with Monte Carlo simulations. Another effect which could cause the algorithm to modify its response is the PMT loss throughout the detector history. In fact, this causes a loss in the efficiency which can be modeled with the Monte Carlo quite well and is almost proportional to the number of dead PMTs.

The above considerations show that the MLP variable is very powerful, and for sure better than the Gatti parameter. Anyway, dedicated tests and studies must be performed in order to assess all the systematics of the method. In principle, given the <sup>210</sup>Po contamination in Borexino Phase-II and the performance shown in Fig. 4.10, the MLP variable could provide an almost  $\alpha$  free spectrum.

## 4.8 $\beta^+/\beta^-$ discrimination

The scintillation time response produced by positrons is different compared to that generated by electrons. The most important source of positrons in the Borexino detector is the cosmogenic <sup>11</sup>C, which is a crucial background for the detection of pep  $\nu$ . Before annihilating in two back-to-back  $\gamma$ 's, the positron loses its energy in the medium and, when at rest, it forms a bound state with an electron in the scintillator, the “positronium”. This state might be formed in the spin singlet state (para-positronium), or in the spin triplet state (ortho-positronium). The para-positronium is a very short lived state, with a mean life of 125 ps in the vacuum, while ortho-positronium has a mean life of 140 ns. The relative probability of para/ortho-positronium formation could be easily computed in the vacuum, counting the available spin combinations for the couple of particles. However, in the scintillator, both the probability formation of the two states and their life times are modified by the interaction of the particles with the medium, through processes

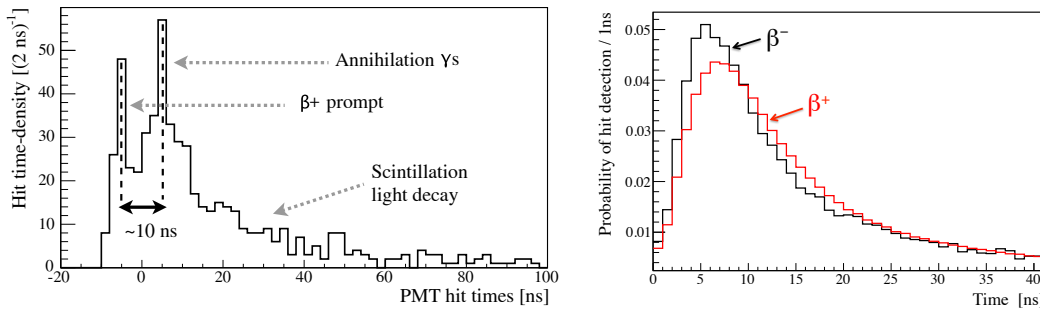


**Fig. 4.11:** *Left panel:* Example of hit time distribution for an ortho-positronium event in the scintillator. Picture from Ref. [214]. *Right panel:* Comparison between the hit time distributions of electrons and positrons with respect to the start of the cluster. Picture from Ref. [214].

such as spin-flip, or pick-off annihilation on collision with an anti-parallel spin bulk electron. Therefore, these parameters must be determined experimentally. Dedicated measurements for Borexino’s scintillator found out that the ortho-positronium formation probability is around 53%, and its life time is around 3.1 ns [223]. The para-positronium life time is *zero* with a very high accuracy, if compared to the ns time scale of scintillation processes.

The delay introduced in the case of the ortho-positronium formation is comparable to the fastest scintillation component of the scintillation pulse (around 4 ns, see Sec. 5.8.3), and for this reason it is expected to introduce a measurable distortion in the time distribution of hit PMTs with respect to pure  $\beta$  events. Additional distortions are expected from the diffuse topology of this kind of event which has a sort of prompt component (the positron energy loss) and possibly a delayed and disperse energy release due to the annihilation gammas.

The left panel of Fig. 4.11 shows an event where there is a clear time separation between the energy deposit by the positron and that of the two annihilation gammas. Only  $\sim 1\%$  of ortho-positronium events have a so evident time separation, since generally, it is small enough that only a broadening of the primary time distribution is observed.

The right panel of Fig. 4.11 shows the average over many events of the distribution of decoded hits for electron events (selected from the  $^{214}\text{Bi}$ - $^{214}\text{Po}$  sample) and positron candidates selected with the Three Fold Coincidence (TFC) algorithm described in Sec. 6.3. The TFC algorithm vetoes space-time regions of the detector after muon plus neutron coincidences in order to exclude the subsequent  $^{11}\text{C}$  decays. By selecting these vetoed regions, it is possible to construct a sample of positron events uniformly distributed both in space and in time during the detector data taking. The delay and broadening of the peak in the average time distribution of positron events due to the ortho-positronium formation is evident.

During Borexino Phase-I analysis, a discrimination parameter based on the neural network algorithm of the Boosted Decision Tree (BDT) was developed. Many variables were inputed to the neural network, such as the Gatti parameters both for  $\alpha/\beta$  and

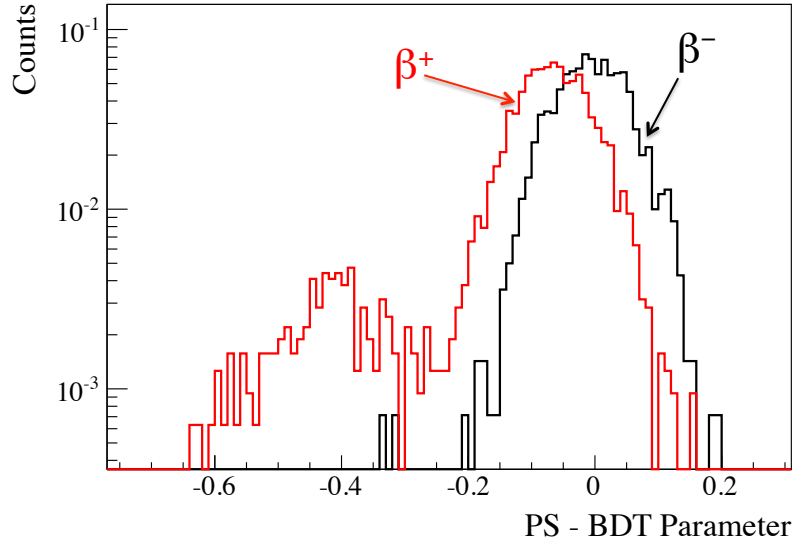


**Fig. 4.12:** BDT pulse shape discrimination parameter power, after the training for Borexino data. Picture from Ref. [214].

$\beta^+/\beta^-$  (see Sec. 4.7.1), the mean, variance, skewness and kurtosis of the emission time distribution, various tail to totals and many others. The result on the separation capability is shown in Fig. 4.12. The presence of the second peak in the positron distribution of the BDT is due to the long-lived ortho-positronium events. On average, the positron events have a BDT which is slightly shifted with respect to that of electrons, mainly because the non punctual energy deposits of the annihilation gammas slightly modify the time and event shape variables.

The BDT algorithm was used successfully during Phase-I analysis, but it has some drawbacks. Within the analysis which led to the first evidence of pep  $\nu$  [224], the statistics and the choice of the training samples needed to develop the BDT were one of the most important limiting factors. In addition to this, the BDT shares some of the critical points already discussed for the MLP in Sec. 4.7.2, such as a quite pronounced energy dependence or the risk of over training. For this reason, within the Phase-II analysis which is one of the goal of this PhD thesis, the attention was focused on another variable much simpler than the BDT and which can provide a even better discrimination, i. e. the value at the end of the maximization of the likelihood of the position reconstruction  $\mathcal{L}_{pos}$  presented in Sec. 4.6. This is discussed more extensively in Sec. 6.6.2.

## 4.9 Thermal stability, $^{210}\text{Po}$ evolution and $^{210}\text{Bi}$ constraint

One of the most critical backgrounds for the experimental detection of CNO  $\nu$  is radioactive  $^{210}\text{Bi}$  dissolved in the liquid scintillator. Because of the almost degenerate spectra of CNO  $\nu$  and  $^{210}\text{Bi}$  (see Fig. 4.3), the only way to disentangle the two components

is to independently tag the  $^{210}\text{Bi}$ . A possible method has been considered since the time of the Borexino prototype CTF, and it is discussed e.g. in Ref. [225].  $^{210}\text{Bi}$  is the parent of  $^{210}\text{Po}$  and both belong to the  $^{238}\text{U}$  radioactive chain. Under some assumptions, by tagging  $^{210}\text{Po}$  events thanks to the pulse shape discrimination (see Sec. 4.7), it might be possible to infer the  $^{210}\text{Bi}$  rate in the scintillator independently from the spectral fit. In fact, one could expect that  $^{210}\text{Bi}$  and  $^{210}\text{Po}$  are decaying in secular equilibrium within the  $^{238}\text{U}$  chain. This would simply mean that the rate of  $^{210}\text{Bi}$  decays is equal to the rate of those of  $^{210}\text{Po}$  (which are tagged with the pulse shape discrimination). However, this is not the case in Borexino, where the observed  $^{210}\text{Po}$  rate is much higher than that of  $^{210}\text{Bi}$  [214]. The high rate of  $^{210}\text{Po}$ , out of equilibrium with the rest of the  $^{238}\text{U}$  chain, may be due to  $^{210}\text{Po}$  coming from the surfaces of the scintillator storage tanks and pipes. Following the arguments of Ref. [225], the activities of  $^{210}\text{Po}$  and  $^{210}\text{Bi}$  in the scintillator, namely  $a_{\text{Po}}$  and  $a_{\text{Bi}}$ , can be related by:

$$a_{\text{Po}}(t) = a_{\text{Po},0} e^{-t/\tau_{\text{Po}}} + \langle a_{\text{Bi}}(t) + S_{\text{Po}}(t) \rangle, \quad (4.10)$$

where  $a_{\text{Po},0}$  is the polonium activity at the beginning of the data taking,  $\tau_{\text{Po}}$  is the  $^{210}\text{Po}$  mean life,  $S_{\text{Po}}(t)$  is an external source of  $^{210}\text{Po}$  and the angle brackets indicate a sort of time average, which, for a generic function  $f(x)$  would be defined as the following convolution:

$$\langle f(t) \rangle = \frac{1}{\tau_{\text{Po}}} \int_0^t f(t-t') e^{-t'/\tau_{\text{Po}}}. \quad (4.11)$$

In the assumption of an absolutely stable detector, where there are no motions in the liquid and the diffusion is negligible<sup>9</sup>, the source term  $S_{\text{Po}}(t)$  is zero. Therefore, in this condition, the bismuth activity could be related directly to the polonium activity, which can be easily tagged thanks to the pulse shape determination. Eq. (4.10) follows directly from the basic laws describing radioactive decays and it becomes even easier if one adds the condition that bismuth activity is constant:

$$a_{\text{Po}}(t) = (a_{\text{Po},0} - a_{\text{Bi}}) e^{-t/\tau_{\text{Po}}} + a_{\text{Bi}}. \quad (4.12)$$

This is a good approximation since  $\tau_{\text{Pb}} = 32.3$  years while  $\tau_{\text{Po}} \sim 200$  days. Of course, it assumes that  $^{210}\text{Bi}$  is in secular equilibrium, since there has been no evidence so far that this is not the case. One should expect deviations from the trend predicted by Eq. (4.12) if the data taking extends to many years, since it would not be negligible anymore with respect to  $\tau_{\text{Pb}}$ . This method makes quite a lot of assumptions which must be checked carefully, such as the absence of external polonium sources, the polonium and bismuth uniformity in the FV and the fact that  $^{210}\text{Bi}$  is in secular equilibrium with the lead, i.e. there were no other sources of bismuth in the detector other than the lead since the detector construction. Provided these assumptions, Eq. (4.12) shows that, if one can

<sup>9</sup>This is actually the case, since polonium could diffuse to the innermost FV only starting from the IV. However, the time constant for the pure diffusion through the liquid scintillator would be much bigger than  $\tau_{\text{Po}}$ , thus implying that practically polonium could not make it to the FV only through diffusion.

measure  $a_{\text{Po}}(t)$  as a function of time with a high accuracy, an independent constraint for the bismuth rate can be inputed to the spectral fit. This is essential for a potential CNO  $\nu$  detection.

#### 4.9.1 $^{210}\text{Po}$ time and space evolution

Thanks to the pulse shape discrimination methods described in Sec. 4.7, it is possible to tag with high efficiency  $^{210}\text{Po}$  events, and thus study their time and space evolution. The polonium activity inside Borexino is constantly monitored on a weekly basis. Figure 4.13 shows the  $^{210}\text{Po}$  count rate observed in the whole Borexino Phase-II after tagging the events with the MLP variable. At least in its first part, the trend shown in the plot agrees with that predicted by Eq. (4.12). Then, mixing of the scintillator takes place. These events can be correlated almost perfectly with sudden temperature variations in the Hall C of the Gran Sasso National Laboratory where Borexino is located. The temperature variations could trigger convection motions able to bring polonium from the outermost shells to the fiducial volume. More in detail, the scintillator in contact with the vessel or its endcaps is moved inside, bringing in the contaminant. These motions are slow, with a time constant of months, and the only solution to prevent them is to assure a very stable temperature around the detector.

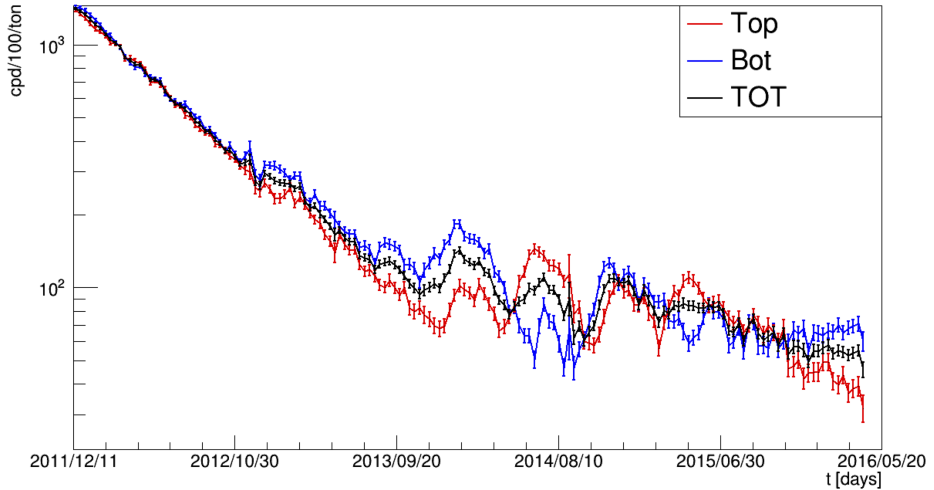


**Fig. 4.13:**  $^{210}\text{Po}$  time evolution in Borexino Phase-II. The red line shows the count rate for the upper hemisphere of the FV, while the blue refers to the lower one. Besides the characteristic exponential decay of  $^{210}\text{Po}$ , features indicating mixing of the scintillator are present, since the rates in the two detector portions vary non monotonically.

#### 4.9.2 Borexino thermal insulation

The major obstacle to the  $^{210}\text{Po}$  stabilization goal is the recontamination occurring in the fiducial volume from particulate, most likely sitting on the surface of the IV and

stirred up by convection of scintillator. The only way in order to thermally decouple Borexino from the environment is to insulate it. Actually, the bottom of the Borexino detector is in contact with a heat sink, provided by the rock. Its temperature is much lower than that of the air in Hall C ( $7 \div 8^\circ\text{C}$ , to be compared to  $\sim 15^\circ\text{C}$ ) and for this reason it acts as a natural way for preventing convections, keeping a vertical temperature gradient. However, without insulation, the temperature of all the remaining external surface of the WT is highly influenced by air currents in Hall C. For these reasons, in 2015 the Borexino detector WT was covered with two layers of 10 cm thick mineral wool, as shown in Fig. 4.14. Temperature sensors were placed in contact with the WT and between the two isolation layers in order to constantly monitor the situation and study how the external temperature changes propagate inside the system.

In parallel to this activity, an active temperature control on the top of the WT was developed. In principle, if the detector is perfectly isolated apart from the bottom surface, after some time the whole system would cool down, asymptotically reaching a uniform temperature equal to that of the rock. This should be avoided, for the sake of assuring the presence of a vertical temperature gradient which can prevent convection motions. At the moment, the system has not been turned on yet, since the observed temperature variations due to the installation of the insulation are so slow, that for the next years no significant reduction of the temperature gradient is expected.



**Fig. 4.14:** Pictures of the Borexino detector water tank covered with the insulation layer, partially in the left picture, and totally in the right one.

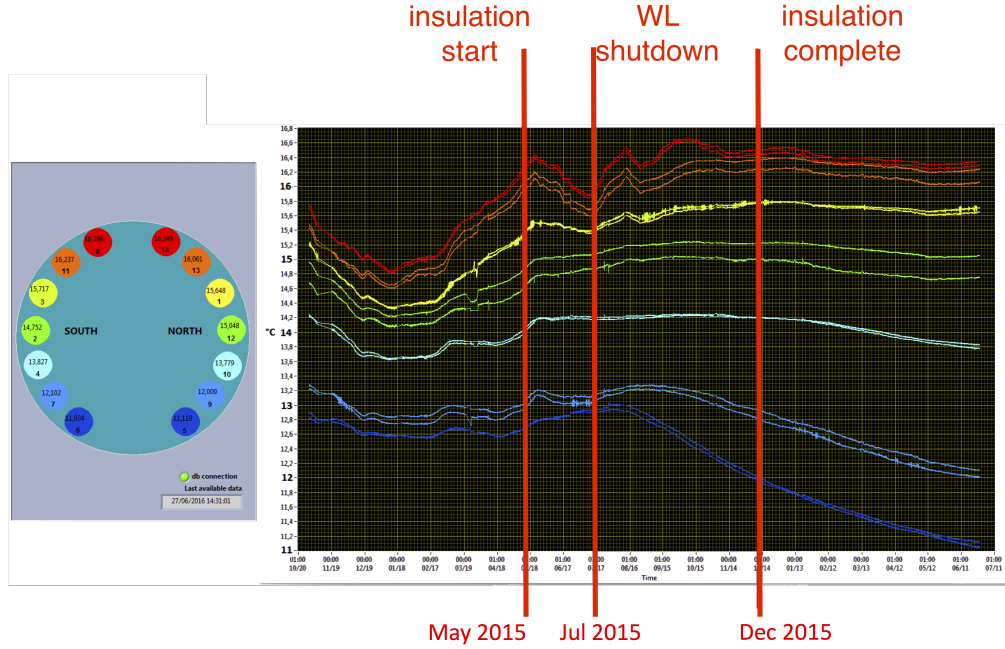


**Fig. 4.15:** Time evolution of the temperatures measured by sensors placed in the Borexino outer buffer. On the left, a scheme of the positions of the sensors is shown. Particularly, two sets of sensors are placed from the bottom to the top of the sphere (color scale), one set being on the north side of the detector and the other one on the south one. For a more detailed description of the events marked by the red vertical lines, refer to the text.

The time evolution of the temperatures measured by many sensors all around Borexino is shown in Fig. 4.15. These sensors are placed inside the outer buffer and they are divided in two groups: one of them lays on the northern side of the detector (geographically) and the other one on the southern. Each group contains sensors from the bottom to the top of the sphere. The leftmost scheme in Fig. 4.15 provides the color legend for the different sensor positions. Three major events are marked by the vertical red lines. The first one refers to the date in which the insulation work started. It is clearly visible how, prior to the presence of the insulation, all the temperatures were quite unstable. The second vertical line corresponds to the water loop (WL) shut down. In standard Borexino operations, the water in the WT was kept recirculating by the WL. This system released some heat in the water. In order to prevent an increase of the detector temperature in the bottom after the insulation installation, the WL was shut down, in order to avoid the risk of triggering convection motions by a sudden increase of the temperature at the base of the detector. As shown in the plot, after the WL shutdown, the temperatures of the sensors located closer to the bottom suddenly drop. This is supposed not to be a problem, since this trend increases the top-bottom temperature gradient, assuring thermal stability. The last red vertical line indicates the end of the insulation operations, and after this point, the successful stabilization of the temperature inside the detector is particularly evident (apart from the effects induced by the shutdown of the WL).

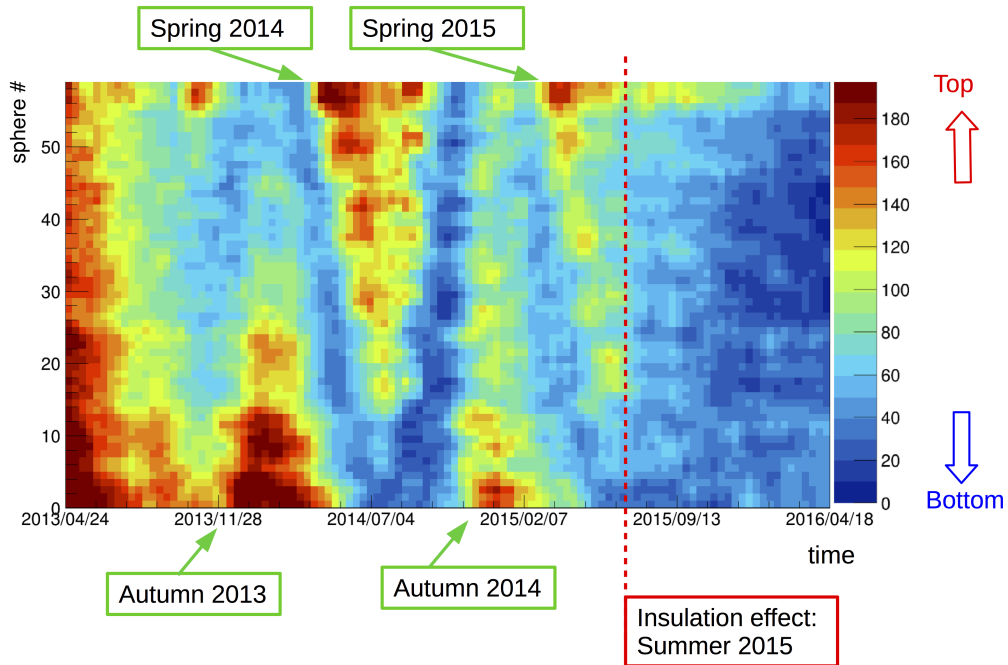


**Fig. 4.16:**  $^{210}\text{Po}$  count rate in the 59 spheres considered in the analysis in the last 3 years of Borexino. The sphere numbers go from 0 to 58, 0 being at the bottom and 58 at the top. The color scale refers to the cpd/100 ton of  $^{210}\text{Po}$  observed in each cube. The time binning is 10 days. The main seasonal variations together with the time in which the insulation was installed are also highlighted.

In order to better understand the detector behavior and possibly predict the future happenings, a thermal simulation of the system is being developed. The simulation is performed with the FLUENT software [226] and the system geometry and boundary conditions make it particularly hard. The early stages of the work included simplified steps, which could be easily understood, in order to validate the simulation, such as convection only scenarios or simplified geometries. The goal is to be able to “predict” the past  $^{210}\text{Po}$  movements in the scintillator (it can actually be used as a tracker of the scintillator motion), thus validating the simulation. Once this is achieved, the future detector behavior might possibly be predicted and the active temperature control could be manually managed in a controlled way.

#### 4.9.3 $^{210}\text{Po}$ distribution in Borexino

In order to study the  $^{210}\text{Po}$  spatial distribution in Borexino as a function of time on a weekly basis, the innermost FV (in this case a sphere of 3 m radius) is studied considering 59 smaller spheres of  $1.5 \text{ m}^3$  each, whose centers are placed so that they span almost the entire FV. Interestingly enough, since in the first stages of the analysis the 59 spheres were actually cubes with 1.5 m sides, inside the Borexino collaboration the 59

spheres might actually be referred to as 59 “cubes”. The spheres cover the 3 m FV being arranged on 6 layers and overlap with each other, since it is not possible to entirely cover the volume of a sphere with separated spheres. The numbers of the spheres increase from the bottom to the top, 0 corresponding to the extreme bottom and 58 to the extreme top. The reason for which the analysis has to be performed in such big volumes is the statistics. Fortunately, in fact, the  $^{210}\text{Po}$  contamination in Borexino is so low that smaller volumes would not collect enough statistics in one week in order to perform the analysis. The weekly basis was chosen in order to correlate possible  $^{210}\text{Po}$  variations to those of the IV shape, although no correlations of this kind have been observed yet.

$^{210}\text{Po}$  events are selected thanks to the MLP variable and in order to assure a reliable estimation of the rate, corrections for the MLP inefficiency and time variations along the Borexino data taking are considered.

Figure 4.16 shows the count rate of  $^{210}\text{Po}$  in the spheres as a function of time, from 2013 to 2016. The motion of the liquid scintillator is evident and it is well tracked by the polonium. Particularly, during the winter  $^{210}\text{Po}$  is brought in the FV from the bottom, while in the summer it falls down from the top. Anyhow, the convective motions and the  $^{210}\text{Po}$  net flux from the outer shells towards the FV observed before the summer 2015 made it completely impossible to establish  $^{210}\text{Bi}$  through the  $^{210}\text{Po}$  tagging. However, Fig. 4.16 shows unambiguously that the insulation, besides stabilizing the temperatures (see Sec. 4.9.2), worked very effectively in reducing the convective motions inside the scintillator. After the completion of the insulation installation, in fact, the  $^{210}\text{Po}$  distribution looks almost uniform. This seems very promising in order to try to extract a  $^{210}\text{Bi}$  constraint through Eq. (4.12) in the near future.

## 4.10 Borexino Phase-I results

Using Borexino Phase-I data, many important measurements have already been achieved. Results regard naturally the measurements of solar neutrino fluxes, but not only. In this section, a brief overview on these results is presented.

### 4.10.1 $^7\text{Be} \nu$

The measurement of the flux of  $^7\text{Be} \nu$  was the primary goal for Borexino. The first observation was published in the summer of 2007, after only 3 months of data taking [227]. A subsequent refinement of the first measurement is reported in Ref. [228]. The signal of  $^7\text{Be}$  solar neutrinos is extracted from the data through a fit of the energy spectrum of the events collected in the FV. The main backgrounds are due to the radioactive decay of the isotopes  $^{85}\text{Kr}$ ,  $^{210}\text{Po}$  and  $^{210}\text{Bi}$ , but their contributions can be disentangled very efficiently through the spectral fit.

The rate of the neutrino-electron elastic scattering interactions from 862 keV  $^7\text{Be} \nu$  solar neutrinos in Borexino resulted of  $46.0 \pm 1.5 \text{ (stat.)} \pm 1.5 \text{ (sys.) cpd/100 ton}$  [229]. This corresponds to a  $\nu_e$ -equivalent  $^7\text{Be} \nu$  flux of  $(3.10 \pm 0.15) \times 10^9 \text{ cm}^{-2}\text{s}^{-1}$  and, under the assumption of  $\nu_e$  transition to other active neutrino flavors, yields an electron neutrino

survival probability of  $0.51 \pm 0.07$  at 862 keV. The no flavor change hypothesis is ruled out at  $5.0\sigma$ , assuming the prediction on the unoscillated flux by the Solar Standard Model. Borexino also investigated the potential day-night asymmetry in the  ${}^7\text{Be}$  solar neutrino interaction rate. The measured asymmetry is  $0.001 \pm 0.012$  (stat.)  $\pm 0.007$  (sys.) [230], in agreement with the prediction of the MSW-LMA solution for neutrino oscillations.

#### 4.10.2 pep $\nu$ and CNO $\nu$

Thanks to the development of novel data analysis techniques for the rejection of cosmogenic  ${}^{11}\text{C}$  and of external gammas (the main backgrounds in the  $1 \div 1.5$  MeV region), a first evidence of pep solar neutrinos could be obtained. Particularly, the TFC vetoing method [219] for the  ${}^{11}\text{C}$  suppression discussed in Sec. 6.3 was developed. In addition, the BDT variable (see Sec. 4.8) allowed a further discrimination of the remaining positrons against the electron recoils. The spectral fit was then performed with a multivariate approach, fitting simultaneously the energy spectrum, the BDT pulse shape discrimination variable and the radial distribution of the events, in order to decouple the uniformly distributed neutrino-like events from the external gammas.

The interaction rate of pep neutrinos in Borexino is  $3.1 \pm 0.6$  (stat.)  $\pm 0.3$  (sys.) cpd/100 ton [224]. The absence of the solar neutrino signal is disfavored at 99.97% C.L., while the absence of the pep signal is disfavored at 98% C.L. . The strongest constraint on the CNO  $\nu$  interaction rate ( $< 7.9$  cpd/100 ton, at 95% C.L. [224]) could also be obtained.

#### 4.10.3 pp $\nu$

Being the keystone of the pp-chain, the measurement of the pp  $\nu$  flux is a major experimental milestone in solar neutrino physics, and paves the way to a deeper understanding of the Sun dynamics. Low energy pp  $\nu$  were observed in the past by radiochemical experiments. However, Borexino could perform the first real-time detection of pp  $\nu$  with good accuracy. The measurement was made possible by the very low radioactive backgrounds, particularly in  ${}^{85}\text{Kr}$ , achieved after an extensive purification campaign performed in 2010-2011. Furthermore, the rate of one of the most important backgrounds, i. e.  ${}^{14}\text{C}$ , was estimated independently and constrained in the fit. The other crucial aspect in order to perform the measurement was the understanding of the event pileup in the low energy part of the spectrum. Particularly, the pileup component was determined using an independent, data-driven method: real triggered events with no cuts are artificially overlapped with random data obtained from the ends of real trigger windows, uncorrelated with the triggering event. The synthetic events are then reconstructed with the same software used for real events, and selected with the same criteria. Using this method, it is possible to obtain the true rate and spectral shape of pileup in the detector.

The pp  $\nu$  interaction rate measured by Borexino is  $144 \pm 13$  (stat.)  $\pm 10$  (sys.) cpd/100 ton [218]. The absence of pp  $\nu$  is excluded with a statistical significance of  $10\sigma$ . Assuming the MSW-LMA model of solar neutrino oscillations, the resulting pp  $\nu$  flux is  $(6.6 \pm 0.7) \times 10^{10} \text{ cm}^{-2}\text{s}^{-1}$ , in agreement with the SSM prediction.

#### 4.10.4 ${}^8\text{B} \nu$

Borexino could measure for the first time  ${}^8\text{B}$  solar neutrinos with an energy threshold of only 3 MeV. The rate of  ${}^8\text{B} \nu$ -induced electron scattering events above this energy in Borexino is  $0.217 \pm 0.038$  (stat.)  $\pm 0.008$  (sys.) cpd/100 ton [200], which corresponds to a total solar neutrino flux of  $(2.4 \pm 0.4) \times 10^6 \text{ cm}^{-2}\text{s}^{-1}$  in the assumption of the MSW-LMA model, in good agreement with the measurements from SNO and SuperKamiokaNDE.

#### 4.10.5 Geo-neutrinos

Borexino could perform the first observation at more than  $3\sigma$  C.L. of geo-neutrinos [231]. These anti-neutrinos are detected effectively and quite unambiguously through the IBD process (see Sec. 4.1). The measurement was subsequently refined in Ref. [232], and finalized in Ref. [233] where an improved result from 2056 days of data taking is presented. The total exposure is of  $(5.5 \pm 0.3) \times 10^{31} \times \text{proton} \times \text{yr}$ . The non-null observation of geo-neutrinos with Borexino alone has a significance of  $5.9\sigma$  C.L. . In addition, a geo-neutrino signal from the mantle is obtained at 98% C.L., also restricting the radiogenic heat production for U and Th to the range  $23 \div 36$  TW.

#### 4.10.6 Other Borexino measurements

Borexino is a large ultra-pure calorimeter and, apart from solar and geo neutrinos, could investigate many other rare processes. Other results include the study of solar and other unknown anti-neutrino fluxes [234], a measurement of neutrino velocity [235], a characterization of the muon flux at the Gran Sasso National Laboratory depth [236], limits on Pauli-forbidden transitions in  ${}^{12}\text{C}$  nuclei [237], searches for solar axions [238], experimental limits on heavy neutrinos [239] and a test of the electric charge conservation and electron decay [240].

### 4.11 Outlook and Phase-II goals

The high impact of Borexino Phase-I on neutrino physics is very well summarized by Fig. 4.17, where the survival probability of solar neutrinos is plotted as a function of the neutrino energy. For all the solar neutrino components that Borexino measured, the trend is in good agreement with the MSW-LMA prediction. Nonetheless, improvements on all such measurements are possible within Borexino Phase-II data analysis, both thanks to the reduction of the internal contaminations due to the purification campaign which took place between Phase-I and Phase-II, and also thanks to improved data analysis techniques and a better detector understanding. One of the main goals of Borexino Phase-II, the detection of CNO  $\nu$ , is anyhow difficult and depends on the detector evolution and its stabilization, in order to reliably assess independently the  ${}^{210}\text{Bi}$  rate and constrain it in the fit. Therefore, this target is not addressed extensively in this PhD thesis. Besides the potential CNO  $\nu$  detection, an improvement of the precision on all the other solar neutrino flux measurements would be really important. Particularly, the goal of a 3%

measurement of the  ${}^7\text{Be} \nu$  flux could be crucial for a further evolution of SSMs, since the theoretical prediction has a higher uncertainty (see Tab. 4.1). In addition, another goal is to reach an evidence on the pep  $\nu$  interaction rate with a significance greater than  $3\sigma$ . The increased statistics and improved analysis techniques should lead to substantial progresses in the precision of the determination of pp  $\nu$  and  ${}^8\text{B} \nu$  as well.

The most important goal of the Borexino Phase-II analysis consists in measuring the solar neutrino fluxes (excluding the  ${}^8\text{B} \nu$ , which, because of the higher energy and lower flux, needs a separate analysis) in a *global analysis fit*. In fact, all the Borexino Phase-I results on the fluxes presented in Sec. 4.10 were obtained with dedicated analysis and fits. Thanks to the improved detector response understanding, it was possible to develop a Phase-II global analysis, where pp  $\nu$ ,  ${}^7\text{Be} \nu$  and pep  $\nu$  are fitted simultaneously. Ultimately, this is the goal of this PhD thesis. This effort is described in chapter 6 and it relies on a substantial upgrade of the Borexino Monte Carlo simulation which is presented in chapter 5.

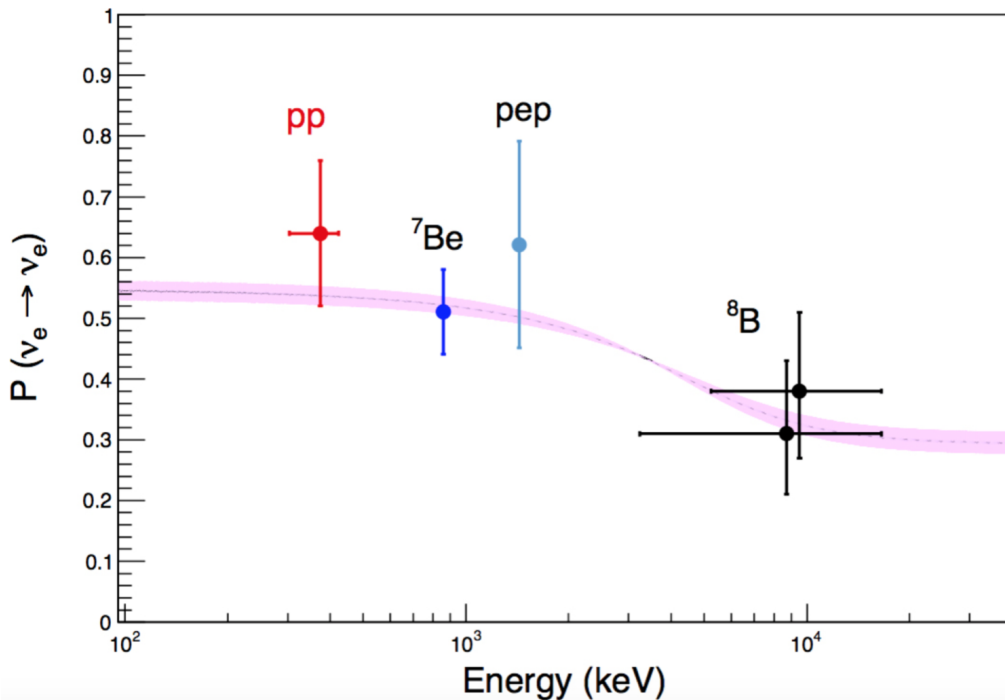


**Fig. 4.17:** Survival probability of electron neutrinos produced by the different nuclear reactions in the Sun averaged over their energy spectra.. All the experimental numbers are from Borexino's measurements. The violet band corresponds to the  $\pm 1\sigma$  prediction of the MSW-LMA solution.

## 4.12 Borexino (near) future: the SOX project

The standard three-flavor neutrino oscillation paradigm has been established since long, as discussed in Sec. 1.1. However, some long standing anomalies in datasets of

different origins (those from accelerator experiments like LSND and MiniBoone [241, 242], those from reactor experiments [243, 244] and those from the gallium solar neutrino experiments [245] like Gallex and SAGE already presented in Sec. 1.9) led to the hypothesis of the existence of at least one additional sterile neutrino state. In fact, the reactor and gallium anomalies may be explained by oscillations into one or more sterile components. However, regardless of the possible theoretical interpretations, the existence of these anomalies is an experimental problem that must be investigated by better and more sensitive experiments. In Ref. [246], a comprehensive program to be carried out with the Borexino experiment facility and named “Short distance neutrino Oscillations with BoreXino” (SOX) is discussed. In practice, a very intense  $\bar{\nu}_e$  source placed at the bottom of the Borexino detector could allow for a precision measurement of the anti-neutrino interaction rate, thus either proving the existence of new physics or excluding the anomaly.

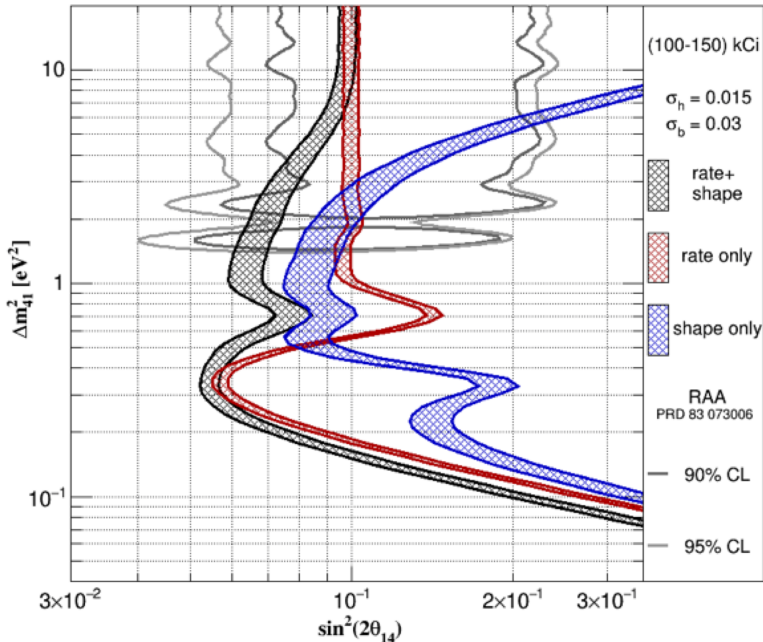


**Fig. 4.18:** Projected sensitivity of Ce-SOX in the case of rate-only analysis (red band), shape-only analysis (blue band) and combined analysis (black band). The widening of the bands corresponds to values of the initial source activity in the range  $100 \div 150$  kCi. The regions of the anomalies (RAA) are depicted with grey lines with different darkness according to the different C.L. of significance.  $\sigma_h$  is the supposed percentage accuracy on the heat measurement, while  $\sigma_b$  is the error on the  $^{144}\text{Pr}$  shape factor, which describes the emitted anti-neutrino energy spectrum.

The SOX experiment foresees the deployment of a  $^{144}\text{Ce}-^{144}\text{Pr}^{10} \bar{\nu}_e$  with a  $\sim 150$  kCi activity at the bottom of Borexino, at a distance of 8.25 m from the detector center. The current schedule predicts the start of the data taking at the beginning of 2018. Right

<sup>10</sup>For this reason, usually the project is also referred to as “Ce-SOX”.

beneath the Borexino detector, there is a cubical pit that was built at the time of the experiment construction with the purpose of housing possible neutrino sources. The existence of this tunnel is one of the reasons why the SOX experiment can be done with no changes to the Borexino layout. Furthermore, since the  $^{144}\text{Ce}$ - $^{144}\text{Pr}$  source produces  $\bar{\nu}_e$ , the detection in Borexino has a very high efficiency through the IDB tagging and is background free. In fact, the total number of anti-neutrino interactions predicted for the SOX experiment is of the order of  $10^4$  in a couple of years, which should be compared to the background coming from geo-neutrinos (a few tens per year), which is negligible, even if it represents the highest one.

The key points assuring a very high sensitivity to the SOX project are the Borexino experiment itself, which is very sensitive to neutrinos and anti-neutrinos and background free, and a very accurate determination of the source activity, and thus of the anti-neutrino flux produced. The activity measurement is performed through a calorimetric technique, which has demonstrated to reach a precision better than 1% [247]. This goal is obtained thanks to the careful design of a vacuum calorimeter and the precisely known radioactive contaminations present inside the cerium source. The calorimetric measurement allows to perform a rate-only analysis, in which the number of anti-neutrino interactions induced in Borexino by the source is compared to the predicted one. However, Borexino can measure the event position with quite good precision (see Sec. 4.6) and thus, if oscillations to sterile states on the  $\sim \text{m}$  length scale occur, it might be possible to observe “wiggles” in the spatial density of anti-neutrino interactions, proving the existence of new physics without any assumption on the source activity. This method is called usually “shape analysis”. Of course, the best sensitivity is obtained when the rate and the shape analyses are combined. Figure 4.18 shows the projected sensitivity for the Ce-SOX experiment in the case of rate-only analysis, shape-only analysis and combination of the two. The region of the anomalies is almost completely covered thanks to the very high accuracy of the experiment.



## Chapter 5

# The Borexino full Monte Carlo simulation

A solid determination of solar neutrino interaction rates was achieved in the past both through an analytical modeling of the detector response and a detailed Monte Carlo (MC) simulation of the detector, which allowed to extract the fluxes through a spectral fit. Particularly, Monte Carlo simulation comparisons with data allow to understand to a greater extent the features, the physics and the evolution of Borexino's response. The data analysis is of course strengthened by the co-existence of the analytical and the Monte Carlo methods, but a precision solar neutrino flux measurement, and a full understanding of the detector in the whole energy range ( $\sim 200 \text{ keV} \div 3 \text{ MeV}$ ) and for the whole data set ( $\sim 5\text{-year-long}$ ), requires an accurate simulation, which is able to describe non uniformities, time dependences, detector's response over volume, trigger efficiency, spatial reconstruction of the events, time response and pulse shape variables very efficiently. This chapter contains details on how this understanding was achieved and implemented in a detailed Monte Carlo simulation which reproduces the data (with and without calibration sources) at the level of 1% or better for all quantities relevant for the analysis. The improvements implemented within the Borexino Monte Carlo simulation, which underwent a substantial revision and upgrade in 2013 in view of the Phase-II analysis, are one of the major goal of this PhD thesis and are here discussed.

The chapter is structured as follows. Section 5.1 discusses the principles of the MC simulation, Sec. 5.2 describes the geometry simulation, Sec. 5.3 illustrates the light generation mechanisms, Sec. 5.4 details the light propagation model adopted in the simulation, Sec. 5.5 shows the results on the measurements of the refractive index dependence upon the temperature, Sec. 5.6 describes the event generators, Sec. 5.7 discusses the electronics simulation, Sec. 5.8 details the tuning of the simulation procedure, Sec. 5.9 shows the strategy for  $^{210}\text{Po}$  event simulation, Sec. 5.10 describes the novel approach for external background simulation, Sec. 5.11 illustrates the pileup understanding thanks to the MC method and Sec. 5.12 discusses further developments foreseen for Borexino's MC simulation.

## 5.1 Simulation principles and structure

The accuracy of the relations between measured observables (energy estimators or PMT hit times) and physical quantities (deposited energy, position, type of particles generating the signal) depends on the knowledge and understanding of the processes governing the particle energy loss in the various materials, as well as the scintillator light production, propagation and detection. Besides, it also depends on the characteristics of the electronics and of the triggering system. Particles depositing energy in the IV or in the buffer regions produce scintillation and Čerenkov photons which propagate inside the detector and possibly reach the PMTs, yielding a detectable signal. The Borexino MC simulation was designed and optimized to fully model and reproduce all these processes up to the signal detection and electronics processing. Simulated events are produced in the very same format as that of real data. In this way, simulated and real data can share the same reconstruction and analysis algorithms.

The Borexino MC simulation consists of a chain of numerical codes that:

- simulate all interesting events: solar neutrino interactions, radioactive decays, geo-neutrinos, and calibration source events.
- simulate the energy loss of each specific particle in every material present in the detector, either active (the scintillator in the IV, the buffers and the water in the OD) or passive.
- generate a number of scintillation or Čerenkov photons taking into account the particle energy loss in the media and the properties of the scintillator and/or the buffer.
- track each single scintillation photon including its interaction with the scintillator and with the materials until a photomultiplier is reached or the photon is lost.
- generate the PMT pulse signals, the front end outputs and the digital electronics behavior of Borexino's data acquisition system.
- simulate the trigger response and produce the final output for triggered events.
- produce a set of data formally identical to the real raw data. These simulated data are then analyzed with the same tools (decoding and reconstruction codes) used to analyze the real data to obtain the physical information (energy, position and pulse shape variables of the event).

The code is structured in three independent programs. The generation of the events is implemented within the Geant4 [248] framework. Geant4 is an object oriented C++ toolkit for the simulation of the passage of particles through matter. Its areas of application include high energy, nuclear and accelerator physics, as well as studies in medical and space science. The first version of the Geant4 implementation of Borexino's simulation was called `g4bx`. As anticipated, a substantial upgrade and refactoring of `g4bx` was carried

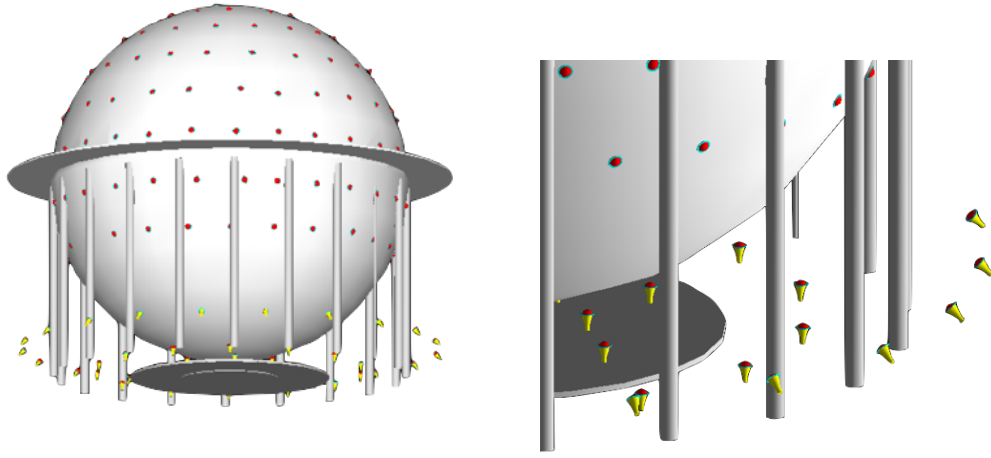


**Fig. 5.1:** Simulated geometry for the Borexino OD in `g4bx2`.

out in 2013, yielding to a new version of the algorithm, named `g4bx2`, which is the main subject of this chapter. `g4bx2` takes care of simulating particle interactions in the detector, producing scintillation photons and tracking them until they are possibly detected by the PMTs. Once photoelectrons are created, the simulation of the whole electronics chain of Borexino takes place, in an independent software, developed completely by the Borexino collaboration and named `bxelec`. It simulates the charge and time response of the PMTs, as well as the behavior of the front ends and of the trigger. The output of `bxelec` is a binary file with the same structure as that of the files produced by the main Borexino data acquisition system. This is then an input of the reconstruction algorithm `echidna`, which is the same both for MC and real events.

The developments of the code were driven by the constant comparison of simulations with calibration data. Section 5.8 discusses why calibrations were also essential in order to validate the whole simulation algorithm as well as for the tuning procedure of some of the physical inputs needed by the MC.

## 5.2 Detailed geometry simulation

A high precision simulation is subordinated to a very careful description of the system geometry. This includes the implementation of proper materials, sizes and physical properties of all the objects. The geometrical idealization of the system for the simulation in the Geant4 framework which is presented here, should be compared to the detailed mechanical project of the detector discussed in Sec. 4.2 and shown in Fig. 4.1.

### 5.2.1 Outer Detector geometry

In Fig. 5.1, a sketch of the simulation of the outer detector geometry is presented. Particularly, one can notice the OD structure (in reality enclosed in the WT), the legs supporting the SSS and the steel platforms at the bottom of the detector, which were designed originally as a shield against the rock radioactivity [215]. PMTs are placed on the floor of the WT and on the outer surface of the SSS. The schematization of the OD PMT geometry directly follows the real design, as it is shown in Fig. 5.2. PMTs are enclosed in an outer shielding against water and pressure, and this is reproduced in the simulation. The whole PMT structure is not visible for PMTs attached to the SSS, since they are fixed to the SSS but tyvek foils cover the ensemble SSS-PMTs only leaving the photocathodes facing the water. The tyvek foils placed on the inner surface of the WT are also simulated.

Besides the geometrical details implemented in the simulation, the optical properties of all the materials involved are taken into account according to specific measurements or data available in literature. In the specific case of the OD simulation, particularly important is the tyvek reflectivity dependence upon the wavelength, the PMT QEs and the water properties.



**Fig. 5.2:** Comparison between the schematization of the OD PMTs in the simulation and the actual objects.

### 5.2.2 Inner Detector Geometry

Figure 5.3 shows a cut of the simulated Borexino, revealing the inner detector. All the most relevant geometrical features are simulated, such as the PMTs with their real distribution, the nylon vessels and their endcaps. Particularly, the IV is simulated with the shape inferred from real data on a weekly basis, as discussed in Sec. 4.2, and when simulating data throughout a long period of time, the vessel evolution is taken into account. This is important, since the vessel shape can affect the amount of external contaminations reaching the standard FV or the energy response of the detector (see e.g. Sec. 5.8.2 and Sec. 5.10.4). The granularity with which the real vessel shape is simulated

is adjustable by the user, but optimal values are usually around  $\sim 5$  cm (i. e. the shape is approximated with a polygonal shape in the  $r - \theta$  plane with sides of  $\sim 5$  cm). This is a good compromise, which takes into account both the intrinsic uncertainty of the vessel shape determination (a few cm [214]) and an optimized code performance.

In Fig. 5.3, also vessel endcaps are visible. They support the vessel and provide the connection between the innermost volumes and the Borexino plants in Hall C at LNGS. A careful simulation of the endcaps is important, since their effect of light shadowing and reflection for events close to the north and the south poles of the IV is quite important.

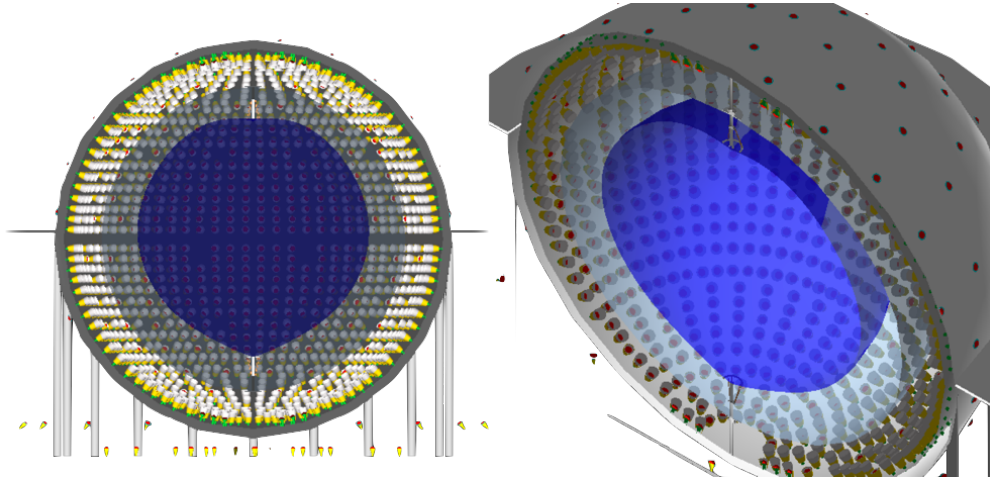


**Fig. 5.3:** Simulated geometry for the Borexino ID in g4bx2: the realistic IV shape is taken into account on a weekly basis.

The crucial objects in the Borexino geometry simulation are the ID PMTs. In fact, their features, materials and optical properties highly influence the detector response. In Fig. 5.4, a comparison between the real PMTs mounted on the inner surface of the SSS and the MC idealization is shown. As anticipated in Sec. 4.2, 1828 PMTs are equipped with light concentrators, while 384 are not. The two different configurations are shown both in the left and right panels of Fig. 5.4. The schematization of the ID PMTs is made of a common PMT base (almost invisible, but in green in the right panel of Fig. 5.4) on top of which the photocathode is placed (red in the picture). The photocathode is made of bialkali and it is a portion of a hemisphere. The whole PMT body is surrounded by a conical  $\mu$ -metal shielding (yellow in the picture) which reduces the effect of the Earth magnetic field on the PMT response.

The light concentrators (“light cones” or simply “cones”) were designed to enhance the collection of the light coming from the innermost 3 m sphere [249]. Their shape is thus carefully reproduced in the simulation (with a sub-cm precision), since it significantly affects the amount of photoelectrons collected as a function of the event position. PMTs without light concentrators are equipped with a small steel ring which surrounds the photocathode and supports it. PMTs with concentrators are simulated in g4bx2 as shown in top of the right panel of Fig. 5.4, while PMTs without concentrators are simulated as



**Fig. 5.4:** *Left Panel:* Borexino ID PMTs mounted on the SSS. *Right Panel:* MC schematization of the PMTs with (top) and without (bottom) concentrators.

shown in the bottom of the same panel.

Particular care is devoted in the implementation of the optical properties of the simulated materials in the ID, since they are the most relevant for solar neutrino analyses. Apart from scintillator and buffer's properties, which are discussed in more detail in Sec. 5.4, the nylon vessel absorption length as a function of wavelength and index of refraction are inputed in the simulation. The vessel transparency was measured with a dedicated measurement campaign carried out at the moment of the vessel construction. The PMT quantum efficiency spectral dependence was implemented according to the measured curve, which is shown in Fig. 5.5. Furthermore, the light cones and the SSS inner surface are modeled such that with some probability, the incoming light is reflected or absorbed. In the case of reflection, the photon can be reflected specularly or diffusively (Lambertian diffusion). The same holds for the steel rings of the PMTs not equipped with cones, since it somehow acts as a little concentrator on its own. The precise determination of all these coefficients can be done only in an effective way through the tuning procedure outlined in Sec. 5.8. In fact, even if one knew the measured values for all these properties (reflectivity, absorbance, ratio between specular and diffusive reflection, wavelength dependence...) in the laboratory, it would be impossible to predict the effective physical values with a superb precision when the individual components are all placed inside the detector.

### 5.3 Energy loss and light generation

“Low energy electrons”, i. e. with energies much lower than the critical energy for which the Bremsstrahlung becomes important, lose energy in the scintillator mainly through ionization and, for those above the threshold, through Čerenkov light production. A small fraction of the energy lost through ionization is converted in optical photons by the liquid scintillator. For low energy solar neutrinos, the Čerenkov contribution

in optical photons is pretty low (a few % with respect to scintillation for electrons of 1 MeV), but still it should be taken into account properly, when aiming at reaching a very sensitive measurement. In this section, the scintillation mechanism in Borexino and its actual modeling in the MC simulation are described, as well as the modeling of the Čerenkov photon production.

### 5.3.1 Generation of scintillation light

The photon emission and its time distribution in the PC+PPO mixture depend on the details of the energy loss processes and on the molecular interaction between solvent and solute in the scintillator. In fact, fluorescence is a property of single molecules in organic scintillators. Carbon bonds in aromatic molecules, such as those of PC and PPO, are constituted by electrons lying in the so called  $\sigma$  and  $\pi$  bonds. The  $\sigma$  bond is responsible for the hexagonal planar structure of the scintillator molecule, through shared electrons among the carbon atoms. The electrons in p orbitals, orthogonal to the hexagon, form  $\pi$  bonds, creating toroidal regions below and above the lines connecting the carbon atoms in which electrons can move. The  $\pi$  electron energy levels are quantized in a series of singlet  $S_{ij}$  and triplet  $T_{ij}$  states, where  $i = 0, 1, 2..$  denotes the electron energy levels and  $j = 0, 1, 2, ..$  vibrational sub-levels.  $\pi$  electrons are those responsible for the scintillation mechanism. Fluorescence light is emitted when  $\pi$  electrons decay from the first excited state  $S_1$  to one of the vibrational energy levels of the fundamental state.

Several processes may happen, such as :

- the excitation of a  $\pi$  electron in a singlet  $S_{ij}$  state. Electrons cannot be directly excited into a triplet state because the transition  $S_{0j} \rightarrow T_{ij}$  is forbidden due to simple spin selection rules.
- the ionization of a  $\pi$  electron. The emitted  $\pi$  electron can be potentially re-captured by the molecule in a singlet or triplet excited state.
- the excitation of  $\sigma$  electrons that then decay to their ground states without emitting light.
- the ionization of  $\sigma$  electrons that may leave damaged molecules that can absorb scintillation light.

Charged particles lose energy in the scintillator mainly interacting with the solvent (in a 1.5 g/L solution, the mass ratio between solvent and fluor is around  $\sim 0.2\%$ ). The energy is then transferred to the solute either by radiative (emission of photons from the solvent and absorption from the fluor) or non radiative processes (dipole-dipole interactions between excited solvent and solute molecules). For solute concentrations like the one in Borexino, non radiative transfer should dominate. Once PPO is excited, it can emit fluorescence light only through the de-excitation of  $\pi$  electrons. Excited electrons of the fluor promptly reach (through non radiative processes) the first excited state  $S_{10}$ , from where they decay to the fundamental state  $S_{0j}$  emitting scintillation light, following an exponential time distribution with a time constant of 1.6 ns. In case some

of the excitation energy is lost by collisions, and the electron is transferred to a triplet excitation state,  $T_{10}$ , it is impossible for the electron both to de-excite emitting light and to return to the singlet state by non-radiative transition (being  $E_{T_{10}} < E_{S_{10}}$ ). The only way out is the interaction with another solvent molecule in the same triplet state, thus generating delayed fluorescence.

This discussion points out why the generation of scintillation photons is the only process in **g4bx2** which cannot be performed *ab initio*. This would require too many molecules and processes to be taken into account, resulting in a practically infinite simulation time. Therefore, the emission of fluorescence light is modeled effectively.

Both the time distribution and the net light yield of the emitted fluorescence photons depend on how the energy is released, i. e. on the value of the energy lost per unit path,  $dE/dx$ . In turns,  $dE/dx$  depends on the particle type: heavy ionizing particles like  $\alpha$  particles have a big  $dE/dx$  which produces large ionization or excitation density, therefore increasing the probability to get  $T_{10}$ -like excited states and thus delayed fluorescence. Simultaneously, the ionization density may favor molecular processes in which the energy is dissipated in non radiative ways, resulting in a substantial quenching of the scintillation light.

The most widely spread quenching model, i. e. a model able to predict the fluorescence light emission as a function of the energy loss, is the semi-empirical Birks model [250]. It depends on the average ionization particle energy loss  $dE/dx$ , and on the so called Birks parameter  $kB$ , a characteristic constant which depends on the medium and on the primary particle. The Birks formula computes the scintillation light yield  $dL$  produced when a particle loses energy along a path  $dx$  with the stopping power  $dE/dx$  as:

$$\frac{dL}{dx} = Y_0 \frac{dE/dx}{1 + kB \cdot dE/dx}, \quad (5.1)$$

where  $Y_0$  is the scintillation yield in absence of quenching ( $kB = 0$ ).

The Birks parametrization is a macroscopic description of the quenching, and can not be used directly in a stochastic approach as in Monte Carlo simulations. In fact, the model assumes that all energy deposits due to secondaries (like  $\delta$ -rays or X-rays) belong to the primary particle, but in the Monte Carlo approach each particle is treated and tracked independently. A correct implementation of the Birks formalism requires therefore the evaluation of the quenching factor for the primary ionizing particle. Each daughter inherits the same quenching factor of the parent. This approach requires an *a priori* parametrization of the energy loss  $dE/dx$  for the different primary particles considered as required by Eq. (5.1), and a table of quenching factors as a function of the energy, which is built at the initialization phase in order to speed up the simulation.

The total number of emitted scintillation photons is obtained by integration of Eq. (5.1):

$$L(E) = Y_0 \int_0^E \frac{dE}{1 + kB \cdot dE/dx}, \quad (5.2)$$

where  $kB$  is of the order of  $10^{-2}$  cm/MeV, but its precise value has to be determined for every particular scintillator and particle, as it is discussed in Sec. 5.8. As an example of

a limit case such as that of electrons of some MeV,  $kB \cdot dE/dx \ll 1$  and thus Eq. (5.2) becomes simply:

$$L(E) \simeq Y_0 E. \quad (5.3)$$

If the approximation  $kB \cdot dE/dx \ll 1$  does not hold, the light yield is lower than that of Eq. (5.3), resulting in an intrinsic non linearity between the deposited energy  $E$  and the emitted scintillation  $L(E)$ . The quenching factor  $Q_p(E)$  describing the deviations from the linear behavior is defined as:

$$Q_p(E) = \frac{1}{E} \int_0^E \frac{dE}{1 + kB \cdot dE/dx}. \quad (5.4)$$

$Q_p(E)$  is always lower than 1 and it represents the ratio between the “true light yield” and the one expected from the simple linear law of Eq. (5.3). The suffix  $p$  recalls that  $Q_p(E)$  depends on the particle type  $p$  (e.g.  $\alpha$ ,  $\beta$ , or proton). Actually, as it is pointed out in Sec. 5.8, for the case of  $\alpha$  particles, a single parameter  $kB$  is not sufficient to describe the non linearity induced by the high  $dE/dx$ . In such a case, the Birks model of the second order is adopted (see the discussion in Sec. 5.8.4 for more details).

The deviation of the measured light yield from Eq. (5.3) is increasingly important for protons,  $\alpha$  particles, and nuclear fragments due to the high ionization per unit length. The quenching effect is relevant also for  $\gamma$  rays. The amount of scintillation light emitted when a  $\gamma$  with energy  $E$  is fully absorbed by the scintillator is significantly lower than the amount of light emitted by an electron with the same energy  $E$ . This effect originates from the fact that  $\gamma$  rays cannot directly excite the molecules of the scintillator but they can only do it through their previous interactions with the electrons. Every daughter electron deposits in the scintillator an amount of energy  $E_i$  which is a fraction of the initial energy of the  $\gamma$  ray. Therefore the amount of scintillation light  $Y_\gamma$  generated by the  $\gamma$  is obtained summing up all the electron contributions  $i$  obtaining the following relation [214]:

$$Y_\gamma = Y_0 \sum_i E_i Q_\beta(E_i) \equiv Y_0 \cdot Q_\gamma(E) \cdot E, \quad (5.5)$$

which defines  $Q_\gamma(E)$ . Since  $Q_\beta(E)$  decreases as a function of the energy, it results that  $Q_\gamma(E)$  is smaller than  $Q_\beta(E)$  for the same energy  $E$ . As a result, the quenching factor is not negligible for  $\gamma$  rays with  $E$  in the MeV range.

In view of the above considerations, the number of photons as a function of the incident particle and of its initial energy is computed using the quenching factor of the parent as of Eq. (5.4) and assigning it to all the daughters produced by the primary interaction. The precise values of  $Y_0$  and  $kB$  were obtained through the tuning and the comparison of simulations with calibration data, as described in Sec. 5.8.4. The energy spectrum of optical photons produced by the scintillation is that of the fluor, the PPO, and it is shown in Fig. 5.5. The picture also shows the spectral response of the PMTs (in terms of nominal QE) and the emission spectrum of the pure PC, which is important for

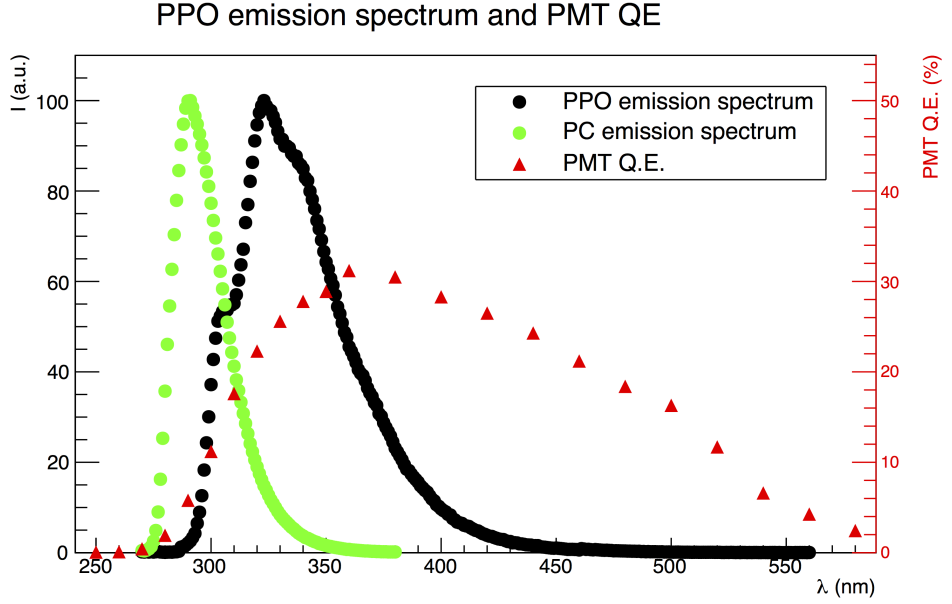


**Fig. 5.5:** The picture shows, overlapped, the PPO (black) and PC (green) emission spectra. The two curves are normalized to 100 at the maximum. The red points show the PMT QE as a function of the wavelength.

the scintillation in the buffer and for the absorption-reemission processes described in Sec. 5.4.

The phenomenological model describing as a whole the time evolution of the photon production due to the solvent excitation, energy transfer to the fluor and finally its scintillation is that of four exponentials, as anticipated in Sec. 3.7.1. Therefore, the light emission time  $t$  in the PC+PPO scintillator is generated in the Monte Carlo according to the formula:

$$P(t) = \sum_{i=1}^4 \frac{w_i}{\tau_i} \exp^{-t/\tau_i}, \quad (5.6)$$

where the  $\tau_i$  values and their weights  $w_i$  were obtained with the dedicate experimental setup described in Ref. [210]. The precise values are then optimized thanks to the tuning procedure, as described in Sec. 5.8.3. The values of the weights and of the time constants<sup>1</sup> are much different for  $\alpha$ 's and  $\beta$ 's: this is the key factor that allows the pulse shape discrimination to work efficiently, as described in Sec. 4.7.

As a final remark, the light generation in the buffer medium (PC+DMP at 2 g/L) is modeled using the available measured data [251]. The total photon yield in the buffer is estimated to be equal to 4% of that of Borexino's scintillator. The spectrum of the

<sup>1</sup>As already mentioned in Sec. 3.7.1, this model is just phenomenological, with the fastest time constant being the only one with the physical meaning of describing the energy transfer from the solvent to the solute.

optical photons is that of the pure PC as shown in Fig. 5.5 and their time distribution follows an exponential with a time constant of 2.8 ns.

In g4bx2, the energy loss and the creation and tracking of the secondaries is handled through the standard Geant4 libraries. Instead, the implementation of the Birks formula and the creation of optical photons with the proper energy spectrum and time profile are managed by custom classes developed specifically for Borexino.

### 5.3.2 Generation of Čerenkov light

The spectrum of Čerenkov light is generated according to the standard expression [7]:

$$\left( \frac{d^2 N_{Ch}}{dxd\lambda} \right)_{Ch} \propto \frac{1}{\lambda^2} \left( 1 - \frac{c^2}{v^2 \cdot n^2(\lambda)} \right), \quad (5.7)$$

where  $n(\lambda)$  is the refraction index as a function of the wavelength and  $v$  is the particle speed in the scintillator. Naturally, in order for the effect to take place, the Čerenkov threshold condition must be satisfied, i. e.

$$\left( 1 - \frac{c^2}{v^2 \cdot n^2(\lambda)} \right) > 0. \quad (5.8)$$

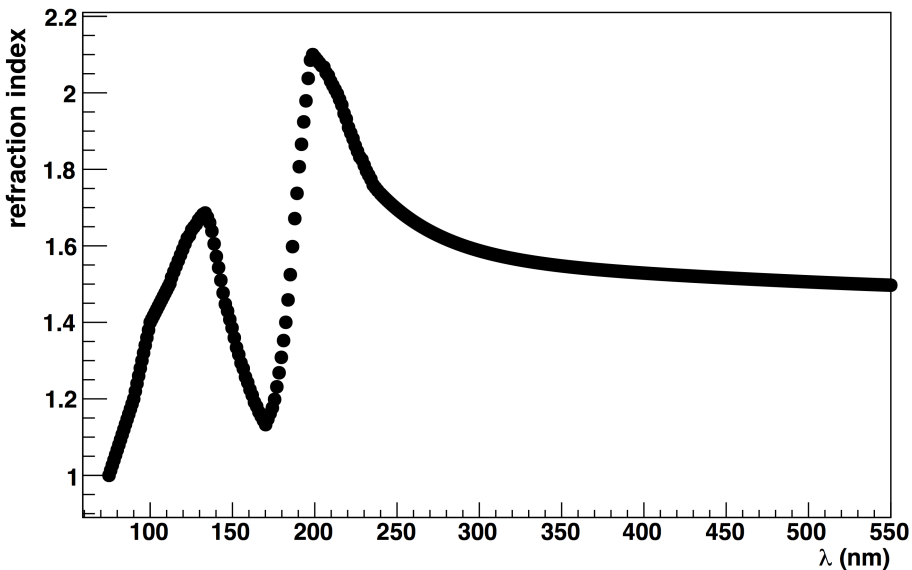


**Fig. 5.6:** Refractive index of the Borexino scintillator as a function of the wavelength.

The primary spectrum of Čerenkov light extends into the ultraviolet (UV) region which is not directly detectable by the PMTs. However, as described in Sec. 5.4, UV light is almost immediately absorbed and (possibly) reemitted by the scintillator with longer wavelength, thus allowing an almost direct detection also of the Čerenkov photons.

As outlined by Eq. (5.7), a proper simulation of the Čerenkov effect requires the knowledge of the dispersion relation  $n = n(\lambda)$ . Direct measurements performed at the University of Genoa in the past allowed to obtain  $n(\lambda)$  in the wavelength range (245, 1688) nm. The methodology and the instrument used to carry out the measurements is the same presented in Sec. 5.5. Since the number of photons produced by the Čerenkov effect is proportional to  $\lambda^{-2}$  (Eq. (5.7)), the knowledge of  $n(\lambda)$  in the UV region is fundamental. Unfortunately, direct measurements for such low wavelengths are not available for Borexino’s scintillator, but since the trend at higher wavelengths is almost the same as that of benzene, the measured data for benzene [252] was used to extend the  $n(\lambda)$  curve in the UV region for Borexino’s scintillator. Furthermore, the data points are extrapolated to the value  $n = 1$  in the deep ultraviolet region. Figure 5.6 shows the global  $n(\lambda)$ , which is used for the Čerenkov photon generation and propagation. It has to be noted that the resonant behavior of  $n(\lambda)$  at lower wavelengths is simply denoting the presence of a non null imaginary component of the index of refraction, i. e. the presence of absorption. In fact, as discussed in Sec. 5.4, the information on  $n(\lambda)$  alone does not allow to properly quantify the total amount of detectable Čerenkov photons, since there is quite of a lack of knowledge about the reemission probability of the scintillator in the UV region of the spectrum.

From the technical point of view of the implementation, the Geant4 class describing the Čerenkov effect had to be extended, since in its standard configuration it works only for monotonic functions for  $n(\lambda)$  (since it assumes that there is no absorption), which is not the Borexino case, as shown in Fig. 5.6.

### 5.3.3 Algorithm optimization

In order to speed up the simulation, a trick is implemented in `g4bx2`. The most demanding activity from the CPU time point of view is the tracking of all the scintillation and Čerenkov photons. A possibility allowing to track less photons consists in generating less of them and, contemporarily, renormalizing the values of the PMT QEs. In practice, if the theoretical number of photons to be tracked was  $N$ , the number of the actually produced and tracked photons would be  $N \times QE_{max}$ , where  $QE_{max} = 0.312$  is the maximum value of the QE among all the PMTs. Of course, given the lower number of produced photons, the QEs of all PMTs are normalized to  $QE_{max}$ . This procedure could be summarized by saying that instead of producing a certain amount of photons and detecting them with a 1/3 probability, only 1/3 of the photons are produced and are detected with a probability of 1. Of course, the two statements are not equivalent, since in the second case the simulation is effectively *biased*, and this must be taken into account. For instance, the number of photoelectrons detected from an event in the center of the sphere obtained with the two methods, would show the same mean values, but different variances. If the fluctuation is computed according to Poisson statistics on the original number of photons  $N$  which are supposed to be produced, but then only  $N \times QE_{max}$  are tracked, the resulting distribution would result squeezed. This is known as variance reduction. The effect is taken into account by letting fluctuate the number of photons around  $N \times QE_{max}$ , instead of considering the original percentage fluctuation on  $N$ .

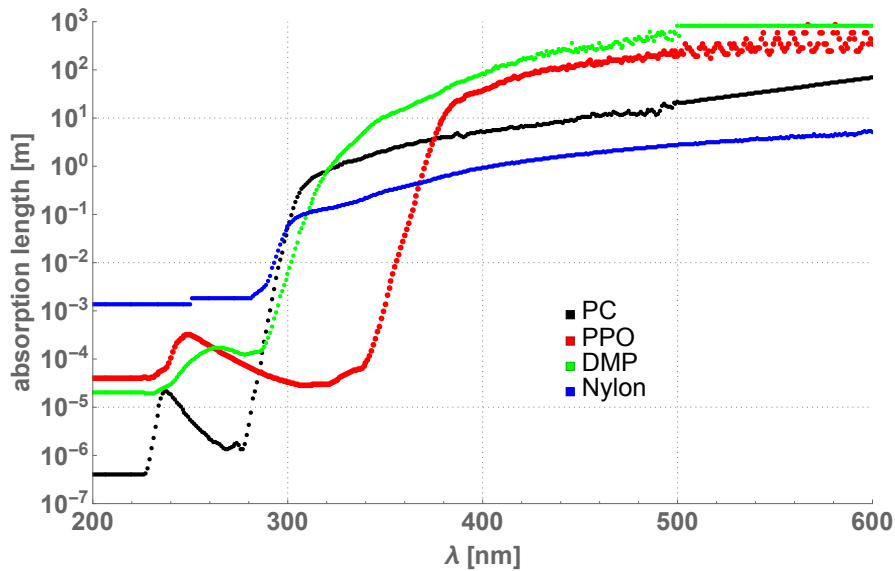


**Fig. 5.7:** Attenuation length of PC (black), PPO (red), DMP (green) and nylon (blue) as a function of the wavelength.

Actually, this is just an approximation, and an additional Fano factor is introduced in order to match the resolution observed in calibration data and that coming out from the simulation. It has to be noted that if this trick is not applied, and thus the total number  $N$  of photons is tracked, there is no need to introduce an additional Fano factor to describe the detector resolution. This allows to prove that this factor is just a statistical need, which does not bring any other information regarding the physics of the light production.

## 5.4 Light tracking and propagation

`g4bx2` tracks individually each optical photon, taking into account its interactions with each single component of the scintillator or the buffer. These processes include elastic Rayleigh scattering, absorption and reemission of photons by PPO molecules, absorption of photons by DMP and also photon absorption in the thin nylon vessels. The cross-sections (or equivalently the wavelength dependent attenuation length  $\Lambda(\lambda)$ ) for these interactions were obtained from dedicated spectrophotometric measurements and are shown in Fig. 5.7.

Photons emitted by scintillation or Čerenkov processes can interact with PC, PPO, DMP or nylon molecules in their ways to PMTs. In the model implemented in `g4bx2`, if photons interact with DMP or nylon molecules, they are simply absorbed. In case of interaction with PC, two distinct cases are considered, and their definitions are related to the PC emission spectrum shown in Fig. 5.5. Optical photons with a wavelength  $\lambda > 310$  nm undergo Rayleigh scattering with an angular distribution  $P(\theta) = 1 + \cos^2 \theta$ ,

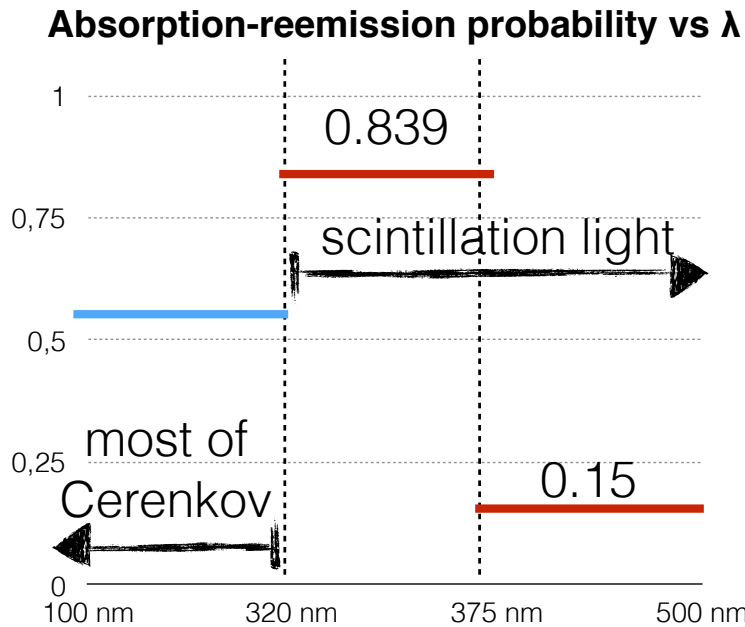


**Fig. 5.8:** Model for the reemission probability after absorption by PPO molecules as a function of the wavelength, as it is implemented in g4bx2.

without time delay, and with no shift in energy. At shorter wavelengths, the interaction with PC is simulated as absorption by PC molecules, followed by the energy transfer to PPO (if the interaction happens in the IV). With a probability of 82%, the PPO subsequently reemits the photon with an exponentially distributed emission time with a constant  $\tau_{PC \text{to} PPO} = 3.6 \text{ ns}$ . In the buffer medium, where PPO is not present, the interaction with PC for  $\lambda < 310 \text{ nm}$  is followed by subsequent PC scintillation according to the PC spectrum of Fig. 5.5 with a probability of 0.04 and with an exponential time distribution with  $\tau_{PC} = 2.8 \text{ ns}$ .

Even if PC molecules are the most abundant, most of the optical photon interactions (which have the energy spectrum of PPO, see Fig. 5.5) are with the PPO molecules, as it is clear from the attenuation length plot in Fig. 5.7. Thus, the absorption and potential reemission of optical photons due to their interaction with PPO is the most important effect to be taken into account regarding the light propagation in Borexino. The attenuation length as a function of the wavelength of PPO molecules was measured quite accurately (Fig. 5.7), but an experimental determination of the reemission probability as a function of the optical photon energy  $P_{rem}(\lambda)$  is not easy to achieve. The optical model describing  $P_{rem}$  adopted in g4bx2 is depicted in Fig. 5.8. In practice, it is a three-plateau function, where for  $320 \text{ nm} < \lambda < 375 \text{ nm}$   $P_{rem} = 0.839$  (where the most of the optical photons are produced) and for  $\lambda > 375 \text{ nm}$   $P_{rem} = 0.15$ . No experimental data are available for  $\lambda < 320 \text{ nm}$ , and thus the value of  $P_{rem}$  for this wavelength range was determined effectively, through the tuning with calibration data described in Sec. 5.8.4. This region of the optical photon spectrum is very important for Čerenkov photons, and

thus the value of  $P_{rem}$  found in the tuning corresponds to an effective parameter which sums up the uncertainties on  $n(\lambda)$  for such low wavelengths and that of the reemission probability itself. If photons absorbed by PPO are reemitted, they are produced with an isotropic distribution, according to the standard PPO energy spectrum (presumably non-radiative interactions delete the memory of incoming photons) and with an exponential time distribution with a time constant of  $\tau_{PPO} = 1.6$  ns.

The MC simulation takes also into account the interactions of optical photons with interfaces (e. g. the refraction induced by the presence of the nylon vessels) and surfaces (reflections on the cone surfaces, on the SSS, on the PMT photocathodes). This light propagation model was already validated in the CTF detector (Borexino’s prototype) [253], apart from the treatment of UV photons due to Čerenkov production, which is a novel development introduced in g4bx2.

In the end, photons reach photocathodes. They are detected with a probability which depends on their energy, as shown in the PMT QE curve of the left panel of Fig. 5.9. All PMTs are assumed to have the same spectral dependence of the QE, but different peak values. This allows to take into account the slight differences which are present among the different channels. Actually, the intrinsically different QE values for the PMTs are not enough in order to properly characterize the time behavior of the detector, since the global detection efficiency of a single channel might vary with time. For this reason, the values of the single PMT QE (actually, this should not be referred to as “quantum efficiency”, since it describes the global channel, PMT plus front end plus digital electronics, photo-detection efficiency) are computed on a weekly basis with the data driven method which is outlined in the next Sec. 5.4.1.

### 5.4.1 Effective Quantum Efficiencies

All Borexino PMTs have slightly different light detection efficiencies, this being caused by different intrinsic properties of the photocathodes. These relative quantum efficiencies were measured in the past, prior to the PMT installation in Borexino [254]. Their distribution is shown in the right panel of Fig. 5.9, and they refer to the peak value of the spectral response of the PMT QE (shown in the left panel of Fig. 5.9), normalized to the best PMT in the set. Actually, what matters in order to map precisely all the possible sources of non uniformity in the detector, is the global photo-detection efficiency of each single channel. This number is an extension of the relative QE mentioned above, and is usually called “effective quantum efficiency”. The effective quantum efficiency is the probability of a hit signal detection in case of a photoelectron, normalized to the solid angle of observation and to the total number of photons in that event. This definition, besides taking into account the intrinsic QE differences among the PMTs, also describes effects such as light propagation non uniformities and electronic channel properties.

In order to dynamically estimate the effective quantum efficiencies, real events in the center of the detector are selected with a spherical radius of 2 m. In this way, solid angle differences among the PMTs are negligible. PMTs with and without concentrators are of course treated separately, since the detection efficiency is much higher for PMTs with the cone. The class of events which is selected in order to compute the effective QE

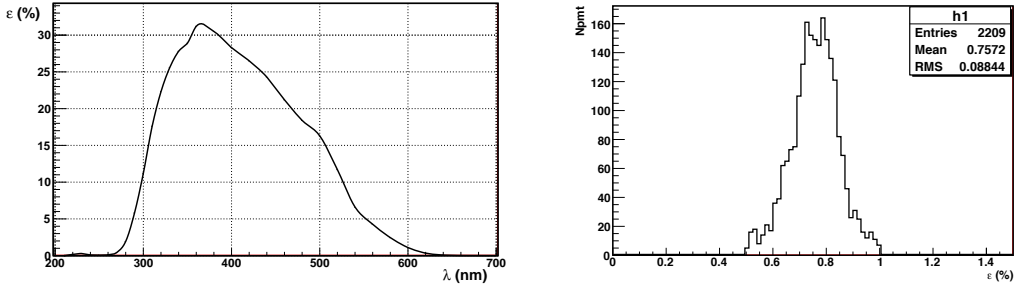


**Fig. 5.9:** *Left Panel:* Borexino PMT spectral dependence of the QE. *Right Panel:* Relative QE among the whole set of Borexino PMTs. The values are normalized so that 1 corresponds to the highest measured QE.

corresponds to  $^{14}\text{C}$  events, thanks to their relatively high statistics, their uniform volume distribution and steady rate. Thus, the effective quantum efficiency for each channel is proportional to the hit count rate on each channel, caused by  $^{14}\text{C}$  selected in the innermost 2 m sphere. In order to have a precise estimation, the dark noise contribution for each PMT, which is evaluated weekly during the electronics calibration campaign, is subtracted, so that the hit rate associated to each channel can be attributed to the real  $^{14}\text{C}$  events (within statistical fluctuations).

Some time dependent non-uniformities in the values of the effective quantum efficiencies are actually present in the data, but the most important effect is the one induced by the intrinsic differences among the PMTs, shown in the right panel of Fig. 5.9.

## 5.5 Refractive index dependence upon the temperature

A long standing issue regarding Borexino's position reconstruction has been reported since the first calibration campaign of the detector [216]. As already mentioned in Sec. 4.6, a  $^{222}\text{Rn}$  source was deployed in  $\sim 200$  positions, in order to optimize the position reconstruction algorithm implemented in `echidna`. The source position inferred from the data through the algorithm described in Sec. 4.6 was compared to the source position measured by the CCD camera system used during calibrations. While the performances of the algorithm along the  $x$  and  $y$  axes turned out to be very good, a shift in the reconstruction of the  $z$  coordinate was observed. This does not happen in MC simulations. The situation is summarized in Fig. 5.10. Red points show the difference between the reconstructed  $z$  position by `echidna` and that of the CCD camera as a function of the  $z$  coordinate. There is a parabolic mismatch which has a maximum of  $3 \div 4$  cm at the center of the detector. This feature is not observed in MC simulations. Figure 5.10 also shows the behavior of position reconstruction very close to the vessel endcaps (blue points), which shadow the light and thus affect the whole algorithm. However, these geometrical points are very far away from the FV used for the analysis, and for this reason the observed trend is not worrying.

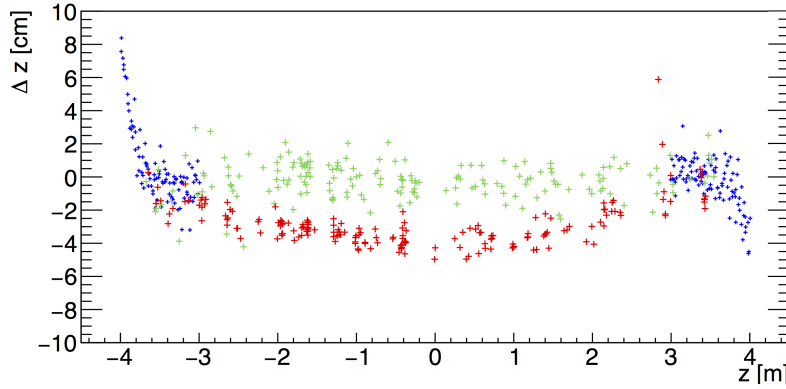


**Fig. 5.10:**  $\Delta z$ , i.e. reconstructed position minus “true position” (input position in the case of the simulations, CCD camera position for real data), versus the  $z$  coordinate, for  $^{222}\text{Rn}$  events in the 182 positions of real calibration data (red) and MC simulation (green). The blue points are MC simulated for  $|z| \gtrsim 3.5$  m and do not have a counter part in real calibration data. The sharp deviations from  $\Delta z = 0$  at large radii are induced by the shadowing effect of the endcaps and the asymmetry north-south is due to the vessel shape.

Many hypotheses were considered, in order to try to explain the observed shift along the  $z$  direction in the FV. Anyhow, it has to be noted that the impact on the systematics of the FV determination of this shift is totally negligible [214], and thus the present discussion is motivated by the curiosity of understanding the phenomenon instead of assessing a crucial point of the analysis. Among the considered effects able to explain the  $z$  shift there are: a small offset in the position of the PMT coordinate system, not precisely measured cable delays, troubles in the CCD camera reconstruction system and algorithm or some physical phenomenon affecting light propagation. As discussed in Sec. 4.9.2, a vertical thermal gradient is present in Borexino: a potentially non negligible temperature (and thus  $z$ ) dependence of the index of refraction could be able to explain the observed  $z$  mismatch.

### 5.5.1 Simple model for the effect of $n(z)$ on the reconstruction

It is possible to develop a very simplified model, which assumes a detector with a spherical geometry as that of Borexino and only two PMTs, one at the south and the other at the north pole. Two photons are emitted by an event along the  $z$  axis, one going upwards and the other going downwards. The position of the event is inferred by the time difference of the hits produced by the photons on the PMTs. This is much simpler than what happens in reality in Borexino but the physical principle is exactly the same as that described in Sec. 4.6. Recalling what was already discussed in Sec. 4.6, the refractive index  $n$  is intended here as the effective refractive index  $n_{\text{eff}}$ , as defined in Eq. (4.8), which describes the propagation of single photons, i.e. wave packets. Since the index of refraction variations can be supposed to be “small”, a linear parameterization

can be assumed, i. e.  $n_{eff} = n_0 + az$ . Therefore, the difference of the two photons times of flight is:

$$t_S - t_N = \frac{1}{c} \int_{-R}^{z_0} n_{eff}(z) dz - \frac{1}{c} \int_{z_0}^R n_{eff}(z) dz = \frac{2n_0 z_0}{c} + \frac{a}{c} (z_0^2 - R^2), \quad (5.9)$$

where  $t_N$  ( $t_S$ ) is the hit time for the PMT at the top (bottom) of the sphere,  $z_0$  is the  $z$  coordinate of the event and  $R$  is the distance of the two PMTs from the center. If one assumes  $a = 0$ , thus neglecting any variation of the effective refractive index, the reconstructed position  $z_R$  would simply be

$$z_R = (t_S - t_N)v_R \rightarrow z_R = z_0 \Leftrightarrow v_R = \frac{c}{2n_0}, \quad (5.10)$$

where  $v_R$  is the effective velocity used by this very simple reconstruction algorithm. In this context, it is clear that assuming the procedure of Eq. (5.10) while Eq. (5.9) holds with  $a \neq 0$ , yields to a mismatch between  $z_R$  and  $z_0$ :

$$\Delta z \equiv z_R - z_0 = \frac{a}{2n_0} (z_0^2 - R^2). \quad (5.11)$$

A reasonable assumption concerning  $a$  comes from considering the expected variation of the index of refraction upon the density of the liquid, which is of course related to the temperature and thus to the  $z$  coordinate in Borexino. Since  $\Delta n/n \ll 1$ , it can be assumed  $\Delta n \propto \rho$ ,  $\rho$  being the scintillator density. Particularly, to a greater density it corresponds a bigger  $n$ . This means that  $a < 0$ . Furthermore, assuming a total temperature difference of 5°C between the top and the bottom and the data for benzene (very similar to PC) [255], one can quantify a global variation of  $n$  of 0.15%, which would correspond, for  $R = 4.25$  m and  $n_0 = 1.53$ , to  $a \sim -3 \cdot 10^{-4}$  m $^{-1}$ . The shift in the center of the detector quantified through Eq. (5.11) is around 5 mm upwards. This is off an order of magnitude and, most of all, the sign is completely wrong, if compared to the one observed in real data and shown in Fig. 5.10. Therefore, it seems that the temperature dependence of the index of refraction due to the density effect can not be responsible for the  $z$  shift present in data.

### 5.5.2 Density effect and $dn/d\lambda$

The parameter governing the optical photon speed in the scintillator is  $n_{eff}$ . Thus, not only the amplitude of  $n$  is important (whose variations are driven by the density effect), but also the shape of  $dn/d\lambda$  is fundamental in the determination of the effective refractive index. A rough estimation of the effective refractive index could be obtained by simply computing

$$n_g = \int_{-\infty}^{+\infty} E_{PPO}(\lambda) n_{eff}(\lambda) d\lambda, \quad (5.12)$$

where  $n_g$  is the effective index of refraction describing the speed of optical photon wave packets and  $E_{PPO}(\lambda)$  is the normalized PPO emission spectrum reported in Fig. 5.5.

In practice,  $n_{eff}$  is mediated on the spectrum of the optical photons produced by the scintillation. This is an approximation, since the mean should be performed on the spectrum of the photons reaching the PMTs (which is red shifted with respect to the pure PPO emission spectrum because of absorption and reemission) and the Čerenkov effect is neglected, but it works very well, since by the *a priori* computation one finds  $n_g \sim 1.67$ , while the actual value of  $n_g$  used in **echidna** and optimized thanks to the calibration campaign is 1.68.

It is possible to assume that the temperature induces a variation on the shape of  $n$  as a function of  $\lambda$ . This in turn would mean a variation of  $n_{eff}$ , which could explain the  $z$  shift. If one assumes a variation on  $dn/d\lambda$  as high as 10% and more precisely a growing (in modulus) slope as a function of the temperature, one gets:

$$\frac{n_g^{top}}{n_g^{bottom}} \sim 1.01, \quad (5.13)$$

which goes in the direction of the observed data and has the proper order of magnitude, since in the notation of Sec. 5.5.1 it would correspond to  $a \sim 3 \cdot 10^{-3} \text{ m}^{-1}$  and thus to a shift of  $3 \div 5 \text{ cm}$  downwards (see Eq. (5.11)). A set of measurements performed at the Princeton University in the past showed that such shape modification could be possible. This motivated the development of a setup for a new measurement campaign of the refractive index spectral dependence as a function of the temperature. It is described in the next Sec. 5.5.3.

### 5.5.3 The experimental setup and the measurements

The wavelength dependence of the refractive index was measured at the University of Genova with a commercial setup. It is the ellipsometer “J.A. Woollam M-2000”. Ellipsometry is an optical technique for measuring the change of polarization of light upon reflection or transmission by the medium one wants to study. In the setup used for the measurements described here, photons are emitted by a xenon light source and linearly polarized by a polarizer. The light is then directed on the PC+PPO sample. The fraction of light reflected by the PC+PPO liquid surface is injected into a second polarizer and then into a light sensor. Actually, the Woollam M-2000 allows to perform automatic wavelength scans: a monochromator out of the xenon lamp is able to select light with fixed  $\lambda$ , with a sub-nm precision. The system compares the polarization of the detected light signal to that of the original ray of light. More information on this technique can be found e. g. in Ref. [256].

The system by itself does not allow any temperature control of the sample. Furthermore, the scintillator is very sensitive to the presence of humidity in the air, and thus it must be kept in a controlled atmosphere during the measurement. For these reasons, the glass container filled with the PC+PPO mixture was put in contact with a Peltier cell, so that it can be cooled down with respect to the room temperature (in fact, the temperature in Borexino is in the range  $10 \div 20^\circ \text{C}$ ). The Peltier cell is attached with thermal paste to a copper support, which acts as a heat dissipator. The whole system

is placed inside a closed box<sup>2</sup> which is kept in a nitrogen over-pressure. This allows to prevent oxygen diffusion inside the scintillator and possible humidity condensation on its surface. The temperature is controlled with two sensors, with a precision of 0.1°C, which are placed in two different parts of the sample, allowing to test its thermal stability. The whole system is shown in Fig. 5.11.

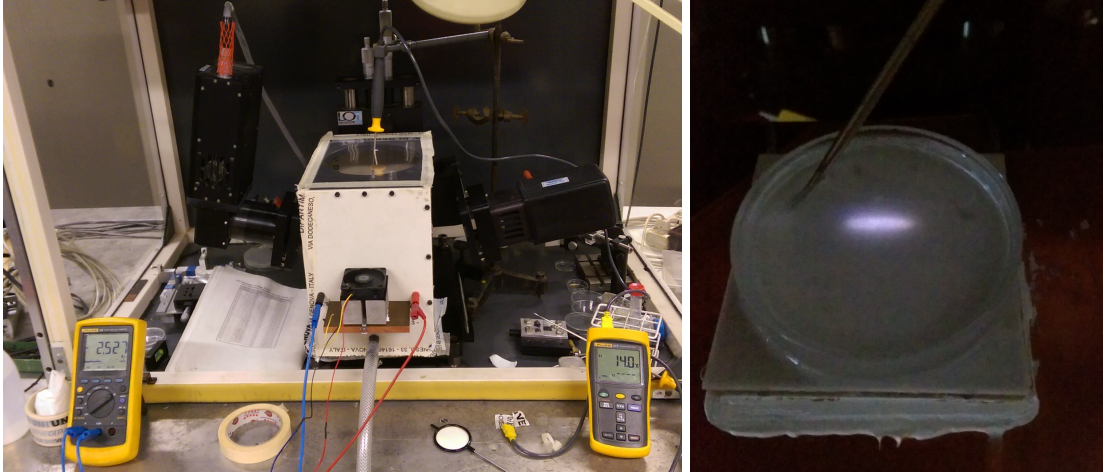


**Fig. 5.11:** *Left Panel:* The box containing the PC+PPO sample is placed in the middle of the ellipsometer system, which in principle was not designed to perform measurements in a controlled temperature condition. *Right panel:* Zoom on the PC+PPO sample. It is contained in a small glass case placed on top of the Peltier cell which is in thermal contact with the copper support. The spot of incident light coming from the ellipsometer is visible. The steel probe measures constantly the sample temperature.

Many consistency checks were performed. The stability of the system was monitored over few hour periods, by repeating the same measurement and comparing the obtained results. This allows to quantify the sensitivity of the system in  $\Delta n \sim 0.005$  for a given wavelength. The absolute response of the detector was checked by performing several measurements on distilled water samples. Critical aspects of the measurement were identified to be the sample stability over time (contamination by oxygen and water condensation) and vibrations of the liquid surface due to external noise. These aspects were anyway taken under control by optimizing the measurement procedure in the preliminary system studies.

The left panel of Fig. 5.12 shows as an example the experimental data points for the PC+PPO index of refraction at a temperature of 12.5°C. The data points are fitted with the Cauchy equation, since it is typically adopted for the description of dispersion relations:

$$f(\lambda) = B + \frac{C}{\lambda^2} + \frac{D}{\lambda^4}. \quad (5.14)$$

<sup>2</sup>Actually, two holes are present, and they allow the light rays of the ellipsometer to come in and out.

The results of the measurement campaign carried out on PC+PPO at different temperatures are shown in the right panel of Fig. 5.12. The data points for each single temperature are fitted according to Eq. (5.14) and the resulting Cauchy curves are reported. No temperature effect on the  $n(\lambda)$  shape is evident with this system setup. However, the density dependence (and thus the temperature dependence) of the refractive index is clearly evident, and it is pretty much the same as that of benzene, as reported in Sec. 5.5.1.

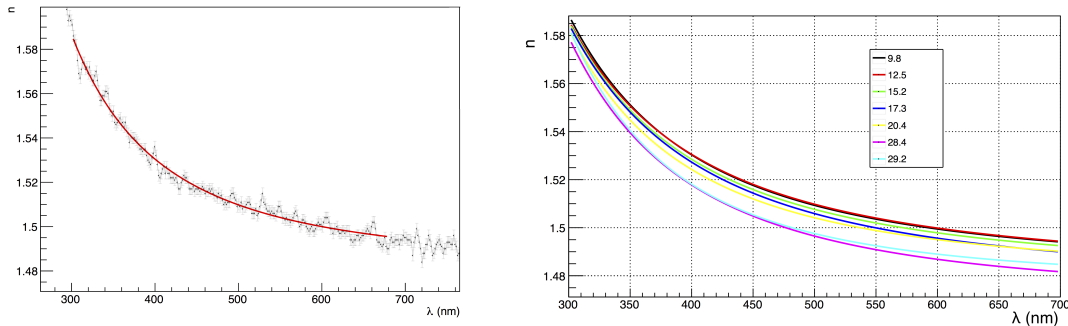


**Fig. 5.12:** *Left Panel:* Example of fit on the refractive index data of PC+PPO at  $T = 12.5^\circ\text{C}$  with the Cauchy formula. *Right Panel:* Set of Cauchy curves resulting from the fits of experimental data for the index of refraction of PC+PPO at different temperatures (in Celsius).

#### 5.5.4 Outlook

The measurements reported in Sec. 5.5.3 seem to exclude the possibility that the  $z$  shift is explained by a consistent variation of the index of refraction, and thus of the group velocity, as a function of the temperature. The density effect is too small and would explain an effect with an opposite sign with respect to what is observed. In order to eliminate all the doubts, a new set of more sensitive measurements is being carried out at the Princeton University, with the goal of reducing the uncertainty down to  $\Delta n \lesssim 0.001$ . The setup used in this case is different, since it is simply a refractometer. Conversely, it can be calibrated more efficiently and thus the expected precisions are very high. It seems reasonable to say that with a low probability a big enough dependence of  $dn/d\lambda$  upon the temperature will be observed in order to explain the  $z$  shift. With this respect, one of the most probable explanations left is that of a problem in the calibration of the CCD camera algorithm. During the next calibration of Borexino, every effort will be made in order to sort out this issue, even if, as already discussed, its impact on all the analyses is totally negligible.

## 5.6 Event generators

Several generators were developed in `g4bx2` in order to properly simulate radioactive decays inside the scintillator, solar neutrinos, anti-neutrinos and radioactive sources

encapsulated in holders such as those used in the calibration campaign. Most of the radioactive decays are simulated by letting the parent decay so that it produces the secondary particles, with Geant4 managing all the involved processes. Unfortunately this is not possible for all the radioactive contaminants, since some of the decays are not easily described theoretically, and thus the Geant4 implementation might be inaccurate. In this section, some details on the event generation procedure are given. However, the details concerning the generation of external background events are described in much greater detail in Sec. 5.10. The procedure for the MC pileup generation is addressed in Sec. 5.11. The development of the algorithms for these two latter spectral components are among the most important achievements of g4bx2.

### 5.6.1 Solar neutrino generation

A dedicated solar neutrino generator simulates their elastic scattering off electrons. The primary solar neutrino energy spectra are those computed by John Bahcall and his collaborators [257]. The electron solar neutrino survival probability is then computed according to Eq. (1.52) and specifically according to Ref. [258]. The mixing parameters are currently those reported in Ref. [259]. Depending on whether the solar neutrino oscillated to a  $\mu$  or  $\tau$  flavor or not, the neutrino cross section as a function of energy with electrons is computed according to Ref. [213]. Then, the recoiled electron energy is sampled from the shape which takes into account radiative corrections and which is presented in Ref. [213].

### 5.6.2 “Special” radioactive decays

Among the radioactive decays which are treated separately from the Geant4 standard approach there are those of  $^{14}\text{C}$  and  $^{210}\text{Bi}$ .

The beta decay of  $^{14}\text{C}$  into  $^{14}\text{N}$  is an allowed ground-state-to-ground-state transition. This decay was investigated both theoretically and experimentally by many groups, but some unsatisfactory features remain. For instance, its anomalously long lifetime with respect to “standard” beta decays has been subject of considerable interest. In addition, there have been different experimental investigations in order to assess the deviations from the expected allowed decay spectrum, since accidental cancellations in the matrix element calculations might cause a non-statistical shape of the spectrum [260]. The g4bx2 generator allows to simulate the  $^{14}\text{C}$  beta decay spectrum with a shape factor, i. e. a quantification of the deviation from the allowed shape, either from Ref. [260] or from Ref. [261].

The  $^{210}\text{Bi}$  decay is a first-forbidden beta decay and thus there is some uncertainty on its spectral shape. In g4bx2, the  $^{210}\text{Bi}$  event generation is handled in such a way that the shape factor can be modified, in order to use the differences between the various models to evaluate the systematics associated to the uncertainty on the decay spectrum. The standard spectral shape is that reported in Ref. [262], which is the only one which can account for uncertainties. Systematics can be evaluated comparing with the spectral shape proposed in Ref. [263], which shows differences of only a few % with the standard

used in `g4bx2`. A new measurement campaign of the  $^{210}\text{Bi}$  spectral shape is being carried out in Dresden within the framework of the Borexino Collaboration, with the aim of improving the current knowledge of this important background both for pep and CNO neutrinos.

As a final remark, the case of  $^{85}\text{Kr}$  is not as important as the two mentioned above, since fortunately in Borexino Phase-II the content of this potentially dangerous contaminant is very low, i. e.  $< 5 \text{ cpd}/100 \text{ ton}$  at 95% C.L. .

### 5.6.3 Positron generator

$^{11}\text{C}$  and  $^{10}\text{C}$   $\beta^+$  decays are described with a custom generator in `g4bx2`, in order to take into account all the physical processes that positrons undergo in the liquid scintillator. They are summarized in Sec. 4.8. From the point of view of the implementation, positrons are generated with an energy sampled from the decay spectrum implemented in Geant4. The code lets them lose energy and produce scintillation photons. When the positron is at rest, it is removed from the simulation, and `g4bx2` decides if the annihilation process goes through ortho- (53%) or para-positronium (47%) formation, generating two back-to-back gammas after a time sampled from an exponential with the proper lifetime (immediately for the para- and 3.1 ns for the ortho-positronium). The gammas are then tracked individually until they lose their energies completely.

### 5.6.4 Anti-neutrino generator

Anti-neutrino detection is important for geo-neutrino investigations and for the Ce-SOX experiment. As discussed in Sec. 4.1, anti-neutrinos are detected through inverse beta decay. Thus, the event generation in the MC is actually split in two separate events. The prompt event corresponds to the generation of a positron with an energy which depends on the anti-neutrino source (geo-neutrinos, reactor neutrinos or neutrinos from the SOX source). The energy spectra for geo-neutrinos are computed from the  $\beta^-$  spectrum of  $^{238}\text{U}$  and  $^{232}\text{Th}$ . Energy spectra of reactor antineutrinos are computed according to Ref. [264]. Regarding SOX anti-neutrinos, the  $\beta$  spectrum of  $^{144}\text{Pr}$  is generated according to Fermi's theory, taking into account corrections for the finite size and mass of the nucleus, weak interaction finite size corrections, radiative corrections, screening, weak magnetism and shape factor as discussed in Ref. [265].

The neutron is emitted together with the positron, but because of the very high quenching of proton and nuclear recoils, the light generation associated to its thermalization is practically null. The delayed event, consisting in the neutron capture by a proton or by a carbon nucleus followed by the emission of a gamma, is completely handled by `g4bx2`. It tracks the neutron until it is captured, and a gamma with the proper energy is emitted. From the point of view of the simulation, the vertex associated to the delayed event is separated from the prompt vertex. The relative time information between the two events is anyhow stored, so that `bxelec` and `echidna` can handle the temporal and spatial correlations between the two events.

### 5.6.5 Radioactive source generator

During the calibration campaign extensively described in Ref. [216] and briefly recalled in Sec. 5.8.1, vials containing radioactive sources were deployed inside Borexino. The information coming from calibrations was essential for the development of the MC simulation of the detector, as it is clear from Sec. 5.8. Therefore, an accurate reproduction of calibration data by simulations needs a detailed simulation of the source containers. This was implemented, in order to match in the code both the geometry and the materials with which the vials were produced. In the case of the  $^{241}\text{Am}$ - $^{9}\text{Be}$  neutron source, it was particularly important to reproduce properly the full geometry of the container, so that neutrons could be captured by the different nuclei surrounding the source and emit all the gammas observed in the real data.

## 5.7 Electronics simulation

`g4bx2` tracks optical photons until they are detected by the PMTs. `bxelec` simulates the electronics chain and the trigger system response, based on the information of the fired PMTs and of the hit times. One of the most important features of `bxelec` is the fact that it simulates the detector electronics following the real detector status over time. Both during the data taking and the offline analysis, the detector is continuously monitored in order to assure the data quality and its stability. Many parameters are recorded in a database which is then used by `bxelec` to simulate on a run by run basis (6h per run) a response as close as possible to the real one. Because of the intrinsic loss of PMTs [214] and since some acquisition boards might be disabled during part of some runs, it is crucial that `bxelec` follows the real time evolution of the PMTs actually running. This happens on an event basis, thanks to the information stored on the database during the standard data taking. Other parameters are obtained offline and due to the need to accumulate some statistics, their implementation cannot occur on a event basis. The dark rate of individual PMTs, the effective QE for each channel and the PMT gains are injected in the simulation on a weekly basis. The knowledge of all these parameters is crucial for allowing `bxelec` to reproduce the status of the detector as a function of time.

### 5.7.1 `bxelec` operation and features

At the initialization phase, the detector status is set: according to the run number, the features of the detector are retrieved from the database. While `g4bx2` simulates events without taking into account the time correlations between events (apart from the prompt-delayed coincidences for the neutron or anti-neutrino interaction simulation), `bxelec` implements the actual flow of time. Dark hits, generated according to the measured dark rate of each PMT, are summed up with the real hits due to scintillation. The typical dark noise rate is below  $\sim 1$  kHz for most of the PMTs.

For each photoelectron recorded at the end of a `g4bx2` event, the code fully simulates the response of the analog and digital electronics chains, which are briefly described in Sec. 4.4. The effective QE associated to the hit PMT is used at this stage to assess if the

photoelectron actually makes it to form a detectable signal. Then, the charge associated to each photoelectron is sampled from an exponential plus gaussian distribution. The specific parameters describing this curve for each PMT (different in the case of dark noise events and real scintillation events) were measured channel by channel, and an example is shown in the left panel of Fig. 5.13. A PMT pulse with that given charge is generated, according to a reference shape for the signal which was acquired directly from the output of the front end. This shape is a mean one and equal for all the PMTs. It is shown in the right panel of Fig. 5.13. The generation of the analog output of the inverted and amplified PMT pulse, as it is produced by the front end, allows the simulation of the double threshold logic of the Laben board discriminators described in Sec. 4.4. For each hit, the PMT transit time spread is simulated, and with a fixed probability of 0.028, the creation of an after-pulse hits is considered. The program reproduces the gate-less integrator circuit present in the front ends as outlined in Sec. 4.4. The 140 ns Laben board dead time is of course included in the simulation. It is crucial to reproduce the response of the front end modules as close as possible to the real one. Otherwise, the simulation of the energy response of the detector as a function of the position of the events and their energy cannot be accurate enough.

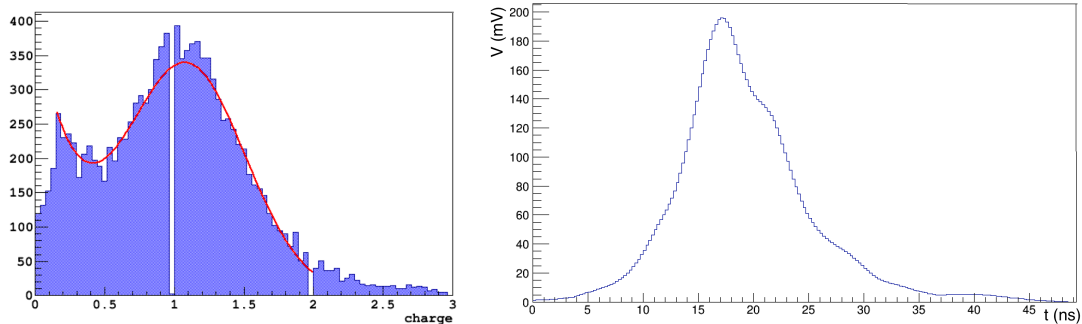


**Fig. 5.13:** *Left Panel:* Example of single photoelectron charge response of a PMT channel in the case of laser calibration events. *Right Panel:* Mean single photoelectron waveform, output of the front end. It is rescaled according to the hit charge and used for the Laben threshold condition evaluation.

A physical trigger in Borexino and in the MC simulation happens when  $N$  hits are detected within a time window  $\Delta t$ . Typically,  $N = 20 \div 30$  and  $\Delta t = 100$  ns. The value of  $N$  changes within the Borexino history (mainly because of the loss of the live PMTs). Run by run, the actual number of  $N$  is correctly taken into account in `bxelec`. `bxelec` also reproduces the time structure of the acquired data which is due to details of the design of the digital boards. This allows the trigger evaluation conditions to be the same both in the detector and in the simulation. There are two different strategies for the search of the trigger condition in `bxelec`: a time flow based one and a “boosted” one. The former consists in letting the time flow with the steps of the time resolution of the trigger board. The condition for the occurrence of the trigger is evaluated as the time flows. This has the advantage of being able to generate a trigger event even if the

“real” event generated with `g4bx2` is not present and the hits are due to the dark rate or the noise. The disadvantage consists in a very slow simulation. The boosted technique, instead, looks for the occurrence of the trigger condition in a time window around the physical Geant4 events. This is much faster, but the generation of the triggered event is related to the presence of the simulated vertex by `g4bx2`. In normal simulations, this is the working condition, while the first one might be useful for trigger efficiency studies.

When the trigger is generated, all the hits within the acquisition gate of  $\sim 16.5\mu\text{s}$  are acquired. The information about the hits is stored in the same way of real data, in order to be processed by the same reconstruction algorithm (`echidna`). For each event, apart from the electronics response of each channel, the information of the “MC truth” (information regarding some input parameters of `g4bx2`) is stored in a dedicated structure, that can be then accessed after the processing of the simulated events through the reconstruction code.

Apart from events temporally related (fast coincidences, neutron captures...), `g4bx2` events are not correlated in time. The temporal information is added by `bxelec`, which assigns a real time to the event, by sampling from an exponential distribution whose time constant can be picked by the user and varies accordingly to the events which are simulated. Multiple scintillation events due to fast radioactive decays may produce events with hits in the same gate, or with a time distance which depends on the physical interactions simulated in `g4bx2`. The MC takes into account this effect: for these special cases, the timing information is copied from `g4bx2` to `bxelec`, which correlates in time the events.

Finally, the code includes the effect of noisy, bad channels and detector inefficiencies by default in a time dependent way. For some studies, it is important to simulate the detector response in the ideal case, i. e. with all PMTs turned on and without any asymmetry due to effective QEs. Such possibility is implemented in `bxelec` and allows to study the deviations in the detector behavior induced mainly by the loss of PMTs.

## 5.8 Tuning of the MC simulation

The precision simulation of scintillation and light propagation requires the knowledge of a large number of input parameters, which characterize all the materials the detector is made of. Among the others, these parameters include attenuation lengths, reflectivity, reemission probability, indexes of refraction and so on. Data acquired during the detector calibration campaigns have been fundamental in order to optimize the MC accuracy and validate it. A brief summary on the calibrations [216] is given in Sec. 5.8.1. Part of the calibration data were used as a tuning sample (to fix the free parameters) while another independent set of calibration data (or data coming from the standard data taking) were used as test of the performance of the simulation. Great care was devoted in simulating the source runs, taking into account all the known non idealities of the detector and its status as a function of time, as discussed in the previous sections.

Most of the parameters inputed in the simulation were measured in dedicated laboratory setups. However, it might be possible that some of the measurements were

not performed in the actual experimental condition of the Borexino data taking. For instance, all the laboratory characterization of the Borexino liquid scintillator might result inaccurate, simply because of the purity of the sample which cannot be as high as that of Borexino (this is the same problem discussed in many occasions when commenting the measurements reported in chapter 3). In addition, some of the parameters are by definition effective (e.g. the reemission probability of Čerenkov photons in the UV region discussed in Sec. 5.4), thus their nominal values have to be slightly adjusted in the simulation.

The main difficulty in the tuning procedure comes from the correlations among the parameters. Most of the physical effects (which are connected to the material properties) are mutually dependent. For example, the energy response is strictly related to the time response, which in turn depends on light propagation effects and transparencies. For these reasons, the tuning was performed iteratively and following the strategy outlined in Fig. 5.14.

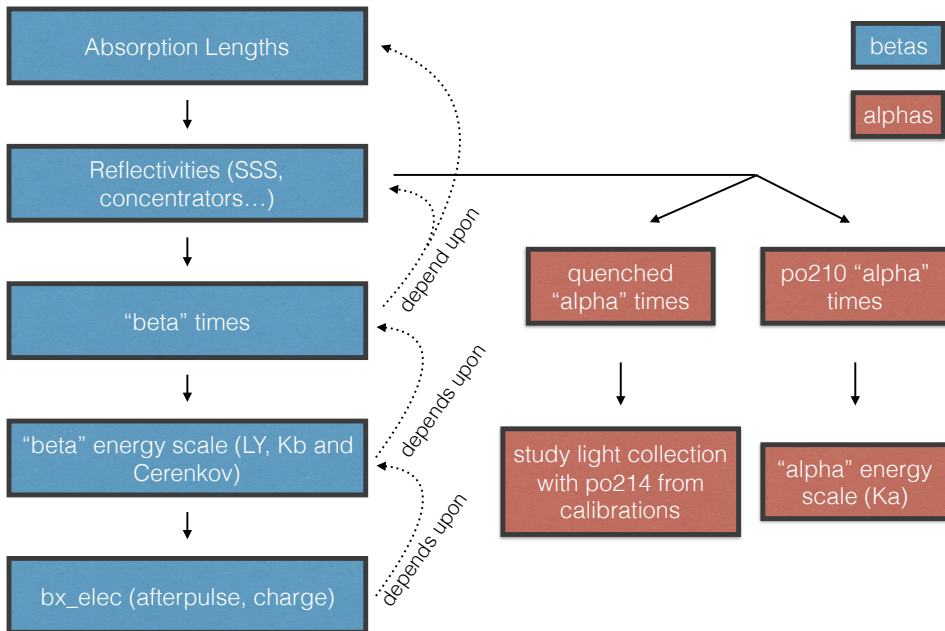


**Fig. 5.14:** Sketch of the “tuning strategy”.

At the beginning, all the parameters are initialized to measured values and a global check of the simulation is performed by direct comparison with results from calibrations. In this condition, the simulated detector response differs from the measured one by at most some tens of percent. As shown in Fig. 5.14, the first step consists in varying the material attenuation lengths and reflectivity, in order to roughly reproduce the light

collection in the various points of the detector. Then, the time response (time constants and weights of the exponentials describing the scintillation) for alpha particles contained in the vial used for calibrations (see Sec. 5.8.1) is tuned, so that these calibration points can be used for a precise tuning of the reflectivity and attenuation lengths. This part of the tuning of the parameters is referred to as “quenched  $\alpha$  times” and “study light collection with  $^{214}\text{Po}$  from calibrations” in Fig. 5.14. The goal for the light collection accuracy was  $\lesssim 1\%$ . Then, the procedure starts from the beginning, using  $\beta$ -like events, and cross checking the time response of the simulation with the tuned parameters for the attenuation lengths (because of absorption and reemission, attenuation lengths influence the time response) and reflectivity. Then, the specific parameters of the scintillation times for  $\beta$ 's and  $\alpha$ 's are tuned, as well as the energy scale. The energy scale for  $\beta$  events is tuned together with some parameters of `bxelec`, since the amount of reconstructed photons depends both on the intrinsic scintillator response and on the electronics. In the next sections, more details on all the steps of the tuning are given, as well as an overview on the calibration campaign.

### 5.8.1 The calibration campaigns

A set of calibration campaigns with various types of radioactive sources inserted into the detector were carried out between 2008 and 2009. In 2010 an external  $^{228}\text{Th}$   $\gamma$  source [266] was placed very close to the SSS (thorough dedicated pipes) in order to study the external  $\gamma$  background. The hardware for a safe, air-tight, clean and accurate deployment of small radioactive sources in several locations within the Borexino active volume is described in [216].

The goals of the Borexino calibration campaigns included:

- measuring the accuracy of the event position reconstruction for events generated in the IV.
- calibrating the absolute energy scale and characterizing the energy resolution with particular emphasis on the solar neutrino energy window.
- studying the non-uniformity of the energy response as a function of the event position and of its energy.
- producing signals mimicking the external  $\gamma$  background.

The radioactive sources deployed within the IV were selected in order to study the detector response in the energy region between 122 keV and 7 MeV with  $\alpha$ ,  $\beta$ ,  $\gamma$  and neutron interactions in the liquid scintillator. In order to avoid the introduction of unwanted contaminations, the source containers were carefully designed. A quartz sphere of 1" diameter was filled either with  $^{14}\text{C}$ - $^{222}\text{Rn}$  loaded scintillator or with  $\gamma$  emitters in aqueous solution. The source vial was attached to a set of stainless steel bars that allowed to locate the source in almost any position within the IV. A special procedure was developed to minimize the quenching of the scintillation light by oxygen for the case of the  $^{14}\text{C}$ - $^{222}\text{Rn}$  source. In fact, being the container sealed outside Borexino, one

can not expect the purity of that scintillator to be as high as that of Borexino's one.  $\beta$  and  $\alpha$  events from the  $^{14}\text{C}$ - $^{222}\text{Rn}$  source have been used to study the accuracy of the position reconstruction and of the uniformity of the energy response in the whole IV volume (light collection). The  $\gamma$  lines provided the absolute energy scale along the whole region of interest. The available  $\gamma$  lines were:  $^{57}\text{Co}$  (122 keV),  $^{139}\text{Ce}$  (165 keV),  $^{203}\text{Hg}$  (279 keV),  $^{85}\text{Sr}$  (514 keV),  $^{54}\text{Mn}$  (834 keV),  $^{65}\text{Zn}$  (1115 keV) and  $^{40}\text{K}$  (1460 keV). A commercial  $^{241}\text{Am}$ - $^{9}\text{Be}$  neutron source was used to study the neutron propagation and capture inside the scintillator. In this case, the vial containing the source was a little more complicated [216], since low energy gamma rays from the source should be shielded before entering the scintillator.

### 5.8.2 Non uniformity of the energy response within the inner vessel

The first step consists in the tuning of the optical attenuation lengths and of some reflectivity of the materials. These parameters mainly influence the non uniformity of the energy response of the detector, i. e. the difference in the amount of light collected by the PMTs when the same scintillation event happens in different positions inside the IV. The candidate events to perform such a study are those coming from the  $^{14}\text{C}$ - $^{222}\text{Rn}$  source, which was deployed in  $\sim 200$  different positions within the scintillator volume. Particularly, the chosen reference is the position of the  $^{214}\text{Po}$  peak. For the reasons discussed above, the precision tuning and study of the light collection could be performed after a preliminary cross check of the performances and after a dedicated tuning of the time response of the scintillator contained in the source vial.  $^{214}\text{Po}$  events are almost point like and have a visible energy which is relatively low (less than 1 MeV,  $\sim 300$   $npmts$ ). This allows to study the effects of the light propagation without caring much of the simulation of electronics effects, since the PMTs are in single photoelectron regime, and thus good energy estimators are  $npmts$  and  $nhits$ , which mildly depend on electronics effects at low energy.

Attenuation lengths as functions of the photon wavelength for PC, PPO, DMP and nylon were measured with spectrophotometric techniques using samples with small volumes of liquid. During the tuning procedure, the absolute values of the attenuation lengths were slightly adjusted by scaling them with a multiplicative factor ( $\Lambda$ ). Other important parameters, which describe the asymmetry in the light collection inside the detector, are the values of reflectivity of the light concentrators and of the SSS. Particularly, the shape of the cones is effective in enhancing the light collection for events in the innermost 3.5 m, whereas the concentration efficiency is not as high for large radii. Besides a good reproduction of the shape, it is crucial that the reflectivity of the aluminum of which the cones are made of and the ratio of specular and diffusive reflections (modeled as Lambertian reflection) are fixed solidly according to the data from calibrations. The key distributions in order to tune these parameters are basically two:

- the ratio of the fired PMTs with and without light concentrators (“cone/no cone ratio”).

- the ratio of the fired PMTs close ( $< 4$  m) and far ( $> 4$  m) from the source (“near/far ratio”).

At this stage, the matching of the absolute value of the fired PMTs between calibration and simulation is not a real concern, and differences of a few percents are tolerated. The fine tuning of the energy scale of the detector is done as a last step. The cone/no cone ratio allows to determine the reflectivity of the inner and outer surfaces of the light concentrators and the specular/diffusive ratio. The same holds for the reflectivity of the steel ring mounted on the PMTs without concentrator. The near/far ratio allows to study the attenuation lengths. Actually, both the attenuation lengths and the reflectivity affect the two ratios at the same time, since the concentrator efficiency depends on the distance of the event from the PMT. For this reason, these two distributions, plus their combinations (such as cone/no cone ratio considered individually for near or far PMTs, or near/far ratio considered for PMTs with concentrator only or for those without) were considered and studied for  $\sim 20$  different source positions all over the IV volume. The statistical estimators considered in order to select the best parameter configurations were the  $\chi^2$  and Kolmogorov-Smirnov tests. Figure 5.15 shows examples of the cone/no cone ratio and near/far ratio distributions for selected points inside the IV. In the plot, the results of the Kolmogorov-Smirnov and  $\chi^2$  tests are also reported. Figure 5.16 shows instead the combination of the two ratios, and particularly the different cone/no cone distributions for near and far PMTs. The two distributions are clearly different and a good reproduction of such behaviors is crucial in order to describe the detector response in the whole volume.

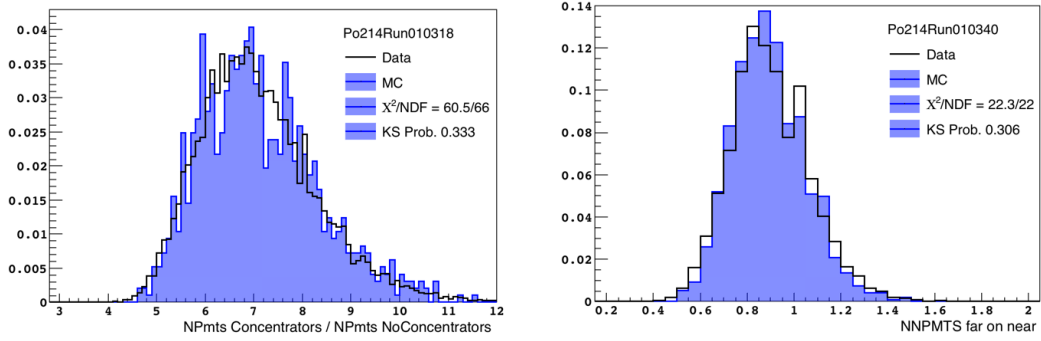


**Fig. 5.15:** Left Panel: MC-data comparison of the cone/no cone ratio in a selected point in the IV. Right Panel: MC-data comparison of the near/far ratio in a selected point in the IV.

The results of the attenuation length and reflectivity tuning are shown in Tab. B.2, where the starting and tuned values are reported. It has to be noted that the values of the reflectivity are also influenced by the time response of the detector (see Sec. 5.8.3) and thus the final result can only be reached through an iterative approach. The precision goal regarding light collection was set to be  $\lesssim 1\%$  and the achieved performance is shown in the left panel of Fig. 5.17, where the relative discrepancy, i. e. in the case of  $npmts$ :  $(npmts_{MC} - npmts_{data}) / npmts_{data}$ , is plotted as a function of the source radial position.

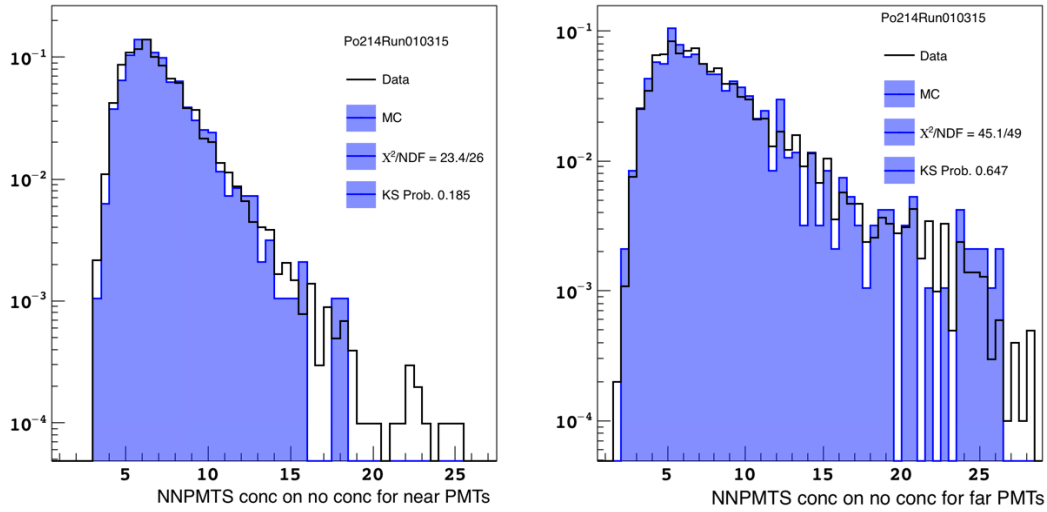


**Fig. 5.16:** Cone/no cone ratios for near (left) and far (right) PMTs.

Inside the 3.5 m sphere, all the points are contained in the  $\pm 0.5\%$  band, thus showing that the goal was reached. In order to reach a so good accuracy, the nylon attenuation length effective parameter, an improved computation of the effective QE and a very precise simulation of the light concentrators and of their optical properties were crucial. The results here presented are much more accurate than those shown in Ref. [214]. The right panel of Fig. 5.17 shows the comparison in terms of absolute values regarding the reconstructed energy (*nhits*) of the  $^{214}\text{Po}$  peak position. It can be seen directly on the data points that the light collection is not uniform inside the whole IV by some percents. Figure 5.17 is relative to the *nhits* energy estimator, but very similar results have been achieved both with *npmts* and *charge*. Regarding this last, it has to be noted that some discrepancies of the order of a few percents are still present at higher energies ( $> 2$  MeV): this has to be investigated and improved in view of SOX, but it is not a real concern for the solar analysis. Furthermore, the fact that the discrepancy is observed only at high energy indicates that probably some electronics detail is not simulated accurately enough.

### 5.8.3 Time distribution of the collected light

The main parameters describing the time response of the detector are the scintillation time constants, the absorption-reemission delays and the electronics response of the detector. In order to decouple the physics of scintillation and light propagation, “low energy” sources in the center of the detector were chosen both for  $\alpha$ ’s and  $\beta$ ’s. This allows to study the response of the system with all the PMTs in the single photoelectron condition. Particularly, for  $\alpha$ ’s,  $^{210}\text{Po}$  events from real data were selected through the MLP discrimination parameter in the innermost 1 m sphere. Regarding  $\beta$ ’s, data

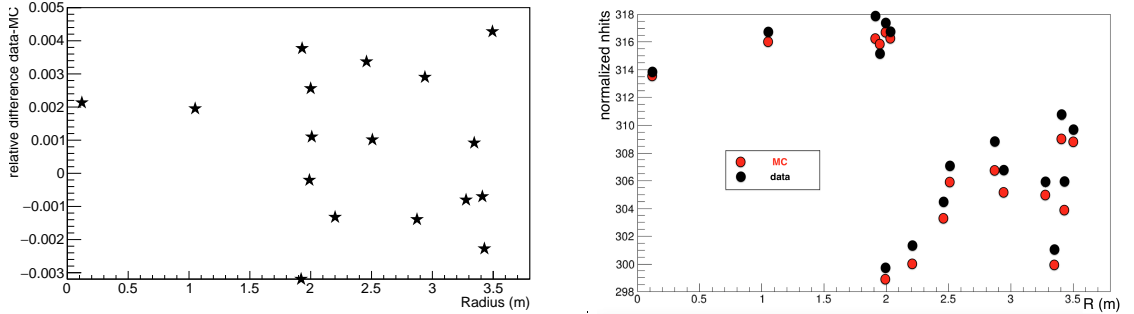


**Fig. 5.17:** *Left Panel:* Relative difference of the  $^{214}\text{Po}$  peak position in MC and data as a function of the radial distance of the source. The statistical uncertainty on the points is around  $\sim 0.1\%$ . *Right Panel:*  $^{214}\text{Po}$  peak position in MC and data as a function of the radial distance of the source.

acquired with the  $^{85}\text{Sr}$  source in the center of the detector were used as benchmark for the simulations. Both the  $^{85}\text{Sr}$  and  $^{210}\text{Po}$  have a visible energy of around  $\sim 200$   $nhits$ , which is relatively low and the electronics effects are minimized. Note that it is not possible to tune the response to  $\alpha$  particles using any of the data from the calibration campaign, since in that case the scintillation happened in the vial and not in the actual Borexino scintillator. The tuning is performed for these classes of events in the center, and then the agreement is checked for different source positions. This allows also to test whether the attenuation lengths were properly selected at the previous stage, since the time response is affected by the amount of absorption and reemission.

The most important variables which were studied in order to fine tune the parameters describing the time response are depicted in Fig. 5.18 and Fig. 5.19. The variables used are very basic, and thus their good reproduction guarantees a good agreement also with more complex variables, which are based on the basic ones. Particularly, the agreement of the decoded hit times distribution was tested it is shown in Fig. 5.18. The plot shows the agreement of the decoded hit times, relative to the first hit identified in the cluster. This curve is the convolution of the four exponential response function used to describe the scintillation process and the simulated absorption and reemissions. It is possible to distinguish the shape due to the sum of the four exponentials, but some additional features are evident, such as the structure at approximately  $\sim 100$  ns, which is due to the reflection of photons on the SSS and the tail at larger times, which is due to the contribution of after-pulse hits and dark noise.

The agreement between the decoded hit time distributions in data and MC assures that all the other variables based on timing (pulse shape discrimination, position reconstruction) are well understood. Figure 5.19 shows the MC-data comparison of other timing variables, based on the decoded hit time distribution, such as mean and RMS time of the hits in the cluster, reconstructed hit time distribution (which means hit time distribution corrected for the time of flight based on the reconstructed position) and  $\alpha/\beta$  Gatti parameter.

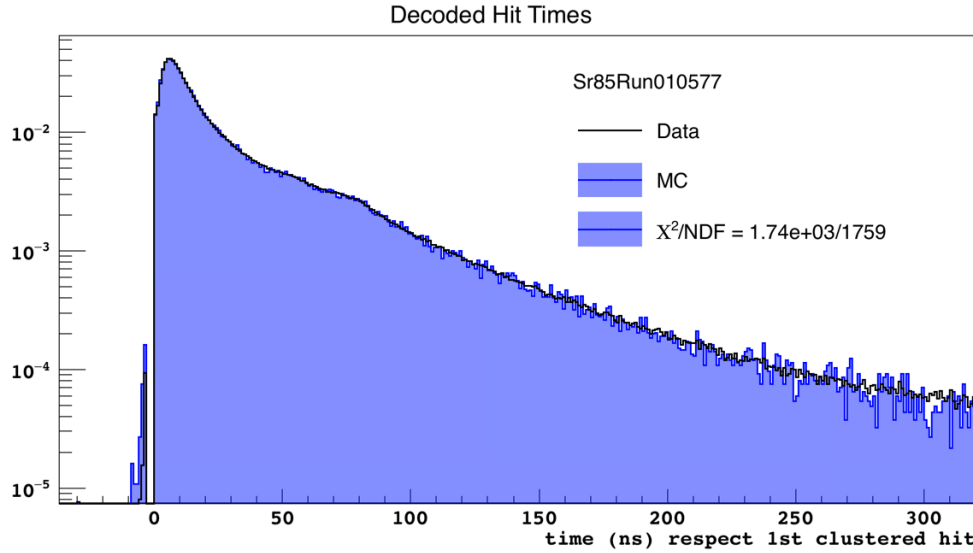


**Fig. 5.18:** Light curve (i. e. decoded hit times with respect to the first hit in the cluster) for  $^{85}\text{Sr}$  events in the center of the detector.

The tests adopted in order to select the best parameter configuration were again the Kolmogorov-Smirnov and  $\chi^2$  tests. The results on the tuning of the parameters are reported in Tab. B.3. The exponential parameters were only slightly adjusted with respect to the experimentally determined ones (coming from Ref. [210]). This is acceptable, because of the different purity of the two scintillators. A very good result is the fact that the MC works already well without any modification of the characteristic times of absorption and reemission. Particularly, the most important parameter in the game is  $\tau_{PPO}$ , which affects significantly the time distribution of photons (most of the primary light is absorbed and reemitted within a few cm from the interaction point).  $\tau_{PPO}$  is quite well established in the literature, and thus the absence of the need of a modification is an argument for the solidity of the optical model of the detector in g4bx2.

#### 5.8.4 The energy scale

The last step of the tuning of the simulation is the reproduction of the absolute energy scale. All the input numbers, apart from the ones describing the quenching and the scintillation times, are common to the  $\beta$  and  $\alpha$  energy response. Crucial parameters influencing the energy scale are the absolute scintillation yield  $Y_0$ , the quenching parameter  $kB$  and the yield of the Čerenkov light. Furthermore, some electronics fine tuning might be required for a high precision simulation of the *charge* variable. As discussed in Sec. 5.4, there is no experimental data available for the  $P_{rem}$  parameter for  $\lambda < 320$  nm. Therefore, this is an effective parameter which allows the tuning of the total Čerenkov emission, given also the fact that the knowledge on the index of refraction in the near UV is not very precise.

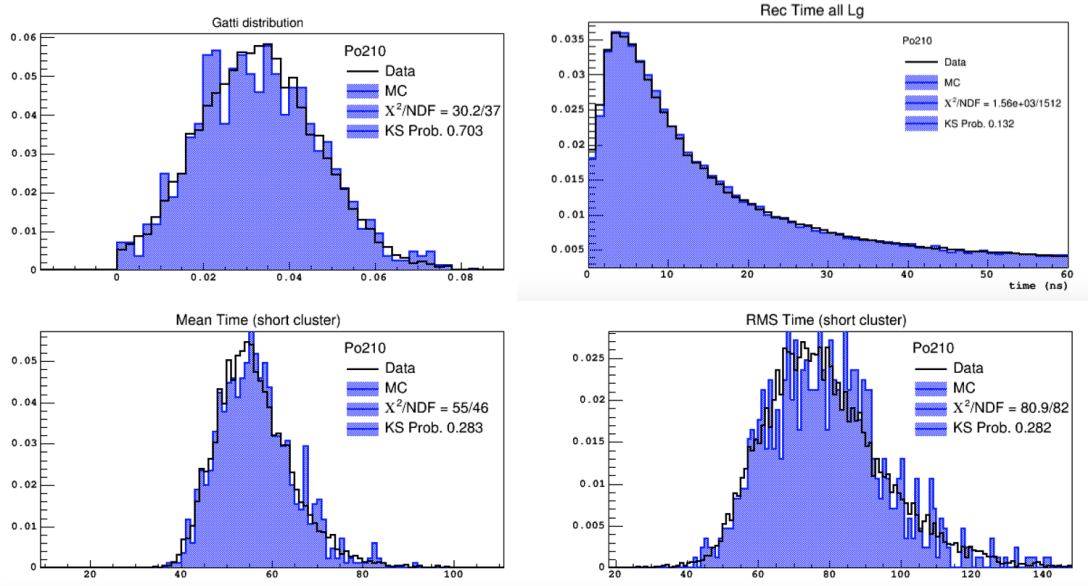


**Fig. 5.19:** Data-MC agreement for some timing variables for  $^{210}\text{Po}$  events in the center. In the top left panel the  $\alpha/\beta$  Gatti distribution is shown, the top right panel contains the reconstructed hit time distribution (hit time distribution corrected for the time of flight), the bottom left (right) panel shows the mean (RMS) time of the hits in the cluster.

The reproduction of the energy response of  $\beta$  particles was optimized varying the light yield  $Y_0$ , the quenching factor  $kB$ , the reemission probability at low wavelengths and the “pmtgainscale”, which is an overall multiplicative parameter rescaling the simulated single photoelectron gains of the PMTs. This is needed since the lack of some details in the electronics simulation might require a few percent adjustment. In particular, it is necessary to overcome the approximation in `bxelec` for which the reference shape for the pulse of the PMTs is unique for all the channels. All the other parameters in the simulation were kept fixed and the measured energy estimators were compared with the simulated ones for events in the center of the detector. A comparison of the  $\gamma$  peak positions for the `nhits` and `npmts` variables are shown in Fig. 5.20. The goodness of the agreement is comparable also for the `charge` variable for  $E \lesssim 2$  MeV, but a detailed discussion is not carried out here, since for the analysis presented in this PhD thesis, the `nhits` and `npmts` variables are more relevant (see the discussion in chapter 6).

The energy spectra of  $^{57}\text{Co}$ ,  $^{139}\text{Ce}$  and  $^{203}\text{Hg}$  overlap with the tail of  $^{14}\text{C}$  spectrum. A volume cut is not sufficient to obtain clean peaks and thus a proper subtraction of background events (evaluated with dedicated runs before and after the source insertion) was performed. The agreement between data and simulation is evaluated comparing the reconstructed energy peaks of each gamma source. They are fitted with a Gauss function plus a constant (the irreducible background due to radioactive decays or neutrinos) to obtain the mean value and the RMS of the energy estimator. The goodness of the energy

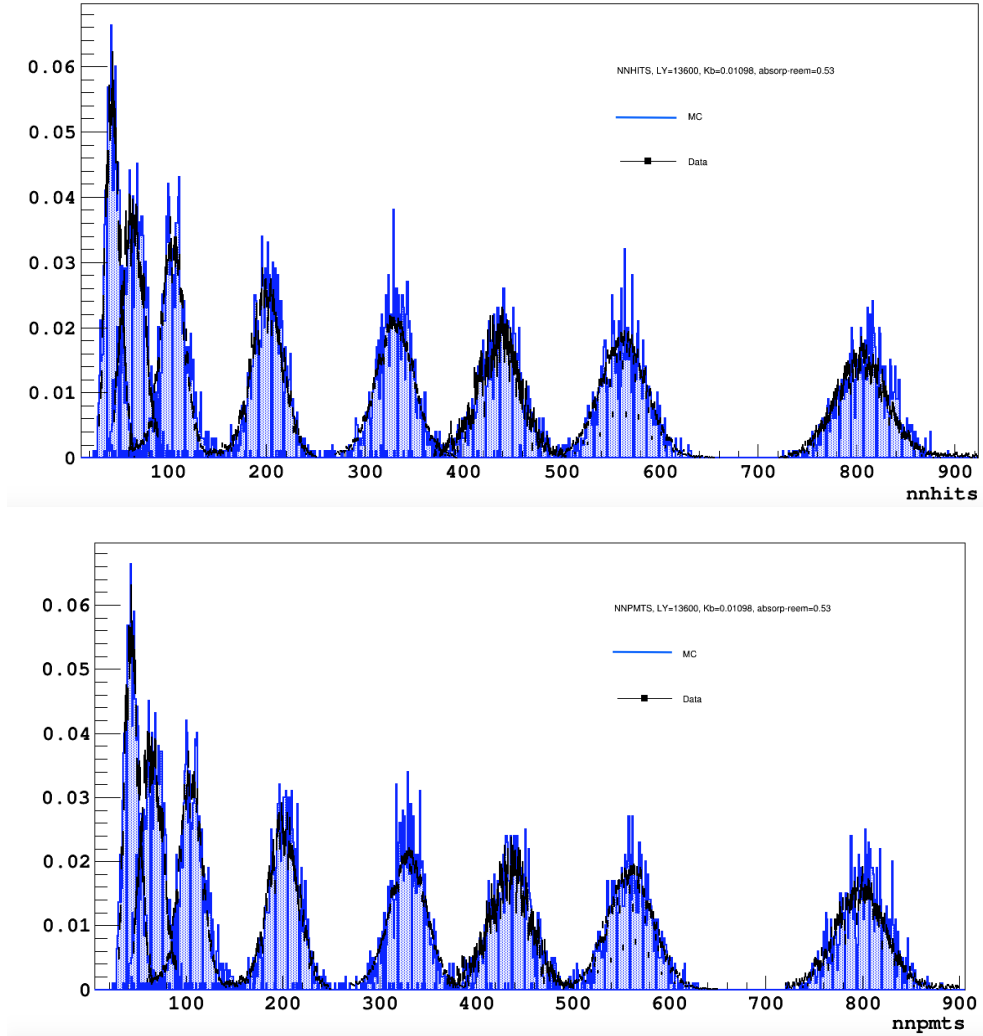


**Fig. 5.20:** *Top panel:* Data-MC agreement for the  $nhits$  energy estimator for the  $\gamma$  sources listed in Sec. 5.8.1 with the addition of the 2.22 MeV gamma events from the neutron capture of the  $^{241}\text{Am}$ - $^{9}\text{Be}$  source in the center of the detector. *Bottom Panel:* Data-MC agreement for the  $npmts$  energy estimator for the  $\gamma$  sources listed in Sec. 5.8.1 with the addition of the 2.22 MeV gamma events from the neutron capture of the  $^{241}\text{Am}$ - $^{9}\text{Be}$  source in the center of the detector.

simulation was defined as [267]:

$$\epsilon = \sum_{sources} \frac{(\mu^{data} - \mu^{MC})^2}{1 + e_{\mu^{data}}^2 + e_{\mu^{MC}}^2}, \quad (5.15)$$

where  $\mu$  is the mean value of the Gauss function from the fit (i.e. the peak position in the energy spectrum) and  $e_\mu$  its error. The optimized set of  $Y_0$ ,  $kB$ , reemission probability and pmtgainscale was been found looking for the minimum value of  $\epsilon$ . This procedure

was followed for each energy estimator (*nhits*, *npmts* and *charge*) and the result does not depend on the energy estimator used.

The required precision of the energy reconstruction is found to be  $\lesssim 1\%$  on the peak position reconstruction. All the sources are reproduced in the center of the detector with a precision better than 0.8%. The results on the tuned parameters are given in Tab. B.1.

The procedure is then repeated once again for the  $\alpha$  particles. In this case, only the quenching parameter ( $kB_\alpha$ ) is free, being all the others fixed by the previous iteration. Since during normal Borexino data taking it is possible to measure non negligibly  $\alpha$ 's coming only from  $^{210}\text{Po}$ , a Birks model with only one parameter is more than enough to describe the  $\alpha$  energy scale (the result on  $kB_\alpha$  is reported in Tab. B.1). However, if one compares the peak positions of other  $\alpha$  contaminants present in Borexino during operations (e. g.  $^{214}\text{Po}$  events), it is clear that a single Birks parameter cannot describe the whole response. A second order Birks model where the light yield is computed as

$$L(E) = Y_0 \int_0^E \frac{dE}{1 + kB_1 \cdot dE/dx + kB_2 \cdot (dE/dx)^2} \quad (5.16)$$

would be needed. This has not been investigated further, since it is of no practical importance for the analysis reported here, and since it does not make much sense to tune a model with two parameters with (in practice) two experimental points.

### 5.8.5 Outlook

The good performances in the light collection and detector response reproduction are crucial in order to simulate the spectral response of neutrinos and backgrounds in Borexino. The next sections and chapters demonstrate that despite the tuning was performed using calibration data from 2009  $\div$  2011, the MC simulation is able to reproduce the detector response very well until 2016. Within this amount of time, the detector has been quite stable, but many things changed (mostly PMTs died). Particularly, the energy response, which was tuned for events in the center, can reproduce automatically, without the addition of any other parameter, the spectral shape of the volume-distributed components inside Borexino. Furthermore, all the tuned parameters have values which are physical and not unreasonable, thus demonstrating the solidity of the whole simulation modeling. A few details can still be improved (e. g. the *charge* response at high energy and for “large” radii), but they are not of any concern for what regards the solar neutrino analysis. In the next sections, the good results of the tuning are used in order to develop new methods for exploiting the MC simulation and reproduce the most difficult features of the Borexino energy spectrum.

## 5.9 $^{210}\text{Po}$ simulation

A solid simulation of  $^{210}\text{Po}$   $\alpha$  events is very important in Borexino. In fact,  $^{210}\text{Po}$  is the most abundant background in Borexino (after the intrinsic  $^{14}\text{C}$ ) and it is crucial for a proper measurement of  $^7\text{Be} \nu$ . The key issues concerning the  $^{210}\text{Po}$  simulation are its non uniformity both in space and in time, which were discussed in Sec. 4.9.1 and Sec. 4.9.3.

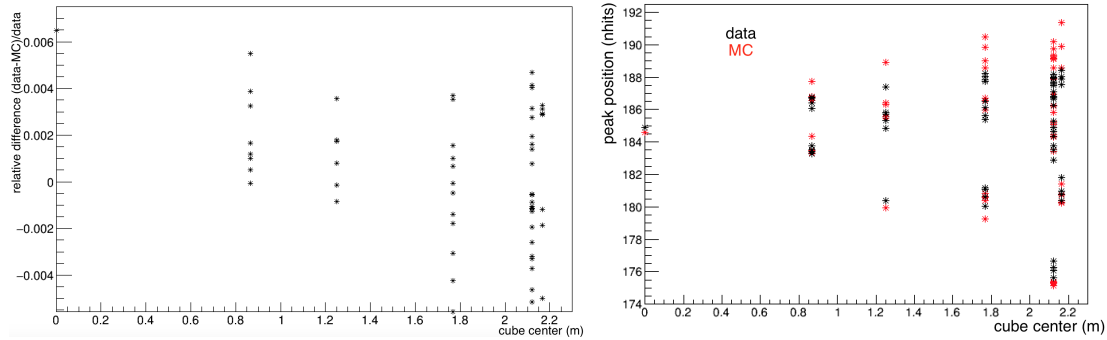


**Fig. 5.21:** *Left panel:* Relative difference between the  $^{210}\text{Po}$  peak position in MC and in data as a function of the cube center position (radius from the center of the detector). The cubes cover completely the innermost 3 m of Borexino’s IV. *Right Panel:*  $^{210}\text{Po}$  peak position in MC and in data ( $nhits$ ) as a function of the cube center position (radius from the center of the detector).

The non uniformity in space together with the small asymmetries in the light collection performance of the detector lead to a modified spectral shape for  $^{210}\text{Po}$  with respect to the “ideal case” of uniform response and background density. The non uniformity in time is intrinsic of the  $^{210}\text{Po}$  contaminant, and it is due to its natural decay and to the fact that towards the end of Borexino Phase-II the count rate induced by  $^{210}\text{Po}$  is quite low (comparable to those of solar neutrino fluxes). An ideal detector, without any time dependence, would not respond differently to different amounts of  $^{210}\text{Po}$ , but after almost 10 years of operations, Borexino experienced a quite significant loss of live PMTs, which results in a different energy response. Furthermore, the PMT deaths also affected the light collection efficiency, since the distribution of dead PMTs changed over time (in the first years, the most of the dead PMTs were at the bottom of the detector, while in the last years the situation evolved towards a more uniform distribution). In the past, this situation was handled by using effective quenching and resolution for  $^{210}\text{Po}$  events. In fact, asymmetries of  $^{210}\text{Po}$  lead both to a different position of the  $\alpha$  peak and to a broadening which cannot be explained with the intrinsic resolution of the detector. The accurate tuning and the precise performances of `g4bx2` and `bxelec` allowed to overcome the need of effective parameters and a very good agreement in the reproduction of the  $^{210}\text{Po}$  peak shape was obtained without any change with respect to what was found after the tuning.

The procedure for a proper simulation of  $^{210}\text{Po}$  events in `g4bx2` consists in simulating events with the same distribution of real events. This is subordinated to a good reproduction of the light collection and of the detector time behavior. On a monthly basis, real  $^{210}\text{Po}$  events are tagged in the detector in cubes (such as those mentioned in Sec. 4.9.3) thanks to the MLP tagging together with energy cuts. For each cube and each month, the number of the events is saved. When simulating the total  $^{210}\text{Po}$  spectral shape for a long period of time, for each run which is simulated (each real run corresponds to  $\sim 6$  hours), the events are simulated according to the measured number of events and

to the measured spatial distribution. A special generator was developed to pursue this goal. Events were selected in 59 cubes (Sec. 4.9.3) both in data and in the MC and the agreement is good (see Fig. 5.21), even better than the goal of 1% accuracy. The demonstration that the technique is solid also for reproducing the time evolution of the detector and  $^{210}\text{Po}$  events comes from the spectral shape used to fit the Borexino energy spectrum, as widely discussed in chapter 6.

## 5.10 External background simulation

In the “high energy” region of the solar neutrino spectrum (i. e. above  $\sim 1$  MeV in terms of electron recoil energy), one of the most important background in Borexino is due to external gammas, traveling from the SSS and the PMTs and reaching the FV. Regarding the pep  $\nu$  and CNO  $\nu$  analyses, apart from the internal  $^{210}\text{Bi}$  tail and the cosmogenic  $^{11}\text{C}$ , external gammas are the most critical components in the background budget. The SSS, the PMTs and the light concentrators are contaminated by non negligible amounts of  $^{232}\text{Th}$ ,  $^{238}\text{U}$  and  $^{40}\text{K}$ , as described in Sec. 4.3. Gammas from  $^{40}\text{K}$  and from the daughter nuclides  $^{208}\text{Tl}$  and  $^{214}\text{Bi}$  can reach the innermost part of the detector. Thus, the knowledge of the energy spectra of these external backgrounds is of great importance. However, a standard MC simulation approach for producing a high statistics sample of events from external backgrounds in the FV is not feasible. The attenuation length of a few MeV  $\gamma$  traveling in Borexino’s scintillator was estimated to be  $\sim 23$  cm from calibration data. Consequently, due to the suppression produced by the buffer liquid, the primary  $\gamma$  flux is reduced by a factor  $\sim 10^{13}$ , meaning that if one needed a few thousands events reaching the innermost volume, around  $\sim 10^{16}$  events should be simulated. This is possible in theory, but it is not in practice, with only a few hundreds CPUs available for a few months. Conversely, it is not possible to simulate  $\gamma$ ’s simply closer to the FV, since the energy spectrum is pretty much affected by the Compton degradation of the  $\gamma$  energy in the buffer. Furthermore, the vessel shape affects in a significant way the visible light which is collected for each event. In fact, the primary  $\gamma$  generation is supposed to be uniform all around the PMTs and the SSS, but the vessel is deformed, thus leading to a different distance traveled by the  $\gamma$ ’s before reaching the scintillating volume as a function of the  $z$  coordinate. In the past, these problems were overcome by generating events on the SSS and on the PMTs, but artificially tracking only the gammas which were moving towards the center [214]. This strategy allowed to produce a reasonable sample of events in the FV, but still it was not efficient enough for a really massive event production throughout many years of Borexino data taking. Furthermore, although the output of the simulation was carefully checked with calibration data and turned out to be satisfactory, the cuts implemented in order to select only “interesting” events were somewhat arbitrary. For these reasons, in `g4bx2` a novel approach was developed, in order to eliminate these problems and have a more efficient simulation production. The method is based on standard variance reduction techniques, with some dedicated modifications in order for it to comply with the Borexino simulation needs. In practice, the simulation is *biased* in a controlled way so that the

effect of the shielding induced by the presence of the buffer can be studied efficiently.

### 5.10.1 Biassing strategy: importance sampling

Event biassing techniques are methods for accelerating simulations of useful events at the expense of the reproduction of accurate fluctuations. “Analogue simulations” use *real* probability density functions (PDFs) to generate correct mean and fluctuations for the parameters of interest. They often include a significant fraction of events or vertexes which are not interesting for the final analysis, i. e. the net efficiency is not as high. “Biased simulations” replace the *real* PDFs with artificial ones, enhancing the production of interesting events. In this way, the MC efficiency is much higher, but the primary distributions are not correct: they must be corrected by weights which take into account the applied biassing. Typically, two classes of biassing techniques are provided by simulation algorithms such as Geant4 [248]. It is possible to apply a “geometrical or acceptance biassing”, which suppresses/enhances events on the basis of the coordinates in the setup, or a “physics biassing”, which allows to modify the production of primary or secondary particles by changing relative branching ratios. In the case of a “passive” shielding, such as that of Borexino’s buffer liquid, the most appropriate approach is that of the geometrical biassing.

The importance sampling is an implementation of a geometrical biassing approach, which was implemented in `g4bx2`. Its purpose consists in saving computing time by sampling less often particles entering “less important” geometry regions, and more often those in “more important” regions. The strategy adopted in `g4bx2` is depicted in the left panel of Fig. 5.22. Geometrical portions of the detector are assigned different “importances”,  $I_n$ . The implementation of the assignment of importances is usually done through a parallel geometry in the simulation code, where the detector is divided in sub-volumes ( $V_n$ ) each of them linked to  $I_n$ . If one assumes  $I_{n+1} > I_n$  and a particle going in the direction  $V_n \rightarrow V_{n+1}$ , at the boundary between  $V_n$  and  $V_{n+1}$  the algorithm splits the original track in  $I_{n+1}/I_n$  different particles. If  $I_{n+1}/I_n$  is not integer, a number of  $\text{int}(I_{n+1}/I_n)$  tracks is created, while an additional particle is added with a probability  $I_{n+1}/I_n - \text{int}(I_{n+1}/I_n)$ . In order to preserve probabilities, the new tracks are assigned a weight  $w = I_n/I_{n+1} \times w_0$ , where  $w_0$  is the weight of the original particle coming out of  $V_n$ . Newly generated particles (not by the biassing algorithm, but by “real” physical events) have  $w_0 = 1$ . If the particle is traveling the opposite direction, namely from  $V_{n+1}$  to  $V_n$  with  $I_{n+1} > I_n$ , then the Russian roulette is played. This consists in killing the particle at the  $V_n - V_{n+1}$  boundary with a probability of  $1 - I_n/I_{n+1}$ . This procedure allows to privilege particles accessing more interesting physical regions of the detector. The information on the weight of the track is crucial, in order to reconstruct the real physical distributions out of the biased ones, and thus remove the distortions induced by the biassing. The choice of the volumes  $V_n$  and of the relative importance between different volumes ( $I_{n+1}/I_n$ ) must be performed taking carefully into account the particle, physical processes and materials involved in the simulation. If the relative importance is too low, or the volumes are too “big”, the algorithm might be inefficient, since particles cannot propagate through the shielding, but they are stopped pretty soon. On the other

hand, if the importance volumes are too “small” or the relative importance is too high, the number of tracked particles might explode, thus yielding to a never ending simulation in the worst case, or to a huge amplification of the primary statistical fluctuations at the end of the simulation. The best strategy is to fine tune the importance values and the parallel geometry by assuring that the number of tracked particles is more or less constant along the shielding which needs to be studied. This guarantees a good performance of the simulation code and the statistical fluctuations observed after the shielding are of the same amplitude of the primary ones (and thus related to the primary event generation statistics). For these reasons, a careful fine tuning of the choice of the volumes and of the importances is important. However, it must be noted that this tuning operation is not related to physics and the importance values are not physical parameters. The tuning is needed only for a proper and efficient operation of the algorithm.

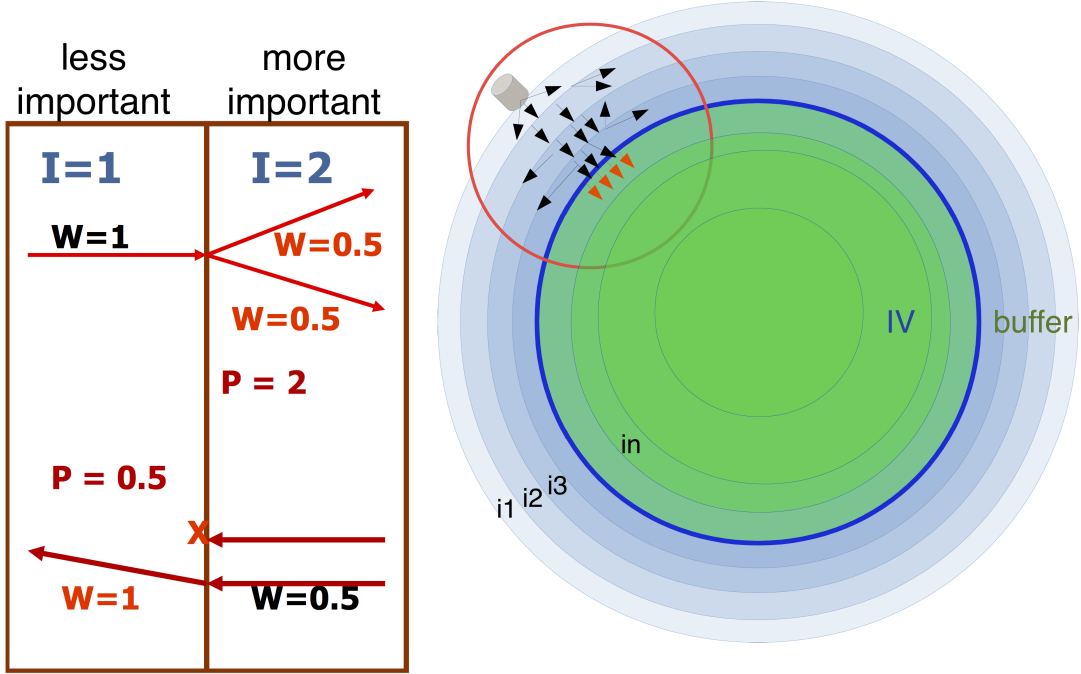


**Fig. 5.22:** *Left panel:* Diagram illustrating the importance sampling technique implemented in g4bx2, where particles entering “more important” regions are split, and for those going towards “less important” ones the Russian roulette is played. *Right Panel:* Parallel geometry implemented in g4bx2 for the proper biased simulation of external  $\gamma$ ’s.

The right panel of Fig. 5.22 shows the parallel geometry implemented for the external  $\gamma$  simulation in Borexino. The whole volume inside the SSS is divided in 1000 concentric shells with (geometrically) increasing importance. The optimal values found for the relative importance of the shells (i.e.  $I_{n+1}/I_n$ , with  $n = 0$  indicating the SSS and  $n = 1000$  the innermost sphere) are 1.032 for  $^{208}\text{Tl}$   $\gamma$ ’s, 1.036 for  $^{214}\text{Bi}$   $\gamma$ ’s and 1.04 for  $^{40}\text{K}$   $\gamma$ ’s.

### 5.10.2 Steps of the simulation

Besides the tracking of  $\gamma$ 's and of their energy deposits in the scintillator, the biased simulation must take care of the optical photons associated to the energy releases. It is not possible to perform the full simulation in one single step, handling all the different needs at the same time (from the biasing of  $\gamma$ 's to tracking of optical photons). For this reason, an automatic script allows to run `g4bx2` three times, in different modes, in order to produce the final output of the external background simulation. The different steps, all of them handled by `g4bx2`, are:

1.  $\gamma$  tracking: in this mode, `g4bx2` tracks  $\gamma$ 's from the SSS or the PMTs towards the center with the biased importance sampling turned on.
2. visible deposits generation: primary  $\gamma$  interactions are reconstructed starting from the biased output, and the visible energy associated to each energy deposit is computed.
3. light generation and tracking: according to the energy deposits, optical photons are generated and tracked, generating the “real” scintillation event.

In the  $\gamma$  tracking mode,  $\gamma$ 's are propagated according to the parallel geometry depicted in the right panel of Fig. 5.22. Every time a  $\gamma$  track interacts with electrons inside the IV scintillator (and thus there is a non negligible light generation) by Compton, photoelectric, Rayleigh or couple production effects the information of the vertex is saved in an entry of a `TTree` (“biasing output”). This procedure discards events which are fully contained in the buffer: these events have a very low visible energy and thus they practically do not generate signals which are able to trigger the detector. As discussed in Sec. 5.11, it is important to simulate also the effects of external  $\gamma$ 's in the buffer for the MC pileup production. Thus, with a simple flag, it is possible to save the energy releases in the whole volume inside the SSS and not only for those events releasing some energy in the IV. The energy, momentum, position and the associated weight  $w$  of the incoming  $\gamma$  and of the scattered electron are recorded. Once all the primary particles are processed, `g4bx2` reads the entries of the biasing output `TTree` just created and reconstructs the vertexes of all the energy releases belonging to the same  $\gamma$  track. This operation must be done after the whole tracking of particles by the biased algorithm, since at every parallel geometry boundary, a track is split with some probability. Therefore, the whole event must be tracked before being able of reconstructing the individual tracks. At the end of the  $\gamma$  tracking step, a second `TTree` (“biasing reduced”) object is filled with objects called `BxBiasedEvent`, which comprise the information about the whole energy deposits due to each track, i. e. type of interactions, position and energy of the scattered electrons or created positrons. One of the most important parameters associated to each `BxBiasedEvent` is the weight, which allows, in the end, to take into account the biasing effects on the distributions. The net output of this first step is the biasing reduced `TTree`, containing many `BxBiasedEvent` objects, in no particular order. These are the raw “reference” events from which the final vertexes will be selected and fully simulated.

In real simulations, the biasing reduced **TTree** is produced with high statistics for each week of data taking, since the only time dependence which is present at this stage of the simulation is the vessel shape evolution that affects the external  $\gamma$  energy and radial distributions (see Sec. 5.10.4).

The visible deposits generation is a step which allows to produce the final reference **TTree** (“biasing filtered”), used in the end for producing the final simulation output. The biasing reduced **TTree** is read, and for each **BxBiasedEvent** entry, the energy deposits are read and the visible energy (i. e. the amount of light to be produced) both accounting for Čerenkov and scintillation is computed. During this step of the simulation, no physical processes or geometrical objects are simulated, in addition to computing the amount of light associated to each energy deposit. The simulation at this step is not biased, and all the entries of the biasing reduced **TTree** are processed. The information thus calculated is saved in another object, called **BxBiasedDeposits**, which contains the details on the visible energy deposits and on the event weight. Meanwhile, the weights of each **BxBiasedDeposits** are read and a special binary file, which contains the cumulative distribution of the weights as a function of the entry number of the events in the biasing filtered **TTree** (which is the same of that of the biasing reduced **TTree**), is produced. This cumulative distribution allows the third step of the simulation to select the events contained in the biasing filtered reference with a radial distribution which is corrected for the biasing alteration. A possible source of technical trouble, which was solved in the case of **g4bx2**, is the precision of commonly used float or double variables of standard operating systems. In fact, the weights are numbers which span a very huge range in terms of orders of magnitude: at least as many as those of the shielding flux reduction. In Borexino’s case, the shielding factor is around  $10^{13}$ , which means that at least (but possibly more) 13 digits of the cumulative distribution are needed. Single precision floating point numbers have around  $6 \div 9$  digit precisions, while double precisions variables are slightly better (at maximum 16), but when combining the numbers, results of arithmetical operations might be unpredictable. For this reason, the Boost libraries [268] were included in **g4bx2**, allowing to handle numbers with at least 20 stable, significant digits.

The light generation and tracking step is the last one and allows to get the final output of the external background simulation. The necessary inputs in order to perform this step are the biasing filtered **TTree** and the binary file which contains the cumulative weight distribution as a function of the event number. A special generator shoots a random number  $rnd$  uniformly in the range  $(0, C_{max})$ , where  $C_{max}$  is the maximum (the last) value of the weight cumulative distribution. According to the cumulative distribution, the event number associated to  $rnd$  is picked and the corresponding **BxBiasedDeposits** in the biasing filtered **TTree** is loaded. At this point, optical photons are generated and tracked exactly as in the case of standard simulations. At the end, **bxelec** and **echidna** are also run. As anticipated previously, for the massive production of these events, usually the first two steps are performed for data sets equivalent to one week long periods of time because of the vessel shape. Events are then selected according to the cumulative weight distribution and processed on a run basis only for the last step.

### 5.10.3 Further optimization strategies

Figure 5.23 shows the radial distribution of  $^{208}\text{Tl}$  events originating on the SSS and propagating towards Borexino's center. This information is obtained after the  $\gamma$  tracking mode of the biased simulation chain. The plot on the left panel shows the  $\gamma$  interaction positions without any weight correction. As an estimator for the position, a barycenter of the visible energy deposits (energy barycenter) is considered:

$$\vec{R}_{bar} = \frac{\sum_i \vec{r}_i E_i}{\sum_i E_i}, \quad (5.17)$$

where  $i$  runs over all the visible energy deposits for a given event,  $\vec{r}_i$  is the position of the  $i$ -th deposit and  $E_i$  its visible energy. The maximum radius for which events are recorded is around the vessel radius (4.25 m), since only events with at least one energy deposit in the IV are recorded. Therefore, the energy barycenter falls inside the IV volume, being the buffer highly quenched. The left panel of Fig. 5.23 shows clearly that the importance value and the parallel geometry definition are chosen so that the mean number of particles at a given radius is more or less constant. The spike around the vessel border is due to events mostly contained in the buffer, but with a small deposition in the scintillator, thus giving rise to an event excess close to the IV boundary.

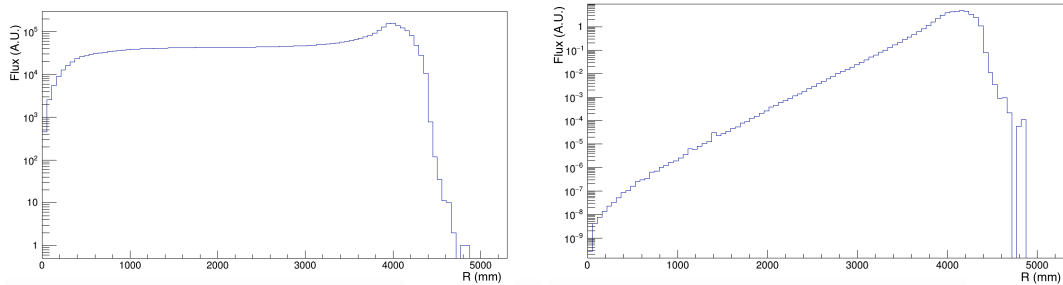


**Fig. 5.23:** *Left panel:* Radial positions of the gamma interaction points after the biased step of the simulation, without taking into account the track weights. *Right Panel:* Radial positions of the gamma interaction points after the biased step of the simulation, corrected for the track weights.

The right panel of Fig. 5.23 shows the energy barycenter radial distribution when the correction of the track weight is applied. This allows to consider the multiplication of the tracks induced by the biasing algorithm. As expected, the distribution is exponential to a very good approximation and it spans several orders of magnitude, even considering only the IV volume.

The definition of the energy barycenter given in Eq. (5.17) is useful since it can be adopted in order to further increase the algorithm efficiency. In fact, when performing the last step of the simulation, events are chosen according to their weights and have a radial distribution very close to that shown in the right panel of Fig. 5.23. In practice, most of the events have a visible energy barycenter which lies very close to the IV border, while common FVs used in solar neutrino analyses consider radial cuts of  $\lesssim 3$  m (see Sec.

6.2.2). Therefore, it is possible to preselect events based on a cut on the visible energy barycenter. This operation might seem to bias the final results, but for spherical FVs of 3.5 m radius, a visible energy barycenter cut of 4 m is already very safe and does not introduce any bias, as shown in the comparison plots in Sec. 5.10.4.

In the case of the MC pileup production (see the more extended discussion in Sec. 5.11), it is important to simulate the light generation by external  $\gamma$ 's in the buffer. Therefore, in this case no cuts are applied, neither on the selection of events which have at least one energy deposit in the IV nor on the visible energy barycenter. The radial distribution of this class of events (starting from the SSS and already corrected by the biasing effects, by taking into account the track weights) is shown in Fig. 5.24. If one considers the distribution where no cut on the total visible energy of the events is applied, the total shielding factor of the scintillator is around  $10^{15}$ : the algorithm implemented in g4bx2 is able to handle quite efficiently the simulation through such a huge primary flux reduction. The various curves shown in Fig. 5.24 highlight the effect of a cut on the visible energy of the events on the radial distribution. This is equivalent to an energy cut (or simply a threshold effect both in triggering or in clustering) applied to the *npmts* or *nhits* energy estimators. Most of the external  $\gamma$  events happen in the buffer, where the scintillation is highly suppressed. Conversely, external  $\gamma$  events in the IV (and even more in the FV) are for sure energy degraded on average due to Compton scattering in the buffer, but they have quite high visible energy.

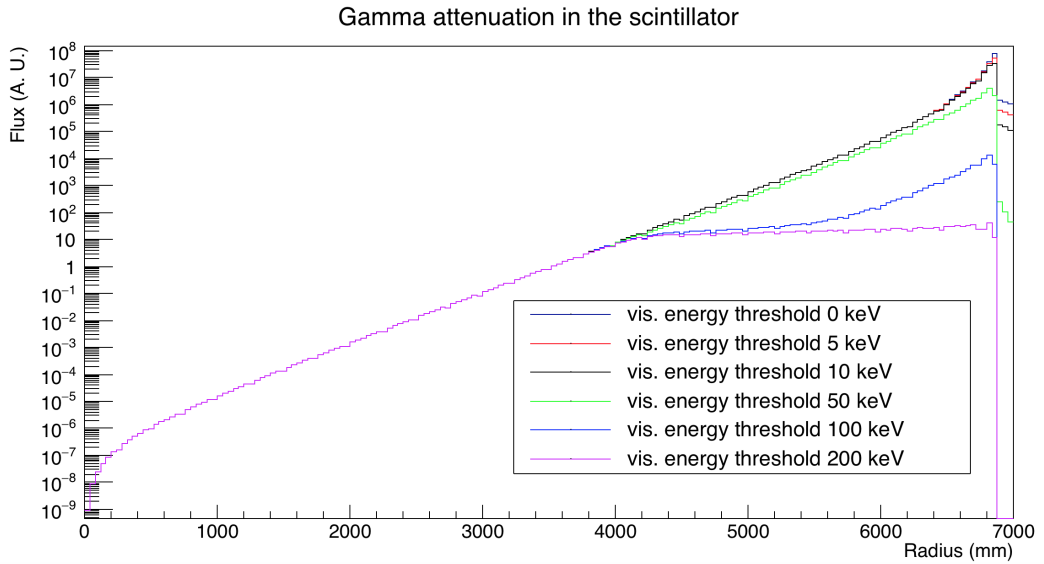


**Fig. 5.24:** Radial distributions of external  $\gamma$  events for different cuts on the total visible energy.

### 5.10.4 Validation of the procedure through comparisons with calibrations

The external  $\gamma$  simulation procedure was validated by direct comparison with real data from calibrations. No parameters were tuned or modified in order to improve the goodness of the simulations, thus all the amount of data from external calibrations was used for testing the already tuned MC code.

	N1	N2	N3	N4	N5	N6	N7	S3	S5	S7
X [m]	2.63	4.16	5.93	6.53	6.07	4.37	2.55	-6.00	-6.06	-2.21
Y [m]	-0.62	-0.81	-1.44	-1.65	-1.08	-0.80	-0.43	0.98	1.02	-0.27
Z [m]	6.29	5.39	3.11	-1.24	-2.99	-5.22	6.34	3.15	-3.03	-6.48

**Tab. 5.1:** Positions of the external calibration source deployments. The coordinates are relative to the center of the detector.

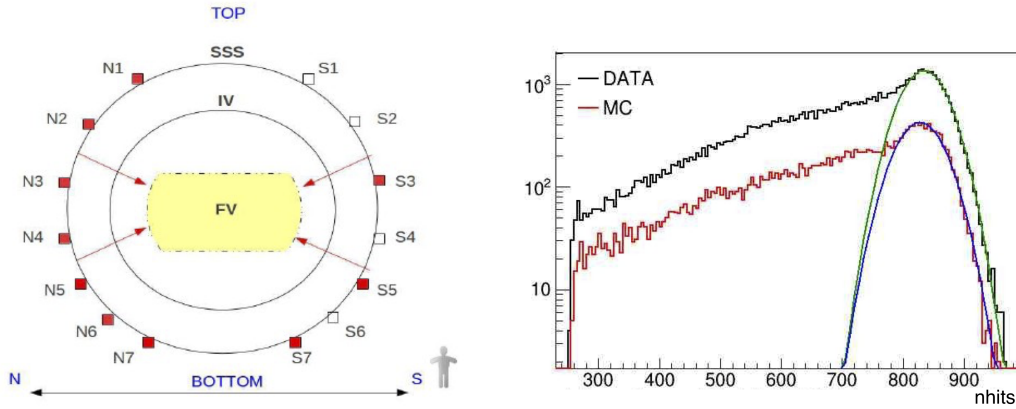


**Fig. 5.25:** *Left Panel:* Sketch of the external source deployment positions listed in Tab. 5.1. *Right Panel:* Gaussian fit examples of the full  $\gamma$  absorption peak for data and MC. The relative normalization of the spectra is meaningless.

The external calibration campaign held in 2011 [216] was carried out using a  $^{228}\text{Th}$  source with an activity of  $\sim 2.9\text{ MBq}$  placed in several positions both in the top and the bottom hemispheres, as listed in Tab. 5.1 and illustrated in the left panel of Fig. 5.25. The usage of a  $^{228}\text{Th}$  calibration source is convenient, since  $^{228}\text{Th}$  is a long-lived nuclide ( $\tau = 2.76\text{ yr}$ ),  $^{208}\text{Tl}$  is one of its daughters and the emission probability of the 2.615 MeV  $\gamma$  line is 35.6%.  $\alpha$  and  $\beta$  particles emitted by daughter nuclides of  $^{228}\text{Th}$  are blocked by the source encapsulation, while low energy  $\gamma$  rays are absorbed in the buffer, very close to the generation point. In addition, the  $^{228}\text{Th}$  source activity needed to be of several MBq, in order to produce a measurable rate of events in the FV. The source was encapsulated and inserted into the detector through dedicated pipes. Data were acquired with the source in positions on two sides of the detector (north and south, geographically) and with different heights with respect to the ground. In Tab. 5.1 and in Fig. 5.25 the “N”

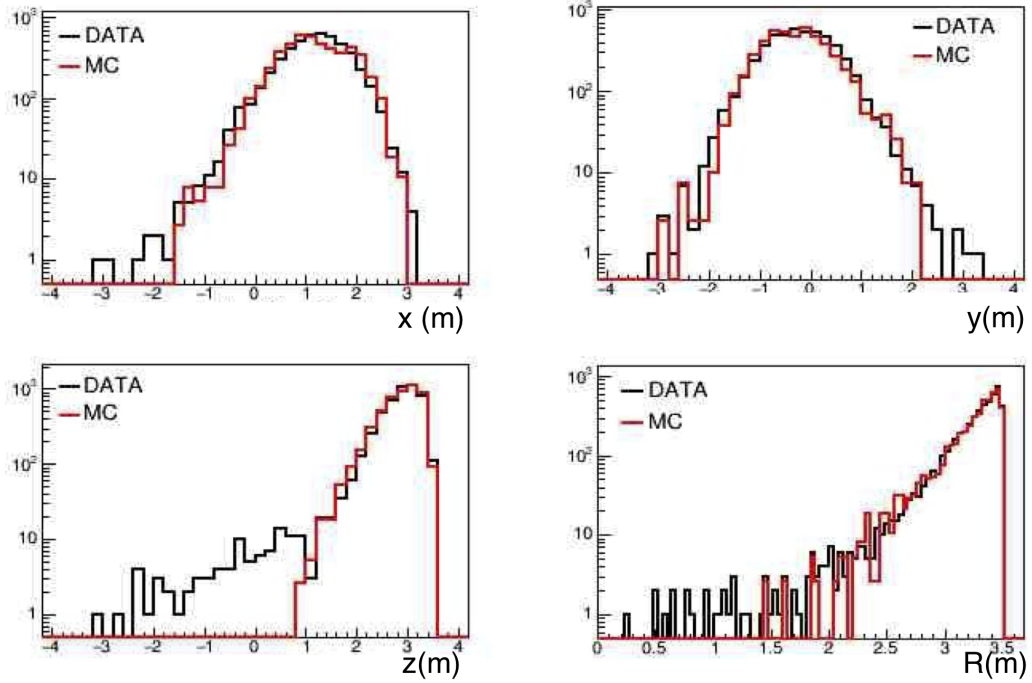


**Fig. 5.26:** Comparisons of the reconstructed positions ( $x$ ,  $y$  and  $z$  coordinates and radius) in MC and calibration data for the source deployed in the N3 position.

("S") letter indicates the north (south) side while the numbers refer to the position's height. It is important to test the detector response to external  $\gamma$ 's in different positions and especially at different heights in order to test both the effect of the vessel shape and that of the asymmetry of the live PMT distribution.

Using the biasing procedure described above,  $^{208}\text{Tl}$  events originating in all the listed positions (see Tab. 5.1) were simulated. The reconstructed spectra and event positions were compared to the measured ones, recording an excellent agreement between simulations and real data. Examples of the goodness of the simulations are given in Fig. 5.26, where the event position reconstruction in data and MC is shown, and in Fig. 5.27, where the  $\gamma$  induced energy spectrum in the  $nhits$  variable is compared for different FV cuts. Both the event position and the energy spectrum are well reproduced. Particularly, it is possible to note a good agreement even with the 3.5 m FV cut (left panel of Fig. 5.27) which is already well beyond the needs of the solar neutrino analysis (good light collection reconstruction in the 3 m sphere). The different shape of the energy spectrum between the two plots in Fig. 5.27 is due to the different FV cut, and thus to the different ratio between the Compton tail (of events degraded in energy by the buffer) and the full absorption peak. Despite the simulation method being efficient, the plots of Fig. 5.27 show that the MC spectra lack of statistics with respect to data. This is mostly due to the fact that the source event rate is pretty high with respect to the standard external background rate and thus a lot of computational power would be needed in

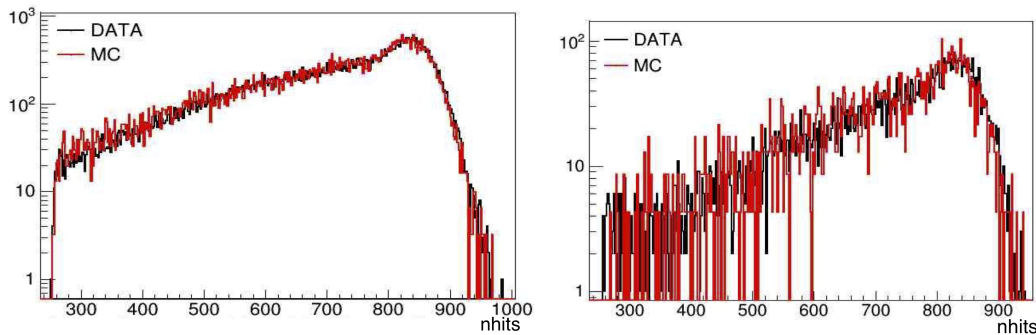


**Fig. 5.27:** *Left Panel:* Comparison of the external  $\gamma$  energy spectrum in the  $nhits$  energy variable for source-induced events from the N3 position. The FV cut consists in a 3.5 m radial cut from the center of the detector. *Right Panel:* Comparison of the external  $\gamma$  energy spectrum in the  $nhits$  energy variable for source-induced events from the N3 position. The FV cut is 3 m.

order to generate enough statistics of  $\gamma$  events reaching the innermost FV for all the source positions.

A more systematic study was performed in order to assess the solidity of the method in the whole IV volume. Particularly, a parameter of interest, which depends mostly on the vessel shape non-uniformity, is the ratio between the number of events in the full absorption peak and in the Compton tail,  $\rho_{\text{peak/tail}}$ . This ratio can be computed very simply, by fitting with a Gaussian (as shown in the right panel of Fig. 5.25) the full absorption peak. Then, the integral of the Gaussian is compared to the total number of events in the spectrum and thus to those in the Compton tail.

Figure 5.28 shows the values of  $\rho_{\text{peak/tail}}$  as a function of the position both for MC and data. The events (in the  $nhits$  variable) are selected in a 3 m FV sphere before fitting with the Gaussian function. This kind of agreement is actually the smoking gun, which proves that the simulation is working properly and accurately. Figure 5.28 also demonstrates once more that the dynamical vessel shape in Borexino is well reproduced and that it is crucial for understanding this kind of backgrounds, since  $\rho_{\text{peak/tail}}$  as a function of the source position is well reproduced by the MC. The error on the MC point for the S7 position of Fig. 5.28 is very big because of the little statistics in the spectrum, which made it difficult to perform the Gaussian fit proficiently.

### 5.10.5 Source-induced background simulation for the SOX experiment

The algorithm here described can be easily used in order to simulate, for instance, the source-induced backgrounds both in terms of  $\gamma$ 's and neutrons for the SOX experiment. The  $^{144}\text{Ce}$  source is pretty powerful, and although a very thick shielding (the tungsten surrounding the source, concrete, water, scintillator...) some  $\gamma$ 's or neutrons could anyhow reach the innermost FV. The biasing algorithm as it is can compute the shielding factor for  $\gamma$ 's (which, in the case of SOX was quantified to be  $\sim 10^{18}$ ) while it would need slight modifications in order to study neutrons. Of course, this requires a detailed simulation of

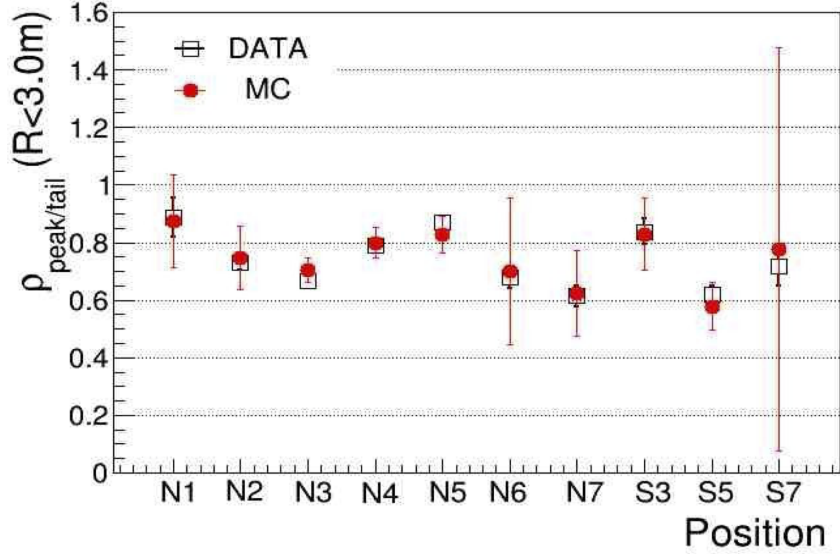


**Fig. 5.28:** Value of the full absorption peak/Compton tail ratio as a function of the source position both in MC and in data.

the geometry of the system (source geometry and materials, their precise locations and details of the surroundings) in addition to the implementation of the parallel geometry assigning importances related to the particular properties of each material. Once all the details are implemented, the simulation is very fast, almost immediate.

## 5.11 Monte Carlo pileup production

The event pileup (or simply “pileup”), i.e. two or more events happening so close in time that the clustering algorithm cannot disentangle them, is the most critical background for very low energy solar neutrino analyses. In particular, its understanding is mandatory for the pp  $\nu$  measurement [218]. Since  $^{14}\text{C}$  events are the most abundant in Borexino’s FV, it is trivial to consider the pileup of two<sup>3</sup>  $^{14}\text{C}$  events as the most important component of the pileup spectrum. The situation is made particularly difficult from the fact that the convolution of the  $^{14}\text{C}$  spectral shape with itself is very similar to the pp  $\nu$ -induced electron recoil in the scintillator. In addition, as visible in Tab. 4.1, the pp  $\nu$  count rate is around 130 cpd/100 ton. Considering the  $^{14}\text{C}$  rate in Borexino as 40 Bq/100 ton [218] and a mean cluster duration of  $\sim 500$  ns, it is very easy to compute the expected rate of pileup events, which is  $\sim 140$  cpd/100 ton. These numbers do not take into account sources of pileup other than the  $^{14}\text{C}$  on  $^{14}\text{C}$ , but they already make the pileup understanding importance very clear.

The inputs for studying the actual pileup shape in Borexino must come from data, since

<sup>3</sup>The pileup of more than two events has such a low probability that it gives a negligible contribution in the region of interest.

it is impossible to establish the pileup composition *a priori*. The most straightforward way consists in studying the spectrum of events acquired in random triggers. This data is acquired without any physical PMT coincidence, and thus it offers the possibility to study the spectrum without any threshold. However, when analyzing the events through the clustering algorithm, a software threshold of  $\sim 20$  fired PMTs is applied (see Sec. 4.5). Most of the random trigger events are actually “empty”, containing only hits from dark rate.

### 5.11.1 Data-driven methods for pileup spectra production

Historically, two different data-driven approaches were considered in order to produce the pileup PDF. The easiest way consists in convolving the analytical or MC PDFs with the spectrum of random trigger events. This has the advantage of being a simple procedure, but it is not able of reproducing the effects induced on the actual pileup events by the reconstruction algorithm and by the cuts. For this reason, another method, called “synthetic pileup”, was developed. It consists in artificially overlapping the hits and processing them and new events. In the  $pp\nu$  analysis presented in Ref. [218], both the methods were used and thus they are here described.

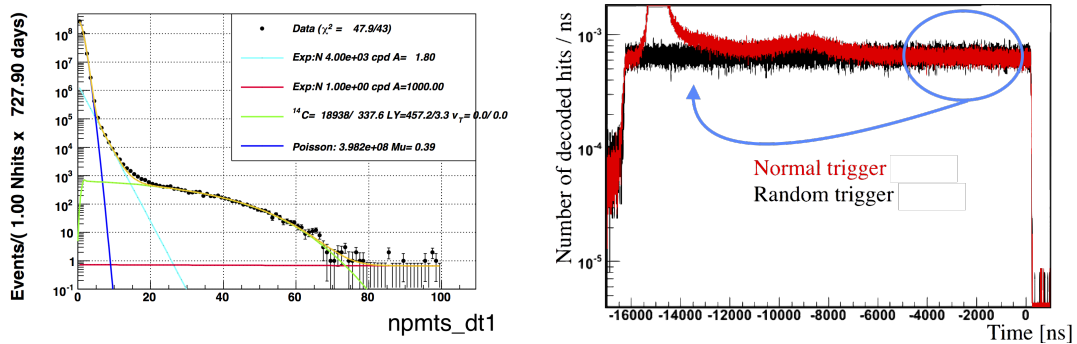


**Fig. 5.29:** *Left Panel:* Random trigger spectrum with an analytical interpretation of its major components. *Right Panel:* Schematic overview of the the procedure of hit overlapping used for the synthetic pileup production.

### Convolution with random triggers

In this method, pileup is not treated as a species of its own. Its contribution is taken into account by convoluting the spectral components used in the fit with the spectrum of random triggers. These events are collected by opening acquisition windows at a 0.5 Hz rate, during normal data-taking. The clustering algorithm does not work for events with less than  $\sim 20$  hits, and thus in order to produce the spectrum of this class of events, which is mostly formed by dark noise, it is necessary to develop a dedicated algorithm, which counts the number of hits in a fixed time window within the gate. The left panel of Fig. 5.29 shows the random trigger spectrum in the  $npmts\_dt1$  variable. At

very low energy, it is dominated by dark noise, while above it can be explained as the sum of  $^{14}\text{C}$  events and another component following an exponential distribution with a good approximation. As anticipated before, the main drawback of this method is the impossibility of taking into account the cut effects on the pileup, especially concerning the position reconstruction and thus the FV cut.

### Synthetic pileup

The synthetic pileup method is based on the assumption that the probability of the overlap of a second event on any given real trigger event is equal to that of recording it in a random time window of the same length as the cluster length. For this reason, the method was applied only to  $npmts\_dt1$  and  $npmts\_dt2$  variables, since the considered length of the cluster is fixed and thus it is simple to compute that probability. Decoded hits from the end of every trigger window (where hit distributions are the same as those of random triggers) are shifted over the top of the accepted range of cluster start times for normal triggering events. The procedure is very simply sketched in the right panel of Fig. 5.29. Normal events and the new synthetic events undergo the same reconstruction program and cuts. The pileup spectrum is defined as the set of synthetic events whose energy (estimated according to  $npmts\_dt1$  or  $npmts\_dt2$ ) changes by at least  $E_{min}$  with respect to the corresponding normal event. This procedure allows the production of the pileup spectrum which can be used for fitting data. The major sources of systematics in this method are the selection of  $E_{min}$ , below which all the additional  $npmts\_dt1$  or  $npmts\_dt2$  on the synthetic event are considered to be from “dark noise”, and from the assumption that all forms of pileup originate from at least one of the events being an event that would have triggered on its own. These effects can be taken under control starting the analysis sufficiently far away from the detector trigger threshold and by combining the use of the synthetic strategy together with the convolution with the random spectrum from 0 up to the value  $E_{min}$ . Another critical point which should be taken into account is the fact that within this procedure, the PMT dark noise is double counted by definition.

#### 5.11.2 Introduction on MC pileup production

The general method for producing pileup events with the MC is shown in Fig. 5.30.

Events of given kinds are produced with `g4bx2`. Two different vertexes (`g4bx2` events) are correlated in time by an external application which creates a new binary file, with the same structure of the output of `g4bx2`. The time correlation is typically created by sampling a random delay between the vertexes uniformly in a range of a few  $\mu\text{s}$  (typical cluster durations are of the order of  $500 \div 1000 \mu\text{s}$ ). The output thus created is then processed through the standard `bx1ec` and `echidna` chain. This procedure has the advantage of replicating what happens in reality. Real events overlap at the level of light production in the scintillator, and the already piled-up pattern of decoded hits undergoes the electronics chain and the reconstruction. This is performed in the same way in the simulation. The disadvantage is the need of knowing the most abundant primary classes of events which contribute non negligibly to the pileup. The final pileup

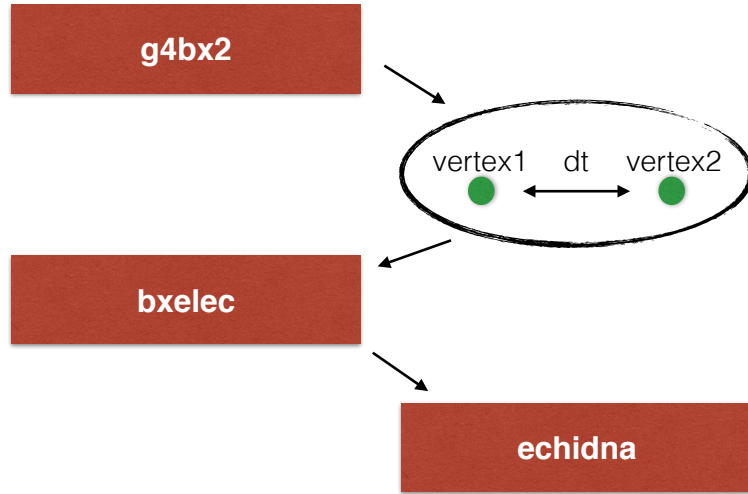


**Fig. 5.30:** Scheme of the software chain for the MC event pileup production.

PDF is constructed by summing up the results of the overlap of pairs of events (such as  $^{14}\text{C}$ - $^{14}\text{C}$ ,  $^{14}\text{C}$ - $^{210}\text{Po}$  and so on). As a final remark, this method allows the inclusion in the analysis of those pileup events which might not trigger the detector individually, but which do if they happen close enough in time. This is not possible with the synthetic pileup method.

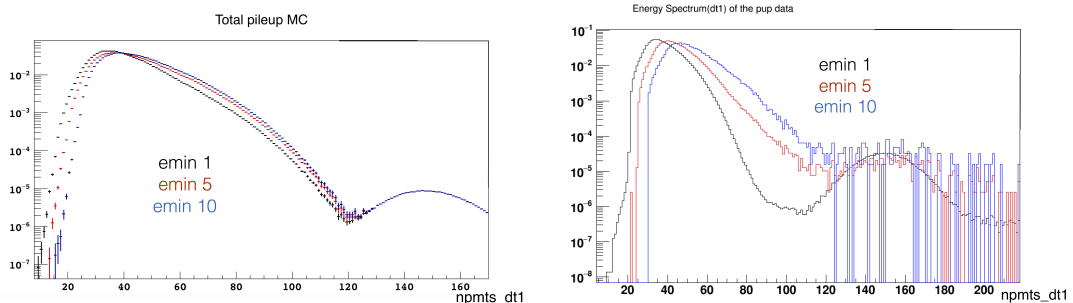


**Fig. 5.31:** *Left Panel:*  $^{14}\text{C}$ - $^{14}\text{C}$  pileup event spectra produced with the MC as a function of  $E_{min}$ . *Right Panel:* Synthetic pileup spectra as a function of  $E_{min}$ .

### 5.11.3 Pileup spectral composition

A possibility in order to study the pileup composition is to use the information both of random trigger events and of the shape of the synthetic pileup produced for the Phase-I analysis [218]. In particular, the key parameter for synthetic events is  $E_{min}$ , which is connected with the mean energy of the primary events which build the pileup. The first step consists in testing the assumption that  $^{14}\text{C}$ - $^{14}\text{C}$  events are the most important

component in the pileup spectrum. The left panel of Fig. 5.31 shows the energy spectrum of MC  $^{14}\text{C}$ - $^{14}\text{C}$  pileup events as a function of  $E_{min}$ . It is possible to evaluate  $E_{min}$  in the MC pileup construction, since the two primary vertexes are also processed independently and, through the MC truth information, it is possible to relate the piled-up energy with that of the first (or second) event only. The spectral shape dependence on  $E_{min}$  observed with the MC should be related to what happens in data and is shown in the right panel of Fig. 5.31. In this case, the MC-data comparison is not satisfactory. The dependence of the pileup spectrum upon  $E_{min}$  is pretty mild in the MC, while it is much more significant in the case of the data, especially when  $E_{min}$  is modified from a few hits to  $\sim 10$ . This is not a real surprise, since the most probable  $^{14}\text{C}$  event energy is around  $\sim 20$   $npmts\_dt1$  and therefore the pileup spectral shape is not expected to depend significantly on  $E_{min}$ , when this is varied in the range  $1 \div 10$ . At very low  $E_{min}$ , the most important contribution is that of dark noise. The mean dark rate is around  $\sim 300$  Hz per PMT, which reads as a global rate of  $\sim 600$  kHz. The mean number of dark hits in a 230 ns time window (the  $npmts\_dt1$  duration) is  $\sim 0.14$  and thus the contribution of the dark rate cannot explain the observed difference in the synthetic spectrum between  $E_{min} = 5$  and  $E_{min} = 10$ . Therefore, some other component must play a significant role in the pileup spectrum construction.

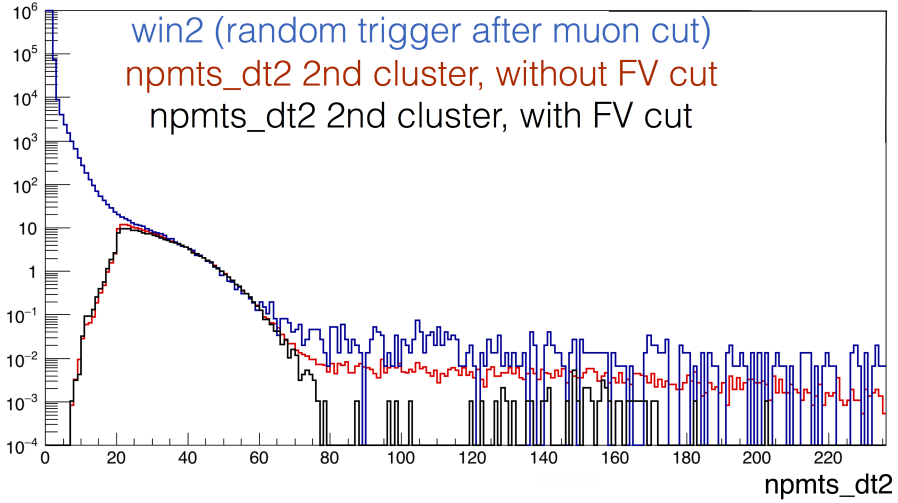


**Fig. 5.32:** Energy spectra of random triggers (blue) and of second clusters (black and red). Second clusters are contained in the normal events with more than one cluster (the first cluster being responsible for triggering): they are subject to no hardware threshold but they undergo clustering, and this explains why the low energy part is cut. The red line is obtained with no cuts, while the black line underwent the FV cut.

Information on the most abundant classes of events in Borexino can come only from the random trigger spectrum. Figure 5.32 shows the energy spectrum of random triggers for different cut choices. The blue line shows the  $npmts\_dt2$  energy estimator for random

trigger events with no cuts. More or less the same spectral shape is obtained if, instead of considering random trigger events, one analyzes second clusters in normal events where the clustering algorithm finds more than one physical event. Second clusters are acquired without trigger threshold, but they have to qualify as clusters, and for this reason the very low energy part of the spectrum is cut. The advantage of second clusters with respect to purely random triggers is that the reconstruction algorithm can be used and thus the FV cut can be applied (black line vs red line). When the FV cut is applied, the events which are left are almost purely  $^{14}\text{C}$ . It is evident that a non negligible component of the random spectrum is removed by the FV cut, thus suggesting its external origin. The developments carried out on the external background simulation (see Sec. 5.10) can help to assess if the order of magnitude of expected external  $\gamma$ 's could explain the physical events in the random trigger which are not  $^{14}\text{C}$ . Particularly, interactions in the buffer and energy degraded gammas reaching the outermost part of the IV might explain the components both above and below the  $^{14}\text{C}$  spectrum. Extrapolating from the measurements of the external contaminations inside the FV [214] according to the radial distribution shown in Fig. 5.24, it is possible to compute an expected count rate of external  $\gamma$ 's of  $\sim 7 \text{ kBq}$  in the whole SSS inner volume. This is in agreement with what is expected by an *a priori* calculation from the measured contaminations in Borexino's materials [193]. The external background rate is much bigger than the total  $^{14}\text{C}$  rate of 120 Bq (neglecting the contribution of the  $^{14}\text{C}$  in the buffer which, given the quenching and the mean decay energy, is totally negligible) and its mean energy is pretty lower than that of  $^{14}\text{C}$  (see the blue line in Fig. 5.32).

At this point of the discussion, the three most abundant components which can enter the pileup construction are external  $\gamma$ 's,  $^{14}\text{C}$  and  $^{210}\text{Po}$ . Polonium is not really important in the understanding of the random trigger spectrum, since its rate is much lower than those of the first two, but it is the third component in terms of number of events in the Borexino spectrum. The smoking gun for demonstrating the arguments here presented is provided by the fit in Fig. 5.33.

The components considered in the fit shown in Fig. 5.33 are the dark rate,  $^{14}\text{C}$  and external  $\gamma$ 's. The spectrum shown in Fig. 5.33 is obtained by selecting hits in a fixed 400 ns window inside the  $16.5 \mu\text{s}$ -long gate opened at random times. The same holds for the MC PDFs creation, where  $^{14}\text{C}$  and external  $\gamma$ 's are simulated as normal events, but then 400 ns-wide windows were selected randomly and the  $npmts_dt2$  energy estimator was extracted. The dark rate is inserted in the fit only for improving the agreement at very low energy (a few hits) and it is modeled analytically with a Poisson distribution.  $^{14}\text{C}$  events are simulated over all the IV volume without any FV cut. External  $\gamma$ 's are simulated originating from the SSS and from the light concentrators, and energy deposits and light production are taken into account both for interactions in the IV and in the buffer. The scintillation in the buffer is quenched, and most importantly it is not wavelength shifted by PPO, thus resulting almost invisible to PMTs. It is anyhow present. The quenching factor in the buffer is around 4%, which corresponds to an average value of a few tens of hits at maximum for  $2 \div 3 \text{ MeV}$  events. Furthermore, the MC must reproduce to a good extent the light collection capabilities of the detector

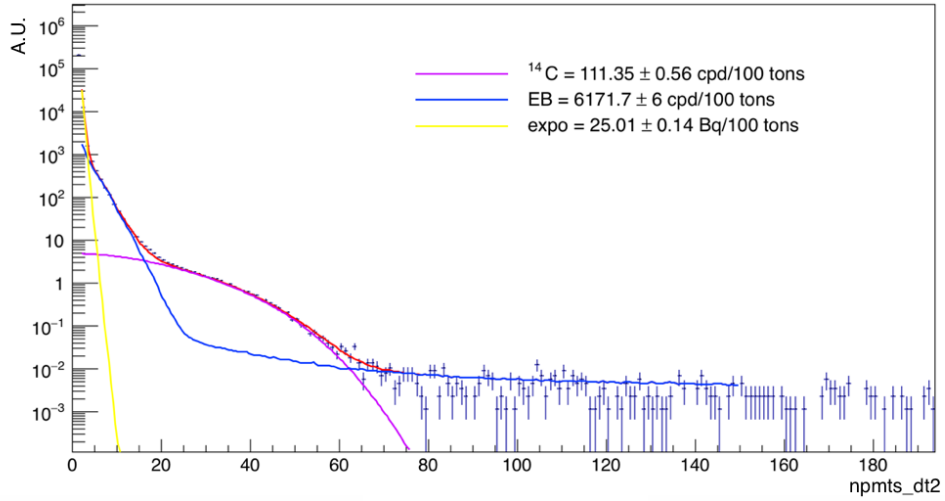


**Fig. 5.33:** Fit of the random trigger spectrum in  $npmts\_dt2$  with MC PDFs. The yellow component is the Poisson dark rate, the purple is  $^{14}\text{C}$  and the blue one is the external background. The values of the rates given for the different species should be considered as arbitrary units, where only the ratios between the components are meaningful.

at very large radii, where the most of the external events are produced. This seems to be the case, since the fit presented in Fig. 5.33 demonstrates that the random event spectrum can be almost perfectly described by external events and  $^{14}\text{C}$ . The shape of the external background spectrum can be divided in two different portions: the low energy part, produced by  $\gamma$  interactions in the buffer (in fact these are the most abundant and produce a few photons), and the higher energy part, which is mostly due to the residual interaction in the outermost part of the IV by  $\gamma$ 's which lost most of their energy in the buffer. These results are consistent with the analytical fit of the random triggers presented in the left panel of Fig. 5.29.

As an outcome of this discussion, the Borexino pileup can be explained by the superposition of external background events,  $^{14}\text{C}$  and  $^{210}\text{Po}$ . It can be easily proved (also by using the MC), that despite being the most abundant source of pileup, the overlap of two external  $\gamma$  events is negligible in practice. Despite the very high rate of external  $\gamma$ 's, in reality most of their pileup events are overlaps of a few hits coming from two external  $\gamma$  depositions. Given the very low visible energy of these events, in practice “none” of them triggers or is identified as a cluster. Therefore, they can be dropped from the analysis. The most important components turn out to be:

1.  $^{14}\text{C}$  over external  $\gamma$ 's.
2.  $^{14}\text{C}$  over  $^{14}\text{C}$ .
3.  $^{210}\text{Po}$  over external  $\gamma$ 's.

The pileup with  $^{210}\text{Po}$  results in an effective smearing of the  $^{210}\text{Po}$  resolution. Furthermore, the contribution of  $^{210}\text{Po}$  over  $^{14}\text{C}$  can be neglected, being of the second order with respect to  $^{210}\text{Po}$  over external  $\gamma$ 's. At this point, the MC production of these three pileup components is straightforward. However, the relative rates must be known in order to sum them up and produce the “final” pileup PDF. The most critical ratio is that of  $^{14}\text{C}$  over external  $\gamma$ 's with respect to  $^{14}\text{C}$  over  $^{14}\text{C}$ . In fact, once this is known, it is possible to infer the rate of  $^{210}\text{Po}$  over external  $\gamma$ 's just by rescaling the  $^{210}\text{Po}$  rate (measured thanks to the MLP tagging) to that of  $^{14}\text{C}$ . It has to be noted that the needed numbers are those of the “true” rate of the primary components ( $^{14}\text{C}$ ,  $^{210}\text{Po}$  and external  $\gamma$ 's) in the detector. Then, the MC procedure is able to simulate the reconstruction and the cut efficiencies.

The ratio of  $^{14}\text{C}$  over external  $\gamma$ 's with respect to  $^{14}\text{C}$  over  $^{14}\text{C}$  can be obtained at least in two ways. The fit of Fig. 5.33 shows that the relative intensity of the two components is around  $\sim 55$ . Taking into account some systematics in the fit procedure, the error on this number can be quantified in  $\sim 10\%$ . Conversely, if one extrapolates the external background rate measured in the FV with the radial distribution as simulated by the MC, the ratio would be:  $\sim 7\text{ kBq}/120\text{ Bq} \approx 66$ . In this case the error is much bigger (at least  $\pm 20$ ), since the uncertainty on the extrapolation is big. However, despite the two numbers are compatible and somehow reasonable, this precision is not enough to constraint the total pileup shape in such a way that the  $\text{pp} \nu$  measurement can be performed. Another strategy was then adopted and it consists in tuning the ratio and then validating the whole MC pileup thanks to the usage of the synthetic pileup, as described in the next Sec. 5.11.4.

#### 5.11.4 Validation of the MC pileup with the synthetic pileup

The key dependence which can test if the MC pileup is accurately describing the real data is the pileup spectral shape behavior as a function of  $E_{\min}$ . The spectral shape subordination on  $E_{\min}$  tests both the rates with which the primary components are inputed in the pileup generation and the MC ability to reproduce the electronics and reconstruction behaviors. The approach consists in fitting the synthetic pileup spectrum with a fixed  $E_{\min}$  in order to establish quite accurately ( $\sim 2\%$  precision) the rates of the primary components. Then, MC pileup spectra are produced for different values of  $E_{\min}$  with no other modifications or assumptions. The fit to the synthetic pileup spectrum produced for Borexino Phase-I and  $E_{\min} = 6$  is shown in Fig. 5.34. The spectral components used for fitting are  $^{14}\text{C}$  over external  $\gamma$ 's,  $^{14}\text{C}$  over  $^{14}\text{C}$  and  $^{210}\text{Po}$  over external  $\gamma$ 's. The values of the obtained rates should be considered to be in arbitrary units, with the relative ratios being meaningful. However, these values are relative to the primary rates of the different components, depurated from the threshold and reconstruction effects (these events are selected in the innermost FV).

The fit is quite accurate and the starting point was selected to be 60  $npmts\_dt1$  (not normalized) since this was the starting point of the fit used in the analysis of Ref. [218]. In that occasion, the synthetic pileup spectral shape with  $E_{\min} = 5$  was used to describe the pileup. The uncertainty of the weights of the different components as obtained from

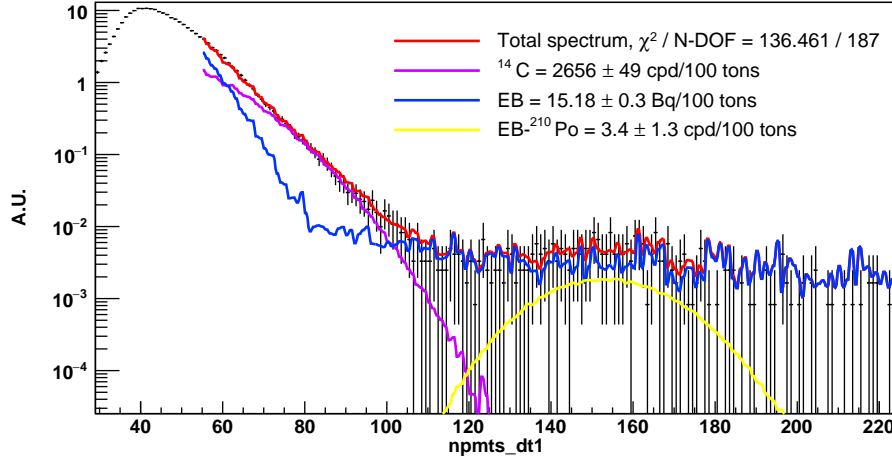


**Fig. 5.34:** Fit of the synthetic pileup spectrum with the considered MC pileup spectral components for  $E_{min} = 6$ . The purple line denoted with “ $^{14}\text{C}$ ” in the legend refers to the pileup of  $^{14}\text{C}$  over  $^{14}\text{C}$ . In the legend, “EB” stands for external background.

the fit should be treated as systematics when fitting the Borexino energy spectrum with this pileup PDF.

Once the various contributions were established with  $E_{min} = 6$ , the MC pileup was validated by comparing the predicted pileup shape with that of the synthetic in the same cut and  $E_{min}$  conditions. The results are shown in Figs. 5.35, 5.36 and 5.37.

The pictures show that the synthetic pileup shape changes a lot as a function of  $E_{min}$  and the MC pileup is able of reproducing it very well. In particular, as  $E_{min}$  grows, the contribution of the pileup with external  $\gamma$ 's is reduced, since the mean visible energy of buffer events is of a few hits. In the case of  $E_{min} = 10$ , the pileup can mostly be explained by  $^{14}\text{C}$  on  $^{14}\text{C}$  events, with a higher energy tail of gammas interacting in the IV and reconstructed in the FV. The agreement of the MC pileup with the synthetic tests not only the procedure of the pileup creation and composition, but also the quenching description, the light collection reproduction, the light propagation modeling and the external background production. In fact, pileup events with a given visible energy are formed by events whose energy, if summed up in real single events, would correspond to a lower quenching, and thus a higher amount of detected light. The energy scale of MC pileup matches very well with that of data, giving confidence on the quenching description solidity. Furthermore, the hit time distribution is essential for reproducing the behavior of position reconstruction. Pileup events happen “far away” in the detector and thus the behavior of the reconstruction algorithm cannot be established *a priori*, since it is based on a maximization. The fact that the MC pileup spectral composition after the cuts agrees with that of the synthetic pileup strengthens the whole simulation procedure.

### 5.11.5 Pileup constraint in the fit

In the final spectral fit of Borexino data aiming at the measurement of  $\text{pp } \nu$ , the pileup contribution must be constrained, because of its degeneracy with the  $\text{pp } \nu$  energy spectrum. The most accurate information on the total pileup rate can be obtained by the measured  $^{14}\text{C}$  rate [218]. The value of  $^{14}\text{C}$  on  $^{14}\text{C}$  pileup rate can be computed by taking into account the mean cluster duration, even if this does not consider the clustering and position reconstruction efficiencies. A more accurate method, which should anyhow be crosschecked with the previous one, consists in computing the total amount of  $^{14}\text{C}$  on  $^{14}\text{C}$  pileup with the MC. One can simulate  $^{14}\text{C}$  on  $^{14}\text{C}$  pileup events with a random delay in a fixed window and then compute how many events survive the cuts and thus form the pileup. It is not really easy to quantify precisely the amount of external background. Once established the  $^{14}\text{C}$  on  $^{14}\text{C}$  rate, it is possible to use the information on the ratios between the two as obtained in Sec. 5.11.4. Otherwise, it is possible to exploit the fact that in the  $\text{pp } \nu$  region of interest the most important component of the pileup is exactly the  $^{14}\text{C}$  on  $^{14}\text{C}$  one. This is clearly visible in Figs. 5.35, 5.36 and 5.37 in the `npmts_dt1` energy range  $\sim 80 \div 100$ . It is therefore possible to constrain the number of counts of the pileup with quite high accuracy in this energy region, which is the most important for the  $\text{pp } \nu$  measurement.

## 5.12 Outlook

The Borexino full Monte Carlo simulation and its applications for solar neutrino measurements are described in this chapter. The upgrade of the simulation carried out throughout 2013, 2014 and 2015 was a major commitment among those presented in these PhD thesis and brought to very good results. The simulation is able of reproducing the detector response all over the FV without the need for effective parameters, the time response is reproduced to a satisfactory extent and the electronics simulation is very close to reality as well. The development of the novel techniques for the external background simulation were a milestone, which also allowed to perform the extensive work on the pileup and to understand its composition in detail. All these achievements are crucial in the analysis presented in the subsequent chapter 6, where the preliminary global analysis of solar neutrino data from Borexino Phase-II is presented.

The work on the MC is of course very important also in view of the SOX experiment. The very good accuracy especially at large radii is important for SOX analysis, where the FV must be kept as big as possible. Of course, the needs of that kind of analysis are different from those of solar neutrino analyses and some minor details still have to be improved (such as the *charge* response at large radii and for high energy events). The next calibration campaign, which will take place at the end of the Phase-II and right before the start of SOX, will be a crucial moment in order to completely finalize the work on the MC simulation code.

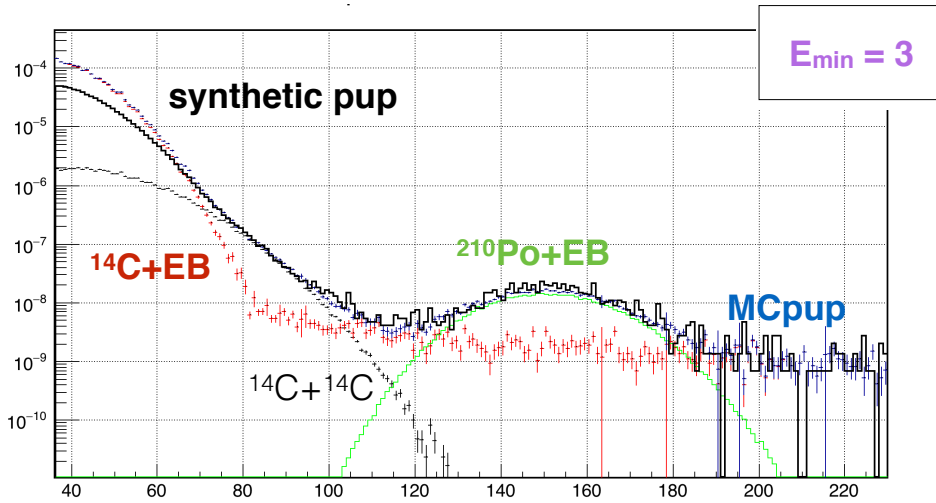


**Fig. 5.35:** Synthetic and MC pileup for  $E_{min} = 3$ . The different components are shown in various colors.

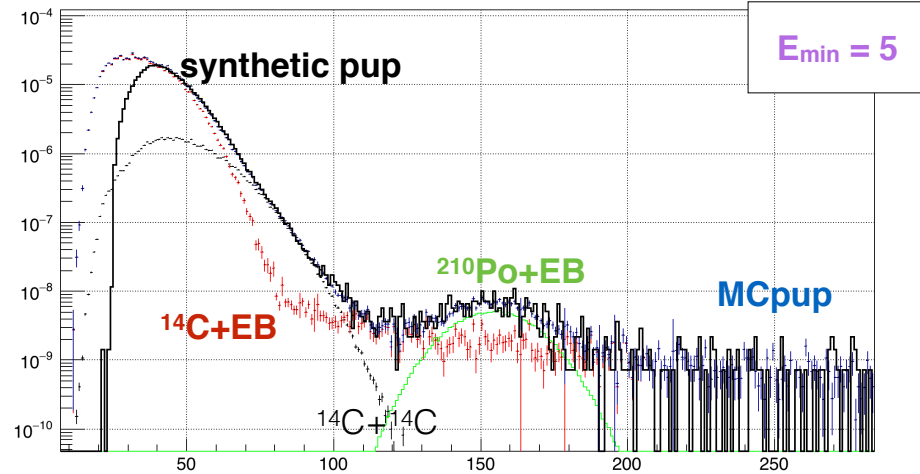


**Fig. 5.36:** Synthetic and MC pileup for  $E_{min} = 5$ . The different components are shown in various colors.

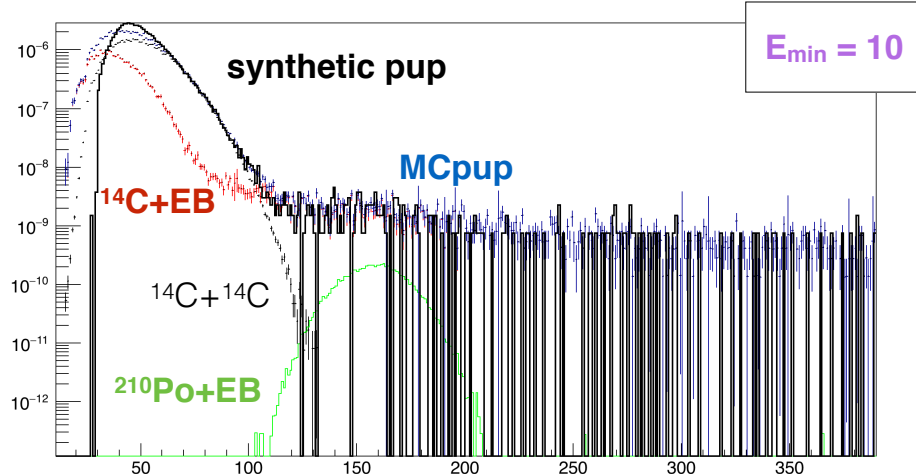


**Fig. 5.37:** Synthetic and MC pileup for  $E_{min} = 10$ . The different components are shown in various colors.

# Chapter 6

## Precision measurement of solar neutrino fluxes with Borexino

In this chapter, the ingredients and the preliminary results of the solar neutrino global analysis of Phase-II Borexino data are presented. The discussion is mainly focused on the spectral fit of the data with the MC PDFs produced thanks to the improved simulation described extensively in chapter 5. Data selection strategies are introduced, as well as the multivariate fitting procedure and the three-fold coincidence method for cosmogenic background reduction. Results from the spectral fit and investigations on systematic uncertainties are also addressed.

The chapter is structured as follows. Section 6.1 describes the data selection, Sec. 6.2 discusses the cuts, Sec. 6.3 illustrates the three-fold coincidence veto, Sec. 6.4 explains the spectrum binning choice, Sec. 6.5 describes the PDF masking procedure, Sec. 6.6 discusses the pulse shape and radial distributions, Sec. 6.7 shows the fitting strategy adopted for the analysis, Sec. 6.8 validates the fitting algorithm, Sec. 6.9 describes the procedure for the goodness of fit evaluation, Sec. 6.10 discusses the three-fold coincidence optimization, Sec. 6.11 describes the fit and the results on  ${}^7\text{Be} \nu$ , pp  $\nu$  and pep  $\nu$ , Sec. 6.12 assesses systematic uncertainties, Sec. 6.13 discusses the pep  $\nu$  measurement and the CNO  $\nu$  limit, Sec. 6.14 summarizes the results and Sec. 6.15 discusses possible outlooks.

### 6.1 Data selection

The data analyzed in this PhD thesis corresponds to Borexino Phase-II data set, which began in December 2011. The data set used for fitting was frozen in May 2016, despite the data acquisition is still ongoing, because developments on the hardware of the trigger system started. As a precaution, while extensive tests on the new trigger system are carried out, data obtained with the new hardware are not considered in this work. For this reason, preliminary results on the analysis are related to the period of time December 2011 - May 2016, while the final results on Borexino Phase-II analysis should be expected beyond this PhD thesis work, with the inclusion of all the data which will be acquired until the beginning of the next calibration campaign. In fact, before the

start of SOX, which is expected at the beginning of 2018, a new calibration campaign will be performed, both for crosschecking the knowledge of the detector for the solar analysis after many years of data taking and for tuning the data analysis tools for the SOX analysis.

Borexino's acquisition is organized in 6-hour long runs. Runs from every single week are grouped in pre-filtered structures (DSTs), where very basic cuts are applied and service triggers are removed. The average Borexino DAQ duty cycle is around 80%. Table 6.1 reports the data set period subdivisions. Periods are named with numbers from 20 to 28, where the tens number indicates “Phase-II”, and the last digit is a progressive number starting from zero. The division of the data set in periods is convenient in order to study the detector stability. Periods were defined to have more or less the same livetime. The last one was frozen when the new trigger system for Borexino was installed.

The total livetime of the data set considered in this thesis before any cut is 1343.45 days.

Period	Start run	End run	Start week	End week	Livetime (days)
20	17328	18406	11 Dec 2011	06 May 2012	129.63
21	18407	19355	13 May 2012	11 Nov 2012	172.68
22	19363	20488	18 Nov 2012	26 May 2013	124.92
23	20489	21293	02 Jun 2013	03 Nov 2013	146.69
24	21294	22181	10 Nov 2013	20 Apr 2014	143.05
25	22182	23213	27 Apr 2014	14 Sep 2014	119.09
26	23214	24558	21 Sep 2014	10 May 2015	206.99
27	24559	25404	17 May 2015	18 Oct 2015	141.14
28	25405	26535	25 Oct 2015	08 May 2016	159.26
all	17328	26300	11 Dec 2011	08 May 2016	1343.45

**Tab. 6.1:** Data set period subdivision for the Borexino Phase-II analysis. For each period, the DAQ first and last run defining the subset, the first day of the first and last DST considered and the livetime (prior to any cut) are reported.

## 6.2 Event selection

Neutrino-like scintillation events are selected according to event-based cuts which are able to eliminate most of external and cosmogenic backgrounds. In particular, a set of “standard cuts” is applied in order to remove muons, some of their daughters, fast coincidences and noise. Independently from these cuts, a FV selection is also applied and its details are described in Sec. 6.2.2. Furthermore, for an additional cosmogenic  $\beta^+$  reduction, the three-fold coincidence veto outlined in Sec. 6.3 is used. In this section, the standard cuts are described.

Muons, short lived cosmogenic backgrounds, fast coincidences and noise are removed by applying the following cuts:

1. muons and muon daughters (300 ms). Muons are defined either by the trigger of the OD or by shape variables describing the hit time distribution in case the OD is not triggered.
2. zero clusters. Only events where the clustering algorithm can recognize at least a point-like scintillation event are kept.
3. fast coincidences. It checks if two clusters happen at a distance shorter than 1.5 m and within a 2 ms time window. The energy of the events are also crosschecked and possibly the couple of events is tagged as  $^{214}\text{Bi}$ - $^{214}\text{Po}$  coincidence.
4. “neutrino trigger”. Events which are generated by service triggers (pulser or calibrations) are removed.
5. multiclusters. Only one-cluster events are kept.
6. start time. Events with the first cluster start time in a strange position within the cluster (thus probably originated by a faulty trigger) are dropped.
7. “Qrec”. The amount of the reconstructed charge for a given event is compared to the number of fired PMTs and if a mismatch is present, the event is removed.
8. crate fraction. If more than 75% of fired PMTs are physically attached to the same crate (out of the 13 currently used), the event is attributed to crate noise and eliminated.

In older analyses [214], other shape cuts such as those for  $\alpha/\beta$  discrimination or for the event sphericity evaluation were applied. They are not applied in the present work, since they affect in a non negligible way the spectrum at the low energies interesting for the pp  $\nu$  analysis. Therefore, coherently to what is presented in Ref. [218] these cuts are not used.

The cut application removes  $\sim 0.15\%$  of good events ( $\ll 1\%$ , thus negligible if compared e.g. with the total systematic uncertainty on  $^7\text{Be} \nu$ , which is of the order of 1.5%, see Sec. 6.12). This was evaluated both on calibration data and on MC. Calibrations were important in order to test the cuts on real data, but the MC usage is fundamental, in order to have a sample of neutrino-like events uniformly distributed in the FV and thus test the position dependence of the cuts. The introduced dead time is dominated by the 300 ms cosmogenic cut which was measured to be of 1.8% [269]. The dead time due to the other cuts is negligible. As a consequence of the fast coincidence cut evaluation, the  $^{214}\text{Pb}$  contamination in the data is estimated according to the measured rate of  $^{214}\text{Bi}$ - $^{214}\text{Po}$  coincidences.

### 6.2.1 Effects of the cuts

Figure 6.1 shows the cut effects on the spectrum. The black line reports the Borexino spectrum without any cut. It is clearly possible to see spikes in the high statistics bin of the black line. These spikes are due to the normalization procedure to 2000 of the

*npmts* variable (see Sec. 4.5). They can be described by the masking procedure introduced in Sec. 6.5.

The blue line in Fig. 6.1 shows the effect of the  $\mu$  cut, which eliminates mostly the high-energy components in the spectrum due to  $\mu$  interactions. Most of the effects on the spectrum are due to the application of the FV cut (red line in Fig. 6.1), which kills most of the external contaminations and of the response non-uniformities. The details on the FV cuts used in Borexino solar neutrino analysis are given in Sec. 6.2.2. After the FV cut, the main spectral features of solar neutrino interactions in Borexino and of contaminations are evident already by eye. In particular, the  ${}^7\text{Be}$   $\nu$  electron recoil shoulder becomes clear around  $250 - 300$  *npmts*.

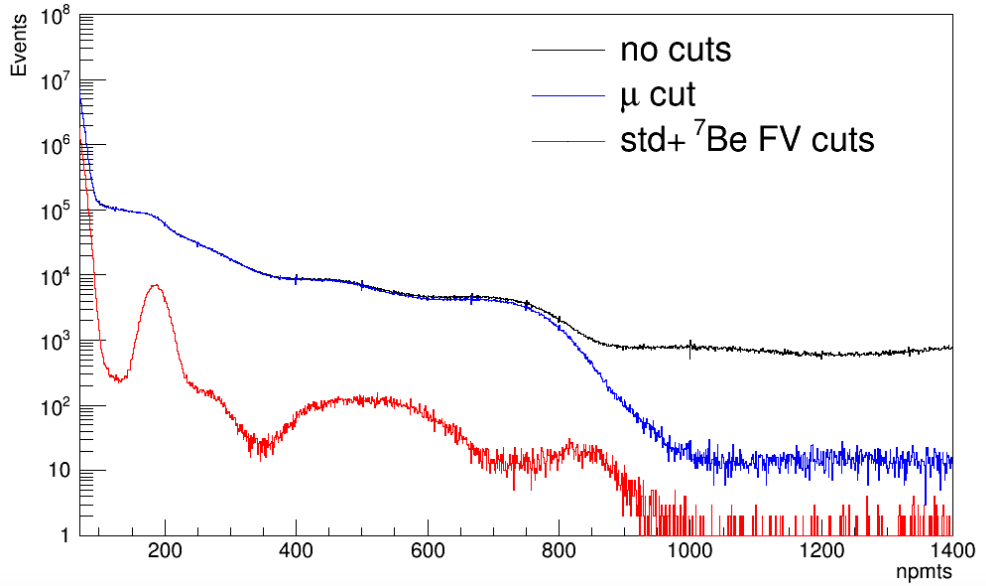


**Fig. 6.1:** Borexino Phase-II spectrum (*npmts* variable) for no cuts (black),  $\mu$  cut (blue) and standard plus FV cuts (red).

### 6.2.2 Fiducial Volume cut

One of the most important cuts is the fiducial volume definition. The main guidelines adopted for the FV definition are:

- maximize the amount of considered mass.
- minimize the amount of external background entering the active volume.
- minimize the light collection non-uniformities in the FV.

While the first condition is obvious, the second one requires to cut as further as possible from the SSS, the IV and the endcaps. The last condition was particularly important

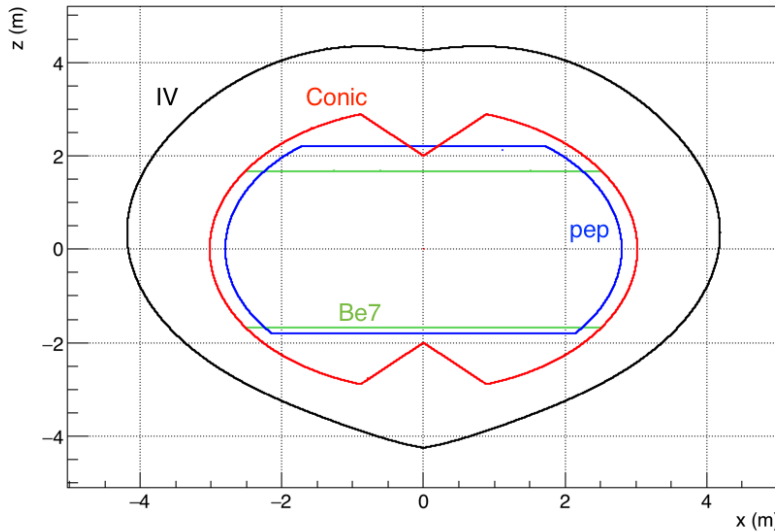


**Fig. 6.2:** Sketch of the different FV definitions in the  $x - z$  plane for the solar neutrino analysis compared to the IV shape as of 15th March 2015.

in the early stages of Borexino, when only the analytical fit approach was adopted and therefore it was not straightforward to model the detector response non uniformity. However, this requirement is not so strict regarding the Phase-II analysis, thanks to the good precision of the MC simulation. However, the selection of the most uniform volume in terms of energy scale is important in order to analyze data with a good energy resolution.<sup>1</sup> Three different FVs are considered for the solar neutrino analysis:  ${}^7\text{Be}$  FV, pep FV and conic cut FV. Their definitions and features are briefly discussed in this section and a scheme is given in Fig. 6.2. The plot shows the different FV shapes in the  $x - z$  plane together with that of the IV.

### ${}^7\text{Be}$ FV

This FV is defined by a radial cut  $R < 3.021\text{ m}$  and a  $z$  cut  $|z| < 1.67\text{ m}$ . This definition was introduced from the very first  ${}^7\text{Be}$   $\nu$  analysis and it is mainly motivated by the identification of a portion of the detector where the energy response is uniform a the % level. The  ${}^7\text{Be}$  FV corresponds to a mass of 75.46 ton.

### pep FV

The cuts describing the pep FV are  $R < 2.8\text{ m}$ ,  $z > -1.8\text{ m}$  and  $z < 2.2\text{ m}$ . The motivation for this FV is the need of a reduction of the external background component, which is crucial for the pep  $\nu$  analysis [224]. The asymmetric  $z$  cut is due to the deformed

<sup>1</sup>The situation could be improved by the definition of position dependent energy estimators.

vessel shape, whose radius is lower in the southern hemisphere. The pep FV corresponds to a mass of 71.30 ton.

### Conic cut FV

A newly defined FV to be used as an alternative of the previous two was introduced for the Phase-II analysis. The radial cut is  $R < 3.021$  m and only two conical portions at the north and south of the sphere are removed. The cones have vertexes in  $(0, 0, 2)$  m and  $(0, 0, -2)$  m and an angular opening of  $\pi/4$ . The conic cut FV corresponds to a mass of 99.33 ton.

### Energy response in the different FVs

A comparison of the Borexino Phase-II spectra in the different FVs is shown in Fig. 6.3. The spectra are normalized to the same exposure. Besides the different statistics (due to the different mass), it is clearly visible that choosing the pep FV reduces quite significantly the external background component in the spectrum at high energy. In other energy regions, the  $^7\text{Be}$  and pep FV cuts produce almost identical spectra. Instead, the conic cut FV produces a spectrum with a different energy response, and this is visible both on the starting point of the  $^{11}\text{C}$  contamination around  $\sim 350$   $nhits$  and also on the  $^{210}\text{Po}$  peak at  $\sim 200$   $nhits$ .

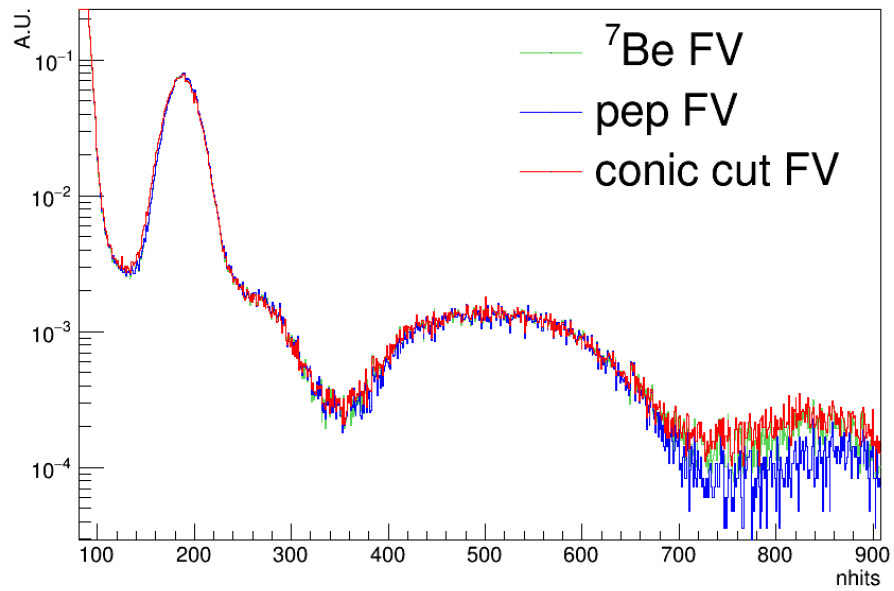


**Fig. 6.3:** Comparison of Borexino spectra in the different FVs normalized to the same exposure.

### 6.3 Three-Fold Coincidence veto

One of the most important backgrounds in the region of interest of pep  $\nu$  and CNO  $\nu$  is  $^{11}\text{C}$ , produced by muon spallation on  $^{12}\text{C}$  (see Sec. 4.3). There are two possible approaches for the  $^{11}\text{C}$  suppression in Borexino spectrum:

- distinguish  $^{11}\text{C}$  events through  $\beta^+/\beta^-$  pulse shape discrimination.
- tag  $^{11}\text{C}$  events through delayed coincidence according to the isotope production scheme.

The two approaches are actually used simultaneously, with the tagging procedure being much more powerful, especially if the systematics associated to the development of a pulse shape parameter (e.g. energy, spatial dependence) are considered. Muon tracking algorithms were developed [270] and thus subsequent neutrons can be correlated to the muon track, allowing the identification of a spatial region of the detector where  $^{11}\text{C}$  could have been created. Neutrons, as already discussed, are identified by the 2.22 MeV (4.95 MeV)  $\gamma$  rays following the hydrogen (carbon) nucleus de-excitations after the neutron captures.

$^{11}\text{C}$  decays could be subtracted by simply putting a cylindrical veto on muon tracks with a radius which depends on the tracking precision. Such an approach would give a theoretical subtraction efficiency close to  $\sim 100\%$ . However, the efficiency of Borexino's muon tracking algorithm is around 50%, making this method not particularly powerful. Therefore, spallation-produced neutrons must be considered as well. Also in this case, the neutron tagging is pretty simple in theory, while it is not straightforward in practice. Muon events produce much more light with respect to the events that Borexino wants to study. In particular, Borexino's electronics is tuned for the detection of sub-MeV events while muons crossing the IV release energies of the order of hundreds of MeV. This might cause overflow and saturation in some Laben boards ("empty boards"), which then need some time before going back to normal operation, resulting in a partial blinding of the detector after very energetic muon events. These facts make the neutron identification for the  $^{11}\text{C}$  subtraction not as straightforward as it might seem.

The TFC algorithm can be summarized by the following steps:

- a 2-hour full volume blackout is applied at the beginning of each DST, since the grouping of data in weekly DSTs makes them independent on each other and the information on muons is not transferred from one DST to another.
- at the beginning of each run, a full volume veto is applied, since muons can be lost in the time window between two runs. The veto time is  $(600 + 3600(1 - e^{-3\Delta t/\tau}))$  s, where  $\Delta t$  is the time interval between the previous run end and the current run start and  $\tau$  is the neutron capture time ( $\sim 0.25$  ms).
- full 2-hour veto for events after muons with high neutron or muon daughter multiplicity or whether the muon track cannot be reconstructed.

- if the neutron position reconstruction is not reliable because of saturation or too many empty boards, a cylindrical veto along the muon track with a radius of  $\sim 1$  m for 2 hours is established.
- if either the FADC or the Laben system identify a neutron, a 2 m sphere cut for 2 hours is applied both around the neutron position and around the projection of the neutron capture on the muon track.
- if the FADC system recognizes more neutrons than the Laben electronics, all muon daughters are treated as detected neutrons.

The possible geometrical veto configurations are shown in the left panel of Fig. 6.4. The effect of the application of the TFC veto on Borexino Phase-II data is shown in the spectra comparison of the right panel of the same Fig. 6.4. The nominal parameters defining the time and geometrical vetoes are reported here as a reference, but their precise values have to be fixed during the tuning of the algorithm. Particularly, a compromise must be reached between the hardness of the cuts and the amount of the exposure which is left in the  $^{11}\text{C}$ -subtracted (“TFC subtracted”) spectrum used for fitting. Since the amount of residual  $^{11}\text{C}$  in the spectrum to be fitted is crucial especially for the pep  $\nu$  determination, the key parameter for the optimization of the TFC cut is the statistical sensitivity reachable on pep  $\nu$  in a given configuration. This is addressed with the MC on MC studies reported in Sec. 6.10.

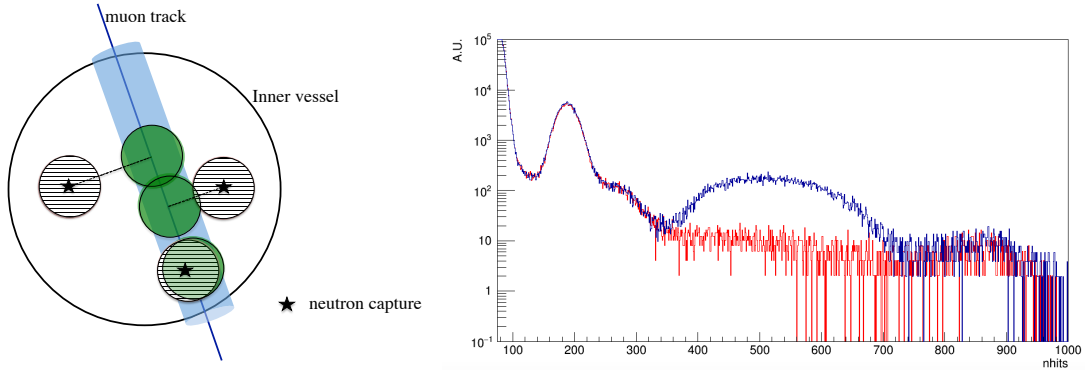


**Fig. 6.4:** *Left Panel:* Sketch of the geometrical veto applied by the TFC algorithm for different situations. Picture from Ref. [214]. *Right Panel:* Comparison between Borexino’s spectrum before (blue) and after (red) the TFC cut in the  $nhits$  variable. The spectra are normalized to the same exposure.

One of the quantities which must be evaluated precisely when applying the TFC cut is the exposure loss, which is quite significant. Typical achieved values range in  $50 \div 60\%$  livetime saved after the cut with a  $^{11}\text{C}$  suppression of  $90 \div 95\%$ . The precise evaluation of the actual saved exposure can be carried out only through a toy MC. In fact, the cut conditions are quite complicated, and it is impossible in practice to predict analytically the amount of dead time introduced. The toy MC procedure consists in

producing fake events with a constant rate (2 Hz) and with a uniform distribution in the FV. The number of events falling in the TFC veto are related to the total, thus resulting in a pretty solid evaluation of the exposure loss.

Besides the evident difference in the  $^{11}\text{C}$  contents, the two spectra shown in the right panel of Fig. 6.4 have a little different content of  $^{210}\text{Po}$ . This is a consequence of the  $^{210}\text{Po}$  decay and of a slightly non constant duty cycle of Borexino DAQ over the time. In fact, at the beginning of Phase-II, the duty cycle was worse than the average on all the period. This means that more full detector vetoes are applied with respect to the period average. The first part of the data taking also coincides with a higher  $^{210}\text{Po}$  content in the detector, and thus the amount of  $^{210}\text{Po}$  in the TFC subtracted spectrum is lower than that of the TFC vetoed one.

## 6.4 Choice of the spectrum binning

The choice of the number of bins to be used for building the spectra to be fitted might not be unique. A too fine binning would potentially make the spectrum a series of 0 or 1, while too few bins could alter the spectrum features. Furthermore, the Borexino spectrum has very different features and needs in different energy regions. For instance, at low energy, the statistics available is pretty high ( $^{14}\text{C}$  dominates), whereas at the pep  $\nu$  energies, especially after the TFC cut, the number of remaining events is “pretty low”. For these reasons, the bin width to be used in the histograms should be determined as a compromise on the whole energy region.<sup>2</sup>

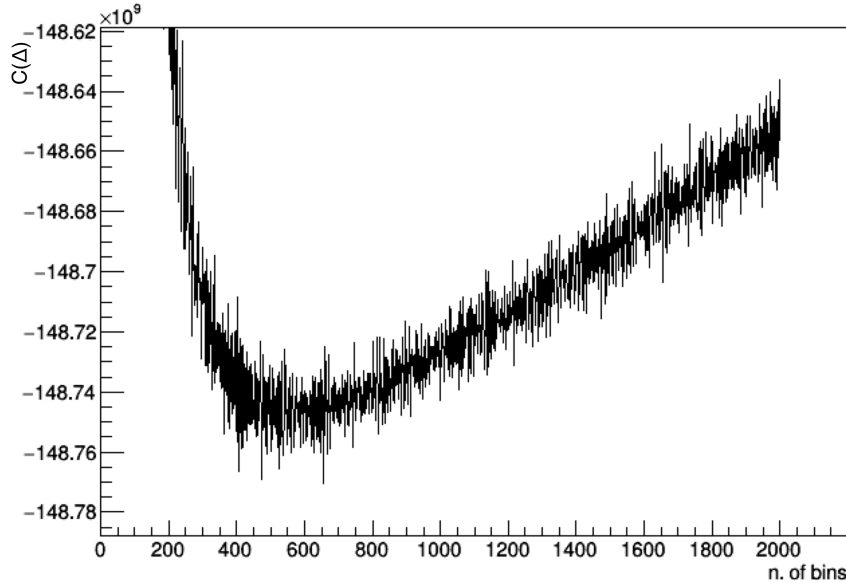


**Fig. 6.5:** Values of  $C(\Delta)$  as a function of the number of bins for Borexino data.

---

<sup>2</sup>Another possibility could be the usage of a non uniform binning, which is not considered here.

A bin width optimization procedure is proposed in Ref. [271]. This method is usually called “Mean Integrated Squared Error” (MISE) binning. It is based on the principle that with the best binning, fluctuations between close bins must be compatible with statistics, avoiding non statistical features. This is formalized by filling the histogram with the available data set assuming a bin width  $\Delta$  and computing a cost function

$$C(\Delta) = \frac{2k - v}{\Delta^2}, \quad \text{where } k = \frac{1}{N} \sum_{i=1}^N k_i \quad \text{and} \quad v = \frac{1}{N} \sum_{i=1}^N (k_i - k)^2, \quad (6.1)$$

with  $N$  being the number of bins and  $k_i$  the content of the  $i$ -th bin. Many histograms are filled with a varying value of  $\Delta$  and the best binning coincides with the situation in which  $C(\Delta)$  is minimum. Figure 6.5 shows the result of the MISE method for Borexino data. In this case, the test was performed on the *charge* variable in the range  $130 \div 800$  p.e. . Being the minimum of  $C(\Delta)$  close to a number of bins  $\sim 600$ , it is clear that the best binning for Borexino is achieved with a bin width of  $\sim 1$  p.e., which is the binning adopted in the work presented in this PhD thesis.

## 6.5 Effect of the normalization: “PDF masking”

During Borexino Phase-II the number of live PMTs diminishes with an almost constant rate in time ( $0 \div 2$  PMTs per week). This fact is normal, especially taking into account that Borexino PMTs have been in operation since 2007. In order to reduce the impact of the varying number of live PMTs on the detector energy scale, the energy variable normalization procedure outlined in Sec. 4.5 is adopted. This requires the calculation on an event basis of the factor  $f_{eq}(t) = 2000/N_{live_{pmt}}$ .  $f_{eq}$  is by definition a rational number. The values of  $N_{live_{pmt}}$  for the events considered in Phase-II analysis are given in the left panel (beta-like events) and right panel (alpha-like events) of Fig. 6.6. There is a clear difference between the  $N_{live_{pmt}}$  histogram for  $^{210}\text{Po}$  tagged events and that of beta-like events. This is due to the polonium decay. In fact, most of the  $^{210}\text{Po}$  events are recorded at the beginning of the data acquisition period and thus were acquired with a higher average number of live PMTs. On the contrary, the rate of beta-like events is almost constant<sup>3</sup> and thus the “weight” of lower values of  $N_{live_{pmt}}$  is almost as high as that of larger values.

When  $f_{eq}$  is multiplied by an integer number, such as the values referring to *npmts* or *nhits* variables, and then the result is inputed to a histogram with a given binning (typically 1 *npmts* or *nhits*), “strange” features with non statistical fluctuations between close bins are observed. This can be easily understood by generating uniform random integer numbers in the interval  $(0, 2000)$ , and then multiplying them by a value of  $f_{eq}$  computed according to the  $N_{live_{pmt}}$  distribution observed in data (either the one of  $\beta$ ’s or  $\alpha$ ’s). If one inputs the numbers thus obtained into a 1-unit bin wide histogram, the result is not a flat binned distribution as shown in the left panel of Fig. 6.7. This distribution

<sup>3</sup>Actually, this is not completely true, since the loss of PMTs affects the energy scale and also the trigger efficiency, reducing the number of  $^{14}\text{C}$  events able to fire the trigger and clustering algorithms.

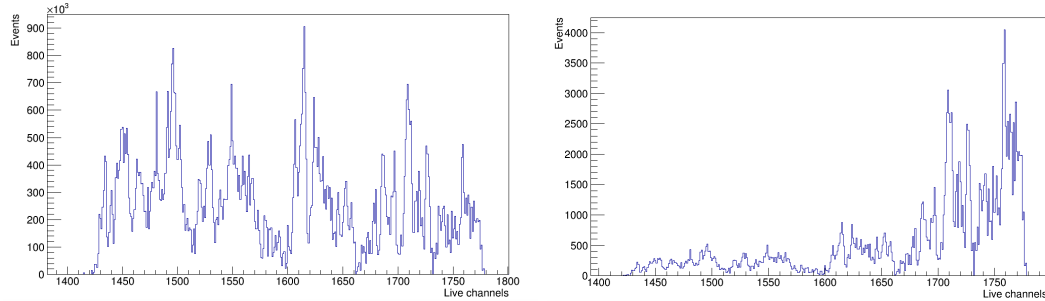


**Fig. 6.6:** *Left Panel:* Number of live PMTs for the events considered in the Phase-II analysis with the exclusion of  $^{210}\text{Po}$ . *Right Panel:* Number of live PMTs for events tagged as  $^{210}\text{Po}$  by the MLP variable.

is usually referred to as “mask”, in order to indicate the specific pattern which describes the filled histogram features. These unphysical peaks can be clearly seen in the high statistics bins of the spectra e.g. in Fig. 6.1. The mechanism originating the effect is simply the interaction of the multiplication of integer numbers with fixed rational coefficients together with the rounding induced by the binning choice. The effect depends on the binning and it is more evident when high statistics is available.

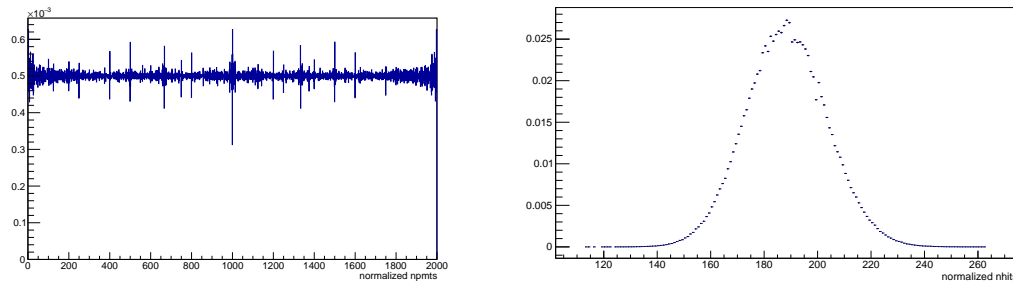


**Fig. 6.7:** *Left Panel:* Histogram filled with a uniform distribution of integer numbers in  $(0, 2000)$  multiplied by  $f_{eq}$  with the  $N_{live_{pmt}}$  distribution obtained from data. *Right Panel:*  $^{210}\text{Po}$  MC PDF prior to the elimination of the binning effects. The fluctuations observed are evidently non statistical.

A proper fit of Borexino data based on normalized “integer” energy variables such as  $npmts$  and  $nhits$  has to take into account this binning effect. In fact, the induced fluctuations between close bins are much higher than the ones allowed statistically, and for this reason they have to be considered in order to obtain a solid fit result.

Since data should not be altered prior to fitting, the PDFs must be multiplied with the mask, in order to introduce the features which the normalization procedure creates. It is possible to describe the spikes observed in the left panel of Fig. 6.7 without using the toy MC mentioned above. The mask contains 2000 bins, from 0 to 2000, and for each bin of the distribution of  $N_{live_{pmt}}$  (such as that shown in one of the panels of Fig. 6.6) a loop is performed over the 2000 bins of the mask. For each mask bin  $i$ , the mask is filled with

$i \times f_{eq}$ , with  $f_{eq}$  corresponding to the precise value of  $N_{live_{pmt}}$  examined. The content of the  $N_{live_{pmt}}$  bin considered is used as a weight to be associated to the value  $i \times f_{eq}$  which is inputed. The mask area is then normalized to the total number of bins (2000). This procedure allows to insert in the mask histogram the binning features induced by the normalization algorithm according to the measured distribution of  $N_{live_{pmt}}$ . By using the mask, it is therefore possible to reproduce the structures present in data or eliminate those originated in MC PDFs. In fact, when simulating data over the whole Phase-II period, the real distribution of  $N_{live_{pmt}}$  is reproduced, and thus the MC PDFs have by definition very prominent features of the binning effect. The spikes are even more evident than those observed in data, since the simulated statistics is typically higher. Of course, the successful application of the mask on MC PDFs is a demonstration that the procedure is effective. This was done especially with respect to the  $^{210}\text{Po}$  peak, since its shape is similar to a gaussian and the simulated statistics is pretty high. The MC PDF in normalized  $npmts$  or  $nhits$  energy variable for  $^{210}\text{Po}$  would look like the one shown in the right panel of Fig. 6.7. If each single bin is divided by the corresponding values contained in the mask for the same bin, the PDF becomes smooth such as that shown in the left panel of Fig. 6.8, and the binning effect disappears completely. This procedure is adopted in order to produce smooth MC PDFs to be used in the fit.

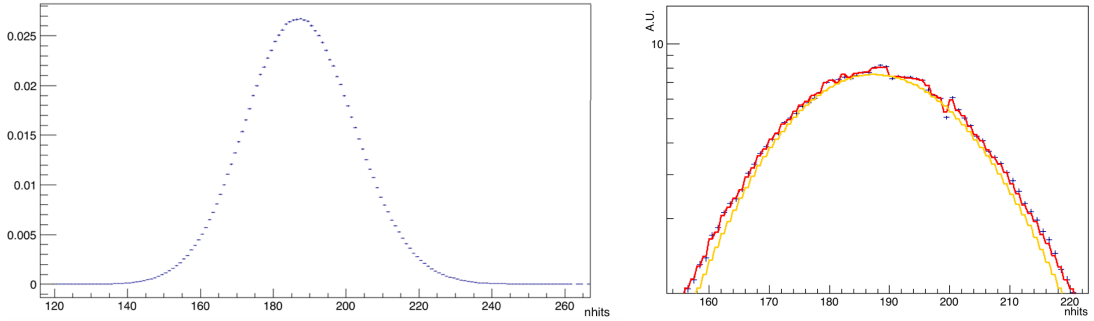


**Fig. 6.8:** *Left Panel:* MC  $^{210}\text{Po}$  PDF in the  $nhits$  normalized variable after the removal of the binning effect with the usage of the mask. *Right Panel:* Zoom of a fit of the  $^{210}\text{Po}$  peak in the  $nhits$  normalized variable where the binning effect present in data is correctly reproduced by the MC PDF to which the mask is applied (the smooth PDF is in yellow, while the red line shows the PDF after the mask application).

Both analytical and MC PDFs for  $npmts$  and  $nhits$  normalized energy variables are thus smooth, while data contains the binning effect. In the fit, PDFs are multiplied by the mask computed as discussed above and therefore the spikes are artificially introduced in the PDFs, which can reproduce quite well the behavior observed in data. The mask computation depends quite heavily on the  $N_{live_{pmt}}$  distribution and thus on the histograms shown in Fig. 6.6. For this reason, two masks are actually computed, independently for  $^{210}\text{Po}$  and beta-like events. An example of a PDF multiplied by the mask can be seen in the right panel of Fig. 6.8, where a zoom around the fit of the polonium peak is shown. The PDF shows the same binning features as the data, thus confirming that the mask is

working properly.

## 6.6 Radial distribution of events and $\beta^+/\beta^-$ pulse shape discrimination

The global fit of Borexino data, including the higher energy region for pep  $\nu$  and CNO  $\nu$  detection, needs the TFC suppression of  $^{11}\text{C}$  and an adequately small FV for the external background reduction. However, additional constraints for the residual  $^{11}\text{C}$  and external  $\gamma$ 's are needed. They are included in the fit according to the procedure outlined in Sec. 6.7. The reference PDFs for the radial distribution and for the  $\beta^+/\beta^-$  pulse shape discrimination must be produced either with the MC or from data. The procedures for building them is briefly outlined in the next subsections.

### 6.6.1 Radial versus energy distribution of events

The spatial distribution of events in Borexino is related to their origin. Neutrino events, cosmogenic<sup>4</sup> and intrinsic<sup>5</sup> contaminants are uniformly distributed, while external contaminations are not, because of the shielding offered by the scintillator itself. While an analytical description of the uniform volume distribution is possible, it is not straightforward to model the external component, since while  $\gamma$ 's lose energy, their interaction cross section with the scintillator varies. Furthermore, the effect of the position reconstruction algorithm cannot be easily modeled for events in which the energy deposits span over tens of cm. These facts led to the construction of two dimensional PDFs of radial distributions versus energy both for uniform and external components using the MC simulation. Figures 6.9 and 6.10 show the two dimensional (together with the projections over the energy axis) distributions of radius versus energy for uniformly distributed and external background events. The reference PDF for the uniform component is obtained by using a toy MC approach. Instead, the radial distribution of the external background is obtained with the full MC simulation and the procedure described in Sec. 5.10. This makes the statistics available for this reference much lower with respect to the uniform component, but still much higher than that of data. The validation of this distribution was performed against calibration data as discussed in Ref. 5.10.4.

### 6.6.2 $\beta^+/\beta^-$ pulse shape discrimination: the likelihood of the position reconstruction

As already introduced in Sec. 4.8, the formation of ortho/para-positronium leads to different time patterns, which could allow  $\beta^+/\beta^-$  discrimination. During Borexino Phase-I analysis, a discrimination parameter based on the neural network algorithm of

<sup>4</sup>Apart from some cosmogenic neutrons, probably produced in the WT or in the rocks, which anyhow lie outside the energy window of interest for the solar neutrino analysis.

<sup>5</sup>Apart from  $^{210}\text{Po}$ , which is not uniform in the volume as discussed in Sec. 4.9.1. However, this is not a problem for disentangling the external background components, since  $^{210}\text{Po}$  lies in a region of the spectrum where external  $\gamma$ 's are negligible.

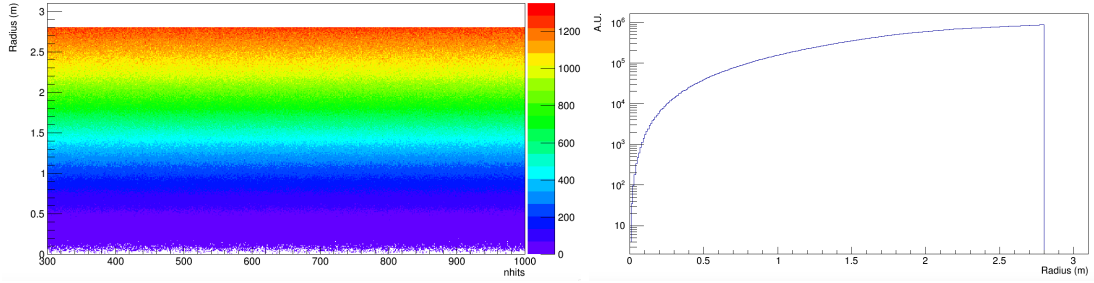


**Fig. 6.9:** *Left Panel:* Radial position versus the  $nhits$  energy estimator for uniformly distributed events in the pep FV. *Right Panel:* Radial distribution (integrated over energy) for uniformly distributed events in the pep FV.

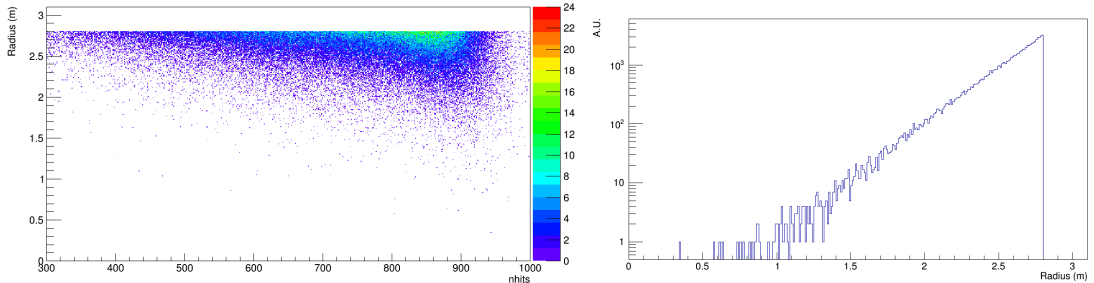


**Fig. 6.10:** *Left Panel:* Radial position versus the  $nhits$  energy estimator for external background events in the pep FV. *Right Panel:* Radial distribution (integrated over energy) for external background events in the pep FV.

the Boosted Decision Tree (BDT) was developed and used. However, for the Phase-II analysis, a novel discrimination approach was discovered. It has the advantages of being less affected by systematics and by energy dependence.

The  $\beta^+$  event topology is very different from that of  $\beta^-$ . In fact, besides the prompt energy release by the positron which loses momentum, the (possibly delayed)  $\gamma$ 's make the pattern of the energy deposits quite wide in space. An algorithm very sensitive to this difference is the position reconstruction (see Sec. 4.6). In fact, the mean travelled distance of 511 keV  $\gamma$ 's in the scintillator is  $\sim 10 \div 20$  cm which is of the same order (or bigger) than the position reconstruction precision on an event basis. The  $\beta^+$  event topology can create multi-maximum structures in the likelihood maximized by the position reconstruction algorithm  $\mathcal{L}_{pos}$ , and in general it is expected that in the case of particularly long lived ortho-positronium events the value of the likelihood at maximum is worse with respect to the analogous pure  $\beta^-$  event. Of course, since the position reconstruction algorithm is based on the collected hits, the value of the likelihood at the maximum has a significant energy dependence, which can be almost completely eliminated by dividing it by the number of fired PMTs. This fact has no rigorous theoretical motivation, but it is justified both by MC simulations and comparisons with data.

The sample of  $\beta^-$  events used to produce the reference PDF for the multivariate fit

(see Sec. 6.7) is extracted from the prompt events of the  $^{214}\text{Bi}$ - $^{214}\text{Po}$  coincidences detected during the water extraction periods (the same events used for tuning the Gatti and MLP parameters for  $\alpha/\beta$  discrimination, see Sec. 4.7). Instead,  $\beta^+$  candidates are extracted among the TFC tagged events, with hard cuts on the energy and on the time correlation with the neutron and muon tracks. A comparison between the  $\beta^+/\beta^-$  discrimination capability of BDT and likelihood of position reconstruction<sup>6</sup> is given in the two panels of Fig. 6.11. Already from Fig. 6.11 it is clearly visible that the discrimination power of the likelihood is not much different from that of the BDT. It should also be noted that in the position reconstruction algorithm, the considered quantity is  $-\ln \mathcal{L}_{\text{pos}}$ , which is minimized (corresponding to the maximization of  $\mathcal{L}_{\text{pos}}$ ). The absolute value at minimum  $-\ln \mathcal{L}_{\text{pos}}|_{\text{min}}$  is considered, and in practice this means that larger values of the likelihood correspond to a worse reconstructed position. For this reason, ortho-positronium events can be identified with the events tagged as  $^{11}\text{C}$  in the tail at higher values of the likelihood in the right panel of Fig. 6.11.

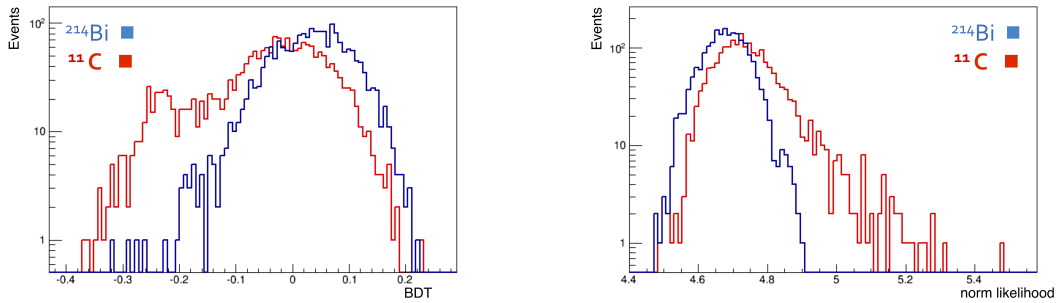


**Fig. 6.11:** *Left Panel:* BDT parameter values for  $\beta^+$  (red) and  $\beta^-$  (blue) events. *Right Panel:* Likelihood of the position reconstruction normalized to the number of fired PMTs for  $\beta^+$  (red) and  $\beta^-$  (blue) events.

The usage of the likelihood instead of the BDT has a number of advantages. First of all, the samples of  $^{11}\text{C}$  and  $^{214}\text{Bi}$  available for the PDF creation are not very large (they are of the order of  $\sim 10^4$  events in the FV). The BDT algorithm needs to use a quite significant fraction of the primary events in order to be trained, and thus the amount of events effectively available for fitting is reduced to a few thousands in total. Furthermore, the systematics associated to the neural network training are not easy to assess. In fact, one of the most important systematic errors in the pep  $\nu$  analysis presented in Ref. [224] comes from the  $\beta^+/\beta^-$  pulse shape parameter. An additional difficulty is introduced by the features of the  $^{214}\text{Bi}$  used for training and fitting. As already discussed in Sec. 4.7 and shown in the right panel of Fig. 4.8, the  $^{214}\text{Bi}$ - $^{214}\text{Po}$  coincidences in Borexino are mostly concentrated in the upper hemisphere. In addition, those events are selected in a very short period of time prior to the beginning of Phase-II. Therefore, while  $^{11}\text{C}$  events are selected uniformly by the TFC both in space and in time and are representative of

<sup>6</sup>From now on, unless explicitly stated, when referring to the likelihood of the position reconstruction, its absolute value is intended to be divided by the number of fired PMTs.

the time evolution of the detector response,  $^{214}\text{Bi}$  events are asymmetric and do not take into account of the effects of the PMT loss. The possible bias induced by these facts is hard to quantify when using a neural network which depends non trivially on many variables. It has anyhow to be noted, that the PMT loss effect was almost negligible for the analysis presented in Ref. [224], since the water extraction period was much closer in time to the data used for fitting and the amount of statistics was much less than that of Phase-II.

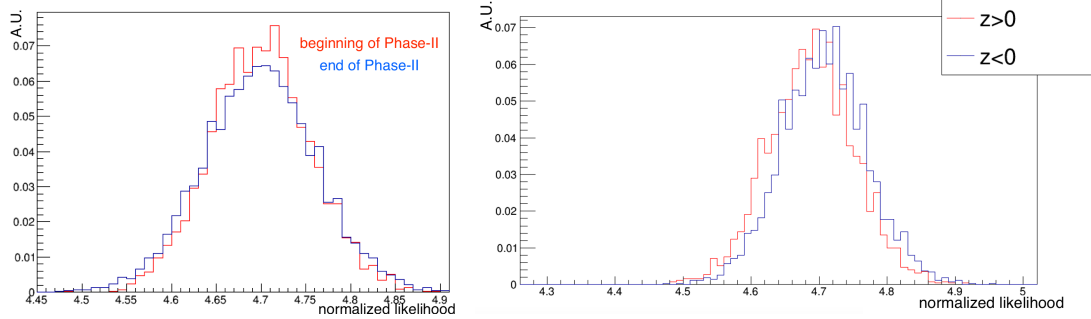


**Fig. 6.12:** *Left Panel:* Normalized likelihood distribution for uniformly distributed electron events in the  $^{11}\text{C}$  energy range for run conditions equivalent to the beginning (red) and to the end (blue) of Phase-II. *Right Panel:* Normalized likelihood distribution for uniformly distributed electron events in the  $^{11}\text{C}$  energy range and selected in the upper (red) and lower (blue) hemispheres.

Another critical point of the BDT approach is the difficulty of reproducing it with MC simulations reliably. In fact, the precision in the simulation needed on all the variables involved in the BDT computation is not straightforward to get. This makes it impossible to study the impact of the PMT loss and of the non uniform  $^{214}\text{Bi}$  event distribution on the BDT algorithm with simulations. On the contrary, position reconstruction works reliably in MC and it reproduces pretty well the data, allowing the study of these two mentioned effects and possibly correct the reference PDFs to take them into account. The left panel of Fig. 6.12 shows the MC simulated likelihood of position reconstruction of uniformly distributed electrons in the  $^{11}\text{C}$  energy range for two different runs, one at the beginning of Phase-II and the other one towards the end. The effect of the PMT loss is evident, since the observed distribution widens (thus the position reconstruction gets worse) as less PMTs are operative. On the right panel of Fig. 6.12, electrons are simulated uniformly in the FV for a given run number, but then they are split in two families, according to the hemisphere to which they belong. Since most of the dead PMTs are at the bottom of Borexino, the position reconstruction is worse for events at the bottom with respect to those in the North hemisphere. Both these facts can be described and predicted by the MC and must be taken into account when producing the reference PDFs for fitting. In parallel to the MC correction, a data driven method can be adopted and the runs from water extractions could be reprocessed with lower values of live PMTs, according to the measured distribution during Phase-II. However, this method cannot take into account the modifications on the position reconstruction likelihood induced by

the asymmetry of the events in the FV.

The good discrimination power of the normalized likelihood of the position reconstruction and its milder energy dependence with respect to that of the BDT are outlined in Fig. 6.13. The two dimensional distributions of BDT and likelihood versus energy (in this case the *charge* energy estimator) are given and whereas the BDT energy dependence is evident, the normalized likelihood appears almost energy independent. Intrinsically, it should not be possible to define a pulse shape discrimination variable for  $^{11}\text{C}$  based on the collected light which does not depend on the energy at all, since the different amount of energy released by the positron deceleration alters the hit pattern quite significantly. However, the milder energy dependence shows that the normalized likelihood is actually based on the identification of the characteristics defining the emission of the two back-to-back  $\gamma$ 's. This results in a more effective discrimination power, as shown in the rightmost panel of Fig. 6.13. Here, the correlation between BDT and likelihood is shown: in the regions of the plot where the two variables are not linearly correlated, the BDT seems to be degenerate whereas the likelihood assumes a continuum of values which could probably be associated to the different lifetimes of the ortho-positronium states producing those events.

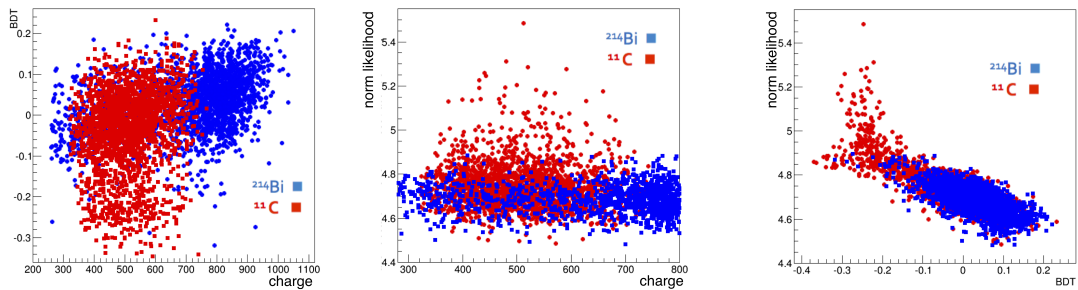


**Fig. 6.13:** *Left Panel:* BDT versus *charge* for  $^{11}\text{C}$  (red) and  $^{214}\text{Bi}$  (blue) events. *Central Panel:* Normalized position reconstruction likelihood versus *charge* for  $^{11}\text{C}$  (red) and  $^{214}\text{Bi}$  (blue) events. *Right Panel:* Normalized position reconstruction likelihood versus BDT for  $^{11}\text{C}$  (red) and  $^{214}\text{Bi}$  (blue) events.

For the reasons above discussed, the pulse shape parameter which is used in the analysis presented in this PhD thesis is the normalized likelihood of the position reconstruction.

## 6.7 Fitting procedure

The method of maximum likelihood is used in Borexino's analysis to fit the data. This approach is convenient for at least two reasons:

- some of the spectrum bins have low statistics and thus are in the Poisson regime.
- it is possible to generalize the likelihood definition in order to perform a multivariate fit, where the information from pulse shape parameters and radial distribution is

added to the energy spectrum information. The multivariate approach, where the radial distribution is fitted simultaneously with the energy spectrum, was pioneered by the SNO and SuperKamiokaNDE collaborations.

This fitting strategy has already been discussed extensively for the Borexino Phase-I analysis [214, 224, 267], and thus only the most important concepts are recalled here. While for the pp  $\nu$  and  $^7\text{Be}$   $\nu$  measurements the fit of the energy spectrum only is sufficient to get a good result, the investigation of pep  $\nu$  and CNO  $\nu$  requires that external and cosmogenic backgrounds are further suppressed in the fit with the addition of the radial and  $\beta^+/\beta^-$  pulse shape distributions.

The total likelihood to be maximized with respect to the set of parameters  $\vec{\theta}$  is thus:

$$\mathcal{L}_T(\vec{\theta}) = \mathcal{L}_E^{TFC_{sub}}(\vec{\theta}) \cdot \mathcal{L}_E^{TFC_{tagged}}(\vec{\theta}) \cdot \mathcal{L}_{PS}(\vec{\theta}) \cdot \mathcal{L}_{Rad}(\vec{\theta}), \quad (6.2)$$

where  $\mathcal{L}_E^{TFC_{sub}}(\vec{\theta})$  is the likelihood computed on the spectrum after the TFC cut,  $\mathcal{L}_E^{TFC_{tagged}}(\vec{\theta})$  is calculated on the spectrum obtained with the events removed by the TFC (“complementary spectrum”),  $\mathcal{L}_{PS}(\vec{\theta})$  is the likelihood of the  $\beta^+/\beta^-$  pulse shape discrimination parameter and  $\mathcal{L}_{Rad}(\vec{\theta})$  is the likelihood of the radial distribution of the events.

The first two terms are standard Poisson likelihoods on the two input energy spectra (TFC subtracted and TFC tagged):

$$\mathcal{L}_E^{TFC_{sub/tagged}}(\vec{\theta}) = \prod_{i=1}^N \frac{\lambda_i(\vec{\theta})^{k_i} e^{-\lambda_i(\vec{\theta})}}{k_i!}, \quad (6.3)$$

where  $i$  labels the spectrum bins,  $N$  is the total number of bins,  $\lambda_i(\vec{\theta})$  is the expected number of entries in the  $i$ -th bin given the parameters  $\vec{\theta}$  and  $k_i$  the measured number of entries in the  $i$ -th bin. The TFC tagged and TFC subtracted spectra are independent, since the events rejected by the TFC veto come from space-time regions of the sensitive volume which are disjoint from the non-vetoed ones. This allows to fit the two spectra simultaneously simply multiplying their own Poisson likelihood terms. No constraint on the total number of events (i. e. on the sum of the TFC tagged and subtracted spectra) is added to the likelihood.

The TFC tagged and TFC subtracted spectra share the rates of most of the components, such as the neutrinos or internal contaminations. However, cosmogenic components other than  $^{11}\text{C}$  such as  $^{10}\text{C}$  or  $^6\text{He}$  have to be decoupled between the two spectra since their abundances are related to muons, and thus are affected by the TFC cut. As already anticipated in Sec. 6.3, also the  $^{210}\text{Po}$  rate is different in the TFC subtracted and tagged spectra, since the time distribution of the TFC induced vetoes is not uniform, and thus more  $^{210}\text{Po}$  events are present in the TFC tagged spectrum.

The definition of the pulse shape and radial distribution parts of the likelihood has to take into account that the PDFs used for fitting are two dimensional. This requires quite high statistics, and while it is theoretically possible to have it (even if complicated) for the radial distribution, it is not achievable for the pulse shape, since it

is constructed from the data. At the same time, there exists no analytical model able to reproduce these multidimensional PDFs. For these reasons, the pulse shape/radial distribution versus energy is projected and integrated over an energy range larger than the energy spectrum binning, thus creating other one-dimensional histograms of the pulse shape/radial distribution for which the corresponding likelihoods are computed. Of course, this procedure generates a correlation between the number of counts in the different histograms, since the same events which are included in the TFC subtracted spectrum are included in the projections. In order to take this into account, the reference PDFs for pulse shape/radial distribution are normalized to the total number of entries in the projected data histograms to fit. Consequently, the likelihood for the pulse shape/radial distribution is:

$$\mathcal{L}_{PS/Rad}(\vec{\theta}) = \prod_{s=1}^P \prod_{j=1}^M \frac{a_s \lambda_{js}(\vec{\theta})^{k_{js}} e^{-a_s \lambda_{js}(\vec{\theta})}}{k_{js}!}, \text{ where } n_s = a_s \sum_{j=1}^M \lambda_{js}(\vec{\theta}), \quad (6.4)$$

with  $s$  running on the  $P$  energy projections of the pulse shape/radial distribution and  $j$  indexing the  $M$  bins of the projected histograms. The factors  $a_s$  enforce the normalization and take into account the correlation of the projections with the energy spectrum. With a similar notation of that of Eq. (6.3),  $\lambda_{js}(\vec{\theta})$  is the expected content of the  $j$ -th bin of the  $s$ -th pulse shape/radial distribution histogram,  $k_{js}$  is the measured number of entries in that bin and  $n_s$  is the total number of entries in the  $s$ -th projection.

The solidity of the likelihood thus constructed is discussed extensively e. g. in Ref. [267] and many tests to study the fitter biases and correlations are carried out in Sec. 6.8.

### 6.7.1 MC PDF production

MC PDFs are produced by simulating events according to the detector condition throughout the whole Phase-II of data acquisition. The simulated events undergo the same cuts of the real data and are processed by the same algorithms which create the histograms to be fitted. The PDFs are smoothed according to the procedure outlined in Sec. 6.5 (for  $nhits$  and  $npmts$ -like normalized variables). At the level of fitting, the mask computed from the data is applied on the PDFs, which then do not result smooth anymore, but reproduce the features of the data. In principle, the original features present in the MC PDFs prior to the smoothing should be the same as the ones present in data, since the time evolution of the live PMTs is strictly reproduced. This is in fact the case, but, for a more direct comparison with the analytical fit results, the procedure of smoothing is applied, so that the mask with which the data is fitted is the same as the one used in the analytical fit.

For almost all the species, the simulated statistics for the MC PDF creation is  $\sim 200$  times the expected interaction rate in the real data. This allows to neglect the statistical uncertainties on the PDFs with respect to those on data (which are  $\sim \sqrt{200}$  times higher). However, this is not possible for all the species. Although the external background simulation is very efficient, still the computing resources allocated for Borexino do not allow the production of such a high statistics and thus the enhancement factor is only

$\sim 50$ , which however still allows to discard the statistical uncertainty on the PDF. This is true also in consideration of the fact that the count rate of external background is pretty low, and thus the statistical uncertainty on the data is consistent. The case of  $^{14}\text{C}$  is instead a little different. In this case, the statistics is so high, that it is not possible to simulate even the same amount of events present in data. The statistics in the MC is around  $\sim 1/15$  with respect to that of data. Thus, the MC PDF for  $^{14}\text{C}$  has intrinsically a worse statistical error than the data. This is taken into account by using the Scaled Poisson distribution in the likelihood computation for the bins of the spectrum where  $^{14}\text{C}$  dominates. In practice, the data statistics is scaled to that of MC, increasing the error for those bins and thus reducing the weight in the total likelihood computation of this region of the spectrum.

All the species apart from the external background and  $^{14}\text{C}$  are simulated in a spherical volume with 3.75 m radius. Various MC tests allowed to prove that the position reconstruction algorithm selects events inside the FV quite efficiently in this case, and for this reason the generation of the events in the whole IV with the subsequent application of the FV cut is not needed. However, this is not true for external  $\gamma$ 's and  $^{14}\text{C}$ . In the case of external  $\gamma$ 's a preselection on the energy barycenter of the events  $\vec{R}_{bar} < 4$  m (see Eq. (5.17)) was applied, after the verification that this does not introduce biases in the energy spectrum reconstruction or in the FV cut efficiency.  $^{14}\text{C}$  events instead need to be simulated in the whole IV. In fact, the very low energy of most of the  $^{14}\text{C}$  events can make the reconstruction algorithm work not very efficiently, bringing in the FV some events which actually lie outside and vice versa.

## 6.8 Validation of the fit procedure

The fit procedure and behavior was tested with many MC on MC tests. MC PDFs used for fitting the real data are used for sampling data-like spectra which then are fitted with the standard procedure. This is repeated many times and the distribution of the fit results can be studied in order to highlight the most important correlations between the species inserted in the fit and potential biases in the reconstruction of the injected rates. The study of the correlations among the different species is of crucial importance, since the Borexino spectrum is fitted with many parameters and thus their interactions must be well understood before fitting the real data. A first test should be decoupled from the intrinsic degeneracies among the species due to the limitation in statistics. For this reason, a few thousands of data-like histograms were produced from the MC PDFs with a statistics equivalent to  $\sim 100$  times the one of Borexino Phase-II. The standard correlation plot allowing to study the fit results is shown in Fig. 6.14.

In Fig. 6.14, the distribution of the values for the different species (all the rates are expressed in cpd/100 ton) are shown (red histograms) and the two dimensional correlation plots for all the couples of species involved in the fit are attached. The fits reported in Fig. 6.14 were performed by fitting simultaneously the TFC subtracted and TFC tagged spectra with a statistics 100 times higher than that of Phase-II. The residual livetime in the TFC subtracted spectrum was chosen to be the 50% of the total with a

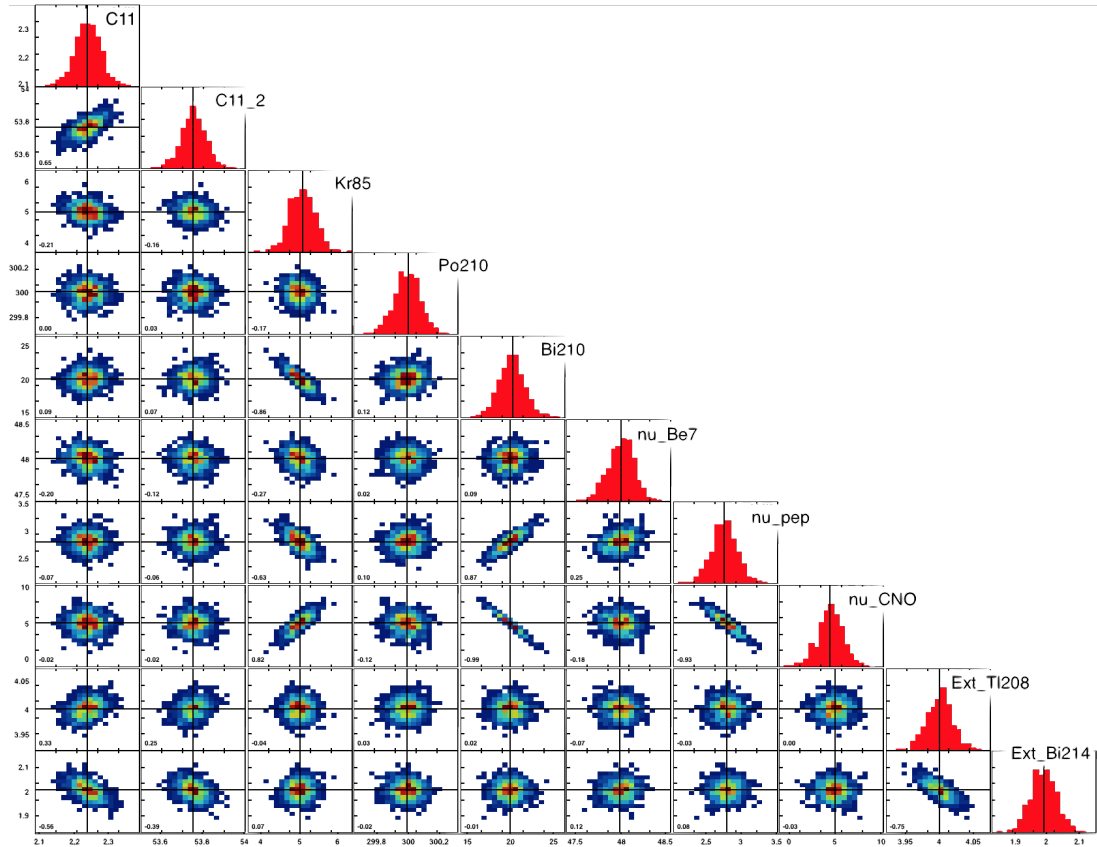


**Fig. 6.14:** Correlation plots of many MC on MC fits of TFC subtracted and TFC tagged spectra corresponding to a statistics  $\sim 100$  times that of Borexino Phase-II. Linear correlation coefficients are shown at the bottom left corner of each two dimensional distribution.

$^{11}\text{C}$  suppression of 92%. In the plot, two independent fit variables for  $^{11}\text{C}$  are included in the fit, namely “C11” and “C11\_2”, since the amount of the residual  $^{11}\text{C}$  after the TFC is not known *a priori*. Studies for different combinations of these two TFC parameters were carried out (see Sec. 6.10 and Ref. [267]), the result being that the conclusions driven in this section would not be altered by a different choice. In the histograms showing the individual fit result distributions of the species rates, black vertical lines indicate the injected values of the rates of the single components. As the plot shows, all the species are reconstructed without any bias, since the result distributions are Gaussian and centered on the injected values of the rates.

The most evident, intrinsic correlation highlighted by Fig. 6.14 is the one between  $^{210}\text{Bi}$  and CNO  $\nu$ : the correlation coefficient is  $R = -0.99$ . This was expected, since  $^{210}\text{Bi}$  and CNO  $\nu$  PDFs are almost degenerate. However, with a very high statistics such as the one simulated for Fig. 6.14, the fitter is able to disentangle the two components. Another important anti-correlation  $R = -0.93$  is the one between CNO  $\nu$  and pep  $\nu$ . In fact, the CNO  $\nu$  end point is almost completely overlapping with the region of the

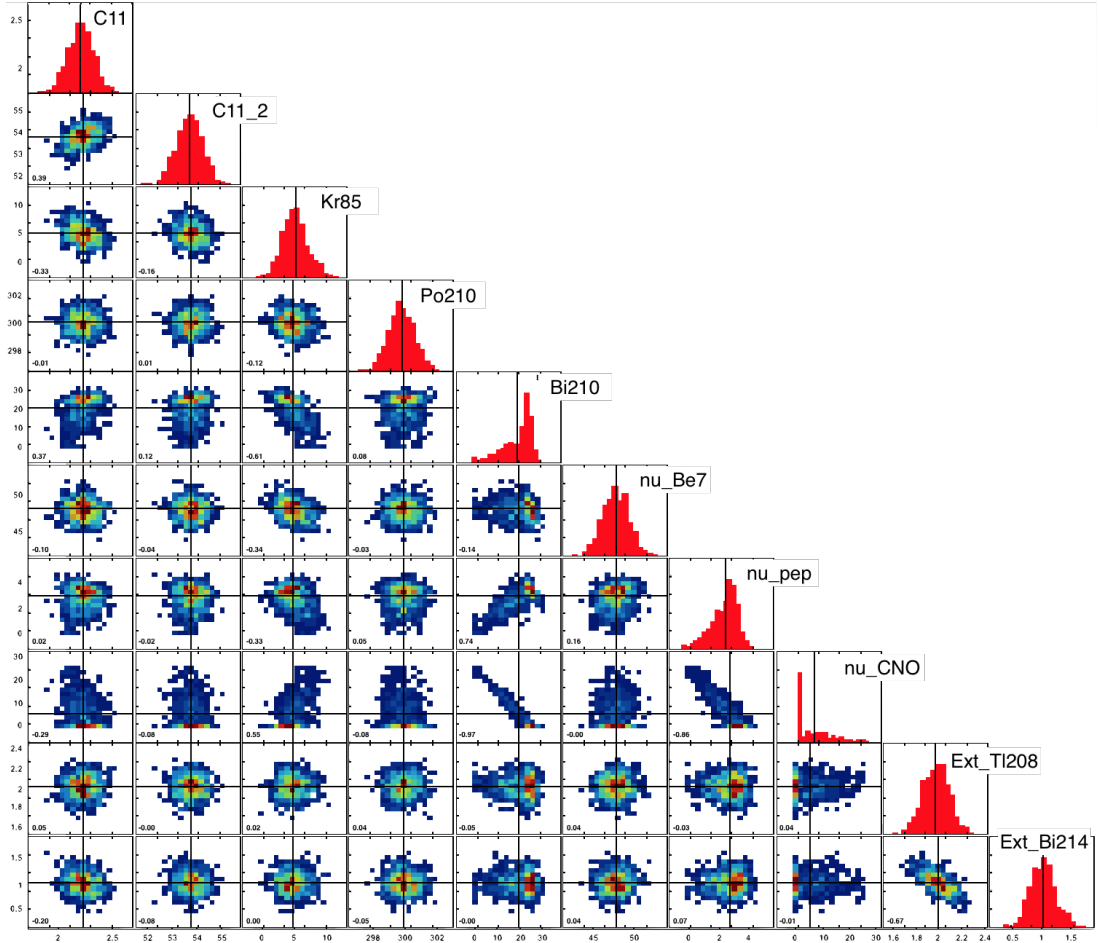


**Fig. 6.15:** Correlation plots of many MC on MC fits with the full multivariate fit procedure (TFC subtracted and tagged spectra, position reconstruction likelihood and radial distributions) corresponding to a statistics of 1200 days, equivalent to that of Borexino Phase-II. Linear correlation coefficients are shown at the bottom left corner of each two dimensional distribution.

pep  $\nu$  shoulder in which the fit is most sensitive. These two anti-correlations induce a positive correlation between pep  $\nu$  and  $^{210}\text{Bi}$ . In turn, the  $^{210}\text{Bi}$  component is also anti-correlated with the  $^{85}\text{Kr}$  one because of their shapes below the  $^7\text{Be}$   $\nu$  electron recoil spectrum and thus, as a consequence, a positive correlation between CNO  $\nu$  and  $^{85}\text{Kr}$  is observed. This correlation map makes already clear the reasons why the CNO  $\nu$  detection is very complicated. The only other notable correlation is the one between the external  $^{208}\text{Tl}$  and  $^{214}\text{Bi}$  components, because of their quite similar shape, which anyhow is not really critical within the solar neutrino analysis.

The correlations mentioned above are physical, and intrinsic of Borexino's spectrum. The injected values for the single species were chosen to be consistent either with the SSM or with independent estimates on Borexino data of the major contaminants (e.g.

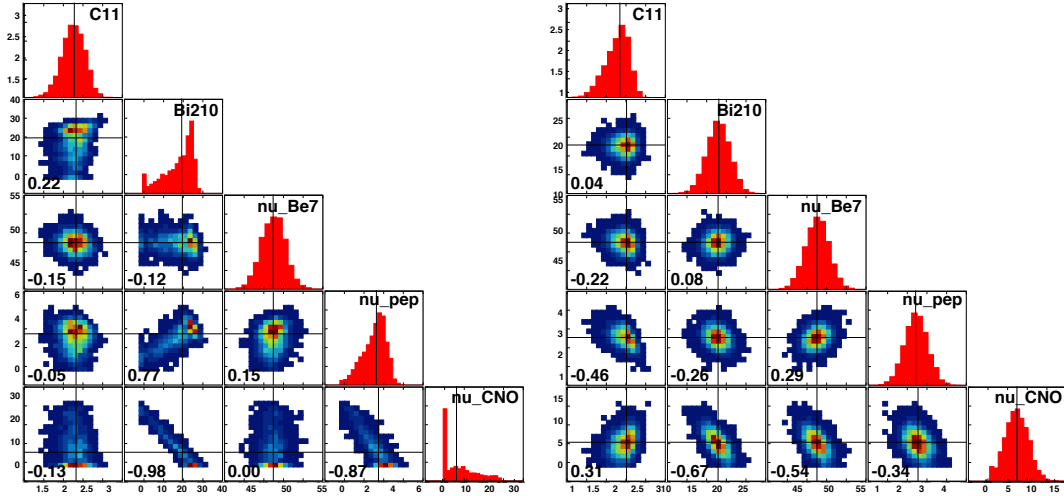


**Fig. 6.16:** *Left Panel:* Correlation plots of MC on MC fits with the full multivariate fit procedure corresponding to a statistics of 1200 days, equivalent to that of Borexino Phase-II. Zoom on a few selected components crucial for  ${}^7\text{Be}$   $\nu$ , CNO  $\nu$  and pep  $\nu$  detection. *Right Panel:* Correlation plots of MC on MC fits with the full multivariate fit procedure corresponding to a statistics of 1200 days, equivalent to that of Borexino Phase-II. Zoom on a few selected components crucial for  ${}^7\text{Be}$   $\nu$ , CNO  $\nu$  and pep  $\nu$  detection. In these fits, the  ${}^{210}\text{Bi}$  is constrained with a parabolic term in the likelihood with a precision of 20% around the true value.

${}^{85}\text{Kr}$  can be estimated by the search of delayed coincidences, as discussed in Sec. 4.3). The absence of any bias also allows to be confident of the fitting procedure algorithm.

The second step for the fit strategy characterization is the production of the correlation plots with many fits obtained from data sets with a statistics comparable to that of Borexino Phase-II and with the full multivariate algorithm working, i. e. in addition to the TFC subtracted and tagged spectra, also the normalized likelihood of the position reconstruction and the radial distribution are added. The result is shown in Fig. 6.15.

The most evident feature in the correlation plots with 1200 days of statistics and without any external constraint is the fact that the fit is not able to resolve the CNO  $\nu$  anymore. The distribution of the results is thus a broad Gaussian, truncated at zero, where most of the fit results lie. As a consequence, the reconstructed  ${}^{210}\text{Bi}$  value are peaked not around the “true” injected  ${}^{210}\text{Bi}$  rate, but to that of the sum of CNO  $\nu$  and  ${}^{210}\text{Bi}$ . The impact of the multivariate fit (both regarding the radial and the pulse shape distributions) is very positive, since the distribution of the pep  $\nu$  reconstructed rates narrows a lot with respect to the case in which only the energy spectrum is fitted. At the same time, all the components are reconstructed by the fit procedure without any bias, thus confirming that the likelihood definition of Eq. (6.2) is solid and consistent.

Figure 6.14 shows that an exposure 100 times bigger than that of Phase-II would allow a measurement of CNO  $\nu$  without the need of any assumption on the  ${}^{210}\text{Bi}$  rate. This is impossible in the realistic case of the Phase-II exposure (see Fig. 6.15). Unfortunately, MC simulations show that the CNO  $\nu$  flux measurement cannot be achieved if the exposure

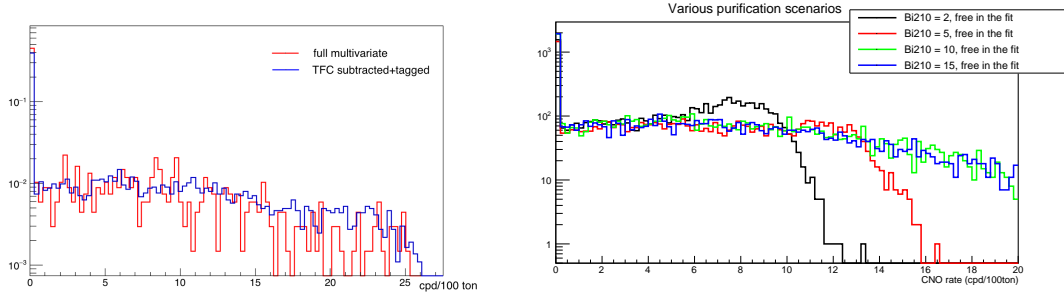


**Fig. 6.17:** *Left Panel:* Reconstructed values for the CNO  $\nu$  rate in MC fits with (red) and without (blue) the usage of the pulse shape and radial distributions in the spectral fit.  $^{210}\text{Bi}$  is left free in the fit. *Right Panel:* Reconstructed values for the CNO  $\nu$  rate in MC fits on data-like samples containing different amounts of  $^{210}\text{Bi}$ , which is left free in the fit.

is increased only by a “tiny” factor (e.g. a factor of 2). The amount of statistics needed for the CNO  $\nu$  determination independently from the  $^{210}\text{Bi}$  has to be at least  $10 \div 20$  times larger than the current one. This is not achievable in practice, also considering the natural aging of the detector over the years.

It is useful to study how the correlations are broken by the introduction of a constraint on  $^{210}\text{Bi}$ . In fact, the major correlations among the parameters left free in the fit are driven by the degeneracy between  $^{210}\text{Bi}$  and CNO  $\nu$ . In Borexino Phase-I analysis [214], the amount of  $^{210}\text{Bi}$  was almost a factor of 2 higher than what is observed in Phase-II. Paradoxically, the higher purity of Borexino makes it even more difficult to disentangle the degeneracy, since the two count rates are closer to each other. Figure 6.16 shows the correlation plots of selected background components which are important for the  $^7\text{Be}$   $\nu$ , pep  $\nu$  and CNO  $\nu$  detection, namely  $^{11}\text{C}$  and  $^{210}\text{Bi}$ . The plot on the left is obtained by fitting without any external constraint, while the picture on the right contains a parabolic penalty in the likelihood which constrains the  $^{210}\text{Bi}$  rate with a precision of 20% around the true value at  $1\sigma$ . The addition of the constraint on the  $^{210}\text{Bi}$  breaks almost completely all the correlations. For this reason, the search of an independent method for the estimation of the  $^{210}\text{Bi}$  is important besides the CNO  $\nu$  detection, since it makes the fit results more stable and reliable also for the pep  $\nu$  measurement.

MC on MC studies allow also to state that for the CNO  $\nu$  detection it is much more important to know independently the amount of  $^{210}\text{Bi}$  present in the scintillator, other than to have it very low. The left panel of Fig. 6.17 shows the reconstructed values for the CNO  $\nu$  rate with MC on MC studies. This plot is essentially a zoom of the CNO  $\nu$  fitted rate histograms presented in the correlation plots of Fig. 6.15 and in the left panel of Fig. 6.16. The addition of the pulse shape and radial distributions is crucial for the pep  $\nu$  measurement, while it is almost useless for the CNO  $\nu$  detection, since the dominating problem is  $^{210}\text{Bi}$ . The reconstructed values are distributed almost flat, ranging from 0 to  $\sim 25$  cpd/100 ton, which corresponds to the amount of counts injected for the sum of  $^{210}\text{Bi}$  and CNO  $\nu$ . The addition of the  $^{210}\text{Bi}$  constraint allows to reconstruct with higher probability the true value of the CNO  $\nu$  rate, as shown in the right panel of Fig. 6.16.

The right panel of Fig. 6.17 shows that even if the true count rate of  $^{210}\text{Bi}$  was reduced to the level of a few cpd/100 ton, it would not be possible to reconstruct the CNO  $\nu$  rate without an independent constraint on bismuth. This effect is directly connected to the almost complete degeneracy between the two PDFs with Borexino Phase-II statistics.

In the previous studies,  $^{14}\text{C}$  and pp  $\nu$  were not introduced. The pp  $\nu$  rate is critically anti-correlated with the pileup rate, which is however constrainable in the fit with independent estimations. Even if the MC on MC studies are enlarged to the lower energy part of the spectrum, no biases are observed and the previous conclusions, which aimed at highlighting the most difficult intrinsic correlations to break, are not modified.

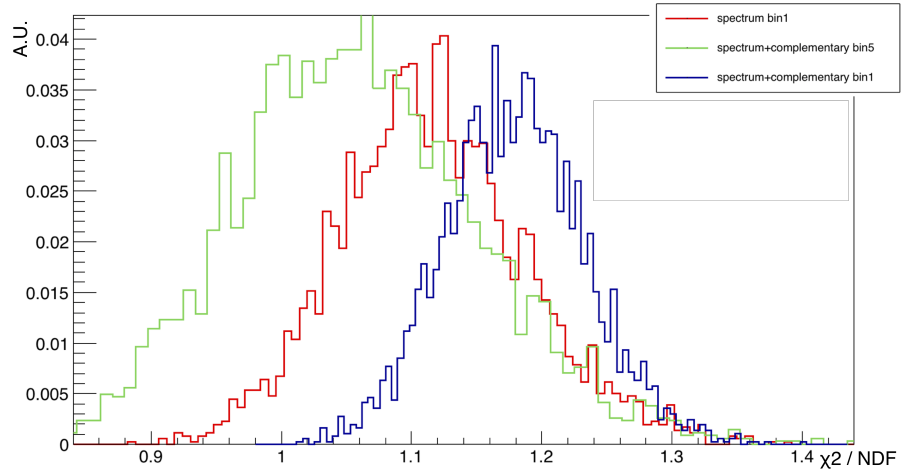
## 6.9 Goodness of fit evaluation

Figure 6.18 shows the  $\chi^2/NDF$  value computed after the likelihood maximization for MC on MC fits in different situations. In particular, the fits were performed on the energy spectrum only (without the TFC application) or on the two energy spectra (TFC subtracted and tagged) with different binning. Since the amount of degrees of freedom is of the order of some hundreds, it is clearly visible that the  $\chi^2/NDF$  value computed after the maximization is not distributed according to a  $\chi^2$  distribution. In fact, almost Gaussian distributions centered around 1 should be observed in Fig. 6.18. Instead, the  $\chi^2/NDF$  at the maximum likelihood depends on the histogram binning and on the application of the TFC cut. This simply means that at least part of the bins do not contain a statistics high enough for the Gaussian fluctuation approximation to be good. This is particularly the case of bin width equal to 1  $nhits$  and when the TFC cut is applied. The removal of  $^{11}\text{C}$ , in fact, leaves many bins dominated by pep  $\nu$  or external  $\gamma$ 's which have low statistics, of the order of a few counts per bin for the whole Phase-II. The  $\chi^2/NDF$  distribution is moved to have mean  $\sim 1$  if a bin width of  $\sim 5$   $nhits$  is chosen, thus confirming that the low statistics bins are responsible for the deviations from the expected  $\chi^2$  distribution.

The only way to test the actual goodness of fit is to perform a toy MC study, in order to extract the expected distribution of the maximum likelihood and then compare the measured value of the likelihood at maximum with the MC distribution. In the specific case, the fit is performed on the data, and the resulting count rates on the species are used as injected values for the generation of many MC on MC fits in the same condition of the real fit on the data. From these fits, the distribution of the likelihood values at maximum is extracted and it is compared to what is observed on the data.

## 6.10 TFC parameter optimization

As introduced in Sec. 6.3, the TFC veto can be optimized so that either the  $^{11}\text{C}$  reduction is very high or the saved livetime after the veto is larger. This can be achieved by hardening or softening some of the parameters defining the time-space geometrical veto of the detector subsequent to  $\mu$  interactions in the scintillator. Therefore, an *a priori* method for the determination of the best parameters for the TFC does not exist. The



**Fig. 6.18:**  $\chi^2/NDF$  distributions for MC on MC fits of the energy spectrum only and bin width 1  $nhits$  (red), of both the TFC tagged and subtracted spectra and bin width 1  $nhits$  (blue) and 5  $nhits$  (green).

approach which has been followed since Ref. [267] consists in evaluating the precision of the pep  $\nu$  determination as a function of the fraction of saved livetime after the TFC veto and of the amount of  $^{11}\text{C}$  surviving in the TFC subtracted spectrum. This result can be achieved by performing a few thousands of MC on MC fits for each combination of these two TFC performance parameters and study the distribution of the error on pep  $\nu$ . Figure 6.19 shows the pep  $\nu$  expected error as a function of the TFC parameters thus obtained. Of course, no study is needed in order to state that a better measurement is obtainable by increasing the saved fraction of livetime and reducing the residual  $^{11}\text{C}$  contamination, but the aim of the study is both to quantify the expected error on pep  $\nu$  and to find out the partial derivatives of the pep  $\nu$  error in the two parameter directions, in order to decide whether to push the  $^{11}\text{C}$  removal or the saving of the livetime. The dotted circle in Fig. 6.19 shows the region of parameters describing the performance of the current TFC veto, thus showing that quite an improvement with respect to the Phase-I pep  $\nu$  measurement should be achieved with the new analysis.

## 6.11 The spectral fit

The spectral fit of Borexino data in the whole region of interest for low energy solar neutrino spectroscopy (i. e. all solar neutrinos apart from  $^8\text{B} \nu$  and hep  $\nu$ ) is performed thanks to the usage of MC PDFs. Before the developments described in this PhD thesis, such global analysis was not possible and a fit where pp  $\nu$ ,  $^7\text{Be} \nu$ , pep  $\nu$  and CNO  $\nu$  were contemporarily studied could not be carried out.

Table 6.2 summarizes the parameters (i. e. the interaction rate of each species) and their role in the fit, which is performed as discussed in Sec. 6.7. The  $^{214}\text{Pb}$  rate is fixed thanks to its determination through the tagging of  $^{214}\text{Bi}$ - $^{214}\text{Po}$  coincidences. However,

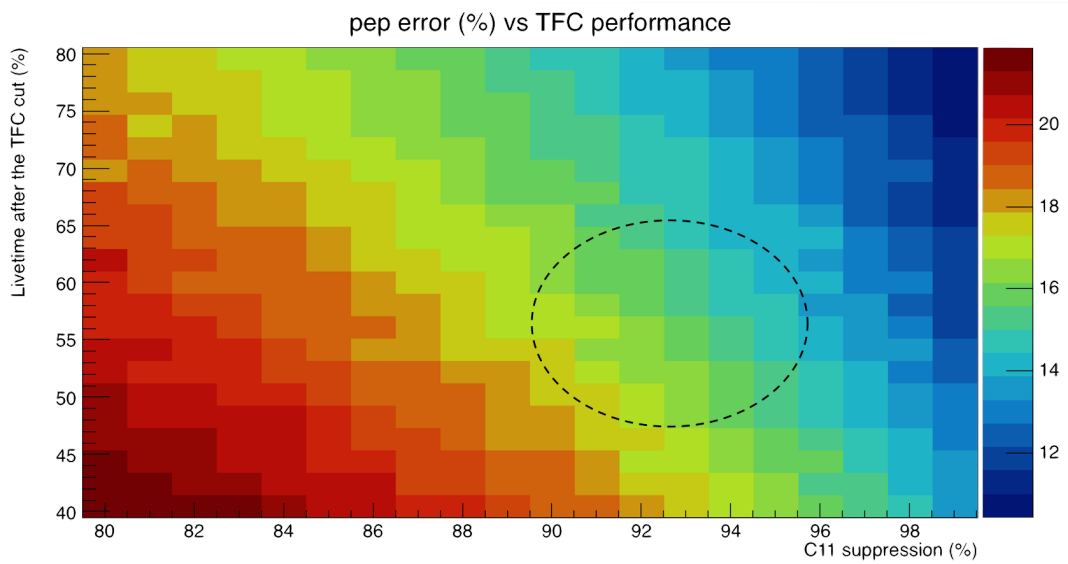


**Fig. 6.19:** Percentage error on the pep  $\nu$  obtained by MC on MC simulations as a function of the fractional livetime after the TFC cut and the  $^{11}\text{C}$  suppression. The dotted line circle highlights the region of parameters achieved by the current TFC code. A substantial improvement on the pep  $\nu$  measurement with the new data set is expected, since the previous measurement had an uncertainty of  $\sim 20\%$ .

this rate is determined to be so low ( $\ll 1\text{cpd}/100\text{ ton}$ ) that the presence of the  $^{214}\text{Pb}$  component in the fit is almost irrelevant. The rate of  $^8\text{B}$   $\nu$  is fixed to the prediction of the *high-Z* SSM, but since the interaction rate is around  $\sim 0.5\text{ cpd}/100\text{ton}$ , also this component is negligible in the low energy part of Borexino's spectrum. The rate of  $^{85}\text{Kr}$  is constrained thanks to its independent determination through the delayed coincidence tagging procedure explained in Sec. 4.3. In addition, the  $^{14}\text{C}$  and pileup rates are constrained according to the arguments discussed in Sec. 5.11.5.

The  $^{10}\text{C}$  and  $^6\text{He}$  components are only present in the TFC tagged spectrum, since the temporal fit of events after muons indicate that their level is negligible in practice in the TFC subtracted spectrum. The addition of these two components in the fit of the TFC subtracted spectrum has anyway no impact on the results.  $^{11}\text{C}$  and  $^{210}\text{Po}$  are the only two species whose rates are independent in the TFC subtracted and tagged spectra. While the explanation of this need is trivial for the case of  $^{11}\text{C}$ , simply because the TFC algorithm was designed to suppress it, one might not expect that the rate of  $^{210}\text{Po}$  could be affected by the application of the TFC veto. The TFC algorithm efficiency depends on the duty cycle of the data taking, since many run interruptions cause a lot of full vetoes of the whole detector for some hours (see Sec. 6.3). The data acquisition became more stable throughout Phase-II, resulting in a net increase of the duty cycle within a few years after the start of the data taking. These facts, combined with the natural  $^{210}\text{Po}$  decay inside the detector, explain the higher number of  $^{210}\text{Po}$  events in the TFC tagged spectrum with respect to the TFC subtracted one. This clarifies the need for

Species	Free?	Common	PS type	Radial distribution
$^{210}\text{Bi}$	Yes	Yes	$\beta^-$	Uniform
$^{10}\text{C}$	Yes	Only TFC tagged	$\beta^+$	Uniform
$^{11}\text{C}$	Yes	No	$\beta^+$	Uniform
$^{14}\text{C}$	Constrained	Yes	$\beta^-$	Uniform
Pileup	Constrained	Yes	$\beta^-$	Uniform
Ext. $^{214}\text{Bi}$	Yes	Yes	$\beta^-$	External
Ext. $^{208}\text{Tl}$	Yes	Yes	$\beta^-$	External
Ext. $^{40}\text{K}$	Yes	Yes	$\beta^-$	External
$^6\text{He}$	Yes	Only TFC tagged	$\beta^-$	Uniform
$^{85}\text{Kr}$	Constrained	Yes	$\beta^-$	Uniform
$^{214}\text{Pb}$	Fixed	Yes	$\beta^-$	Uniform
$^{210}\text{Po}$	Yes	No	-	-
$^8\text{B} \nu$	Fixed	Yes	$\beta^-$	Uniform
$^7\text{Be} \nu$	Yes	Yes	$\beta^-$	Uniform
CNO $\nu$	Yes	Yes	$\beta^-$	Uniform
pep $\nu$	Yes	Yes	$\beta^-$	Uniform
pp $\nu$	Yes	Yes	$\beta^-$	Uniform

**Tab. 6.2:** The table lists the spectral components involved in the fit. The second column shows if the given species rate is free, fixed or constrained. The third column states whether the rate is shared between the TFC subtracted and TFC tagged spectra. The last two columns show if the species is considered  $e^+/e^-$  and externally/uniformly distributed in space in the pulse shape and radial distribution fits. Note that not all the species are effectively involved in the multivariate fit of the pulse shape and of the radial distribution (e. g.  $^{210}\text{Po}$ ), since this information is considered only in the energy ranges where external backgrounds and  $^{11}\text{C}$  are dominant, as clarified also in Tab. 6.3.

uncorrelated  $^{210}\text{Po}$  rates in the two spectra. The duty cycle non uniformity in time only affects  $^{210}\text{Po}$  since its rate is not constant in time but it is exponentially decreasing.

It has to be noted that for a better comparison of the results with those of Phase-I [224], the external background rates are scaled so that the PDF normalization takes into account only the events above a certain threshold ( $\sim 200 \text{ nhits}$ ). At very low energies ( $\text{nhits} < 80$ , thus far away from the starting point of the fit), the external background PDFs grow again because of the many Compton degraded events releasing a little portion of the primary energy inside the IV. The old algorithm used for the external background simulation did not allow to quantify this effect, and a lower threshold on the event energy was applied. In fact, as reported in Ref. [267], the external background rates inferred from the fit were distant up to a factor of 5 from the expectations based on the material contamination measurements. It turns out that if the low energy threshold is not applied to the new PDFs, the absolute count rates of external backgrounds returned from the fit increase by a factor  $3 \div 5$ , thus agreeing better with the predicted rates. However, the absolute value of the external background count rate in Borexino is not a crucial point for the solar neutrino interaction rate determination and for an easier comparison with

the old results the low energy threshold was applied. In view of the final publication, this condition will be probably removed and the “true” value of the rates will be reported.

Parameter	
Bin width	1 <i>nhits</i>
Energy range	92-950 <i>nhits</i>
Pulse shape fit	
Energy range	400-650 <i>nhits</i>
Bin width	250 <i>nhits</i>
Radial distribution fit	
Energy range	500-900 <i>nhits</i>
Bin width	25 <i>nhits</i>

**Tab. 6.3:** The main fit options are summarized. The bin width both in the pulse shape and radial distribution fits indicates the amount of energy bins in *nhits* for which the events are projected over for the respective multivariate fits. In the case of the pulse shape, only one fit is performed, while in the case of the radial distribution 16 additional histograms to be fitted are created, projecting events in 25 *nhits* wide energy bins.

The fit results presented in this PhD thesis were obtained by analyzing data in the pep FV. This choice resembles that of Phase-I analysis for the pep  $\nu$  determination and it is motivated by the need of reducing the external background components. However, consistent results were obtained when fitting data in both the  ${}^7\text{Be}$  and conic cut FVs. Thanks to their larger exposure with respect to the pep one, it is possible that in the future the Borexino Collaboration will release updated (and better) results obtained with a data set coming from either the  ${}^7\text{Be}$  or the conic cut FV.

One of the advantages of the MC fit procedure is the possibility to perform easily many fits with different energy estimators. This is a good crosscheck and allows to quantify the systematics associated to the energy variable definition. The fit presented in this section is obtained with the *nhits* variable and it should be considered as the “reference fit”. In fact, the *nhits* variable was the most studied one at the stage of MC tuning and validation and thus it can be considered as the “golden variable” for MC fitting. However, the MC is able to reproduce the energy spectrum in all the other energy variables and thus the fit was performed on the whole energy spectrum also using *npmts*, *npmts\_dt1* and *npmts\_dt2*. Consistent results were obtained also using the *charge* energy estimator, but they are not reported here, since the *charge* energy variable does not allow to fit the lower energy part of the spectrum. This problem is not connected with the MC but it is an intrinsic feature of *charge*: at low energy, the contribution of dark noise or of other “strange” effects, such as radioactivity or Čerenkov light in the PMT glass, spoils the *charge* energy estimator. The results of the fits performed using *npmts*, *npmts\_dt1* and *npmts\_dt2* as energy variables are considered in Sec. 6.12 when evaluating systematic uncertainties and are reported in App. C.

Table 6.3 summarizes the main fit options, such as the energy ranges for the fit and for the application of the multivariate fits of the  $\beta^+/\beta^-$  pulse shape and radial

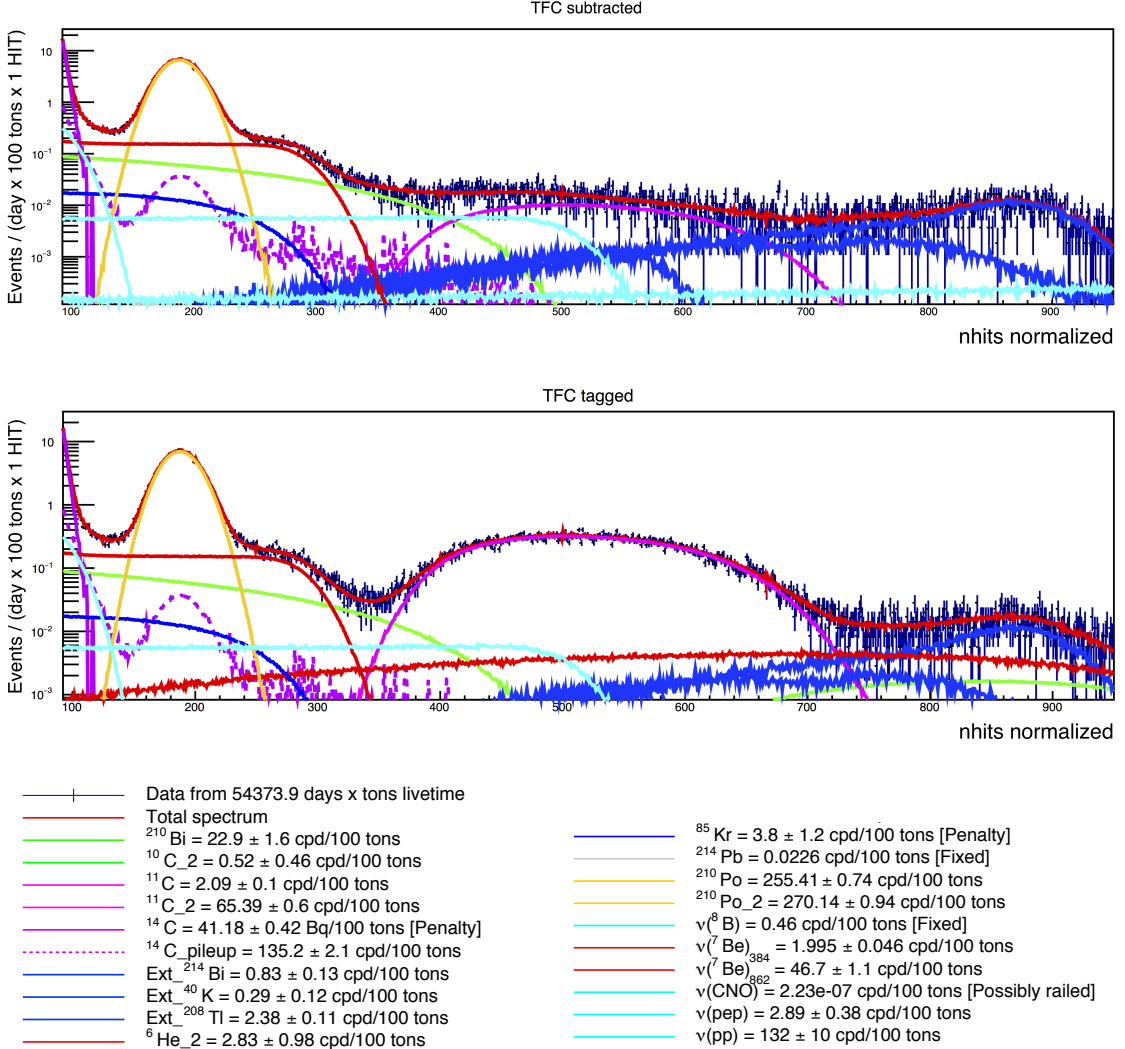


**Fig. 6.20:** *Top Panel:* Picture of the fit of the two energy spectra (TFC subtracted and TFC tagged) using  $nhits$  as energy variable. *Bottom Panel:* Best fit values of the interaction rates of the different components. The suffix “\_2” indicates the rate in the TFC tagged spectrum for the species whose rates are uncorrelated in the TFC tagged and subtracted spectra. Note that the rates of the species with the label “\_2” are normalized to the livetime of the TFC tagged spectrum and not to the total livetime. Species marked with the label “Penalty” are constrained (as outlined in Tab. 6.2). The best fit rate for CNO  $\nu$  is zero (indicated as “railed”): the limit for its interaction rate in Borexino is discussed in Sec. 6.13. Note that the value of the pileup event rate in Borexino is reported in the fit results as “ $^{14}\text{C}_\text{pileup}$ ”, namely only the  $^{14}\text{C}-^{14}\text{C}$  component of the pileup rate is highlighted, since it is the most critical one for the pp  $\nu$  determination.

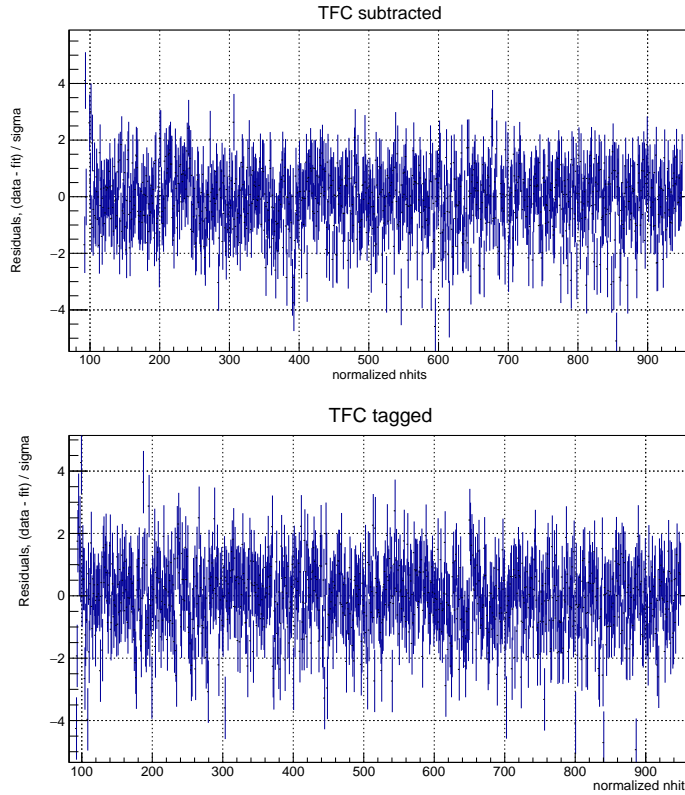


**Fig. 6.21:** *Top Panel:* Residuals of the spectral fit of the TFC subtracted spectrum shown in Fig. 6.20. *Bottom Panel:* Residuals of the spectral fit of the TFC tagged spectrum shown in Fig. 6.20.

distribution. An important improvement brought by the usage of the normalized position reconstruction likelihood as pulse shape parameter instead of the BDT is the possibility to project the events in only one energy bin. In the previous analysis, the BDT energy dependence made this impossible and thus the BDT parameter was fitted in 5 different energy projections. Since the statistics of the pulse shape references is limited, splitting the events in many energy bins results in an increased systematic error. This problem does not affect the fit of the radial distribution of the data, since in this case the reference PDFs are produced by MC and the statistics is not an issue.

As discussed in Sec. 4.9, the CNO  $\nu$  determination is strictly linked to the independent constraint of  $^{210}\text{Bi}$ . The Borexino Collaboration efforts in assessing  $^{210}\text{Bi}$  are still ongoing and for this reason all the fits presented in this PhD thesis are performed without any  $^{210}\text{Bi}$  constraint. It has also to be noted that the final publication of solar neutrino fluxes with Borexino Phase-II will be released some months after the deadline for the termination of this PhD thesis. Presumably, the data set available for the publication will be larger than the one used in the analysis presented here. This could also imply that the precise values of the solar neutrino fluxes measured at this stage might be slightly

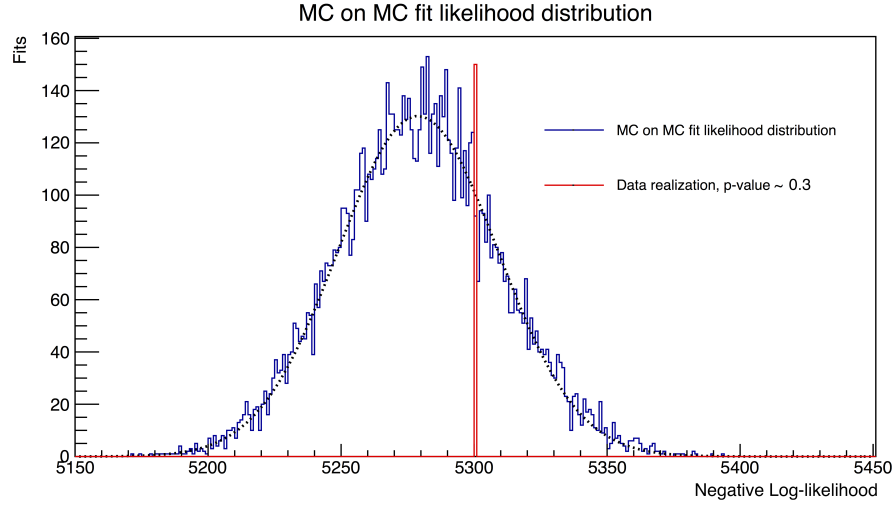


**Fig. 6.22:** Goodness of fit evaluation according to the procedure outlined in Sec. 6.9. The blue line indicates the distribution of the negative log-likelihood values for MC on MC fits with injected rates equal to those of the best fit on data. The red bin shows the data realization of the negative log-likelihood value.

modified thanks to an improved statistics.

Figure 6.20 shows the spectral fit result in the *nhits* variable. The two energy spectra (TFC subtracted and tagged) are fitted simultaneously. The fit results are shown in the lower panel of Fig. 6.20. Residuals for both the spectra are instead shown in Fig. 6.21. The residuals distributions show that the quality of the fit is good. The only points which are a few  $\sigma$  away from zero are those at very low energy, where the fluctuations in the  $^{14}\text{C}$  MC PDF dominate due to the lack of MC statistics. However, as it is discussed in Sec. 6.7.1, this does not represent a problem since it is taken into account in the likelihood computation. In order to quantify the goodness of fit, the procedure outlined in Sec. 6.9 was followed. Many MC on MC fits with injected rates for the species corresponding to the best fit values from the fit on data were generated and the distribution of the likelihood value at minimum<sup>7</sup> was built. The comparison between the negative log-likelihood value realization on data and the MC distribution is shown in Fig. 6.22. The corresponding p-value is around  $\sim 0.3$ .

Together with the energy spectra of Fig. 6.20, also the pulse shape and radial distribution were fitted and the results are reported in Fig. 6.23. The goodness of these individual parts of the fit is evaluated simply with  $\chi^2$  tests, whose values are reported in the pictures. The addition of the pulse shape and radial information to the spectral fit is very helpful in order to get stable results and break some correlations between the species involved in the fit. As it is shown in Fig. 6.23, a non negligible fraction of bins contains a few counts, thus suggesting that  $\chi^2$  tests might not be very accurate for the goodness of fit evaluation. Nevertheless, while the agreement between data and the model is evident

<sup>7</sup>Instead of maximizing the likelihood, the negative log-likelihood is minimized for simplicity.

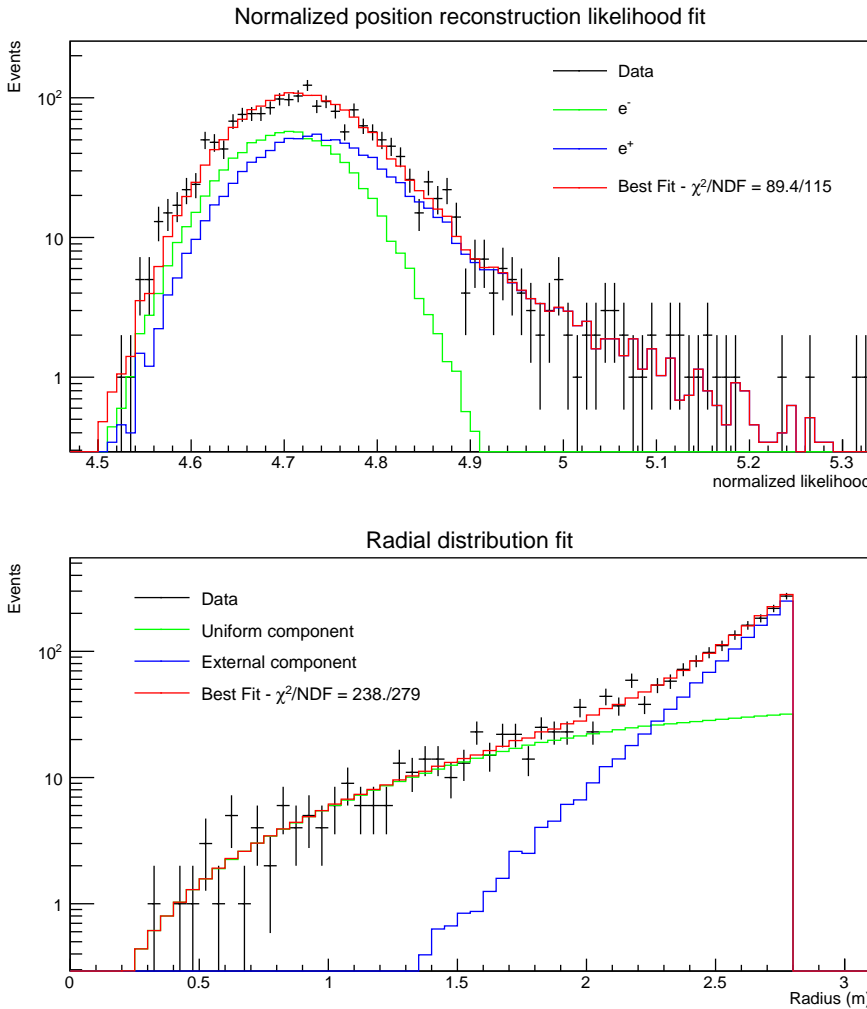


**Fig. 6.23:** *Top Panel:* Fit of the normalized position reconstruction likelihood for  $\beta^+/\beta^-$  discrimination. *Bottom Panel:* Fit of the radial distribution of the events for disentangling external contaminations. The picture shown here is the sum of the 16 histograms actually used to perform the radial distribution fits in different energy windows.

for low statistics bins,  $\chi^2$  tests performed only on the bins with higher statistics show a good description of the data by the fit.

## 6.12 Systematic uncertainties

Systematic uncertainties were evaluated by performing hundreds of fits varying the choice of parameters in the fit configuration, such as fit range, penalties<sup>8</sup> and setups

<sup>8</sup>A ‘penalty’ is intended here as an external constraint on some (free) parameter in the fit.

of the pulse shape and radial distribution fits. An ideal approach for disentangling all the correlations among the different parameters would consist in modifying all of them simultaneously, building the central value distribution of the results from which the systematic uncertainty can be determined. In practice, this is not possible because of the very big computational power which would be needed. For this reason, the different parameters were grouped in independent subsets. For each subset, the parameters were varied performing hundreds of fits and the final uncertainty is obtained by summing up in quadrature the contributions from the different groups. However, the results presented in this PhD thesis are preliminary, in the sense that the Borexino Collaboration is still working in order to crosscheck them through the fit with an analytical modelling of the detector response (and, as already mentioned, in order to possibly improve them by adding more statistics). The first outcome of these investigations shows very consistent results between the MC and the analytical fit of the spectrum. This increases the confidence on the numbers presented in this thesis.

There is a subset of quantities (e.g. the exposure) which do not depend directly on the fit and which can be evaluated *a priori*, in an uncorrelated way from all the other uncertainties. The various details on the considered sources of systematics are discussed in the next subsections. The final results on the neutrino interaction rates are presented so that the systematic uncertainty is symmetric (i.e. in case of asymmetric systematics, the central values of the results are shifted so that the uncertainty is symmetric).

### 6.12.1 Uncertainty on the exposure

The systematic uncertainty related to the fiducial volume determination from position reconstruction was performed in the same way as reported in Ref. [229, 269, 267]. A conservative uncertainty can be quantified as [267]  $+0.6, -1.1\%$  for the pep FV and for an energy range which includes most of the  ${}^7\text{Be} \nu$ , pep  $\nu$  and CNO  $\nu$  PDFs. The same error is also adopted here for the pp  $\nu$  interaction rate determination, even if the mean energy of these events is lower. However, this should not be a real problem, since the error on the FV is almost negligible with respect to the other sources of uncertainties on the pp  $\nu$  flux measurement.

The computation of the livetime was performed as discussed in Ref. [269] and the uncertainty can be quantified as  $\sim 0.05\%$ . The uncertainty on the scintillator density is of more or less of the same order. Both of them are negligible for the determination of  ${}^7\text{Be} \nu$ , pep  $\nu$  and pp  $\nu$  interaction rates. The statistical uncertainty associated with the toy MC used for the estimation of the residual exposure after the TFC veto (see Sec. 6.3) is  $< 0.5\%$ . It has only an impact for the pep  $\nu$  determination and it is negligible in practice, compared to the other sources of error for this neutrino flux measurement.

### 6.12.2 Fit configuration

The systematics from the fit configuration was studied by varying simultaneously the fit range, the central values of the penalties on  ${}^{14}\text{C}$  and pileup and the threshold of application of the scaling of PDF errors in the region where  ${}^{14}\text{C}$  events are dominating

(see Sec. 6.7.1). The starting point of the fit was varied in the range [89, 102]  $nhits$ . For these values, the outcomes of the fit are pretty stable as shown in Fig. 6.24, where the fitted values for  ${}^7\text{Be} \nu$  and pp  $\nu$  are shown as a function of the starting point of the fit. Below  $\sim 90$   $nhits$ , results are no more stable and this is probably due to the very different statistics of  ${}^{14}\text{C}$  events in data and in MC. This part of the spectrum is anyway dominated by  ${}^{14}\text{C}$  events and is not much sensitive neither to pp  $\nu$  nor to  ${}^7\text{Be} \nu$ . At energies higher than  $\sim 100$   $nhits$ , the fit is not sensitive anymore neither to  ${}^{14}\text{C}$  or pp  $\nu$ , and thus the results become meaningless. The fitted pep  $\nu$  rate depends very mildly on the starting point of the fit. The ending point was varied in the range [940, 960]  $nhits$  with negligible effects on any of the species involved in the fit.

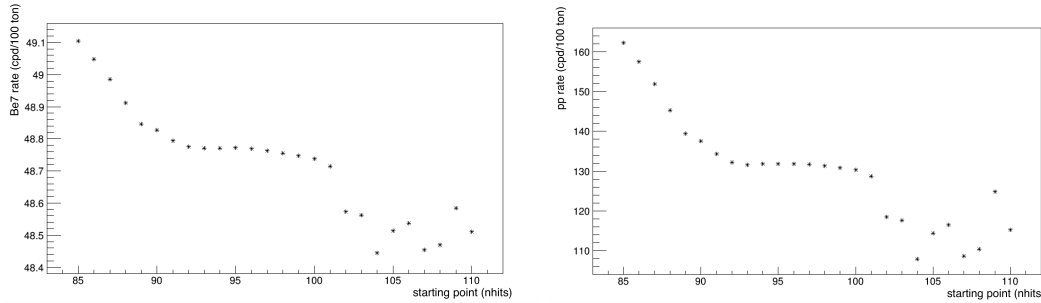


**Fig. 6.24:** *Left Panel:* Results for the  ${}^7\text{Be} \nu$  interaction rate for different starting points in the fit. *Right Panel:* Results for the pp  $\nu$  interaction rate for different starting points in the fit.

Together with the fit range, the central values of the penalties of both  ${}^{14}\text{C}$  and pileup events were modified in their allowed  $1\sigma$  range. This allows to be sure that the systematics associated to the particular evaluation of those penalty values does not bias the final results. In practice, this is important only for the pp  $\nu$  determination, since it might be possible that the injected value for the pileup rate penalty determines univocally the pp  $\nu$  rate, given the substantial degeneration of the two spectral shapes. Actually, the degeneration is not complete and the fit results are pretty stable even if the pileup penalty central value is varied a little.

As discussed in Sec. 6.7.1, the errors associated to the MC  ${}^{14}\text{C}$  PDF are increased thanks to the usage of a Scaled Poisson distribution. This is applied to those energy bins where  ${}^{14}\text{C}$  events dominate. However, with the aim of ensuring that this is not biasing the results, the energy starting point for this procedure has been a little varied and its impact is included in the fit configuration systematics.

Figure 6.25 shows the impact of the fit configuration options on the  ${}^7\text{Be} \nu$ , pp  $\nu$  and pep  $\nu$  results. The RMS's of the plotted distributions are taken as the systematic uncertainties associated with the choice of the best fit configuration for each neutrino species.

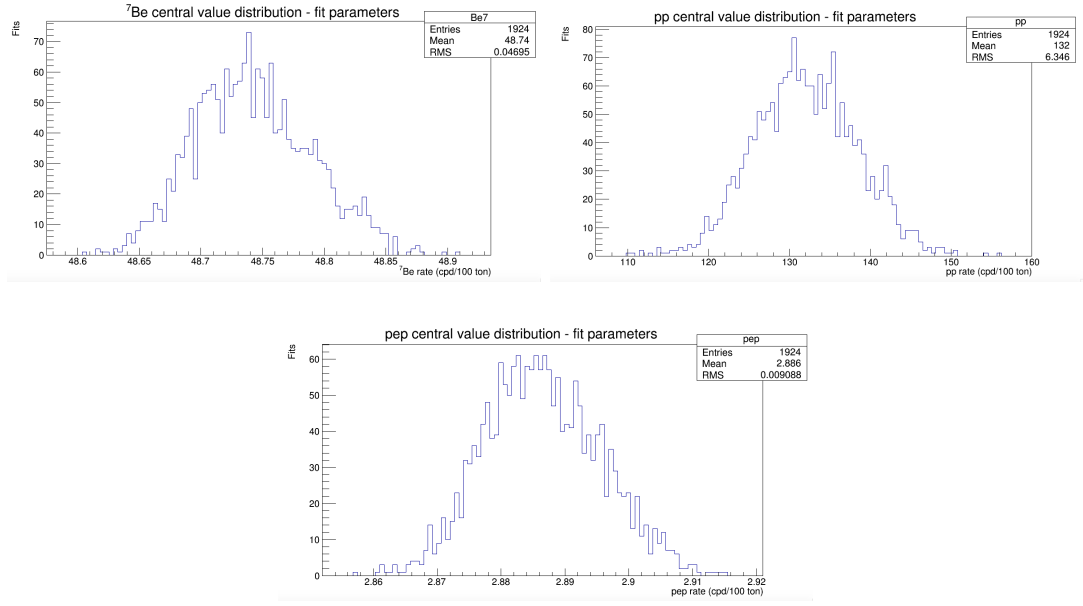


**Fig. 6.25:** Distributions of  ${}^7\text{Be}$   $\nu$ , pp  $\nu$  and pep  $\nu$  results for many fits with different fit configurations.

### 6.12.3 Energy scale

The energy scale uncertainty was estimated by fitting spectra obtained with different energy variables. The different outcomes of the fits for the different spectra account for the systematic error associated with the energy variable definition and for its modeling through the MC simulation. In addition to  $nhits$ , fits were performed using  $npmts$ ,  $npmts_dt1$  and  $npmts_dt2$  and the results are reported in App. C. The difference in the central value for the pep  $\nu$  interaction rate for the  $npmts_dt1$  and  $npmts_dt2$  energy variables is not considered as a systematics, since these variables are known to be worse than  $nhits$  and  $npmts$  at higher energy.

In addition, MC PDFs obtained with the  $nhits$  energy variable were modified by applying random energy shifts in the range  $[-5, 5]$   $nhits$  and by convolving with Gaussian functions with RMS in the range  $[0, 5]$   $nhits$ . This allows to study the impact of a possibly wrong response function in the MC. These PDF modifications are applied independently on  $\alpha$ ,  $\beta^-$  and  $\beta^+$  events, since in principle their energy scales are different. In this case, only the fits with an acceptable goodness of fit<sup>9</sup> were kept for the systematics evaluation. The outcome of this investigation is that there is not much freedom in the energy response description of the detector, since when the energy scale is moved a little, the fit results get bad relatively quickly. This is one of the advantages of the global fit on the whole energy range, since it does not leave much freedom in terms of degenerate parameters in the detector response description.

The most important contribution to the energy scale uncertainty comes from fits

<sup>9</sup>The expected distribution of  $\chi^2/\text{NDF}$  for the fit was built on the basis of MC on MC fits.

performed with different energy variables. In this PhD thesis, the central values for the neutrino interaction rates are obtained as the mean value between the two most extreme outcomes and their difference is interpreted as the double RMS of a Gaussian distribution describing the associated error. This is just a preliminary estimation and it is expected that the final published central values will be obtained from a distribution of fits where the energy variable, together with the other parameters, are varied simultaneously.

#### 6.12.4 Multivariate fit options

The options for the multivariate fits of the pulse shape and radial distributions shown in Tab. 6.3 were a little varied, in order to take into account the error and the fit stability associated with the fit of these parameters. The impact of these options is almost negligible for  ${}^7\text{Be} \nu$  and pp  $\nu$ , while it is higher (as expected) for pep  $\nu$ . Naturally, a small impact is present also on  ${}^7\text{Be} \nu$ , even if the energy range where  ${}^7\text{Be} \nu$  recoils are present is not involved neither in the pulse shape nor in the radial distribution fits. This is due to the fact that the correlations between pep  $\nu$ , CNO  $\nu$  and  ${}^{210}\text{Bi}$  induce a dependency also on the fitted  ${}^7\text{Be} \nu$  rate. The starting and ending points of the multivariate analysis were modified of  $\pm 50$   $nhits$  with respect to what is reported in Tab. 6.3. In addition, the number of energy bins was also modified (25 or 50  $nhits$  for the radial distribution and 250 or 50  $nhits$  for the pulse shape). The most important improvement on the systematic uncertainty for the pep  $\nu$  evaluation comes from the reduced error on the pulse shape variable. As reported in Ref. [267], one of the biggest contributions to the systematics in Phase-I analysis came from the reduced statistics in the pulse shape PDFs. The usage of the normalized position reconstruction likelihood reduces a lot this error. In fact, a much bigger sample of events can be used as pulse shape reference, since there is no need to train a neural network algorithm.<sup>10</sup>

#### 6.12.5 ${}^{85}\text{Kr}$ and ${}^{210}\text{Bi}$ spectral shapes

The systematic uncertainty associated with the knowledge of the  ${}^{85}\text{Kr}$  and  ${}^{210}\text{Bi}$  spectral shapes was evaluated according to Ref. [229, 269] and to Ref. [224, 267], respectively. The impact of the  ${}^{85}\text{Kr}$  spectral shape on Phase-II result is expected to be lower with respect to that of Phase-I, simply because of the different amount of  ${}^{85}\text{Kr}$  in the detector after purifications. Thus, the given uncertainty on the  ${}^{85}\text{Kr}$  spectral shape is conservative. At the same time, an updated measurement of the  ${}^{210}\text{Bi}$  spectral shape is being carried out within the Borexino Collaboration in Dresden, and it is possible that the currently quoted uncertainty for  ${}^{210}\text{Bi}$  will be decreased in the future.

#### 6.12.6 ${}^{85}\text{Kr}$ external constraint

The  ${}^{85}\text{Kr}$  rate is constrained in the fit thanks to the independent information coming from the delayed coincidence tagging (see Sec. 4.3). In practice, the likelihood is multiplied

---

<sup>10</sup>The training of the former BDT variable required the selection of a subset of events only for the purpose of training, thus reducing the size of the remaining sample used as fitting PDF.

by a Poisson distribution whose mean gives the limit of 5 cpd/100 ton at 95% C.L. The systematics associated to the introduction of this constraint is conservatively estimated by performing the fit with and without the penalty, and by quoting the difference as the double RMS of this error. The fit results for  $^{85}\text{Kr}$  without any constraint ( $\sim 4$  cpd/100 ton) are consistent with the limit and the differences induced by the constraint on all neutrino fluxes are well under control.

### 6.12.7 Oscillation parameters and $^8\text{B}$ $\nu$ rate

The uncertainties on the knowledge of the oscillation parameters and of the neutrino-electron differential cross section are almost totally negligible for the presented measurement of  $^7\text{Be}$   $\nu$ , pp  $\nu$  and pep  $\nu$ . As discussed e. g. in Ref. [269], their contribution to the total uncertainty is much smaller than 1%. The  $^8\text{B}$   $\nu$  interaction rate in Borexino is fixed to the *high-Z* SSM prediction (see Tab. 4.1). A variation of the central value of the  $^8\text{B}$   $\nu$  rate of  $\sim 30\%$  ( $\sim 3$  times the theoretical uncertainty) shows negligible effects on the pep  $\nu$  rate and zero effects on the other solar neutrino fluxes, as outlined in Ref. [267].

### 6.12.8 Systematics budget for $^7\text{Be}$ $\nu$

Table 6.4 shows the main contributions to the total systematic uncertainty for the  $^7\text{Be}$   $\nu$  interaction rate measurement. The fit results for the 862 keV line of  $^7\text{Be}$   $\nu$  interaction rate in Borexino obtained with different energy variables and reported in Fig. 6.20 and App. C are:

- $46.7 \pm 1.1(\text{stat.})$  cpd/100 ton ( $nhits$ ).
- $46.4 \pm 1.1(\text{stat.})$  cpd/100 ton ( $npmts$ ).
- $46.3 \pm 1.1(\text{stat.})$  cpd/100 ton ( $npmts\_dt1$ ).
- $46.4 \pm 1.0(\text{stat.})$  cpd/100 ton ( $npmts\_dt2$ ).

$^7\text{Be}$ $\nu$	Nominal error	Shift (%)	Symmetric systematic error (%)
FV	+0.6%, -1.1%	-0.25%	0.85%
$^{85}\text{Kr}$ penalty	-0.82%	-0.41%	0.41%
Bi210 and Kr85 shape			0.8%
Fit parameters			0.1%
Energy scale		-0.41%	1.0%
Multivariate parameters			0.25%
<b>Total systematics</b>			<b>1.61%</b>

**Tab. 6.4:** Summary of the main systematic uncertainties for the  $^7\text{Be}$   $\nu$  interaction rate measurement in Borexino. The first column indexes the different sources as discussed in Sec. 6.12, the second column reports the net effect on the measured  $^7\text{Be}$   $\nu$  rate prior to symmetrization, the third one quantifies the shift applied and the last one shows the symmetric uncertainty.

### 6.12.9 Systematics budget for pp $\nu$

Table 6.5 shows the main contributions to the total systematic uncertainty for the pp  $\nu$  interaction rate measurement. The fit results for the pp  $\nu$  interaction rate in Borexino obtained with different energy variables and reported in Fig. 6.20 and App. C are:

- $132 \pm 10$ (stat.) cpd/100 ton ( $nhits$ ).
- $138 \pm 10$ (stat.) cpd/100 ton ( $npmts$ ).
- $139 \pm 12$ (stat.) cpd/100 ton ( $npmts_dt1$ ).
- $134 \pm 11$ (stat.) cpd/100 ton ( $npmts_dt2$ ).

pp $\nu$	Nominal error	Shift (%)	Symmetric systematic error (%)
FV	+0.6%, -1.1%	-0.25%	0.85%
$^{85}\text{Kr}$ penalty	-2.2%	-1.1%	1.1%
Fit parameters			4.7%
Energy scale		+2.65%	3.6%
Multivariate parameters			0.8%
<b>Total systematics</b>			<b>6.1%</b>

**Tab. 6.5:** Summary of the main systematic uncertainties for the pp  $\nu$  interaction rate measurement in Borexino. The first column indexes the different sources as discussed in Sec. 6.12, the second column reports the net effect on the measured pp  $\nu$  rate prior to symmetrization, the third one quantifies the shift applied and the last one shows the symmetric uncertainty.

### 6.12.10 Systematics budget for pep $\nu$

Table 6.6 shows the main contributions to the total systematic uncertainty for the pep  $\nu$  interaction rate measurement. The fit results for the pep  $\nu$  interaction rate in Borexino obtained with different energy variables and reported in Fig. 6.20 and App. C are:

- $2.89 \pm 0.38$ (stat.) cpd/100 ton ( $nhits$ ).
- $2.91 \pm 0.38$ (stat.) cpd/100 ton ( $npmts$ ).
- $3.06 \pm 0.4$ (stat.) cpd/100 ton ( $npmts_dt1$ ).
- $2.89 \pm 0.98$ (stat.) cpd/100 ton ( $npmts_dt2$ ).

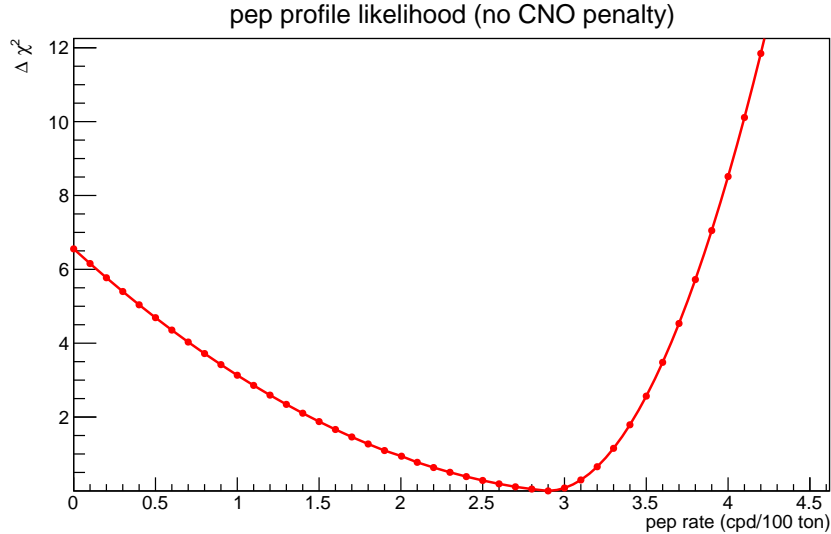
It has to be noted that the statistical errors shown above for the pep  $\nu$  rate are not accurate, since they are obtained through the HESSE algorithm, which approximates the likelihood around the minimum with a “parabolic” function. More details are given in Sec. 6.13.

pep $\nu$	Nominal error	Shift (%)	Symmetric systematic error (%)
FV	+0.6%, -1.1%	-0.25%	0.85%
$^{85}\text{Kr}$ penalty	-3.8%	-1.9%	1.9%
Fit parameters			$\ll 1\%$
Energy scale		+0.35%	1.8%
Multivariate parameters			5.9%
<b>Total systematics</b>			<b>7.2%</b>

**Tab. 6.6:** Summary of the main systematic uncertainties for the pep  $\nu$  interaction rate measurement in Borexino. The first column indexes the different sources as discussed in Sec. 6.12, the second column reports the net effect on the measured pep  $\nu$  rate prior to symmetrization, the third one quantifies the shift applied and the last one shows the symmetric uncertainty.

### 6.13 Likelihood profile for pep $\nu$ and CNO $\nu$ limit

Likelihood ratio tests were performed both for assessing the pep  $\nu$  detection significance and the CNO  $\nu$  limit. Fits were performed by fixing either the pep  $\nu$  or the CNO  $\nu$  component and the corresponding  $\Delta\chi^2$  profile was studied. In fact,  $-\Delta 2 \ln \mathcal{L}$  can be interpreted as a  $\Delta\chi^2$  with one degree of freedom if one parameter is fixed, as checked for Phase-I analysis in Refs. [224, 267]. As discussed in Ref. [267], the frequentist interpretation of the CNO  $\nu$  interaction rate limit and of the confidence level for the pep  $\nu$  detection inferred from the  $\Delta\chi^2$  profile was tested studying the distribution of the CNO  $\nu$  and pep  $\nu$  interaction rates out of MC on MC fits.



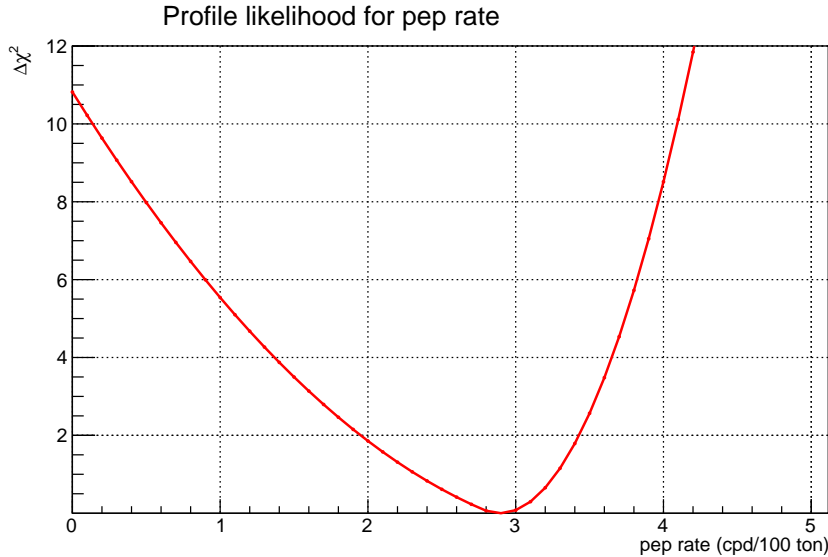
**Fig. 6.26:**  $\Delta\chi^2$  profile obtained from a likelihood ratio test between the likelihood of the best fit result and the maximum likelihood returned by the fit when the pep  $\nu$  rate is fixed to different values.

Figure 6.26 shows the  $\Delta\chi^2$  profile obtained from a likelihood ratio test between the likelihood of the best fit result and the maximum likelihood for fits with the pep  $\nu$  rate fixed to different values. The profile of Fig. 6.26 shows that the absence of pep  $\nu$  signal is rejected at  $2.6\sigma$  C.L.. The corresponding pep  $\nu$  interaction is  $2.9^{+0.4}_{-1.0}$  cpd/100 ton, considering only the statistical uncertainty from the profile at  $1\sigma$ .

The main correlation which enlarges the negative error on the pep  $\nu$  interaction rate is that between CNO  $\nu$  and pep  $\nu$  itself. This effect can be reduced if an external constraint on the CNO  $\nu$  rate is inserted into the likelihood computation. The most conservative  $\Delta\chi^2$  profile providing a limit on the CNO  $\nu$  interaction rate in Borexino is the one obtained in Phase-I analysis, with the *nhits* energy estimator and without any constraint on the pep  $\nu$  rate in the fit, as shown in Ref. [267]. The limit can be approximated by the following curve:

$$\Delta\chi^2 = 0.18 \cdot R_{CNO} + 0.0065 \cdot R_{CNO}^2, \quad (6.5)$$

where  $R_{CNO}$  is the rate of CNO  $\nu$  in cpd/100 ton. The pep  $\nu$  likelihood profile, which can be obtained if the limit of Eq. (6.5) is used, is shown in Fig. 6.27. In this case, the absence of the pep  $\nu$  signal is rejected at  $3.3\sigma$  and the corresponding interaction rate is  $2.9^{+0.4}_{-0.6}$  cpd/100 ton. Better results can be achieved if  $^{210}\text{Bi}$  is constrained independently. In fact, in this case the likelihood profile becomes symmetric and the correlation between pep  $\nu$  and CNO  $\nu$  is substantially broken (see Sec. 6.8).



**Fig. 6.27:**  $\Delta\chi^2$  profile obtained from a likelihood ratio test between the likelihood of the best fit result and the maximum likelihood returned by the fit when the pep  $\nu$  rate is fixed to different values and the constraint on CNO  $\nu$  rate from Eq. (6.5) is added to the total likelihood computation.

The same procedure was used in order to assess the limit on the CNO  $\nu$  interaction rate in Borexino. Figure 6.28 shows the  $\Delta\chi^2$  profiles for the CNO  $\nu$  interaction rate. The

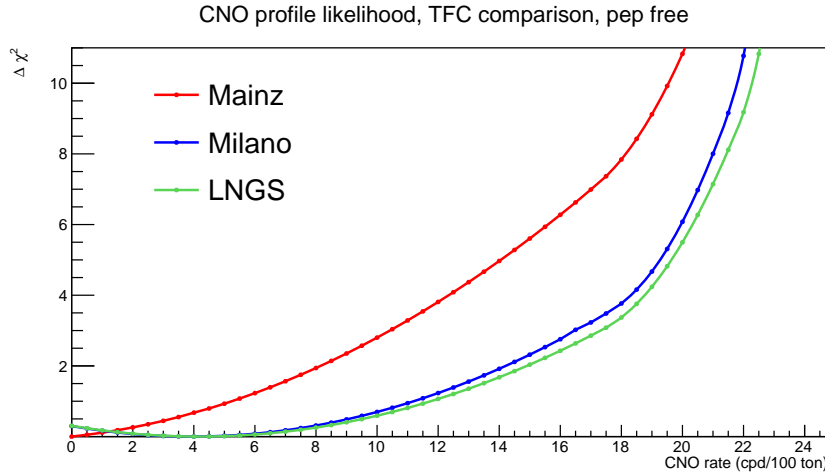


**Fig. 6.28:**  $\Delta\chi^2$  profile obtained from a likelihood ratio test between the likelihood of the best fit result and the maximum likelihood returned by the fit when the CNO  $\nu$  rate is fixed to different values. The different curves are obtained from the fit to energy spectra built using different TFC algorithms for the  $^{11}\text{C}$  suppression.

different curves are obtained by fitting data sets obtained with different TFC algorithms (the names are relative to the places where the people who developed the code work). The LNGS code has an efficiency on  $^{11}\text{C}$  rejection of  $\sim 93\%$ , but only a fraction  $\sim 48\%$  of the livetime is saved in the TFC subtracted spectrum. On the contrary both Mainz and Milano codes have an efficiency around  $\sim 92\%$  and livetimes after the TFC of  $\sim 60\%$  (slightly higher for Mainz). The qualitative difference between the three TFCs consists in the best fit value for CNO  $\nu$ . Despite it is different from zero with the usage either of Milano or LNGS TFC, the statistical significance of the value being different from zero is almost null. As a matter of fact, LNGS TFC turns out to provide the worst limit on CNO  $\nu$ , even if its performances are not dramatically different with respect to those of the other two codes. Therefore, a conservative approach suggests that the LNGS TFC result should be considered in order to assess the limit on the CNO  $\nu$  interaction rate. It has to be noted that a particular choice of the TFC does not affect the pep  $\nu$  result. In fact, the central values obtained for the pep  $\nu$  rate with spectra produced with different TFCs are very close to each other (inside the systematic error band generated by the other contributions to the error). In addition, a discrepancy on the central values (statistically compatible with each other) should not be considered as a systematics, since the data sets are correlated but not exactly equal, and thus statistical fluctuations are expected.

The limit shown in Fig. 6.28 is not very competitive, because of the well known correlations among CNO  $\nu$ ,  $^{210}\text{Bi}$  and pep  $\nu$ . The bound becomes much stricter if the pep  $\nu$  rate is fixed to the value predicted by SSM and MSW-LMA. The result is presented in Fig. 6.29. Even considering conservatively the result from LNGS TFC, the limit is pushed further down with respect to that of Phase-I to 8 cpd/100 ton at  $3\sigma$  C.L..

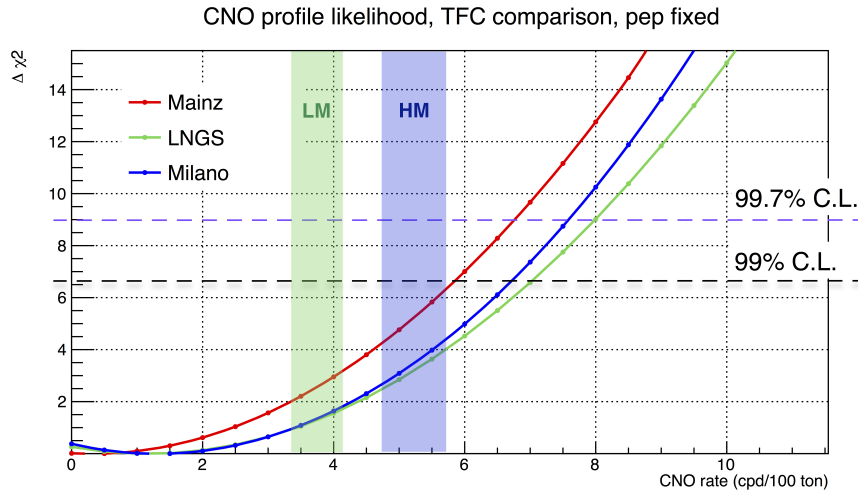


**Fig. 6.29:**  $\Delta\chi^2$  profiles obtained from a likelihood ratio test between the likelihood of the best fit result and the ( $\sim 4$  cpd/100 ton) likelihood returned by the fit when the CNO  $\nu$  rate is fixed to different values and the pep  $\nu$  rate is fixed to 2.8 cpd/100 ton. The different curves are obtained from the fit to energy spectra built using different TFC algorithms for the  $^{11}\text{C}$  suppression. The blue band shows the  $1\sigma$  prediction for the CNO  $\nu$  rate according to the *high-Z* (GS98) SSM, while the green band shows the  $1\sigma$  expectation from the *low-Z* (AGSS09) SSM (see Tab. 4.1).

## 6.14 Results

The MC fit of the whole low energy spectrum from Borexino Phase-II was performed for the first time yielding to the simultaneous measurement of the interaction rates of  $^7\text{Be} \nu$ , pp  $\nu$  and pep  $\nu$  and to the determination of the best limit on CNO  $\nu$ . This is a remarkable result, since before the analysis presented in this PhD thesis a global fit of Borexino's energy spectrum was not possible. In addition, the measurement on the whole energy range increases the confidence on the result, since it demonstrates that the detector response is well under control. All the solar neutrino interaction rates obtained as a result of this effort are better than those published before. However, it must be noted that these results are only preliminary, since further consistency checks are still ongoing inside the Borexino Collaboration. The final results are expected to be published a few months after the deadline by which this PhD thesis had to be completed, and for this reason it is possible that the actual final numbers will be slightly modified in the future.

A summary of the final results, where both statistical and systematic uncertainties are reported, is given below:

- The interaction rate of the 862 keV  $^7\text{Be} \nu$  in Borexino is found to be  $46.2 \pm 1.1(\text{stat.}) \pm 0.8(\text{sys.})$  cpd/100 ton. The total error was lowered down to 3% (to be compared to  $\sim 7\%$  coming from theoretical calculations). In the assumption of the MSW-LMA model of solar neutrino oscillations this corresponds to a flux of  $(4.89 \pm 0.13) \cdot 10^9 \text{ cm}^{-2}\text{s}^{-1}$ . This flux is compatible with both *high-Z* and *low-*

$Z$  SSMs at  $1\sigma$ . The expected interaction rate in Borexino from the two lines of  ${}^7\text{Be}$   $\nu$  within the *high-Z* SSM in absence of solar neutrino oscillations is  $77 \pm 5$  cpd/100 ton and thus the no oscillation hypothesis is rejected at  $5.2\sigma$ . In the assumption of the *high-Z* SSM the value of the observed survival probability is  $P_{ee} = 0.52 \pm 0.06$ .

- The interaction rate of pp  $\nu$  in Borexino is  $134 \pm 10(\text{stat.}) \pm 8(\text{sys.})$  cpd/100 ton. The total error is around 9.5%, a little better with respect to the previous result from Borexino which quoted an uncertainty of  $\sim 12.5\%$ . In the assumption of the MSW-LMA model of solar neutrino oscillations this corresponds to a flux of  $(6.1 \pm 0.6) \cdot 10^{10} \text{ cm}^{-2}\text{s}^{-1}$ , which is compatible with both *high-Z* and *low-Z* SSMs at  $1\sigma$ . In the assumption of the *high-Z* SSM the value of the observed survival probability is  $P_{ee} = 0.57 \pm 0.09$ .
- The interaction rate of pep  $\nu$  in Borexino is  $2.9_{-1.0}^{+0.4}(\text{stat.}) \pm 0.2(\text{sys.})$  cpd/100 ton without any constraint on the CNO rate. The hypothesis of null signal from pep  $\nu$  is rejected at  $2.6\sigma$  C.L.. If a conservative constraint on the CNO  $\nu$  rate from Borexino Phase-I is applied, the result improves:  $2.9_{-0.6}^{+0.4}(\text{stat.}) \pm 0.2(\text{sys.})$  cpd/100 ton, corresponding to a rejection of the absence of the pep  $\nu$  signal at  $3.3\sigma$  C.L.. The result obtained with the constraint on the CNO  $\nu$  rate corresponds to a flux of  $(1.5_{-0.32}^{+0.22}) \cdot 10^8 \text{ cm}^{-2}\text{s}^{-1}$  in the assumption of the MSW-LMA model. This agrees with both *low-Z* and *high-Z* SSMs at  $1\sigma$ . The expected interaction rate in Borexino from pep  $\nu$  within the *high-Z* SSM in absence of solar neutrino oscillations is  $4.47 \pm 0.05$  cpd/100 ton. The no oscillation hypothesis is rejected at  $3.4\sigma$ . In the assumption of the *high-Z* SSM the value of the observed survival probability is  $P_{ee} = 0.56_{-0.21}^{+0.12}$ .
- The interaction rate of CNO  $\nu$  in Borexino can be constrained to be  $< 8$  cpd/100 ton at 99.7% C.L. ( $< 7$  cpd/100 ton at 99% C.L.) assuming the SSM rate with MSW-LMA oscillation probability for the pep  $\nu$  rate. Without any external constraint on  ${}^{210}\text{Bi}$ , it is not possible to even hope for a CNO  $\nu$  rate determination. This result corresponds to a limit on the flux of  $< 8.1 \cdot 10^8 \text{ cm}^{-2}\text{s}^{-1}$  at 99.7% C.L. if the MSW-LMA model is assumed.

## 6.15 Outlook

The results here presented from Borexino Phase-II were obtained thanks to an improved understanding of the detector response in the whole region of interest of low energy solar neutrinos and to unprecedently low backgrounds. One of the most important prospects for Borexino is the investigation of the CNO  $\nu$  rate. The efforts in order to understand  ${}^{210}\text{Bi}$ , i. e. the most important and subtle background, are ongoing. The ultra low radioactive levels reached in Borexino make it the only experiment able to carry out this investigation at present (and probably for many years thereafter). Either an improved limit or a first indication of a signal from CNO  $\nu$  would be extremely precious for the scientific community.

Additional prospects could foresee the improvement of the measurements of the currently measured solar neutrino fluxes with the usage of both Phase-I and Phase-II data sets. In particular, the re-analysis of Phase-I data with the new tools could allow to lower down the systematics, even if it is expected that most of the improvement could be provided by the increase of statistics.



# Chapter 7

## Conclusions

The work presented in this PhD thesis studied the phenomenology of  $0\nu\beta\beta$ , both assessing theoretical uncertainties and experimental expectations for the next decade. It turns out that ton or multi-ton scale detectors are needed in order to probe values of the Majorana Effective mass allowed by current constraints from cosmological surveys. The expected sensitivity of a new generation experiment hunting for  $0\nu\beta\beta$  by dissolving  $^{136}\text{Xe}$  in Borexino's liquid scintillator at high pressure was discussed. The ultra low background environment provided by Borexino and its relatively good energy resolution make the case for very promising results. As complementary investigations, the experimental efforts concerning the determination of optical properties of liquid scintillators loaded with xenon at high pressure were also reported.

The other important aspect of this PhD thesis regards the advancements of the Borexino full Monte Carlo simulation which yielded to the fit of the whole low energy spectrum from Borexino Phase-II. This allowed, for the first time, the simultaneous measurement of the interaction rates of  $^7\text{Be} \nu$ , pp  $\nu$  and pep  $\nu$  and to the determination of the best limit on CNO  $\nu$ .

The final results on the solar neutrino flux measurements carried out in this thesis are reported below, while Fig. 7.1 summarizes the impact of these measurements in terms of solar neutrino survival probability in the assumption of the High Metallicity (*high-Z*) Solar Standard Model (SSM). The results are perfectly compatible to the prediction of the MSW-LMA model. The current results cannot disentangle High Metallicity and Low Metallicity SSMs since no definitive answer on CNO  $\nu$  is achieved.

- The interaction rate of the 862 keV  $^7\text{Be} \nu$  in Borexino is found to be  $46.2 \pm 1.1(\text{stat.}) \pm 0.8(\text{sys.}) \text{ cpd}/100 \text{ ton}$ . In the assumption of the MSW-LMA model of solar neutrino oscillations this corresponds to a flux of  $(4.89 \pm 0.13) \cdot 10^9 \text{ cm}^{-2}\text{s}^{-1}$ . The observed survival probability is  $P_{ee} = 0.52 \pm 0.06$  for the *high-Z* SSM prediction of the flux.
- The interaction rate of pp  $\nu$  in Borexino is  $134 \pm 10(\text{stat.}) \pm 8(\text{sys.}) \text{ cpd}/100 \text{ ton}$ . In the assumption of the MSW-LMA model of solar neutrino oscillations this corresponds to a flux of  $(6.1 \pm 0.6) \cdot 10^{10} \text{ cm}^{-2}\text{s}^{-1}$ . The observed survival probability is  $P_{ee} = 0.57 \pm 0.09$  for the *high-Z* SSM prediction of the flux.

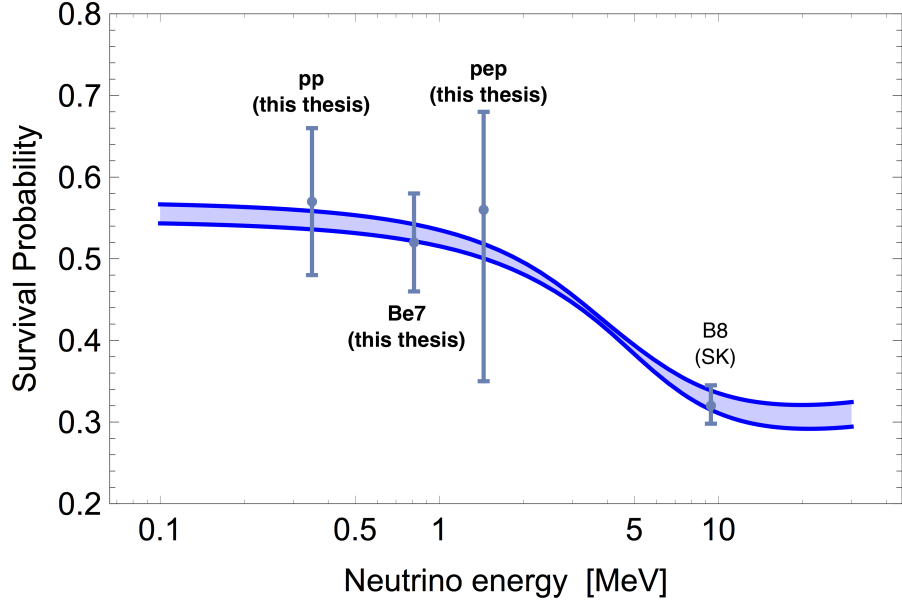


**Fig. 7.1:** Survival probability for solar neutrinos in the assumption of the High Metallicity Solar Standard Model. The experimental points for pp  $\nu$ ,  $^7\text{Be} \nu$  and pep  $\nu$  correspond to the results obtained in this PhD thesis, while the point for  $^8\text{B} \nu$  is relative to the measurement by Super-Kamiokande [53]. The colored band shows the prediction of the MSW-LMA model with the corresponding  $1\sigma$  uncertainty.

- The interaction rate of pep  $\nu$  in Borexino is  $2.9_{-1.0}^{+0.4}(\text{stat.}) \pm 0.2(\text{sys.}) \text{ cpd}/100 \text{ ton}$  without any constraint on the CNO rate. The hypothesis of null signal from pep  $\nu$  is rejected at  $2.6\sigma$  C.L.. If a conservative constraint on the CNO  $\nu$  rate from Borexino Phase-I is applied, the result improves:  $2.9_{-0.6}^{+0.4}(\text{stat.}) \pm 0.2(\text{sys.}) \text{ cpd}/100 \text{ ton}$ , corresponding to a rejection of the absence of the pep  $\nu$  signal at  $3.3\sigma$  C.L.. The result obtained with the constraint on the CNO  $\nu$  rate corresponds to a flux of  $(1.5_{-0.32}^{+0.22}) \cdot 10^8 \text{ cm}^{-2}\text{s}^{-1}$  in the assumption of the MSW-LMA model. The no oscillation hypothesis is rejected at  $3.4\sigma$  and in the assumption of the *high-Z* SSM the value of the observed survival probability is  $P_{ee} = 0.56_{-0.21}^{+0.12}$ .
- The interaction rate of CNO  $\nu$  in Borexino can be constrained to be  $< 8 \text{ cpd}/100 \text{ ton}$  at 99.7% C.L. ( $< 7 \text{ cpd}/100 \text{ ton}$  at 99% C.L.) assuming the SSM rate with MSW-LMA oscillation probability for the pep  $\nu$  rate. This result corresponds to a limit on the flux of  $< 8.1 \cdot 10^8 \text{ cm}^{-2}\text{s}^{-1}$  at 99.7% C.L. if the MSW-LMA model is assumed.

## Appendix A

# Coherence and decoherence in neutrino oscillations

In this appendix, the concepts behind the disappearance of the oscillation phenomenon due to the decoherence of quantum states is discussed following Ref. [10].

Once a neutrino is produced in a weak interaction process and it starts to propagate freely, the three mass eigenstates start to travel independently in the space. Since they have different masses, they propagate at different speeds:

$$v_i = \frac{|\vec{p}_i|}{E_i} \sim 1 - \frac{m_i^2}{2E^2}, \quad (\text{A.1})$$

where the ultra-relativistic approximation was used. The leptonic wave packet is a superposition of the three overlapping mass wave packets, which it is possible to describe with Gaussian distributions with a standard deviation  $\sigma_x$ . This in turn means that the spread in the momentum space would be  $\sigma_p \sim 1/\sigma_x$  for the Heisenberg principle. During the neutrino propagation, the three mass components move with different group velocities  $v_i$ , and therefore at a certain point the mass eigenstates will physically be separated. The overlap between two components, say  $\nu_i$  and  $\nu_j$ , is significant only if the separation of the centers of their wave packets is smaller than  $\sim 2\sigma_x$ . This brings to the definition of the coherence length  $L^{coh}$  as

$$L^{coh} = \frac{2\sigma_x}{|v_i - v_j|} \sim \frac{4E^2\sigma_x}{|\Delta m_{ij}^2|} \quad (\text{A.2})$$

where  $\Delta m_{ij}^2 = m_i^2 - m_j^2$ . After a path  $L \gtrsim L^{coh}$  the wave packets that correspond to the different mass eigenstates are separated. At this point the coherence between the different neutrinos is lost and oscillations are not present any more. An observer at a distance much greater than  $L^{coh}$  from a neutrino source that generates neutrinos of a given flavor, detects neutrinos of all flavors with probabilities independent from the distance. The coherence length is important in practice only in the case of neutrinos produced in distant supernovae [10].



## Appendix B

# Parameters in the Monte Carlo simulation after the tuning

In this appendix, the results on the tuning of the parameters are reported together with the comparison between the starting and the tuned values for each quantity. A full discussion on the tuning procedure and on the meaning of the numbers inside the following tables can be found in Sec. 5.8. Table B.1 reports the results for the parameters related to the energy scale, Tab. B.2 those concerning attenuation lengths and reflectivity while Tab. B.3 summarizes the results on the time response of the scintillator. The results are quite good, since the targeted precision could be achieved (see Sec. 5.8) and also because the tuned values are *not too far* from the measured ones, thus highlighting that the modeling of the detector is accurate and the involved parameters are physical and describe properly the phenomena. Tuned parameters resulting too far away from physical values would prove the presence of some effect not taken into account properly.

Parameter	Measured value	Tuned value
$Y_0$ (photons/MeV)	11000	13600
$kB$ ( $\beta$ , cm MeV $^{-1}$ )	0.0109	0.01098
$kB$ ( $\alpha$ , cm MeV $^{-1}$ )	0.012	0.01055
pmtgainscale	1	1.015
$P_{rem}(\lambda < 320 \text{ nm})$	0.2	0.53

**Tab. B.1:** Results on the tuning of the parameters describing the energy response. The PMT gain scale (“pmtgainscale”) allows to slightly vary the gains of the PMTs in the simulation (whose values anyhow come from real, automatic measurements) in order to compensate for possible discrepancies between the reality and the simulation idealization.  $P_{rem}(\lambda < 320 \text{ nm})$  is the parameter discussed in Sec. 5.4.

Parameter	Measured value	Tuned value	Parameter	Measured value	Tuned value
$\Lambda_{\text{PC}}$	1	1.35	$\tau_{1,\beta}$ (ns)	3.95	3.7
$\Lambda_{\text{nylon}}$	1	0.75	$\tau_{2,\beta}$ (ns)	23.56	24
$\Lambda_{\text{DMP}}$	1	1.1	$\tau_{3,\beta}$ (ns)	78.86	60
$\Lambda_{\text{PPO}}$	1	1.15	$\tau_{4,\beta}$ (ns)	546.39	600
$R_{\text{SSS}}$	0.49	0.55	$q_{1,\beta}$	0.933	0.889
$R_{\text{SSS}}^{\text{spike}}$	0.4	0.12	$q_{2,\beta}$	0.024	0.055
$R_{\text{cathode}}$	0.1	0	$q_{3,\beta}$	0.022	0.027
$R_{\mu\text{-metal}}$	0.4	0.4	$q_{4,\beta}$	0.021	0.029
$R_{\text{PMT ring}}$	0.6	0.75	$\tau_{1,\alpha}$ (ns)	4.15	3.9
$R_{\text{PMT ring}}^{\text{spike}}$	0.8	0.88	$\tau_{2,\alpha}$ (ns)	19.90	26
$R_{\text{conc. int.}}$	0.88	0.95	$\tau_{3,\alpha}$ (ns)	99.91	110
$R_{\text{conc. int.}}^{\text{spike}}$	0.8	0.985	$\tau_{4,\alpha}$ (ns)	617.96	630
$R_{\text{conc. ext.}}$	0.88	0.95	$q_{1,\alpha}$	0.679	0.674
$R_{\text{conc. ext.}}^{\text{spike}}$	0.8	0.975	$q_{2,\alpha}$	0.144	0.146
$R_{\text{nylon ring}}$	0.4	0.3	$q_{3,\alpha}$	0.102	0.103
			$q_{4,\alpha}$	0.075	0.077
			$\tau_{PC}$ (ns)	28	28
			$\tau_{PPO}$ (ns)	1.6	1.6
			$\tau_{PCtoPPO}$ (ns)	3.6	3.6

**Tab. B.2:** Results on the tuning of the parameters related to attenuation lengths and reflectivity.  $\Lambda$  is the the multiplicative coefficient which multiplies the measured curves of the attenuation lengths,  $R$  is the reflectivity and  $R^{\text{spike}}$  is the fraction of specular reflection with respect to diffusive reflection. “PMT ring” denotes the stainless steel small ring mounted on the PMTs without concentrators (see Sec. 5.2.2).  $R_{\text{nylon ring}}$  is the value of the reflectivity of the nylon endcaps on top and bottom of the IV.

**Tab. B.3:** Results on the tuning of the scintillation time parameters for  $\alpha$  and  $\beta$  particles. It has to be noted that all these numbers are correlated to some of the reflectivity values (especially SSS and concentrator’s). The constants describing the exponentials are related to the primary scintillation events, while the three last rows describe absorption and reemission time constants, as discussed in Sec. 5.4. The starting values for the exponential parameters come from [210].

## Appendix C

### Fit results with $npmts$ , $npmts\_dt1$ and $npmts\_dt2$ variables

In this appendix, the results of the global fit of Borexino's energy spectrum with  $npmts$ ,  $npmts\_dt1$  and  $npmts\_dt2$  as energy estimators are reported. The fit is performed in the full multivariate configuration (TFC tagged and subtracted spectra together with pulse shape and radial distributions) for the three energy variables, but it is expected that the sensitivity to pep  $\nu$  and CNO  $\nu$  is worse with  $npmts\_dt1$  and  $npmts\_dt2$  because of more prominent saturation effects. Therefore, when assessing systematic uncertainties on the pep  $\nu$  interaction rate, the small differences between the values measured with  $nhits$  and  $npmts$  and those obtained with  $npmts\_dt1$  and  $npmts\_dt2$  are neglected.

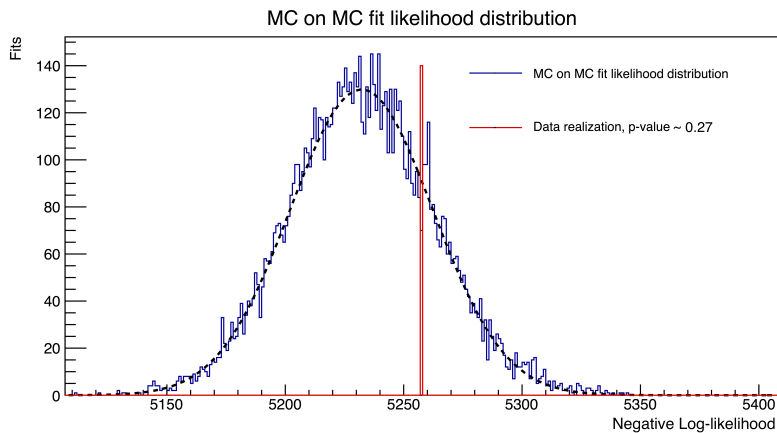


**Fig. C.1:** The blue line indicates the distribution of the negative log-likelihood value for MC on MC fits with injected rates equal to those of the best fit on data. The red bin shows the data realization of the negative log-likelihood value.

The goodness of the fit performed with the *npmts* energy variable can be evaluated according to Fig. C.1, which has been obtained as outlined in Sec. 6.9. Figure C.2 shows the pulse shape and radial distribution fits. The energy spectrum plots and the rate results are summarized in Fig. C.3.

The results obtained with *npmts\_dt1* and *npmts\_dt2* are summarized in Fig. C.4 and Fig. C.5, respectively. All the results are fully compatible, thus giving robustness to the fit strategy and to the MC modeling of the detector.

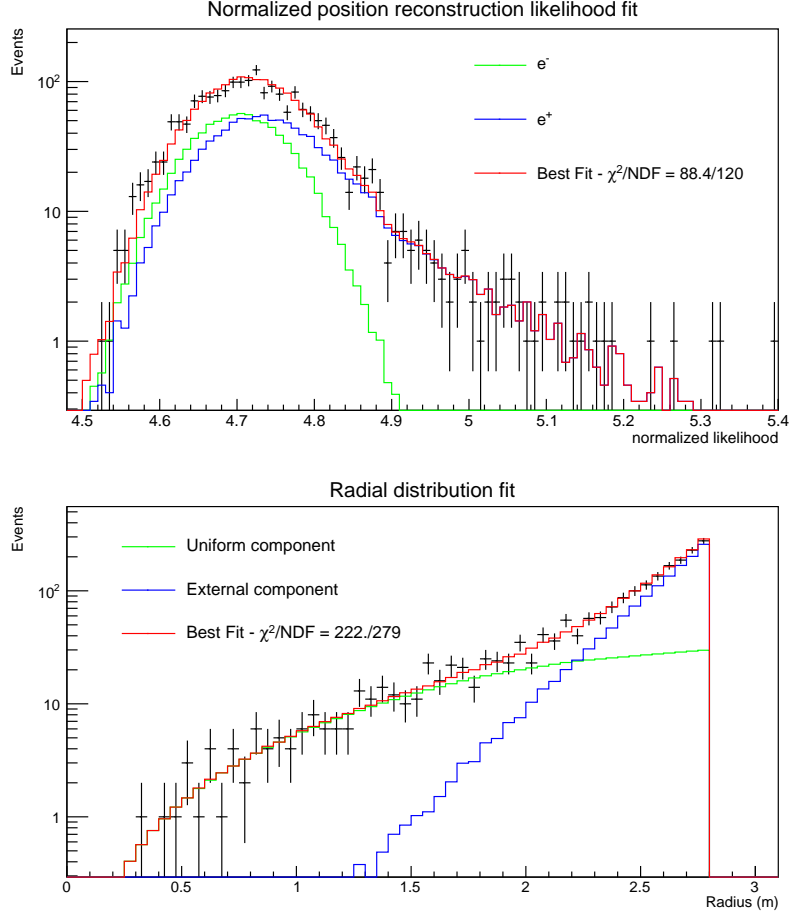


**Fig. C.2:** *Top Panel:* Fit of the normalized position reconstruction likelihood for  $\beta^+/\beta^-$  discrimination using *npmts* as energy variable. *Bottom Panel:* Fit of the radial distribution of the events using *npmts* as energy variable.

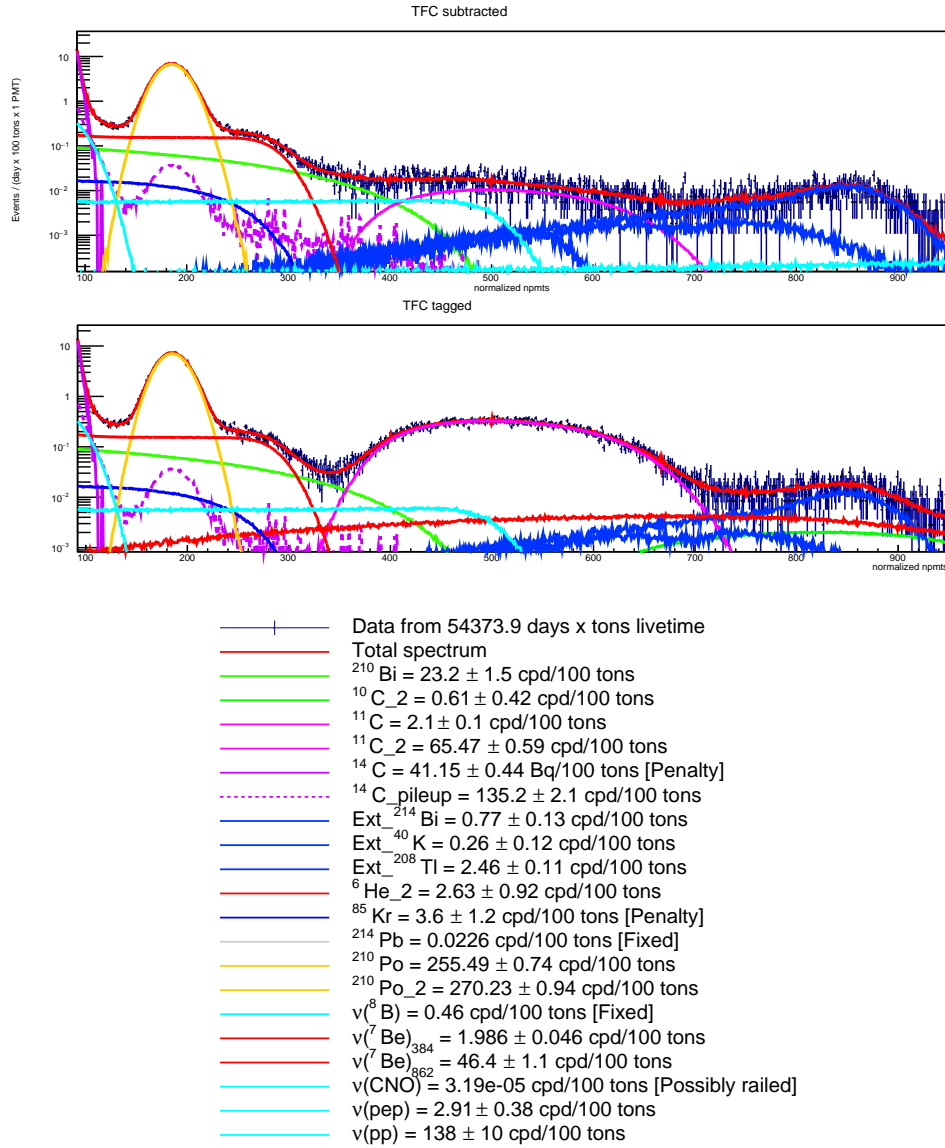


**Fig. C.3:** *Top Panel:* Pictures of the fit of the two energy spectra in the  $npmts$  energy variable. *Bottom Panel:* Best fit values of the interaction rates of the different components.

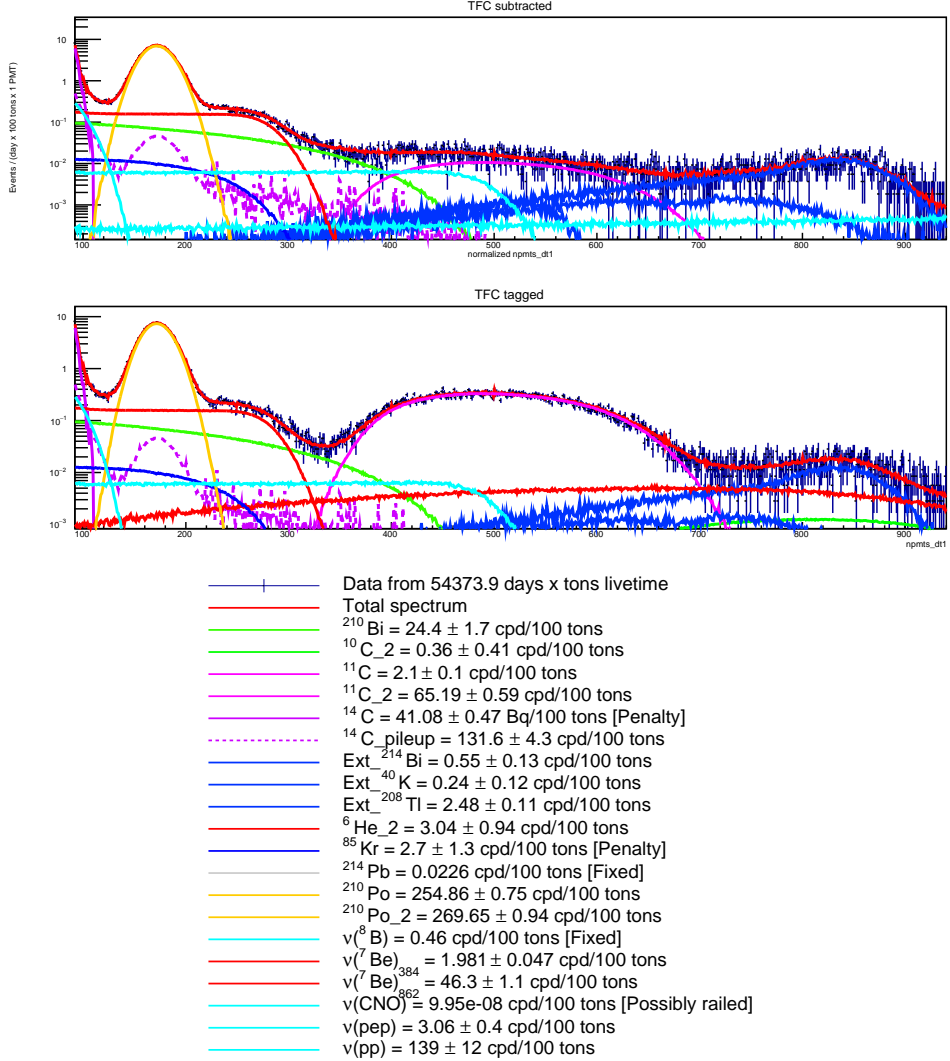


**Fig. C.4:** *Top Panel:* Pictures of the fit of the two energy spectra in the *npmts\_dt1* energy variable. *Bottom Panel:* Best fit values of the interaction rates of the different components.

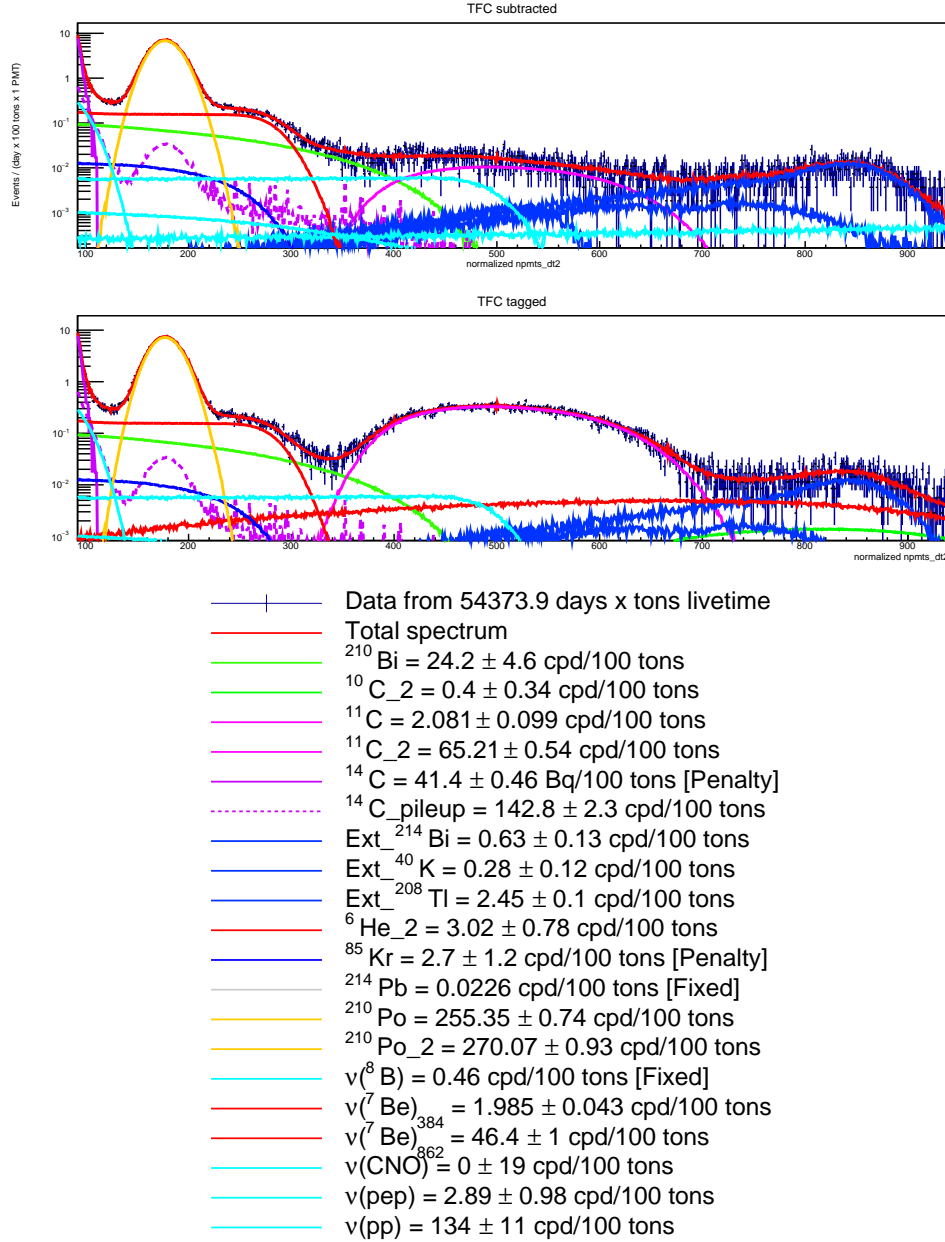


**Fig. C.5:** *Top Panel:* Pictures of the fit of the two energy spectra in the  $npmts\_dt2$  energy variable. *Bottom Panel:* Best fit values of the interaction rates of the different components.



# Bibliography

- [1] S. Dell’Oro, S. Marcocci, and F. Vissani, Phys. Rev. **D90**, 033005 (2014), [1404.2616](#). [x](#), [29](#), [40](#), [49](#), [52](#), [53](#)
- [2] S. Dell’Oro, S. Marcocci, M. Viel, and F. Vissani, JCAP **1512**, 023 (2015), [1505.02722](#). [x](#), [29](#), [50](#), [52](#), [53](#)
- [3] S. Dell’Oro, S. Marcocci, M. Viel, and F. Vissani, Adv. High Energy Phys. **2016**, 2162659 (2016), [1601.07512](#). [x](#), [29](#), [30](#), [33](#), [34](#), [36](#), [37](#), [41](#), [48](#)
- [4] W. Pauli, Tübingen conference (4th Dec. 1930). [1](#)
- [5] F. Reines and C. L. Cowan, Phys. Rev. **92**, 830 (1953), <http://link.aps.org/doi/10.1103/PhysRev.92.830>. [1](#)
- [6] C. L. Cowan, F. Reines, F. B. Harrison, H. W. Kruse, and A. D. McGuire, Science **124**, 103 (1956), ISSN 0036-8075, <http://science.sciencemag.org/content/124/3212/103>. [1](#)
- [7] K. A. Olive et al. (Particle Data Group), Chin. Phys. **C38**, 090001 (2014). [1](#), [2](#), [4](#), [5](#), [145](#)
- [8] L. Goldhaber, M. Grodzins and M. Sunyar, Phys. Rev. **109**, 1015 (1958). [2](#)
- [9] C. Spiering, European Physical Journal H **37**, 515 (2012), [1207.4952](#). [3](#)
- [10] P. Lipari (2003), <https://cds.cern.ch/record/677618>. [2](#), [8](#), [9](#), [10](#), [241](#)
- [11] K. Hirata et al., Phys. Rev. Lett. **58**, 1490 (1987), <http://link.aps.org/doi/10.1103/PhysRevLett.58.1490>. [3](#)
- [12] K. Bays et al. (Super-Kamiokande), Phys. Rev. **D85**, 052007 (2012), [1111.5031](#). [3](#)
- [13] M. G. Aartsen et al. (IceCube), Phys. Rev. Lett. **113**, 101101 (2014), [1405.5303](#). [4](#)
- [14] G. J. Feldman, J. Hartnell, and T. Kobayashi, Adv. High Energy Phys. **2013**, 475749 (2013), [1210.1778](#). [4](#)
- [15] F. Vissani, PoS **GSSI14**, 001 (2015), [1412.8386](#). [4](#), [5](#), [10](#)

- [16] A. Strumia and F. Vissani (2006), [hep-ph/0606054](#). 6, 8, 9, 10, 22, 23, 24
- [17] L. Wolfenstein, Phys. Rev. D **17**, 2369 (1978), <http://link.aps.org/doi/10.1103/PhysRevD.17.2369>. 10
- [18] S. Mikheev and A. Y. Smirnov, Sov. J. Nucl. Phys. **42**, 913 (1985). 10
- [19] Bahcall, J. N. and Fowler, William A. and Iben, Jr. and Sears, R. L., Astrophysical Journal **137**, 344 (1963). 12
- [20] A. Serenelli, Eur. Phys. J. **A52**, 78 (2016), [1601.07179](#). 12, 13, 14, 15, 21, 22
- [21] W. C. Haxton, R. G. Hamish Robertson, and A. M. Serenelli, Ann. Rev. Astron. Astrophys. **51**, 21 (2013), [1208.5723](#). 12, 16, 20, 21
- [22] S. L. Bi, T. D. Li, L. H. Li, and W. M. Yang, Astrophysical Journal Letters **731**, L42 (2011), [1104.1032](#). 12
- [23] A. M. Serenelli, Astrophys. Space Sci. **328**, 13 (2010), [0910.3690](#). 12
- [24] A. Serenelli, S. Basu, J. W. Ferguson, and M. Asplund, Astrophys. J. **705**, L123 (2009), [0909.2668](#). 12
- [25] W. M. Yang and S. L. Bi, Astrophys. J. **658**, L67 (2007), [0805.3644](#). 12
- [26] J. N. Bahcall, Phys. Scripta **T121**, 46 (2005), [hep-ph/0412068](#). 12
- [27] J. N. Bahcall and C. Pena-Garay, New J. Phys. **6**, 63 (2004), [hep-ph/0404061](#). 12
- [28] J. N. Bahcall, eConf **C030626**, THAT04 (2003), [astro-ph/0310030](#). 12
- [29] S. Watanabe and H. Shibahashi, Publ. Astron. Soc. Jap. **53**, 565 (2001), [astro-ph/0105445](#). 12
- [30] J. N. Bahcall, M. H. Pinsonneault, and S. Basu, Astrophys. J. **555**, 990 (2001), [astro-ph/0010346](#). 12
- [31] G. Fiorentini and B. Ricci, Nucl. Phys. Proc. Suppl. **81**, 95 (2000), [astro-ph/9905341](#). 12
- [32] J. N. Bahcall, Nucl. Phys. B Proc. Suppl. **77**, 64 (1999), [astro-ph/9808162](#). 12
- [33] J. N. Bahcall, M. H. Pinsonneault, S. Basu, and J. Christensen-Dalsgaard, Phys. Rev. Lett. **78**, 171 (1997), [astro-ph/9610250](#). 12
- [34] J. N. Bahcall and M. H. Pinsonneault, in *Neutrino '96. Proceedings, 17th International Conference on Neutrino Physics and Astrophysics, Helsinki, Finland, June 13-19, 1996* (1996), pp. 56–70, [hep-ph/9610542](#). 12
- [35] J. N. Bahcall and M. H. Pinsonneault, Rev. Mod. Phys. **67**, 781 (1995), [hep-ph/9505425](#). 12, 15

- [36] J. N. Bahcall, AIP Conf. Proc. **272**, 1111 (2008), [hep-ph/9211291](https://arxiv.org/abs/hep-ph/9211291). [12](#)
- [37] J. N. Bahcall and M. H. Pinsonneault, Rev. Mod. Phys. **64**, 885 (1992), <http://link.aps.org/doi/10.1103/RevModPhys.64.885>. [12](#)
- [38] J. N. Bahcall, Neutrino Astrophysics, Cambridge University Press (1989). [12](#)
- [39] A. Best, A. Caciolli, Z. Fülöp, G. Gyürky, M. Laubenstein, E. Napolitani, V. Rigato, V. Roca, and T. Szücs, Eur. Phys. J. **A52**, 72 (2016), [1601.00188](https://arxiv.org/abs/1601.00188). [13](#)
- [40] A. Formicola, P. Corvisiero, and G. Gervino, Eur. Phys. J. **A52**, 73 (2016). [13](#)
- [41] C. Gustavino, M. Anders, D. Bemmerer, Z. Elekes, and D. Trezzi, Eur. Phys. J. **A52**, 74 (2016). [13](#)
- [42] A. Boeltzig et al., Eur. Phys. J. **A52**, 75 (2016). [13](#)
- [43] M. Asplund, N. Grevesse, A. J. Sauval, and P. Scott, Annual Review of Astronomy & Astrophysics **47**, 481 (2009), [0909.0948](https://arxiv.org/abs/0909.0948). [13](#)
- [44] E. Caffau, H.-G. Ludwig, M. Steffen, B. Freytag, and P. Bonifacio, Solar Physics **268**, 255 (2011), ISSN 1573-093X, <http://dx.doi.org/10.1007/s11207-010-9541-4>. [13, 14](#)
- [45] N. Grevesse and A. Noels, Origin and Evolution of the Elements p. 15 (1993). [13](#)
- [46] N. Grevesse and A. J. Sauval, Space Science Reviews **85**, 161 (1998). [13](#)
- [47] B. Beeck et al., Astronomy & Astrophysics **539**, A121 (2012), ISSN 0004-6361. [14](#)
- [48] A. G. Kosovichev et al., Solar Physics **170**, 43 (1997), ISSN 1573-093X, <http://dx.doi.org/10.1023/A:1004949311268>. [15](#)
- [49] J. Christensen-Dalsgaard, Rev. Mod. Phys. **74**, 1073 (2003), [astro-ph/0207403](https://arxiv.org/abs/astro-ph/0207403). [15](#)
- [50] S. Basu and H. M. Antia, Phys. Rept. **457**, 217 (2008), [0711.4590](https://arxiv.org/abs/0711.4590). [15](#)
- [51] C. Casella et al., Nuclear Physics A **706**, 203 (2002), ISSN 0375-9474, <http://www.sciencedirect.com/science/article/pii/S0375947402007492>. [17](#)
- [52] M. Junker et al. (The Luna Collaboration), Phys. Rev. C **57**, 2700 (1998), <http://link.aps.org/doi/10.1103/PhysRevC.57.2700>. [17](#)
- [53] S. Fukuda et al. (Super-Kamiokande), Phys. Rev. Lett. **86**, 5651 (2001), [hep-ex/0103032](https://arxiv.org/abs/hep-ex/0103032). [17, 240](#)
- [54] B. Aharmim et al. (SNO), Astrophys. J. **653**, 1545 (2006), [hep-ex/0607010](https://arxiv.org/abs/hep-ex/0607010). [17](#)
- [55] C. Howard (SNO) (2009), [0906.0040](https://arxiv.org/abs/0906.0040). [17](#)

- [56] G. Gyurky et al., Phys. Rev. **C75**, 035805 (2007), [nucl-ex/0702003](https://arxiv.org/abs/nucl-ex/0702003). 17
- [57] M. Marta et al. (LUNA Collaboration), Phys. Rev. C **83**, 045804 (2011), <http://link.aps.org/doi/10.1103/PhysRevC.83.045804>. 19
- [58] P. J. LeBlanc et al., Phys. Rev. C **82**, 055804 (2010), <http://link.aps.org/doi/10.1103/PhysRevC.82.055804>. 19
- [59] J. Bergstrom, M. C. Gonzalez-Garcia, M. Maltoni, C. Pena-Garay, A. M. Serenelli, and N. Song, JHEP **03**, 132 (2016), [1601.00972](https://arxiv.org/abs/1601.00972). 20
- [60] A. M. Serenelli, W. C. Haxton, and C. Pena-Garay, The Astrophysical Journal **743**, 24 (2011), <http://stacks.iop.org/0004-637X/743/i=1/a=24>. 21
- [61] Christensen-Dalsgaard, J., Di Mauro, M. P., Houdek, G., and Pijpers, F., Astronomy & Astrophysics **494**, 205 (2009), <http://dx.doi.org/10.1051/0004-6361:200810170>. 21
- [62] F. L. Villante, A. M. Serenelli, F. Delahaye, and M. H. Pinsonneault, The Astrophysical Journal **787**, 13 (2014), <http://stacks.iop.org/0004-637X/787/i=1/a=13>. 21
- [63] J. E. Bailey et al., Nature **517**, 56 (2015), <http://dx.doi.org/10.1038/nature14048>. 21
- [64] M. Maltoni and A. Yu. Smirnov, Eur. Phys. J. **A52**, 87 (2016), [1507.05287](https://arxiv.org/abs/1507.05287). 23
- [65] B. T. Cleveland et al., The Astrophysical Journal **496**, 505 (1998), <http://stacks.iop.org/0004-637X/496/i=1/a=505>. 24, 25
- [66] W. Hampel et al., Physics Letters B **447**, 127 (1999), ISSN 0370-2693, <http://www.sciencedirect.com/science/article/pii/S0370269398015792>. 25
- [67] J. N. Abdurashitov et al. (SAGE), J. Exp. Theor. Phys. **95**, 181 (2002), [Zh. Eksp. Teor. Fiz. 122, 211(2002)], [astro-ph/0204245](https://arxiv.org/abs/astro-ph/0204245). 25
- [68] V. N. Gavrin, Phys. Usp. **54**, 941 (2011). 26
- [69] K. S. Hirata et al., Phys. Rev. Lett. **63**, 16 (1989), <http://link.aps.org/doi/10.1103/PhysRevLett.63.16>. 26
- [70] Y. Fukuda et al., Phys. Rev. Lett. **77**, 1683 (1996), <http://link.aps.org/doi/10.1103/PhysRevLett.77.1683>. 26
- [71] S. Fukuda et al., Physics Letters B **539**, 179 (2002), ISSN 0370-2693, <http://www.sciencedirect.com/science/article/pii/S0370269302020907>. 26

- [72] S. Fukuda et al., Nuclear Instruments and Methods in Physics Research Section A: Accelerators, Spectrometers, Detectors and Associated Equipment **501**, 418 (2003), ISSN 0168-9002, <http://www.sciencedirect.com/science/article/pii/S016890020300425X>. 26
- [73] T. Kajita, Rev. Mod. Phys. **88**, 030501 (2016), <http://link.aps.org/doi/10.1103/RevModPhys.88.030501>. 26
- [74] A. B. McDonald, Rev. Mod. Phys. **88**, 030502 (2016), <http://link.aps.org/doi/10.1103/RevModPhys.88.030502>. 26, 27
- [75] K. Eguchi et al. (KamLAND Collaboration), Phys. Rev. Lett. **90**, 021802 (2003), <http://link.aps.org/doi/10.1103/PhysRevLett.90.021802>. 27
- [76] S. Abe et al. (KamLAND), Phys. Rev. **C84**, 035804 (2011), [1106.0861](https://arxiv.org/abs/1106.0861). 27
- [77] T. Araki et al., Nature **436**, 499 (2005), <http://dx.doi.org/10.1038/nature03980>. 27
- [78] S. Andringa et al. (SNO+ Collaboration), Adv. High Energy Phys. **2016**, 6194250 (2015). 28, 48, 51, 80, 97
- [79] D. Franco et al. (2015), [1510.04196](https://arxiv.org/abs/1510.04196). 28
- [80] P. Agnes et al. (DarkSide), Phys. Rev. **D93**, 081101 (2016), [1510.00702](https://arxiv.org/abs/1510.00702). 28
- [81] G. Bellini, M. Campanella, D. Giugni, and R. Raghavan, Borexino Proposal (Yellow Book) (1991). 29, 54, 101
- [82] R. S. Raghavan, Phys. Rev. Lett. **72**, 1411 (1994). 29, 54
- [83] P. A. M. Dirac, Proc. Roy. Soc. Lond. A **117**, 610 (1928). 29, 31
- [84] P. A. M. Dirac, Proc. Roy. Soc. Lond. A **118**, 351 (1928). 29, 31
- [85] E. Majorana, Nuovo Cim. **14**, 171 (1937). 29, 31
- [86] G. Racah, Nuovo Cim. **14**, 322 (1937). 30
- [87] W. H. Furry, Phys. Rev. **56**, 1184 (1939). 30, 33
- [88] M. Goeppert-Mayer, Phys. Rev. **48**, 512 (1935). 30
- [89] S. Weinberg, Phys. Rev. Lett. **43**, 1566 (1979). 30
- [90] E. Fermi, Nuovo Cim. **11**, 1 (1934). 31
- [91] A. D. Sakharov, Pisma Zh. Eksp. Teor. Fiz. **5**, 32 (1967). 32
- [92] G. 't Hooft, Phys. Rev. Lett. **37**, 8 (1976). 32

- [93] V. A. Kuzmin, V. A. Rubakov, and M. E. Shaposhnikov, Phys. Lett. B **155**, 36 (1985). [32](#)
- [94] J. Harvey and M. S. Turner, Phys. Rev. D **42**, 3344 (1990). [32](#)
- [95] A. Bochkarev and M. Shaposhnikov, Mod. Phys. Lett. A **2**, 417 (1987). [32](#)
- [96] K. Kajantie, M. Laine, K. Rummukainen, and M. E. Shaposhnikov, Nucl. Phys. B **466**, 189 (1996). [32](#)
- [97] M. Fukugita and T. Yanagida, Phys. Lett. B **174**, 45 (1986). [32](#)
- [98] M. Shaposhnikov (2012), [Presentation at [Cosmo 2012](#), Beijing, China, September 2012]. [32](#)
- [99] S. Weinberg, Phys. Rev. **128**, 1457 (1962). [32](#)
- [100] A. Cocco, G. Mangano, and M. Messina, J. Cosm. Astropart. Phys. **0706**, 015 (2007). [32](#)
- [101] A. J. Long, C. Lunardini, and E. Sabancilar, J. Cosm. Astropart. Phys. **1408**, 038 (2014). [32](#)
- [102] J. Schechter and J. W. F. Valle, Phys. Rev. D **25**, 2951 (1982). [34](#)
- [103] M. Duerr, M. Lindner, and A. Merle, J. High Energy Phys. **1106**, 091 (2011). [34](#)
- [104] F. Capozzi, E. Lisi, A. Marrone, D. Montanino, and A. Palazzo (2016), [1601.07777](#). [35](#)
- [105] S. Abe et al. (KamLAND Collaboration), Phys. Rev. Lett. **100**, 221803 (2008). [36](#)
- [106] P. Ghoshal and S. T. Petcov, J. High Energy Phys. **1103**, 058 (2011). [36](#)
- [107] P. A. R. Ade et al. (Planck Collaboration) (2015), [1502.01589](#). [37](#), [39](#)
- [108] Y. B. Zel'dovich and M. Y. Khlopov, Sov. Phys. Usp. **24**, 755 (1981). [37](#)
- [109] G. L. Fogli, E. Lisi, A. Marrone, A. Melchiorri, A. Palazzo, P. Serra, and J. Silk, Phys. Rev. D **70**, 113003 (2004). [37](#)
- [110] J. R. Primack, J. Holtzman, A. Klypin, and D. O. Caldwell, Phys. Rev. Lett. **74**, 2160 (1995). [37](#), [38](#)
- [111] S. W. Allen, R. W. Schmidt, and S. L. Bridle, Mon. Not. Roy. Astron. Soc. **346**, 593 (2003). [37](#), [38](#)
- [112] R. A. Battye and A. Moss, Phys. Rev. Lett. **112**, 051303 (2014). [37](#), [38](#)
- [113] N. Palanque-Delabrouille et al., J. Cosm. Astropart. Phys. **1502**, 045 (2015). [37](#), [38](#), [50](#), [52](#)

- [114] J. Lesgourgues, G. Mangano, G. Miele, and S. Pastor, *Neutrino Cosmology* (Cambridge University Press, 2013). [37](#)
- [115] S. Kovalenko, M. I. Krivoruchenko, and F. Šimkovic, Phys. Rev. Lett. **112**, 142503 (2014). [38](#)
- [116] Y. Y. Y. Wong, Ann. Rev. Nucl. Part. Sci. **61**, 69 (2011). [38](#)
- [117] J. Lesgourgues and S. Pastor, New J. Phys. **16**, 065002 (2014). [38](#)
- [118] N. Palanque-Delabrouille et al., J. Cosm. Astropart. Phys. **1511**, 011 (2015). [39](#)
- [119] E. Di Valentino, E. Giusarma, O. Mena, A. Melchiorri, and J. Silk (2015), [1511.00975](#). [39](#)
- [120] X. Zhang (2015), [1511.02651](#). [39](#)
- [121] A. J. Cuesta, V. Niro, and L. Verde (2015), [1511.05983](#). [39](#)
- [122] T. J. Loredo and D. Q. Lamb, Phys. Rev. D **65**, 063002 (2002). [39](#)
- [123] G. Pagliaroli, F. Rossi-Torres, and F. Vissani, Astropart. Phys. **33**, 287 (2010). [39](#)
- [124] C. Kraus et al., Eur. Phys. J. C **40**, 447 (2005). [39](#)
- [125] V. N. Aseev et al., Phys. Rev. D **84**, 112003 (2011). [39](#)
- [126] A. Osipowicz et al. (KATRIN Collaboration) (2001), [hep-ex/0109033](#). [39](#)
- [127] B. Alpert et al., Eur. Phys. J. C **75**, 112 (2015). [39](#)
- [128] P. J. Doe et al. (Project 8 Collaboration), Conf. Proc. C13-07-29.2 (2013), [1309.7093](#). [39](#)
- [129] P. C. O. Ranitzsch, J. P. Porst, S. Kempf, C. Pies, S. Schafer, D. Hengstler, A. Fleischmann, C. Enss, and L. Gastaldo, J. Low Temp. Phys. **167**, 1004 (2012). [39](#)
- [130] V. I. Tretyak, F. A. Danevich, S. S. Nagorny, and Y. G. Zdesenko, EPL (Europhysics Letters) **69**, 41 (2005), <http://stacks.iop.org/0295-5075/69/i=1/a=041>. [40](#)
- [131] H. Primakoff and S. P. Rosen, Rep. Prog. Phys. **22**, 121 (1959), <http://stacks.iop.org/0034-4885/22/i=1/a=305>. [40](#)
- [132] J. Kotila and F. Iachello, Phys. Rev. C **85**, 034316 (2012). [40, 42, 48, 49, 51, 60, 63](#)
- [133] S. Stoica and M. Mirea, Phys. Rev. C **88**, 037303 (2013). [40](#)
- [134] D. Štefánik, R. Dvornický, F. Šimkovic, and P. Vogel, Phys. Rev. C **92**, 055502 (2015). [40](#)

- [135] J. Barea, J. Kotila, and F. Iachello, Phys. Rev. C **91**, 034304 (2015). [41](#), [42](#), [43](#), [48](#), [49](#), [51](#), [63](#)
- [136] F. Šimkovic, V. Rodin, A. Faessler, and P. Vogel, Phys. Rev. C **87**, 045501 (2013). [41](#)
- [137] J. Menéndez, A. Poves, E. Caurier, and F. Nowacki, Nucl. Phys. A **818**, 139 (2009). [41](#), [43](#)
- [138] E. Caurier, G. Martinez-Pinedo, F. Nowacki, A. Poves, and A. P. Zuker, Rev. Mod. Phys. **77**, 427 (2005). [41](#)
- [139] J. Hyvarinen and J. Suhonen, Phys. Rev. C **91**, 024613 (2015). [41](#)
- [140] F. F. Deppisch and J. Suhonen (2016), [1606.02908](#). [41](#)
- [141] F. Šimkovic, G. Pantis, J. D. Vergados, and A. Faessler, Phys. Rev. C **60**, 055502 (1999). [41](#)
- [142] J. Barea, J. Kotila, and F. Iachello, Phys. Rev. C **87**, 014315 (2013). [41](#), [42](#), [43](#)
- [143] F. Feruglio, A. Strumia, and F. Vissani, Nucl. Phys. B **637**, 345 (2002). [42](#)
- [144] V. A. Rodin, A. Faessler, F. Šimkovic, and P. Vogel, Phys. Rev. C **68**, 044302 (2003). [42](#)
- [145] V. A. Rodin, A. Faessler, F. Šimkovic, and P. Vogel, Nucl. Phys. A **766**, 107 (2006). [42](#)
- [146] F. Šimkovic, S. M. Bilenky, A. Faessler, and T. Gutsche, Phys. Rev. D **87**, 073002 (2013). [42](#)
- [147] A. Faessler, G. L. Fogli, E. Lisi, V. Rodin, A. M. Rotunno, and F. Šimkovic, J. Phys. G **35**, 075104 (2008). [42](#)
- [148] J. Suhonen and O. Civitarese, Phys. Lett. B **725**, 153 (2013). [42](#)
- [149] E. Lisi, A. Rotunno, and F. Šimkovic, Phys. Rev. D **92**, 093004 (2015). [42](#)
- [150] M. Konieczka, P. Baczyk, and W. Satula (2015), [1509.04480](#). [42](#)
- [151] J. Engel, F. Šimkovic, and P. Vogel, Phys. Rev. C **89**, 064308 (2014). [43](#)
- [152] F. Cappuzzello, C. Agodi, M. Bondì, D. Carbone, M. Cavallaro, and A. Foti, J. Phys. Conf. Ser. **630**, 012018 (2015). [43](#)
- [153] D. M. Chernyak, F. A. Danevich, A. Giuliani, E. Olivieri, M. Tenconi, and V. I. Tretyak, The European Physical Journal C **72**, 1989 (2012), ISSN 1434-6052, <http://dx.doi.org/10.1140/epjc/s10052-012-1989-y>. [44](#)

- [154] R. G. H. Robertson, *Mod. Phys. Lett. A* **28**, 1350021 (2013). [44](#), [45](#)
- [155] R. Saakyan, *Ann. Rev. Nucl. Part. Sci.* **63**, 503 (2013). [45](#)
- [156] O. Cremonesi and M. Pavan, *Adv. High Energy Phys.* **2014**, 951432 (2014). [46](#)
- [157] S. R. Elliott and P. Vogel, *Ann. Rev. Nucl. Part. Sci.* **52**, 115 (2002). [47](#)
- [158] E. Andreotti et al., *Astropart. Phys.* **34**, 822 (2011). [48](#)
- [159] K. Alfonso et al. (CUORE Collaboration), *Phys. Rev. Lett.* **115**, 102502 (2015). [48](#)
- [160] H. V. Klapdor-Kleingrothaus et al., *Eur. Phys. J. A* **12**, 147 (2001). [48](#)
- [161] C. E. Aalseth et al. (IGEX Collaboration), *Phys. Rev. C* **59**, 2108 (1999). [48](#)
- [162] C. E. Aalseth et al. (IGEX Collaboration), *Phys. Rev. D* **65**, 092007 (2002). [48](#)
- [163] K. H. Ackermann et al. (GERDA Collaboration), *Eur. Phys. J. C* **73**, 2330 (2013). [48](#)
- [164] M. Agostini et al. (GERDA Collaboration), *Phys. Rev. Lett.* **111**, 122503 (2013). [48](#)
- [165] R. Arnold et al. (NEMO Collaboration), *Phys. Rev. D* **89**, 111101 (2014). [48](#)
- [166] J. B. Albert et al. (EXO Collaboration), *Nature* **510**, 229 (2014). [48](#), [61](#)
- [167] A. Gando et al. (KamLAND-Zen Collaboration), *Phys. Rev. Lett.* **110**, 062502 (2013). [48](#), [54](#), [55](#)
- [168] K. Asakura et al. (KamLAND-Zen Collaboration), *AIP Conf. Proc.* **1666**, 170003 (2015). [48](#), [54](#)
- [169] A. Gando et al. (KamLAND-Zen Collaboration), *Phys. Rev. Lett.* **117**, 082503 (2016), <http://link.aps.org/doi/10.1103/PhysRevLett.117.082503>. [48](#), [49](#), [50](#), [54](#), [56](#), [61](#)
- [170] B. Schwingenheuer, *First data release GERDA Phase II: Search for  $0\nu\beta\beta$  of  $^{76}\text{Ge}$*  (29th June 2016). [48](#)
- [171] D. R. Artusa et al. (CUORE Collaboration), *Adv. High Energy Phys.* **2015**, 879871 (2015). [48](#), [51](#)
- [172] G. Wang et al. (CUPID) (2015), [1504.03599](#). [48](#), [51](#)
- [173] G. Wang et al. (CUPID) (2015), [1504.03612](#). [48](#), [51](#)
- [174] N. Abgrall et al. (MAJORANA Collaboration), *Adv. High Energy Phys.* **2014**, 365432 (2014). [48](#), [51](#)

- [175] J. Martín-Albo et al., Journal of High Energy Physics **2016**, 1 (2016), ISSN 1029-8479, [http://dx.doi.org/10.1007/JHEP05\(2016\)159](http://dx.doi.org/10.1007/JHEP05(2016)159). **48**, **51**
- [176] V. Alenkov et al. (AMoRE) (2015), [1512.05957](https://arxiv.org/abs/1512.05957). **48**, **51**
- [177] I. Ostrovskiy (2015), [To appear in the proceedings of the XIV International Conference on Topics in Astroparticle and Underground Physics (TAUP 2015), Torino, Italy, September 2015]. **48**, **51**, **61**
- [178] X. Ji (2015), [Presentation at the International Workshop on Baryon and Lepton Number Violation (BLV 2015), Amherst, MA, USA, April 2015]. **48**, **51**
- [179] K. Asakura et al., AIP Conference Proceedings **1666**, 170003 (2015), <http://scitation.aip.org/content/aip/proceeding/aipcp/10.1063/1.4915593>. **48**
- [180] R. Arnold et al. (NEMO-3 Collaboration), Phys. Rev. D **92**, 072011 (2015). **48**, **51**
- [181] S. Blot (2015), [To appear in the proceedings of the XIV International Conference on Topics in Astroparticle and Underground Physics (TAUP 2015), Torino, Italy, September 2015]. **48**
- [182] E. L. Fireman, Phys. Rev. **74**, 1238 (1948). **47**
- [183] E. L. Fireman, Phys. Rev. **75**, 323 (1949). **47**
- [184] S. R. Elliott, A. A. Hahn, and M. K. Moe, Phys. Rev. Lett. **59**, 2020 (1987). **47**
- [185] R. Brugnera and A. Garfagnini, Adv. High Energy Phys. **2013**, 506186 (2013). **51**
- [186] D. R. Artusa et al. (CUORE Collaboration), Eur. Phys. J. C **74**, 3096 (2014). **49**
- [187] P. A. R. Ade et al. (Planck Collaboration), Astron. Astrophys. **571**, A16 (2014). **50**
- [188] N. Palanque-Delabrouille et al., Astron. Astrophys. **559**, A85 (2013). **50**, **51**
- [189] V. Cirigliano, A. Kurylov, M. J. Ramsey-Musolf, and P. Vogel, Phys. Rev. Lett. **93**, 231802 (2004). **53**
- [190] V. Tello, M. Nemevsek, F. Nesti, G. Senjanovic, and F. Vissani, Phys. Rev. Lett. **106**, 151801 (2011). **53**
- [191] S. Alekhin et al. (2015), [1504.04855](https://arxiv.org/abs/1504.04855). **53**
- [192] B. Caccianiga and M. G. Giammarchi, Astropart. Phys. **14**, 15 (2000). **54**, **97**, **98**
- [193] C. Arpesella et al. (BOREXINO), Astropart. Phys. **18**, 1 (2002), [hep-ex/0109031](https://arxiv.org/abs/hep-ex/0109031). **54**, **55**, **187**
- [194] G. Bellini et al., The European Physical Journal C - Particles and Fields **19**, 43 (2001), ISSN 1434-6052, <http://dx.doi.org/10.1007/s100520100594>. **54**

- [195] F. An et al. (JUNO), J. Phys. **G43**, 030401 (2016), [1507.05613](https://arxiv.org/abs/1507.05613). **56, 80, 97**
- [196] J. Zhao, L.-J. Wen, Y.-F. Wang, and J. Cao (2016), [1610.07143](https://arxiv.org/abs/1610.07143). **56**
- [197] *Yale Nuclear Theory: Double beta decay site (nucleartheory.yale.edu)*. **60**
- [198] J. J. Gomez Cadenas, *Talk at the Gran Sasso Summer Institute 2014*. **61**
- [199] A. Caminata, *Studio di esperimenti per la ricerca del doppio decadimento beta senza neutrini con scintillatori liquidi (Italian)* (2010). **61, 62**
- [200] G. Bellini et al. (Borexino Collaboration), Phys. Rev. D **82**, 033006 (2010), <http://link.aps.org/doi/10.1103/PhysRevD.82.033006>. **62, 130**
- [201] G. Bellini et al., Journal of Cosmology and Astroparticle Physics **2013**, 049 (2013), <http://stacks.iop.org/1475-7516/2013/i=08/a=049>. **62, 110**
- [202] S. Marcocci, *Sviluppo di un apparato per lo studio di scintillatori liquidi drogati con xenon per la ricerca del doppio decadimento beta senza neutrini (Italian)* (2013). **65, 71, 73, 74, 75, 77, 78, 79, 85**
- [203] S. Marcocci et al. (Borexino), Nuovo Cim. **C38**, 51 (2015). **65, 75, 77, 78**
- [204] *Hamamatsu R1584 datasheet*, <http://www.hamamatsu.com/us/en/R1584.html>. **68**
- [205] *Hamamatsu R6091 datasheet*, <http://www.hamamatsu.com/us/en/R6091.html>. **69**
- [206] G. Alimonti et al., Nuclear Instruments and Methods in Physics Research Section A: Accelerators, Spectrometers, Detectors and Associated Equipment **609**, 58 (2009), ISSN 0168-9002, <http://www.sciencedirect.com/science/article/pii/S0168900209014247>. **70**
- [207] R. Brun and F. Rademakers, Nucl. Instrum. Meth. **A389**, 81 (1997). **73**
- [208] F. Elisei et al., Nucl. Instrum. Meth. **A400**, 53 (1997). **87, 88, 90, 91, 92**
- [209] F. Gatti, G. Morelli, G. Testera, and S. Vitale, Nucl. Instrum. Meth. **A370**, 609 (1996). **87**
- [210] P. Lombardi, F. Ortica, G. Ranucci, and A. Romani, Nucl. Instrum. Meth. **A701**, 133 (2013). **90, 92, 99, 144, 167, 244**
- [211] G. Hooft, Physics Letters B **37**, 195 (1971), ISSN 0370-2693, <http://www.sciencedirect.com/science/article/pii/0370269371900505>. **102**
- [212] J. N. Bahcall, Rev. Mod. Phys. **59**, 505 (1987), <http://link.aps.org/doi/10.1103/RevModPhys.59.505>. **102**

- [213] J. N. Bahcall, M. Kamionkowski, and A. Sirlin, Phys. Rev. **D51**, 6146 (1995), [astro-ph/9502003](https://arxiv.org/abs/astro-ph/9502003). 102, 156
- [214] G. Bellini et al. (Borexino), Phys. Rev. **D89**, 112007 (2014), [1308.0443](https://arxiv.org/abs/1308.0443). 102, 103, 105, 106, 108, 110, 115, 116, 118, 119, 121, 122, 123, 139, 143, 151, 158, 165, 172, 187, 195, 200, 210, 216
- [215] G. Alimonti et al. (Borexino), Nucl. Instrum. Meth. **A600**, 568 (2009), [0806.2400](https://arxiv.org/abs/0806.2400). 102, 103, 138
- [216] H. Back et al. (Borexino), JINST **7**, P10018 (2012), [1207.4816](https://arxiv.org/abs/1207.4816). 105, 114, 115, 150, 158, 160, 162, 163, 179
- [217] G. Alimonti et al., Physics Letters B **422**, 349 (1998), ISSN 0370-2693, <http://www.sciencedirect.com/science/article/pii/S0370269397015657>. 107
- [218] G. Bellini et al. (BOREXINO), Nature **512**, 383 (2014). 107, 114, 129, 182, 183, 185, 189, 191, 195
- [219] C. Galbiati, A. Pocar, D. Franco, A. Ianni, L. Cadonati, and S. Schönert, Phys. Rev. C **71**, 055805 (2005), [http://link.aps.org/doi/10.1103/PhysRevC.71.055805](https://link.aps.org/doi/10.1103/PhysRevC.71.055805). 110, 129
- [220] V. Lagomarsino and G. Testera, Nucl. Instrum. Meth. **A430**, 435 (1999). 110
- [221] G. E. and F. De Martini, Nuclear Electronics II. Proceedings of the Conference on Nuclear Electronics. **5** (1962). 117
- [222] E. Gatti et al., Energia Nucleare, 17 **34** (1970). 117
- [223] D. Franco, G. Consolati, and D. Trezzi, Phys. Rev. C **83**, 015504 (2011), [http://link.aps.org/doi/10.1103/PhysRevC.83.015504](https://link.aps.org/doi/10.1103/PhysRevC.83.015504). 121
- [224] G. Bellini et al. (Borexino Collaboration), Phys. Rev. Lett. **108**, 051302 (2012), [http://link.aps.org/doi/10.1103/PhysRevLett.108.051302](https://link.aps.org/doi/10.1103/PhysRevLett.108.051302). 122, 129, 197, 207, 208, 210, 220, 229, 232
- [225] F. Villante, A. Ianni, F. Lombardi, G. Pagliaroli, and F. Vissani, Physics Letters B **701**, 336 (2011), ISSN 0370-2693, <http://www.sciencedirect.com/science/article/pii/S0370269311006125>. 123
- [226] *ANSYS Fluent Computational Fluid Dynamics*, <http://www.ansys.com/Products/Fluids/ANSYS-Fluent>. 127
- [227] C. Arpesella et al., Physics Letters B **658**, 101 (2008), ISSN 0370-2693, <http://www.sciencedirect.com/science/article/pii/S0370269307011732>. 128
- [228] C. Arpesella et al. (Borexino Collaboration), Phys. Rev. Lett. **101**, 091302 (2008), [http://link.aps.org/doi/10.1103/PhysRevLett.101.091302](https://link.aps.org/doi/10.1103/PhysRevLett.101.091302). 128

- [229] G. Bellini et al. (Borexino Collaboration), Phys. Rev. Lett. **107**, 141302 (2011), <http://link.aps.org/doi/10.1103/PhysRevLett.107.141302>. [128](#), [226](#), [229](#)
- [230] G. Bellini et al., Physics Letters B **707**, 22 (2012), ISSN 0370-2693, <http://www.sciencedirect.com/science/article/pii/S037026931101389X>. [129](#)
- [231] G. Bellini et al., Physics Letters B **687**, 299 (2010), ISSN 0370-2693, <http://www.sciencedirect.com/science/article/pii/S0370269310003722>. [130](#)
- [232] G. Bellini et al., Physics Letters B **722**, 295 (2013), ISSN 0370-2693, <http://www.sciencedirect.com/science/article/pii/S0370269313003092>. [130](#)
- [233] M. Agostini et al. (Borexino Collaboration), Phys. Rev. D **92**, 031101 (2015), <http://link.aps.org/doi/10.1103/PhysRevD.92.031101>. [130](#)
- [234] G. Bellini et al., Physics Letters B **696**, 191 (2011), ISSN 0370-2693, <http://www.sciencedirect.com/science/article/pii/S037026931001422X>. [130](#)
- [235] P. Alvarez Sanchez, G. Bellini, et al., Physics Letters B **716**, 401 (2012), ISSN 0370-2693, <http://www.sciencedirect.com/science/article/pii/S0370269312009185>. [130](#)
- [236] G. Bellini et al. (Borexino), JCAP **1205**, 015 (2012), [1202.6403](#). [130](#)
- [237] G. Bellini et al. (Borexino Collaboration), Phys. Rev. C **81**, 034317 (2010), <http://link.aps.org/doi/10.1103/PhysRevC.81.034317>. [130](#)
- [238] G. Bellini et al. (Borexino collaboration), Phys. Rev. D **85**, 092003 (2012), <http://link.aps.org/doi/10.1103/PhysRevD.85.092003>. [130](#)
- [239] G. Bellini et al. (Borexino Collaboration), Phys. Rev. D **88**, 072010 (2013), <http://link.aps.org/doi/10.1103/PhysRevD.88.072010>. [130](#)
- [240] M. Agostini et al. (Borexino Collaboration), Phys. Rev. Lett. **115**, 231802 (2015), <http://link.aps.org/doi/10.1103/PhysRevLett.115.231802>. [130](#)
- [241] A. Aguilar-Arevalo et al. (LSND), Phys. Rev. **D64**, 112007 (2001), [hep-ex/0104049](#). [132](#)
- [242] A. A. Aguilar-Arevalo et al. (MiniBooNE Collaboration), Phys. Rev. Lett. **105**, 181801 (2010), <http://link.aps.org/doi/10.1103/PhysRevLett.105.181801>. [132](#)
- [243] J. Kopp, P. A. N. Machado, M. Maltoni, and T. Schwetz, JHEP **05**, 050 (2013), [1303.3011](#). [132](#)
- [244] C. Zhang, X. Qian, and P. Vogel, Phys. Rev. **D87**, 073018 (2013), [1303.0900](#). [132](#)
- [245] C. Giunti, M. Laveder, Y. F. Li, Q. Y. Liu, and H. W. Long, Phys. Rev. **D86**, 113014 (2012), [1210.5715](#). [132](#)

- [246] G. Bellini et al. (Borexino Collaboration), J. High Energy Phys. **1308**, 038 (2013). [132](#)
- [247] L. Papp et al., Nuclear Instruments and Methods in Physics Research Section A: Accelerators, Spectrometers, Detectors and Associated Equipment **824**, 699 (2016), ISSN 0168-9002, frontier Detectors for Frontier Physics: Proceedings of the 13th Pisa Meeting on Advanced Detectors, <http://www.sciencedirect.com/science/article/pii/S0168900215014114>. [133](#)
- [248] S. Agostinelli et al., Nuclear Instruments and Methods in Physics Research Section A: Accelerators, Spectrometers, Detectors and Associated Equipment **506**, 250 (2003), ISSN 0168-9002, <http://www.sciencedirect.com/science/article/pii/S0168900203013688>. [136](#), [173](#)
- [249] L. Oberauer, C. Grieb, F. Feilitzsch, and I. Manno, Nuclear Instruments and Methods in Physics Research Section A: Accelerators, Spectrometers, Detectors and Associated Equipment **530**, 453 (2004), ISSN 0168-9002, <http://www.sciencedirect.com/science/article/pii/S016890020401085X>. [139](#)
- [250] J. B. Birks, Proceedings of the Physical Society. Section A **64**, 874 (1951), <http://stacks.iop.org/0370-1298/64/i=10/a=303>. [142](#)
- [251] M. Chen, F. Elisei, F. Masetti, U. Mazzucato, C. Salvo, and G. Testera, Nucl. Instrum. Meth. **A420**, 189 (1999). [144](#)
- [252] R. A. MacRae, M. W. Williams, and E. T. Arakawa, The Journal of Chemical Physics **61**, 861 (1974), <http://scitation.aip.org/content/aip/journal/jcp/61/3/10.1063/1.1682026>. [146](#)
- [253] G. Alimonti et al. (Borexino), Nucl. Instrum. Meth. **A440**, 360 (2000). [149](#)
- [254] A. Ianni, P. Lombardi, G. Ranucci, and O. Smirnov, Nucl. Instrum. Meth. **A537**, 683 (2005), [physics/0406138](https://arxiv.org/abs/physics/0406138). [149](#)
- [255] R. M. Waxler and C. E. Weir, *Effect of pressure and temperature of the refractive indices of benzene, carbon tetrachloride, and water*. [152](#)
- [256] H. Haitjema, *Ellipsometry* (Springer Berlin Heidelberg, Berlin, Heidelberg, 2014), pp. 453–458, ISBN 978-3-642-20617-7, [http://dx.doi.org/10.1007/978-3-642-20617-7\\_16705](http://dx.doi.org/10.1007/978-3-642-20617-7_16705). [153](#)
- [257] J. Bahcall, *Web site* (2005), <http://www.sns.ias.edu/~jnb>. [156](#)
- [258] P. C. de Holanda, W. Liao, and A. Yu. Smirnov, Nucl. Phys. **B702**, 307 (2004), [hep-ph/0404042](https://arxiv.org/abs/hep-ph/0404042). [156](#)
- [259] F. Capozzi, G. L. Fogli, E. Lisi, A. Marrone, D. Montanino, and A. Palazzo, Phys. Rev. D **89**, 093018 (2014). [156](#)

- [260] V. V. Kuzminov and N. J. Osetrova, Physics of Atomic Nuclei **63**, 1292 (2000), ISSN 1562-692X, <http://dx.doi.org/10.1134/1.855786>. 156
- [261] J. Montara, S. Freedman, B. Fujikawa, and others., Tech. Rep., Argonne Nat. Lab. NSD Report (1998). 156
- [262] H. Daniel, Nuclear Physics **31**, 293 (1962), ISSN 0029-5582, <http://www.sciencedirect.com/science/article/pii/0029558262907459>. 156
- [263] D. Flothmann, W. Wiesner, R. Löhken, and H. Rebel, Zeitschrift für Physik **225**, 164 (1969), ISSN 0044-3328, <http://dx.doi.org/10.1007/BF01392517>. 156
- [264] M. Baldoncini, I. Callegari, G. Fiorentini, F. Mantovani, B. Ricci, V. Strati, and G. Xhixha, Phys. Rev. D **91**, 065002 (2015), <http://link.aps.org/doi/10.1103/PhysRevD.91.065002>. 157
- [265] P. Huber, Phys. Rev. C **84**, 024617 (2011), <http://link.aps.org/doi/10.1103/PhysRevC.84.024617>. 157
- [266] W. Maneschg et al., Nuclear Instruments and Methods in Physics Research Section A: Accelerators, Spectrometers, Detectors and Associated Equipment **680**, 161 (2012), ISSN 0168-9002, <http://www.sciencedirect.com/science/article/pii/S0168900212003749>. 162
- [267] S. Davini, Ph.D. thesis, University of Genoa (2012). 169, 210, 211, 213, 218, 220, 226, 229, 230, 232, 233
- [268] B. Schling, *The Boost C++ Libraries* (XML Press, 2011), ISBN 0982219199, 9780982219195. 176
- [269] R. N. Saldanha, Ph.D. thesis, Princeton University (2012). 195, 226, 229, 230
- [270] G. Bellini et al., Journal of Instrumentation **6**, P05005 (2011), <http://stacks.iop.org/1748-0221/6/i=05/a=P05005>. 199
- [271] H. Shimazaki and S. Shinomoto, Neural Computation **19**, 1503 (2007), <http://dx.doi.org/10.1162/neco.2007.19.6.1503>. 202



# Acknowledgments

Here we are, to the (probably) most read part of the thesis. The last three years literally flew away, despite the hard work and the “frustration periods” which characterize inevitably the life of any PhD student. This proves I actually had a lot fun, and this is only thanks to the wonderful people I met and worked with in the Borexino Collaboration, at GSSI and at LNGS.

The first thanks goes to my Advisor, Marco. Everybody knows how I admire him both as a person and as a physicist. I am all the time amazed by the deepness of his understanding of physics, which he can convey in 5-minute chats, communicating deeper concepts than many other people could never let you understand. I have no doubts in saying that my model of “physicist” is you.

Gemma, you have been probably the key person which made a lot of the work in this thesis possible. It was, it is and I hope it will be a pleasure to keep working together. My “twin”, team mate and support (and now senior, good luck!) in these three years was for sure you, Alessio. I am very proud of the work we did and the achievements we accomplished. I have no doubts in saying that I could have not worked with anybody better than you, a great person and a great physicist. As you very well know, many results of this thesis were possible only thanks to your work and our Skype calls at 10.30pm!

It’s also impossible not to recognize the value of the always useful discussions and opinion exchanges with Aldo and Stefano D., as well as their help in my thesis work. All this happened in the amazing environment of LNGS, where many bx\_lngs people were precious to me and made the last three years unique and unforgettable. Marcin and Nicola, it was great to chat and spend time with you, I enjoyed every single moment. I don’t know if we’ll ever measure CNO, for sure the correct answer is anthropic principle. Ilia, you had the natural ability of driving me crazy, speaking of Borexino 24/24 and 7/7, even at 7am in the car going to LNGS or at 10pm, coming back from LNGS. But I have to say, I had a lot of fun. Lee, Matteo and Chiara...you’re probably the “most normal” people at LNGS, please never change! :-D

Then of course I have to thank all the Borexino Collaboration for giving me the opportunity to work in one of the best experiments ever built and that we’ll likely remain unique for many decades. In this context, all the bx\_nusol analysis working group was

always stimulating and a very nice environment to work in, so thank you, Barbara, Livia, Alessandra, Silvia, Davide D., Davide B., Emanuela, Oleg, Alina and Francesco.

I want to explicitly thank one of my thesis referees, Luciano Pandola. You gave me very nice suggestions and useful corrections. I hope to interact again with you in the future!

Moving to GSSI people, the first guy to thank is for sure you, Francesco, our coordinator, neutrino professor and most importantly good friend. You are one of the best people I have ever met (now I can say this, it's not a conflict of interest anymore). Dello (I'm sorry, I could not use Stefano D. since that is Davini!) I enjoyed a lot pretending to be a phenomenologist with you and Francesco and in general it was great to be able to make fun of you for your accent. Thank you! Then a special mention goes to all the other guys who made our stay in L'Aquila for 3 years enjoyable, so thank you Lu, Maria, Michele, Marta, Sarah, Axel, Fede, Valerio and Luigi.

Back to Genova (probably my second house right now, Savona being absolutely irreplaceable), in that bunker which is the DIFI there are the people who did not work with me directly, but whom I shared a lot of my time with, as if we still were students at the university. Fede, thank you and I don't even have to explain why. And thanks to all the other crazy inhabitants of the "piccionaia", Pisto, Coppe, Lollo, Rugge, Chiara, Alessio (the young one :-P), Luca, Ruben, Lea. It was also great to spend time in L202, of course the best lab of the entire DIFI, and this is thanks to the people working there and to their kindness, so thanks Roberto, Sandra, Giuliano, Daniel and Sergio (btw, thanks for the opportunity with the high school student stage: it was fantastic!).

Ma la verità è che ci sono 3 persone senza le quali nulla di ciò che ho fatto da quando sono nato sarebbe stato possibile. Parlo chiaramente della mia mamma, di mio papà e del mio fratellino Gianlu (ormai sciu megù, quindi dategli del lei). Non dovrebbe servire che lo ripeta, ma non avrei potuto chiedere di meglio. Siete fantastici. Non riesco anche a non pensare ai miei secondi genitori, Teddy e Mirko. A me sembra ieri, ma sono passati 20 anni da quando imparavamo  $(a+b)(a-b)$  sotto il castagno davanti a casa. All'epoca volevo probabilmente fare il medico...ma senza dubbio, tutto questo è anche grazie a voi. Un ultimo ringraziamento speciale va alla mia SW K., chè mi sopporti e mi vuoi bene per come sono.

It appears that now, at 27, I'm finally done with school. Years ago I was looking forward to this moment. Now I'm "older" and in addition to black and white only, I'm starting seeing also the grey shades of life and emotions. Something will change, I'll be an adult probably, also professionally, but I honestly hope not to grow too much.

Finally, many thanks to all the people who are mad for not being mentioned here.